2010

QCD
and
High Energy Interactions

Sponsored by

. CNRS (Centre National de la Recherche Scientifique)
. CEA (Commissariat à l'Énergie Atomique)
. IN2P3 (Institut National de Physique Nucléaire et de Physique des Particules)
. NSF (National Science Foundation)
. FNRS (Fond National de la Recherche Scientifique)
. BSP (Belgian Science Policy)

XLVth Rencontres de Moriond
La Thuile, Aosta Valley, Italy – March 13-20, 2010

2010 QCD and High Energy Interactions

Proceedings of the XLVth RENCONTRES DE MORIOND

QCD and High Energy Interactions

La Thuile, Aosta Valley Italy *March 13-20, 2010*

2010

QCD and High Energy Interactions

edited by

Etienne Augé,

Jacques Dumarchez,

Bolek Pietrzyk

and

Jean Trân Thanh Vân

The XLVth Rencontres de Moriond

2010 QCD and High Energy Interactions

was organized by :

Etienne Augé (IN2P3, Paris)
Jacques Dumarchez (LPNHE, Paris)

with the active collaboration of :

U. Bassler (CEA - IRFU/SPP - Saclay)
E. Berger (A.N.L. Argonne)
S. Bethke (M.P.I. Munich)
A. Capella (L.P.T. Orsay)
A. Czarnecki (U. Alberta)
D. Denegri (C.E.A. Saclay)
N. Glover (Durham)
B. Klima (Fermilab)
M. Krawczyk (University of Warsaw)
L. McLerran (Brookhaven Nat. Lab.)
B. Pietrzyk (L.A.P.P. Annecy)
Chung-I Tan (Brown University)
J. Trân Thanh Vân (L.P.T. Orsay)
U. Wiedemann (CERN)

2010 RENCONTRES DE MORIOND

The XLVth Rencontres de Moriond were held in La Thuile, Valle d'Aosta, Italy.

The first meeting took place at Moriond in the French Alps in 1966. There, experimental as well as theoretical physicists not only shared their scientific preoccupations, but also the household chores. The participants in the first meeting were mainly french physicists interested in electromagnetic interactions. In subsequent years, a session on high energy strong interactions was added.

The main purpose of these meetings is to discuss recent developments in contemporary physics and also to promote effective collaboration between experimentalists and theorists in the field of elementary particle physics. By bringing together a relatively small number of participants, the meeting helps develop better human relations as well as more thorough and detailed discussion of the contributions.

Our wish to develop and to experiment with new channels of communication and dialogue, which was the driving force behind the original Moriond meetings, led us to organize a parallel meeting of biologists on Cell Differentiation (1980) and to create the Moriond Astrophysics Meeting (1981). In the same spirit, we started a new series on Condensed Matter physics in January 1994. Meetings between biologists, astrophysicists, condensed matter physicists and high energy physicists are organized to study how the progress in one field can lead to new developments in the others. We trust that these conferences and lively discussions will lead to new analytical methods and new mathematical languages.

The XLVth Rencontres de Moriond in 2010 comprised three physics sessions:

- March 06 - 13: "Electroweak Interactions and Unified Theories"
- March 13 - 20: "QCD and High Energy Hadronic Interactions"
- March 13 - 20: "Cosmology"

We thank the organizers of the XLVth Rencontres de Moriond:

- A. Abada, J. Conrad, S. Davidson, P. Fayet, J.-M. Frère, P. Hernandez, L. Iconomidou-Fayard, P. Janot, M. Knecht, J. P. Lees, S. Loucatos, F. Montanet, L. Okun, A. Pich, S. Pokorski, D. Wood for the "Electroweak Interactions and Unified Theories" session.

- E. Augé, U. Bassler, E. Berger, S. Bethke, A. Capella, A. Czarnecki, D. Denegri, N. Glover, B. Klima, M. Krawczyk, L. McLerran, B. Pietrzyk, Chung-I Tan, J. Trân Thanh Vân, U. Wiedemann for the "QCD and High Energy Hadronic Interactions" session.

- R. Ansari, M. Arnaud, P. Astier, Ch. Charmousis, F. Combes, J. Dumarchez, K. Ganga, Y. Giraud-Héraud, C. Magneville, S. Maurogordato, H. McCracken for the "Cosmology" session.

and the conference secretariat and technical staff:

V. de Sa-Varanda and C. Bareille, I. Cossin, G. Dreneau, D. Fligiel, N. Ribet, V. Zorica.

We are also grateful to Andrea Righetto, Gioacchino Romani, Erik Agostini and the Planibel Hotel staff who contributed through their hospitality and cooperation to the well-being of the participants, enabling them to work in a relaxed atmosphere.

The Rencontres were sponsored by the Centre National de la Recherche Scientifique, the Institut National de Physique Nucléaire et de Physique des Particules (IN2P3-CNRS), the Commissariat à l'Energie Atomique (DSM and IRFU), the Fonds de la Recherche Scientifique (FRS-FNRS), the Belgium Science Policy and the National Science Foundation. We would like to express our thanks for their encouraging support.

It is our sincere hope that a fruitful exchange and an efficient collaboration between the physicists and the astrophysicists will arise from these Rencontres as from previous ones.

E. Augé, J. Dumarchez and J. Trân Thanh Vân

Contents

4. Higgs

5. Top

6. New Phenomena

7. Light mesons

8. Structure function, Spin, Diffraction, Forward physics

9. Heavy Ion

10. Summary

1.
LHC start-up

LHCb COMMISSIONING

CATERINA DEPLANO
on behalf of the LHCb Collaboration
INFN Cagliari, Italy

LHCb is a dedicated detector for b and c physics at the LHC. The construction and the installation of the LHCb detector have been completed. This presentation reviews the status of the commissioning and the various steps taken so far are described. The results of the first beam-beam interactions recorded in the Winter 2009 are briefly presented.

1 Introduction

The LHCb experiment [1] is a forward spectrometer dedicated to the study of heavy flavour physics at the Large Hadron Collider. Its primary goal is to look for indirect evidence of new physics in CP violation and rare decays of beauty and charm hadrons. During the 2009 data taking, at $s^{1/2} = 900$ GeV, about 7 μb^{-1} integrated luminosity has been collected while the expected integrated luminosity for the next 2010-11 long run is about 1 fb^{-1} at $s^{1/2} = 7$ TeV. In nominal conditions, at an energy in the center of mass of 14 TeV, the expected integrated luminosity in one year of data taking is 2 $fb^{-1}/10^7 s$, which corresponds to 10^{12} $b\bar{b}$ pairs. The LHCb experiment will exploit the high $b\bar{b}$ cross-section of 500 μb, about 0.6 % of the total. Therefore there will be a large amount of B and D mesons to be studied, but with a high background rate. For this reasons the detector is required to have a highly selective trigger, a good vertex reconstruction and a good particle identification.

2 The LHCb Detector

The schematic view of the LHCb detector is shown in Fig. 1. Since $b\bar{b}$ pairs are mostly produced in the forward or backward direction, the LHCb detector was designed as a forward spectrometer, covering a pseudo-rapidity range of $1.9 < \eta < 4.9$. The LHCb experiment is made of several detector subsystems. The two beams, called Beam1 and Beam2, cross inside the vertex locator system, called VELO, which is a silicon detector. The Beam1 comes in the forward direction of the LHCb spectrometer, from the VELO through all the detector, while the Beam2 comes from backward. To achieve an excellent K π separation in the momentum range from 2 to 100 GeV/c, there are two Ring Imaging Cherenkov counters (RICH1 and RICH2), which use Aerogel, C_4F_{10} and CF_4 as radiators. The RICH1 is just after the VELO, while the RICH2 is before the calorimeters system. Between the two RICHes the tracking system is located. It is made up of a Trigger Tracker (a silicon microstrips detector, called TT) in front of the magnet, and three tracking stations behind it, made of silicon microstrips for the Inner Tracker parts (IT) and of Kapton/Al straws for the Outer Tracker parts (OT). The spectrometer magnet is a warm dipole, providing an integrated field of 4 Tm. The calorimeter system is composed of a

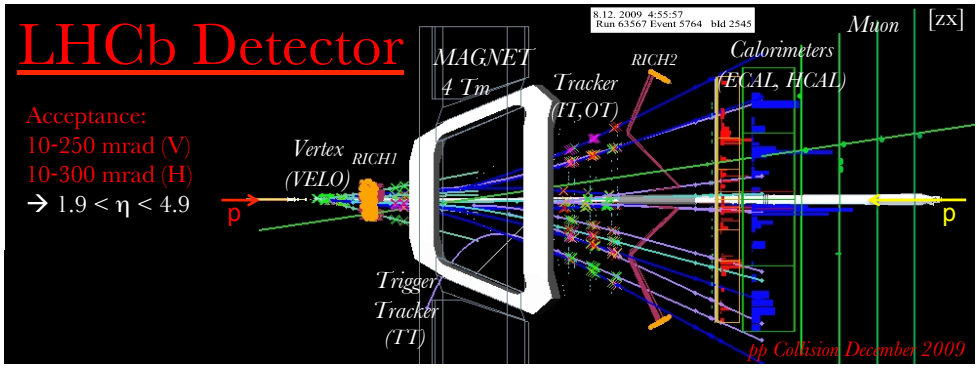

Figure 1: Schematic view of the LHCb detector, from the event display.

Scintillator Pad Detector and Preshower (SPD/PS), an electromagnetic calorimeter (ECAL) and a hadronic calorimeter (HCAL). Finally, the muon detection system providing μ identification and contributing to the Level-0 trigger of the experiment, is composed by five stations of MWPCs except in the highest rate region, where triple-GEM detectors are used. The trigger architecture is conceived in two levels. An hardware level, or Level0 (L0), reduces the effective input rate of 12 MHz to 1 MHz. It takes information from the VELO, Calorimeters and Muon systems at 40 MHz rate and it is based on the identification of muon, electromagnetic and hadron high p_T candidates while rejecting multiple interactions. The software level, called High Level Trigger (HLT), is organized in two stages, the first one (HLT1) checks the L0 candidate using information coming from the tracking sub-detectors and adds impact parameters and lifetime cuts. The second one (HLT2) is able to perform global event reconstructions and decay channel selections. The output of the HLT corresponds to a rate of 2 kHz and an event size of about 40 kB.

3 Commissioning without beam

The LHCb commissioning started in 2007. The main purposes were initially to test and calibrate each detector subsystem individually and finally run the LHCb detector as a whole. It is possible to divide the detector commissioning into two phases: the first without beam while the second with circulating beams and the first pp collisions. In the first phase, the hardware operations controls and monitoring have been tested for each sub-detector individually. Calibration pulses (using LED, radioactive source or test pulse) have been used to test the response of the hardware, allowing to check cables connectivity, channels mapping and to spot any dead or noisy electronic channel. An internal time alignment of about 1 ns between the electromagnetic and the hadronic calorimeter was reached while each muon station has been internally aligned at about 3 ns. From the data produced by each sub-detector, the initial settings of time and spatial alignment had been set to reasonable values for each subsystem individually while no relative time alignment was set among different sub-detectors.

3.1 Commissioning with cosmic rays

Even if the cosmics rate related to the LHCb geometrical acceptance in a 100 m underground cavern is less than 1 Hz/m^2, about 4 M events have been collected starting from the Spring of 2008. The cosmics are well visible only in the external regions of the large area sub-detectors: the Muon, the Calorimeters and the Outer Tracker and were very useful to test the operation of the trigger logic. In order to acquire cosmics events, a dedicated selection has been used for the L0 trigger: thresholds on p_T and E_T have been lowered in order to be sensitive to minimum

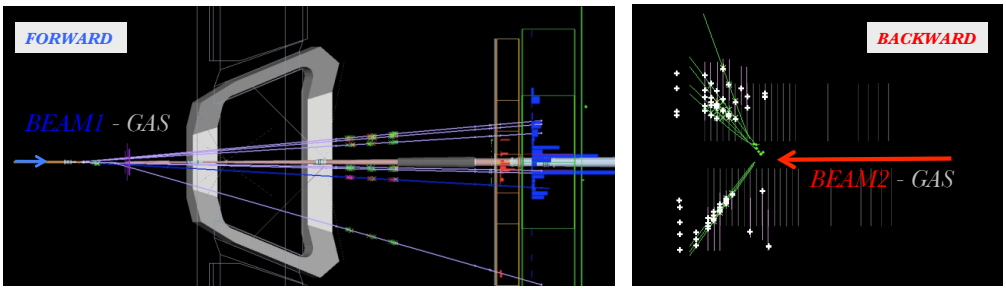

Figure 2: Beam-Gas interaction. Left: Beam1-gas; right: Beam2-gas.

ionizing particles (10 Hz rate); the coincidence of the two last muon stations (4 Hz rate) or the central muon station alone (60 Hz rate) has been required; tracks have not been constrained to point to any vertex. Moreover instead of acquiring a single bunch crossing (25 ns) per event, a time windows of several bunch crossing centered on the triggered one was opened, to allow the start of the time alignment among different sub-detectors. Calorimeters and Muon detectors were aligned at 3 ns for forward cosmics tracks. An improvement of the Muon detector internal time alignment was possible using cosmics data: the r.m.s. time distribution from 9 ns (first cosmics 2008) to about 4 ns (last measurements 2010).

4 Commissioning with beam

On September 2008 the beams started to circulate in the LHC. We could profit of the LHC injection tests to continue the time alignment between sub-detectors and to start the spatial alignment. The beam-gas interactions and the first beam collisions in the Winter of 2009 allowed to tune the LHCb detector calibration and to see the commissioning results.

4.1 LHC injection test

Several injection tests have been performed by the LHC group. In the first-one the beam was injected from the SPS into the LHC to test the new injection lines. The Beam2 was dumped on the injection line beam stopper (TED) about 350 m downstream of the LHCb experiment: the particles come from behind the detector and the fluence was about 10 particles/cm^2 in the center of the shower. In a second step, the beam was stopped 50 m from the LHCb detector in a collimator/beam stopper (TDI) just after the kicker injection magnet: in this case the fluence was 100 times higher. Finally, the beam was injected and passed through the LHCb experiment. Beam induced data have been used to perform a more precise time and spatial alignment, especially for those detectors which could not make use of cosmic events. In particular was possible the check of the space alignment of the VELO in itself and the relative alignment between the VELO and the TT, which is within the specifications: the track residuals correspond to about 500 μm with offset between 150 and 300 μm, while the expected uncertainty in VELO-TT extrapolation is about 300 μm.

4.2 Beam-gas interaction

The circulating beams interact with the residual gas inside the beam pipe. On November 2009 about 80 k interactions between the beams and the residual gas have been collected and then reconstructed by the VELO. In Fig. 2 two events of beam-gas interaction are reported. On the left there is one interaction related to the Beam1, where the event is triggered by the Calorimeters. While on the right an event related to the Beam2 and triggered by the VELO

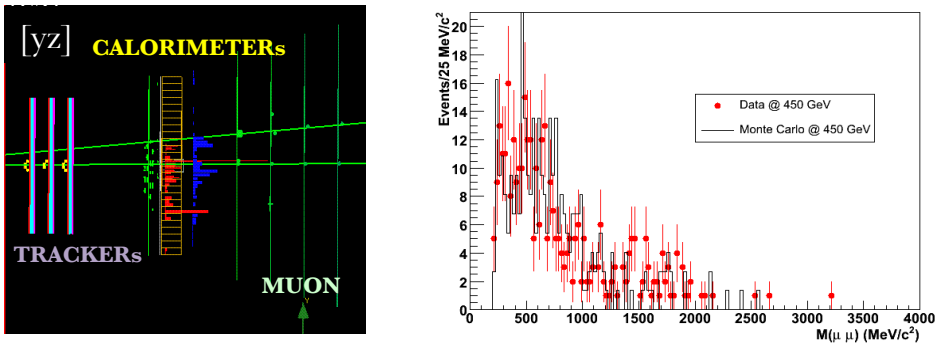

Figure 3: Dimuons from 2009 runs. Left: one dimuon event; right: the dimuon invariant mass distribution.

backward silicon stations is shown. The VELO is made with retractable detector halves which must be open (30 mm per side) during injection, to avoid detector damage, and can be closed in stable beam condition ($E_{beam} > 2$ TeV). During the 2009 runs ($E_{beam} = 450$ GeV) the VELO was open at 15 mm per side and a crossing angle of 2 mrad between Beam1 and Beam2 on the [xz] bending plane have been reconstructed as expected with the full magnetic field, of the LHCb dipole magnet, at $E_{beam} = 450$ GeV.

5 First Result from 2009 beam-beam collisions and Conclusions

In the 2009 runs about 7 μb^{-1} of integrated luminosity [2] of minimum bias triggers were recorded with all the sub-detectors operational, which correspond to about 260 k pp collisions, beam-gas subtracted, at $E_{beam} = 450$ GeV. Several particles have been reconstructed, whose mass is agreement with the PDG value, such as:

- π^0, routinely monitored on-line, $< m >= (133 \pm 3) MeV/c^2$, $\sigma = (11 \pm 4) MeV/c^2$.
- Λ, reconstructed only with the tracking detectors:
  $< m >= (1115.6 \pm 0.2) MeV/c^2$, $\sigma = (3.1 \pm 0.2) MeV/c^2$. Using the full tracking power, including VELO (still open at 15 mm per side) was measured a $\sigma = (1.4 \pm 0.1) MeV/c^2$. More details on V0 production can be found in [3].
- Φ, reconstructed using the RICH particle identification,
  $< m >= (1019.61 \pm 0.22) MeV/c^2$, $\sigma_{Gauss} = (1.75 \pm 0.32) MeV/c^2$.

The muon detector time resolution is in perfect agreement with expectation ($\sigma = 3.6$ ns) and the invariant mass distribution of the dimuons events is reported in Fig. 3.

In conclusion the LHCb detector is in good shape! Cosmics data and the initial LHC accelerator operation have been very useful for the commissioning of the LHCb detector. Beam-induced events and the first collisions were used to conclude the commissioning while high statistics will be used to fine tune the calibrations.

References

1. The LHCb Collaboration, The LHCb Detector at the LHC, Journal of Instrumentation vol. 3 2008.
2. see the presentation of Vladik Balagura, Luminosity measurement at LHCb.
3. see the presentation of Mathias Knecht, Prompt V0-production in inelastic pp-collisions at LHCb.

Luminosity measurement in the first LHCb data

V.Balagura on behalf of LHCb collaboration
CERN, CH-1211 Geneva 23, Switzerland

Using a novel method of beam profile reconstruction with beam-gas interactions a preliminary measurement of the luminosity in the LHCb detector is presented for the LHC pilot run of December 2009. The integrated luminosity for the runs considered is found to be $6.8\pm1.0\ \mu\text{b}^{-1}$.

1 Introduction to beam-gas method

In December 2009 LHC delivered first collisions for its four experiments. In the first physics runs LHC worked without acceleration, so that protons injected from SPS accelerator were collided in December at the SPS energy of 450 GeV per beam. In 2010 – 2011 the LHC collision energy will be 3.5+3.5 TeV, and after the 2012 upgrade it will be raised close to 7+7 TeV. Even though the energy and the statistics accumulated in December commissioning run was small, it was still possible for LHCb to perform its first physics measurement on the topic of K^0_S production in the forward region [1]. This paper describes the LHCb luminosity measurement needed to calculate the K^0_S cross section.

In general, there are several ways to measure luminosity in accelerators. When LHCb acquires large data samples it will be possible to determine the luminosity through normalising to physics processes with well known cross-sections, such as $pp \to ZX \to \mu^+\mu^- X$ and $pp \to pp\gamma\gamma$. In 2009 we instead relied on a direct method. In this approach the luminosity was obtained through measurements of the beam profiles made by LHCb in beam-gas and beam-beam collisions, and knowledge of the LHC beam intensities. Consider the formula for the instantaneous luminosity [2]

$$L = f N_1 N_2 K \cdot \int \rho_1(\vec{r},\, t)\rho_2(\vec{r},\, t)\, d^3\vec{r}\, dt. \tag{1}$$

Here $K = \sqrt{(\vec{v}_1 - \vec{v}_2)^2 - \frac{(\vec{v}_1 \times \vec{v}_2)^2}{c^2}}$ is the kinematic relativistic factor, $N_{1,2}$ are the number of particles in the colliding bunches all moving with the velocities $\vec{v}_{1,2}$ ($|\vec{v}_1 \approx |\vec{v}_2| \approx c$), $\rho_{1,2}(\vec{r},t)$ are the normalized particle densities so that $\int \rho_{1,2}(\vec{r},t)\, d^3\vec{r} = 1$ at any time t, and $f = f_r \cdot n_{bb}$ is the frequency of collisions precisely known from the LHC revolution frequency $f_r = 11.246$ kHz and the number of colliding bunches in the ring n_{bb} (in December 2009 it was either 2 or 8). The bunches were analysed individually. Their intensities $N_{1,2}$ were measured in LHC by the so called Fast BCT (Beam-to-Current Transformers) and DC (Direct Current) BCT systems. The latter had better accuracy but measured only the total current in the ring. The fraction of intensity in the individual bunch was taken from Fast BCT measurements available per-bunch. The LHC design precision of N_1N_2 product measurement is 2%, but during commissioning in December it was 12% which led to this uncertainty becoming a dominating error.

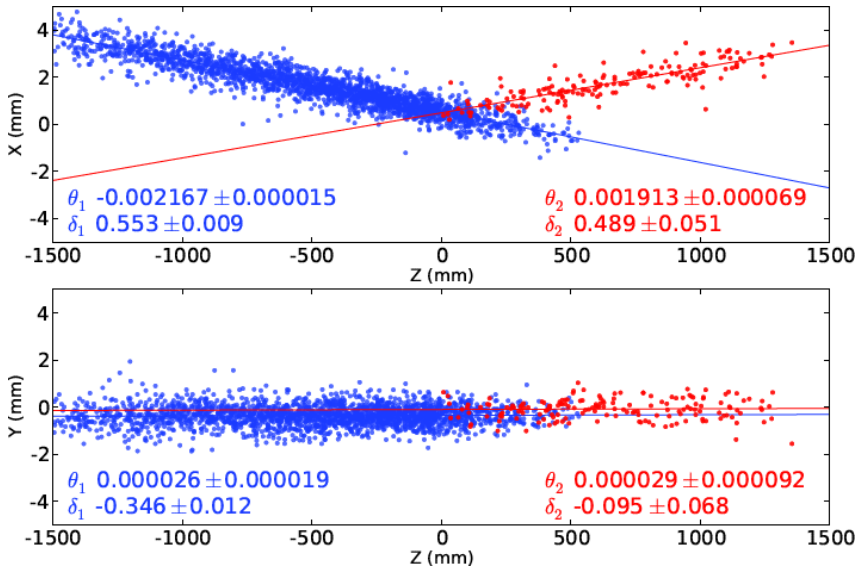

Figure 1: Images of the first (left) and the second (right) LHC beams reconstructed in the beam-gas interactions in the horizontal x-z (top) and vertical y-z (bottom) planes. Statistics for the second beam is lower due to smaller trigger efficiency. The crossing angle in the x-z plane is due to the LHCb dipole magnet.

Due to the bending field of the LHCb dipole the proton beams collide with a finite crossing angle of 2α. At beam energies of 450 GeV $\alpha = 2.1$ mrad. This crossing angle is evident from the top plot of Fig. 1 which shows the reconstructed vertices of beam-gas interactions in the bending plane x-z. The lower plot is the corresponding picture in the non-bending plane y-z. Here the z-axis is chosen to be along the direction $\Delta\vec{v} = \vec{v}_1 - \vec{v}_2$. With the conventions $\vec{v}_0 = (\vec{v}_1 + \vec{v}_2)/2$, $\vec{v}_{1,2} = \vec{v}_0 \pm \Delta\vec{v}/2$, we may integrate Eq. 1 over z and t:

$$\begin{aligned}
\frac{L}{fN_1N_2} &= K \int \rho_1(\vec{r} - \vec{v}_1 t,\, 0)\, \rho_2(\vec{r} - \vec{v}_2 t,\, 0)\, d^3(\vec{r} - \vec{v}_0 t)\, dt = \\
&= \frac{K}{|\Delta\vec{v}|} \int \rho_1(x, y,\, z - \tfrac{|\Delta\vec{v}|}{2} t,\, 0)\, \rho_2(x, y,\, z + \tfrac{|\Delta\vec{v}|}{2} t,\, 0)\, d(z - \tfrac{|\Delta\vec{v}|}{2} t)\, d(z + \tfrac{|\Delta\vec{v}|}{2} t)\, dx\, dy \approx \\
&\approx \int \rho_1^{\perp}(x, y)\, \rho_2^{\perp}(x, y)\, dx\, dy, \qquad (2)
\end{aligned}$$

where $\rho_{1,2}^{\perp}(x, y) = \int \rho_{1,2}(x, y, z, 0)\, dz$ are the projections of the densities onto x-y plane. They are determined by measuring the beam profiles visible in the beam-gas interactions assuming that the small amount of gas remaining in the beam pipe is distributed uniformly in the transverse x-y plane. This is a novel method suggested in [3] and relying on the unique LHCb vertex resolution. It is used here to measure the luminosity for the first time. For simplicity, the beam shape was approximated in the following as a Gaussian.

2 LHCb run in December 2009

LHCb is a forward single-arm spectrometer. A full description may be found in [4]. The most important subdetector for the present analysis is the precision Vertex Locator (VELO).

Since the event rate in December was low ($\lesssim$ 20 Hz) it was possible to record almost all interactions with a very loose minimum bias trigger. The event was selected if it had either $\geq$ 240 MeV energy deposition in the hadron calorimeter and $\geq$ 3 fired pads in the Scintillator Pad Detector in front of the calorimeters, or $\geq$ 8 hits in the upstream VELO layer. The first (second) requirement also effectively selected the beam-gas interactions for the first (second) beam going in (opposite to) the direction of LHCb detector. The trigger efficiency for the second beam was lower, the corresponding statistics of reconstructed vertexes is shown in Fig. 1 on the right.

The VELO detector contains 21 layers of silicon wafer pairs with r and ϕ readout. Every layer has left and right parts. Due to safety reasons they are kept in retracted positions far from the beams until the LHC conditions become stable and the physics run starts. The LHC beams get narrower with the energy. At 450 GeV in December they were broad. Because of this and the relatively large crossing angle it was not possible for reasons of detector and machine safety to close fully the VELO halves. Therefore during data taking they were positioned 15 mm away from the nominal x positions. The VELO vertex resolution was determined from data in the following way. N vertex tracks were randomly split into two equal halves to form two independent vertexes. Their separation divided by $\sqrt{2}$ gave a resolution estimate for a vertex with $N/2$ tracks. The resolution was parametrized as a double Gaussian with sigmas linearly dependent on z position for the beam-gas interactions, and approximately as $1/\sqrt{N}$ on the number of tracks. The resolution for the beam-beam interactions with larger opening angles between the tracks was slightly better than for the beam-gas vertexes. The parametrization was used in the following to deconvolve the resolution from the reconstructed beam profiles.

In addition to the bunches colliding at LHCb, the accelerator contained also the bunches for three other experiments. In LHCb these bunches did not collide and produced only beam-gas interactions, like those shown in Fig. 1. Only the bunches which collided in LHCb are relevant for the luminosity measurement. These bunches produced both beam-beam and beam-gas interactions. They could be distinguished using the vertex z position. The luminous region around a nominal interaction point $z = 0$ was dominated by the beam-beam interactions ($\approx$99%), while the region $|z| > 150$ mm contained a pure sample of the beam-gas vertexes. Projections of the latter to the beam transverse planes deconvolved with the VELO resolution gave the beam profiles. It was checked that the position $\mu^{\text{Lum.}}$ and the width $\sigma^{\text{Lum.}}$ of the luminous region were compatible with the predictions obtained from the beam profiles. In the simple case of Gaussian beams without crossing angle, $\mu^{\text{Lum.}}$ and $\sigma^{\text{Lum.}}$ are related to the corresponding parameters of the individual beams via the following formulas

$$\sigma^{\text{Lum.}} = \sqrt{\frac{\sigma_1\sigma_2}{\sigma_1^2+\sigma_2^2}}, \quad \mu^{\text{Lum.}} = \frac{\mu_1/\sigma_1^2+\mu_2/\sigma_2^2}{1/\sigma_1^2+1/\sigma_2^2}. \tag{3}$$

This constraint corrected numerically for the small crossing angle in the x-z plane was then used in the overall fit of beam-beam and two beam-gas profiles. It considerably improved precision due to the large statistics of the beam-beam events. One example of the fit in the vertical projection for one of the colliding bunch pairs is presented in Fig. 2, with the contribution from VELO resolution superimposed.

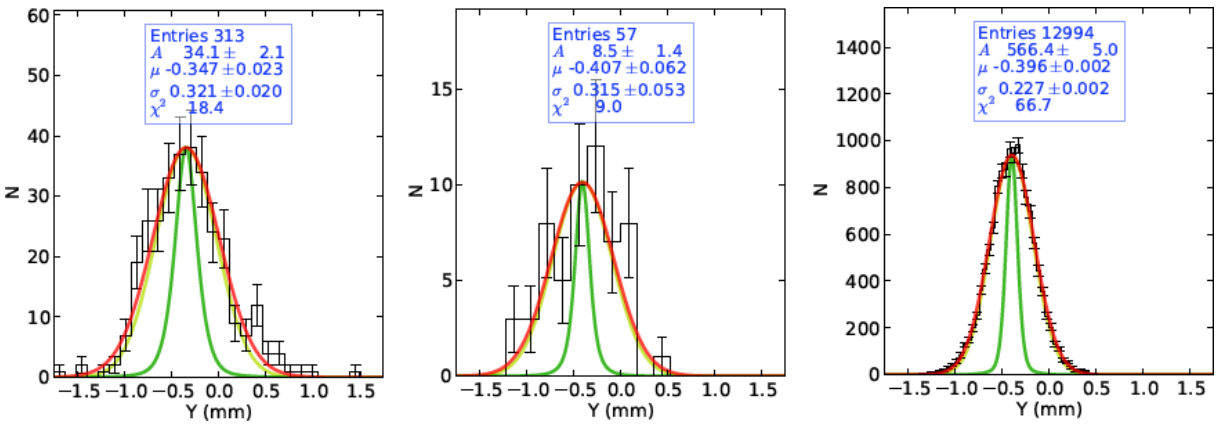

Figure 2: From left to right: LHCb preliminary profiles of the beam-gas interactions for the first and the second beam and of the luminous region in the vertical direction, for a single colliding bunch pair, fit to the Gaussian convoluted with the vertex resolution. The latter is superimposed separately in the center for comparison.

The fit gave Gaussian beam widths transverse to *the beams*. In Eq. 2, however, for the overlap integral we need projections transverse to z *axis*. Due to the crossing angle between z and the beams in x-z plane, the particle spread along the beams produced an extra spread in the x projection. Therefore we added $\sigma_z \sin\alpha$ in quadrature to the widths measured in x, where the Gaussian width along the beams σ_z was estimated from the z width of the luminous region, $\sigma_z = \sqrt{2}\sigma_z^{\rm Lum.}$, assuming that σ_z for both beams was the same. This correction reduced the resulting luminosity by a factor of 0.92.

Using the reconstructed profiles $\rho^{\perp}_{1,2}(x,y)$ and Eq. 2, the luminosity was measured in four different periods with various running conditions. The ratio between obtained results was consistent with the ratio of the number of reconstructed beam-beam vertexes in the same samples. We selected the best running period containing 25% of all available statistics, with two colliding bunches and a good alignment of the two beams to minimize the influence of the beam position uncertainty on the overlap integral. The luminosity measured in this period was extrapolated to the entire sample using the number of reconstructed beam-beam vertexes, yielding the preliminary result $L_{\rm int} = 6.8 \pm 1.0\ \mu{\rm b}^{-1}$. The systematic uncertainty received contributions from the measurements of the beam intensities (12%), widths (5%), relative positions (3%) and the crossing angle correction (1%).

3 Conclusions

The integrated luminosity collected in LHCb during the first physics run in December 2009 is measured to be $6.8 \pm 1.0\ \mu{\rm b}^{-1}$. This result is preliminary. It is determined from the beam profiles reconstructed in the beam-gas interactions. This novel method relies on the precision LHCb vertex reconstruction and is applied for the first time. The systematic error of the measurement (14%) is dominated by the beam intensity uncertainty. In 2010 it should be considerably improved allowing to achieve precision in future luminosity measurements at the level of $\sim 5\%$.

References

1. "Prompt K^0_S production in pp collisions at $\sqrt{s} = 900$ GeV", LHCb collaboration, contribution to this conference.
2. C. Møller, K. Danske Vidensk. Selsk. Mat.-Fys. Medd. **23**, 1 (1945);
   for later papers see e.g. O. Napoly, Part. Acc. **40**, 181 (1993); W. Herr, B. Muratory, "Concept of Luminosity", Proceedings of CERN Accelerator School, 361 (2003).
3. M. Ferro-Luzzi, *Nucl. Instrum. Methods* A **553**, 388 (2005).
4. A. A. Alves *et al.*, *JINST* **3**, S08005 (2008).

Tracking Performance at CMS

D. Giordano,
on behalf of the CMS Collaboration
CERN, European Organization for Nuclear Research,
Geneva, Switzerland

The first LHC collisions at center of mass energies of 900 GeV and 2360 GeV were recorded by the CMS detector in December 2009. The trajectories of charged particles produced in the collisions were reconstructed using the all-silicon CMS Tracker and their momenta were measured in the 3.8 T solenoidal magnetic field. In this paper the results from track reconstruction are presented to demonstrate the overall performance of the CMS Tracker.

1 Introduction

CMS [1] is one of the four detectors at the Large Hadron Collider (LHC) of CERN. It has been designed primarily to perform new physics studies at the highest energies achievable with the LHC. The main components of CMS are a muon detection system, electromagnetic and hadronic calorimeters, and an inner tracking system (Tracker). The Tracker provides robust, efficient, and precise reconstruction of the charged particle trajectories inside a 3.8 T axial magnetic field. The design transverse momentum resolution is typically 0.7 (5)% at 1 (1000) GeV/c in the central region and the impact parameter resolution for high momentum tracks approaches 10 μm.

The CMS Tracker [1], consists of two main detectors: a Silicon Pixel Detector, located close to the interaction region, and a Silicon Strip Detector, covering the region from $\approx$ 25 cm to $\approx$110 cm in radius, and $\approx$ 270 cm on either side of the collision point along the LHC beam axis. The pixel detector has 66 million active elements instrumenting a surface area of about 1 m^2. It is designed to provide three high precision three-dimensional determinations of particle trajectory points. The strip detector has 9.3 million active elements instrumenting a surface area of 198 m^2. It is designed to provide 9-13 high precision determinations of particle trajectory points in the region of pseudorapidity $|\eta| < 2.4$; about half of the coordinates originate from a sensor pair where one of the two sensors is tilted by 0.1 radians, hence providing also a measurement of the z coordinate.

The results presented in this paper were obtained using data samples collected by the CMS experiment during LHC operation in December 2009 at proton-proton center-of-mass energies of 900 GeV and 2360 GeV. Due to the relatively low LHC luminosity, the event selection was mainly based on a minimum bias trigger system consisting of beam scintillator counters [2]. The total number of selected minimum bias events is about 305 000, corresponding to an integrated luminosity of approximately 10 μb^{-1} at 900 GeV and 0.4 μb^{-1} at 2360 GeV.

Prior to the LHC *pp* collisions, the CMS detector was commissioned using about 10 million cosmic muon events, collected under detector and magnetic field conditions similar to the conditions during *pp* collisions [3]. The analysis of cosmic muon data provided good initial operating

points for the pixel detector, the strip detector and the tracker alignment. For instance, the precision achieved for the Tracker alignment parameters (∼3-4 μm in the pixel barrel local x and y coordinates) is already adequate for the precise determination of impact parameters and the reconstruction of secondary vertices.

2 Track Reconstruction

The track reconstruction algorithms rely on a good estimate of the proton-proton interaction region, referred to as the beamspot. The beamspot is used as a precise estimate of the primary interaction point (in the transverse direction) prior to primary vertex reconstruction. After the beamspot is known, an initial round of tracking and vertexing is done using only pixel hits. The pixel vertices found at this stage are used in the standard tracking.

The standard track reconstruction at CMS is performed by the combinatorial track finder (CTF) [4]. Tracks are seeded from either triplets of hits in the tracker or pairs of hits with an additional constraint from the beamspot or a pixel vertex, yielding an initial estimate of the trajectory, including its uncertainty. The seed is then propagated outward in a search for compatible hits. As hits are found, they are added to the trajectory and the track parameters and uncertainties are updated. This search continues until either the boundary of the tracker is reached or no more compatible hits can be found. An additional search for hits is performed starting from the outermost hits and propogating inward. In the final step, the collection of hits is fit to obtain the best estimate of the track parameters, and tracks are filtered to remove those that are likely fakes.

The current implementation of the CTF performs multiple iterations. Between each iteration, hits that can be unambiguously assigned to tracks in the previous iteration are removed from the collection of tracker hits to create a smaller collection that can be used in the subsequent iteration. The first iterations look for prompt tracks, progressively of lower momentum. The following iterations are intended to find displaced tracks or tracks lacking pixel hits.

Finally, starting from the track collection, the primary interaction vertices in the event are reconstructed using an adaptive vertex fit.

3 Tracking Performance

Before using the tracks in further reconstruction of resonances or other objects, a comparison of basic distributions (number of hits per track, transverse momentum, angular parameters impact parameters, normalized χ^2) between the data and simulation was performed, revealing a general agreement in the shape of all variables.

After that, a careful study of the primary vertex and the beamspot reconstruction was performed. The beamspot measurement was performed during each LHC fill, confirming the stability of the luminous region along these first runs: variations in the position of the beamspot were at the level of ∼0.5 mm in x and y and ∼2 cm in z.

The resolution of the primary vertex was evaluated as a function of the two quantities that most affect this measurement: the multiplicity of tracks used in fitting the vertex and the p_t of those tracks. Figure 1 shows the x and z resolutions for different average p_t ranges. While the resolution differs considerably depending on p_t and multiplicity, the simulation accurately reproduces the data results.

More details about the tracking performance during the 2009 data-taking can be found at [5].

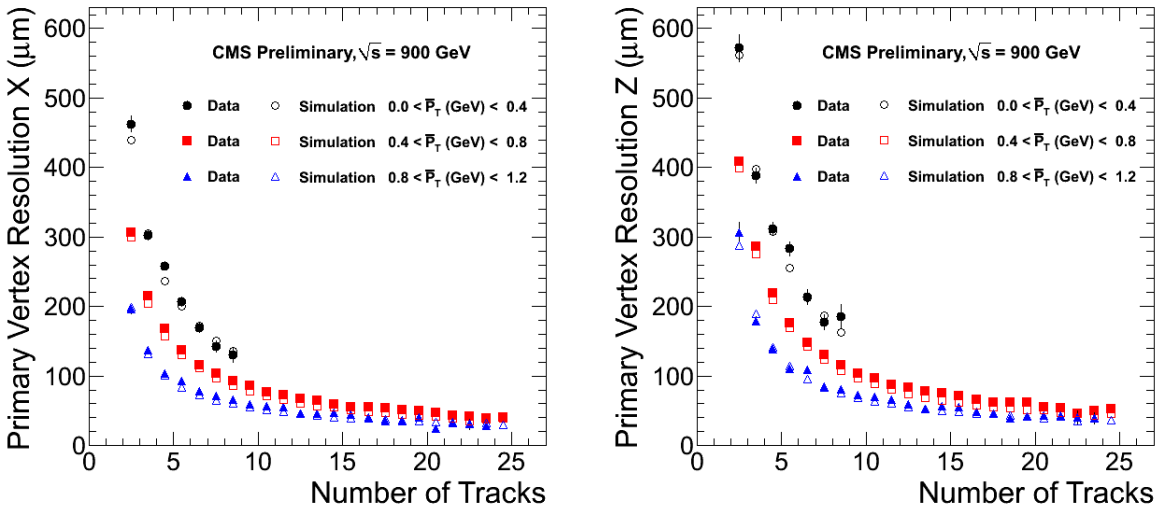

(a) (b)

Figure 1: Primary vertex resolution in x (a) and z (b) versus number of tracks. The three sets of results in each plot show different average p_t ranges and within each p_t range, data and simulation are compared.

3.1 Reconstruction of Resonances

The collection of tracks was then used to reconstruct the decays of K^0_S, Λ^0, $\Xi^{\pm}$, and $K^{\star}(892)$. The measurement of the masses and lifetimes of these well-known particles provides an initial validation of the reconstruction (for both prompt and displaced tracks), vertexing, and the magnetic field.

The K^0_S and Λ^0 candidates were reconstructed by their decay to $\pi^+\pi^-$ and $p\pi^-$ (+ charge conjugate), respectively. The K^0_S candidates were then combined with charged tracks from the primary vertex to search for the strong decay $K^*(892)^- \to K^0_S\pi^-$. The Ξ^- was reconstructed through its decay to $\Lambda^0\pi^-$. As the Ξ^- is a long-lived baryon, the π^- from the Ξ^- decay is detached from the primary vertex rather than originating from the primary vertex.

The mass distributions, along with the overlaid fits, are shown in Fig. 2. The mass values obtained fitting the data distributions are in good agreement with the world average values (PDG [6]), as shown in Table 1.

Table 1: Summary of PDG and data masses. Uncertainties for data results are statistical only.

	Mass (MeV/c^2)	
particle	Data	PDG
K^0_S	497.68 ± 0.06	497.61 ± 0.02
Λ^0	1115.97 ± 0.06	1115.683 ± 0.006
$K^*(892)^{\pm}$	888.3 ± 3.2	$891.66 \pm .26$
Ξ^-	1322.8 ± 0.8	1321.71 ± 0.07

For the K^0_S and Λ^0, the lifetime was also measured. The yield of the reconstructed candidates under the mass peak was correlated with the proper decay length ($ct = mL/p$) of the candidates. Appropriate correction factors, evaluated on simulated data, were applied to the measured yield, in order to take into account the efficiency variation versus lifetime. The goodness of the exponential fit of the calibrated yield versus ct indicates the accuracy of the estimated correction factors. The results, $\tau_{K^0_S} = 90.0 \pm 2.1$ ps and $\tau_{\Lambda^0} = 271 \pm 20$ ps, are both within 1 σ of the world average [6].

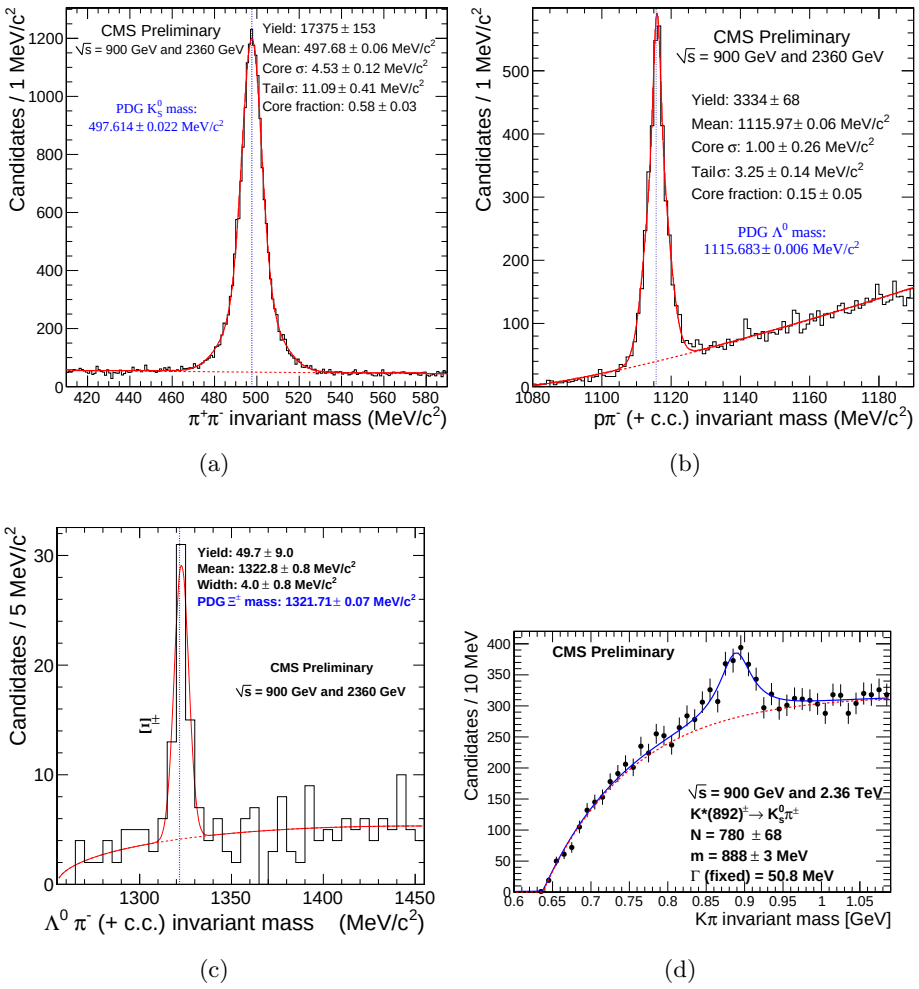

Figure 2: Invariant mass, with fit, of the $\pi^+\pi^-$ pairs - for the K^0_S - (a), of the $p\pi^-$ (+ charge conjugate) pairs - for the Λ^0 - (b), of the $\Lambda^0\pi^-$ (+ charge conjugate) pairs - for the $\Xi^\pm$ - (c), and of the $K^0_S\pi^-$ (+ c.c.) pairs - for the $K^*(892)^\pm$. Uncertainties shown are statistical only.

3.2 Particle identification with dE/dx

Although the primary function of the strip tracker is to provide hit position information for track reconstruction, the charge collected in a hit cluster provides a measure of the energy loss (dE/dx) of a particle while traversing the silicon sensor. A dE/dx estimator based on the measurements in the strip tracker modules traversed by a particle, is used in combination with the measured momentum p of the track to identify the mass (particle type) of the traversing particle.

Figure 3(a) shows the relationship between the dE/dx estimator and momentum in the 900 GeV data. In the figure, clear bands can be seen for kaons and protons and to a much lesser extent for deuterons. Figure 3(b) shows the mass distribution of tracks as determined by the same dE/dx methods. Clear kaon and proton peaks can be observed, as well as good agreement for the peaks with a Monte Carlo simulation. The particle identification technique was validated for protons and kaons using data driven methods based on reconstructed samples of $\Lambda^0 \to p\pi^-$ and $\phi(1020) \to K^+K^-$ decays. These decays provide clean samples of protons and kaons, subsequently identified by the dE/dx tool. This technique can be used to aid in the detection of very massive charged states, such as heavy stable charged particles [7].

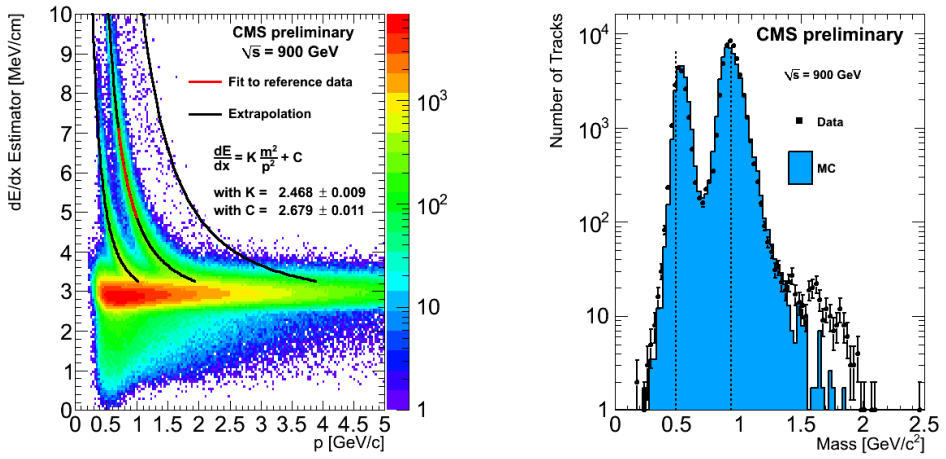

(a) (b)

Figure 3: dE/dx estimator versus particle momentum (a). Frequency of tracks as a function of mass as determined by the measured energy loss (b). The generator used for the simulation, PYTHIA, does not produce deuterons, although they can be produced in the subsequent GEANT hadron showers. This explains the observed deficit in the Monte Carlo prediction.

3.3 Reconstruction of Photon Conversions and Nuclear Interactions

Photon interactions with the tracker material can produce e^+e^- conversion pairs while for hadrons, a nuclear interaction can produce multiple hadrons. These interactions could reduce the efficiency for low energy photon finding by the electromagnetic calorimeter, as well as the resolution of many hadronic observables such as jets or missing transverse energy. To improve the description of the reconstructed event the identification of conversions and nuclear interactions is part of the tracker reconstruction.

The December 2009 collision data allowed to validate the performance of the identification procedures, and to confirm our understanding of the material in the Tracker. For instance, the distribution of the interaction positions provides a means of observing material in the detector. The distribution versus radial position ρ of the nuclear vertices, compared to the simulation, is shown in Fig. 4. The simulation histogram is normalized to the total number of nuclear interactions found in data in the full z range. The good agreement between the data and simulation indicates a consistent description of the material distribution in this region.

4 Conclusions

The performance of the CMS Tracker has been studied using the collision data at center-of-mass energies of 0.9 and 2.36 TeV. The tracking and vertexing resolutions are in agreement with the expected design performance in minimum bias events, for the level of the alignment achieved. Studies of the decays of K^0_S, Λ^0, Ξ^-, and $K^*(892)^-$ test the capability to reconstruct displaced vertices and agree well with predictions from simulation, providing strong tests of our understanding of the magnetic field, tracker material, and detector performance. The accuracy of the tracker material description is demonstrated by the agreement between data and simulation for photon conversions and nuclear interactions. Ionization energy loss measurements in the tracker provide good particle identification at low momentum.

The excellent tracking performance in the early collision running demonstrates that the all-silicon CMS Tracker fully meets its design specifications.

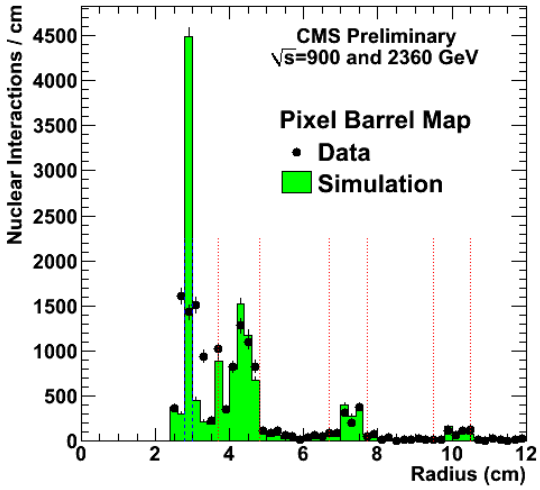

Figure 4: The nuclear interaction vertices: distribution of the radial position ρ for $|z| < 26$ cm. The beam pipe at radius of 3 cm, as well as the three barrel pixel layers at average radii of 4.3 cm, 7.3 cm, and 10.2 cm, are clearly seen. In the data, the beam pipe center is offset from the pixel detector center resulting in a smeared distribution versus radius.

References

1. CMS Collaboration. The CMS experiment at the CERN LHC. *JINST* **0803**, S08004 (2008).
2. CMS Collaboration. Transverse momentum and pseudorapidity distributions of charged hadrons in pp collisions at $\sqrt{s} = 0.9$ and 2.36 TeV. *JHEP* **02**, 04 (2010).
3. CMS Collaboration. Commissioning of the CMS experiment and the cosmic run at four tesla. *JINST* **5**, T03001 (2010).
4. W. Adam, B. Mangano, Th. Speer, and T. Todorov. Track Reconstruction in the CMS Tracker. *CMS Note* **2006/041**, (2006).
5. CMS Collaboration Tracking and Vertexing Results from First Collisions. http://cms-physics.web.cern.ch/cms-physics/public/TRK-10-001-pas.pdf *CMS Physics Analysis Summary* **TRK-10-001**, (2010)
6. C. Amsler et al. Review of Particle Physics. *Physics Letters* **B667**, 1 (2008).
7. M. Fairbairn et al. Stable massive particles at colliders. *Phys. Rept.* **438**, 1–63 (2007).

ATLAS Tracking Results from the first Collision data-taking Period

A. SALZBURGER for the ATLAS Collaboration
CERN PH-ADP, mailbox E25620,
1211 Geneva 23, Switzerland

The first collision data taking period with stable beam conditions at the LHC at $\sqrt{s} = 900$ GeV in December 2009 provided stringent tests of the ATLAS track reconstruction. The detailed understanding of the performance of the track and vertex reconstruction chains has been an integral component of the first charged particle distribution measurements in proton-proton collisions published by the ATLAS collaboration. The very good description of the data by the ATLAS Monte Carlo simulation for track quantities and the reconstruction of weakly decaying particles is shown.

1 Introduction

The data shown here was taken during the stable LHC[1] running periods between December 6 and 15 2009, when the ATLAS tracking detectors[2] were in full operational mode and the magnetic field of the solenoid was on. Approximately half a million events were collected by requiring a hit on either side of the minimum bias trigger scintillators. To reduce the contribution from beam backgrounds, a reconstructed primary vertex was required. The understanding of the detector in terms of e.g. material budget or inactive modules is important for performance studies and physics analyses. Therefore the observed LHC and detector conditions including inactive modules and channels were used in the Monte Carlo (MC) simulation.

2 Track Reconstruction Performance in the Inner Detector

The main reconstruction sequence in the inner detector is an inside-out track reconstruction chain. Track candidates are formed from space points in the silicon detector, which consists of the innermost pixel detector which is inside a silicon microstrip detector (SCT). These track candidates are then extended into the transition radiation tracker (TRT) that provides additional particle identification. A loose track selection was chosen: tracks within a pseudorapidity[a] range of $|\eta| < 2.5$, a reconstructed transverse momentum p_{T} greater than 500 MeV, and with a minimum of 7 hits in the silicon detector were selected. Additional requirements, such as a maximum number of holes and shared hits on a track are applied in the pattern recognition. There is a very good description of the data by the ATLAS MC simulation. Figure 1 illustrates this by comparing the number of associated pixel hits per selected track. The number of holes — i.e. expected hits not associated to a track — is an even stronger test of the pattern recognition performance and is shown for the SCT detector. A more complete performance study for the inner detector track reconstruction using the same track selection can be found elsewhere [3].

[a] Pseudorapidity is defined as $\eta = -\ln\tan(\theta/2)$

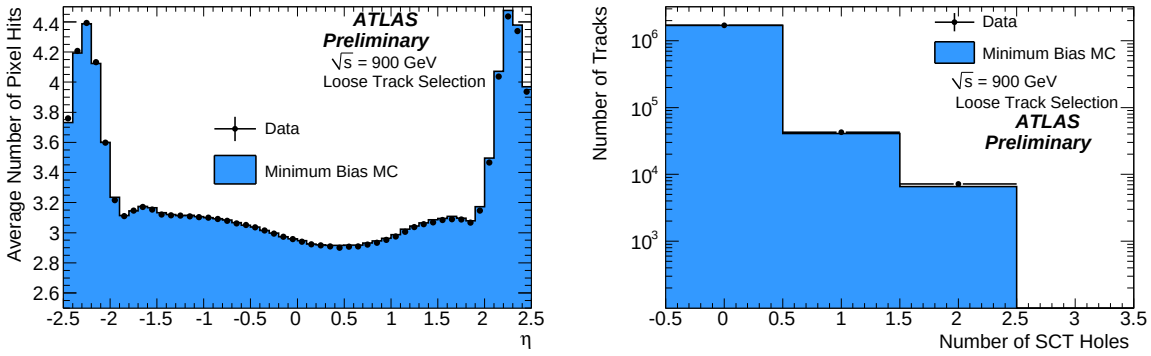

Figure 1: Left: Average number of pixel hits per selected track as a function of pseudorapdity. The distributions are shown for both simulation and data. The structure is mainly influenced by the inactive modules that have been also masked in the digitisation process of the simulation samples to reproduce the run conditions. Right: Total number of SCT holes on a track.

Figure 2 (left) shows the transverse impact parameter distribution of tracks with respect to the primary vertex in linear and logarithmic scale. The difference in the core distribution is due to module misalignment in data. The agreement in the tails indicates that both the secondary production rate and the material budget in the simulation are in good agreement with data. The high quality track reconstruction allowed track-based alignment algorithm to achieve residual distributions close to those of a perfectly aligned detector (see Fig. 2, right).

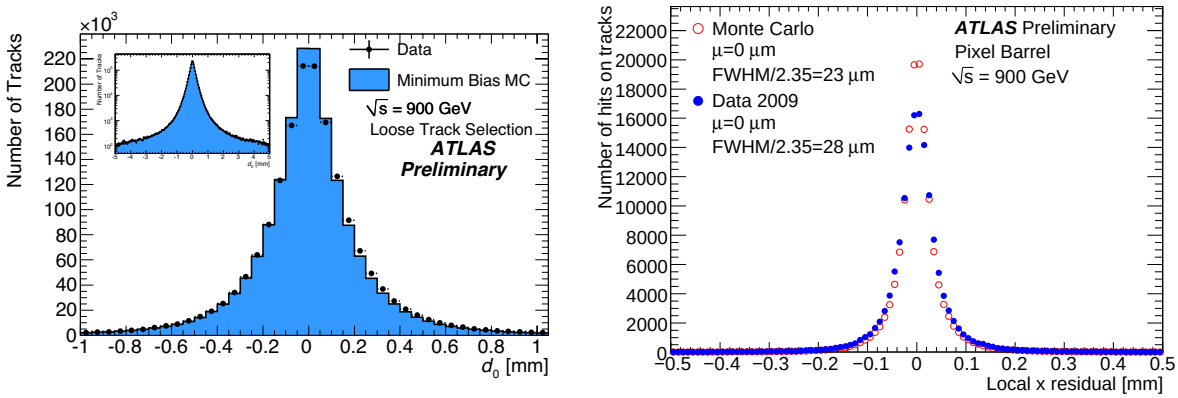

Figure 2: Left: Transverse impact parameter distributions d_0 in linear and logarithmic scale in Monte Carlo and data. The impact parameter is expressed with respect to the reconstructed vertex. Right: The unbiased pixel barrel residual in the local x coordinate after track-based alignment using the 2009 dataset.

3 Primary Vertex and Beam Spot Reconstruction

The interaction point of the proton-proton collision is reconstructed on an event by event basis by a dedicated primary vertex reconstruction algorithm. The efficiency of reconstructing a primary vertex has been determined from data and is close to 100% for events with more than 2 reconstructed tracks[4]. The primary vertices are used to measure the luminous region (beam spot) of the LHC inside the ATLAS detector. This is done for every whole run but also every 2 luminosity blocks[b] to be able to monitor any drifting or widening of the beam spot during

[b] A luminosity block is a defined data-taking time interval.

a run. Figure 3 shows the reconstructed vertex position in one transverse component and the estimated beam spot position and its stability throughout a data-taking run.

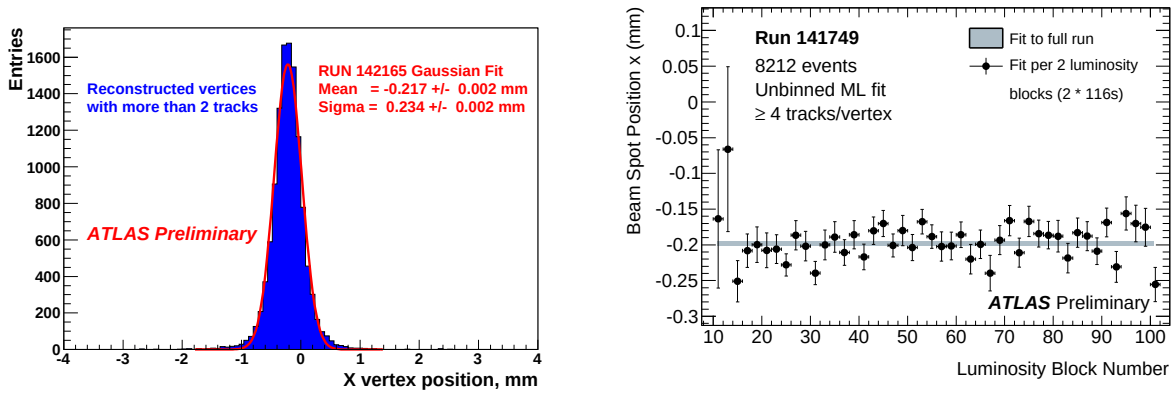

Figure 3: Left: The reconstructed primary vertex position in the transverse coordinate x for a single run. Right: Stability of the beam spot position as a function of luminosity block for a single run.

4 Electron Reconstruction and Photon Conversions

A unique element of the ATLAS inner detector is the TRT detector. It provides electron-pion separation using transition radiation (TR). TR is emitted by a particle traversing materials with strongly differing dielectric constants and is proportional to the Lorentz factor $\gamma = E/m$ of the particle. Figure 4 (left) shows the probability of a high threshold hit induced by transition radiation in the TRT end-cap. Electron candidates with $\gamma > 10^3$ were selected for this study from reconstructed photon conversions into electron-positron pairs. The estimation of the rate of photon conversions is a very powerful approach to estimate the material budget of the detector from data. There is a good agreement between the MC prediction and data within the limited statistics[5].

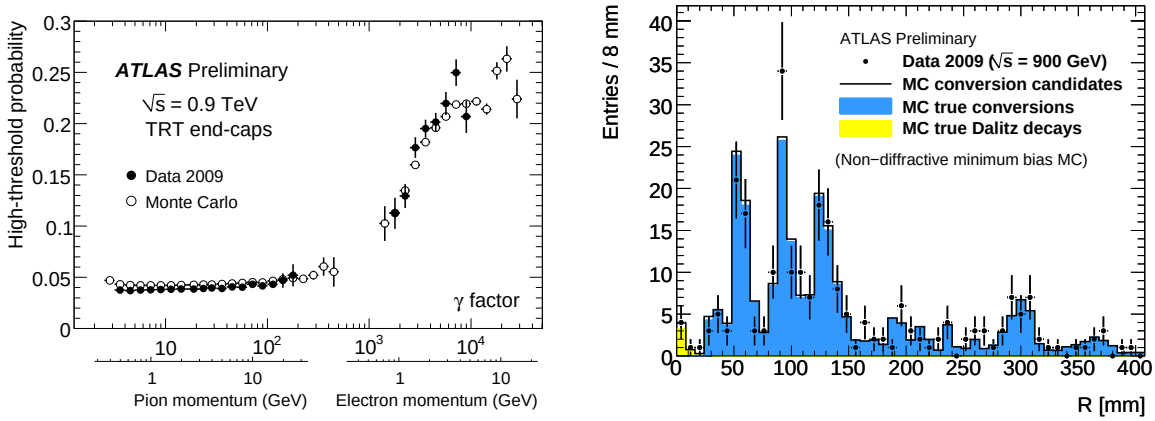

Figure 4: Left: The probability of a TRT high-threshold (HT) hit as a function of the Lorentz factor $\gamma = E/m$ for the TRT end-caps. Right: Distribution of photon conversion radii in the Silicon tracker volume comparing data and MC.

5 Weakly Decaying Particles

Secondary vertex reconstruction was used to identify decay products from weakly decaying particles, such as K_S and Λ. Figure 5 shows the invariant mass distribution of vertices reconstructed from two tracks of opposite charge. The flight direction of the K_S candidate was required to be compatible with the location of the reconstructed primary vertex. No mass constraint was applied during the vertex fit and the invariant mass is calculated by assuming that both tracks are pions. Data and MC show a very good agreement of both the fitted K_S mass and the width. The invariant mass distribution of K_S can been used to provide a constraint on the detector material. Underestimating the ionisation energy loss correction in the track fit shifts the mean of the reconstructed K_S mass. A global scale offset causes the reconstructed K_S mass to depend on the decay radius of the K_S because the decay products traverse different lengths of excess material. Figure 5 (right) compares the fitted K_S mass in data and in MC samples with an excess of 10% and 20% of extra material to MC samples with nominal material in the ID. The presented study[6] shows a disagreement of data with the 10 (20)% excess material MC.

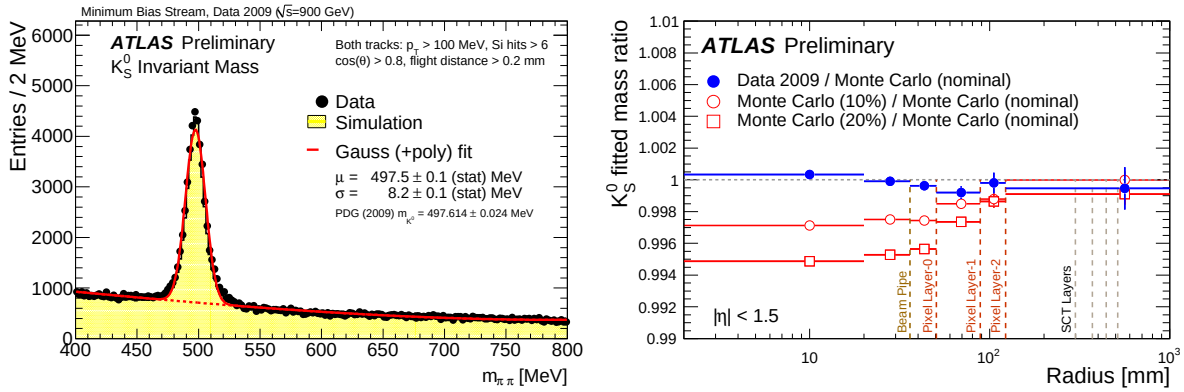

Figure 5: Left: Invariant mass distribution of vertices formed from two tracks of opposite charge, only statistical errors are shown. Right: Ratio of fitted K_S mass in bins of decay radii to the value obtained with the nominal ATLAS MC simulation. Data is compared to MC simulation with the material budget enhanced by 10 and 20 %.

6 Conclusion

The first data-taking period at $\sqrt{s} = 900$ GeV demonstrated excellent performance of the ATLAS tracking system. Close to 98 % of all channels in the inner detector were active and provided stable data taking conditions. The ATLAS Monte Carlo simulation describes the data to a very high level of accuracy. First estimates of the potential deficits in the description of the inner detector material budget were obtained from both photon conversions and the fitted K_S mass. This indicates a good level of agreement between the detector and its simulation model.

References

1. Evans L., (ed.), Bryant P., (ed.), LHC Machine, JINST 3 S08001 (2008).
2. The ATLAS Collaboration, JINST 3 S08003 (2008).
3. The ATLAS Collaboration, ATLAS-CONF-2010-011.
4. The ATLAS Collaboration, Phys. Lett. B 688, Issue 1 (2010).
5. The ATLAS Collaboration, ATLAS-CONF-2010-007.
6. The ATLAS Collaboration, ATLAS-CONF-2010-019.

ATLAS Calorimeter Results

E. MONNIER,
on behalf of the ATLAS Collaboration
CPPM, Aix Marseille Université,CNRS/IN2P3, Marseille, France

This report presents results obtained with the ATLAS detector. These are based on the first Large Hadron Collider (LHC) proton-proton collision data accumulated up to December 2009 at 900 GeV and at 2.36 GeV center of mass energy. The performances of the ATLAS calorimeter system are presented. Highlights are put on its responses to missing transverse energy, jets, photons and electrons including combined performances with the tracking system. In addition it shows the very good description of the data by the ATLAS Monte Carlo simulation. Finally early physics results such as the measured reconstructed $\gamma\gamma$ invariant mass are given, illustrating the very good performances of the calorimeter system.

1 Introduction

At the end of 2009, the Large Hadron Collider [1], at CERN, Geneva, started to produce its first high energy proton-proton collisions at 900 GeV and 2.36 TeV and the ATLAS detector [2] began to accumulate its first collision events. From cosmic to test beam and single beam data, the ATLAS calorimeter system has been commissioned and thoroughly studied. Its performances can now be assessed on high energy data. This report presents results obtained with half a million collision events, so-called Minimum Bias events, selected requiring a hit on either side of the minimum bias trigger scintillators [3].

2 The calorimeter system

The calorimeter system is one of the main components of the ATLAS detector [2]. It has a dual role: record energy deposits to identify electromagnetic (EM) and hadronic components (γ, electrons, jets, transverse/missing energy...), and transmit the information to the trigger system. From the outer core to the inner core, are first a hadronic barrel and extended barrel covering the pseudo rapidity [a] $|\eta| < 1.7$ region, made of flat iron plates, as absorber, and scintillating plastic tiles readout by photomultipliers as active zone. It has 9800 channels and is more than 98% fully operational. Then further in are liquid Argon Calorimeters (LAr) organized in a barrel electromagnetic calorimeter (EMB, $|\eta| < 1.475$), closed by two end-caps, each made of an electromagnetic (EMEC, $1.375 < |\eta| < 3.2$), a hadronic (HEC, $1.375 < |\eta| < 3.2$), and a forward (FCAL, $3.1 < |\eta| < 4.9$) calorimeter. These are sampling calorimeters with liquid argon as active material and absorbers made of lead for the electromagnetic (EMB, EMEC, 173312 channels, 98,6% operational), copper (HEC, 5632 channels, 99.9% operational, FCAL section 1) or tungsten (FCAL section 2 and 3, 3524 channels total, 100% operational). The

[a] $\eta = -ln(\tan(\theta/2))$ where θ is the particle momentum direction versus beam axis polar angle

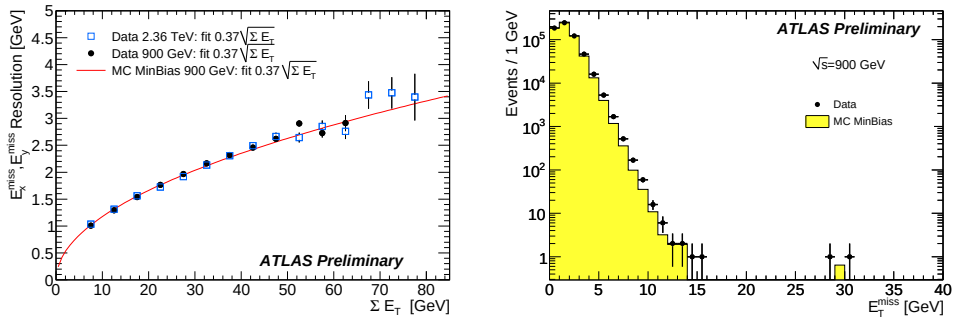

Figure 1: $E_{\mathrm{x}}^{\mathrm{miss}}$ and $E_{\mathrm{y}}^{\mathrm{miss}}$ resolution as a function of $\sum E_{\mathrm{T}}$ (Left) and $E_{\mathrm{T}}^{\mathrm{miss}}$ distribution (Right).

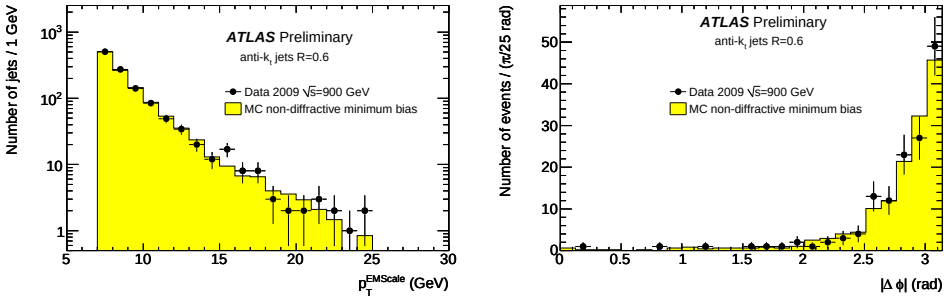

Figure 2: Jet p_T distribution (Left) and two highest p_T jets azimuthal angle difference distribution (Right).

calorimeter system and its related trigger component have a full azimuthal angle (ϕ) and up to $|\eta| < 4.9$ coverage. There are three or four longitudinal layers with different granularity in each. The EMB and EMEC calorimeters have a highly granular accordion layer up to $|\eta| < 2.5$ and a presampler up to $|\eta| < 1.8$, providing information to trigger and identify electromagnetic objects and ensure proper electron/photon identification and measurements. The calorimeter system has first been commissioned using cosmic data then single beam data, so called splash events since issued from a "target" located far upstream of the detector. With those first data, then with the very first collision data, the first level calorimeter trigger then the calorimeters have been properly timed to the nanosecond level.

3 Missing transverse energy and Jet reconstruction

Looking first at raw cell energy distribution, a very good agreement of the simulation, using simulated non diffractive minimum bias events, with the data is observed over the full calorimeter range. Then, the first level calorimeter trigger performances have been looked at. Comparing the trigger tower energy to the calorimeter offline readout, an excellent correlation was found as well as turn on curves at the expected threshold values. Moreover the transverse energy trigger resolution was measured to be better than the 5% design value.

Then after having performed those crosschecks, transverse missing energy ($E_{\mathrm{T}}^{\mathrm{miss}}$) reconstruction, one key element for future physics analysis was studied [4]. Transverse missing energy along the vertical and the horizontal axis, total and missing transverse energy, are calculated using topological clusters at the electromagnetic scale seeded by cell energy above $4\sigma(noise)$ over the full calorimeter range $|\eta| < 4.9$. The transverse missing energy distribution and the resolution of its two axial components as a function of the $\sum E_{\mathrm{T}}$, show a good agreement between the simulation, normalized to the number of events, and the data as can be seen in Fig. 1. Soon, refined transverse missing energy will be provided using hadronic calibration, reconstructed muons and more generally using physics object calibrations (for Jets, Electrons, Photons) as well as taking into account dead material.

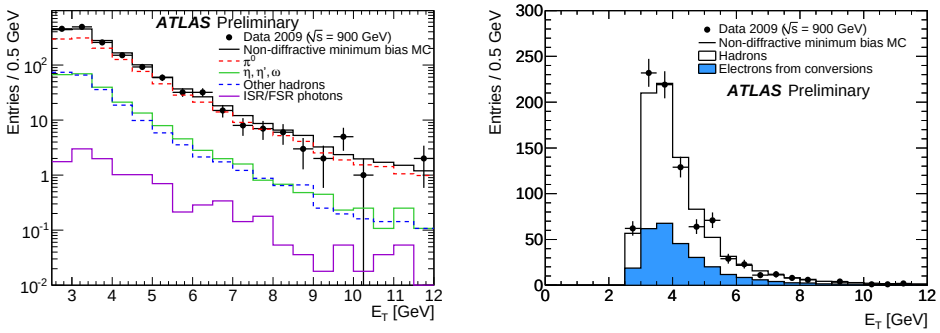

Figure 3: Cluster E_T for all selected photons (Left) and for all selected electron (Right) candidates.

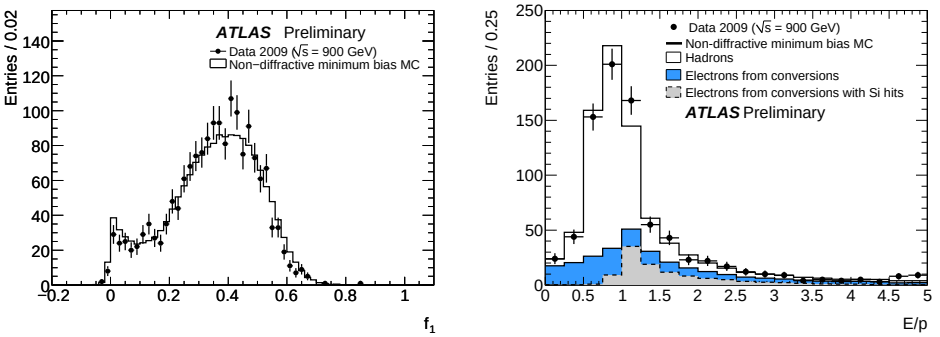

Figure 4: f1 distribution for photon candidates (Left) and E/p distribution for electron candidates (Right).

With those topological clusters, jet algorithms can be performed such as the Anti-K_T, $R = 0.6$ algorithm with $p_T^{\mathrm{EMScale}} > 7$ GeV and $|\eta| < 2.6$. The related jet distributions exhibit an excellent agreement of the simulation with the data as shown in Fig. 2 for the Jet transverse momentum distribution and for the distribution of the azimuthal angle difference between the two highest energy jets. The simulation is normalized to the number of jets or di-jets. Even more complex distributions such as the energy over momentum (E/p) ratio for isolated tracks turn to be in good agreement illustrating promising performances for the future jet energy calibration and the result of years of test beam studies and Geant 4 simulation tuning.

4 Electrons and photons

Out of the first 384000 minimum bias events, using a sliding window clustering, excluding the $1.37 < |\eta| < 1.52$ crack region, 1694 photon candidates with $E_T > 2.5$ GeV and $|\eta| < 2.37$ were selected. Similarly, adding a matched track with $P_T > 0.5$ GeV, and a cut at 2.47 instead of 2.37, 879 electron candidates were selected as well [5]. For those candidates, the different kinematic distributions are in good agreement between the non diffractive minimum bias simulation and the data as shown in Fig. 3 for the momentum distribution for both selected candidates. Then, to further select those electromagnetic physics objects, several shower profile variables have been defined and again the simulation and the data are in good agreement as can be seen for example in Fig. 4 for the fraction of energy in the front layer (f1). In addition, applying cuts on the shower shapes of the electron candidates, including a track matching, track based distributions for those selected candidates can be studied in further details. They are found to be well described by hadrons and electrons from conversions as can be seen in Fig. 4 for the E/p ratio. Matching angular distributions present similar agreement.

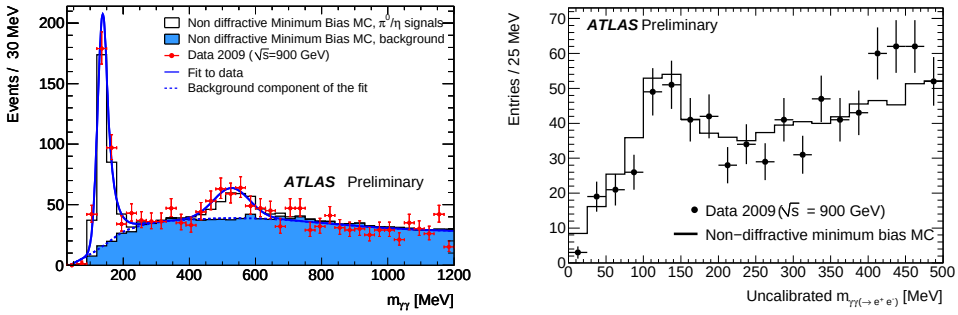

Figure 5: $\gamma\gamma$ (Left) and $\gamma(\gamma \rightarrow e^+e^-)$ (Right) invariant mass spectrum.

5 π^0 and η^0 reconstruction

Looking further into the data, physics signals can be extracted. Selecting photon candidates, similarly as above but using a topological EM cluster seed approach to include low energy photons and with additional cuts such as $E_{\mathrm{T}}^{\mathrm{cluster}} > 0.4$, $P_{\mathrm{T}}^{\mathrm{pair}} > 0.9$ GeV and $f_1 > 0.1$ with a dedicated low E_{T} photon calibration, then fitting the reconstructed $\gamma\gamma$ invariant mass spectrum with the sum of a Gaussian and a Crystal-Ball function for the signal and a 4^{th} order Chebyshev polynomial for the background, a signal peak of $1.34 \pm 0.02.10^4 \pi^0$ candidates is extracted with $m_{\pi^0} = 134.0 \pm 0.8(\mathrm{stat})$ MeV, $\sigma = 24.0$ MeV for the data. The simulation is in good agreement with $m_{\pi^0} = 132.9 \pm 0.2(\mathrm{stat})$ MeV, $\sigma = 25.2$ MeV. There is a 1% uncertainty on the fitted π^0 mass arising from the background modelling. Cutting further, $E_{\mathrm{T}}^{\mathrm{cluster}} > 0.8$, $P_{\mathrm{T}}^{\mathrm{pair}} > 2.2$ GeV, and adding a track veto cluster, the reconstructed $\gamma\gamma$ invariant mass spectrum, shown in Fig. 5, contains a π^0 peak but also exhibit a clear η^0 peak at a fitted $m_{\eta^0} = 527 \pm 11(\mathrm{stat})$ MeV for the data and $m_{\eta^0} = 544 \pm 3(\mathrm{stat})$ MeV for the simulation. All distribution agrees well in spectrum as well as in width and peak positions for the signals. Using photon candidates and converted photon candidates instead, a reconstructed $\gamma\gamma$ invariant mass spectrum is produced with $P_{\mathrm{T}}^{\gamma e^+e^-} > 0.9$ GeV, as shown in Fig. 5, with a similar π^0 peak illustrating the very good performances of the ATLAS calorimeter as well as tracking system.

6 Conclusion

The first 900 GeV and 2.36 TeV pp collision data were produced fall 2009 by the LHC and recorded by the ATLAS detector. Its calorimeter system performances were thoroughly studied. This system, at this early stage, is performing very well showing a good agreement between simulation and data. Missing transverse energy, calorimeter jets, electrons and photons reconstruction, identification and trigger performances are as expected, thanks to detailed simulation, test beam campaigns and a long commissioning with cosmic and single beam data. Preliminary results on π^0 and η^0 reconstruction look very promising with di-photon invariant masses reconstructed at the expected values. ATLAS is now at the edge of a promising era already accumulating in 2010 its first 7 TeV data. The performance studies will continue with the calorimeter system and will gradually switch to physics analysis that we hope will be very fruitful.

References

1. Evans L., (ed.), Bryant P., (ed.), LHC Machine, JINST **3**, S08001 (2008).
2. The ATLAS Collaboration *JINST* **3**, S08003 (2008).
3. The ATLAS Collaboration *Phys. Lett.* B **688**, Issue 1 (2010).
4. The ATLAS Collaboration ATLAS-CONF-001 and ATLAS-CONF-008
5. The ATLAS Collaboration ATLAS-CONF-005, ATLAS-CONF-006, ATLAS-CONF-007.

Studies of Jets and MET At CMS

Salvatore Rappoccio for the CMS Collaboration
Johns Hopkins University, Baltimore MD

During the LHC early commissioning phase, CMS recorded about 350000 minimum bias events from proton-proton collisions at $\sqrt{s} = 900$ GeV, and 20000 minimum bias events from proton-proton collisions at $\sqrt{s} = 2360$ GeV. Three types of jets and missing transverse energy are reconstructed: from calorimeter energy depositions, from combined calorimeter and tracker information, and from particle flow candidates. We present the properties of inclusive jets and dijet events, as well as missing transverse energy from inclusive events. The collision data are in good agreement with predictions from PYTHIA minimum bias events simulated with the full CMS detector simulation.

1 Introduction

In 2009 CMS recorded roughly 350k and 20k minimum bias events from LHC proton-proton collisions at $\sqrt{s} = 900$ GeV and $\sqrt{s} = 2360$ GeV respectively. Here we present studies of jets and missing transverse energy, reconstructed from different detector inputs, with the intention to demonstrate that the jet and MET reconstruction in CMS is performing well at these energies.

Three different types of jet and MET reconstruction are employed by CMS [1], characterized by the way that the sub-detector inputs are used.

Calorimeter jets and MET are reconstructed using energy deposits in the electromagnetic and hadronic calorimeter cells.

The **Jet-Plus-Tracks and Track-Corrected MET** (JPT, tcMET) algorithms [2] correct the energy and the direction of calorimeter jets and MET using the excellent CMS tracking detectors [3].

The **Particle Flow** (PF) algorithm [4] aims to reconstruct, identify and calibrate each individual particle in the event by combining the information from all CMS sub-detector systems. PF particles are reconstructed as a combination of charged particle tracks and clusters in the electromagnetic and hadronic calorimeters, as well as signals in either of the two CMS pre-shower detectors and the muon system.

Jets are reconstructed with the anti-k_{T} algorithm [5], and corrected using Pythia [6] QCD events from proton-proton collisions at $\sqrt{s} = 900$ GeV and $\sqrt{s} = 2360$ GeV which were further processed with the full, GEANT4 [7] based, CMS detector simulation. They consist of two stages: the relative (Rel) correction that makes the jet response uniform in η, by calibrating, on average, to the response in the central region of the calorimeters ($|\eta| < 1.3$); the absolute (Abs) correction that removes the p_{T} dependence of the jet response.

First we examine a sample of dijet events for which both jets with the highest transverse momentum p_{T} in the event are back-to-back in azimuth φ. The resulting high purity dijet sample allows the study of jet properties with loose additional jet quality criteria and serves as a benchmark sample for the jet commissioning.

Secondly, beyond the dijet selection, we also report on the characteristics of jets inclusively. In the absence of topological constraints, the purity of the inclusive jet sample is enhanced by applying tight kinematic selection requirements and jet quality criteria.

Finally, the missing transverse energy in an inclusive sample is examined. There are no physical sources of true missing transverse energy in the collisions at this time since the rate of such processes is much lower than the collected luminosity, so this gives a measurement of the missing transverse energy resolution.

2 Cleaning and Object Identification

In the jet results, jets are purified in two selections, "loose" for the dijet results, and "tight" for the inclusive jet results. The loose selection requires that jets are inconsistent with sources of calorimeter noise (both hadronic and electromagnetic), and the tight selection additionally rejects very "narrow" jets that are consistent with electronics noise.

In the $\not\!\!E_T$ results, several sources of noise are identified, including anomalous noise from hybrid photo-diodes (HPDs) in the hadronic barrel and hadronic endcap calorimeters (HB/HE), and photomultiplier window hits in the forward hadronic calorimeter (HF). Only the second source is removed for the $\not\!\!E_T$ results because the probability of HPD noise overlapping with real events is measured to be negligible.

3 Results

For brevity, only the results of 900 GeV data are shown. Please see References [8–10] for full results and the 2360 GeV comparisons. Results of dijet comparisons for the 900 GeV data and MC are shown in Figure 1. Results of inclusive $\not\!\!E_T$ comparisons for the 900 GeV data and MC are shown in Figure 2.

Good agreement is seen between the data and the MC in the distributions examined.

References

[1] **CMS** Collaboration, "The CMS Experiment at the CERN LHC", *JINST* **3** (2009) S08004.

[2] **CMS** Collaboration, "Jet Plus Tracks Algorithm for Calorimeter Jet Energy Corrections in CMS", *CMS PAS* **JME-09-002** (2009).

[3] **CMS** Collaboration, "Tracking and Vertexing Results from First Collisions", *CMS PAS* **TRK-10-001** (2010).

[4] **CMS** Collaboration, "Particle-Flow Event Reconstruction in CMS and Performance for Jets, E_T^{miss}, and Taus", *CMS PAS* **PFT-09-001** (2009).

[5] M. Cacciari, G. P. Salam, and G. Soyez, "The anti-kt jet clustering algorithm", *JHEP* **0804:063** (2008).

[6] T. Sjostrand, S. Mrenna, and P. Skands, "PYTHIA 6.4 physics and manual", *JHEP* **05:026** (2007).

[7] S. Agostinelli and et al., "Geant 4 – A Simulation Toolkit", *Nucl.Inst.A* **506** (2003) 250–303. doi:10.1016/S0168-9002(03)01368-8.

[8] **CMS** Collaboration, "Jets in 0.9 and 2.36 TeV pp Collisions", *CMS Physics Analysis Summary* **JME-10-001** (2010).

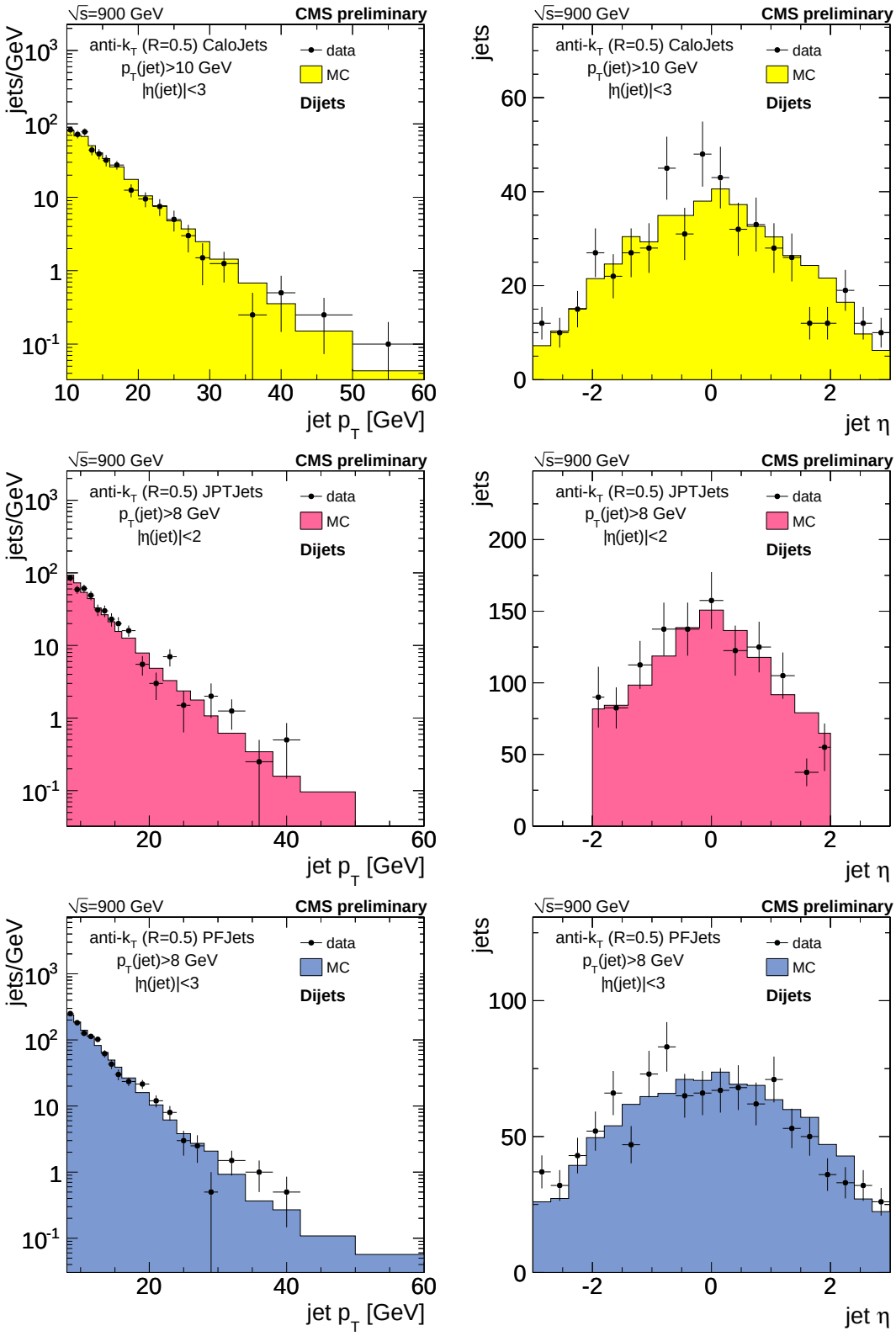

Figure 1: Comparisons of data and MC distributions for the two leading jets for selected $\sqrt{s} = 900$ GeV dijet events. Jet p_{T} is plotted on the left, jet η on the right. The calorimeter-only jets are plotted in the first row, track-corrected calorimeter jets ("jet-plus-tracks" jets) in the second, and the PF jets are plotted in the third row. Jets are reconstructed with the anti-k_{T} $R = 0.5$ algorithm.

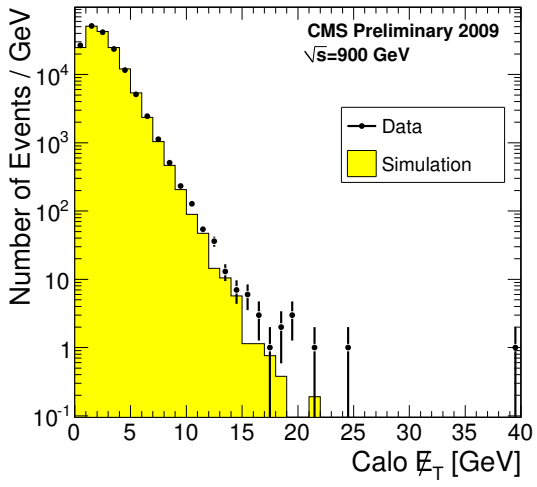

(a) Calo$\not\!\!E_T$ distribution

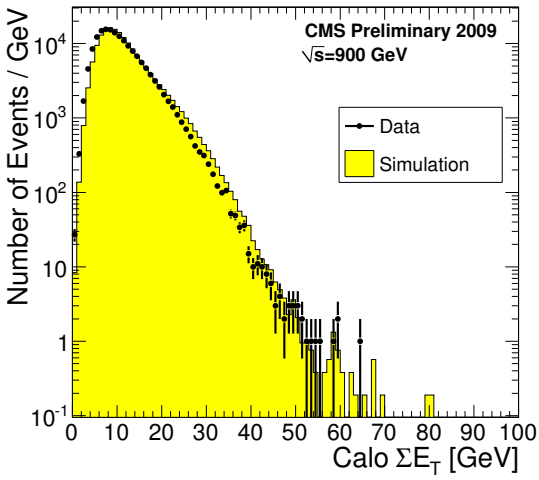

(b) Calo$\Sigma E_{\rm T}$ distribution

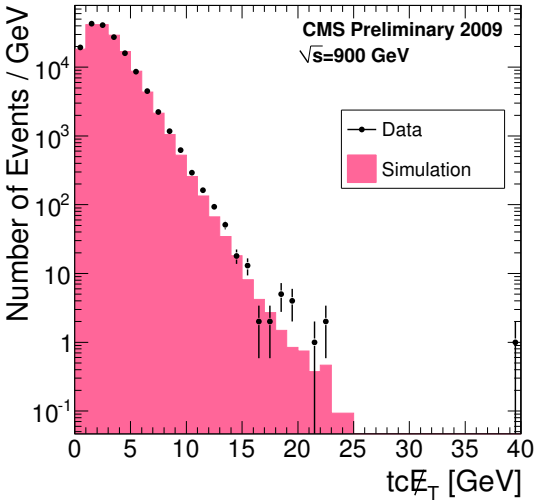

(c) tc$\not\!\!E_T$ distribution

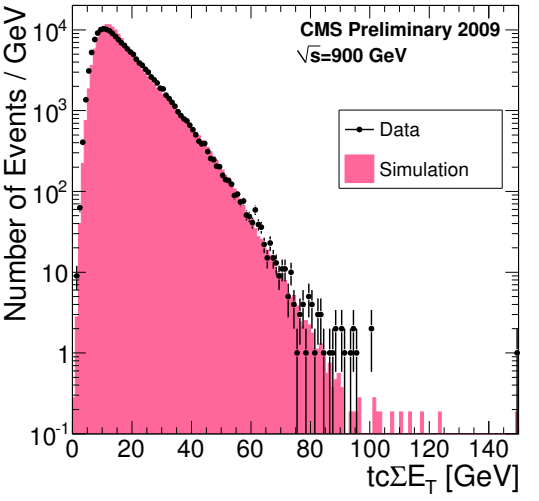

(d) tc$\Sigma E_{\rm T}$ distribution

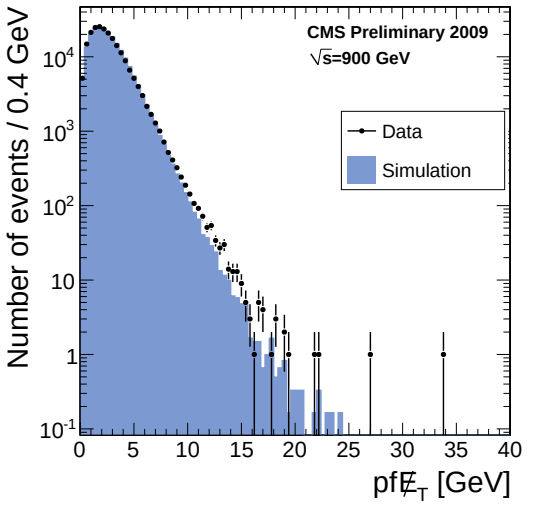

(e) pf$\not\!\!E_T$ distribution

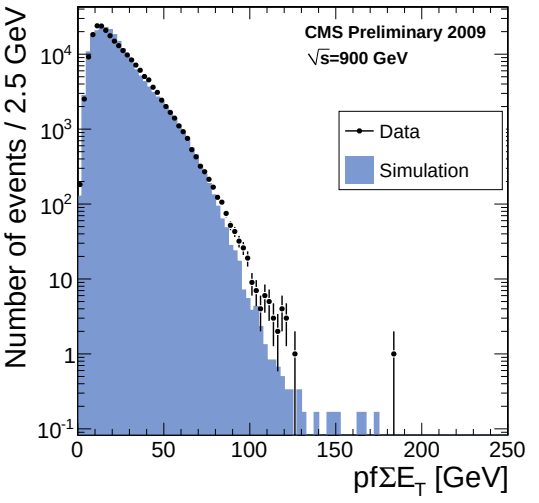

(f) pf$\Sigma E_{\rm T}$ distribution

Figure 2: Comparisons of data and MC for the $\not\!\!E_T$ distributions (after cleanup procedure) in the 900 GeV data. $\not\!\!E_T$ is plotted on the left, $\Sigma E_{\rm T}$ is plotted on the right. The calorimeter-only $\not\!\!E_T$ is plotted in the first row, track-corrected $\not\!\!E_T$ in the second, and the PF $\not\!\!E_T$are plotted in the third row.

[9] **CMS** Collaboration, "Missing ET in 0.9 and 2.36 TeV pp Collisions", *CMS Physics Analysis Summary* **JME-10-002** (2010).

[10] **CMS** Collaboration, "Commissioning of the Particle-Flow Event Reconstruction with the first LHC collisions recorded in the CMS detector", *CMS Physics Analysis Summary* **PFT-10-001** (2010).

PHOTONS AND ELECTRONS STUDIES AT CMS

C. ROVELLI, on behalf of the CMS Collaboration
Università La Sapienza and INFN Roma1,
P.le Aldo Moro 2, 00185 Roma, Italy

Reconstructing electrons and photons with high efficiency and good momentum resolution is crucial for many physics channels at the CMS experiment. This goal is challenging in view of the high material budget in front of the electromagnetic calorimeter and the presence of a strong magnetic field. The reconstruction algorithms are described here. The use of data from the first proton-proton collisions recorded by CMS at the center of mass energy of 900 GeV to commission the reconstruction of electrons and photons is discussed.

1 Introduction

CMS is one of the two multipurpose experiments collecting data at the Large Hadron Collider at CERN. The LHC started the data taking at the end of 2009 providing the experiments proton-proton collisions at the centre-of-mass energies of 0.9 and 2.36 TeV. Data at $\sqrt{s}$=7 TeV have been collected starting in 2010.
The detection of electrons and photons is of primary importance at the LHC as these particles characterize the final state for many SUSY or extra dimensions scenaria, Higgs decay channels and Standard Model processes. Several reconstruction tools have been developed in recent years and are currently being tested with collision data. Data collected at $\sqrt{s}$=900 GeV have been used to check the basic ingredients contributing to the reconstruction and identification of electromagnetic physics objects and to compare them with the simulation. Given the low integrated luminosity the study has been performed without identification requirements. Most of the reconstructed candidates are therefore due to fakes and the comparison is mainly carried out for background [1].

2 The CMS detector

A detailed description of the CMS detector can be found in [2]. The central feature of the CMS apparatus is a superconducting solenoid of 6 m internal diameter, providing an uniform magnetic field of 3.8 T. Within the magnetic field are the tracker, the electromagnetic calorimeter and the brass/scintillator hadron calorimeter. Gas-based detectors embedded in the steel return yoke are used to measure muons.
A crucial role in the electron and photon measurement is played by the electromagnetic calorimeter (ECAL) and the tracker. ECAL is a homogeneous calorimeter made of 75848 lead tungstate scintillating crystals. It consists of a central barrel covering the pseudorapidity region up to $|\eta|$=1.5; the coverage for precision measurements extends up to $|\eta|$=2.6 including two endcaps.

A silicon preshower detector also covers the region between $|\eta|$=1.6 and $|\eta|$=2.6.
The tracker is made of 1440 silicon-pixel and 15148 silicon-strip detector modules and measures charged particles trajectories within the pseudorapidity range $|\eta|$ <2.5. The pixel tracker consists of three barrel layers and two endcap disks on each side of the barrel section. The barrel layers are located at a radius of 4.4 cm, 7.3 cm and 10.2 cm respectively.

3 Event selection

The results discussed here use about 200k minimum bias events recorded at $\sqrt{s}$=900 GeV in 2009. The events are selected by a trigger signal in any of the scintillator planes located in front of the Hadron Calorimeter Forward detectors (BSC). From these sample, collision events are selected offline by requiring them to be in time with a valid beam crossing measured by the coincidence of the two beam pickup monitors. The absence of a beam halo trigger, the presence of at least one hit with energy greater than 2 GeV in each of the Forward Hadron calorimeter detectors and a high fraction (>25%) of high purity tracks are also requried. Finally at least one primary vertex must be reconstructed in the event.
Collision data are compared to a full Monte Carlo simulation based on Geant4 of minimum bias events. The simulation is carried out using mis-alignments, mis-calibrations and dead channel lists corresponding to the startup conditions of the CMS detector.

4 Energy clustering

The reconstruction of electrons and photons starts by the detection of energy clusters in the electromagnetic calorimeter. Electromagnetic showers deposit their energy in several ECAL crystals. The presence of material in front of the calorimeter results in electron bremsstrahlung and photon conversions and because of the strong magnetic field the energy reaching the calorimeter is spread in ϕ. The energy is therefore clustered at the ECAL level by building a cluster of clusters (supercluster), which is extended in ϕ to minimize the cluster containment variations [3]. The clustering threshold is approximately 1 GeV in transverse energy E_T. Containment variations are corrected for as a function of energy and pseudorapidity using functions which can be extracted from data.
Kinematic and shower shape variables have been compared in data and Monte Carlo for superclusters in the ECAL fiducial region with E_T greater than 2 GeV. In total 3226 superclusters satisfying these requirements have been reconstructed in data, of which about 2/3 in the barrel. A good agreement is observed between data and simulation for all the considered variables, including clusters in the preshower detector. As an example, Fig.1 on the left shows the distribution in the barrel of $R9$, the ratio of the energy contained in the 3x3 region around the seed crystal and the total supercluster energy. $R9$, which is used to discriminate between converted and unconverted photons, can be larger than one due to fluctuations in the electronic noise.

5 Electron reconstruction

Electrons are characterized by the presence of a charged track pointing to the electromagnetic supercluster. Two different algorithms are used in CMS at the track seeding stage. In the ECAL driven seeding, roads are built from the supercluster to search for hits in the innermost part of the tracker. This algorithm is optimised for isolated electrons in the p_T range relevant for Z or W decays down to ∼5 GeV/c. It is complemented by the tracker driven seeding, which starts from hits in the tracker and is more suitable for low p_T and not isolated electrons.
As the bremsstrahlung radiation severely affects the track propagation, a dedicated tuning of the trajectory building and a Gaussian Sum Filter [4] track fit are used to well follow the non Gaussian

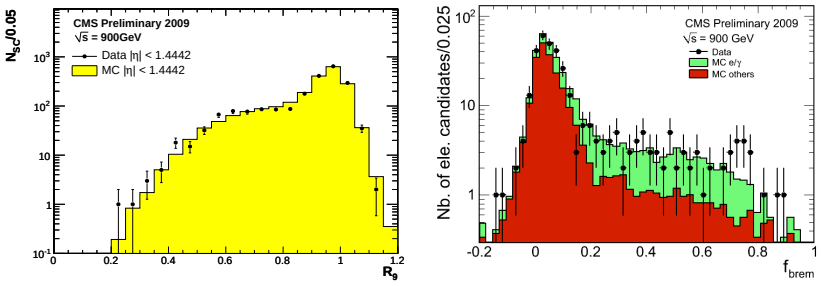

Figure 1: Left: Ratio between the energy contained in the 3x3 region around the seed crystal and the total supercluster energy for barrel superclusters. Right: Relative difference between the track momentum estimate at the innermost and at the outermost position. The Monte Carlo expectation for electron candidates matched to a generated electron or photon is also shown (filled green histogram). In both figures: The black dots correspond to data and the filled histogram to simulated minimum bias events. The Monte Carlo is normalized to the total number of candidates observed in data.

tails in the energy loss. As a result, the track hits can be collected up to the ECAL front face and this allows to obtain an unbiased estimate of the track momentum at both track ends. This procedure also gives a tracker measurement of the fraction of energy lost by bremsstrahlung ($fbrem$), defined as the relative difference between the momentum at the vertex and the momentum at the last point. Based on $fbrem$, different track-cluster patterns are defined and used to derive specific corrections as well as estimates of the electron quality [5].
In the collected minimum bias events only very low p_T electrons are expected and the sample of electron candidates is dominated by charged hadrons or electrons coming from photon conversions. In total 351 electron candidates have been reconstructed in data, of which about 2/3 in the barrel. Being at low p_T most of the candidates are reconstructed from the tracker driven algorithm; the relative fraction of electron candidates found by the two algorithms is well reproduced by the simulation. Several quantities used in the electron reconstruction have been compared between data and Monte Carlo. As an example, Fig.1 on the right shows the $fbrem$ distribution for the electron candidates, which is peaked at $fbrem$=0 since most of the candidates are fakes. A discrepancy in this variable would mean problems in the behaviour of the GSF algorithm or in the parameterization of the tracker material budget. The agreement between data and Monte Carlo is good. In general a good agreement is observed for all the considered variables.

6 Electromagnetic objects identification and isolation

At reconstruction level some cuts are applied in the seeding step and a first candidate preselection is done. Further electron identification is then achieved using shower shape variables and refined track-cluster matching. Electron classes based on the different observed patterns can be used to optimize the electron identification using probability distributions per class.
Isolation requirements can be imposed to suppress the QCD background. A simple and powerful isolation criterion comes from tracks originating from a common vertex as the electron. Also, the sum of the transverse energy reconstructed in ECAL individual channels or in HCAL towers around the reconstructed candidate can be used.
Isolation and shower shape variables for supercluster candidates can also be used for photon isolation and identification. All the checked isolation and identification variables show a good agreement between data and simulation.

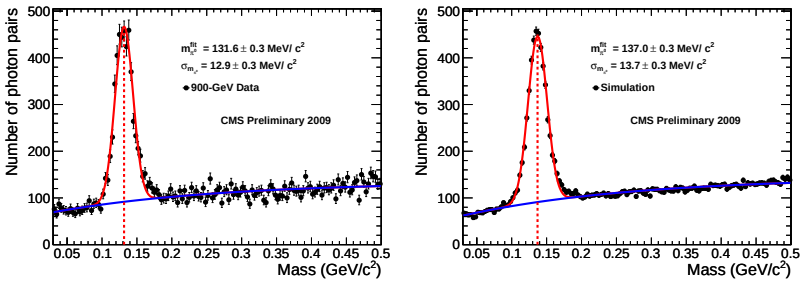

Figure 2: Photon-pair invariant-mass distribution ($|\eta|$ <1) in data (left) and Monte Carlo (right). Also shown is a fit of the π^0 mass peak by a Gaussian (red line). The fit mean value and resolution are 131.6±0.3 and 12.9±0.3 MeV/c^2 respectively for the data and 137.0±0.3 and 13.7±0.3MeV/c^2 for the simulation. The combinatorial background is fit by an exponential function (blue line).

7 Reconstruction of electromagnetic objects with the first LHC data

Resonances decaying into two photons have been searched for in the first collision data. A clear π^0 peak was observed just after few days, proving the good understanding of the detector. The η peak has been also observed and the π^0/η yields ratio measured in data is in good agreement with the one in the simulation. Due to the combined effect of not containment and readout thresholds the peak is expected to be at a value somehow lower than the real one. The shift in mass is well reproduced in the simulation, such as the peak width and the signal-to-background ratio. The uncorrected π^0 and η peaks are currently being used for the calibration of the electromagnetic calorimeter from data.

For physics studies Monte Carlo-based corrections determined from simulated single photons have been applied to the cluster energies. The photon-pair invariant mass distribution for candidates reconstructed within $|\eta|$ <1 is shown in Fig. 2 for data and Monte Carlo. The agreement for the measured mass value with the world average is within 2%, demonstrating the suitability of the simulation-based absolute ECAL cluster calibration for low-energy photons [6].

8 Summary

Using the first proton-proton collision data collected with the CMS detector at $\sqrt{s}$ =900 GeV many quantities entering the reconstruction of electromagnetic objects have been compared between data and Monte Carlo. Due to the limited statistics the comparison has been done without identification requirements, so the sample is dominated by background. All the considered variables show a good agreement between data and Monte Carlo, leading to the conclusion that the response of the subdetectors is well modeled in the simulation and that the algorithms behavior is consistent with expectations. The commissioning of the electromagnetic physics objects is continuing with the new LHC data at higher center of mass energy.

References

1. CMS Collaboration, CMS-PAS-EGM-10-001
2. CMS Collaboration, JINST 3 (2008) S08004.
3. CMS Collaboration, CERN-LHCC-2006-001 (2006).
4. W. Adam et al., J. Phys. G: Nucl. Part. Phys. 31 (2005) N9-N20
5. S. Baffioni et al., Eur. Phys. J. C 49 (2007).
6. CMS Collaboration, CMS-PAS-PFT-10-001

MUON STUDIES AT CMS

G. MASETTI
on behalf of the CMS collaboration
Università di Bologna, Department of Physics, Viale Berti-Pichat 6/2,
40127 Bologna, Italy

Detection and reconstruction of muons is one of the most important goal of the detectors at LHC. In the first part of this paper, the CMS muon system is described. Then, the muon reconstruction performance, measured with the cosmic-ray sample collected during the data-taking exercise performed in 2008, is presented. Finally, the first J/ψ candidate in di-muon final states collected in CMS is described.

1 CMS Muon System

The Compact Muon Solenoid [1] (CMS) is a general purpose detector designed to optimize the discovery potential of the LHC collider.

Final states with muons are a signature for important processes produced in CMS. Goal of the CMS muon system is muon identification, momentum measurement and trigger. The muon system is the outermost detector in CMS (Fig.1). It consists of three independent subsystems: the Drift Tubes (DT), the Cathode Strips Chambers (CSC) and the Resistive Plate Chambers (RPC).

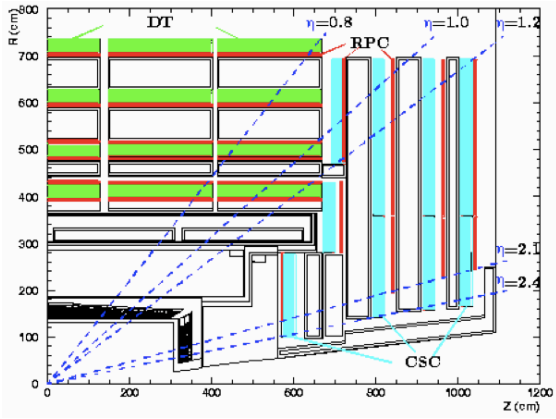

Figure 1: CMS Muon System.

1.1 Drift Tubes

In the barrel region, where the neutron-induced background is small and the muon rate is low, the Drift Tubes technology has been chosen. The detector is composed by four stations forming

concentric cylinders around a beam line. The DT chambers are 250, for a total of 172000 sensitive wires. The pseudorapidity coverage is $|\eta| < 1.2$.

DT performances have been extensively tested during the commissioning of the apparatus using cosmic-rays [2] [3]. The resolution of single reconstructed hits is on the order of 260 μm in all chambers, while the muon position within one station can be measured with a precision of about 100 μm. The local reconstruction efficiency is measured to be about 99% in all chambers. The overall local trigger efficiency, when the proper time of arriving muon is taking into account, is 97% for any trigger quality.

1.2 Cathode Strip Chambers

The endcap region is characterized by a large and varying magnetic field, and by a higher particle rate: cathode strip chambers are used. CSC are composed by trapezoidal chambers mounted on eight stations (four in each endcap). There are 468 chambers in total. The pseudorapidity coverage is $0.9 < |\eta| < 2.4$.

CSC performance have been measured with cosmic-rays [5]: the efficiencies for local charged track triggers, for hit and for segments reconstruction are above 99%. The fraction of noisy or dead channels is less then 1%. The spatial resolution for local muon reconstruction varies from 47 μm to 243 μm .

1.3 Resistive Plate Chambers

To improve the muon trigger efficiency, a complementary trigger system, consisting of resistive plate chambers, have been placed both in the barrel and in the endcap region. RPC have a fast time response ($\sigma_t \sim 2$ ns) and the pseudorapidity coverage is $|\eta| < 1.6$. There are a total of 6 layer of RPC in the barrel and a plane in each of the first 3 stations of the endcap.

More than 98% of the channels were operational during the cosmic-ray data taking exercise with typical detection efficiency of 90% [6].

2 Muon Reconstruction Performance

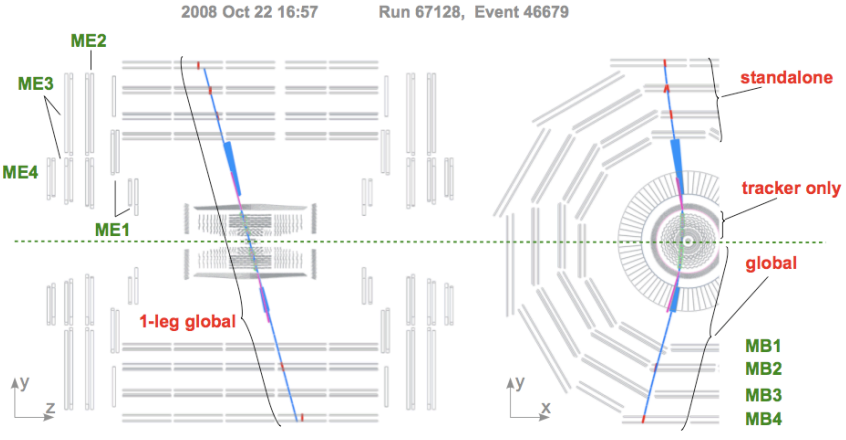

Figure 2: Event display of a cosmic muon crossing CMS.

The performance of muon reconstruction in CMS has been widely tested with the data sample of cosmic muons [7]. Fig. 2 shows, as an example, the event display of a cosmic muon crossing the whole CMS detector: muons tracks can be reconstructed using informations from

the muon system only (*standalone muons*), from the tracker system only (*tracker tracks*) or from all CMS (*global muons*).

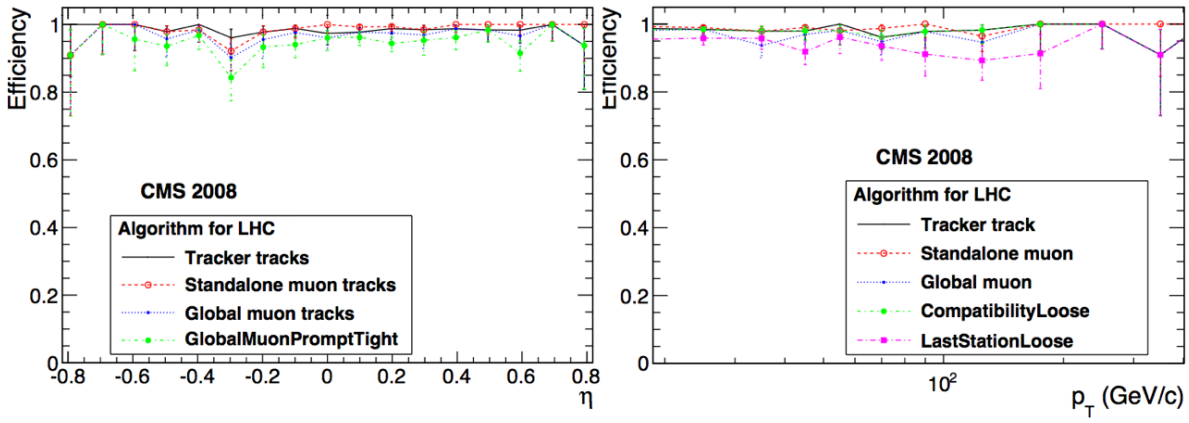

Figure 3: Muon reconstruction efficiency as a function of η (left) and p_T (right).

Cosmic-ray events have been used to measure the muon reconstruction efficiency: events with a good-quality muon reconstructed in one hemisphere have been selected and the corresponding track in the other hemisphere were searched in the region of $|\Delta\phi| < 0.3$ and $|\Delta\eta| < 0.3$ around the direction of the reference global-muon track. To be sure that all the detector is traversed, only global-muon with $p_T > 10$ GeV/c at the point of closest approach to the beam line have been considered. Fig 3 show the measured muon reconstruction efficiency for the standard LHC-like algorithms (a detailed description of the algorithms can be found in Ref. [4]).

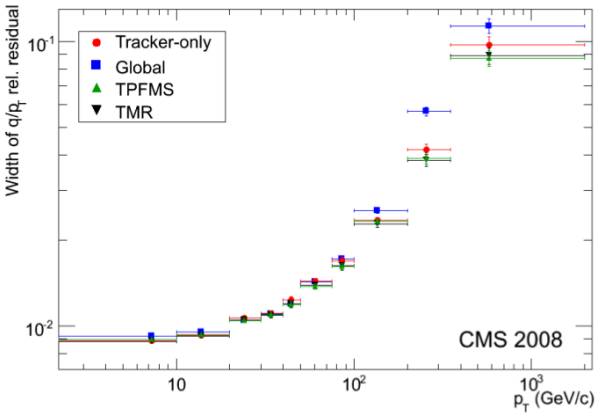

Figure 4: Widths of Gaussian fits to the distribution of the relative residuals for various muon reconstruction algorithm, as a function of p_T of the reference track.

The muon momentum resolution can be measured by the width of the distribution of the relative residuals, R(q/p_T):

$$R(q/p_T) = \frac{(q/p_T)^{upper} - (q/p_T)^{lower}}{\sqrt{2}(q/p_T)^{lower}} \quad (1)$$

where $(q/p_T)^{upper}$ and $(q/p_T)^{lower}$ are the ratios of the charge sign to the transverse momentum for muon tracks in the upper and lower detector halves, respectively. Figure 4 shows the muon momentum resolution as a function of the p_T: below 200 GeV/c the contribution of muon detector hits is low; for high p_T the resolution will improve once that a better detector alignment will be in place.

3 Dimuons in CMS at 900 and 2360 GeV

At the end of 2009, about 12 μb^{-1} of integrated luminosity has been collected by the CMS detector with a centre of mass energy of 900 GeV and 2360 GeV. A selection, searching for final states with 2 muons, has been applied: an event (Fig.5) in the 3.0 - 3.2 GeV mass window (centered in the J/ψ mass peak) has been selected.

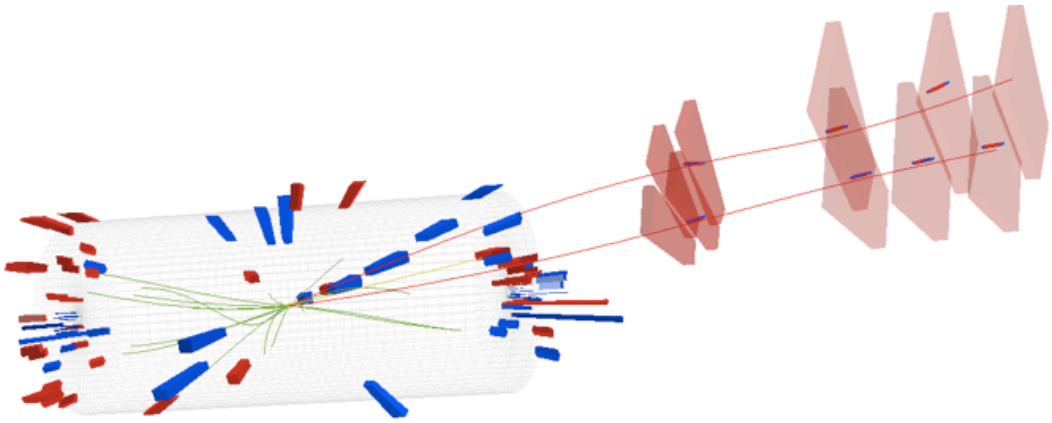

Figure 5: J/ψ candidate. Reconstructed mass: 3.04 GeV/c^2; p_T: 5.38 GeV/c; Dimuon vertex chi^2 prob.: 57%; $c\tau$: -17±81 μm

4 Conclusion

The CMS muon system, composed by three independent subsystems, has been fully commissioned in the past years. Cosmic-ray data taking allowed to evaluate the performances of the detector. The first events coming from proton-proton interaction confirm that CMS is ready for the LHC era. With the first few pb^{-1} collected, it will be possible to reconstruct the J/ψ and Υ resonances, and therefore measure the muon efficiencies and resolution at low momenta (<20 GeV/c). Already with ~ 10 pb^{-1}, several thousands of $Z \rightarrow \mu\mu$ events are expected to be identified in the di-muon reconstructed mass distribution: thus it will be possible to measure muon efficiencies and resolution at high momenta (>20 GeV/c).

References

1. R. Adolphi *et al.* [CMS Collaboration], *JINST* **0803** (2008) S08004
2. S. Chatrchyan *et al.* [CMS Collaboration], *JINST* **5** (2010) T03015
3. S. Chatrchyan *et al.* [CMS Collaboration], *JINST* **5** (2010) T03003
4. G. L. Bayatian *et al.* [CMS Collaboration], "CMS physics: Technical design report," *CERN/LHCC* **2006-001**. CMS TDR 8.1
5. S. Chatrchyan *et al.* [CMS Collaboration], *JINST* **5** (2010) T03018
6. S. Chatrchyan *et al.* [CMS Collaboration], *JINST* **5** (2010) T03017
7. S. Chatrchyan *et al.* [CMS Collaboration], *JINST* **5** (2010) T03022

Multiplicity measurements in proton–proton collisions at $\sqrt{s} = 0.9$ and 2.36 TeV with ALICE

Jan Fiete Grosse-Oetringhaus for the ALICE Collaboration
CERN, 1211 Geneva 23, Switzerland

This paper presents multiplicity measurements that have been performed with ALICE based on minimum-bias data at 0.9 and 2.36 TeV. Results are shown of the pseudorapidity density and the multiplicity distribution in different phase space windows. The analysis and correction procedures are discussed and the results are compared to previous measurements and to model predictions.

1 Introduction

ALICE[1] is a general-purpose particle detector optimized to study heavy-ion collisions at the LHC. The detector's unique features are high-precision tracking and particle identification in an environment of very high particle densities over a large range of momenta, from tens of MeV/c to over 100 GeV/c, thereby accessing topics starting from soft physics to high-p_T particle production and jets. In ALICE it is possible to reconstruct the primary vertex with a resolution of about 100 μm in pp collisions and 10 μm in Pb+Pb collisions. In addition, secondary vertices of e.g. hyperon and heavy quark meson decays can be determined with a resolution of about 100 μm.

The detector consists of a central barrel part ($|\eta| < 0.9$) optimized for the measurement of hadrons, electrons and photons, a muon spectrometer at forward rapidities ($-2.5 < \eta < -4.0$) as well as additional forward and trigger detectors. The central barrel is contained in a magnetic field of up to 0.5 T.

2 Detectors and data sample

The results described in this paper were obtained with the Silicon Pixel Detector (SPD) which consists out of two layers sourrounding the beam pipe at radii of 3.9 and 7.6 cm. The layers cover a pseudorapidity range of $|\eta| < 2$ and $|\eta| < 1.4$, respectively. In addition to the SPD, two scintillator hodoscopes called VZERO were used for triggering. These are placed on both sides of the interaction region with distances of 3.3 and 0.9 m and cover the pseudorapidity regions $2.8 < \eta < 5.1$ and $-3.7 < \eta < -1.7$, respectively.

Results are presented for inelastic (INEL) and non-single-diffractive (NSD) events. For the INEL sample a trigger requiring a signal in either the SPD or one VZERO side was used ($\mathrm{MB_{OR}}$). This trigger is sensitive to 95–97 % of the inelastic cross sections (shown by simulations[2] with PYTHIA[3,4] 6.4.14 tune D6T[5] and PHOJET[6] 1.12 used with PYTHIA 6.2.14). For the NSD sample a different trigger is used which reduces the amount of single-diffractive events while retaining most of the NSD events. It requires a signal on both VZERO sides ($\mathrm{MB_{AND}}$). Fig. 1 shows the trigger efficiency for both these triggers as function of multiplicity.

The events used in this analysis were taken during the commissioning of the LHC in December 2009 at the nominal magnetic field of 0.5 T. About 150 000 and 40 000 interactions for the 0.9 and 2.36 TeV data, respectively, were used. The analysis uses so-called tracklets[7] consisting of hits in the two SPD layers. By correlating these hits the primary vertex is reconstructed. Subsequently, tracklets are constructed that point to this vertex. This method allows to reconstruct particles with a transverse momentum of about 50 MeV/c or larger.

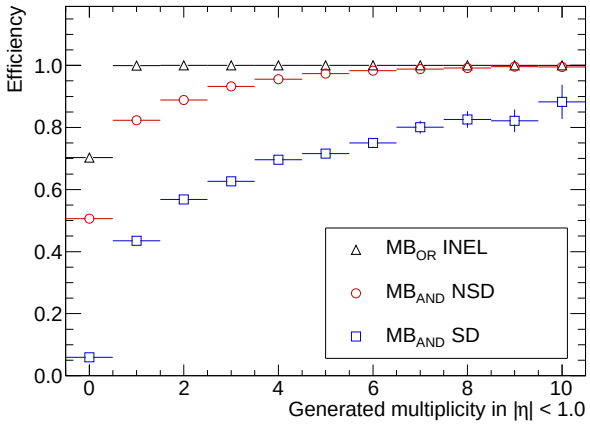

Figure 1: Trigger efficiency for INEL events with the MB_{OR} selection (triangles), and for NSD (circles) and SD events (squares) with the MB_{AND} selection.

3 Analysis

The pseudorapidity density $dN_{ch}/d\eta$ is measured by counting the number of events and the number of tracks, and correcting bin-by-bin for the detector acceptance and tracklet finding efficiency. Furthermore, secondaries need to be subtracted. The effect of the vertex reconstruction and trigger efficiency is considered. By using all triggered events for the normalization including those with no reconstructed vertex the correction to the number of events is rather small. Beam-induced and accidental background was subtracted using control triggers that take data when only a single bunch or no bunch is passing the experiment.

The multiplicity distribution is determined by unfolding the measured distribution applying χ^2 minimization with regularization[8]. This is based on the detector response (measured tracklets vs. generated particles) determined for a given pseudorapidity range with simulations. Subsequently, it is corrected for the vertex reconstruction and trigger efficiencies as function of the unfolded multiplicity.

Systematic uncertainties have been evaluated for both analyses considering the effects of cuts during tracklet reconstruction, material budget, detector alignment, composition of produced particles, the p_T spectrum below the p_T cut off, ratios of diffractive cross sections, detector efficiency, and thresholds for the VZERO. The model dependency was assessed by using two

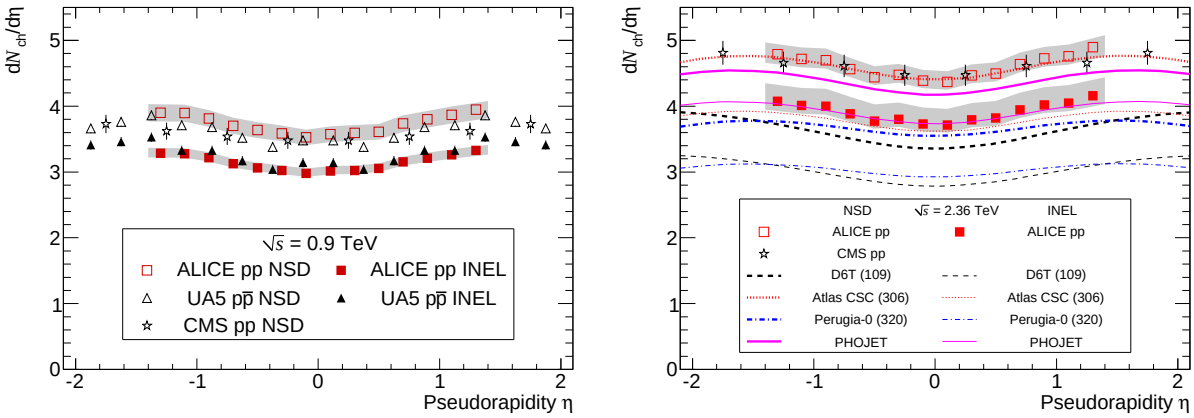

Figure 2: Pseudorapidity density measurements at 0.9 (left) and 2.36 TeV (right). ALICE data (squares) is compared to UA5 (triangles, only at 0.9 TeV), CMS (stars, only NSD) and MC generator predictions (lines, only at 2.36 TeV). The shaded area indicates the systematic uncertainty.

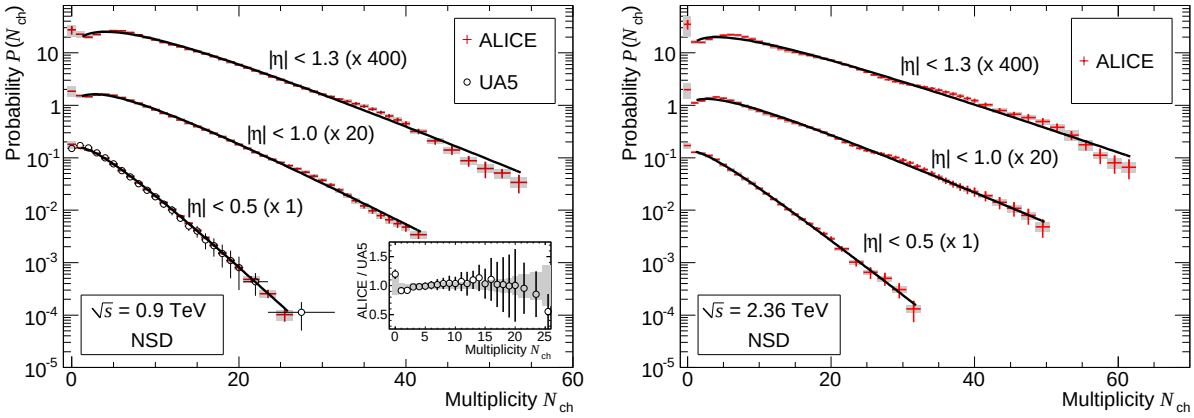

Figure 3: Multiplicity distribution measurements for NSD events at 0.9 (left) and 2.36 TeV (right). The shaded area indicates the systematic uncertainty. The lines are NBD fits to the data. In the left figure UA5 data is also shown; the inset shows the comparison to UA5, here the shaded area is the combined statistical and systematic uncertainty.

different event generators (PYTHIA and PHOJET). The largest contributions to the systematic uncertainty are due to diffractive processes and the detector efficiency.

More details about these correction procedures are found in Ref.[9] and about this specific analysis in Ref.[10].

4 Results

Fig. 2 shows the pseudorapidity density at 0.9 and 2.36 TeV for INEL and NSD events compared to results from UA5[11] and CMS[12] and MC generator predictions of PYTHIA tune D6T, ATLAS-CSC[13], and Perugia-0[14] as well as PHOJET. At mid-rapidity the values measured with ALICE at 0.9 TeV are $3.02 \pm 0.01(stat.)\ ^{+0.08}_{-0.05}(syst.)$ and $3.58 \pm 0.01\ ^{+0.12}_{-0.12}$ for the INEL and NSD sample, respectively. At 2.36 TeV, these are $3.77 \pm 0.01\ ^{+0.25}_{-0.12}$ (INEL) and $4.43 \pm 0.01\ ^{+0.17}_{-0.12}$ (NSD). Our results are consistent with results from UA5 and CMS. At the higher energy, model comparisons show that only PYTHIA tune ATLAS-CSC and PHOJET are close to the data. D6T and Perugia-0 significantly underestimate the pseudorapidity density.

The increase of the pseudorapidity density at mid-rapidity from 0.9 to 2.36 TeV is found to be $(24.7 \pm 0.005\ ^{+0.057}_{-0.028})$ % and $(23.7 \pm 0.005\ ^{+0.046}_{-0.011})$ % for the INEL and NSD sample, respectively. The considered MC generators predict an increase between 17–20 % (INEL) and 14–19 % which understimates the measured value significantly. This trend has been shown to continue at 7 TeV[15].

Fig. 3 shows the multiplicity distribution measured in three pseudorapidity ranges, $|\eta| < 0.5$, 1.0, and 1.3, at 0.9 and 2.36 TeV for NSD events. In the two larger pseudorapidity intervals, small wavy fluctuations are seen at multiplicities above 25. While visually they may appear to be significant, one should note that the errors in the deconvoluted distribution are correlated over a range comparable to the multiplicity resolution. We concluded that these are not significant, and that the uncertainty bands should be seen as one-standard-deviation envelopes of the deconvoluted distributions (see also[10]).

The ratio to the UA5 measurement[16] at the lower energy shows good agreement. Negative-binomial distributions (NBDs) that have shown to fit distributions at lower energies[17,18] provide a reasonable description of the data. Fig. 4 compares the distribution in $|\eta| < 1$ at 2.36 TeV with predictions from PYTHIA and PHOJET. Only PYTHIA tune ATLAS-CSC and PHOJET are close to the data but both differ significantly over large areas of multiplicity.

5 Summary

Pseudorapidity density and multiplicity distributions have been measured in pp collisions at 0.9 and 2.36 TeV. The pseudorapidity density at mid-rapidity is found to increase significantly faster than predicted by the MC generators PYTHIA and PHOJET. The multiplicity distribution in limited η-regions is described by a NBD while the considered MC generators have difficulties describing it. More information about this analysis can be found in Ref.[10]. A similar measurement has been performed at 7 TeV[15].

References

1. ALICE Collaboration, K. Aamodt et al., J. Instrum **3**, S08002 (2008)
2. ALICE Collaboration, R. Brun et al., Nucl. Instrum. Meth. A **502**, 339 (2003)
3. T. Sjöstrand, Comput. Phys. Commun. **82**, 74 (1994)
4. T. Sjöstrand, S. Mrenna, P. Skands, J. High Energy Phys. **2006**, 05 026 (2006)
5. M.G. Albrow et al. (Tev4LHC QCD Working Group), arXiv:hep-ph/0610012 (2006)
6. R. Engel, J. Ranft, S. Roesler, Phys. Rev. D **52**, 1459 (1995)
7. PHOBOS Collaboration, B.B. Back et al., Phys. Rev. Lett. **85**, 3100 (2000)
8. V. Blobel, in *8th CERN School of Comp 84*, Spain, CERN-85-09, 88, (1985)
9. J.F. Grosse-Oetringhaus, PhD thesis, Univ. of Münster, Germany, CERN-THESIS-2009-033 (2009)
10. ALICE Collaboration, K. Aamodt et al., to be published in Eur. Phys. J. C, arXiv:1004.3034[hep-ex] (2010)
11. UA5 Collaboration, G.J. Alner et al., Z. Phys. C **33**, (1986) 1
12. CMS Collaboration, V. Khachatryan et al., JHEP **2010** 02 041 (2010)
13. A. Moraes (ATLAS Collaboration), ATLAS Note ATL-COM-PHYS-2009-119 (2009)
14. P.Z. Skands, arXiv:0905.3418[hep-ph] (2009)
15. ALICE Collaboration, K. Aamodt et al., submitted to Eur. Phys. J. C, arXiv:1004.3514[hep-ex] (2010)
16. UA5 Collaboration, R.E. Ansorge et al., Z. Phys. C **43**, 357 (1989)
17. UA5 Collaboration, G.J. Alner et al., Phys. Lett. B **160**, 193 (1985)
18. J.F. Grosse-Oetringhaus and K. Reygers, to be published in J. Phys. G, arXiv:0912.0023[hep-ph] (2009)

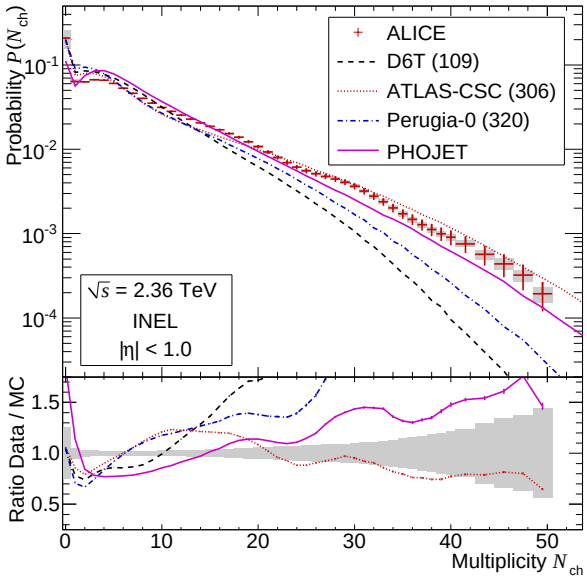

Figure 4: Multiplicity distribution for INEL events in $|\eta| < 1$ at 2.36 TeV compared to MC generator predictions. The shaded area indicates the systematic uncertainty. The lower part shows the ratio to the predictions where the shaded area is the combined statistical and systematic uncertainty.

Momentum spectra of identified particles in pp collisions with the ALICE detector

F. Noferini for the ALICE collaboration
University of Bologna, Dipartimento di Fisica, via Irnerio 46, Bologna 40126, Bologna

The performance of the ALICE detector for charged hadrons identification turned out to be effective immediately after the start of the first pp collisions. The central barrel detectors (ITS, TPC and TOF) have provided π, K, p identification in a wide range of momenta. The ALICE detector was designed to perform such a study in a very efficient way by using the energy-loss dependence in the lower p_T region (with the ITS and the TPC) and the time-of-flight measurement in the higher p_T region (with the TOF). The capability to reconstruct a wide set of particles is also shown.

1 Introduction

The study presented here is based on the excellent capability of the ALICE detector [1] in particle identification. The Time-Projection Chamber (TPC) [2], the main tracking system, provides dE/dx information in a momentum range limited by the absorption in the material closer to the collision zone and by the crossing of the dE/dx curves to high momenta. The dE/dx information from the Inner Tracking System (ITS) [1] allows us to extend the limits towards lower momenta, while the additional information in the Time-Of-Flight detector (TOF) [3,4] makes the identification possible up to 2.5 GeV/c.

The ALICE detector is a dedicated heavy ion experiment, designed to cope with the high particle multiplicities expected for central $Pb-Pb$ collisions at $\sqrt{s} = 5.5$ TeV. The central barrel (midrapidity) detectors of ALICE consist of a six-layer silicon detector (ITS), located at 3.9 - 48.9 cm from the beam axis, a Time Projection Chamber (TPC) at 85 - 250 cm, a Transition Radiation Detector (TRD) for electron identification at 290 - 368 cm (not presented in this analysis), and a Time-Of-Flight (TOF) detector at 370 - 399 cm. The detectors are sitting in a solenoidal magnetic field of $B = 0.5$ T with a rapidity coverage of $-0.9 < \eta < 0.9$. The experiment setup and the expected performance are described in detail in [5] and [6], respectively.

The results presented in this article are based on the analysis of charged particle tracks in the ITS, TPC and TOF.

The data presented were collected during the commissioning of the LHC at CERN in the fall of 2009 with pp collisions. The energy of each beam was 450 GeV (i.e. injection energy). The collider was run with 4×4 bunches per beam, resulting in two bunch crossing (BC) per beam circulation period (89 μs) at the ALICE interaction point. The remaining two bunches were passing through the ALICE detector and served to estimate the contribution of beam-gas interactions. The average rate was a few events per second and pile-up within one bunch crossing was, therefore, negligible.

Moreover, the ITS capability in reconstructing secondary vertex allowed us to identify un-

stable particles like K^0_s, Λ and Ξ in the first collisions at 900 GeV.

2 Particle identification performance

As mentioned before the PID (Particle IDentification) performance is very good in a wide range of momenta. Combining the information of the three detectors is possible to cover a range from 0.1 GeV/c to 2.5 GeV/c. The ITS dE/dx covers the range at very low momenta ($0.1 < p < 0.5$ GeV/c), the TPC dE/dx is good at intermediate momenta ($0.3 < p < 1$ GeV/c) and the TOF is ideal for high momenta ($0.5 < p < 2.5$ GeV/c). A summary of the performance is reported in Fig. 1, where dE/dx vs. momentum (ITS and TPC) and β vs. momentum (TOF) plots are shown. In the same figure is also reported a sketch with the detector momentum ranges and the complementarity of the three detectors can be noted.

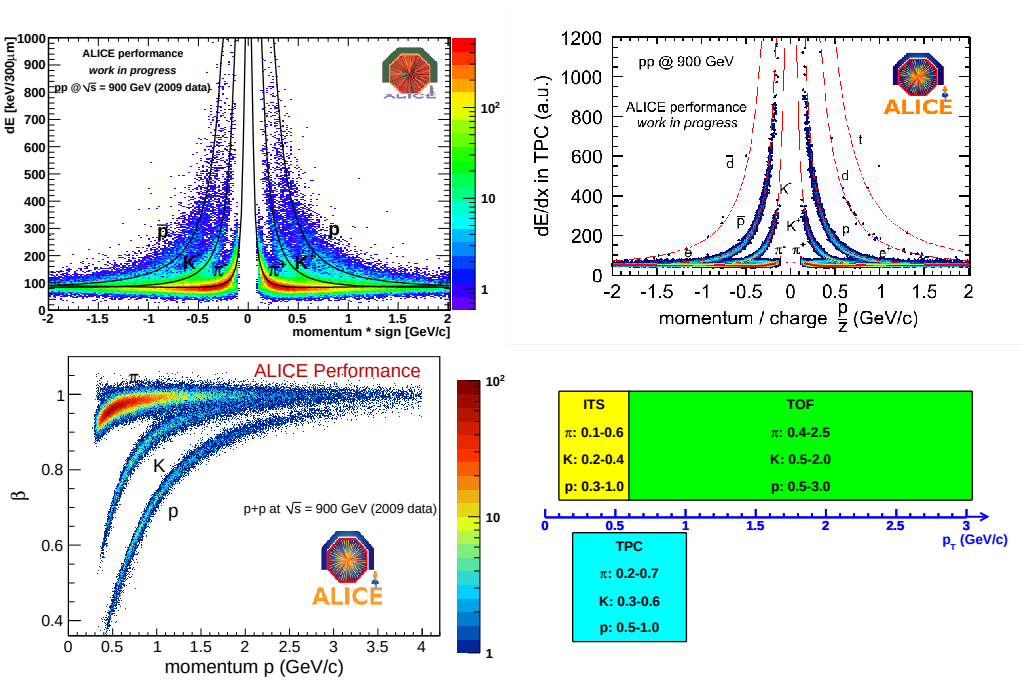

Figure 1: dE/dx vs momentum and β vs. momentum for the ALICE subdetectors (top: ITS and TPC, bottom: TOF) in the central barrel ($|\eta| < 0.9$). A sketch on the performance of combined Particle IDentification (PID) is also shown.

A more detailed picture is given in Fig. 2, Fig. 3 and Fig. 4 where fits to the different detector response functions were performed in order to extract the yields in different p_T slices. In order to improve the particle identification with TOF a proper variable was choosen to guarantee the gaussian response, especially for the pion and kaon cases. In fact the variable $(t^\pi + t^K)_{calc}/2 - t_{TOF}$ is a good compromise to realize a symmetric behaviour for pions and kaons; where t^π_{calc} and t^K_{calc} are the expected times for pion and kaon hypotheses and t_{TOF} is the time measured by TOF.

These plots represent the main way to extracts yields for different particle species and so to measure identified particle spectra in the first pp collisions at 900 GeV with the ALICE detector. These preliminary results are very promising so that the final identified spectra will be published very soon in a future article.

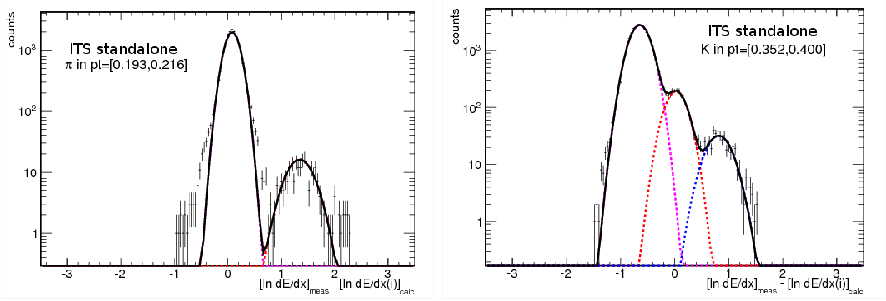

Figure 2: The dE/dx distribution measured with the ITS for momenta between 193 MeV and 216 MeV (left pannel) and 352 MeV and 400 MeV (right pannel).

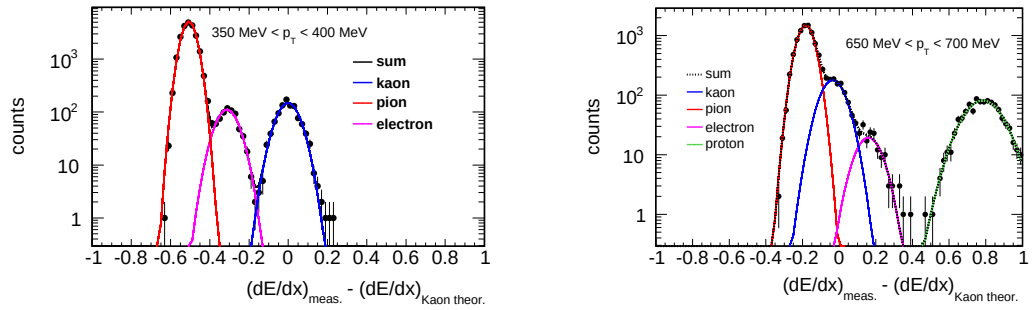

Figure 3: The dE/dx distribution measured with the TPC for momenta between 350 MeV and 400 MeV (left pannel) and 650 MeV and 700 MeV (right pannel)

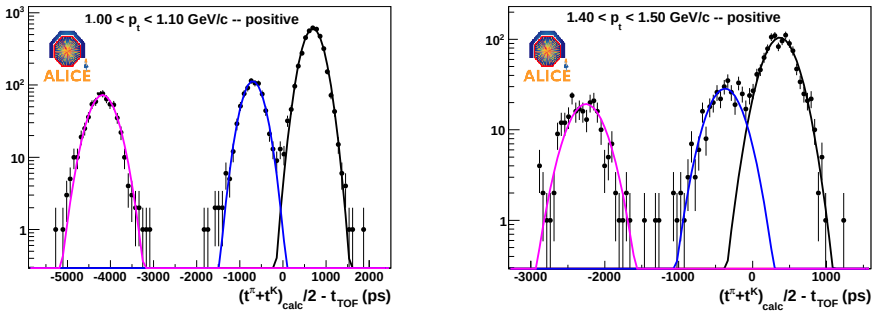

Figure 4: The arrival time distribution for 1.0 GeV $< p_T <$ 1.1 GeV (left panel) and 1.5 GeV $< p_T <$ 1.6 GeV (right panel).

3 Week decays and resonances through reconstructed secondary vertex and kaon identification

Another topic of this work is the measurement of resonances and weak decaying particles. Some of the first observations of ALICE were the K^0_s and Λ particle using the secondary vertex reconstruction. Some results are reported in Fig. 5 which show the good capability of the Inner Tracking System in resolving these signals from the combinatorial background.

Moreover the PID in the central barrel allowed us to reconstuct several resonances decaying in the kaon channel. In particular ϕ and K^{*0} mesons were identified using the TPC and TOF response.

In Fig. 6 the results for TOF stand alone analysis are reported for both of these resonances.

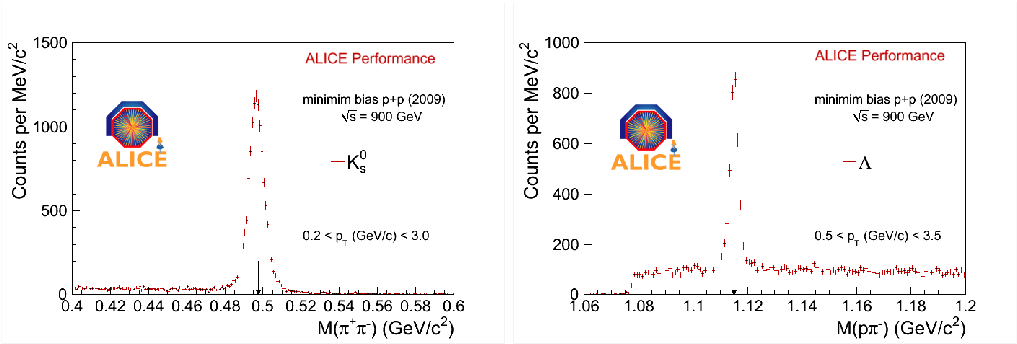

Figure 5: K^0_s and Λ invariant mass after the secondary vertex selection.

The requirement of the TOF identification selects the transverse momentum region above 1 GeV/c for both decay channels.

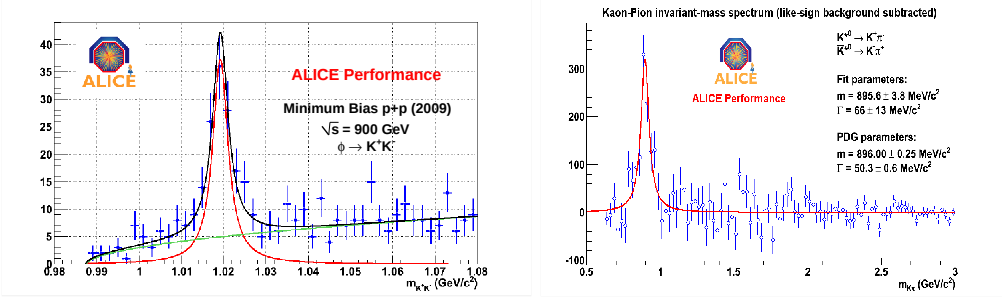

Figure 6: ϕ and K^{*0} invariant mass ($p_T > 1$ GeV/c) using the TOF PID.

4 Conclusion

The ALICE performance for particle identification has been shown in this work. It is quite good also considering that it was obtained for the very first pp collision in 2009 ($\sqrt{s} = 900$ GeV).

It was shown how the several subdetectors (ITS, TPC and TOF) at midrapidity allow to perform the measurement for identified particle spectra in a wide p_T-region and in a complementary way, even if final results will be available in a future work.

The PID performance can be also used to identify several particles in a number of different channels, taking advantage both from the secondary vertex reconstrucion in the ITS and from the good K/π separation up to high momenta.

References

1. K. Aamodt et al. [ALICE Collaboration], *JINST* 3 S08002, 2008.
2. J. Alme et al., arXiv:1001.1950 [physics.ins-det].
3. A. Akindinov et al., *Nucl. Instrum. Methods* A615 37, 2010.
4. A. Akindinov et al., *Nuovo Cimento* C32 123, 2009.
5. B. Alessandro et al. [ALICE Collaboration], *J. Phys.* G32 1295, 2006.
6. F. Carminati et al. [ALICE Collaboration], *J. Phys.* G30 1517, 2004.

Transverse-momentum and pseudorapidity distributions of charged hadrons in pp collisions at $\sqrt{s} = 0.9$ and 2.36 TeV

C. Roland for the CMS Collaboration
Massachusetts Institute of Technology, Cambridge, MA, USA

Measurements of inclusive charged-hadron transverse-momentum and pseudorapidity distributions are presented for proton-proton collisions at $\sqrt{s} = 0.9$ and 2.36 TeV. The data were collected with the CMS detector during the LHC commissioning in December 2009. For non-single-diffractive interactions, the average charged-hadron transverse momentum is measured to be 0.46 ± 0.01 (stat.) $\pm$ 0.01 (syst.) GeV/c at 0.9 TeV and 0.50 ± 0.01 (stat.) $\pm$ 0.01 (syst.) GeV/c at 2.36 TeV, for pseudorapidities between -2.4 and $+2.4$. At these energies, the measured pseudorapidity densities in the central region, $dN_{\rm ch}/d\eta|_{|\eta|<0.5}$, are 3.48 ± 0.02 (stat.) $\pm$ 0.13 (syst.) and 4.47 ± 0.04 (stat.) $\pm$ 0.16 (syst.), respectively. The results at 0.9 TeV are in agreement with previous measurements and confirm the expectation of near equal hadron production in $\rm p\bar{p}$ and pp collisions.

1 Introduction

Measurements of transverse-momentum ($p_{\rm T}$) and pseudorapidity (η) distributions are reported for charged hadrons produced in proton-proton (pp) collisions at centre-of-mass energies ($\sqrt{s}$) of 0.9 and 2.36 TeV at the CERN Large Hadron Collider (LHC) [1]. The data were recorded with the Compact Muon Solenoid (CMS) experiment in December 2009 during two 2-hour periods of the LHC commissioning.

The bulk of the particles produced in pp collisions arises from soft interactions, which are only modeled phenomenologically. Therefore experimental results have to provide guidance for the tuning of these widely-used models and event generators. Soft collisions are usually divided into several categories, namely elastic scattering, inelastic single-diffractive (SD) and double-diffractive (DD) dissociation (Double Pomeron Exchange is treated as DD in this paper), and inelastic non-diffractive (ND) scattering [3]. The distributions shown in this paper are measured for inelastic non-single-diffractive (NSD) interactions to minimize the model dependence of the necessary corrections for the event selection, and to enable a comparison with earlier experiments.

2 Experimental Methods

A detailed description of the CMS experiment can be found in Ref. [2]. The detectors used for the present analysis are the pixel and silicon-strip tracker (SST) covering the η range to $|\eta| < 2.5$, embedded in a 3.8 T magnetic field. The pixel tracker consists of three barrel layers and two end-cap disks at each barrel end. The forward calorimeter (HF), which covers the region $2.9 < |\eta| < 5.2$, was used for event selection. The detailed Monte Carlo simulation (MC) of the CMS detector response is based on GEANT4 [4].

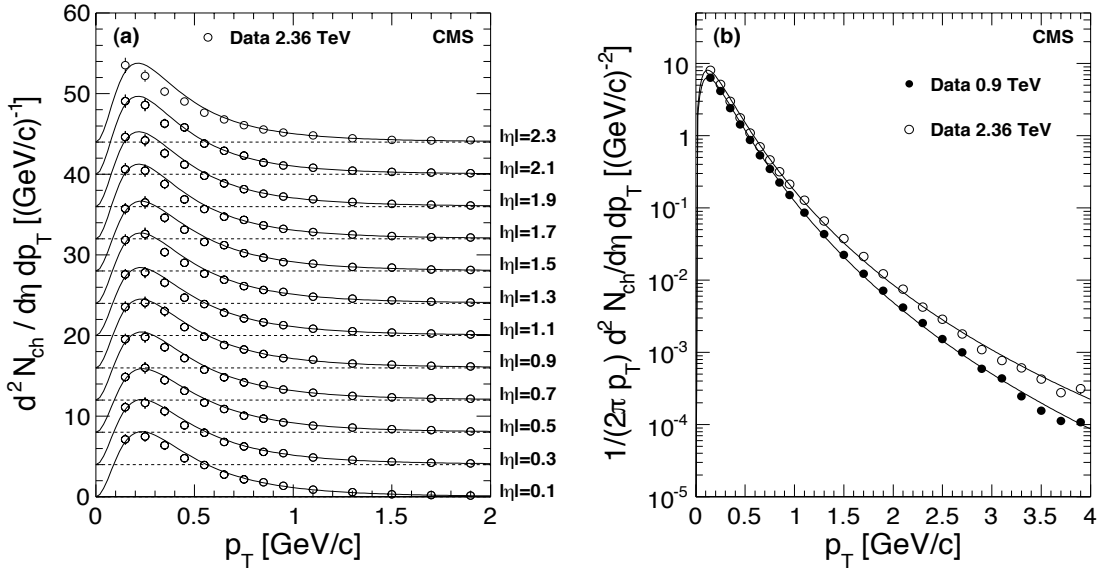

Figure 1: (a) Measured differential yield of charged hadrons in the range $|\eta| < 2.4$ in 0.2-unit-wide bins of $|\eta|$ for the 2.36 TeV data. The measured values with systematic uncertainties (symbols) and the fit functions (Eq. 1) are displayed. The values with increasing η are successively shifted by four units along the vertical axis. (b) Measured yields of charged hadrons for $|\eta| < 2.4$ with systematic uncertainties (symbols), fit with the empirical function (Eq. 1).

For the purpose of this analysis, predominantly NSD events were selected by requiring a primary vertex (PV) to be reconstructed with the tracker, together with at least one HF tower with more than 3 GeV total energy on each side. The event selection efficiency was estimated with simulated events using the PYTHIA[6] and PHOJET[7,8] event generators. The measurements were corrected for the selection efficiency of NSD processes and for the fraction of SD events contained in the data sample after the event selection.

The $dN_{\rm ch}/d\eta$ distributions were obtained with three methods based on counting (i) reconstructed clusters in the barrel part of the pixel detector; (ii) pixel tracklets composed of pairs of clusters in different pixel barrel layers; and (iii) tracks reconstructed in the full tracker volume. The latter method also allows a measurement of the $dN_{\rm ch}/dp_{\rm T}$ distribution. The three methods are sensitive to particles down to $p_{\rm T}$ values of about 30, 50 and 100 MeV/c, respectively, and a correction was applied to the final results of the three methods to extrapolate to $p_{\rm T} = 0$. The measurements were corrected for the geometrical acceptance, efficiency, fake and duplicate tracks, low-$p_{\rm T}$ particles curling in the axial magnetic field, decay products of long-lived hadrons, photon conversions and inelastic hadronic interactions in the detector material. A more detailed description of the event selection and analysis methods can be found in Ref.[5].

3 Results

The $dN_{\rm ch}/dp_{\rm T}$ distributions of charged particles were measured in 12 different η bins, within $|\eta| < 2.4$. The average charged-hadron yields in NSD events are shown in Fig. 1(a), as a function of $p_{\rm T}$ and $|\eta|$. The Tsallis parametrization[9,10]:

$$E\frac{d^3N_{\rm ch}}{dp^3} = \frac{1}{2\pi p_T}\frac{E}{p}\frac{d^2N_{\rm ch}}{d\eta dp_T} = C\frac{dN_{\rm ch}}{dy}\left(1+\frac{E_T}{nT}\right)^{-n} \quad (1)$$

was fit to the data. The $p_{\rm T}$ spectrum of charged hadrons, $1/(2\pi p_{\rm T})d^2N_{\rm ch}/d\eta dp_{\rm T}$, measured in the range $|\eta| < 2.4$ is shown in Fig. 1(b). The fit to the data (Eq. 1) is mainly used for

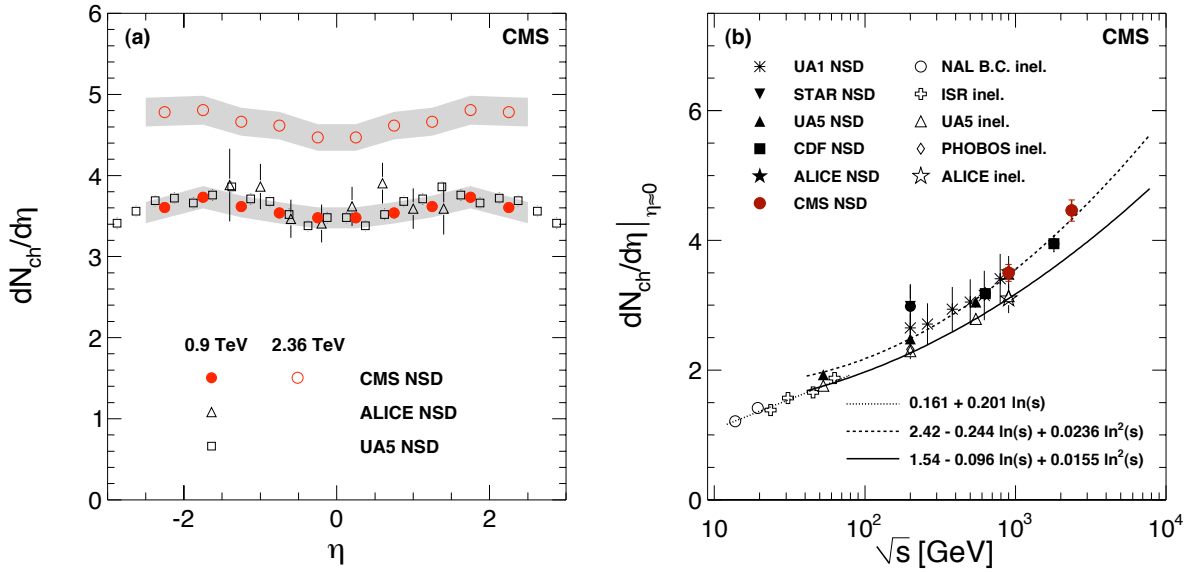

Figure 2: (a) Reconstructed $dN_{\rm ch}/d\eta$ distributions averaged over the cluster counting, tracklet and tracking methods (circles), compared to data from the UA5 (open squares) and from the ALICE (open triangles) experiments at 0.9 TeV, and the averaged result over the three methods at 2.36 TeV (open circles). The CMS and UA5 data points are symmetrized in η. The shaded band represents systematic uncertainties of this measurement, which are largely correlated point-to-point. The error bars on the UA5 and ALICE data points are statistical only. (b) Charged-hadron pseudorapidity density in the central region as a function of centre-of-mass energy in pp and p$\bar{\rm p}$ collisions including lower energy data, together with various empirical parameterizations fit to the data corresponding to the inelastic (solid and dotted curves with open symbols) and to the NSD (dashed curve with solid symbols) event selection. The error bars indicate systematic uncertainties, when available.

extrapolations to $p_{\rm T}$=0, but is not expected to give a perfect description of the data in all η bins with only two parameters. For the 0.9 TeV data, the inverse slope parameter and the exponent were found to be $T = 0.13 \pm 0.01$ GeV and $n = 7.7 \pm 0.2$. For the 2.36 TeV data, the values were $T = 0.14 \pm 0.01$ GeV and $n = 6.7 \pm 0.2$. The average transverse momentum, calculated from the measured data points adding the low- and high-$p_{\rm T}$ extrapolations from the fit is $\langle p_{\rm T} \rangle = 0.46 \pm 0.01$ (stat.) $\pm$ 0.01 (syst.) GeV/c for the 0.9 TeV and 0.50 ± 0.01 (stat.) $\pm$ 0.01 (syst.) GeV/c for the 2.36 TeV data. The summary of results on the pseudorapidity density distribution of charged hadrons is shown in Fig. 2. The results from the three different analysis methods are in agreement and are combined to form the final measurement. The resulting $dN_{\rm ch}/d\eta$ distributions are shown in Fig. 2a for $\sqrt{s}$ = 0.9 and 2.36 TeV and are compared to measurements by other experiments. The shaded error band on the CMS data indicates systematic uncertainties, while the error bars on the data from UA5 [14] and ALICE [16] display statistical uncertainties only. For $|\eta| < 0.5$, the corrected results average to $dN_{\rm ch}/d\eta = 3.48 \pm 0.02$ (stat.) $\pm$ 0.13 (syst.) and $dN_{\rm ch}/d\eta = 4.47 \pm 0.04$ (stat.) $\pm$ 0.16 (syst.) for NSD events at $\sqrt{s}$ = 0.9 and 2.36 TeV. The collision energy dependence of the measured $dN_{\rm ch}/d\eta|_{\eta \approx 0}$ is shown in Fig. 2b, which includes data from the NAL Bubble Chamber [12], the ISR [13], and UA1 [11], UA5 [14], CDF [15], STAR [17], PHOBOS [18] and ALICE [16]. The $dN_{\rm ch}/d\eta$ measurement reported here is consistent with the previously observed trend.

4 Summary

Inclusive measurements of charged-hadron densities, $dN_{\rm ch}/dp_{\rm T}$ and $dN_{\rm ch}/d\eta$, have been presented based on the first pp collisions recorded at $\sqrt{s}$ = 0.9 and 2.36 TeV by the CMS experiment.

For NSD interactions, the average charged-hadron transverse momentum has been measured to be 0.46 ± 0.01 (stat.) $\pm$ 0.01 (syst.) GeV/c at 0.9 TeV and 0.50 ± 0.01 (stat.) $\pm$ 0.01 (syst.) GeV/c at 2.36 TeV. The pseudorapidity density in the central region, $dN_{\rm ch}/d\eta|_{|\eta|<0.5}$, has been measured to be 3.48 ± 0.02 (stat.) $\pm$ 0.13 (syst.) at 0.9 TeV and 4.47 ± 0.04 (stat.) $\pm$ 0.16 (syst.) at 2.36 TeV. The results at 0.9 TeV have been found to be in agreement with previous measurements in $\rm p\bar{p}$ and pp collisions. The increase of $(28.4 \pm 1.4 \pm 2.6)\%$ from 0.9 to 2.36 TeV is significantly larger than the 18.5% (14.5%) increase predicted by the PYTHIA (PHOJET) model tunes used in this analysis.

Acknowledgments

We congratulate and express our gratitude to our colleagues in the CERN accelerator departments for the excellent performance of the LHC. We thank the technical and administrative staff at CERN and other CMS institutes, and acknowledge support from: FMSR (Austria); FNRS and FWO (Belgium); CNPq, CAPES, FAPERJ, and FAPESP (Brazil); MES (Bulgaria); CERN; CAS, MoST, and NSFC (China); COLCIENCIAS (Colombia); MSES (Croatia); RPF (Cyprus); Academy of Sciences and NICPB (Estonia); Academy of Finland, ME, and HIP (Finland); CEA and CNRS/IN2P3 (France); BMBF, DFG, and HGF (Germany); GSRT (Greece); OTKA and NKTH (Hungary); DAE and DST (India); IPM (Iran); SFI (Ireland); INFN (Italy); NRF and WCU (Korea); LAS (Lithuania); CINVESTAV, CONACYT, SEP, and UASLP-FAI (Mexico); PAEC (Pakistan); SCSR (Poland); FCT (Portugal); JINR (Armenia, Belarus, Georgia, Ukraine, Uzbekistan); MST and MAE (Russia); MSTDS (Serbia); MICINN and CPAN (Spain); Swiss Funding Agencies (Switzerland); NSC (Taipei); TUBITAK and TAEK (Turkey); STFC (United Kingdom); DOE and NSF (USA).

References

1. L. Evans, (ed.) and P. Bryant, (ed.), *JINST* **3** (2008) S08001.
2. **CMS** Collaboration, "The CMS experiment at the CERN LHC," S. Chatrchyan et al., *JINST* **3** (2008) S08004.
3. W. Kittel and E. A. De Wolf, "Soft Multihadron Dynamics". (World Scientific, Singapore, 2005).
4. **Geant4** Collaboration, S. Agostinelli et al., *Nucl. Instrum. and Methods* **A506** (2003) 250.
5. **CMS** Collaboration, V. Khachatryan et al., JHEP **1002**, (2010) 041.
6. T. Sjöstrand, S. Mrenna, and P. Skands, "PYTHIA 6.4 Physics and Manual; v6.420, tune D6T," *JHEP* **05** (2006) 026.
7. F. W. Bopp, R. Engel, and J. Ranft, `arXiv:hep-ph/9803437v1`.
8. R. Engel, J. Ranft, and S. Roesler, *Phys. Rev.* **D52** (1995) 1459.
9. C. Tsallis, *J. Stat. Phys.* **52** (1988) 479.
10. G. Wilk and Z. Wlodarczyk, *Eur. Phys. J.* **A40** (2009) 299.
11. **UA1** Collaboration, C. Albajar et al., *Nucl. Phys.* **B335** (1990) 261.
12. J. Whitmore, *Phys. Rept.* **10** (1974) 273.
13. **Aachen-CERN-Heidelberg-Munich** Collaboration, W. Thome et al., *Nucl. Phys.* **B129** (1977) 365.
14. **UA5** Collaboration, G. J. Alner et al., *Z. Phys.* **C33** (1986) 1.
15. **CDF** Collaboration, F. Abe et al., *Phys. Rev.* **D41** (1990) 2330.
16. **ALICE** Collaboration, K. Aamodt, *Eur. Phys. J.* **C65** (2010) 111.
17. **STAR** Collaboration, B. I. Abelev et al., *Phys. Rev.* **C79** (2009) 034909.
18. **PHOBOS** Collaboration, R. Nouicer et al., *J. Phys.* **G30** (2004) S1133.

ATLAS first results
Charged-particle multiplicities in pp interactions at $\sqrt{s} = 900$ GeV

W. H. Bell on behalf of the ATLAS Collaboration
Université de Genève, Section de Physique, 24 rue Ernest Ansermet, CH-1211 Geneve 4

The first physics results from pp collisions measured with the ATLAS detector [1] at the Large Hadron Collider (LHC) [2] are presented. The analysis within the kinematic range $p_{\mathrm{T}} > 500$ MeV, $|\eta| < 2.5$, and at least one charged-particle in this range, is summarised. The charged-particle multiplicity per event and unit of pseudorapidity at $\eta = 0$ is measured to be $1.333 \pm 0.003(\mathrm{stat.}) \pm 0.040(\mathrm{syst.})$, which is 5–15% higher than the Monte Carlo model predictions.

1 Introduction

The charged-particle spectra produced in inelastic pp and $p\bar{p}$ collisions have previously been studied over a wide range of centre-of-mass energies [3–10]. These experimental results have been used to tune phenomenological models of soft QCD interactions. Measurements of charged-particle multiplicities have been presented as inelastic, non-diffractive and non-single-diffractive results, with and without trigger and primary vertex reconstruction corrections. Results are most commonly presented as non-single-diffractive measurements. The selection of these events typically involves a double-arm coincidence trigger, where the remaining single-diffractive events are removed either with measurements from a single-arm trigger or by using a Monte Carlo model. In the cases where the trigger or vertex-reconstruction efficiencies have not been corrected for, it is difficult to determine the effects of these requirements at the particle-level. In general, previous measurements have included events with no charged particles within the acceptance of the tracking volume. These events may be accepted due to beam-induced-background, electronic noise, or inelastic interactions with no reconstructed tracks. Therefore, a Monte Carlo is used to determine the trigger efficiency, which introduces model dependence into these measurements.

These proceedings discuss the first ATLAS measurements of charged-particle multiplicities at 900 GeV [3], within the kinematic range $p_{\mathrm{T}} > 500$ MeV and $|\eta| < 2.5$ and the requirement of at least one charged-particle within this range. Primary charged particles were defined as charged particles with a mean lifetime $\tau > 0.3 \times 10^{-10}$ s directly produced in pp interactions or from subsequent decays of particles with a shorter lifetime. The distributions of tracks reconstructed in the ATLAS inner detector were corrected to obtain the particle-level distributions:

$$\frac{1}{N_{\mathrm{ev}}} \cdot \frac{\mathrm{d}N_{\mathrm{ch}}}{\mathrm{d}\eta}, \quad \frac{1}{N_{\mathrm{ev}}} \cdot \frac{1}{2\pi p_{\mathrm{T}}} \cdot \frac{\mathrm{d}^2 N_{\mathrm{ch}}}{\mathrm{d}\eta \mathrm{d}p_{\mathrm{T}}}, \quad \frac{1}{N_{\mathrm{ev}}} \cdot \frac{\mathrm{d}N_{\mathrm{ev}}}{\mathrm{d}n_{\mathrm{ch}}} \quad \text{and} \quad \langle p_{\mathrm{T}} \rangle \text{ vs. } n_{\mathrm{ch}},$$

where N_{ev} is the number of events with at least one charged-particle inside the selected kinematic range, N_{ch} is the total number of charged particles, n_{ch} is the number of charged particles in an event and $\langle p_{\mathrm{T}} \rangle$ is the average p_{T} for a given number of charged particles.

2 Event Selection

A total of 455,593 events were selected with a single-arm scintillator trigger covering the region of ($2.09 < |\eta| < 3.84$) at $z = \pm 3.56$ m from the centre of the detector. Tracks were reconstructed within the inner detector volume $|\eta| < 2.5$ from measurements within the silicon pixel detector (Pixel), silicon microstrip detector (SCT) and transition radiation tracker. Events were required to contain a reconstructed primary vertex fit from three or more $p_{\mathrm{T}} > 150$ MeV tracks with transverse impact parameter with respect to the beam-spot position $d_0^{\mathrm{BS}} < 4$ mm. Tracks were selected for the multiplicity measurements by requiring $p_{\mathrm{T}} > 500$ MeV, a minimum of one Pixel and six SCT hits, and transverse and longitudinal impact parameters calculated with respect to the primary vertex $d_0 < 1.5$ mm and $z_0 \cdot \sin\theta < 1.5$ mm respectively. The multiplicity of these selected tracks is denoted by n_{Sel}. Events were required to have one or more selected tracks.

3 Analysis and Results

The selected-track distributions were corrected back to the particle-level. The vertex-reconstruction efficiency was parameterized in terms of selected tracks with a requirement of $d_0^{\mathrm{BS}} < 4$ mm, matching the primary vertex fit preselection, and without requirements on the impact parameters with respect to the primary vertex. The multiplicity of these tracks within an event is denoted as $n_{\mathrm{Sel}}^{\mathrm{BS}}$. The trigger efficiency was defined in a similar manner, but from a sample selected with a control trigger. The trigger and vertex efficiency were derived from data and are illustrated in Fig. 1(a) and 1(b). The $n_{\mathrm{Sel}}^{\mathrm{BS}}$ value for a given event was used to select the trigger and vertex-reconstruction efficiency values. The selected tracks in the given event were then weighted by the reciprocal of the product of these two values. The trigger requirement was found to introduce no dependency on p_{T} or η. The small dependency introduced through the primary vertex requirement on the selected-track η for events with one selected-track was also corrected for.

The track-reconstruction efficiency was determined from a Geant4 simulation as a function of p_{T} and η and is illustrated in profile form in Fig. 1(c) and 1(d). The effects of this efficiency on the p_{T} and η distributions were corrected for on a track-wise basis by weighting each track with the reciprocal of the binned efficiency function. The track-weight also included a term for the fraction of secondary tracks as a function of p_{T} and tracks migrating into the selected kinematic range due to reconstruction resolution.

The charged-particle multiplicity (n_{ch}) was determined from the track multiplicity (n_{Sel}) on an event-by-event basis via Bayesian unfolding [11]. The n_{ch} spectrum was also corrected for the migration of events with $n_{\mathrm{ch}} \geq 1$ to $n_{\mathrm{Sel}} = 0$ by using a correction factor of the form $1/(1-(1-\epsilon(n_{\mathrm{ch}}))^{n_{\mathrm{ch}}})$, where $\epsilon(n_{\mathrm{ch}})$ is the mean track-reconstruction efficiency. Final results and the comparison with different Monte Carlo models and tunes are shown in Fig. 2.

4 Conclusions

The first ATLAS charged-particle multiplicity measurements from pp collisions at $\sqrt{s} = 900$ GeV have been discussed. Particle-level inclusive-inelastic distributions are presented within the kinematic range $p_{\mathrm{T}} > 500$ MeV and $|\eta| < 2.5$ and the requirement of at least one charged-particle within this range. The charged-particle multiplicity per event and unit of pseudorapidity at $\eta = 0$ is measured to be $1.333 \pm 0.003(\mathrm{stat.}) \pm 0.040(\mathrm{syst.})$, which is 5–15% higher than the Monte Carlo model predictions. The selected kinematic range, precision of this analysis, and the absence of additional model dependent corrections, highlights clear differences between Monte Carlo models and the measured distributions.

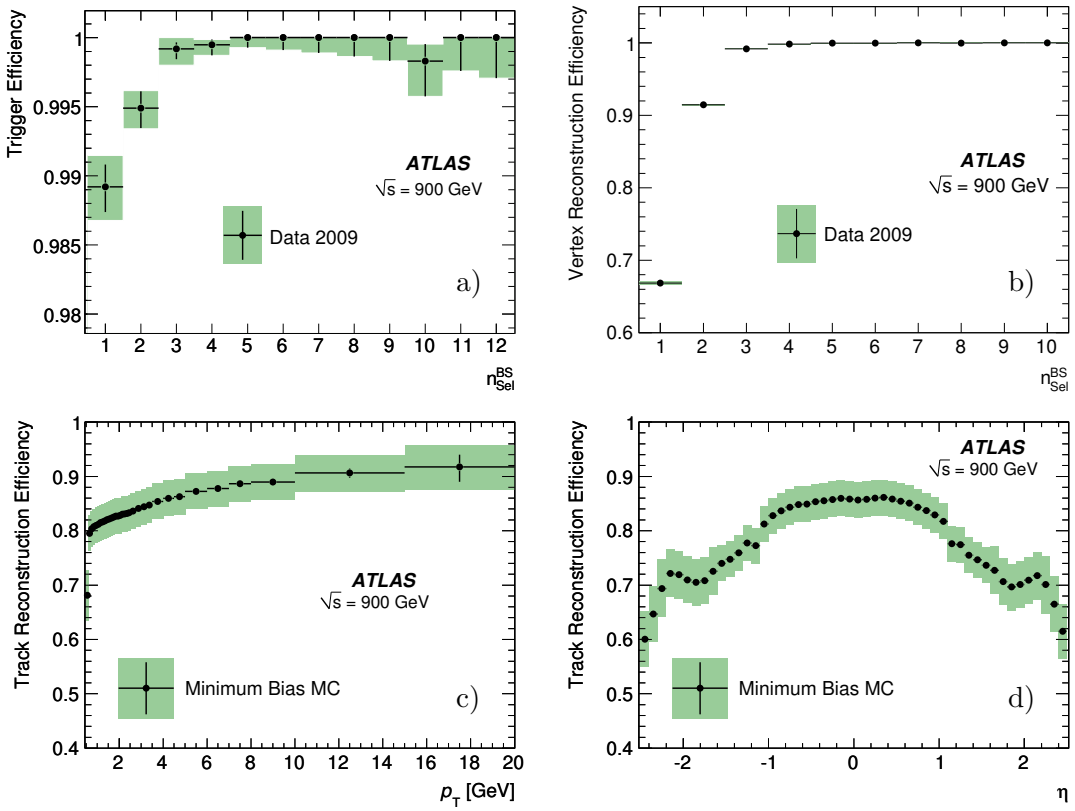

Figure 1: Trigger (a) and vertex-reconstruction (b) efficiencies as a function of $n^{\mathrm{BS}}_{\mathrm{Sel}}$ reconstructed tracks; track-reconstruction efficiency as a function of p_{T} (c) and of η (d). The vertical bars represent the statistical uncertainty, while the shaded areas represent the statistical and systematic uncertainties added in quadrature. The two bottom panels were derived from the PYTHIA ATLAS MC09 sample.

Acknowledgments

The work was undertaken within the framework of the ATLAS Collaboration. This paper presents results that were obtained from LHC *pp* collisions, using the ATLAS collaboration reconstruction and Geant4 simulation software. The author therefore thanks all of those involved in these areas of research, together with colleagues who contributed directly to the analysis presented.

References

1. G. Aad, et al. The ATLAS Collaboration. *JINST*, 3:S08003, 2008.
2. Lyndon Evans, (ed.) and Philip Bryant, (ed.). *JINST*, 3:S08001, 2008.
3. G. Aad, et al. The ATLAS Collaboration. *Phys. Lett.*, B688:21–42, 2010.
4. V. Khachatryan, et al. CMS Collaboration. *JHEP*, 02:041, 2010.
5. K. Aamodt, et al. ALICE Collaboration. *Eur. Phys. J.*, C65:111–125, 2010.
6. T. Aaltonen, et al. CDF Collaboration. *Phys. Rev.*, D79:112005, 2009.
7. T. Alexopoulos, et al. E735 Collaboration. *Phys. Lett.*, B336:599–604, 1994.
8. C. Albajar, et al. UA1 Collaboration. *Nucl. Phys.*, B335:261, 1990.
9. R. E. Ansorge, et al. UA5 Collaboration. *Z. Phys.*, C37:191–213, 1988.
10. A. Breakstone, et al. ABCDHW Collaboration. *Phys. Rev.*, D30:528, 1984.
11. G. D'Agostini. *Nucl. Instr. Meth.*, A362:487–498, 1995.

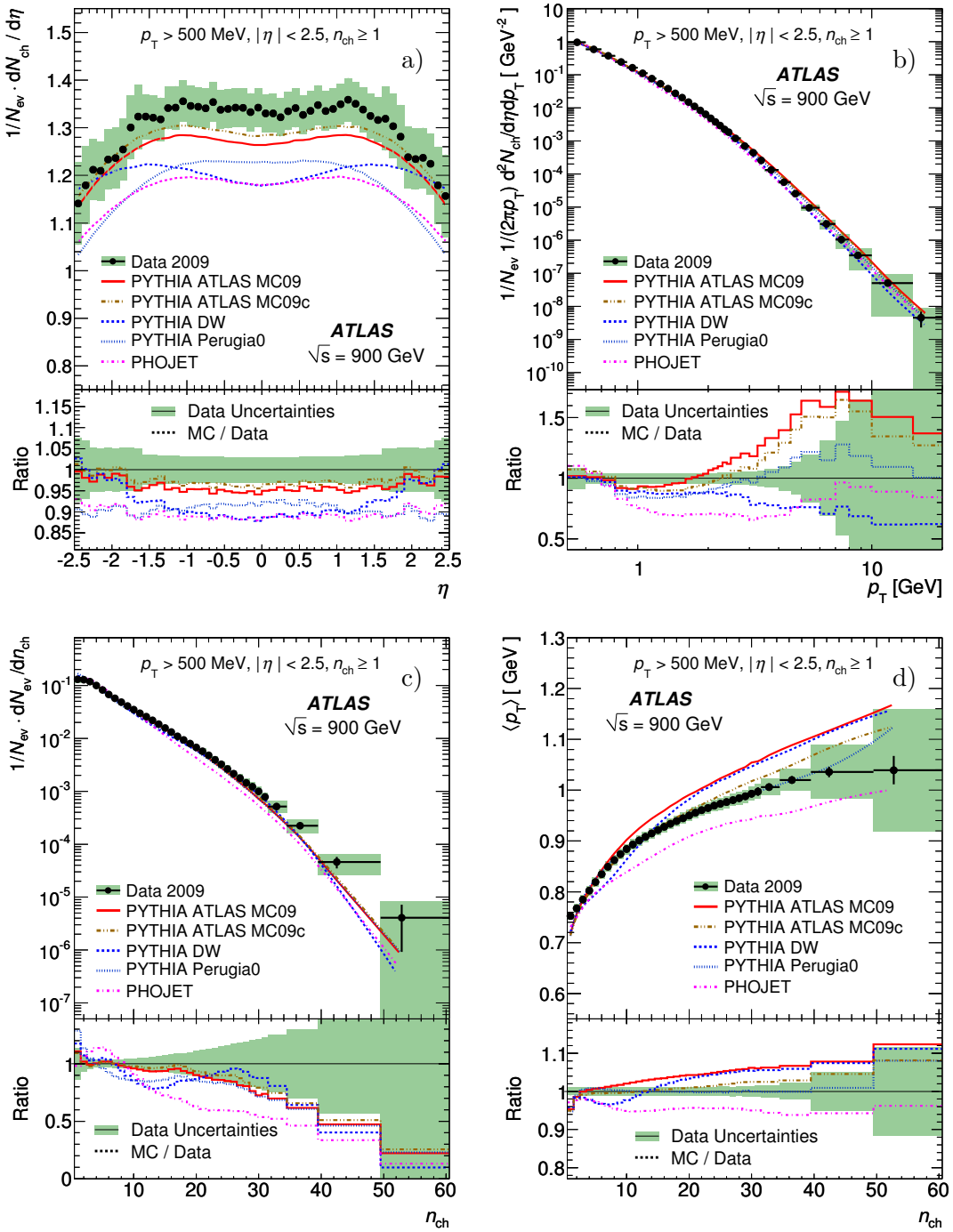

Figure 2: Charged-particle multiplicities for events with $n_{\mathrm{ch}} \geq 1$ within the kinematic range $p_{\mathrm{T}} > 500$ MeV and $|\eta| < 2.5$. The panels show the charged-particle multiplicity as a function of pseudorapidity (a) and of the transverse momentum (b), the charged-particle multiplicity (c), and the average transverse momentum as a function of the number of charged particles in the event (d). The dots represent the data and the curves the predictions from different MC models. The vertical bars represent the statistical uncertainties, while the shaded areas show statistical and systematic uncertainties added in quadrature. The values of the ratio histograms refer to the bin centroids.

2.
Heavy Flavours

THE LANDSCAPE OF FLAVOUR PHYSICS

Guy Wilkinson
University of Oxford, Denys Wilkinson Building, Keble Road, Oxford, OX1 3RH, United Kingdom

The importance of Flavour Physics as a method to search for non-Standard Model effects is explained. A brief summary is given of some of those topics in Flavour Physics where there are intriguing discrepancies between measurement and expectation. The prospects are discussed for the LHCb experiment in helping to make progress in these and other areas.

1 The Importance of Flavour Physics

There are many good reasons why flavour physics[a] will play a central role in high energy physics in the LHC era and beyond:

- Many of the open questions in the Standard Model (SM) are found in the flavour sector. Why are there three generations? What determines the extreme hierarchy of quark masses? What determines the elements and structure of the Cabibbo-Kobayashi-Maskawa (CKM) matrix? What is the origin of CP-violation (CPV)?
- Progress in flavour physics may have consequences for our understanding of cosmology, as it is well known that the CPV which can be accommodated in the SM is inadequate to explain the matter dominated universe that we observe.
- Flavour physics is a proven tool of discovery. The observed rate of kaon mixing and the suppressed decay $K_L^0 \to \mu^+\mu^-$ necessitated the construction of the GIM mechanism and hence predicted the existence of the charm quark. Explaining CPV in the kaon system within the SM required invoking a third quark generation. The first indication that the top quark was very massive followed from the observation of B-mixing.

It is the last point in particular which is worth stressing in this, the first full year of LHC operation. The LHC has been constructed to search for evidence of new physics (NP) at the TeV energy scale. As well as looking for direct production of new particles associated with this NP, however, an equally valid approach is to make precise measurements of processes which are suppressed in the SM and hope to discover deviations with respect to the SM predictions.

2 The Legacy of the B-factories

The B-factory experiments, BABAR and Belle, are close to finalising the analysis of their complete $\Upsilon(4S)$ datasets of ~ 400 fb^{-1} and ~ 700 fb^{-1} respectively. The results from these experiments, together with the measurement of B_s^0 mixing from the Tevatron, and that of ϵ_K in the

[a] In this review, given the nature of the conference, flavour physics is interpreted as hadronic flavour physics, although many of the arguments advanced apply equally well to leptons.

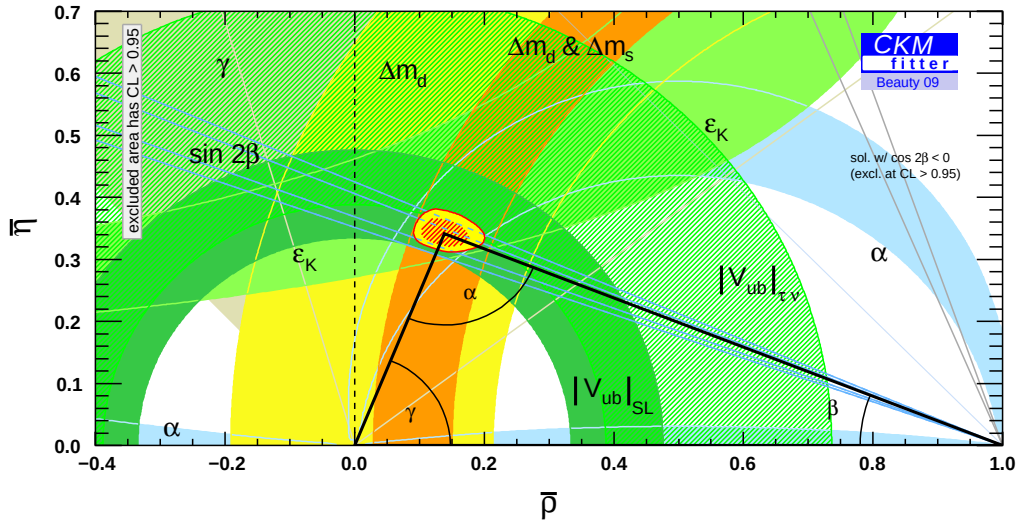

Figure 1: The CKM unitarity triangle, as drawn with inputs valid in Autumn 2009 [1].

kaon sector, tell a clear message - that the CKM-mechanism is the dominant source of CPV in nature, or at least those phenomena which make up the classical unitarity triangle, which is the usual way of assessing the consistency of the results within the CKM-paradigm. The present status of the unitarity triangle is shown in Fig. 1. All measurements are seen to be consistent with a single solution for the apex of the triangle.

The apparent self-consistency of the unitarity triangle, and the agreement of other flavour observables with Standard Model expectation (these include, for example, the D^0-mixing parameters x_D and y_D, where the SM predictions are very imprecise, but some NP models give values very different from those observed [2]), is frustrating for those who hoped for NP to be revealed by the B-factory programme. Indeed this fact is a priori surprising, as it contradicts the two commonly held beliefs that NP is present at the TeV scale, and that many flavour observables should in general be sensitive to the effects of this NP. Assuming that the former assumption is correct, one concludes that the NP must have a very specific flavour structure which has so far masked its discovery. An extreme possibility would be that the NP flavour couplings are pure-CKM and thus identical to the SM. Theories with this feature are classed as 'Minimal Flavour Vilolation' (MFV) models. MFV is unappealing to the experimental Flavour Physicist as it makes NP discovery very challenging indeed.

3 Hope in the Desert: Oasis or Mirage?

Are we then in the MFV desert with no hope of making a Flavour Physics measurement in contradiction with SM prediction? There are good reasons why we should not yet draw this conclusion. In particular there are already several observables where unexpected behaviour exists. Here we summarise some of the most intriguing:

- **Unitarity Triangle Tensions**
  The superficial consistency of the unitarity triangle masks certain internal 'tensions'. For example, comparison of the direct measurement of $\sin 2\beta$ with other triangle inputs shows far-from-perfect agreement. This feature can be looked at in various ways (see for example [3]). Figure 2 shows a comparison between the triangle apex as found by measurements of the B^0 mass splitting Δm_d and the $B^+ \to \tau^+ \nu_\tau$ branching ratio, and the prediction

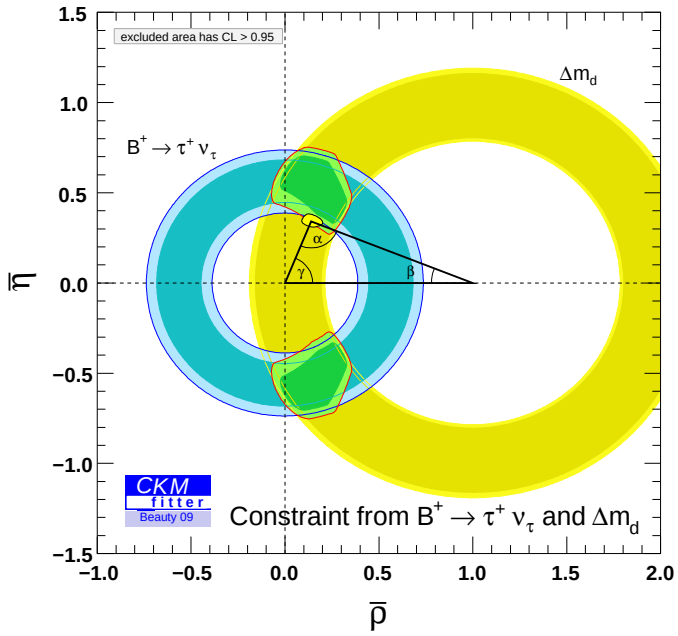

Figure 2: Comparison of the unitarity triangle apex as determined by Δm_d and the $B^+ \to \tau^+ \nu_\tau$, and from the global fit [1].

coming from the global fit. The poor consistency of the two approaches may point to the sub-dominant contribution of NP effects in one or more of the observables.

Whatever the source of this inconsistency, it is clear that it is important to improve significantly our experimental knowledge of the unitarity triangle, particularly of the poorly known parameters such as the angle γ. This need will become more acute as the uncertainties on lattice QCD inputs to the triangle fit decrease, as they are expected to do over the coming few years.

- **$B \to K\pi$ asymmetry puzzle**
  Tne naïve expectation is that the CP-asymmetry in the decay $B^\pm \to K^\pm \pi^0$ should be the same as that in $B^0, \bar{B}^0 \to K^\pm \pi^\mp$, however the measured values of the two asymmetries differ by over 5 sigma [4]. Some commentators believe this result can be explained by SM effects, such as large colour suppressed tree amplitudes [5], whereas others interpret it as a clear sign of NP, for example hinting at the existence of a fourth fermion generation [6].

  In order to make progress it will be necessary to make measurements in complementary channels. An improved measurement of the CP-asymmetry in $B^0, \bar{B}^0 \to K^0_S \pi^0$, presently measured with an uncertainty of ≈ 0.25 [4], will certainly clarify the situation [7], as will studies of modes such as $B \to \rho K$ and $K^* \pi$.

- **A_{FB} in $B \to K^* \ell^+ \ell^-$**
  The decay $B \to K^{(*)} \ell^+ \ell^-$, which proceeds through a $b \to s$ loop transition, is a system which provides a host of powerful observables which are sensitive to non-SM contributions [8,9], in particular the helicity structure of any NP couplings. One of the most interesting of these observables available in $B^0 \to K^{*0} \ell^+ \ell^-$ decays is the forward-backward asymmetry of the angle between the lepton and the B-meson in the di-lepton rest frame. This asymmetry is expected to evolve with, q^2, the invariant mass of the lepton pair in a

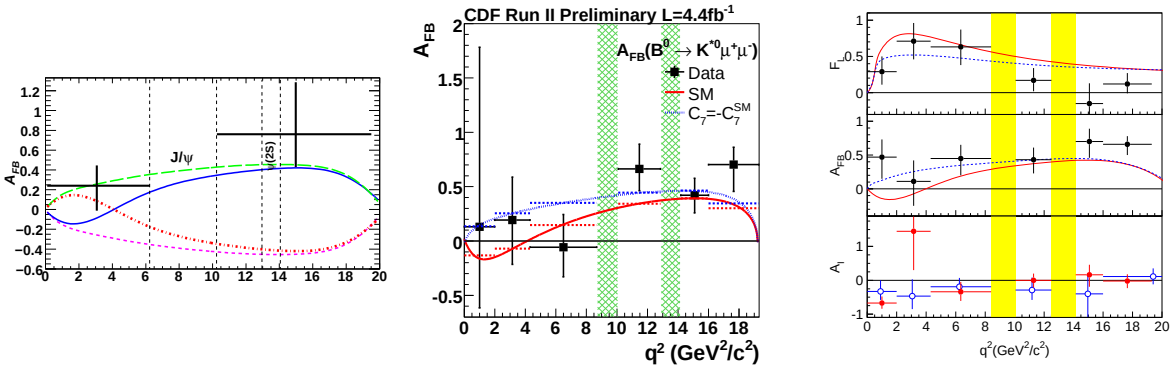

Figure 3: BABAR [11] (left), CDF [13] (middle) and Belle [12] (right centre) results for A_{FB} in $B^0 \to K^* \ell^+ \ell^-$ as a function of the invariant mass squared of the dilepton system. In all plots the charmonium resonance regions have been excluded, the solid curve (blue for BABAR, red for CDF and Belle) is the SM prediction and the higher dashed curve (green for BABAR, blue for CDF and Belle) is the expectation when the sign of the effective Wilson coefficient C_7^{eff} is swapped.

manner which differs between the SM and many New Physics scenarios. Too few of these decays ($\sim$ 450 in total) have so far been reconstructed at the B-factories and the Tevatron for any clear picture to emerge, but the early indications, shown in Fig. 3, are intriguing, with a tendency for the data to lie above the SM prediction.

- ϕ_s
  The mixing induced CP-violation in the decay $B_s^0 \to J/\psi$ is expected to be very small in the SM. Furthermore any NP phase appearing in the box-diagram which drives this observable, here (but not universally) designated ϕ_s, would be largely invisible to the unitarity triangle tests discussed in Sec. 2. For this reason the early results from the Tevatron [14] for this quantity have caused excitement, as they show consistency between CDF and D0, but a two sigma discrepancy with the SM prediction (see Fig. 4). [b]

4 Discovery Potential at LHCb

LHCb has been designed and constructed to take full advantage of the very high cross-section for heavy-flavour production at the LHC [17]. Even with the reduced collision energy of 7 TeV which is being used in the present run, a value of around 0.5 mb is expected for the $b\overline{b}$ cross-section, and around ten times higher for $c\overline{c}$ production [18]. LHCb is optimised for heavy-flavour physics: in particular it has a dedicated trigger system, a vertex detector which approaches to within 8 mm of the beamline, and two RICH detectors providing good π-K separation over a momentum range 2-100 GeV/c.

In December 2009 LHCb collected 6.8 ± 0.1 μb^{-1} of data at $\sqrt{s} = 0.9$ TeV in the LHC pilot run. These data were sufficient to establish that the fundamentals of the experiment work well. Figure 5 for example shows an attempt to form a $\phi \to K^+K^-$ signal without and then with RICH information. The effectiveness of the particle identification is evident. Shown in Fig. 6

[b] It should be remarked that since the conference new results from CDF have showed improved agreement with the SM [15]. On the other hand, a recent measurement from D0 on the flavour specific B_s^0 asymmetry [16], a different but related observable to ϕ_s, has shown a 3 σ excursion from expectation. The picture remains unclear.

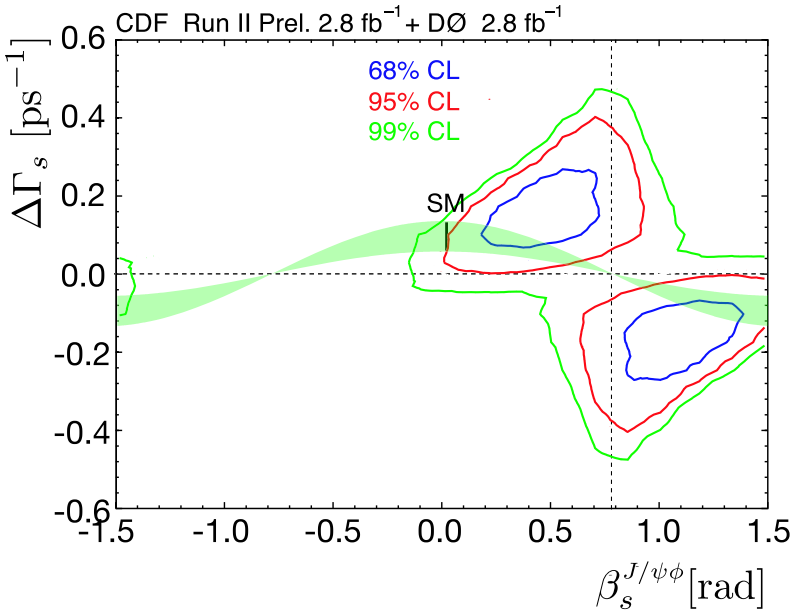

Figure 4: CDF and D0 combined profile likelihood as confidence contours of the CP-violating phase $\beta_s^{J/\psi\phi}$ in $B_s^0 \to J/\psi\phi$ (referred to as ϕ_s in the main text) and the width splitting between the mass eigenstates, $\Delta\Gamma_s$. The SM expectation and uncertainty is indicated by the black line. The sinusoidal green band indicates that region allowed in NP models. [14]

are K_S^0 and Λ (plus $\bar{\Lambda}$) signals also from the pilot run. Results are reported elsewhere at this conference from the first physics studies with LHCb data [19].

The physics programme of LHCb is aimed at making progress in many of the areas outlined in Sec. 3 [20]. In particular, with the 1 fb^{-1} of data expected in the 2010 run LHCb will:

- Begin to improve our knowledge of the unitarity triangle angle γ. The sensitivity with 10 fb^{-1} of data is estimated to be $\approx 2^\circ$ and so it is clear that significant measurements will already be possible with smaller datasets.
- Embark on a detailed study of charmless B-decays, collecting large samples of $B \to hh$ and $B \to 3h$ events.

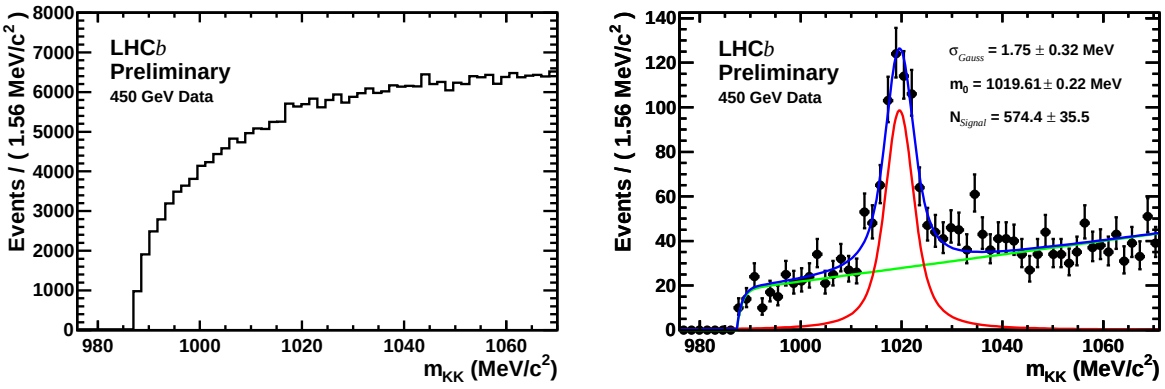

Figure 5: A reconstructed $\phi \to K^+K^-$ peak from the 2009 LHC run at $\sqrt{s} = 0.9$ TeV. Left: without RICH. Right: with RICH identification of both kaon candidates.

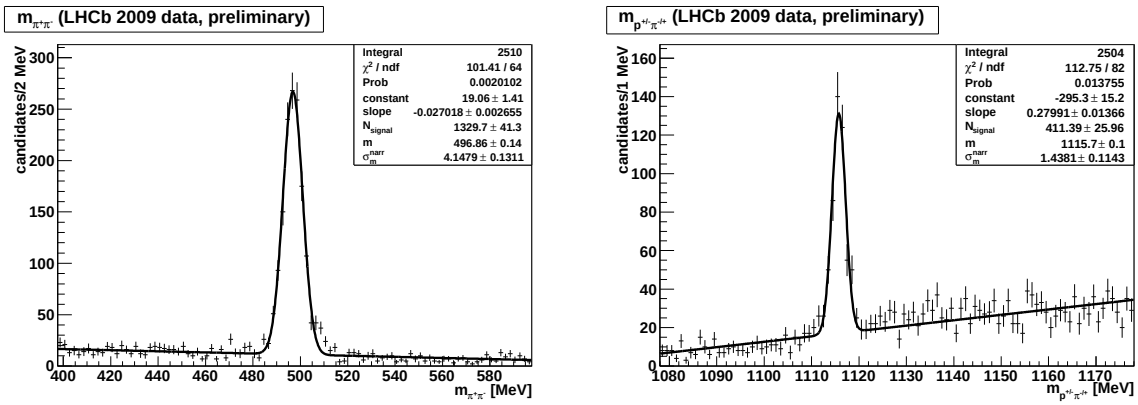

Figure 6: Reconstructed K^0_S and Λ (plus $\bar{\Lambda}$) signals from the 2009 LHC run at $\sqrt{s} = 0.9$ TeV.

- Collect a sample of $\sim$1200 $B^0 \to K^*\mu^+\mu^-$ events, which will be used to decide whether the intriguing behaviour in the existing A_{FB} results are more than a statistical fluctuation.

- Make a measurement of ϕ_s with a precision significantly better than the existing measurements at the Tevatron, and indeed better than the expected 'final' Tevatron measurements as projected from the present results (see Fig. 7).

In addition to these studies, LHCb will make important contributions to many other areas, not yet discussed, where NP effects could be visible. One of the most promising of these is the search for the very rare decay $B^0_s \to \mu^+\mu^-$. In the SM the branching ratio is both highly suppressed and precisely predicted ($\mathcal{B}(B^0_s \to \mu^+\mu^-) = (3.35 \pm 0.32) \times 10^{-9}$ [21]), whereas significant enhancements can occur in many NP models. Figure 8 shows how the 90% confidence level exclusion limit will evolve at LHCb as a function of integrated luminosity. It can be seen that sensitivity in the 10^{-9} regime should be achievable well before the end of 2011.

5 Conclusions

Studies of heavy flavour decays are an excellent way to search for NP effects. Furthermore, when NP is discovered, it will be necessary to characterise its flavour structure in order to understand its true nature. It has been seen that there already exist certain hints of non-SM behaviour in a variety of observables. LHCb, which began operation successfully in the LHC pilot run of late 2009, has the capabilities to advance our understanding in many of these areas. Beyond LHCb, other projects (not discussed here) will be able to achieve still higher sensitivities. These include an upgraded LHCb itself, as well as experiments at a very high luminosity e^+e^- 'super-flavour factory'.

Acknowledgments

I thank the organisers for hosting a very interesting conference in a beautiful location.

References

1. J. Charles *et al.* (CKMfitter group), Eur. Phys. J. **C 41** (2005) 1, updated results and plots available at : http://ckmfitter.in2p3.fr/ (results shown here as of 2009 Autumn).
2. E. Golowich *et al.*, Phys. Rev. **D 98** (2007) 095009.

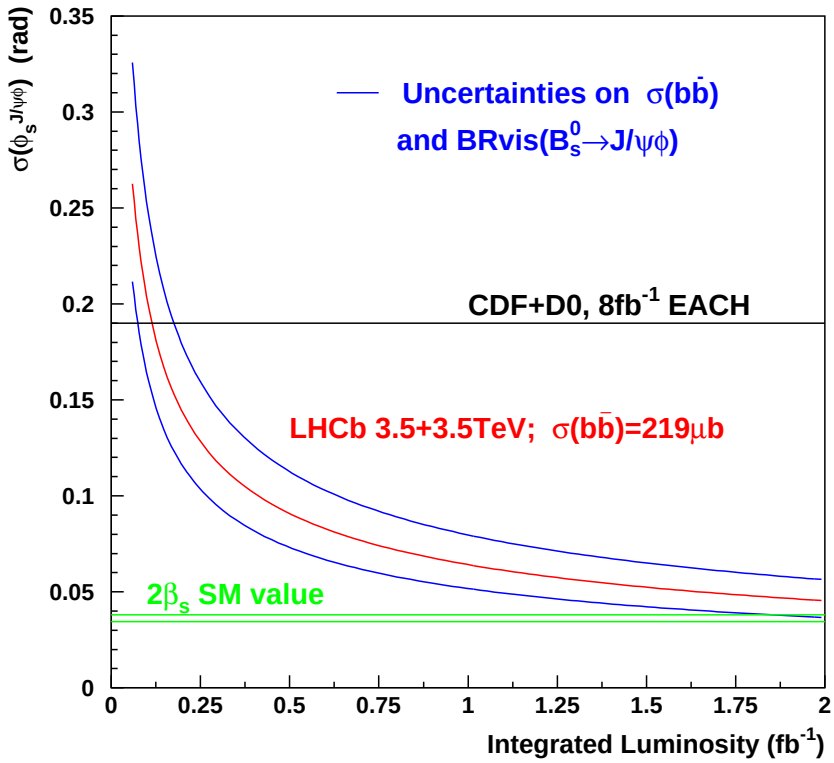

Figure 7: LHCb precision on ϕ_s using $B_s^0 \to J$ as a function of integrated luminosity. Also shown is the expected Tevatron precision with 8 fb^{-1} as extrapolated from the results which existed at the time of the conference.

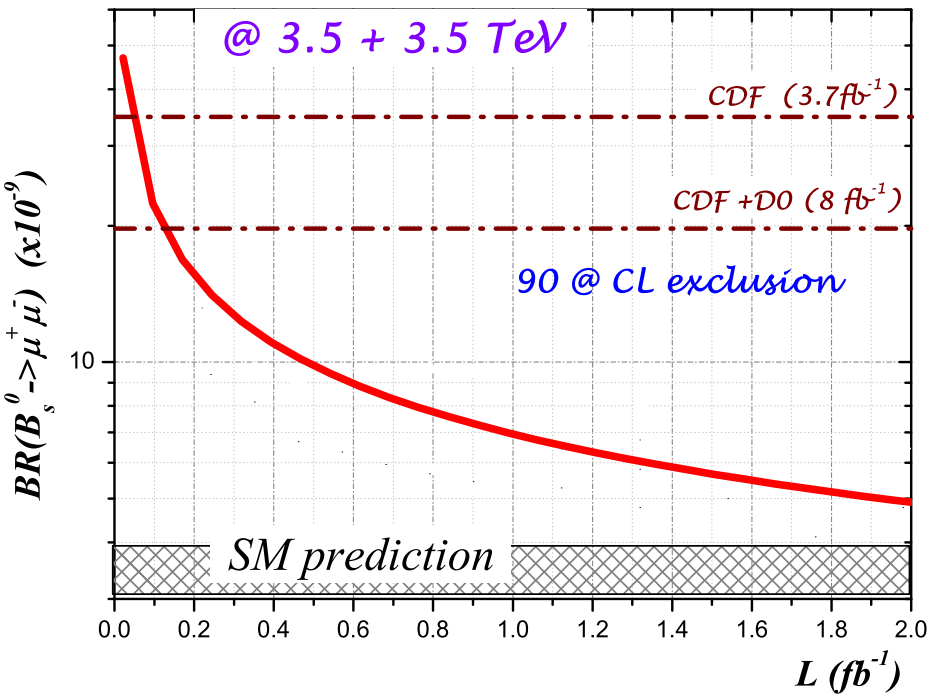

Figure 8: Expected exclusion limit for $B_s^0 \to \mu^+\mu^-$ as a function of integrated luminosity.

3. E. Lunghi and A. Soni, *Unitarity triangle without semileptonic decays*, arXiv:0912.0002 [hep-ph].
4. C. Amsler *et al.* (Particle Data Group), Phys. Lett. **B 667** (2008) 1.
5. M. Gronau and J.L. Rosner, Phys. Rev. **D 74** (2006) 057503.
6. A. Arhrib and W-S. Hou, Phys. Rev. **D 80** (2009) 076005.
7. M. Gronau, Phys. Lett. **B 627** (2005) 82.
8. A. Ali *et al.*, Phys. Lett. **B 273** (1991) 505.
9. F. Kruger and J. Mathias, Phys. Rev. **D 71** (2005) 094009.
10. B. Aubert *et al.* (BABAR Collaboration), Phys. Rev. Lett. **102** (2009) 091803.
11. B. Aubert *et al.* (BABAR Collaboration), Phys. Rev. **D 79** (2009) 031102.
12. J.T. Wei *et al.* (Belle Collaboration), Phys. Rev. Lett. **103** (2009) 171801.
13. CDF Collaboration, *Measurement of Forward-Backward Asymmetry in* $B \to K^{(*)}\mu^+\mu^-$ *and First Observation of* $B_S^0 \to \phi\mu^+\mu^-$, CDF note 10047.
14. CDF/D0 $\Delta\Gamma_s$, β_s Combination Working Group, *Combination of D0 and CDF Results on* $\Delta\Gamma_s$ *and the CP-Violating Phase* $\beta_s^{J/\psi\phi}$, CDF note 9787, D0 note 5928, July 2009.
15. L. Oakes (CDF Collaboration), *Measurement of* β_s *at CDF*, talk at FPCP 2010, May 2010, Torino.
16. V.M. Abazov *et al.* (D0 Collaboration), *Evidence for an anomalous like-sign dimuon charge asymmetry*, arXiv:1005.2757 [hep-ex].
17. A. Augusto Alves Jr. *et al.*, (LHCb Collaboration), JINST **3** (2008) S08005.
18. Results obtained with Pythia 6.4.
19. V. Balagura and M. Knecht, this conference; LHCb Collaboration, *Prompt* K_S^0 *production in pp collisions at* $\sqrt{s} = 900$ *GeV*, LHCb-CONF-2010-008.
20. B. Adeva *et al.* (LHCb Collaboration), *Roadmap for selected key measurements of LHCb*, arXiv:0912.4179 [hep-ex].
21. M. Blanke *et al.*, JHEP **10** (2006) 003.

MEASUREMENTS OF THE MASSES, LIFETIMES AND DECAY MODES OF HADRONS AT TEVATRON

M. DORIGO on behalf of the CDF and DØ collaborations
Department of Physics, University of Trieste,
and INFN, Trieste Section, Trieste, Italy

The Tevatron provides 1.96 TeV $p\bar{p}$ collisions and allows for collection of rich b-hadron samples to the two experiments CDF and DØ. The study of heavy flavor properties represents a fruitful opportunity to investigate the flavor sector of the Standard Model (SM) and to look for hints of New Physics (NP). Here we report the first measurement of polarization amplitudes in B_s^0 charmless decays, world leading results on b-hadron lifetimes, and measurements of several other properties of b-hadrons.

1 $B_s^0 \to \phi\phi$ polarization measurement

The $B_s^0 \to \phi\phi$ decay proceeds through a $b \to s\bar{s}s$ quark level process, whose dominant diagram is the $b \to s$ penguin: it is potentially sensitive to NP that could manifest itself through the presence of new particles in the penguin loop. In addition, the $B_s^0 \to \phi\phi$ is a decay of a pseudo-scalar meson to two vector mesons whose differential decay rate is determined by three independent amplitudes corresponding to different polarizations: one longitudinal (A_0) and two transverse, with spins parallel ($A_\parallel$) or perpendicular ($A_\perp$) to each other.[a] In the SM, $|A_0|^2 \gg |A_\parallel|^2 + |A_\perp|^2$ is naively expected in B decays to two light vector mesons.[1] This was experimentally confirmed by BaBar and Belle in tree-dominated transitions.[2] In contrast, it was found $|A_0|^2 \simeq |A_\parallel|^2 + |A_\perp|^2$ in $b \to s$ penguin decays.[3] In order to shed light on this "polarization puzzle" additional experimental information is required and $b \to s$ penguins in charmless B_s^0 decays are a promising opportunity. The $B_s^0 \to \phi\phi$ decay has been observed in its $K^+K^-K^+K^-$ final state for the first time by CDF in 2005 in 180 pb^{-1} of integrated luminosity: 8 events have been counted, and the branching ratio ($\mathcal{B}$) has been measured.[4] Recently, CDF presents an updated analysis with 2.9 fb^{-1} of data collected with the displaced track trigger.[5] The reconstructed signal events are $295 \pm 20(\text{stat}) \pm 12(\text{syst})$ and $\mathcal{B} = [2.40 \pm 0.21(\text{stat}) \pm 0.86(\text{syst})] \times 10^{-5}$, which is consistent with the previous result and with the theoretical prediction.[9]

We report the first polarization measurement of such decays using the same data set of the branching fraction update.[6] In this analysis, the untagged time-integrated decay rate as a function of three angular variables of the final state decay products is considered. The polarization amplitudes are corrected for the expected lifetime difference for the B_s^0 mass eigenstates using the world average B_s^0 lifetime and width difference,[7] and the tiny CP phase in B_s^0 mixing is neglected, as expected in the SM.[b, 7] Thus, a fit to the reconstructed B_s^0 mass and to the

[a] The three polarization amplitudes are constrained by the unitarity condition: $|A_0|^2 + |A_\parallel|^2 + |A_\perp|^2 = 1$.

[b] Anyway, the effect related to a possible non vanishing CP-violating phase in mixing at a level consistent with the current world average is included in the systematic treatment.

decay product angular distributions is performed. The approach is validated by performing a similar measurement using $B_s^0 \to J/\psi\phi$ decays, collected via the same trigger, and comparing the obtained results with the current experimental information on the polarization in such a decay.[8] The measured polarization amplitudes and the cosine of $\delta_\parallel = \arg(A_0^\star A_\parallel)$ are: $|A_0|^2 = 0.348 \pm 0.041(\text{stat}) \pm 0.021(\text{syst})$, $|A_\parallel|^2 = 0.287 \pm 0.043(\text{stat}) \pm 0.011(\text{syst})$, $|A_\perp|^2 = 0.365 \pm 0.044(\text{stat}) \pm 0.027(\text{syst})$ and $\cos\delta_\parallel = -0.91^{+0.15}_{-0.13}(\text{stat}) \pm 0.09(\text{syst})$. This measurement indicates that the expected amplitudes hierarchy is disfavored in this charmless B_s^0 decay, being $|A_0|^2 < |A_\parallel|^2 + |A_\perp|^2$. The plot in Fig. 1 (a) shows the estimates point for $f_0 = |A_0|^2$ versus $f_\parallel = |A_\parallel|^2$ compared with the prediction of different theoretical models developed in the SM.[9,10]

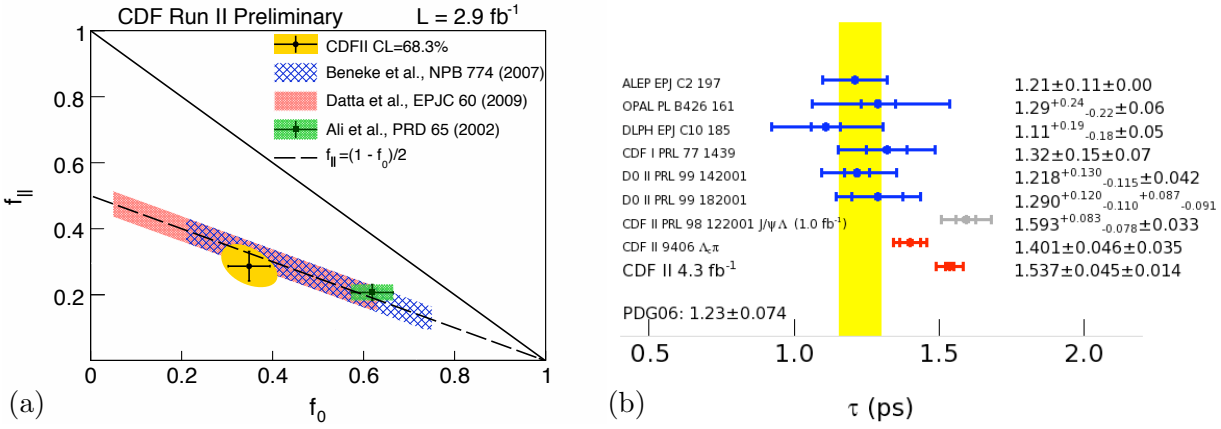

Figure 1: (a) Comparison between the $B_s^0 \to \phi\phi$ polarization measurement and several theoretical predictions. (b) Λ_b^0 lifetime: comparison between the new result and selected previous measurements.

2 Lifetimes

The lifetime of the ground state hadrons containing a b quark and lighter quarks is largely determined by the charged weak decay of the b quark. Ignoring the lighter quarks in the hadron, the spectator model predicts equal lifetimes for all b-hadrons. However, several effects change these expectations by up to about 10%. The lifetime ratio $\tau(B^+)/\tau(B^0)$ is predicted to be in the range 1.04–1.08;[11] for the $\tau(\Lambda_b^0)/\tau(B^0)$ the range is wider, from 0.83 to 0.93.[12]

Using a 4.3 fb^{-1} data sample, CDF searches for fully reconstructed b-hadron decays with a J/ψ decaying to muon pairs: $B^+ \to J/\psi K^+$, $B^0 \to J/\psi K^{0\star}$, $B^0 \to J/\psi K_S^0$ and $\Lambda_b^0 \to J/\psi\Lambda^0$.[13] The data are collected by the dimuon trigger, which has no biasing effects on the observed proper time distribution. The analysis consists of a maximum likelihood fit to the mass, the proper decay time and the proper decay time uncertainty of the reconstructed candidates. The measured lifetimes are reported in Tab. 1: they are the most precise determination of the B^+, B^0 and Λ_b^0 lifetimes. Several systematic uncertainties have been studied with Monte Carlo samples; while the overall systematic uncertainties remain small, the uncertainty on the extracted lifetime values is dominated by the silicon detector alignment uncertainty in the case of B mesons and by the resolution effects in the case of the Λ_b^0. A cancellation of some common systematic uncertainties in the lifetime ratios is achieved by using the vertex of the two tracks from the J/ψ, common to all decay modes, as an estimate of the transverse decay length.[c]

The Λ_b^0 lifetimes measurement has particular interest (see Fig. 1 (b)): until 2006 all measurements were in agreement and lay at the lower end of the theoretically expected value. Then,

[c] The transverse decay length is the projection of the decay lenght in the plane transverse to the beam.

CDF performed two high precision measurements [14] which are significantly above previous results; this is confirmed by the latest result here reported.

Table 1: Lifetime measurements of b-hadrons.

Hadron	Lifetime [ps]	Lifetime ratio (over $\tau(B^0)$)	PDG 08 [ps]
B^+	$1.639 \pm 0.009(\text{stat}) \pm 0.009(\text{syst})$	$1.088 \pm 0.009(\text{stat}) \pm 0.004(\text{syst})$	1.638 ± 0.011
B^0	$1.507 \pm 0.010(\text{stat}) \pm 0.008(\text{syst})$	1	1.530 ± 0.009
Λ_b^0	$1.537 \pm 0.045(\text{stat}) \pm 0.014(\text{syst})$	$1.020 \pm 0.030(\text{stat}) \pm 0.008(\text{syst})$	$1.383^{+0.049}_{-0.048}$

3 $\Lambda_b^0 \to \Lambda_c^+\pi^-\pi^+\pi^-$ resonance structure

Since CDF has recently observed the resonant structure in the $\Lambda_b^0 \to \Lambda_c^+\pi^-\pi^+l^-\nu$ decay mode,[15] a similar resonance structure is expected in the corresponding hadronic decay mode $\Lambda_b^0 \to \Lambda_c^+\pi^-\pi^+\pi^-$, where the $l^-\nu$ pair is replaced by a ud quarks pair.

Last year CDF performed an analysis aimed at the first observation of the $\Lambda_b^0 \to \Lambda_c^+\pi^-\pi^+\pi^-$ and of the following intermediate resonant states: $\Lambda_c(2595)^+\pi^-$, $\Lambda_c(2625)^+\pi^-$, $\Sigma_c(2455)^{++}\pi^-\pi^-$ and $\Sigma_c(2455)^0\pi^+\pi^-$. The analysis uses an integrated luminosity of 2.4 fb^{-1} of data collected by the CDF trigger on two displaced tracks. The Λ_c^+ is reconstructed in the $pK^-\pi^+$ decay mode and three tracks, assumed to be pions, are added to reconstruct the $\Lambda_b^0 \to \Lambda_c^+\pi^-\pi^+\pi^-$. The relative branching fractions of the resonant states to the total ($\mathcal{B}_{\text{rel}}$) are measured using the yields of each decay mode estimated by fitting the data mass distributions. The final results are listed in Tab. 2.

Table 2: $\Lambda_b^0 \to \Lambda_c^+\pi^-\pi^+\pi^-$ resonance structure: yields and branching fractions.

Λ_b^0 decay mode	Yield	$\mathcal{B}_{\text{rel}}$ in 10^{-2}
$\Lambda_b^0 \to \Lambda_c(2595)^+\pi^-$	$46.6 \pm 9.7(\text{stat})$	$2.5 \pm 0.6(\text{stat}) \pm 0.5(\text{syst})$
$\Lambda_b^0 \to \Lambda_c(2625)^+\pi^-$	$114 \pm 13(\text{stat})$	$6.2 \pm 1.0(\text{stat})^{+1.0}_{-0.9}(\text{syst})$
$\Lambda_b^0 \to \Sigma_c(2455)^{++}\pi^-\pi^-$	$81 \pm 15(\text{stat})$	$5.2 \pm 1.1(\text{stat}) \pm 0.8(\text{syst})$
$\Lambda_b^0 \to \Sigma_c(2455)^0\pi^+\pi^-$	$41.5 \pm 9.3(\text{stat})$	$8.9 \pm 2.1(\text{stat})^{+1.2}_{-1.0}(\text{syst})$

4 Masses: the Ω_b^- observation

The quark model predicts a rich spectrum of baryons containing b quarks.[17] In 2007, the accumulation of large data sets from the Tevatron allowed the first observation of new baryons, the Ξ_b^- and the $\Sigma_b^{(\star)}$.[18,19] The Ω_b^- is the latest observed of such heavy states: in 2008, DØ made its discovery using 1.3 fb^{-1} of data,[20] while CDF observed it last year in 4.2 fb^{-1}.[21] In both cases, the Ω_b^- observation is made through the decay chain $\Omega_b^- \to J/\psi\Omega^-$, where $J/\psi \to \mu^+\mu^-$, $\Omega^- \to \Lambda K^-$, and $\Lambda \to p\pi^-$.[d] However, the two experiments measure a Ω_b^- mass in significant disagreement. The DØ analysis is built on the Ξ_b^- discovery;[18] a yield of $17.8 \pm 4.9(\text{stat}) \pm 0.8(\text{syst})$ Ω_b^- events is extracted, with a significance of 5.4 Gaussian standard deviations that the observed peak is not due to background fluctuations. The estimated Ω_b^- mass is $6165 \pm 10(\text{stat}) \pm 13(\text{syst})$ MeV/c^2.

In the Ω_b^- observation, in addition to its mass, CDF measures for the first time its lifetime. Moreover, in the same analysis, CDF updates the Ξ_b^- mass measurement and performs its first lifetime measurement.[e] CDF measures the Ω_b^- mass, $m = 6054.4 \pm 6.8(\text{stat}) \pm 0.9(\text{syst})$ MeV/c^2, and lifetime, $\tau = 1.13^{+0.53}_{-0.40}(\text{stat}) \pm 0.02(\text{syst})$ ps, using a signal of $16^{+6}_{-4}(\text{stat})$ (5.5 σ significance),

[d] Charge conjugate modes are included implicitly.

[e] Using the decay chain $\Xi_b^- \to J/\psi\Xi^-$, where $J/\psi \to \mu^+\mu^-$, $\Xi^- \to \Lambda\pi^-$, and $\Lambda \to p\pi^-$.

and the Ξ_b^- mass, $m = 5790.9 \pm 2.6(\text{stat}) \pm 0.8(\text{syst})$ MeV/c^2, and lifetime, $\tau = 1.56^{+0.27}_{-0.25}(\text{stat}) \pm 0.02(\text{syst})$ ps. The small systematic uncertainties in the CDF measurements are due to the ability to reconstruct the actual trajectory of the long-lived hyperons from their hits in the silicon tracker.

The disagreement between the CDF and DØ Ω_b^- mass measurements consists of about six standard deviations. In addition, the measured Ω_b^- production rates relative to the Ξ_b are different between the two experiments, being $f_{\text{CDF}} = 0.27 \pm 0.12(\text{stat}) \pm 0.01(\text{syst})$ and $f_{\text{D}\emptyset} = 0.80 \pm 0.32(\text{stat})^{+0.14}_{-0.22}(\text{syst})$. Neither measurement is very precise; nevertheless, CDF indicates a rate substantially lower than DØ. The mass obtained by CDF agrees with theoretical estimates.[17] Clearly, further studies are needed to resolve the discrepancies and analysis updates are ongoing with the addition of new available data.

5 Conclusions

In the latest years, the CDF and DØ heavy flavor programs reached maturation, yielding results that are competitive to the B factories ones for the $B^{\pm}$ and B^0 properties measurement, and complementary to them for the study of the b-baryons and the B_s^0 meson. We presented here a small sampling of recent results, including the first measurement of decay-polarization structure in a charmless B_s^0 decay, world-leading measurements of b-hadron lifetimes, the structure study of a Λ_b^0 hadronic decay mode and the observation of the Ω_b^- baryon. These are obtained using just a fraction of the presently available data-samples, which keep increasing at a pace of 70 pb^{-1} per week. The large amount of data, and ever improving analysis technique suggest a few years of exciting competition with the LHCb experiment that has just started its operations.

References

1. H. Y. Cheng *et al.*, *Phys. Rev.* D **65**, 094023 (2002); M. Suzuki, *ibid.* **64**, 117503 (2001).
2. B. Aubert *et al.*, *Phys. Rev. Lett.* **98**, 111801 (2007); A. Somov *et al.*, *ibid.* **96** 171801 (2006);
3. P. Goldenzweig *et al.*, *Phys. Rev. Lett.* **101**, 231801 (2008); B. Aubert *et al.*, *ibid.* **99**, 201802;
4. D. Acosta *et al.*, *Phys. Rev. Lett.* **95**, 031801 (2005).
5. CDF Collaboration, CDF Public Note 10064 (2010).
6. CDF Collaboration, CDF Public Note 10120 (2010).
7. C. Amsler *et al.*, (Particle Data Group) *Phys. Lett.* B **667** 1 (2008), and 2009 partial update.
8. T. Aaltonen *et al.*, *Phys. Rev. Lett.* **100**, 121803 (2008).
9. M. Beneke *et al.*, *Nucl. Phys.* B **774** 64-101 (2007);
10. A. Datta *et al.*, *Eur. Phys. J.* C **60** 279-284 (2009); A. Ali *et al.*, *Phys. Rev.* D **76**, 074018 (2007).
11. C. Tarantino, *Eur. Phys. J.* C **33**, S895 (2004); F. Gabbiani *et al.*, *Phys. Rev.* D **70** 094031 (2004); I. I. Bigi *et al.*, in *B Decays*, ed. S. Stone (World Scientific, Singapore, 1994); I. I. Bigi *et al.*, *Phys. Lett.* B **280** (1992) 271.
12. I. I. Bigi *et al.*, *Ann. Rev. Nucl. Part. Sci.* **47** 591-661 (1997); M. Neubert *et al.*, *Nucl. Phys.* B **483** (1997) 339; G. Bellini *et al.*, *Phys. Rept.* 289 (1997) 1; P. Colangelo *et al.*, *Phys. Lett.* B **387** (1996) 307; N. Uraltsev, *Phys. Lett.* B **376** (1996) 303.
13. CDF Collaboration, CDF Public Note 10071 (2010).
14. A. Abulencia *et al.*, *Phys. Rev. Lett.* **98**, 122001; T. Aaltonen*et al.*, *ibid.* **104**, 102002 (2010).
15. T. Aaltonen *et al.*, *Phys. Rev.* D **79**, 032001 (2009).
16. CDF Collaboration, CDF Public Note 10001 (2009).
17. E. Jenkins, *Phys. Rev.* D **77**, 034012 (2008); R. Lewis *et al.*, *ibid.* **79**, 014502 (2009); D. Ebert *et al.*, *ibid.* **72**, 034026 (2005); M. Karliner *et al.*, *Ann. Phys.* (N.Y.) **324**, 2 (2009); A. Valcarce *et al.*, Eur. Phys. J. A **37**, 217 (2008).
18. V.M. Abazov *et al.*, *Phys. Rev. Lett.* **99**, 052001; T. Aaltonen *et al.*, *Phys. Rev. Lett.* **99**, 052002.
19. T. Aaltonen *et al. Phys. Rev. Lett.* **99**, 202001 (2007).
20. V.M. Abazov *et al.*, *Phys. Rev. Lett.* **101**, 232002 (2008).
21. T. Aaltonen *et al. Phys. Rev.* D **80**, 072003 (2009).

CLEO RESULTS ON CHARM LEPTONIC AND SEMILEPTONIC DECAYS

S. STONE
Department of Physics, Syracuse University,
Syracuse, NY, 13244, USA

1 Introduction

Here I will review a small selection of recent CLEO results on purely leptonic and semileptonic decays mostly of the D_s^+ meson. In leptonic decays the quark and antiquark in the meson annihilate via a virtual W that materializes as a lepton (ℓ) anti-neutrino pair. To lowest order, the decay width is given by

$$\Gamma(P \to \ell\nu) = \frac{G_F^2}{8\pi} f_P^2 \; m_\ell^2 M_P \left(1 - \frac{m_\ell^2}{M_P^2}\right)^2 |V_{q_1 q_2}|^2 \;\; , \tag{1}$$

where M_P is the P mass, m_ℓ is the ℓ mass, $V_{q_1 q_2}$ is the Cabibbo-Kobayashi-Maskawa (CKM) matrix element between the constituent quarks $q_1\bar{q}_2$ in P, and G_F is the Fermi coupling constant. The parameter f_P is the decay constant, the quantity to be measured or calculated, that is related to the wave-function overlap of the quark and antiquark.

2 Leptonic Decays

Near 4.170 GeV in center-of-mass energy e^+e^- collisions produce $D_s D_s^*$ pairs with about a 1 nb cross-section. The presence of the $D_s^* \to \gamma D_s$ transition makes the analysis of D_s^+ decays somewhat more complicated than studies at 3.770 GeV where D^+D^- and $D^0\overline{D^0}$ pairs are produced.

To study D^+ decays we fully reconstruct a D^- and then we use the conservation of energy and momentum to infer the presence of a missing neutrino in $D^+ \to \ell^+\nu$ (leptonic) or $D^+ \to h\ell^+\nu$ (semileptonic) decays. This is done by calculating the missing mass squared as

$$\mathrm{MM}^2 = \left(E_{\mathrm{beam}} - E_{\mu^+}\right)^2 - \left(-\mathbf{p}_{D^-} - \mathbf{p}_{\mu^+}\right)^2 , \tag{2}$$

here E_{beam} is the beam energy, $\mathbf{p}_{D^-}$ is the three-momentum of the fully reconstructed D^-, and $E_{\mu^+}(\mathbf{p}_{\mu^+})$ is the energy (momentum) of the μ^+ candidate. MM^2 peaks at zero for a missing ν.

To reconstruct D^- tags we require that the tag candidates have a measured energy consistent with the beam energy, and have a "beam constrained mass," m_{BC}, consistent with the D^- mass, where $m_{\mathrm{BC}} = \sqrt{E_{\mathrm{beam}}^2 - (\sum_i \mathbf{p}_i)^2}$, and i runs over all the final state particles three-momenta.

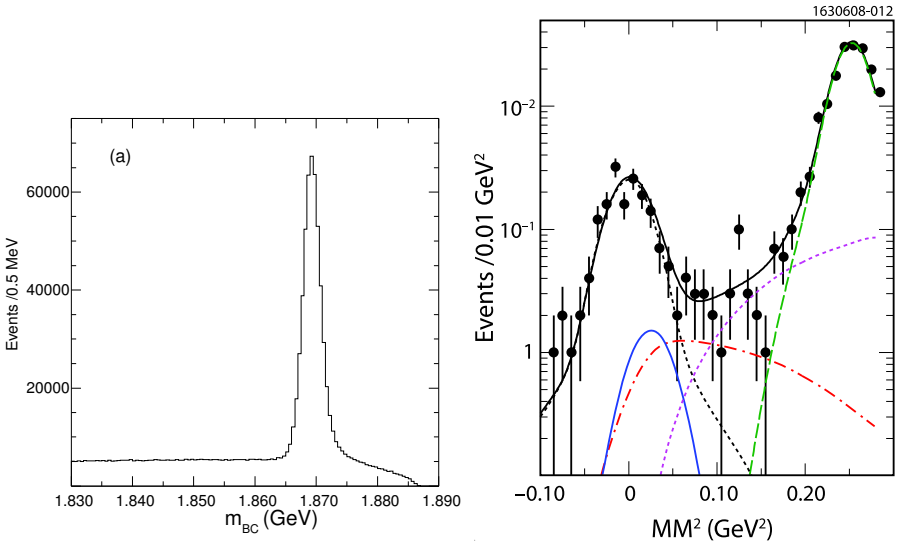

Figure 1: (a) The beam-constrained mass distributions summed over D^- decay candidates in the final states: $K^+\pi^-\pi^-$, $K^+\pi^-\pi^-\pi^0$, $K_s\pi^-$, $K_s\pi^-\pi^-\pi^+$, $K_s\pi^-\pi^0$ and $K^+K^-\pi^-$. (b) Fit to the MM^2. Data are points with error bars. The black (dashed) curve centered at zero shows the signal $\mu^+\nu$ events. The dot-dashed (red) curve that peaks around 0.05 GeV^2 shows $D^+ \quad \tau^+\nu$, $\tau^+ \quad \pi^+\bar{\nu}$. The solid (blue) Gaussian shaped curve centered on the pion-mass squared shows residual $\pi^+\pi^0$. The dashed (purple) curve that falls to zero around 0.03 GeV^2 is the sum of all the other background components, except the $\overline{K}^0\pi^+$ tail which is shown by the long-dashed (green) curve that peaks up at 0.25 GeV^2. The solid (black) curve is the sum of all the components.

Fig. 1(a) shows the m_{BC} distribution summed over all the decay modes we use for tagging. There are 460,055±787 plus 89,472 backgrounds. The fit to the MM^2 distribution shown in Fig. 1(b) contains separate shapes for signal, $\pi^+\pi^0$, $\overline{K}^0\pi^+$, $\tau^+\nu$ ($\tau^+ \to \pi^+\bar{\nu}$), and a background shape describing three-body decays. Here we constrain the ratio of the $\tau^+\nu/\mu^+\nu$ components to the SM ratio of 2.65. We also veto events with an extra neutral energy cluster > 250 MeV which removes most $\pi^+\pi^0$ events. The normalizations of the signal, $\overline{K}^0\pi^+$, and 3-body background shapes are allowed to float. The final result, including radiative corrections is [1]

$$f_{D^+} = (206.7 \pm 8.5 \pm 2.5) \text{ MeV} \ . \tag{3}$$

For D_s^+ studies we first cut on the the invariant mass of the decay products of D_s^- tag candidates shown in Fig. 2(a), then detect an additional photon candidate from the D_s^* decay, and construct

$$\text{MM}^{*2} = (E_{\text{CM}} - E_{D_s} - E_\gamma)^2 - (\mathbf{p}_{\text{CM}} - \mathbf{p}_{D_s} - \mathbf{p}_\gamma)^2 \, , \tag{4}$$

where E_{CM} ($\mathbf{p}_{\text{CM}}$) is the center-of-mass energy (momentum), E_{D_s} ($\mathbf{p}_{D_s}$) is the energy (momentum) of the fully reconstructed D_s^- tag, and E_γ ($\mathbf{p}_\gamma$) is the energy (momentum) of the additional photon. In performing this calculation we use a kinematic fit that constrains the decay products of the D_s^- to the known D_s mass and conserves overall momentum and energy. All photon candidates in the event are tried, except for those that are decay products of the D_s^- tag candidate. Regardless of whether or not the photon forms a D_s^* with the tag, for real $D_s^*D_s$ events the missing mass-squared MM^{*2}, recoiling against the photon and the D_s^- tag should peak at the D_s^+ mass-squared.

The MM^{*2} distributions for events in the D_s^- invariant mass signal region (±17.5 MeV from the D_s mass) are shown in Fig. 2(b). In order to find the number of tags used for further analysis we perform a two-dimensional binned maximum liklihood fit of the MM^{*2} distribution and the invariant mass distribution in the interval ±60 MeV from the D_s mass and $3.50 <$ MM^{*2} < 4.25 GeV^2. The background has two components, both described by 5th order Chebyshev polynomials; the first comes from the background under the invariant mass peak, defined by

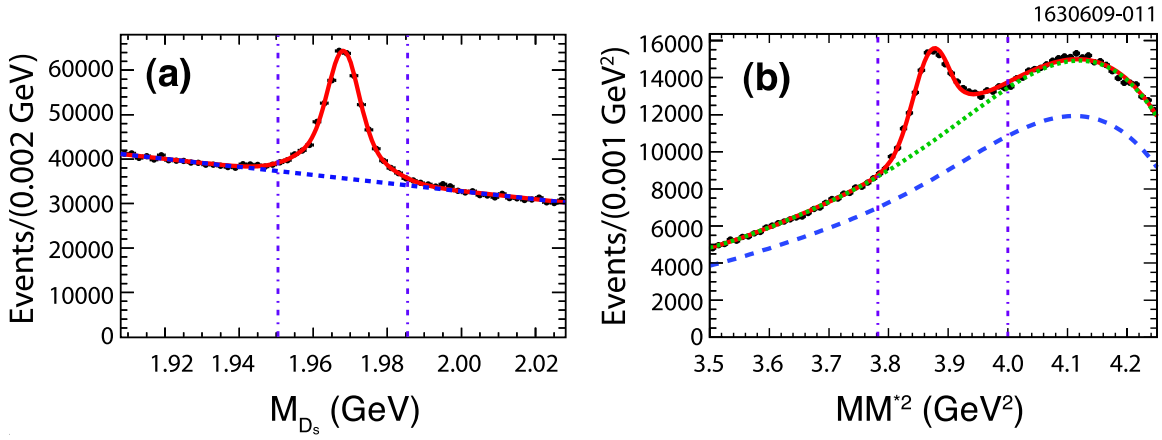

Figure 2: (a) Invariant mass of D_s^- candidates summed over the decay modes: $K^+K^-\pi^-$, K_sK^-, $\eta\pi^-$, $\eta'\pi^-$, $K^+K^-\pi^-\pi^0$, $\pi^+\pi^-\pi^-$, $K^{*-}K^{*0}$, $\eta\rho^-$, and fit to a two-Gaussian signal shape plus a linear background. No MM^{*2} cut has been applied. (b) The MM^{*2} distribution. The curves show a Crystal Ball function for signal and two 5th order Chebyshev background functions; the dashed curve shows the background from fake D_s^- tags, while the dotted curve in (b) shows the sum of the backgrounds from multiple photon combinations and fake D_s^- tags. The vertical dashed lines in (a) and (b) show the region of events selected for further analysis.

the sidebands, and the second is due to multiple photon combinations. In both cases we allow the parameters to float. We find a total of 43859±936±877 signal events in the interval $3.782 < \mathrm{MM}^{*2} < 4.000$ GeV^2 and having an invariant mass within ±17.5 MeV of the D_s mass.

With these tag samples CLEO measured the $D_s^+ \to \mu^+\nu$ and $\tau^+\nu$ final states with $\tau^+ \to \pi^+\nu$ and $\rho^+\nu$. The $\tau^+ \to e^+\nu\bar{\nu}$ was measured using a sub-set of invariant mass tags only. Here the sum of all of the energy deposited in the electromagnetic calorimeter, E_{extra}, that is not associated with either the tag or the τ^+ decay is used as an additional discriminant; for signal events E_{extra} should be zero.

The $\tau^+ \to \rho^+\nu$ analysis is quite novel. Here some backgrounds peak while the signal shape, that is extremely well known, is rather flat. E_{extra} is also used in this analysis. The MM^2 distribution computed from a D_s^- tag, a photon and a ρ^+ is shown on Fig. 3. A clear excess of signal events is present. A summary of measurements of $f_{D_s^+}$ by several groups are listed in Table 1.[1]

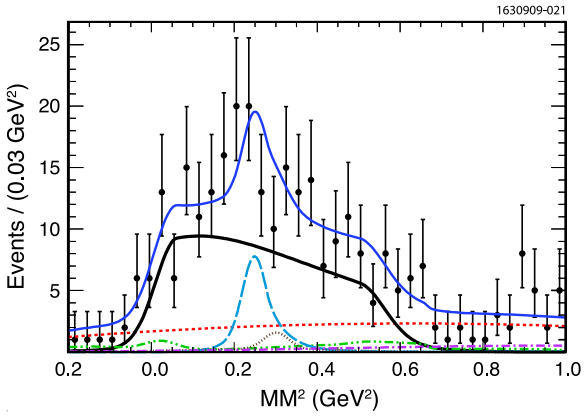

Figure 3: Fit to the data (points) for $E_{\mathrm{extra}} < 0.1$ GeV. The various components are signal (thick solid line), $\eta\rho^+$ (dotted), fake D_s^- (dashed), $K^0\pi^+\pi^0$ (long dash), sum of $\pi^+\pi^0\pi^0$, $\eta\pi^+$, $\phi\pi^+$, τ^+ $(\pi^+ + \pi^+\pi^0\pi^0)\overline{\nu}$, $\mu^+\nu$, and $X\mu^+\nu$ (dash-dot-dot), and other backgrounds (dashed-dot). The thinner solid curve shows the total.

The decay constant average for $f_{D_s^+}$ is (257.5 ± 6.1) MeV. Two unquenched lattice QCD calculations using 3 light fermion loops (unquenched) are available.[7] HPQCD now quotes a value of (247±2) MeV, a 2σ change from their published value of (241±3) MeV. The updated Fermilab/MILC result is (261.4±7.7±5.0 MeV). They also predict $f_{D_+} = 220.3 \pm 8.0 \pm 4.3)$ MeV. Thus these preliminary theoretical results are in agreement with the data.

3 Semileptonic Decays

CLEO has observed $D_s^+ \to f_0(980)e^+\nu$; $f_0 \to \pi^+\pi^-$, measured the form-factor as a function of q^2, and determined the mass and width of the f_0, parameters that are not well known.[8] The rate

Table 1: Experimental results for $\mathcal{B}(D_s^+ \to \mu^+\nu)$, $\mathcal{B}(D_s^+ \to \tau^+\nu)$, and $f_{D_s^+}$.

Experiment	Mode	$\mathcal{B}$	$f_{D_s^+}$ (MeV)
CLEO-c [2]	$\mu^+\nu$	$(5.65 \pm 0.45 \pm 0.17) \times 10^{-3}$	$257.6 \pm 10.3 \pm 4.3$
Belle [3]	$\mu^+\nu$	$(6.38 \pm 0.76 \pm 0.57) \times 10^{-3}$	$274 \pm 16 \pm 12$
Average	$\mu^+\nu$	$(5.80 \pm 0.43) \times 10^{-3}$	261.5 ± 9.7
CLEO-c [2]	$\tau^+\nu$ $(\pi^+\overline{\nu})$	$(6.42 \pm 0.81 \pm 0.18) \times 10^{-2}$	$278.0 \pm 17.5 \pm 3.8$
CLEO-c [4]	$\tau^+\nu$ $(\rho^+\overline{\nu})$	$(5.52 \pm 0.57 \pm 0.21) \times 10^{-2}$	$257.8 \pm 13.3 \pm 5.2$
CLEO-c [5]	$\tau^+\nu$ $(e^+\nu\overline{\nu})$	$(5.30 \pm 0.47 \pm 0.22) \times 10^{-2}$	$252.6 \pm 11.2 \pm 5.6$
BaBar [6]	$\tau^+\nu$ $(e^+\nu\overline{\nu})$	$(4.54 \pm 0.53 \pm 0.40 \pm 0.28) \times 10^{-2}$	$233.8 \pm 13.7 \pm 12.6$
Average	$\tau^+\nu$	$(5.58 \pm 0.35) \times 10^{-2}$	255.5 ± 7.5
Average	$\mu^+\nu + \tau^+\nu$		257.5 ± 6.1

and form-factor for $D_s^+ \to \phi e^+\nu$ was also measured. The ratio of these two rates at q^2 of zero was predicted [9] to be similar to that of $\Gamma(B_s \to J/\psi f_0)/\Gamma(B_s \to J/\psi\phi)$.

Figure 4 shows the q^2 distributions. The $\phi e^+\nu$ channel is fit using the form factors determined by the BaBar collaboration letting the normalization float.[10] For $f_0 e^+\nu$ a simple pole model is used: $|f_+(q^2)| = 1/(1 - q^2/M^2_{\rm pole})$, resulting in $M_{\rm pole}$=$(1.7^{+4.5}_{-0.7} \pm 0.2)$ GeV. Using the fits we find that at q^2 of zero the f_0/ϕ yield is (42±011)%.

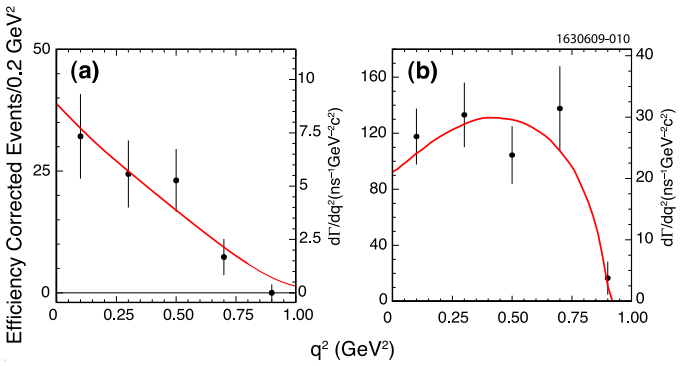

Figure 4: The q^2 distributions for (a) $D_s^+ \to f_0 e^+\nu$ (b) $D_s^+ \to \phi e^+\nu$. The fits are described in the text.

Acknowledgments

I thank the U. S. National Science Foundation for Support. I thank my CLEO colleagues especially M. Artuso, J. Rosner and L. Zhang. I apologize for the large amount of omitted material.

References

1. J. L. Rosner and S. Stone arXiv:1002.1655v2 [hep-ex].
2. J. P. Alexander *et al.*, (CLEO Collab.), *Phys. Rev.* D**79**, 052001 (2009); M. Artuso *et al.*, (CLEO Collab.), *Phys. Rev. Lett.* **99**, 071802 (2007).
3. L. Widhalm *et al.*, (Belle Collab.), *Phys. Rev. Lett.* **100**, 241801 (2008).
4. P. Naik *et al.*, (CLEO Collab.), *Phys. Rev.* D**80**, 112004 (2009).
5. P.U.E. Onyisi *et al.*, (CLEO Collab.), *Phys. Rev.* D**79**, 052002 (2009); K.M. Ecklund *et al.*, (CLEO Collab.), *Phys. Rev. Lett.* **100**, 161801 (2008).
6. J. Dingfelder, "Hot topics from Babar: Leptonic and Semileptonic B and D decays," presented at Moriond QCD and High Energy Interactions, La Thuile, Italy March 2010; J. P. Lee *et al.*, (BaBar Collab.) [arXiv:1003.3063].
7. C. Bernard, "Leptonic B and D Decays on the Lattice," Lattice QCD Meets Exp. Workshop, Ferimlab, April, 2010.
8. K. M. Ecklund *et al.*, (CLEO Collab.), *Phys. Rev.* D**80**, 052009 (2009); J. Yelton, *et al.*, (CLEO Collab.), *Phys. Rev.* D**80**, 052007 (2009).
9. S. Stone and L. Zhang, *Phys. Rev.* D**79**, 074024 (2009).
10. B. Aubert *et al.* (BaBar Collab.), *Phys. Rev.* D**78**, 051101 (2008).

Hadronic D^0, D^+, and D_S^0 Decays

M. ARTUSO on behalf of the CLEO-c Collaboration
Department of Physics, Syracuse University,
Syracuse, NY 13244

Hadronic decays of the charmed mesons D^0, D^+, and D_S^0 offer unique opportunities to probe non-perturbative strong dynamics. In this report we summarize recent CLEO-c results, and we compare them with predictions from phenomenological models. Finally, we discuss their impact on our knowledge of light quark spectroscopy.

1 Introduction

Hadronic charm decays are driven by the complex interplay between short distance and long distance dynamics, which introduces a variety of complex phases resultin in enhancements and suppressions through interference effects. In these proceedings we will summarize recent CLEO-c hadronic D^0,D^+, and D_S^0 decays, based on the full CLEO-c data set,[1] with 818 pb^{-1} at the $\psi(3770)$ center-of-mass energy, and 586 pb^{-1} at $\sqrt{s}$=4.170 GeV(unless otherwise noted). They correspond to 3×10^6 $D^0\bar{D}^0$ pairs, and 5.3×10^5 $D_S^{\pm}D_S^{\star\mp}$pairs.

2 Charm decays to two pseudoscalars

Cleo-c has recently published an extensive set of measurements of branching fractions of hadronic D^0, D^+, and D_S^0 into two pseudoscalars. Bhattacharya and Rosner [2] have proposed a diagrammatic approach to analyze these modes in the framework of flavor $SU(3)$. The decay amplitudes are expressed in terms of topological quark flow diagrams: each diagram represents an amplitude which accounts for weak and strong interaction effects, to all orders, including long distance effects. The key amplitudes include a color-favored tree (T), a color-suppressed tree (C), an exchange (E) and an annihilation (A). The role of the annihilation term, especially in D_S^0 decays, is very interesting as it provides information relevant to annihilation effects in charmless semileptonic decays.

Table 1 compares the results from the best fit to the quark flow diagram formalism in the case of the Cabibbo favored and the singly Cabibbo suppressed decays. The experimental information is sufficient to use the Cabibbo favored (CF) decays to fit for the quark flow diagram amplitudes, their relative phases, and the octet-singlet mixing angle θ_η, which they determine to be 11.7°. This value of θ_η is used to predict singly-Cabibbo-suppressed (CS) and doubly-Cabibbo-suppressed (DCS) decays. This approach does not work very well for singly Cabibbo suppressed decays, for example it overestimates $\mathcal{B}(D^0 \to \pi^+\pi^-)$ and underestimates $\mathcal{B}(D^0 \to K^+K^-)$.

Table 1: Comparison between CLEO-c data and theoretical predictions from Bhattacharya and Rosner. The theoretical predictions quoted are derived with their favorite singlet-octect mixing angle $\theta_\eta = 11.7^\circ$ ($\phi_1 = 45^\circ - \frac{\phi_2}{2}$, and $\phi_2 = 19.5^\circ$).

Mode	$\mathcal{B}$ (%) (CLEO-c) [1]	Representation	Predicted $\mathcal{B}$ (%) [2]	
$D^0 \to K^-\pi^+$	3.906 ± 0.077	T+E	3.891	
$D^0 \to \bar{K}^0\pi^0$	2.38 ± 0.085	(C-E)/$\sqrt{2}$	2.380	
$D^0 \to \bar{K}^0\eta$	0.962 ± 0.060	$\frac{\mathrm{C}}{\sqrt{2}}\sin(\theta_\eta+\phi_1) - \frac{\sqrt{3}\mathrm{E}}{\sqrt{2}}\cos(\theta_\eta+2\phi_1)$	0.962	
$D^0 \to \bar{K}^0\eta'$	1.900 ± 0.108	$-\frac{\mathrm{C}}{\sqrt{2}}\cos(\theta_\eta+\phi_1) - \frac{\sqrt{3}\mathrm{E}}{\sqrt{2}}\sin(\theta_\eta+2\phi_1)$	1.900	
$D^+ \to \bar{K}^0\pi^+$	3.074 ± 0.097	C+T	3.074	
$D_S^0 \to \bar{K}^0K^+$	2.98 ± 0.17	C+A	2.980	
$D_S^0 \to \pi^+\eta$	1.84 ± 0.15	$\mathrm{T}\cos(\theta_\eta+\phi_1) - \sqrt{2}\mathrm{A}\sin(\theta_\eta+\phi_1)$	1.840	
$D_S^0 \to \pi^+\eta'$	3.95 ± 0.34	$\mathrm{T}\sin(\theta_\eta+\phi_1) + \sqrt{2}\mathrm{A}\cos(\theta_\eta+\phi_1)$	3.950	
			$\lvert T'\rvert > \lvert C'$	$\lvert T'\rvert < \lvert C'$
$D^0 \to \pi^-\pi^+$	0.145 ± 0.005	-(T′ +E′)	0.224	0.224
$D^0 \to \pi^0\pi^0$	0.081± 0.005	-(C′ - E′)/$\sqrt{2}$	0.135	0.136
$D^0 \to K^-K^+$	0.407 ± 0.010	(T′ +E′)	0.193	0.192
$D^0 \to K^0\bar{K}^0$	0.032 ± 0.002	0	0	
$D^+ \to \pi^0\pi^+$	0.0118 ± 0.006	-(T′ +C′)/$\sqrt{2}$	0.089	0.088
$D^+ \to K^+\bar{K}^0$	0.612 ± 0.022	(T′ - A′)	0.615	0.073
$D_S^0 \to \pi^+K^0$	0.252 ± 0.027	-(T′ -A′)	0.308	0.037
$D_S^0 \to \pi^0K^+$	0.062 ± 0.023	-(C′ +A′)/$\sqrt{2}$	0.085	0.086

3 $K^0\bar{K}^0$ Interference

The decay rates for $D^0 \to K_S\pi^0$ and $D^0 \to K_L\pi^0$ are not the same because of the interference between the CF component $D^0 \to \bar{K}^0\pi^0$ and the DCS $D^0 \to \bar{K}^0\pi^0$ which has a positive sign fo the decay $D^0 \to K_S\pi^0$ and a negative sign when the K_S is replaced by K_L. The amplitudes $D^0 \to \bar{K}^0\pi^0$ and $D^0 \to \bar{K}^0\pi^0$ are related by U-spin (interchange of u and s quark). Thus, assuming U-spin symmetry, $A(D^0 \to K^0\pi^0) = \tan^2\theta_c \times A(D^0 \to \bar{K}^0\pi^0)$ and the decay rate asymmetry is given by:

$$R(D^0) \equiv \frac{\Gamma(D^0 \to K_S\pi^0) - \Gamma(D^0 \to K_L\pi^0)}{\Gamma(D^0 \to K_S\pi^0) + \Gamma(D^0 \to K_L\pi^0)} = 2\tan^2\theta_c = 0.109 \quad (1)$$

CLEO-c, using a partial sample of 281 pb^{-1}, measures $R(D^0)$ exploiting kinematic constraints to reconstruct the K_L in the final state with a missing mass square technique [3] and obtains:

$$R(D^0)_{exp} = 0.108 \pm 0.025 \pm 0.024, \quad (2)$$

which is in excellent agreement with the expectations based on U-spin symmetry. The theoretical treatment of a similar asymmetry $R(D^+)$ in D^+ decays is more complex; the diagrammatic approach [2] predicts

$$R(D^+) = -0.005 \pm 0.013, \quad (3)$$

in excellent agreement with

$$R(D^+) = 0.022 \pm 0.016 \pm 0.018. \quad (4)$$

4 D_S^0 decays with ω in the final state and weak annihilation

D_S^0 decays are important to shed light on the poorly known weak annihilation effects which influence the extraction of $|V_{ub}|$ from inclusive charmless semileptonic B decays.[4, 5] Hadronic D_S^0 decays present interesting puzzles concerning weak annihilation effects.[6, 7] Decays including ω in the final state are expected to be mediated predominantly by the annihilation diagram $c\bar{s} \to u\bar{d}$. G-parity of a J=0 $u\bar{d}$ quark-antiquark pair suggests that only D_S^0 decays including an odd number of πs are allowed. This is contradicted by the observation of $D_S^0 \to \omega\pi$ and the

Table 2: Summary of the CLEO-c data on exclusive and inclusive decays $D_S^0 \to \omega X$. The sum of the measured exclusive branching fraction is (5.4±1.0)%

Mode	$\mathcal{B}$ (%) (CLEO-c) [9, 10]
$D_S^0 \to \pi^+\omega$	0.21 ± 0.09 ±0.01
$D_S^0 \to \pi^+\pi^0\omega$	2.78 ± 0.65 ±0.25
$D_S^0 \to \pi^+\pi^+\pi^-\omega$	1.58 ± 0.45 ±0.09
$D_S^0 \to \pi^+\eta\omega$	0.85 ± 0.54 ±0.06
	< 2.3 (90% CL)
$D_S^0 \to K^+\omega$	< 0.24 (90% CL)
$D_S^0 \to K^+\pi^0\omega$	< 0.82 (90% CL)
$D_S^0 \to K^+\pi^+\pi^-\omega$	< 0.54 (90% CL)
$D_S^0 \to K^+\eta\omega$	< 0.79 (90% CL)
$D_S^0 \to \pi^0 K^+$	0.062 ± 0.023
$D_S^0 \to \omega X$	6.1 ±1.4

non-observation of $D_S^0 \to \rho\pi$. [8] Table 2 summarizes the CLEO-c measurements of inclusive and exclusive D_S^0 decays including ω in the final state. These data show that the measured branching fractions account for the inclusive rate, but the interplay between annihilation and rescattering makes a simple model based on annihilation and G-parity conservation inadequate to describe these decays.

5 The Dalitz Decay $D_S^0 \to K^+K^-\pi^+$

The kinematics of the 3-body decay $D \to ABC$ is fully described in terms of the invariant masses M_{AB}^2 and M_{BC}^2 of two pair of final state mesons. The "Dalitz analysis" of these decays, involving the measurement of the differential distribution $d\Gamma/dM_{AB}^2 M_{BC}^2$ provides an impressive wealth of information relevant to D and B meson dynamics, as well as light meson spectroscopy, in particular the poorly known scalar meson sector. I will illustrate this point with the Dalitz analysis of $D_S^0 \to K^+K^-\pi^+$.

An example, recently studied by CLEO-c,[11] is the decay $D_S^0 \to K^+K^-\pi^+$. Table 3 gives the the relevant isobar model fit parameters. This study is based on 12K $D_S^0 \to K^+K^-\pi^+$ decays, to be compared with the pioneering E687 [12] analysis based on 701 events. CLEO-c confirms the strength of the dominant s-wave component ($f_0(890)$). The best fit to the CLEO-c data is achieved by adding another scalar mesons, the $f_0(1370)$.[13] This meson is strongly overlapping with the broad $f_0(600)$ and the narrow $f_0(1500)$. Its mass and width[8] have large uncertainties due to the small fraction of these decays into two π or K. The CLEO-c fit with floating resonance parameters gives $M_{f_0(1370)} = (1315 \pm 34)$ MeV/c^2, and $\Gamma_{f_0(1370)} = 276 \pm 39$ MeV/c^2, where the quoted errors are statistical only. CLEO-c obtains a reasonably good fit, χ^2/d.o.f = 178/117, using these resonances.

6 Conclusions

This report gives a quick snapshot of some of the many important contributions towards our understanding of fundamental interactions provided by CLEO-c studies of hadronic charm decays. Excellent reviews [14, 15] offer a broader picture of the experimental and theoretical landscape.

Acknowledgments

This work was supported by the US National Science Foundation. I would like to thank the organizers for a lovely conference with spirited discussions, great physics, and wonderful skiing opportunities, and my CLEO collaborators for all the years of shared fun and discoveries.

Table 3: Summary of the six resonance model (Model A) fit to the $D_S^0 \to K^+K^-\pi^+$ Dalitz plot. Fit parameters are shown with their statistical and systematic uncertainty respectively. The "δMean" and "RMS" account for variation of the fit parameters in the systematic cross checks as discussed in the text. The "Total" is a quadratic sum of "δMean" and "RMS" and after rounding is the systematic uncertainty given in the second column. The results of the E687 Model are also shown for comparison.

Parameter	Model A	δMean	RMS	Total	E687 Model
$m_{K^*(892)}$	894.9±0.5±0.7	0.088	0.654	0.660	895.8±0.5
$\Gamma_{K^*(892)}$	45.7±1.1±0.5	0.148	0.499	0.520	44.2±1.0
$a_{K_0^*(1430)}$ (a.u.)	1.51±0.11±0.09	-0.024	0.089	0.092	1.76±0.12
$\phi_{K_0^*(1430)}$ (°)	146±8±8	-0.623	8.442	8.465	145±8
$a_{f_0(980)}$ (a.u.)	4.72±0.18±0.17	-0.029	0.167	0.170	3.67±0.13
$\phi_{f_0(980)}$ (°)	157±3±4	-0.343	4.036	4.051	156±3
$a_{\phi(1020)}$ (a.u.)	1.13±0.02±0.02	0.004	0.017	0.018	1.15±0.02
$\phi_{\phi(1020)}$ (°)	−8±4±4	0.081	3.850	3.851	−15±4
$a_{f_0(1370)}$ (a.u.)	1.15±0.09±0.06	-0.003	0.063	0.063	
$\phi_{f_0(1370)}$ (°)	53±5±6	-0.536	5.820	5.845	
$a_{f_0(1710)}$ (a.u.)	1.11±0.07±0.10	-0.004	0.098	0.098	1.27±0.07
$\phi_{f_0(1710)}$ (°)	89±5±5	0.195	4.916	4.920	102±4
FF[$K^*(892)$] (%)	47.4±1.5±0.4	0.016	0.357	0.4	48.2±1.2
FF[$K_0^*(1430)$] (%)	3.9±0.5±0.5	0.036	0.460	0.5	5.3±0.7
FF[$f_0(980)$] (%)	28.2±1.9±1.8	0.096	1.792	1.8	16.8±1.1
FF[$\phi(1020)$] (%)	42.2±1.6±0.3	0.018	0.277	0.3	42.7±1.3
FF[$f_0(1370)$] (%)	4.3±0.6±0.5	0.044	0.488	0.5	
FF[$f_0(1710)$] (%)	3.4±0.5±0.3	0.044	0.311	0.3	4.4±0.4
$\sum_R$ FF$_R$ (%)	129.5±4.4±2.0	0.020	1.981	2.0	117.3±2.2
χ^2/ν	178/117				278/119

References

1. H. Mendez *et al.* [CLEO Collaboration], Phys. Rev. D **81** (2010) 052013 [arXiv:0906.3198 [hep-ex]].
2. B. Bhattacharya and J. L. Rosner, Phys. Rev. D **81**, 014026 (2010) [arXiv:0911.2812 [hep-ph]].
3. Q. He *et al.*CLEO Collaboration], Phys. Rev. Lett. {**100**,091801 (2008).
4. M. B. Voloshin, Mod. Phys. Lett. A **17** (2002) 245 [arXiv:hep-ph/0202028].
5. Z. Ligeti, M. Luke and A. V. Manohar, arXiv:1003.1351 [hep-ph].
6. M. Gronau and J. L. Rosner, Phys. Rev. D **79**, 074022 (2009) [arXiv:0903.2287 [hep-ph]].
7. F. E. Close and H. J. Lipkin, Phys. Lett. B **551** (2003) 337 [arXiv:hep-ph/0208217].
8. C. Amsler *et al.* [Particle Data Group], Phys. Lett. B **667** (2008) 1.
9. J. Y. Ge *et al.* [CLEO Collaboration], Phys. Rev. D **80** (2009) 051102 [arXiv:0906.2138 [hep-ex]].
10. S. Dobbs *et al.*[CLEO Collaboration], Phys. Rev. D **76**, 112001 (2007).
11. R. E. Mitchell *et al.* [CLEO Collaboration], Phys. Rev. D **79** (2009) 072008 [arXiv:0903.1301 [hep-ex]].
12. P. L. Frabetti *et al.* [E687 Collaboration], Phys. Lett. B **351**, 591 (1995).
13. S. Spanier, N. A. Tornqvist and C. Amsler, Phys. Lett. B **667** (2008) 1.
14. M. Artuso, B. Meadows and A. A. Petrov, Ann. Rev. Nucl. Part. Sci. **58**, 249 (2008) [arXiv:0802.2934 [hep-ph]].
15. A. Ryd and A. A. Petrov, arXiv:0910.1265 [hep-ph].

FROM Ω^- TO Ω_b

M. KARLINER
Raymond and Beverly Sackler School of Physics and Astronomy
Tel Aviv University, Tel Aviv, Israel

I discuss several recent highly accurate theoretical predictions for masses of baryons containing the b quark, especially Ω_b (ssb) very recently reported by CDF. I also point out an approximate effective supersymmetry between heavy quark baryons and mesons and provide predictions for the magnetic moments of Λ_c and Λ_b. Proper treatment of the color-magnetic hyperfine interaction in QCD is crucial for obtaining these results.

1 Introduction

QCD describes hadrons as valence quarks in a sea of gluons and $\bar{q}q$ pairs. At distances above ~ 1 GeV^{-1} quarks acquire an effective *constituent mass* due to chiral symmetry breaking. A hadron can then be thought of as a bound state of constituent quarks. In the zeroth-order approximation the hadron mass M is then given by the sum of the masses of its constituent quarks m_i, $M = \sum_i m_i$. The binding and kinetic energies are "swallowed" by the constituent quarks masses. The first and most important correction comes from the color hyper-fine (HF) chromo-magnetic interaction,

$$M = \sum_i m_i + V_{i<j}^{HF(QCD)}; \qquad V_{ij}^{HF(QCD)} = v_0 \, (\vec{\lambda}_i \cdot \vec{\lambda}_j) \, \frac{\vec{\sigma}_i \cdot \vec{\sigma}_j}{m_i m_j} \, \langle \psi | \delta(r_i - r_j) | \psi \rangle \tag{1}$$

where v_0 gives the overall strength of the HF interaction, $\vec{\lambda}_{i,j}$ are the $SU(3)$ color matrices, $\sigma_{i,j}$ are the quark spin operators and $|\psi\rangle$ is the hadron wave function. This is a contact spin-spin interaction, analogous to the EM hyperfine interaction, which is a product of the magnetic moments,

$$V_{ij}^{HF(QED)} \propto \vec{\mu}_i \cdot \vec{\mu}_j = e^2 \, \frac{\vec{\sigma}_i \cdot \vec{\sigma}_j}{m_i m_j} \tag{2}$$

in QCD, the $SU(3)_c$ generators take place of the electric charge. From eq. (1) many very accurate results have been obtained for the masses of the ground-state hadrons. Nevertheless,

several caveats are in order. First, this is a low-energy phenomenological model, still awaiting a rigorous derivation from QCD. It is far from providing a complete description of the hadronic spectrum, but it provides excellent predictions for mass splittings and magnetic moments. The crucial assumptions of the model are: (a) HF interaction is considered as a perturbation which does not change the wave function; (b) effective masses of quarks are the same inside mesons and baryons; (c) there are no 3-body effects.

2 Quark masses

Table I shows the quark mass differences obtained from mesons and baryons [1]. The mass difference between two quarks of different flavors denoted by i and j are seen to have the same value to a good approximation when they are bound to a "spectator" quark of a given flavor.

On the other hand, Table 1 shows clearly that *constituent quark mass differences depend strongly on the flavor of the spectator quark*. For example, $m_s - m_d \approx 180$ MeV when the spectator is a light quark but the same mass difference is only about 90 MeV when the spectator is a b quark.

Since these are *effective masses*, we should not be surprised that their difference is affected by the environment, but the large size of the shift is quite surprising and its quantitative derivation from QCD is an outstanding challenge for theory. Let us now discuss the HF splitting in mesons and baryons. We have

$$M(K^*) - M(K) = 4v_0 \frac{\vec{\lambda}_u \cdot \vec{\lambda}_s}{m_u m_s} \langle\psi|\delta(r)|\psi\rangle, \qquad (3)$$

$$M(\Sigma^*) - M(\Sigma) = 6v_0 \frac{\vec{\lambda}_u \cdot \vec{\lambda}_s}{m_u m_s} \langle\psi|\delta(r_{rs})|\psi\rangle \qquad (4)$$

Table I. Quark mass differences.

observable	baryons		mesons $J=1$		mesons $J=0$		Δm_{Bar} MeV	Δm_{Mes} MeV
	B_i	B_j	$\mathcal{V}_i$	$\mathcal{V}_j$	$\mathcal{P}_i$	$\mathcal{P}_j$		
$\langle m_s - m_u\rangle_d$	sud	uud	$s\bar{d}$	$u\bar{d}$	$s\bar{d}$	$u\bar{d}$	177	179
	Λ	N	K^*	ρ	K	π		
$\langle m_s - m_u\rangle_c$			$c\bar{s}$	$c\bar{u}$	$c\bar{s}$	$c\bar{u}$		103
			D_s^*	D_s^*	D_s	D_s		
$\langle m_s - m_u\rangle_b$			$b\bar{s}$	$b\bar{u}$	$b\bar{s}$	$b\bar{u}$		91
			B_s^*	B_s^*	B_s	B_s		
$\langle m_c - m_u\rangle_d$	cud	uud	$c\bar{d}$	$u\bar{d}$	$c\bar{d}$	$u\bar{d}$	1346	1360
	Λ_c	N	D^*	ρ	D	π		
$\langle m_c - m_u\rangle_c$			$c\bar{c}$	$u\bar{c}$	$c\bar{c}$	$u\bar{c}$		1095
			ψ	D^*	η_c	D		
$\langle m_c - m_s\rangle_d$	cud	sud	$c\bar{d}$	$s\bar{d}$	$c\bar{d}$	$s\bar{d}$	1169	1180
	Λ_c	Λ	D^*	K^*	D	K		
$\langle m_c - m_s\rangle_c$			$c\bar{c}$	$s\bar{c}$	$c\bar{c}$	$s\bar{c}$		991
			ψ	D_s^*	η_c	D_s		
$\langle m_b - m_u\rangle_d$	bud	uud	$b\bar{d}$	$u\bar{d}$	$b\bar{d}$	$u\bar{d}$	4685	4700
	Λ_b	N	B^*	ρ	B	π		
$\langle m_b - m_u\rangle_s$			$b\bar{s}$	$u\bar{s}$	$b\bar{s}$	$u\bar{s}$		4613
			B_s^*	K^*	B_s	K		
$\langle m_b - m_s\rangle_d$	bud	sud	$b\bar{d}$	$s\bar{d}$	$b\bar{d}$	$s\bar{d}$	4508	4521
	Λ_b	Λ	B^*	K^*	B	K		
$\langle m_b - m_c\rangle_d$	bud	sud	$b\bar{d}$	$c\bar{d}$	$b\bar{d}$	$c\bar{d}$	3339	3341
	Λ_b	Λ_c	B^*	D^*	B	D		
$\langle m_b - m_c\rangle_s$			$b\bar{s}$	$c\bar{s}$	$b\bar{s}$	$c\bar{s}$		3328
			B_s^*	D_s^*	B_s	D_s		

we can then use eqs. (3) and (4) to compare the quark mass ratio obtained from mesons and baryons:

$$(m_c/m_s)_{Bar} = (M_{\Sigma^*} - M_\Sigma)/(M_{\Sigma_c^*} - M_{\Sigma_c}) = 2.84$$
$$(m_c/m_s)_{Mes} = (M_{K^*} - M_K/(M_{D^*} - M_D) = 2.81 \qquad (5)$$

Similarly, $(m_c/m_u)_{Bar} = 4.36$ and $(m_c/m_u)_{Mes} = 4.46$. We find the same value from mesons and baryons $\pm 2\%$. We can write down an analogous relation for hadrons containing the b quark instead of the s quark, obtaining the prediction for splitting between Σ_b and Λ_b:

$$\frac{M_{\Sigma_b} - M_{\Lambda_b}}{M_\Sigma - M_\Lambda} = \frac{(M_\rho - M_\pi) - (M_{B^*} - M_B)}{(M_\rho - M_\pi) - (M_{K^*} - M_K)} = 2.51 \qquad (6)$$

yielding $M(\Sigma_b) - M(\Lambda_b) = 194\,\mathrm{MeV}$ [1,2], to be compared with the isospin average of the recent measurement by CDF [3], $M(\Sigma_b) - M(\Lambda_b) = 192 \pm 2.3$ MeV. There is also the prediction for the spin splittings, $M(\Sigma_b^*) - M(\Sigma_b) = [M(B^*) - M(B)] \cdot [M(\Sigma^*) - M(\Sigma)]/[M(K^*) - M(K)] = 22\,\mathrm{MeV}$, to be compared with 21 MeV from the isospin-average of CDF measurements [3]. The challenge is to understand how and under what assumptions one can derive from QCD the very simple model of hadronic structure at low energies which leads to such accurate predictions.

3 Effective Meson-Baryon SUSY

Some of the results described above can be understood [2] by observing that in the hadronic spectrum there is an approximate effective supersymmetry between mesons and baryons related by replacing a light antiquark by a light diquark. This supersymmetry transformation goes beyond the simple constituent quark model. It assumes only a valence quark of flavor i with a model independent structure bound to "light quark brown muck color antitriplet" of model-independent structure carrying the quantum numbers of a light antiquark or a light diquark. The mass difference between the meson and baryon related by this transformation has been shown [4] to be independent of the quark flavor i for all four flavors (u, s, c, b) when the contribution of the hyperfine interaction energies is removed as denoted by the "$\sim$" overscript. For the two cases of spin-zero $S = 0$ and spin-one $S = 1$ diquarks [4] (all masses differences in MeV):

$$M(N) - \tilde{M}(\rho)=323 \approx M(\Lambda) - \tilde{M}(K^*)=321 \approx M(\Lambda_c) - \tilde{M}(D^*)=312 \approx M(\Lambda_b) - \tilde{M}(B^*)=310$$
$$\tilde{M}(\Delta) - \tilde{M}(\rho)=518 \approx \tilde{M}(\Sigma) - \tilde{M}(K^*)=526 \approx \tilde{M}(\Sigma_c) - \tilde{M}(D^*)=524 \approx \tilde{M}(\Sigma_b) - \tilde{M}(B^*)=512 \quad (7)$$

4 Magnetic Moments of Heavy Quark Baryons

In Λ, Λ_c and Λ_b baryons the light quarks are coupled to spin zero. Therefore the magnetic moments of these baryons are determined by the magnetic moments of the s, c and b quarks, respectively. The latter are proportional to the chromomagnetic moments which determine the hyperfine splitting in baryon spectra. We can use this fact to predict the Λ_c and Λ_b baryon magnetic moments by relating them to the hyperfine splittings in the same way as given in the original prediction [5] of the Λ magnetic moment,

$$\mu_\Lambda = -\frac{\mu_p}{3} \cdot \frac{M_{\Sigma^*} - M_\Sigma}{M_\Delta - M_N} = -0.61\,\text{n.m.} \qquad (\text{EXP} = -0.61\,\text{n.m.}) \quad (8)$$

We obtain $\mu_{\Lambda_c} = -2\mu_\Lambda \cdot \frac{M_{\Sigma_c^*} - M_{\Sigma_c}}{M_{\Sigma^*} - M_\Sigma} = 0.43$ n.m.; $\mu_{\Lambda_b} = \mu_\Lambda \cdot \frac{M_{\Sigma_b^*} - M_{\Sigma_b}}{M_{\Sigma^*} - M_\Sigma} = -0.067$ n.m.
We view these predictions as a challenge for the experimental community.

5 Predicting the Mass of *b*-Baryons

The Ξ_Q baryons quark content is Qsd or Qsu. They can be obtained from "ordinary" Ξ (ssd or ssu) by replacing one of the s quarks by a heavier quark $Q = c, b$. There is one important difference, however. In the ordinary Ξ, Fermi statistics dictates that two s quarks must couple to spin-1, while in the ground state of Ξ_Q the (sd) and (su) diquarks have spin zero. Consequently, the Ξ_b mass is given by the expression: $\Xi_q = m_q + m_s + m_u - 3v\langle\delta(r_{us})\rangle/m_u m_s$. The Ξ_b mass can thus be predicted using the known Ξ_c baryon mass as a starting point and adding the corrections due to mass differences and HF interactions:

$$\Xi_b = \Xi_c + (m_b - m_c) - 3v\left(\langle\delta(r_{us})\rangle_{\Xi_b} - \langle\delta(r_{us})\rangle_{\Xi_c}\right)/(m_u m_s) \quad (9)$$

Since the Ξ_Q baryon contains a strange quark, and the effective constituent quark masses depend on the spectator quark, the optimal way to estimate the mass difference $(m_b - m_c)$ is from mesons which contain both s and Q quarks: $m_b - m_c = \frac{1}{4}(3B_s^* + B_s) - \frac{1}{4}(3D_s^* + D_s) = 3324.6 \pm 1.4$. On the basis of these results we predicted [7] $M(\Xi_b) = 5795 \pm 5$ MeV. Our paper was submitted on June 14, 2007. The next day CDF announced the result, $M(\Xi_b) = 5792.9 \pm 2.5 \pm 1.7$ MeV, following up on an earlier D0 measurement, $M(\Xi_b) = 5774 \pm 11 \pm 15$ MeV.

Using methods similar to these it is possible to make predictions for many other ground-state and excited baryons containing the b quark [11].

Mass of the Ω_b: For the spin-averaged Ω_b mass we have $\frac{1}{3}(2M(\Omega_b^*) + M(\Omega_b)) = \frac{1}{3}(2M(\Omega_c^*) + M(\Omega_c)) + (m_b - m_c)_{B_s - D_s} = 6068.9 \pm 2.4$ MeV. For the HF splitting we obtain

$$M(\Omega_b^*) - M(\Omega_b) = (M(\Omega_c^*) - M(\Omega_c))\frac{m_c}{m_b}\frac{\langle\delta(r_{bs})\rangle_{\Omega_b}}{\langle\delta(r_{cs})\rangle_{\Omega_c}} = 30.7 \pm 1.3\ \text{MeV} \quad (10)$$

leading to the following predictions: Ω_b=6052.1±5.6 MeV; Ω_b^*=6082.8±5.6 MeV. Fig. 1 shows a comparison of our predictions for the masses of Σ_b, Ξ_b and Ω_b baryons with the data.

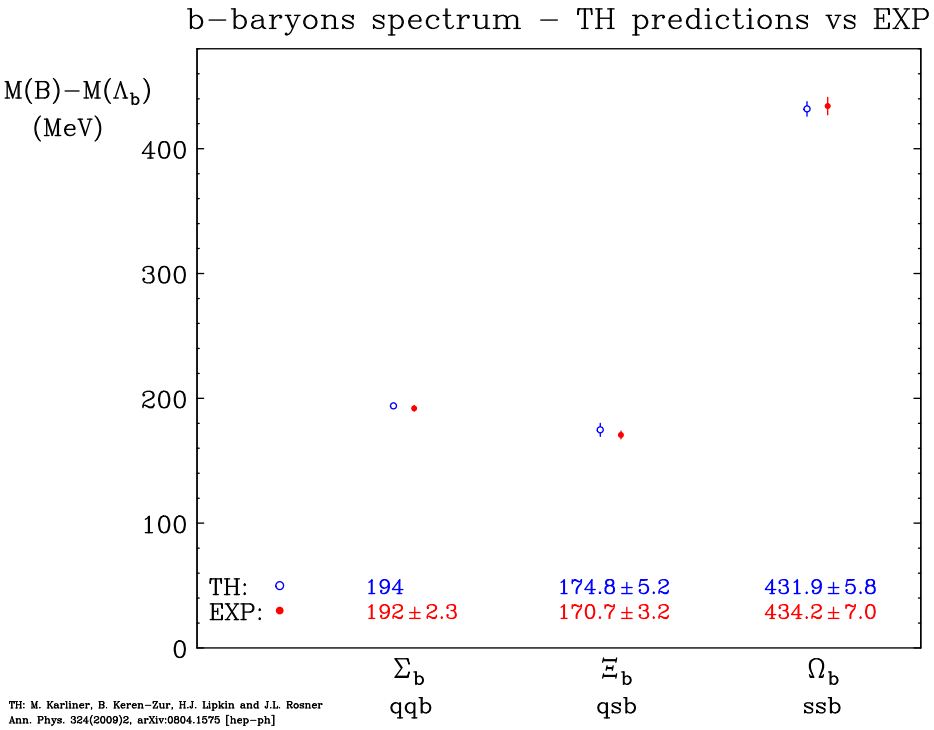

Fig. 1. Masses of b-baryons – comparison of theoretical predictions[7,11] *with experiment.*

The sign in our prediction $M(\Sigma_b^*) - M(\Sigma_b) < M(\Omega_b^*) - M(\Omega_b)$ appears to be counterintuitive, since the color hyperfine interaction is inversely proportional to the quark mass. This reversed inequality is not predicted by other recent approaches[12,13,14]. However the reversed inequality is also seen in the corresponding charm experimental data, $M(\Sigma_c^*) - M(\Sigma_c)(= 64.3 \pm 0.5\text{MeV}) < M(\Omega_c^*) - M(\Omega_c)(= 70.8 \pm 1.5\text{MeV})$. It is of interest to follow this clue theoretically and experimentally. Additional predictions for some excited states of b-baryons are given in Ref. [7,11].

Acknowledgments

The work described here was done in collaboration with B. Keren-Zur, H.J. Lipkin and J. Rosner. It was supported in part by a grant from the Israel Science Foundation.

References

1. M. Karliner and H.J. Lipkin,hep-ph/0307243, Phys. Lett. **B575** (2003) 249.
2. M. Karliner and H. J. Lipkin, Phys. Lett. B **660**, 539 (2008) [arXiv:hep-ph/0611306].
3. T. Aaltonen *et al.* [CDF Collaboration], Phys. Rev. Lett. **99** (2007) 202001.
4. M. Karliner and H. J. Lipkin, Phys. Lett. B **650**, 185 (2007) [arXiv:hep-ph/0608004].
5. A. De Rujula, H. Georgi and S.L. Glashow, Phys. Rev. D12 (1975) 147
6. B. Keren-Zur, Annals Phys. **323**, 631 (2008) [arXiv:hep-ph/0703011].
7. M. Karliner, B. Keren-Zur, H. J. Lipkin and J. L. Rosner, arXiv:0706.2163v1 [hep-ph].
8. V. M. Abazov *et al.* [D0 Collaboration], Phys. Rev. Lett. 99 (2007) 052001.
9. T. Aaltonen *et al.* [CDF Collaboration], Phys. Rev. Lett. 99 (2007) 052002.
10. M. J. Savage, Phys. Lett. B **359**, 189 (1995).
11. M. Karliner, B. Keren-Zur, H. J. Lipkin and J. L. Rosner, arXiv:0708.4027 [hep-ph] (unpublished) and arXiv:0804.1575 [hep-ph], Annals Phys **324**,2 (2009).
12. D. Ebert *et al.*, Phys. Rev. D 72 (2005) 034026; Phys. Lett. B **659** (2008) 612.
13. W. Roberts and M. Pervin, arXiv:0711.2492 [nucl-th].
14. E. E. Jenkins, Phys. Rev. D 77 (2008) 034012.
15. K.-F. Chen *et al.* [Belle Coll.], arXiv:0710.2577 [hep-ex], arXiv:0806.2992 [hep-ex].
16. M. Karliner and H. J. Lipkin, arXiv:0802.0649 [hep-ph].

$\Delta\Gamma_s/\Gamma_s$ from $B_s^0 \to D_s^{(*)+} D_s^{(*)-}$ at $\Upsilon(5S)$

Tariq Aziz
(Representing the Belle Collaboration)
Tata Institute of Fundamental Research,
Mumbai 400 005, India

Using $23.6 fb^{-1}$ data recorded at $\Upsilon(5S)$ by the Belle experiment at the KEKB e^+e^- collider, we have studied $B_s^0 \quad D_s^{(*)+} D_s^{(*)-}$ decays, where each mode is reconstructed exclusively. Assuming that these decay modes saturate decays to CP-even final states, we determine $\Delta\Gamma_s/\Gamma_s$, where $\Delta\Gamma_s$ is the difference in width between the two B_s-$\bar{B_s}$ mass eigenstates, and Γ_s is the mean width, and obtain $\Delta\Gamma_s/\Gamma_s = 0.147^{+0.036+0.044}_{-0.030-0.042}$.

1 Introduction

Study of B_s-$\bar{B_s}$ mixing/oscillation is important to understand the weak Cabibbo-Kobayashi-Maskawa structure of the Standard Model(SM). The decays $B_s^0 \to D_s^{(*)+} D_s^{(*)-}$ provide an opportunity to extract $\Delta\Gamma_s$, the width difference of the two mass eigenstates, which is relatively poorly known. On the other hand, the mass difference between the two respective eigenstates is pretty well measured ($\Delta m_s = 17.77 \pm 0.12 ps^{-1}$) by CDF and D0 experiments [1]. Study of B_s decays at the $\Upsilon(5S)$ provides a complementary approach to measure width or life-time difference without requiring time dependent measurements, rather by just counting the number of events with exclusive decays. First such measurements were performed by ALEPH, CDF and D0 [2]. This kind of measurement is possible because the final state is expected to be predominantly CP-even [3], and the partial width for the Cabibbo-favored $b \to c\bar{c}s$ process dominates the difference in decay widths between the two CP eigenstates, $\Delta\Gamma_s^{CP}$, of B_s-$\bar{B_s}$ system. Thus the branching fraction $\mathcal{B}(B_s^0 \to D_s^{(*)+} D_s^{(*)-})$ determines $\Delta\Gamma_s^{CP}$, if we ignore the CP-violating phase, ϕ_s, which is expected to be small [4] within the SM. However, if the phase turns out to be substantial due to new physics, the study becomes even more interesting.

2 Analysis and Result

The results presented here correspond to $\mathcal{L}_{int} = 23.6 fb^{-1}$ of data recorded by the Belle detector [5] running on the $\Upsilon(5S)$ resonance ($\sqrt{s} = 10.87\ GeV$) at the KEKB e^+e^- collider [6]. The $b\bar{b}$ productions cross section at the $\Upsilon(5S)$ is $\sigma_{b\bar{b}} = 0.302 \pm 0.014\ nb$ [7]. The fraction of $\Upsilon(5S)$ decays leading to B_s mesons is $f_s = 0.193 \pm 0.029$ [1] and the allowed modes are: $B_s\bar{B}_s$, $B_s\bar{B}_s^*$, $B_s^*\bar{B}_s$, $B_s^*\bar{B}_s^*$. In this analysis we use only the last mode which is dominant ($f_{B_s^*\bar{B}_s^*} = 0.901^{=0.038}_{-0.040}$) [8]. In the decay $B_s^* \to B_s\gamma$, the γ is not reconstructed. The number of $B_s\bar{B}_s$ pairs used in the present

analysis are $N_{B_s\bar{B}_s} = \mathcal{L}_{int}.\sigma_{b\bar{b}}.f_s.f_{B_s^*\bar{B}_s^*} = (1.24 \pm 0.20) \times 10^6$.

We select $B_s^0 \to D_s^{*+}D_s^{*-}$, $D_s^{*\pm}D_s^{\mp}$ and $D_s^+D_s^-$ where a D_s^+ decays to $\phi\pi^+$, $K_s^0K^+$, $\bar{K}^{*0}K^+$, $\phi\rho^+$, $K_s^0K^{*+}$ and $\bar{K}^{*0}K^{*+}$. To separate pion from kaon, a combined likelihood based on dE/dx, Cerenkov signal and time of flight information is used. To reconstruct $D_s^{*+} \to D_s^+\gamma$ decays we require the mass difference $M_{\tilde{D}_s^+\gamma} - M_{\tilde{D}_s^+}$ be within 12 MeV/c^2 of the nominal value (143.8 MeV/c^2), where $\tilde{D}_s^+$ denotes the reconstructed D_s^+ candidate. Signal B_s candidates are reconstructed from $D_s^{(*)+}D_s^{(*)-}$ pairs using the beam-energy-constrained mass $M_{\rm bc} = \sqrt{E_{\rm beam}^2 - p_B^2}$ and the energy difference $\Delta E = E_B - E_{\rm beam}$, where p_B and E_B are the reconstructed momentum and energy of B_s^0 candidate, and $E_{\rm beam}$ is the beam energy. These quantities are evaluated in the e^+e^- center of mass (CM) frame. When the B_s^0 is not fully reconstructed e.g. due to loss of γ from $D_s^{*+} \to D_s^+\gamma$, ΔE is shifted down but $M_{\rm bc}$ remains almost unchanged. We extract signal yield by fitting events in the region 5.2 $GeV/c^2 < M_{\rm bc} < 5.45$ GeV/c^2 and -0.15 $GeV < \Delta E < 0.10$ GeV. Multiple $B_s^0 \to D_s^{(*)+}D_s^{(*)-}$ candidates are possible, mostly due to low energy γ's from π^0 decays. In such cases, the best candidate is selected by minimizing the quantity

$$\chi^2 = \frac{1}{(2+N)} \left\{ \sum_{i=1}^{2} [(\tilde{M}_{D_s} - M_{D_s})/\sigma_M]^2 + \sum_{j=1}^{N} [(\Delta\tilde{M} - \Delta M)/\sigma_{\Delta M}]^2 \right\}$$

where $\Delta M = M_{D_s^*} - M_{D_s}$; σ_M and $\sigma_{\Delta M}$ are the uncertainties on M_{D_s} and ΔM; $\tilde{M}$ and $\Delta\tilde{M}$ are reconstructed quantities; and the summation runs over the D_s^+ and D_s^{*+} daughters of a B_s^0 candidate.

Backgrounds that can contribute in the selected region come from $e^+e^- \to q\bar{q}(q = u, d, s, c)$ continuum, $\Upsilon(5S) \to B\bar{B}X$ and $\Upsilon(5S) \to B_s^{(*)}\bar{B}_s^{(*)}$ that are not signal. The continuum events are suppressed using the fact that these are more collimated (jet-like) as compared to signal which tend to be spherical. Using MC signal events and $e^+e^- \to q\bar{q}$ data (taken at a CM energy 60 MeV below the mass of $\Upsilon(4S)$), a Fisher discriminant is formed based on modified Fox-Wolfram moments [9]. This discriminant is used to calculate a likelihood $L_s(L_{q\bar{q}})$ assuming the event is signal ($q\bar{q}$ background). Using a value of $R = L_s/(L_s + L_{q\bar{q}}) > 0.2$ we retain 95% signal and reject $> 80\%$ of $q\bar{q}$ events. This cut leads to an estimate of 0.05 ± 0.02 events as $q\bar{q}$ background in the total of all the three signal regions mentioned above. The remaining backgrounds from $\Upsilon(5S) \to B_s^{(*)}\bar{B}_s^{(*)} \to D_s^+X$ and $\Upsilon(5S) \to B\bar{B}X$ are estimated from MC and found to be 0.25 events for $D_s^+D_s^-$, 0.23 events for $D_s^{*\pm}D_s^{\mp}$, and 0.11 events for $D_s^{*+}D_s^{*-}$. These estimates are checked using the $M_{\rm bc}$ data side-band where a good agreement is observed.

To extract signal, we perform a two dimensional extended unbinned maximum-likelihood fit to $M_{\rm bc} - \Delta E$ distribution, simultaneous over three modes. For each sample, we include probability density function (PDFs) for signal and background. As the three types of backgrounds have similar shapes in $M_{\rm bc}$ and ΔE, we use a single PDF taken to be ARGUS function [10] for $M_{\rm bc}$ and a third-order Chebyshev polynomial for ΔE. All shape parameters are taken from MC.

The signal PDFs have three components: correctly reconstructed decays (CR); wrong combination(WC) in which a non-signal track or photon is included in place of a true daughter track or photon; and cross-feed(CF) decays in which a $D_s^{*\pm}D_s^{\mp}$ or $D_s^{*+}D_s^{*-}$ is reconstructed as $D_s^+D_s^-$ or $D_s^{*\pm}D_s^{\mp}$, respectively, or else a $D_s^+D_s^-$ or $D_s^{*\pm}D_s^{\mp}$ is reconstructed as $D_s^{*\pm}D_s^{\mp}$ or $D_s^{*+}D_s^{*-}$. In the former(latter) case the signal decay has lost(gained) a photon and ΔE is typically shifted lower(higher) by $100 - 150$ MeV. The PDF for CR events is modeled with a single Gaussian

for $M_{\rm bc}$ and a double Gaussian with common mean for the ΔE. The means and widths of these Gaussians are taken from MC, where means are calibrated using $B^0_s \to D^{(*)-}_s \pi^+$ and widths are calibratd using $B^- \to D^{(*)-}_s D^0$ control samples. The PDFs for WC and CF events are modeled from MC samples. The fractions of WC and CF-down events (like $D^{*+}_s D^{*-}_s \to D^{*+}_s D^-_s$) are taken from MC. The fractions of CF-up events(like $D^+_s D^-_s \to D^{*+}_s D^-_s$) which are difficult to accurately simulate, are floated in the fit. As the CF-down fractions are fixed, the three distributions ($D^+_s D^-_s$, $D^{*\pm}_s D^{\mp}_s$, and $D^{*+}_s D^{*-}_s$) are fitted simultaneously. The systematics error due to fixing CF fractions is estimated using the $B^0_s \to D^{(*)+}_s \pi^-$ control sample.

The fit results are listed in Table 1, and the fit projections in ΔE and $M_{\rm bc}$ are shown in Figure 1. The branching fractions for three channels is calculated using yield, MC selection ef-

Table 1: Signal yields (Y), efficiencies including intermediate branching fractions (ϵ), branching fractions ($\mathcal{B}$), and signal significance (S) including systematic uncertainly. The first error listed is statistical, the second is the systematics due to analysis procedure, and the third denotes systematics due to external inputs.

Mode	Y (events)	$\epsilon(\times 10^{-4})$	$\mathcal{B}(\%)$	S(σ)
$D^+_s D^-_s$	$8.5^{+3.2}_{-2.6}$	3.31	$1.03^{+0.39+0.15}_{-0.32-0.13} \pm 0.21$	6.2
$D^{*\pm}_s D^{\mp}_s$	$9.2^{+2.8}_{-2.4}$	1.35	$2.75^{+0.83}_{-0.71} \pm 0.40 \pm 0.56$	6.6
$D^{*+}_s D^{*-}_s$	$4.9^{+1.9}_{-1.7}$	0.643	$3.08^{+1.22}_{-1.04} \pm 0.56 \pm 0.63$	3.2
Sum	$22.6^{+4.7}_{-3.9}$		$6.85^{+1.53+1.26}_{-1.30-1.25} \pm 1.41$	

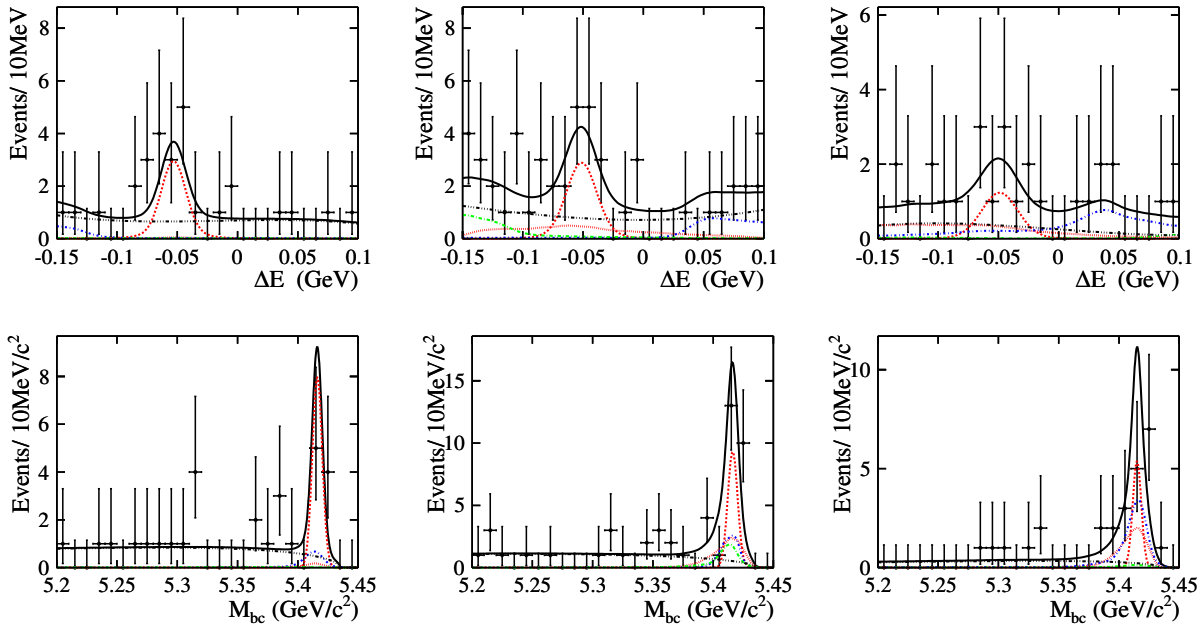

Figure 1: ΔE and M_{bc} projections of the fit results. The left (top and bottom) correspond to $B^0_s \quad D^+_s D^-_s$, middle (top and bottom) to $B^0_s \quad D^{*\pm}_s D^{\mp}_s$ and right (top and bottom) to $B^0_s \quad D^{*+}_s D^{*-}_s$ respectively. The dashed (dotted) curves show RC(WC) signal, the dashed-dotted curves show CF components, the dashed-3-dotted curves show background, and solid curves show the total.

ficiency with intermediate branching fraction [1] included. The statistical significance is calculated as $\sqrt{-2\ln(\mathcal{L}_0/\mathcal{L}_{max})}$, where $\mathcal{L}_0$ and $\mathcal{L}_{max}$ are the values of likelihood function when the signal yield is fixed to zero and when it is the fitted value, respectively. The effect of systematic uncertainly is included in the significance by smearing the likelihood function by a Gaussian having a width equals to total systematic error to the signal yield. These are given in Table 1. We note that $\mathcal{B}(B_s^0 \to D_s^{*\pm}D_s^{\mp})$ with 6.6σ significance is the first observation and $\mathcal{B}(B_s^0 \to D_s^{*+}D_s^{*-})$ with 3.2σ significance is the first evidence.

The systematic errors are dominated by $D_s^{(*)}$ branching fraction, tracking and $K^{\pm}$ identification as well as the $\Upsilon(5S)$ cross-section, f_s, $f_{B_s^*\bar{B}_s^*}$.

Using the branching fraction measurements given in the Table 1, we determine $\Delta\Gamma_s/\Gamma_s$. We assume that CP-violation is negligible and that the above mentioned decay modes saturate the decay width [3].This leads to the relation $\Delta\Gamma_s/\Gamma_s = 2\mathcal{B}/(1-\mathcal{B})$. From our measurement in Table 1, we obtain

$$\Delta\Gamma_s/\Gamma_s = 0.147^{+0.036+0.044}_{-0.030-0.042}$$

where the first error is statistical and the second is systematic. Systematic uncertainties arising from theoretical estimates is expected to be about $\pm 3\%$ [3] where contributions from three-body final states are neglected.

In conclusion we have measured the branching fractions for $B_s^0 \to D_s^{(*)+}D_s^{(*)-}$ using data taken at $\Upsilon(5S)$ resonance. Our results constitute the first observation of $B_s^0 \to D_s^{*\pm}D_s^{\mp}$ and the first evidence for $B_s^0 \to D_s^{*+}D_s^{*-}$. Using our measured decay branching fractions, we determine the decay width difference $\Delta\Gamma_s/\Gamma_s$ for B_s-$\bar{B}_s$ mass eigen states which is an improvement over previous measurements. Expecting another $\sim 100 fb^{-1}$ of data soon to be analyzed, we hope to improve these measurements significantly.

Acknowledgments

I am grateful to members of the Belle collaboration for many fruitful discussions and suggestions, in particular S.Esen, A. Schwartz and K. Trabelsi.

References

1. C.Amsler*et al.* Particle Data Group,*Phys. Lett.* B **667**, 1 (2008) and 2009 update.
2. R.Barate *et al*, ALEPH Collab., *Phys. Lett.* B **486**, 286 (2000).
   T.Altonen *et al*, CDF Collab.,*Phys. Rev. Lett.* **100**, 021803 (2008).
   V.M.Abazov *et al*, *Phys. Rev. Lett.* **102**, 091801 (2009).
3. R.Aleksan *et al.Phys. Lett.* B **316**, 567 (1993).
4. A.Lenz, U.Nierste, JHEP **06**, 072 (2007).
5. A.Abashian *et al.* Belle Collab. *Nucl. Instrum. Methods* A **479**, 117 (2003).
6. S.Kurokawa and E.Kikutani,*Nucl. Instrum. Methods* A **499**, 1 (2003).
7. G.S.Huang *et al.* Cleo Collab. PRD **75**, 012002 (2007),
   M.Artuso *et al.* Cleo Collab. PRL **95**, 261801 (2005),
   A.Drutskoy *et al.* Belle Collab. PRL **98**, 052001 (2007).
8. R.Louvet *et al.* Belle Collab. PRL **102**, 021801 (2009).
9. G.C.Fox and S.Wolfram, PRL **41**, 1581 (1978).The modified moments used here are described in S.H.Lee *et al.* Belle Collab. PRL **91**, 261801 (2003).
10. H.Albrecht *et al.* ARGUS Collab. PLB **241**, 278 (1190).

LEPTONIC AND SEMILEPTONIC D- AND B-MESON DECAYS FROM *BABAR*

J. DINGFELDER
(representing the *BABAR* Collaboration)
Physikalisches Institut Bonn, Nussallee 12,
53115 Bonn, Germany

Recent results on semileptonic and leptonic decays of D and B mesons from the *BABAR* experiment are reviewed. The results are based on large samples of D, D_s and B mesons produced in e^+e^- collisions in the PEP-II asymmetric-energy storage rings at the SLAC National Accelerator Laboratory.

1 Overview

In these proceedings, we briefly review a selection of recent preliminary results on semileptonic and leptonic decays of D and B mesons from the *BABAR* experiment. Three different analyses are discussed:

- charmless semileptonic B-meson decays $B \to \pi\ell\nu$ and $B \to \rho\ell\nu$ and determination of the Cabibbo-Kobayashi-Maskawa (CKM) matrix element $|V_{ub}|$ [1];
- semileptonic D-meson decays $D^+ \to K^-\pi^+e^+\nu_e$ and a detailed study of the $K\pi$ system in these decays [2];
- leptonic D_s-meson decays $D_s^+ \to \tau^+\nu_\tau$ and the determination of the decay constant $f_{D_s^+}$ [3].

The results of these analyses are based on large data samples that correspond to an integrated luminosity of 349 fb^{-1} (427 fb^{-1} for the $D_s^+ \to \tau^+\nu_\tau$ analysis) recorded with the *BABAR* detector in e^+e^- collisions at the $\Upsilon(4S)$ resonance.

2 $B \to \pi\ell\nu$ and $B \to \rho\ell\nu$

The $B \to \pi\ell\nu$ decay is the most promising exclusive decay mode, both experimentally and theoretically, for a precise determination of the CKM matrix element $|V_{ub}|$, a fundamental parameter of the Standard Model that describes the coupling of the weak charged current to a bottom and an up quark. The differential decay rate for $B^0 \to \pi^-\ell^+\nu$ is given by

$$\frac{d\Gamma(B^0 \to \pi^-\ell^+\nu)}{dq^2} = \frac{G_F^2}{24\pi^3} p_\pi^3 |V_{ub}|^2 |f_+(q^2)|^2, \tag{1}$$

where $q^2 = (p_\ell + p_\nu)^2$ is the four-momentum transfer of the semileptonic decay and $f_+(q^2)$ is the pseudoscalar form factor whose normalization must be predicted by theory. Several theoretical form-factor predictions exist from QCD calculations based on lattice QCD or light-cone sum

rules or from quark models. For $B \to \rho\ell\nu$, due to the vector meson in the final state, three form factors are needed to describe the decay dynamics. A determination of $|V_{ub}|$ from $B \to \rho\ell\nu$ decays is an important cross-check of the $B \to \pi\ell\nu$ results, but suffers from higher backgrounds and from a lack of recent lattice QCD calculations for this decay.

A number of $B \to \pi\ell\nu$ and $B \to \rho\ell\nu$ measurements with different techniques to tag one of the two B mesons in the $B\overline{B}$ event exist, but untagged analyses still provide the most precise results due to their relatively large signal efficiency. *BABAR* presents a new untagged analysis of $B \to \pi\ell\nu$ and $B \to \rho\ell\nu$ decays, in which the neutrino is reconstructed from the missing energy and momentum in the event. Compared to previous *BABAR* analyses [4,5], this analysis is based on a larger data sample and an improved q^2-dependent background suppression using dedicated neural networks for each of the main backgrounds ($B \to X_c\ell\nu$ decays, $e^+e^- \to q\bar{q}$ ($q = u, d, s, c$) continuum events, and non-signal $B \to X_u\ell\nu$ decays). The signal is extracted in a maximum-likelihood fit of the two-dimensional ΔE vs. m_{ES} distribution in several bins of q^2 (6 bins for $B \to \pi\ell\nu$, 3 bins for $B \to \rho\ell\nu$), where ΔE is the difference between the reconstructed and expected B-meson energy and m_{ES} is the beam-energy constrained B mass. The fit is performed simultaneously for the four signal modes $B^0 \to \pi^-\ell^+\nu$, $B^+ \to \pi^0\ell^+\nu$, $B^0 \to \rho^-\ell^+\nu$, $B^+ \to \rho^0\ell^+\nu$, assuming isospin symmetry. The resulting signal yields are ~ 10600 $B \to \pi\ell\nu$ and ~ 3300 $B \to \rho\ell\nu$ candidates. The branching fractions are measured to be $(1.41 \pm 0.05 \pm 0.07) \times 10^{-4}$ for $B \to \pi\ell\nu$ and $(1.75 \pm 0.15 \pm 0.27) \times 10^{-4}$ $B \to \rho\ell\nu$, where the errors are statistical and systematic. The $B \to \pi\ell\nu$ branching fraction agrees well with the current world average [6], while the one for $B \to \rho\ell\nu$ is about 2.5σ lower.

Figure 1 shows the measured q^2 spectra for $B \to \pi\ell\nu$ (left) and $B \to \rho\ell\nu$ (right), and their comparisons with predictions from unquenched lattice QCD, light-cone sum rules and the ISGW2 quark model. For $B \to \pi\ell\nu$, the measured q^2 spectrum agrees best with the one predicted by the HPQCD lattice calculation [7], but shows only marginal agreement with the ISGW2 quark model [8] and in particular with the light-cone sum rules calculation [9]. The $B \to \rho\ell\nu$ spectrum agrees well with the predictions from light-cone sum rules [10] and the ISGW2 quark model [8] within the sizable errors.

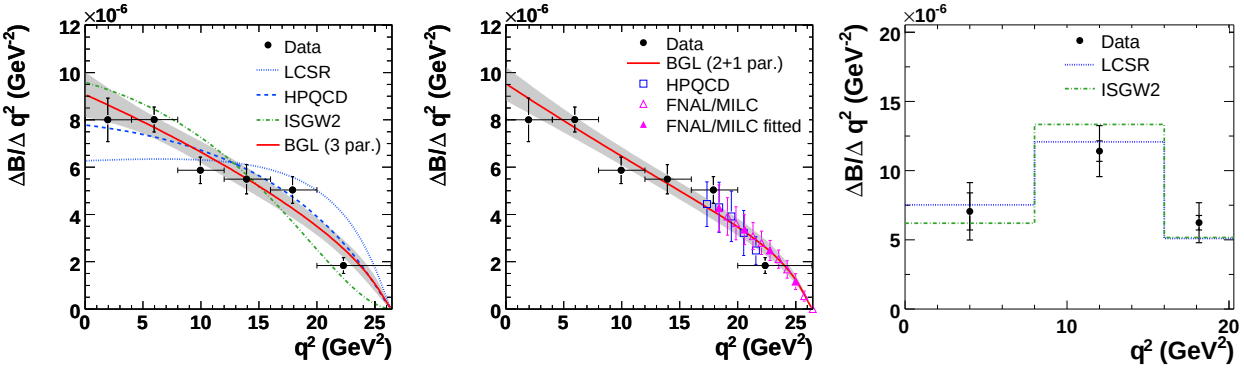

Figure 1: Measured q^2 spectra (unfolded for detector and radiative effects) for $B \to \pi\ell\nu$ and $B \to \rho\ell\nu$. Left: Shape comparisons of the $B \to \pi\ell\nu$ data with various form-factor predictions, normalized to the measured total branching fraction (error bars show the total errors). The results of a fit of the BGL parameterization to the data is shown as red line with error band. Middle: Combined fit of the BGL parameterization to the $B \to \pi\ell\nu$ data and FNAL/MILC predictions. For comparison, the HPQCD predictions are also shown. Right: Shape comparisons of the $B \to \rho\ell\nu$ data with predictions from light-cone sum rules and the ISGW2 quark model (inner and outer error bars show the statistical and total errors, respectively).

BABAR determines $|V_{ub}|$ from $B \to \pi\ell\nu$ with two different approaches. The first is the "classical" approach based on combining the measured partial branching fractions with integrals of the form-factor calculations over a certain q^2 range ($q^2 > 16$ GeV^2 for lattice QCD and $q^2 < 16$ GeV^2 for light-cone sum rules) using the relation $|V_{ub}| = \sqrt{\Delta B/(\tau_0 \Delta\zeta)}$. Here ΔB is the measured

Table 1: $|V_{ub}|$ derived from $B \to \pi\ell\nu$ decays for light-cone sum rules (LCSR) and lattice (HPQCD) form-factor calculations. Quoted errors are experimental uncertainties and uncertainties of the form-factor integral $\Delta\zeta$.

Form-factor calculation	q^2 range (GeV^2)	$\Delta\zeta$ (ps^{-1})	$\lvert V_{ub}\rvert$ (10^{-3})
LCSR [9]	$0-16$	5.44±1.43	$3.63 \pm 0.12^{+0.59}_{-0.40}$
HPQCD [7]	$16-26.4$	2.02±0.55	$3.21 \pm 0.17^{+0.55}_{-0.36}$

partial branching fraction, τ_0 is the B^0 lifetime and $\Delta\zeta = \Gamma/|V_{ub}|^2$ is the normalized partial decay rate predicted by form-factor calculations. Table 1 shows the $|V_{ub}|$ values obtained with this approach. The uncertainty on $|V_{ub}|$ is dominated by the theoretical form-factor uncertainty. In the second approach, $|V_{ub}|$ is determined from a combined fit to *BABAR* data and lattice QCD precictions using the so-called z-expansion (or BGL parametrization) [11] to parameterize $f_+(q^2)$ over the whole q^2 range. This approach makes use of the full shape information from data and the shape and normalization from theory to decrease the uncertainty on $|V_{ub}|$. A fit to data and the FNAL/MILC lattice calculation yields $|V_{ub}| = (2.95 \pm 0.31) \times 10^{-3}$. A similar fit using the HPQCD lattice calculation gives a consistent result. The extracted value of $|V_{ub}|$ has a total relative error of 10%. The error contributions have been estimated to be 3% from the branching-fraction measurement, 5% from the shape of the q^2 spectrum determined with data, and 8.5% from the form-factor normalization obtained from theory. The value of $|V_{ub}|$ is lower by about one standard deviation compared to the results of a combined fit performed by the FNAL group to earlier *BABAR* measurements and the same FNAL/MILC calculation [12].

3 $D^+ \to K^-\pi^+e^+\nu_e$

The semileptonic decay $D^+ \to K^-\pi^+e^+\nu_e$ allows for studies of the hadronic $K\pi$ system in the final state, such as measurements of the contributing $K\pi$ resonant and non-resonant amplitudes and of the properties of the $K\pi$ S-wave or the dominant P-wave component, the $K^*(892)^0$.

BABAR has studied the decay $D^+ \to K^-\pi^+e^+\nu_e$ with a large sample of 245,000 signal events. The signal decay is reconstructed in the following way. A plane perpendicular to the event thrust axis is used to define two hemispheres. A signal candidate corresponds to a positron, a charged kaon and a pion in the same hemisphere. All other tracks in the hemisphere form the "spectator system". The neutrino momentum is estimated from a contrained fit which imposes the D^+ mass to the $(K^-\pi^+e^+\nu_e)$ system and uses estimates of the D^+ direction and neutrino energy and their uncertainties from measurements obtained from all tracks in the event. The backgrounds from $\Upsilon(4S) \to B\overline{B}$ decays and hadronic continuum events (mostly with charm particles) are suppressed by using Fisher discriminants based on variables describing the event topology or the properties of the spectator system.

The information to separate the different hadronic angular momentum components in this decay is available through correlations between the leptonic and hadronic systems. This requires a fit of the differential decay rate over the full five-dimensional phase space, i.e., as a function of five kinematical variables: $m^2_{K\pi}$, q^2, and three decay angles. The nominal fit uses a signal model described by the sum of S- and P-waves, where the latter includes in addition to the dominant $K^*(892)^0$ component a contribution from the $K^*(1410)^0$ radial excitation. The fractions obtained from the fit are $(5.79 \pm 0.16 \pm 0.15)\%$ for the S-wave component, $(94.11 \pm 0.74 \pm 0.75)\%$ for $K^*(892)^0$, and a small contribution of $(0.33 \pm 0.13 \pm 0.19)\%$ for $K^*(1410)^0$, where the errors are statistical and systematic. If an additional D-wave component is added to the fit, a similar fit probability is obtained and the fit yields a D-wave fraction of $(0.19 \pm 0.09 \pm 0.09)\%$, while the $K^*(1410)^0$ fraction becomes $(0.16 \pm 0.08 \pm 0.14)\%$. Considering both statistical and systematic uncertainties, the significances of these two components are slightly below three standard deviations, hence upper limits of are quoted in Ref. [2].

Table 2: Measured parameters of the $K^*(892)^0$ resonance and hadronic form factors compared with the current world averages.

Measured quantity	*BABAR* [2]	PDG average [13]
$m_{K^*(892)^0}$ (MeV)	$895.4 \pm 0.2 \pm 0.2$	896.00 ± 0.25
$\Gamma^0_{K^*(892)^0}$ (MeV)	$46.5 \pm 0.3 \pm 0.2$	50.3 ± 0.6
r_{BW} (GeV^{-1})	$2.1 \pm 0.5 \pm 0.5$	2.72 ± 0.55
$r_V = V(0)/A_1(0)$	$1.463 \pm 0.017 \pm 0.031$	1.62 ± 0.08
$r_2 = A_2(0)/A_1(0)$	$0.801 \pm 0.020 \pm 0.020$	0.83 ± 0.05
m_A (GeV)	$2.63 \pm 0.10 \pm 0.13$	–

BABAR measures the properties of the $K^*(892)^0$, namely its resonance parameters and the hadronic P-wave form factors. Table 2 shows the results for the resonance parameters: the mass $m_{K^*(892)^0}$, the width $\Gamma^0_{K^*(892)^0}$, and the Blatt-Weisskopf parameter r_{BW}. The measured width is significantly smaller than the current PDG world average [13], but agrees with recent measurements from the FOCUS [14] Collaboration and from τ decays [15]. The results for the P-wave form factors (the two axial-vector form factors $A_1(q^2)$ and $A_2(q^2)$ and the vector form factor $V(q^2)$), assuming single-pole dominance, are shown in Table 2 in terms of the form-factor ratios at $q^2 = 0$, $r_V = V(0)/A_1(0)$, $r_2 = A_2(0)/A_1(0)$, and the axial-vector pole mass, m_A, that parameterizes the q^2 dependence of A_1 and A_2. The results for r_V and r_2 represent large improvements in statistical and systematic precision compared to previous measurements. The pole mass m_A has been determined for the first time in this analysis.

The $D^+ \to K^-\pi^+\ell^+\nu_e$ branching fraction is measured relative to the $D^+ \to K^-\pi^+\pi^+$ decay mode, which is used as normalization mode, to be $(4.04 \pm 0.03 \pm 0.04 \pm 0.09) \times 10^{-2}$, where the errors are statistical, systematic and due to external inputs. After subtraction of the S- and $K^*(1410)^0$-wave contributions, the value of the hadronic form factor A_1 at $q^2 = 0$ can be obtained: $A_1(0) = 0.6226 \pm 0.0056 \pm 0.0065 \pm 0.0074$ in the zero-width approximation for the $K^*(892)^0$.

BABAR also measures the phase of the S-wave component as a function of the $K\pi$ mass, fixing the P-wave parameters to the results of the nominal fit. The results are shown in Figure 2. They confirm those obtained from $K\pi$ production at small momentum transfer at fixed-target experiments (LASS [16]), but disagree with similar analyses of three-body decays of D mesons (e.g., $D^+ \to K^-\pi^+\pi^+$ [17,18,19,20]). This result illustrates the importance of final-state interactions in hadronic D-meson decays, i.e., the effect of the additional pion in $D^+ \to K^-\pi^+\pi^+$ decays compared to $D^+ \to K^-\pi^+e^+\nu_e$ decays.

4 $D_s^+ \to \tau^+\nu_\tau$

Leptonic decays of D_s^+ mesons, $D_s^+ \to \ell^+\nu_\ell$, proceed through annihilation of the c and $\bar{s}$ quarks via a virtual W^+ boson that decays to a lepton-neutrino pair. These decays provide access to the pseudoscalar decays constant $f_{D_s^+}$, which describes the amplitude for the c and $\bar{s}$ quarks in the meson to have zero spatial separation, a necessary condition for the annihilation. The decay width in the Standard Model is given to lowest order by

$$\Gamma(D_s^+ \to \ell^+\nu_\ell) = \frac{G_F^2}{8\pi} M_{D_s^+}^3 \left(\frac{m_\ell}{M_{D_s^+}}\right)^2 \left(1 - \frac{m_\ell^2}{M_{D_s^+}^2}\right)^2 |V_{cs}|^2 f_{D_s^+}^2, \qquad (2)$$

where m_ℓ and $m_{D_s^+}$ are the charged-lepton and D_s^+ masses, respectively, and $|V_{cs}|$ is the CKM matrix element describing the coupling of the W boson to the $c\bar{s}$ quark pair. Since the leptonic

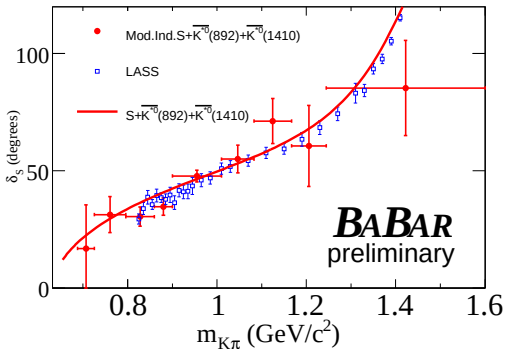

Figure 2: Variation of the S-wave phase with the $K\pi$ mass for $D^+ \to K^-\pi^+e^+\nu_e$ decays, assuming a signal composed of S-wave $+K^*(892)^0+K^*(1410)^0$. The solid red line shows a parametrization of the S-wave variation. The phase variation measured by LASS is shown as blue squares.

decay $D_s^+ \to \ell^+\nu_\ell$ is helicity-suppressed by a factor $m_\ell^2/M_{D_s^+}^2$, the decay sequence $D_s^+ \to \tau^+\nu_\tau$, $\tau^+ \to e^+\nu_e\bar{\nu}_\tau$ is studied. A precise determination of $f_{D_s^+}$ is useful to validate lattice QCD calculations of this quantity. Differences between the measured value and theoretical predictions could also hint at physics beyond the Standard Model, such as models that include a charged Higgs boson (two Higgs doublet models) [21] or leptoquarks [22].

BABAR measures the branching fraction for $D_s^+ \to \tau^+\nu_\tau$ decays relative to that for $D_s^+ \to K_S^0K^+$ decays, whose branching fraction is rather well known. An inclusive D_s^+ sample is selected via the D_s^{*+} production process $e^+e^- \to c\bar{c} \to D_s^{*+}\overline{D}_{tag}\overline{K}^{0,-}X$ and the subsequent decay $D_s^{*+} \to D_s^+\gamma$. Here $\overline{D}_{tag}$ denotes a fully reconstructed hadronic D-meson decay, which is used to suppress the large background from non-charm $q\bar{q}$ production, and X stands for additional charged or neutral pions produced in $c\bar{c}$ fragmentation that are not associated with the $\overline{D}_{tag}$ decay or the kaon. The D_s^{*+} candidate is reconstructed as a missing particle; its four-momentum is computed as $P_{D_s^{*+}} = P_{e^+e^-} - (P_{\overline{D}_{tag}} + P_K + P_X)$. The four-momentum of the D_s^+ candidate is defined as the recoil in the $D_s^{*+} \to D_s^+\gamma$ decay, $P_{D_s^+} = P_{D_s^{*+}} - P_\gamma$. The yields for the signal and normalization modes are determined from unbinned maximum-likelihood fits to the distributions of two variables: the recoil D_s^+ mass and the extra energy in the event. The resulting event yields are $N(D_s \to \tau\nu) = 448 \pm 36$ and $N(D_s \to K_S^0K) = 333 \pm 28$.

The branching fraction for $D_s^+ \to \tau^+\nu_\tau$ is measured to be $(4.5 \pm 0.5 \pm 0.4 \pm 0.3)\%$, where the errors are statistical, systematic and due to external inputs, namely the branching fractions for $D_s^+ \to K_S^0K^+$, $K_S^0 \to \pi^+\pi^-$ and $\tau^+ \to e^+\nu_e\bar{\nu}_\tau$ [13]. Using Eq. 2 and the assumption $|V_{cs}| = |V_{ud}|$, the decay constant is found to be $f_{D_s^+} = (233 \pm 13 \pm 10 \pm 7)$ MeV, where the errors are statistical, systematic and due to external quantities $(m_\tau, m_{D_s^+}, \tau_{D_s^+}, |V_{ud}|)$. The meaured $f_{D_s^+}$ value agrees within one standard deviation with the most recent CLEO-c results from $D_s^+ \to \tau^+\nu_\tau$ decays [23,24] and with recent unquenched lattice QCD calculations [25,26,27]. Further results on leptonic decays of charm mesons can be found in another presentation [28] at this conference.

5 Summary

We presented the most recent results for leptonic and semileptonic D- and B-meson decays from *BABAR*. The branching fractions and q^2 spectra for $B \to \pi\ell\nu$ and $B \to \rho\ell\nu$ decays are mesured with improved accuracy and $|V_{ub}|$ is extracted with a precision of 10% in a combined fit to data and lattice QCD predictions. For $D^+ \to K^-\pi^+\ell^+\nu_e$ decays, several studies of the $K\pi$ system have been performed. The various $K\pi$ contributions are explored down to the $\sim 1\%$ level,

the variation of the S-wave phase with the $K\pi$ mass has been studied for the first time with semileptonic D decays and the $K^*(892)^0$ resonance and hadronic form-factor parameters are measured with a high precision. Using $D_s^+ \to \tau^+\nu_\tau$ decays, the decay constant $f_{D_s^+}$ is measured and is found to be consistent with the current experimental average and with recent lattice QCD calculations. In the future, further improvement for both semileptonic and leptonic decays of D and B mesons can be expected with the large data samples at a Super B factory and progress in lattice QCD calculations.

References

1. *BABAR* Collab., P. del Amo Sanchez *et al.*, submitted to Phys. Rev. D, arXiv:1005.3288 [hep-ex].
2. *BABAR* Collab., preliminary result presented at Moriond QCD and High Energy Interactions, La Thuile, March 2010, to be submitted to Phys. Rev. D.
3. *BABAR* Collab., J. P. Lees *et al.*, submitted to Phys. Rev. D (Rapid Communications), arXiv:1003.3063 [hep-ex].
4. *BABAR* Collab., B. Aubert *et al.*, Phys. Rev. **D72**, 051102 (2005).
5. *BABAR* Collab., B. Aubert *et al.*, Phys. Rev. Lett. **98**, 091801 (2007).
6. Heavy Flavor Averaging Group, E. Barberio *et al.*, e-Print: arXiv:0808.1297 [hep-ex], and recent updates.
7. HPQCD Collab., E. Gulez *et al.*, Phys. Rev. **D73**, 074502 (2006) and Erratum ibid. **D75**, 119906 (2007).
8. N. Isgur, D. Scora, B. Grinstein, and M. B. Wise, Phys. Rev. **D39**, 799 (1989); D. Scora, N. Isgur, Phys. Rev. **D52**, 2783 (1995).
9. P. Ball and R. Zwicky, Phys. Rev. **D71**, 014015 (2005).
10. P. Ball and R. Zwicky, Phys. Rev. **D71**, 014029 (2005).
11. C. G. Boyd, B. Grinstein, and R. F. Lebed, Phys. Rev. Lett. **74**, 4603 (1995); C. G. Boyd and M. J. Savage, Phys. Rev. **D56**, 303 (1997).
12. Fermilab Lattice and MILC Collab., J. Bailey *et al.*, Phys. Rev. **D79**, 054507 (2009).
13. C. Amsler *et al.* (Particle Data Group), Phys. Lett. **B667**, 1 (2008) and 2009 partial update for the 2010 edition.
14. J. M. Link *et al.* (FOCUS Collab.), Phys. Lett. **B535**, 43 (2002).
15. D. Epifanov *et al.* (Belle Collab.), Phys. Lett. **B654**, 65 (2007).
16. D. Aston *et al.*, Nucl. Phys. **B296**, 493 (1988).
17. E. M. Aitala *et al.* (Fermilab E791 Collab.), Phys. Rev. **D73**, 032004 (2006).
18. J. M. Link *et al.* (FOCUS Collab.), Phys. Lett. **B653**, 1 (2007).
19. J. M. Link *et al.* (FOCUS Collab.), Phys. Lett. **B681**, 14 (2009).
20. A. Bonvicini *et al.* (CLEO Collab.), Phys. Rev. **D78**, 052001 (2008).
21. A. G. Akeroyd and C. H. Chen, Phys. Rev. **D75**, 075004 (2007).
22. B. A. Dobrescu and A. S. Kronfeld, Phys. Rev. Lett. **100**, 241802 (2008).
23. P. U. E. Onyisi *et. al.* (CLEO Collab.), Phys. Rev. **D79**, 052002 (2009).
24. P. Naik, *et al.* (CLEO Collab.), Phys. Rev. **D80**, 112004 (2009).
25. E. Follana *et al.* (HPQCD and UKQCD Collab.s), Phys. Rev. Lett. **100**, 062002 (2008).
26. B. Blossier *et al.* (ETMC Collab.), JHEP **0907**, 043 (2009).
27. C. Bernard *et al.* (Fermilab Lattice and MILC Collab.s), PoS LATTICE 2008, 278 (2008).
28. S. Stone, "D and D_s leptonic and semileptonic decays at CLEO", presented at Moriond QCD and High Energy Interactions, La Thuile, March 2010.

CP VIOLATION IN *B* HADRONS AT THE TEVATRON

L.B. OAKES
for the CDF and DØ collaborations
Department of Physics, Subdepartment of Particle Physics, Denys Wilkinson Building, 1 Keble Road, Oxford OX1 3NP, England

The latest results are presented from DØ and CDF on CP violation in the B_s^0 system, including measurements of the CP violating phase $\beta_s^{J/\psi\phi}$, B_s^0 lifetime, τ_s, and width difference, $\Delta\Gamma_s$ using $2.8fb^{-1}$ integrated luminosity. In addition to results from the individual experiments, the Tevatron combined result for $\beta_s^{J/\psi\phi}$ is shown. The improvements made to the analyses for upcoming results from both experiments are also introduced.

1 Introduction

The study of neutral B meson properties can provide important tests of the Standard Model (SM) including constraints on parameters of the CKM matrix. While the B^0 system has been thoroughly investigated by B factories, precision measurements in the B_s^0 system are a more recent development, driven largely by the Tevatron experiments. The $B_s^0 - \bar{B}_s^0$ system has the potential to yield indirect observations of New Physics (NP), through the presence of non-SM particles in second order weak interaction processes such as neutral B meson mixing. Both the CDF and DØ experiments at the Fermilab Tevatron have published measurements of the B_s mixing frequency, Δm_s, but in order to constrain potential NP contributions in this system it is also necessary to precisely measure the CP violating phase, β_s. At the Tevatron, the golden mode for this measurement is $B_s^0 \to J/\psi\phi$. The $J/\psi\phi$ final state is common to B_s^0 and $\bar{B}_s^0$ decays; CP violation occurs in this channel through interference between decays with and without B_s^0 mixing. The phase, β_s, between these two decays is predicted to be close to zero in the SM, so a significant excess would be a clear indication of evidence for NP in this channel.

2 Neutral B_s^0 system phenomenology

The flavour eigenstates of B_s^0 mesons in the SM are not the same as the mass eigenstates, leading to oscillations between $|B_s^0\rangle = (\bar{b}s)$ and $|\bar{B}_s^0\rangle = (b\bar{s})$ via the second order weak interactions. The phenomenology of this weak mixing is described by the Cabibbo-Kobayashi-Maskawa (CKM) matrix. The time evolution of the $B_s^0 - \bar{B}_s^0$ system is governed by the Schrödinger equation

$$i\frac{d}{dt}\begin{pmatrix} B_s^0(t) \\ \bar{B}_s^0(t) \end{pmatrix} = \mathcal{H}\begin{pmatrix} B_s^0(t) \\ \bar{B}_s^0(t) \end{pmatrix} \equiv \left[\begin{pmatrix} M_0 & M_{12} \\ M_{12}^* & M_0 \end{pmatrix} - \frac{i}{2}\begin{pmatrix} \Gamma_0 & \Gamma_{12} \\ \Gamma_{12}^* & \Gamma_0 \end{pmatrix}\right]\begin{pmatrix} B_s^0(t) \\ \bar{B}_s^0(t) \end{pmatrix} \quad (1)$$

where the M and Γ matrices describe the mass and decays of the system. The mass eigenstates can be obtained by diagonalising $\mathcal{H}$; $|B_s^H\rangle = p|B_s^0\rangle - q|\bar{B}_s^0\rangle$ and $|B_s^L\rangle = p|B_s^0\rangle + q|\bar{B}_s^0\rangle$ where

$|q/p| = 1$ in the case of no direct CP violation, as predicted in the $J/\psi\phi$ channel, and the indices H and L label the heavy and light eigenstates respectively. The mass difference, Δm_s, between the heavy and light states is proportional to the frequency of B_s^0 mixing and is approximately equal to $2|M_{12}|$. The mass eigenstates have a small but non negligible lifetime difference, which can be described in terms of the decay width difference $\Delta\Gamma_s = \Gamma_L - \Gamma_H \approx 2|\Gamma_{12}|\cos(2\phi_s)$ where the CP violating phase is defined as $\phi_s = arg(-M_{12}/\Gamma_{12})$ and the mean decay width $\Gamma_s = 1/\tau_s$. The SM predicts ϕ_s^{SM} to be of order 0.004, and it would be expected to increase in the presence of NP. The mixing frequency, Δm_s has been well determined by Tevatron measurements, CDF published a 5σ observation of mixing with $\Delta m_s = 17.77 \pm 0.10$ (stat.) ± 0.07 (syst.)ps^{-1} and DØ 3σ evidence with $\Delta m_s = 18.52 \pm 0.91$ps^{-1}.

3 *CP* violation in $B_s \to J/\psi\phi$

The relative phase, β_s, between decays of a B_s^0 meson to $J/\psi\phi$ directly, and after mixing to $\bar{B}_s^0$, is defined in the SM as

$$\beta_s^{SM} = arg\left(\frac{-V_{ts}V_{tb}^*}{V_{cs}V_{cb}^*}\right) \approx 0.04 \tag{2}$$

A New Physics phase, contributing to the weak mixing diagrams in the neutral B_s^0 system would introduce a new physics phase ϕ_s^{NP} to β_s such that the measured value would be $2\beta_s = 2\beta_s^{SM} - \phi_s^{NP}$. The same NP phase would enhance ϕ_s, giving $\phi_s = \phi_s^{SM} + \phi_s^{NP}$. As both β_s^{SM} and ϕ_s^{SM} are predicted to be close to zero, the NP phase would dominate, and the measured phase would be $2\beta_s \approx -\phi_s \approx \phi_s^{NP}$.

The decay $B_s^0 \to J/\psi(\to \mu^+\mu^-)\phi(\to K^+K^-)$ is fully reconstructed from events which pass the di-muon trigger. The final state is an admixture of CP odd and even states, which can be separated according to their angular momentum. The total angular momentum of the $J/\psi\phi$ state can be $L = 0$, 1, or 2, and the CP of the state is $(-1)^L$, so the $L = 0, 2$ states are CP even, and the $L = 1$ state is CP odd. These CP states can be separated using the angular distribution of the four final state particles, the muons and kaons from the decay of the J/ψ and ϕ. Both CDF and DØ use the transversity basis [1] to define the angular dependence of the final state, where the relative directions of the four particles can be described in terms of three transversity angles, $\{\cos\theta_T, \phi_T, \cos\psi_T\}$ which are defined by the direction of the decaying J/ψ and ϕ mesons. In the transversity basis, the decay amplitude can be separated into three components which represent different linear polarisation states.

The angular analysis is combined with time development and mass dependence in a multivariate likelihood fit. In the simplest case, the fit without flavour tagging information, the likelihood function has a four fold ambiguity under the transformations $\{\beta_s, \Delta\Gamma, \phi_\parallel, \phi_\perp\} \Leftrightarrow \{\phi/2 - \beta_s, -\Delta\Gamma, 2\pi - \phi_\parallel, \pi - \phi_\perp\}$ and $\beta_s \Leftrightarrow -\beta_s$, where the strong phases are defined in terms of the transversity amplitudes, $\phi_\parallel \equiv arg(A_\parallel^* A_0)$ and $\phi_\perp \equiv arg(A_\perp^* A_0)$. By flavour tagging the initial B_s^0 meson, the time development of B_s^0 and $\bar{B}_s^0$ states can be followed separately, which removes the insensitivity to the sign of β_s and $\Delta\Gamma$. This reduces the ambiguity to two points. The flavour of the decaying B meson is tagged using a combination of opposite side (OST) and same side (SST) tagging algorithms. The OST tags on the b quark content of a B meson from the same production vertex as the candidate B_s^0, the SST tags according to the s quark content of a kaon produced with the candidate.

DØ uses the di-muon trigger, followed by cut based selection to find 1967±65 signal events with 2.8fb^{-1} integrated luminosity. The CDF analysis of the same integrated luminosity also uses the di-muon trigger. CDF makes use of a Neural Network (NN) selection procedure to find 3153±55 signal events.

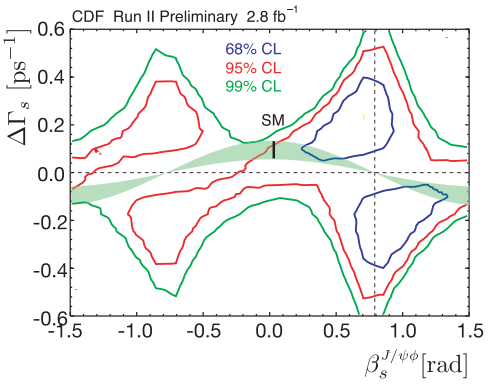

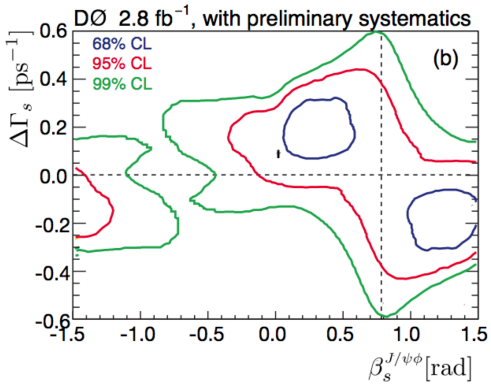

Figure 1: Confidence regions in the $\beta_s^{J/\psi\phi} - \Delta\Gamma_s$ plane, for the CDF analysis (left) and DØ analysis (right). The SM predicted value is marked with a black point.

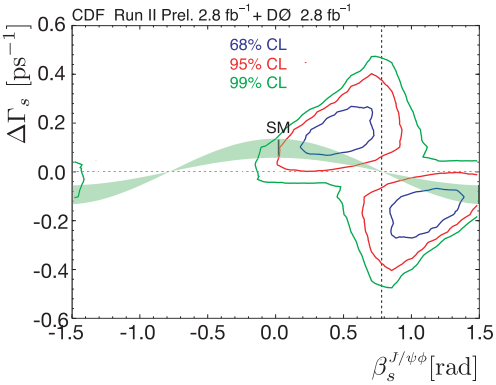

Figure 2: Combined CDF and DØ confidence regions in $\beta_s^{J/\psi\phi} - \Delta\Gamma_s$ plane

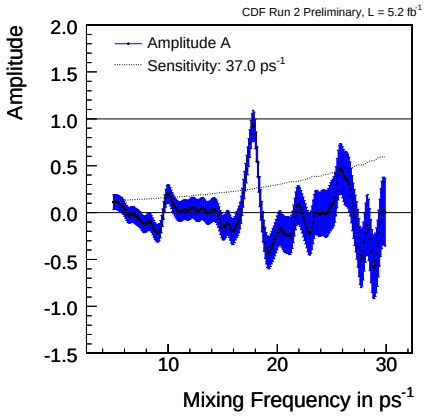

Figure 3: B_s^0 mixing amplitude scan, for calibration of SST

4 Results

In the hypothesis of no CP violation, the CDF experiment presents values of the B_s^0 lifetime, $\tau_s = 1.53 \pm 0.04$ (stat.) $\pm$ 0.01 (syst.) ps, decay width difference $\Delta\Gamma_s = 0.02 \pm 0.05$ (stat.) $\pm$ 0.01 (syst.) ps^{-1} and transversity amplitudes, $|A_\parallel|^2 = 0.241 \pm 0.019$ (stat.) $\pm$ 0.007 (syst.) and $|A_0|^2 = 0.508 \pm 0.024$ (stat.) $\pm$ 0.008 (syst.) using the fit without flavour tagging [4]. The measurements quoted by DØ are in the hypothesis of CP violation, $\tau_s = 1.52 \pm 0.05$ (stat.) $\pm$ 0.01 (syst.) ps, decay width difference $\Delta\Gamma_s = 0.19 \pm 0.07$ (stat.)$^{+0.02}_{-0.01}$ (syst.) ps^{-1} (with flavour tagging) [5], $|A_\parallel|^2 = 0.244 \pm 0.032$ (stat.) $\pm$ 0.014 (syst.) and $|A_0|^2 = 0.555 \pm 0.027$ (stat.) $\pm$ 0.006 (syst.) (without flavour tagging) [6].

Figure 1 shows the individual DØ and CDF likelihood contours in $\beta_s - \Delta\Gamma$. With the current data sample it is not possible for either experiment to quote a point value for the phase β_s due to the symmetries in the likelihood function and the non-Gaussian error distribution. Instead the results are presented as frequentist likelihood contours; a profile-likelihood ratio ordering technique is used to ensure full coverage. To make full use of the available statistics, the Tevatron experiments have produced a combined result [7] shown in Figure 2. The p-value for the SM point in the combined analysis is 3.4%, equivalent to a 2.1σ deviation.

5 Upcoming measurements

Both experiments will produce updated analyses in 2010. The DØ experiment will update to a dataset with integrated luminosity of 6.1fb^{-1}, and make use of a boosted decision tree

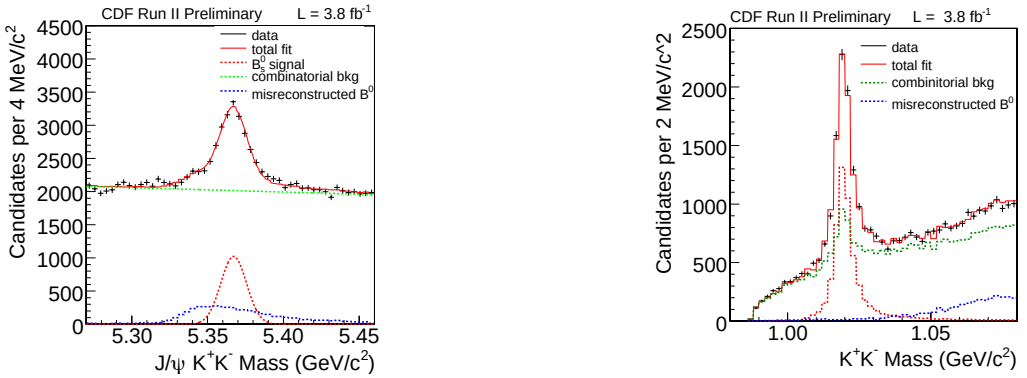

Figure 4: The B_s mass is plotted (left) with a loose ϕ mass cut window, which allows contamination from $B^0 \to J/\psi K^*$ misreconstructed as $B_s^0 \to J/\psi\phi$, this reflection component is fitted with a MC template, the signal B_s mass is fitted with a Gaussian and the combinatorial background with a 1st order polynomial. The invariant KK mass plot(right) is shown with the fractions of each component fixed to that found in the B_s mass fit.

selection to improve the signal to background ratio. CDF plans an update to use 5.2fb^{-1} integrated luminosity, including SST and particle ID for the full data sample, and accounting for contamination of the $B_s^0 \to J/\psi\phi$ signal by $B_s^0 \to J/\psi K^+K^-$ or $B_s^0 \to J/\psi f^0$.

The updated CDF SST is calibrated on a B_s mixing measurement, using the fact that a measured mixing amplitude of ≈ 1 means that the tagger accurately asseses its performance, and an amplitude of > 1 or < 1 implies an under or over estimation of its power, respectively. The amplitude measured for this calibration is $\mathcal{A} = 0.94 \pm 0.15$ (stat.) $\pm$ (syst.), shown in Figure 3. The mixing frequency, $\Delta m_s = 17.79 \pm 0.07$ ps^{-1}, with statistical errors only, is in good agreement with the CDF published measurement.

It has been suggested[8] that a potential contamination of the signal ϕ meson by S-wave f^0 or non-resonant KK of 10-15% could bias the measurement of β_s towards the SM value. The next CDF update includes a full angular analysis of this extra component, however a preliminary study of the invariant KK mass distribution gives no strong indication of a large additional component, as shown in Figure 4.

6 Conclusions

Both of the Fermilab Tevatron experiments have published individual constraints on the CP violating phase $\beta_s^{J/\psi\phi}$ and a combined DØ and CDF result shows a 2σ deviation from the SM prediction. Updated analyses are in progress by both experiments, containing several improvements in addition to the increase from 2.8fb^{-1} to greater than 5fb^{-1} integrated luminosity, including boosted decision tree selection in the DØ analysis, and inclusion of a potential S-wave KK contamination component in the CDF analysis.

References

1. A. S. Dighe, I. Dunietz and R. Fleischer, *Eur. Phys. J. C* **6**, 647 (1999)
2. A.Abulencia et al (CDF collaboration) *Phys. Rev. Lett.* **97**, 242003 (2006)
3. V. Abazov et al (DØ Collaboration) *Phys. Rev. Lett.* **97**, 021802 (2006)
4. The CDF collaboration, Public Note 9458
5. The DØ collaboration, DØ Note 5933-conf
6. V. Abazov et al (DØ Collaboration), arXiv:0810.0037v1
7. http://tevbwg.fnal.gov/results/Summer2009_betas/
8. S.Stone, L.Zhang, arXiv:0812.2832

RARE B-MESON DECAYS AT TEVATRON

D. Tsybychev
Department of Physics and Astronomy, Stony Brook University,
Stony Brook, NY 11794 USA

We present the contributions of the Tevatron experiments, CDF and D0, to the measurements of rare B meson decays and their implications on physics beyond the SM. Both experiments are efficiently collecting data and by now have accumulated data samples corresponding to more than 6 fb^{-1} of integrated luminosity.

1 Introduction

In general, rare decays that involve flavor changing neutral currents (FCNC) are prohibited at a tree level in the Standard Model (SM). The classical examples of such rare decays are $B_{(s)} \to \mu^+\mu^-$. Such decays are possible only at a very low rate through higher-order diagrams. The box diagram through which they proceed makes their rate proportional to $|V^2_{td(s)}|$, and helicity factors further suppress the decay rate. Beyond the SM physics models can have substantial contributions to such FCNC decays, and a measurement of a rate higher than predicted by the SM would clearly indicate the presence of physics processes beyond the SM. Although the mere measurement of such an excess usually reveals little of the underlying physics responsible for the process, it could provide a starting point from which to test various models and limit certain parameters.

Although the Tevatron is the primary facility to study B_s decays, even for B^0 decays the Tevatron experiments have been providing results that are competitive with the experiments at the B factories. The reason for this is that for two-body decays the Tevatron profits best from its large $b\bar{b}$ production cross section. Compared to decays with more particles in the final state, the decay products have relatively large momenta, and therefore the trigger efficiency is relatively high. Due to the three-orders-of-magnitude-larger light quark production cross section at the Tevatron, the background becomes particularly important and much effort is spent in signal selection, which is needed to effectively reject this background. All analyses are developed with a blinded signal region, which is only looked at once the analysis is completed. To calculate branching ratios for observed decays or to set limits usually another well known high branching-ratio decay channel is used for normalization. The same normalization channel is normally used to verify and optimize the analysis. The branching fraction $\mathcal{B}_{sig}$ is then obtained from

$$\mathcal{B}_{sig} = \frac{N_{sig}}{N_{norm}} \frac{\epsilon_{norm}}{\epsilon_{sig}} \frac{f_{norm}}{f_{sig}} \mathcal{B}_{norm},$$

where N_{sig} and N_{norm} are number of observed signal and normalization channel events, ϵ_{sig} and ϵ_{norm} are efficiencies, and f_{sig} and f_{norm} are production fractions for signal and normalization channels respectively.

2 $B_{(s)} \to \mu^+\mu^-$

The $B_{(s)} \to \mu^+\mu^-$ rates have been calculated very precisely[1], $\mathcal{B}(B_s \to \mu^+\mu^-) = (3.35 \pm 0.32) \times 10^{-9}$ and $\mathcal{B}(B^0 \to \mu^+\mu^-) \sim O(-10)$, and will be tested soon by the LHCb experiment at CERN. Even though the SM branching ratio for these decays is probably out of reach for CDF and D0, several plausible physics models can be employed that cause the rate of $B_{(s)} \to \mu^+\mu^-$ to be significantly enhanced. Most of those models are supersymmetric extensions of the SM [2]. Both CDF and D0 have searched for the two decay modes, employing rather similar analysis techniques. The copiously produced $B^+ \to J/\psi K+$ decay mode is used as a normalization channel. Although the kinematic is different, the trigger is based on the two muons. The analysis is optimized through Monte Carlo simulated signal events and background events from the sideband, which are carefully extrapolated into the signal area. The D0 analysis employs a likelihood discriminant to reduce the background, whereas CDF employs an artificial neural network (NN). Due to its superior momentum resolution, CDF is able to define separate signal regions for B_s and B^0, while D0 defines only one mass region. To enhance the sensitivity (by 15%), CDF splits the signal samples into three separate bins in terms of the NN output variable ν_{NN}. The observed event rates were consistent with SM expectations in 3.7 fb^{-1} of data at CDF experiment[2]. Thus a 95% CL limits on the branching ratios were derived:

$$\mathcal{B}(B_s \to \mu^+\mu^-) = 4.3 \times 10^{-8},$$

$$\mathcal{B}(B^0 \to \mu^+\mu^-) = 7.6 \times 10^{-9}$$

At the time of the conference D0 has analyzed [3] data sample of 5 fb^{-1}, but have not unblinded signal region yet. The expected limit is 5.3×10^{-8} at the 95% CL. Those are the most stringent limits to date for $B_{(s)} \to \mu^+\mu^-$ decays. Figure 1 shows the projected sensitivity to observe $B_s \to \mu^+\mu^-$ decay at Tevatron.

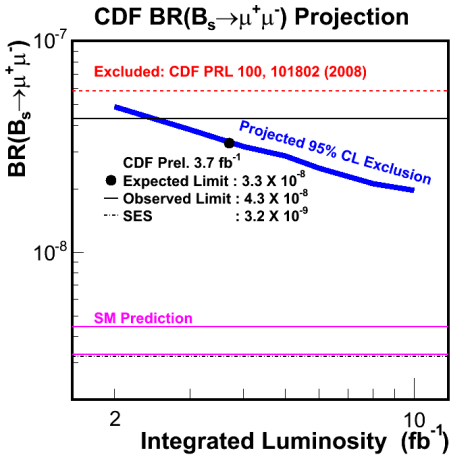

Figure 1: Projected sensitivity for $B_s \to \mu^+\mu^-$ decay at Tevatron as a function of integrated luminosity.

3 $B_{(s)} \to e^+e^-$ and $B_{(s)} \to e^+\mu^-$

Decay rates for $B_{(s)} \to e^+e^-$ are further suppressed by the square of the electron-over-muon-mass ratio, resulting in decay rates of order $10^{?15}$. Other decays, such as $B_{(s)} \to e^+\mu^-$, are completely forbidden in the SM due to lepton flavor violation.

Recently, CDF performed [4] a search for $B_{(s)} \to e^+e^-$ and $B_{(s)} \to e^+\mu^-$ in 2 fb^{-1} of data. The event sample is selected from the displaced two-track trigger by requiring electron and/or muon

signatures, corresponding to the decay mode and is normalized to the copious $B^0 \to K^+\pi^-$ decay mode. The decay $B^0 \to K^+\pi^-$ is separated from the mass peak of $B_s \to hh'$ on a statistical basis. The background contributions considered include combinations of random track pairs and partially reconstructed B-meson decays. The double-lepton misidentification rate was determined by applying electron and muon misidentification probabilities to the number of two-body decays found in the search window. Overall, one event was observed in B_s mass window, and two events were observed in B^0 mass window, which is consistent with a background expectations of 0.8±0.6 and 0.9±0.6 events respectively. Thus 95% CL upper limits on branching ratio were obtained from those observations:

$$\mathcal{B}(B_s \to e^+e^-) = 3.7 \times 10^{-7},$$

$$\mathcal{B}(B^0 \to e^+e^-) = 10.6 \times 10^{-8}$$

$$\mathcal{B}(B_s \to e^+\mu^-) = 2.6 \times 10^{-7},$$

$$\mathcal{B}(B^0 \to e^+\mu^-) = 7.9 \times 10^{-8}$$

The results were further used to derive a low limit on mass of Pati-Salam Leptoquarks [5] $M_{LQ}(B_s \to e^+\mu^-) > 47.8$ TeV/c^2 and $M_{LQ}(B^0 \to e^+\mu^-) > 59.3$ TeV/c^2.

4 $B^{(+)}_{(s)} \to \mu^+\mu^- h^{(+)}$

The decays $B^{(+)}_{(s)} \to \mu^+\mu^- h^{(+)}$, like the $B_{(s)} \to \mu^+\mu^-$ decays, are a FCNC processes and are represented as a $b \to s\mu^+\mu^-$ quark-level transition. When interferences with the much larger $B_s \to J/\psi\phi$ or $B_s \to \psi(2S)\phi$ decay modes are neglected, the theoretical predictions [6] for these decays are approximately 1.6×10^{-6}, where the uncertainties are due to form factors. The exclusive channels $B^+ \to K^+\mu^+\mu^-$ and $B^0 \to K^{*0}\mu^+\mu^-$ were observed by Belle [7] and Babar [8]. However, the analogous decay $B_s \to \phi\mu^+\mu^-$ has not been observed despite searches by CDF [9] and D0 [10]. The branching rations and forward-backward asymmetry A_{FB} are sensitive to Wilson coefficients [11] of the Operator Product Expansion and can indicate whether the underlying dynamics is governed by SM or BSM physics.

CDF studied [12] $B^+ \to K^+\mu^+\mu^-$, $B^0 \to K^{*0}\mu^+\mu^-$ and $B_s \to \phi\mu^+\mu^-$ decays in 4.4 fb^{-1} of data collected with di-muon trigger. After selection criteria based on NN are optimized to maximize statistical significance the B meson are fully reconstructed in corresponding decay chains. The invariant mass spectra for observed decays are shown on Fig. 2, 3, 4. The

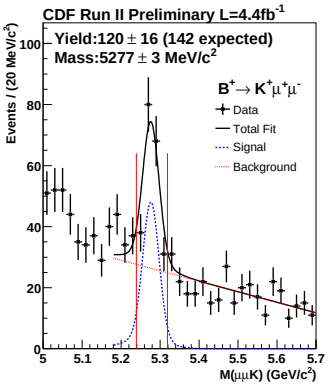

Figure 2: Invariant mass spectrum for the decay $B^+ \to K^+\mu^+\mu^-$.

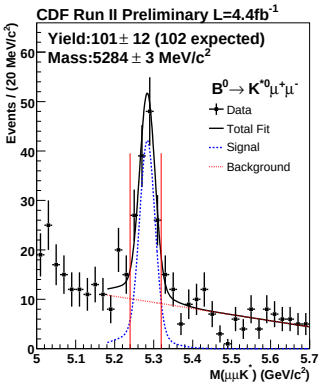

Figure 3: Invariant mass spectrum for the decay $B^0 \to K^{*0}\mu^+\mu^-$.

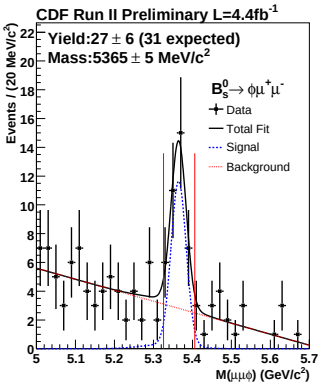

Figure 4: Invariant mass spectrum for the decay $B_s \to \phi\mu^+\mu^-$.

asymmetry A_{FB} and K^{*0} longitudinal polarization F_L are extracted from $\cos\theta_\mu$ and $\cos\theta_K$

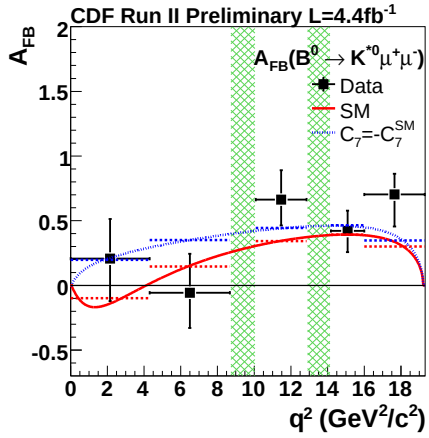

Figure 5: A_{FB} fit result with respect to 5 q^2 bin for $B^0 \to K^{*0}\mu^+\mu^-$. Histogram is the fit result, solid (dotted) curve is the SM ($C_7 = -C_{7SM}^{eff}$) expectation [13], dashed line is the average expectation in each q^2 bin, and hatched regions mean charmonium veto.

distributions, respectively, where θ_μ is the helicity angle between $\mu^+(\mu^-)$ direction and the opposite of the $B(\bar{B})$ direction in the dimuon rest frame, and θ_K is the angle between the kaon direction and the direction opposite to the B meson in the K^{*0} restframe. An unbinned maximum likelihood fit is performed to extract A_{FB} and F_L, the result of which is shown in Fig. 5.

5 Summary

We presented the first observation by CDF of $B_s \to \phi\mu^+\mu^-$ decay mode with 6.3 σ and $\mathcal{B} = [1.44 \pm 0.33(stat) \pm 0.46(syst)] \times 10^{-6}$ in 4.4 fb^{-1} of data as well as the first measurement of A_{FB} in hadron collisions, consistent and competitive with current best results from B factories. In general, all results from rare B-meson decays demonstrate good agreement with the prediction from the SM and can be used to reduce allowed parameter space of a broad spectrum of MSSM models.

References

1. M. Blanke *et al.,* JHEP **610,** 003 (2006).
2. CDF public note 9892.
3. D0 collaboration, Submitted to Phys. Lett. B, arXiv.org:1006.3469.
4. CDF collaboration, Phys. Rev. Lett. **102**, 201801 (2009).
5. J. Pati and A. Salam, Phys. Rev. **D10**, 275 (1974).
6. . Geng CQ, Liu CC. J. Phys. **G29**, 1103 (2003).
7. BELLE Collaboration, Phys. Rev. Lett. **88**, 021801 (2002); BELLE Collaboration Phys. Rev. Lett. **91**, 261601 (2003).
8. BABAR Collaboration, Phys. Rev. Lett. **91**, 221802 (2003).
9. CDF collaboration, Phys. Rev. Lett. **91**, 261601 (2003).
10. D0 collaboration, Phys. Rev. Lett. **91**, 261601 (2003).
11. K. G. Wilson, Phys. Rev. **179**, 1499 (1969).
12. CDF public note 10047.
13. A. Ali, P. Ball, L. T. Handoko, and G. Hiller, Phys. Rev. **D61**, 074024 (2000).

EXOTIC HADRON SPECTROSCOPY

P.N. PAKHLOV (for the Belle Collaboration)
Institute for Theoretical and Experimental Physics,
Moscow, Russia

This review is focused on recent BaBar and Belle results on the quarkonium-like states.

1 Introduction

For many long years the physics of quarkonium remained a seemingly well-understood field, where as was believed the theory described experimental data quite reliably. Over the past few years a new era of charmonium physics began thanks to numerous surprising results obtained mostly in the BaBar and Belle experiments at B-factories, where huge collected integrated luminosity is combined together with various mechanisms of charmonium production. Since 2002, more than ten new states containing the $c\bar{c}$ pair have been observed. Only three of them (h_c, η_c' and χ_{c2}') are identified as possible candidates for charmonium excitations. For the others the term 'charmonium-like' state was introduced, addressing the presence of $c\bar{c}$ pair, but stressing that their properties are poorly consistent with those expected by the charmonium model. This review presents the recent results on the newly observed X, Y and Z charmonium-like states and their probable counterparts in the $s\bar{s}$ and $b\bar{b}$ sectors.

2 X(3872)

The first enigmatic state, the $X(3872)$, was discovered in 2003 by Belle [1] in the $\pi^+\pi^- J/\psi$ invariant mass spectrum from $B^+ \to K^+\pi^+\pi^- J/\psi$ decays. The narrow peak ($\Gamma < 2.3\,\mathrm{Mev}$ at 90% CL) appeared exactly at the $D^0\bar{D}^{*0}$ threshold. This state was soon confirmed by CDF [2], D0 [3] and BaBar [4]. All experiments observed the $\pi^+\pi^-$ system tends to the kinematic limit as if the decay proceed via the isospin-violating $\rho J/\psi$ mode. The observation of radiative transitions to both $\gamma J/\psi$ and $\gamma\psi'$ [5,6] confirmed that the $\pi^+\pi^-$ system has quantum numbers of ρ-meson, thus the observation decay mode is indeed isospin-violating. An angular analysis [7] led to the conclusion that the only possible J^{PC} assignments for the $X(3872)$ are 1^{++} and 2^{-+}.

Two yet undiscovered charmonium states, χ_{c1}' and η_{c2}, correspond to the possible $X(3872)$ quantum numbers. However, the measured $X(3872)$ parameters and decays pattern do not match both assignments. An interpretation of the $X(3872)$ as tetraquark state [8] suggests the existence of another neutral and two charged $X(3872)$-partners with similar masses. BaBar found no evidence for a signal of the X^- in $B \to K\pi^-\pi^0 J/\psi$ decays [9]. In search for the neutral partner, both BaBar [10] and Belle [11] measured the $X(3872)$ mass for $B^+ \to K^+\pi^+\pi^- J/\psi$ and $B^0 \to K_S^0\pi^+\pi^- J/\psi$ decays separately and found mass differences to be consistent with zero. These ruled out a tetraquark hypothesis for the $X(3872)$.

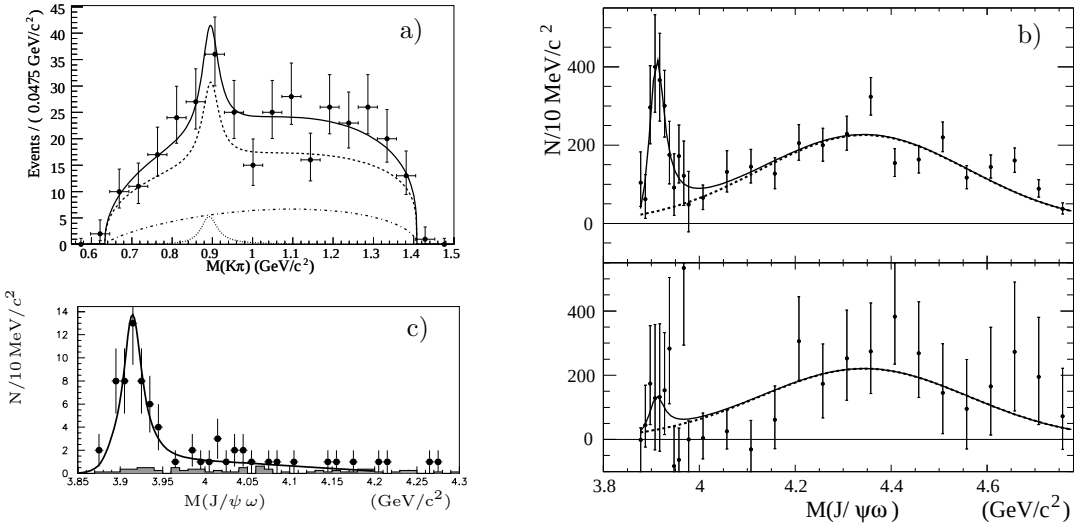

Figure 1: The $K\pi$ mass spectra in $B \to K\pi X(3872)$ decays (Belle). The $\omega J/\psi$ mass spectra (b) in $B \to K\omega J/\psi$ (BaBar) (c) in $\gamma\gamma \to \omega J/\psi$ (Belle).

An intriguing $X(3872)$ feature is the proximity of its mass to the $D^0\bar{D}^{*0}$ threshold, which has stimulated many papers interpreting the $X(3872)$ as a molecule-like system of a D^0 and $\bar{D}^{*0}$, bound by light hadrons exchange [12]. The molecular interpretation meets some difficulty to explain both prompt production in $p\bar{p}$ interaction of such friable object and the J/ψ formation in its decay. A general idea to resolve this is to assume the presence of χ'_{c1} admixture in the $X(3872)$ wave function, which responsible for its production and decay. Therefore it is interesting to compare dynamics of the $X(3872)$ production in B-decays with that of χ_{c1}, *e.g.* in three-body $B \to K\pi X(3872)$ decays. Such a study was reported by Belle in 2008 [11]. It is evident from the $K\pi$ mass spectrum (Fig. 1a) that the $K\pi$ pairs have a phase space-like distribution, with almost no K^* signal. For all of the known charmonium states the K^* dominates in the $K\pi$ system.

3 Y(3940)

In 2005, Belle reported observations of three states with masses near 3940 MeV: the near-threshold $\omega J/\psi$ mass peak, called $Y(3940)$, in the decay $B \to K\omega J/\psi$ [13]; the $X(3940)$, seen in the process $e^+e^- \to J/\psi D\bar{D}^*$ in the $D\bar{D}^*$ mass spectrum [14]; and the $Z(3930)$ seen in $\gamma\gamma$ events and decaying into $D\bar{D}$ [15]. Only the last state was convincingly assigned to the charmonium level χ'_{c2}. In spite of the conventional decay mode, the $X(3940)$ assignment to charmonium excitation is complicated, as the unfilled 0^{-+} state (expected in the studied reaction), η''_c, is supposed to be significantly heavier. The first state, the $Y(3940)$, is the most mysterious: while its mass is well above the thresholds for decays to $D\bar{D}$ or $D\bar{D}^*$ final states, its decays to neither of these modes were observed. While the decay to the first final state can be forbidden by parity conservation, the second decay should dominate for charmonium with such mass.

In 2008, BaBar presented a study of $B \to K\omega J/\psi$ [16]. In their analysis a peak in the $\omega J/\psi$ mass spectrum is qualitatively agrees with the Belle's result (Fig. 1b), however, the BaBar values for mass and width are lower than the corresponding Belle's values: $M = 3914^{+3.8}_{-3.4} \pm 1.6$ MeV, and $\Gamma = 33^{+12}_{-8} \pm 0.6$ MeV. In 2010, Belle reported on observation of a peak in the cross section for $\gamma\gamma \to \omega J/\psi$ [17], called $X(3915)$. The mass and width of the peak in the $\omega J/\psi$ mass spectrum (Fig. 1c) are well consistent with those reported for the $Y(3940)$ by BaBar. The common observation decay mode and similar parameters suggest that the $X(3915)$ and $Y(3940)$ are the same state.

In the absence of the information on quantum numbers it is difficult to find a charmonium assignment for this state. But even more problematic for accommodation of this state as char-

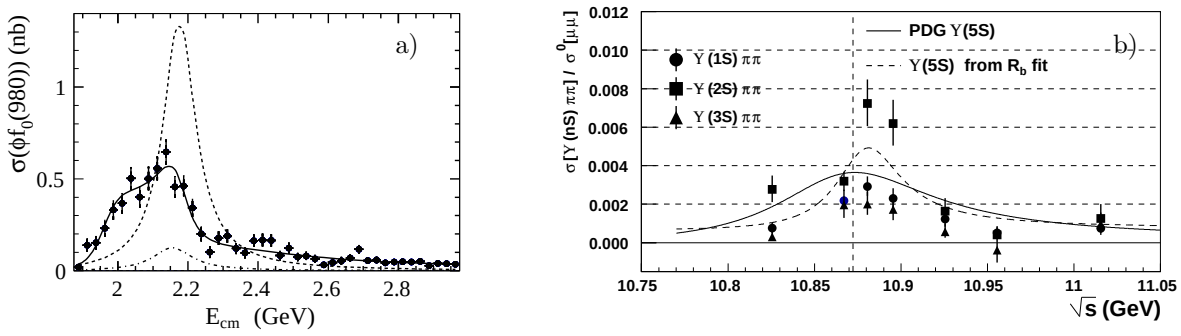

Figure 2: The cross sections for the processes a) $e^+e^- \to \eta\phi f_0$, b) $e^+e^- \to \Upsilon(nS)\pi^+\pi^-$ at Belle.

monium is the large $\omega J/\psi$ partial width. It can be roughly estimated assuming the $B \to KY$ decay branching fraction does not exceed 10^{-3}, typical for two-body B-decays into charmonium states. Using the measured product of branching fractions $\mathcal{B}(B \to KY)\mathcal{B}(Y \to \omega J/\psi)$ and the $Y(3940)$ full width, such an estimate gives $\Gamma(Y \to \omega J/\psi$ of a few MeV. If similar estimates applied for $\gamma\gamma \to X(3915)$ assuming $\Gamma_{\gamma\gamma} \sim 1\,\mathrm{keV}$, typical for charmonium, we find $\Gamma(X(3915) \to \omega J/\psi) \sim 1\,\mathrm{MeV}$. In both cases the estimated values are at least an order of magnitude higher than typical width of charmonium transitions via light hadrons.

4 The charged and strange charmonium-like states

The evidence of the first charged charmonium-like state, $Z(4430)^+$, seen as a peak in the $\pi^+\psi'$ invariant mass spectrum from $B \to K\pi^+\psi'$ decays was reported by Belle [18] in 2008. After BaBar did not confirm the $Z(4430)^+$ peak in their study of $B \to K\pi^+\psi'$ decays [19], Belle reanalysed their data using Dalitz plot technique and confirmed that the observed peak is not a reflection from interfering resonances in the $K\pi$ channel [20]. Besides the $Z(4430)^+$, Belle observed also two resonant states in the $\pi^+\chi_{c1}$ system [21] with the Dalitz analysis of $B \to K\pi^+\chi_{c1}$ decays.

In 2009, CDF presented an evidence for the narrow near-threshold resonance, called $Y(4140)$, in $\phi J/\psi$ system from $B^+ \to K^+\phi J/\psi$ decays [22] with mass $4143.0 \pm 2.9 \pm 1.2\,\mathrm{MeV}$ and width $11.7^{+8.3}_{-5} \pm 3.6\,\mathrm{MeV}$. Belle searched for this state using the same process and found no significant signal [23]. Although the upper limit on the production rate obtained by Belle is lower than the central value of the CDF measurement, Belle result does not contradict with CDF's observation taking into account the large errors. Belle also performed a search for this state in $\gamma\gamma$ fusion, motivated by $D_s^{*+}D_s^{*-}$-molecule interpretation for the $Y(4140)$. While a signal for the $Y(4140)$ is not observed, evidence for another narrow structure at 4350MeV in the $\phi J/\psi$ spectrum is reported with significance of $\sim 3.2\sigma$. Taking into account small significances of both CDF's and Belle's peaks, these states need further confirmation.

5 The 1^{--} quarkonium-like states

In 2005, using the ISR process BaBar studied the cross section for $e^+e^- \to \pi^+\pi^- J/\psi$ at $\sqrt{s} \sim 4\,\mathrm{GeV}$ and discovered a broad peak near $4260\,\mathrm{MeV}$ [24]. This state was confirmed by CLEO [25] and Belle [26]. A year after BaBar reported on a similar structure in the cross section for $e^+e^- \to \pi^+\pi^-\psi'$ but at mass $\sim 60\,\mathrm{MeV}$ higher [27]. Belle confirmed this observation, but in addition found that the structure is formed from two narrower peaks [28]. Unusual decay modes and lack of vacant charmonium levels make the charmonium assignments for these three states very unlikely.

The similar states containing $s\bar{s}$ pair was searched by BaBar in the ISR process in $\phi\pi^+\pi^-$ final state. Two clear structures near $\sqrt{s} = 1680$ and $2175\,\mathrm{MeV}$ were observed; the former is

likely the $\phi(1680)$ state, while the latter was produced predominantly via a ϕf_0 intermediate state, and called $Y(2175)$ [29]. BES confirmed this state in the ϕf_0 invariant mass spectrum of $J/\psi \to \eta\phi f_0$ decays [30]. In the subsequent Belle study [31] this state is also clearly seen (Fig: 2a). However, the widths of the $Y(2175)$ tends to be larger than in previous measurements, that may suggest that it is an excited 1^{--} $s\bar{s}$ state, rather than $s\bar{s}$ counterpart of $Y(4260)$.

In 2008, Belle has reported the observation of enhanced $e^+e^- \to \Upsilon(1S)\pi^+\pi^-$, $\Upsilon(2S)\pi^+\pi^-$, and $\Upsilon(3S)\pi^+\pi^-$ production at the range of $\sqrt{s}$ between 10.83 and 11.02 GeV [32]. The energy-dependent cross sections for $e^+e^- \to \Upsilon(nS)\pi^+\pi^-$ events were found to differ from the shape of the $e^+e^- \to b\bar{b}$ cross section (Fig. 2b).

6 Summary

The number of quarkonium-like states continues to grow. However, today none of the traditional or exotic theoretical models are able to simultaneously explain the variety of their properties.

References

1. S.-K. Choi *et al.* (Belle Collaboration), *Phys. Rev. Lett.* **91**, 262001 (2003).
2. D. Acosta *et al.* (CDF Collaboration), *Phys. Rev. Lett.* **93**, 072001 (2004).
3. V.M. Abazov *et al.* (D0 Collaboration), *Phys. Rev. Lett.* **93**, 162002 (2004).
4. B. Aubert *et al.* (BaBar Collaboration), *Phys. Rev.* D **71**, 071103 (2005).
5. K. Abe *et al.* (Belle Collaboration), hep-ex/0505037 (2005).
6. B. Aubert *et al.* (BaBar Collaboration), *Phys. Rev. Lett.* **102**, 132001 (2009).
7. A. Abulencia *et al.* (CDF Collaboration), *Phys. Rev. Lett.* **98**, 132002 (2007).
8. See, for example: L. Maiani *et al. Phys. Rev.* D **71**, 014028 (2005).
9. B. Aubert *et al.* (BaBar Collaboration), *Phys. Rev.* D **71**, 031501 (2005).
10. B. Aubert *et al.* (BaBar Collaboration), *Phys. Rev.* D **77**, 111101 (2008).
11. I. Adachi *et al.* (Belle Collaboration), arXiv:0809.1224 (2008).
12. See, for example: F.E. Close and P.R. Page, *Phys. Lett.* B **578**, 119 (2004).
13. S.-K. Choi *et al.* (Belle Collaboration), *Phys. Rev. Lett.* **94**, 182002 (2005).
14. K. Abe *et al.* (Belle Collaboration), *Phys. Rev. Lett.* **98**, 082001 (2007).
15. S. Uehara *et al.* (Belle Collaboration), *Phys. Rev. Lett.* **96**, 082003 (2006).
16. B. Aubert *et al.* (BaBar Collaboration), *Phys. Rev. Lett.* **101**, 082001 (2008).
17. S. Uehara *et al.* (Belle Collaboration), *Phys. Rev. Lett.* **104**, 092001 (2010).
18. S.-K. Choi *et al.* (Belle Collaboration), *Phys. Rev. Lett.* **100**, 142001 (2008).
19. B. Aubert *et al.* (BaBar Collaboration), *Phys. Rev.* D **79**, 112001 (2009).
20. R. Mizuk *et al.* (Belle Collaboration), *Phys. Rev.* D **80**, 031104 (2009).
21. R. Mizuk *et al.* (Belle Collaboration), *Phys. Rev.* D **78**, 072004 (2008).
22. A. Aaltonen *et al.* (CDF Collaboration), *Phys. Rev. Lett.* **102**, 242002 (2009).
23. C. Z. Yuan (for the Belle Collaborations), arXiv:0910.3138 (2009).
24. B. Aubert *et al.* (BaBar Collaboration), *Phys. Rev. Lett.* **95**, 142001 (2005).
25. T. Coan *et al.* (CLEO Collaboration), *Phys. Rev. Lett.* **96**, 162003 (2006).
26. C.-Z. Yuan *et al.* (Belle Collaboration), *Phys. Rev. Lett.* **99**, 182004 (2007).
27. B. Aubert *et al.* (BaBar Collaboration), *Phys. Rev. Lett.* **98**, 212001 (2007).
28. X.-L. Wang *et al.* (Belle Collaboration), *Phys. Rev. Lett.* **99**, 142002 (2007).
29. B. Aubert *et al.* (BaBar Collaboration), *Phys. Rev.* D **74**, 091103 (2007).
30. M. Ablikim *et al.* (BES Collaboration), *Phys. Rev. Lett.* **100**, 102003 (2008).
31. C.P. Shen *et al.* (Belle Collaboration), *Phys. Rev.* D **80**, 031101 (2009).
32. K.-F. Chen *et al.* (Belle Collaboration), arXiv:0808.2445 (2008).

Recent progress on h_c and χ_c at BESIII

Wang Zhiyong
For BESII Collaboration

Institute of High Energy Physics, Science Academic of China,
Beijing, 918(1), P.O.Box 100049

Based on about 110M ψ' data sample taken at BESIII detector in 2009, we study the decay of h_c and χ_c. We observed the clear h_c signal in the inclusive decays with and without E1-tagged. Therefore, the h_c signal is further confirm. Meanwhile, we measure the width of h_c for the first time. For χ_c decay, we measure the branching fractions of $\chi_{c0,2} \to PP(P = \pi^0, \eta)$ which are consistent with CLEO's. In addition, we confirmed the decay mode of $\chi_{c0,2} \to \omega\omega, \phi\phi$ and first observed the decay mode of $\chi_{c1} \to \omega\omega, \phi\phi$ which are regarded to be highly suppressed in theory. We also observed the DOZI decay mode of $\chi_c \to \omega\phi$.

1 Introduction

Compared to the vector charmonium states J/ψ and ψ', the χ_{cJ} and h_c are not well studied experimentally and theoretically. In particularly for h_c. Unlike J/ψ and ψ', h_c and χ_{cJ} can not be produced directly in e^+e^- collisions. For h_c, it can only be produced via the magnetic transition of ψ' accompanying by a π^0. Due to the fact that the two photon from π^0 decay are very soft, as well as the lack of understanding on h_c decay modes, it make it very difficult for one to reconstruct the h_c state. Someone predict that the dominant decay mode of h_c is the E1 mode, i.e. $h_c \to \gamma\eta_c$. One is easy to estimate the energy distribution of this E1 photon is about 500 MeV. Experimentally, if we require that such a photon is essential, we take this mode as E1-tagged. For χ_{cJ} decay, the color-octet theory can account for many experimental results, but the theoretical and experimental uncertainties are still large [1,2,3]. New and improved measurements of the branching fraction of the hadronic χ_{cJ} decay channels are mandatory to further test the Color Octet Model(COM) in P-wave charmonium decays. In a recent paper by Zhao [4], it is pointed out that the decay of $\chi_{c0,2}$ in to vector meson pairs(VV), pseudoscalars pairs(PP), and scalar pairs(SS) can be investigated in a general factorization scheme. The purpose is to clarify the role played by the OZI-rule violations and SU(3) flavor breakings in the decay transitions, and their correlations with the final-state meson wavefunctions. Experimental data may suggest that the role of OZI-rule violations is quite different for VV,PP and SS pair production in χ_{c0} decays. While in the PP channel the contribution from the doubly OZI-suppressed processes may be small, large OZI-rule violations may occur in the $\chi_{c0,2} \to SS$ channel due to glueball-$q\bar{q}$ mixing. More precise and new measurements of χ_{cJ} decays may lead to a better understanding on the structure of light scalar mesons.

2 h_c study

The detailed introduction about how to select charged tracks and EMC showers as well as the π^0 candidates can be found in the published paper [6]. Here, we just introduce the general event-level selection criteria. Candidate events must have at least two charged tracks. The continuum background can be suppressed by E_{tot} requirement and the background from $\psi(2S) \to \pi^+\pi^- J/\psi$ and $\psi(2S) \to \pi^0\pi^0 J/\psi$ can be suppressed by the recoiling mass of charged and neutral $\pi\pi$ pair. For E1-tagged mode, we require one photon in the energy range 465-535 MeV. Fig. 1 shows the inclusive π^0 recoil-mass spectra after applying the above selection criteria. The measured results are listed below: $M(h_c) = 3525.40 \pm 0.13 \pm 0.18 MeV/c^2, \Gamma(h_c) = 0.73 \pm 0.45 \pm 0.28 MeV (< 1.44 MeV at 90\% C.L.), \mathcal{B}(\psi' \to \pi^0 h_c) = (8.4 \pm 1.3 \pm 1.0)^{-4}, \mathcal{B}(\psi' \to \pi^0 h + c) \times B(h_c \to \gamma\eta_c) = (4.58 \pm 0.40 \pm 0.50) \times 10^{-4}$, and $\mathcal{B}(h_c \to \gamma\eta_c) = (54.3 \pm 6.7 \pm 5.2)\%$. Our measurements confirm CLEO's results. What is more important is that we give some first measurements.

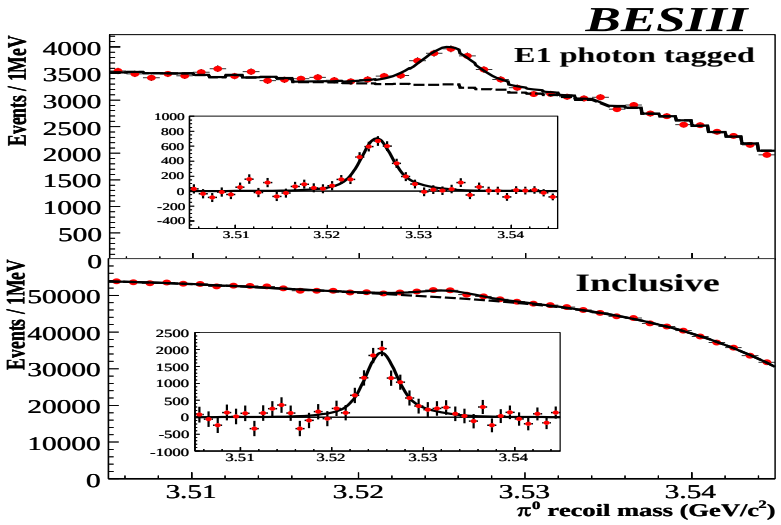

Figure 1: (up)The π^0 recoiling-mass spectrum and fit for the E1-tagged analysis of $\psi' \to \pi^0 h_c, h_c \to \gamma\eta_c$.. (down) for the inclusive analysis of $\psi' \to \pi^0 h_c$.

3 χ_{cJ} study

3.1 $\chi_{c0,2} \to PP(P = \pi^0, \eta)$

Recently, CLEO collaboration has published new results on the $\mathcal{B}(\chi_{c0,2} \to \pi^0\pi^0)$ with much improved precision compared to the previous measurements [5], but their results are about 2σ larger than the PDG's values. CLEO also measured $\chi_{c2} \to \eta\eta$ for the first itme. At BESIII, we studied both $\pi^0\pi^0$ and $\eta\eta$ modes with 5γ final state and the results have been published. [7]. Table 1 listed the measured results for BESIII,CLEO and PDG. One can find that some of our results are consistent with CLEO's. Fig. 2 and **??** shows the radiative photon energy distribution for $\gamma\pi^0\pi^0$ and $\gamma\eta\eta$ final states, respectively. Two clear bumps corresponding to $\chi_{c0,2}$ can be seen in both plots.

3.2 $\chi_{cJ} \to VV(V = \omega, \phi)$

Experimental data χ_{cJ} decays into a pair of vector is rare due to helixity amplitude suppression. Branching fractions are only published for $\chi_{cJ} \to \phi\phi$ and $\chi_{cJ} \to \omega\omega$ according to the BESII's measurements [8] and [9]. Table 2 list the measured results at BESII. Due to imperfect detection

Table 1: Branching fraction of $\chi_{c0,2} \to PP$. The final error items for both BESIII and CLEO are from the uncertainties of $\mathcal{B}(\psi' \to \gamma\chi_{cJ})$

Mode		$\chi_{c0}(\times 10^{-3})$	$\chi_{c2}(\times 10^{-3})$
$\pi^0\pi^0$	BESIII	$3.23 \pm 0.03 \pm 0.23 \pm 0.14$	$0.88 \pm 0.02 \pm 0.06 \pm 0.04$
	CLEO	$2.94 \pm 0.07 \pm 0.32 \pm 0.15$	$0.68 \pm 0.03 \pm 0.07 \pm 0.04$
	PDG	2.43 ± 0.20	0.71 ± 0.08
$\eta\eta$	BESIII	$3.44 \pm 0.10 \pm 0.24 \pm 0.13$	$0.65 \pm 0.04 \pm 0.05 \pm 0.03$
	CLEO	$3.18 \pm 0.13 \pm 0.31 \pm 0.16$	$0.51 \pm 0.05 \pm 0.05 \pm 0.03$
	PDG	2.4 ± 0.4	< 0.5

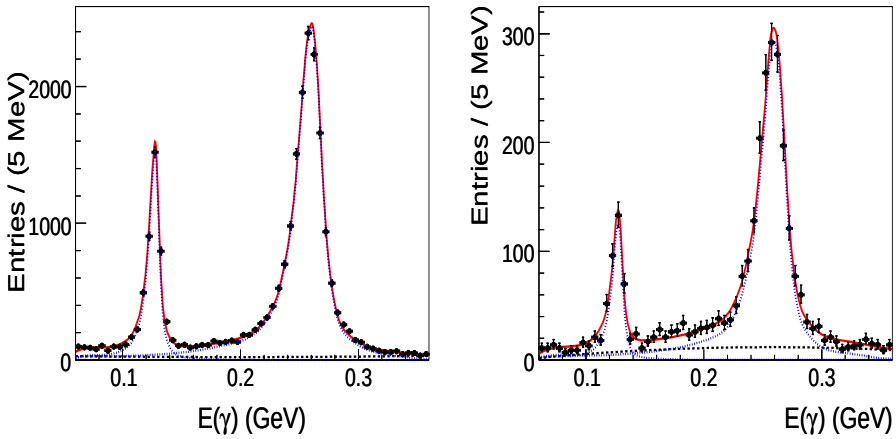

Figure 2: Radiative photon energy distribution of $\chi_c \to \pi^0\pi^0$ events.

resolution and low statistics, we just report the observation of $\chi_{c0,2}$ at that time, hard to judge that there is any χ_{c1} signal in $\phi\phi$ and $\omega\omega$ final state. For the doubly OZI decay mode, $\chi_{cJ} \to \omega\phi$, no any measurement is available before. With the large ψ' data sample taken at BESIII, we observed the clear $\chi_{c0,1,2} \to \omega\omega, \phi\phi$. Particularly, the χ_{c1} signal is firstly observed. Fig. 3 and 4 show the $M_{\phi\phi}$ and $M_{\omega\omega}$ distribution, respectively. Clear χ_{cJ} signal can be seen. For doubly OZI decay, $\chi_{cJ} \to \omega\phi$. We also observed the clear $\chi_{c0,1}$ signal(see fig. 5).

Table 2: Branching fractions of $\chi_{c0,2} \to \phi\phi, \omega\omega$ measured by BESII.

Mode	$\chi_{c0}(\times 10^{-3})$	$\chi_{c2}(\times 10^{-3})$
$\phi\phi$	0.93 ± 0.20	1.5 ± 0.3
$\omega\omega$	2.3 ± 0.7	2.0 ± 0.7

4 conclusion

BESIII has collected a large ψ' data sample. We have performed many study on h_c and χ_c. Some results have been published and some are in progress.

5 acknowledgments

I would like to thank my colleagues of BESIII collaboration. I would also like to thank the organizer for warm hospitality at La Thulei.

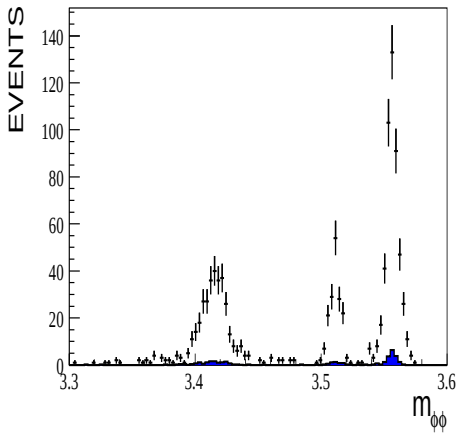

Figure 3: Invariant mass of $\phi\phi$ final state.

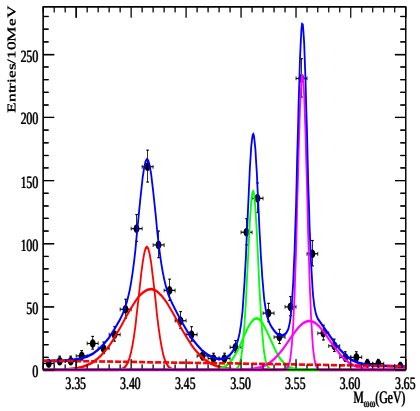

Figure 4: Invariant mass of $\omega\omega$ final state.

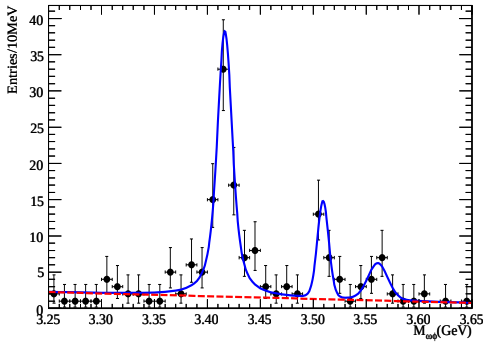

Figure 5: Invariant mass of $\omega\phi$ final state.

1. N.Brambilla *et al*, CERN-2005-05,hep-ph/042158.
2. G.T.Bodwin *et al*, Phys. Rev. D51,1125(1995).
3. H.-W. Huang and K.T.Chao,Phys.Rev.D54,6850(1996).
4. Q.Zhao, Phys.Lett.B 659,221(2008)
5. D.M.Ansner *et al*.(CLEO Collaboration), Phys. Lett.B667,1(2008).
6. Ablikim *et al*,(BES Collaboration),Phys.Rev.Lett. 104,(2010)
7. Ablikim *et al*,(BES Collaboration),Phys.Rev. D81,052005(2010).
8. M.Ablikim *et al*,(BES Collaboration), Phys.Lett.B642,197(2006).
9. M.Ablikim *et al*,(BES Collaboration), Phys.Lett.B630,7(2005).

h_c production in hadron collisions

De-Long Ren[1], Gang Hao[1], YaBing Zuo[1,2], Cong-Feng Qiao[a 1,3]
[1] *Department of Physics, Graduate University, the Chinese Academy of Sciences YuQuan Road 19A, Beijing 100049, China*
[2] *Department of Physics, Liaoning Normal University, Dalian 116029, China*
[3] *Theoretical Physics Center for Science Facilities (TPCSF), CAS, YuQuan Road 19B, Beijing 100049, China*

In this work, we calculate the $h_c(^1P_1)$ production rate at the LHC to leading order of the strong coupling constant, for both color-singlet and -octet mechanisms. Numerical results show that a considerable number of h_c events with moderate transverse momentum p_T will be produced in the early run of the LHC. For h_c production with large transverse momentum, the fragmentation function of gluon splitting into h_c is calculated. The analytic expression is given and the fragmentation probability is found to be 7.1×10^{-7}.

1 Introduction

Since the first charmonium, the J/ψ, was discovered thirty years ago, much effort has been made to explore it and its higher excited states in both theoretical and experimental aspects. These studies have provided deep insights into the heavy quark-antiquark bound states and ideal opportunities to understand both perturbative and non-perturbative properties of quantum chromodynamics(QCD). Although much progress has been made, there are still many unsolved problems left in quarkonium physics. For instance, in the charmonium sector, the $c\bar{c}$ mass spectrum of the naive quark model prediction has not been completely confirmed in experiment yet. Below the open charm threshold, all expected charmonia have been identified in recent years, but experimental measurements of the physical natures of P-wave spin-singlet charmonium, $h_c(^1P_1)$, are quite limited, partly due to the low production rate in leptonic collision and complicated background in hadronic collision. In hadron-hadron collision, the $^1P_1$ state can be formed directly in many ways. The goal of this work is to analyze the h_c production at hadron colliders, e.g. the Large Hardon Collider(LHC).

The rest of this paper is organized as follows: in section 2, h_c production rate at LHC is calculated; in section 3, we give out the analytical expression for the fragmentation function of gluon splitting into h_c; in section 4, a brief conclusion of our results is given.

2 h_c production at the LHC

To obtain more knowledge of the nature of h_c, a key point for experimentalists is to obtain enough h_c data. The newly run collider LHC may supply a good opportunity to study quarkonium physics, including h_c. With a luminosity of about $10^{32} \sim 10^{34} cm^{-2} s^{-1}$ and a center of mass

[a] qiaocf@gucas.ac.cn, corresponding author

energy of $10 \sim 14$ TeV, the LHC will produce copious charmonium data, which in principle will enable the measurement of h_c state precisely. In the following we evaluate the h_c production rate at the LHC .

The differential cross section for h_c hadroproduction is formulated in a standard way,

$$\frac{d\sigma}{dp_T}(pp \to h_c + X) = \sum_{a,b} \int dx_a dy f_{a/p}(x_a) f_{b/p}(x_b) \frac{4p_T x_a x_b}{2x_a - \bar{x}_T e^y} \frac{d\hat{\sigma}}{dt}(a + b \to h_c + X) \ , \tag{1}$$

where $f_{a/p}$ and $f_{b/p}$ denote the parton densities; s, t, and u are Mandelstam variables at the parton level; y stands for the rapidity of produced h_c; $\bar{x}_T \equiv \frac{2m_T}{\sqrt{S}}$ with $m_T = \sqrt{M^2 + p_T^2}$; and the capital $\sqrt{S}$ and M denote the total energy of incident beam and the mass of h_c, respectively. To leading order and with moderate transverse momentum, the dominant partonic sub-processes for h_c hadroproduction evidently include

$$g + g \ \to \ h_c(^1S_0^{[8]}) + g \ , \tag{2}$$

$$g + q(\overline{q}) \ \to \ h_c(^1S_0^{[8]}) + q(\overline{q}) \ , \tag{3}$$

$$q + \overline{q} \ \to \ h_c(^1S_0^{[8]}) + g \ , \tag{4}$$

$$g + g \ \to \ h_c(^1P_1^{[1]}) + g \ , \tag{5}$$

$$g + c(\overline{c}) \ \to \ h_c(^1P_1^{[1]}) + c(\overline{c}) \ , \tag{6}$$

where the first three represent the h_c production processes in the color-octet model(COM)[1,2], while the last two are through color-singlet model(CSM)[3,4,5,6,7].

In our numerical evaluation, the input parameters are taken as follows: $\sqrt{S} = 14$TeV, $m_c = M/2 = 1.78$GeV, the value of the color-singlet matrix element $\langle 0|\mathcal{O}_1^{h_c}(^1P_1)|0\rangle = 0.32$ GeV^5 [9], the value of the color-octet matrix element $\langle 0|\mathcal{O}_8^{h_c}(^1S_0)|0\rangle = 9.8 \times 10^{-3}$ GeV^3 [8], and the pseudorapidity cut $|\eta(h_c)| < 2.2$ is enforced according to the LHC experimental environment, and the CTEQ5L[10] parton distribution function is employed. The numerical results of the integrated cross section for different p_T lower bounds are given in Figure 1. From the figure, it can be found that the contribution from COM is about two orders of magnitude larger than that from CSM in almost every transverse momentum region. Among the three color-octet processes, the contribution from process (2) dominates over the other two. Of the two color-singlet processes, the yield from process (6) overshoots that from process (5) in the large transverse momentum region, in spite of the suppression of the extrinsic charm distribution. Because of the big gap between the yields from the color-singlet and color-octet, one result of this calculation is that the experimental measurement may tell whether the color-octet estimate of h_c production is reliable or not. The calculation details and the possibility of detecting h_c at the LHC can be found elsewhere [11].

3 The gluon fragmentation to h_c

It is well-known that the fragmentation mechanism dominates the heavy quarkonium hadroproduction at large transverse momentum [12,13]. It is hence important to obtain the corresponding fragmentation function in order to properly estimate the production rate of a specific charmonium state. Fortunately it was found that these fragmentation functions for heavy quarkonium production are analytically calculable by virtue of perturbative QCD, with limited universal(phenomenological) parameters.

In the framework of non-relativistic QCD, the fragmentation function of a virtual gluon splitting into heavy quarkonium H reads

$$D_{g\to H}(z,\mu) = \sum_n d_n(z,\mu) \langle 0|\mathcal{O}_n^H|0\rangle \ . \tag{7}$$

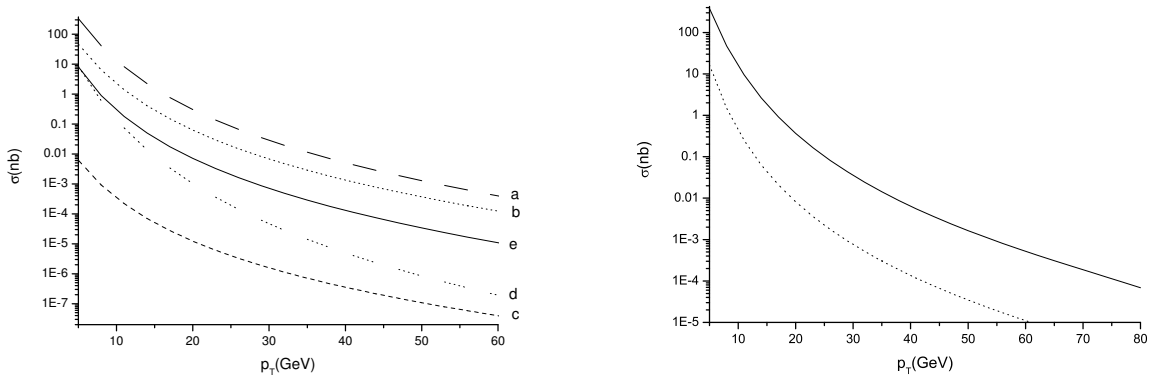

Figure 1: The h_c production rates as a function of the transverse momentum lower bound p_T in pp collision at the center-of-mass energy $\sqrt{S} = 14$ TeV. The left diagram demonstrates the integrated cross-sections of h_c production via processes (2) to (6) shown as lines a to e, respectively. The solid line in the right diagram represents the yield from the color-octet scheme, and the dashed line represents the yield from the color-singlet scheme.

Here, n is the color-spin-orbital quantum number of the heavy quark pair with null relative momentum. The short-distance coefficient $d_n(z,\mu)$, describing the production of heavy quark pair with appropriate quantum number n, is pQCD calculable. $\mathcal{O}_n^H$ are local four-fermion operators in NRQCD, and their vacuum expectation values are proportional to the probabilities of heavy quark pairs with quantum number n hadronizing into quarkonium states. According to NRQCD, in (7) the short distance sector $d_n(z,\mu)$ can be computed order-by-order in strong coupling $\alpha_s(2m_c)$, and the long distance sector, the matrix elements, can be expanded in series of the typical relative velocity v of heavy quarks inside heavy quarkonium [14,15]. In principle the fragmentation function is calculable to any order in α_s and v as desired; in practice, normally the NLO results are enough for phenomenological aim. It should be mentioned that in recently there are discussions about whether the definition of fragmentation function beyond NLO in strong coupling expansion is complete or not in the framework of NRQCD [16,17], whereas it has no influence on our study in this work.

For process of gluon splitting into h_c, there are two classes of processes at leading order of α_s and v. One is the color-singlet process, in which $c\bar{c}$ pair is in spin-singlet, color-singlet and P-wave state (denoted by ${}^1P_1^{(1)}$); the other is color-octet process, in which the quark pair is in spin-singlet, color-octet and S-wave state(${}^1S_0^{(8)}$). The full fragmentation function for $g \to h_c$ then composes of color-singlet and color-octet terms, like

$$D_{g\to h_c}(z,\mu) = d_1(z,\Lambda)\langle 0|\mathcal{O}_1^{h_c}({}^1P_1)|0\rangle + d_8(z)\langle 0|\mathcal{O}_8^{h_c}({}^1S_0)|0\rangle(\Lambda)\,, \tag{8}$$

The factorization scale Λ is introduced to separate the effect at short distance of order $1/m_c$ from the one at long distance in order of heavy quarkonium radius $1/(m_c v)$. $\langle 0|\mathcal{O}_1^{h_c}({}^1P_1)|0\rangle$ and $\langle 0|\mathcal{O}_8^{h_c}({}^1S_0)|0\rangle$ are matrix elements of NRQCD operators, scaling as $m_c^5 v^5$ and $m_c^3 v^5$ according to velocity-scaling rules in NRQCD. Their dependence on Λ can be obtained by renormalization group equations. To leading order of α_s they are [15],

$$\begin{aligned}
\Lambda\frac{d}{d\Lambda}\langle 0|\mathcal{O}_1^{h_c}({}^1P_1)|0\rangle &= 0 \\
\Lambda\frac{d}{d\Lambda}\langle 0|\mathcal{O}_8^{h_c}({}^1S_0)|0\rangle &= \frac{4C_F\alpha_s}{3N_c\pi m_c^2}\langle 0|\mathcal{O}_1^{h_c}({}^1P_1)|0\rangle.
\end{aligned} \tag{9}$$

The calculation for $d_1(z,\Lambda)$ and $d_8(z)$ is straightforward in perturbative QCD, the results

are

$$d_1(z,\Lambda) = f(z) + \frac{5\alpha_s^3(\mu)}{162\pi m_c^5}\Big\{ -\big[-2z^2+3z+2(1-z)\ln(1-z)\big]\ln\frac{\Lambda}{m_c} + w(z)\Big\}, \quad (10)$$

$$d_8(z) = \frac{5\alpha_s^2(\mu)}{96m_c^3}[-2z^2+3z+2(1-z)\ln(1-z)]\,. \quad (11)$$

The functions $f(z)$ and $w(z)$ are Λ-independent, their analytical expressions are shown in Appendix. With the Eq.9, one can easily check the fragmentation function (8) are scale-independent,

$$\frac{d}{d\Lambda}D_{g\to h_c}(z,\Lambda) = 0\,. \quad (12)$$

Integrating the fragmentation function $D_{g\to h_c}(z,2m_c)$ over the momentum fraction z, we get the fragmentation probability,

$$\int_0^1 dz\, D_{g\to h_c}(z,2m_c) = \frac{5\alpha_s^2(2m_c)}{96m_c^3}\Big[\frac{(-54.5)\alpha_s(2m_c)}{216\pi m_c^2}\langle\mathcal{O}_1^{h_c}\rangle + (0.33)\langle\mathcal{O}_8^{h_c}\rangle(m_c)\Big]\,. \quad (13)$$

To make the total probability positive, the lower bound for the magnitude of color-octet matrix element at factorization scale $\Lambda = m_c$ is set to be

$$\langle\mathcal{O}_8^{h_c}\rangle(m_c) > \frac{3\alpha_s(2m_c)}{4\pi m_c^2}\langle\mathcal{O}_1^{h_c}\rangle\,. \quad (14)$$

For numerical evaluation, the input parameters are taken as follows: $m_c = m_{h_c}/2 = 1.78$GeV, $\alpha_s(2m_c) = 0.26$, $\langle 0|\mathcal{O}_1^{h_c}(^1P_1)|0\rangle = 0.32GeV^5$ [9], which enables $\langle 0|\mathcal{O}_8^{h_c}(^1S_0)|0\rangle(m_c) > 6.3\times 10^{-3}GeV^3$, $\langle 0|\mathcal{O}_8^{h_c}(^1S_0)|0\rangle(m_c) = 9.8\times 10^{-3}GeV^3$ [8,11]. With above inputs the fragmentation probability in Eq.(13) is found to be about 7.1×10^{-7}. Compared with the probabilities of gluon fragmenting into χ_{c0}, χ_{c1}, and χ_{c2}, which are 0.4×10^{-4}, 1.8×10^{-4} and 2.4×10^{-4} [13], the value of gluon fragmentation to h_c is smaller by two to three orders, and it is even less than the color-singlet probability of process $g^*\to J/\psi gg$ by an order [14]. The z dependence of the fragmentation function at $\mu = 2m_c$ and $\Lambda = m_c$ is shown in Figure 2.

4 Conclusions

In conclusion, we have evaluated the h_c direct production rate at the LHC, where the h_c indirect yields are much less than the direct ones according to a similar analysis for h_c production at HERA-b [18]. Our calculation is performed to leading order of the strong coupling constant α_s and to second order in the relative velocity v^2 expansion. Both color-singlet and -octet production schemes are taken into account in this work. We find that there will be enough h_c yields at the LHC for a precise measurement on the nature of this P-wave spin singlet. Although as usual the high order corrections may induce some uncertainties in the calculation, as an order-of-magnitude estimate our results should hold. Due to the large discrepancy between predictions from the color-singlet and color-octet schemes, the experimental measurement of the h_c production rate at the LHC may tell to what degree the color-octet mechanism plays a role in charmonium production as well.

At the region of large transverse momentum, the dominant mechanism for heavy quarkonium hadronproduction is fragmentation, hence the fragmentation function is important for h_c production. We have computed in this work the fragmentation function of gluon to P-wave spin singlet quarkonium h_c. While both color-singlet and -octet processes are taken into account, the analytic expression is independent of factorization scale. It is found that the fragmentation probability of a high energy virtual gluon splitting into h_c is about 7.1×10^{-7}. Finally, it is worthy to note that result in this work can be readily applied to the study of h_b physics.

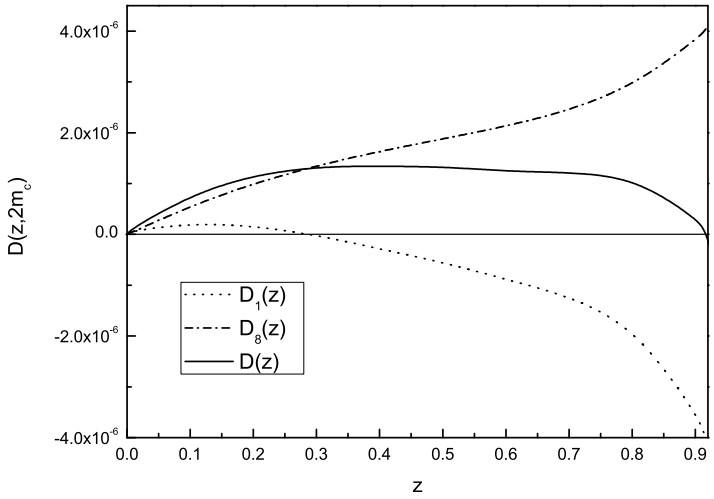

Figure 2: The fragmentation function $D_{g\to h_c}(z,\mu)$ as a function of z for $\mu = 2m_c$ and $\Lambda = m_c$, the dotted line is the contribution from color-singlet process, the dash-dotted line is the contribution from color-octet process and the solid line is the total result.

Acknowledgments

This work was supported in part by the National Natural Science Foundation of China(NSFC) under the grants 10935012, 10928510, 10821063 and 10775179, by the CAS Key Projects KJCX2-yw-N29 and H92A0200S2.

Appendix

$$\begin{aligned} w(z) &= 2(1-z)\ln^2(1-z) + [-2-3(-2+z)z + 3(-1+z)\ln z]\ln(1-z) \\ &\quad + \frac{1}{6}[2\pi^2(1-z) + 3z(-7+8z) + 3z(-3+2z)\ln z] - 2(1-z)Li_2(1-z) - (1-z)Li_2(z)\,, \end{aligned} \tag{15}$$

and

$$\begin{aligned} f(z) &= \frac{5\alpha_s^3(\mu)}{20736\pi m_c^5}\int_0^z dr\int_{(r+z^2)/2z}^{(1+r)/2} dy \frac{1}{(1-y)^4(y^2-r)^2}\left\{\frac{(1+r^2)-4yz+2z^2}{(1-r)^2}h(y,r)\right. \\ &\quad \left. + \frac{1}{(y-r)^5}\sum_{i=0}^{2} z^i\left((r-y)f_i(y,r) + \frac{g_i(y,r)}{\sqrt{y^2-r}}\ln\frac{y-r+\sqrt{y^2-r}}{y-r-\sqrt{y^2-r}}\right)\right\} \end{aligned} \tag{16}$$

with functions $w(z)$, $h(y,r)$, $f_i(y,r)$ and $g_i(y,r)$ read

$$\begin{aligned} h(y,r) &= (1+11r-5r^2+r^3)(1-20r+6r^2-4r^3+r^4) + (2-20r+606r^2-280r^3+94r^4-20r^5+2r^6)y \\ &\quad +(4+468r-792r^2+232r^3-44r^4+4r^5)y^2 + (8-1120r+560r^2-96r^3+8r^4)y^3 \\ &\quad +(-240+1072r-208r^2+16r^3)y^4 + (544-448r+32r^2)y^5 + (-448+64r)y^6 + 128y^7\,, \end{aligned} \tag{17}$$

$$\begin{aligned} f_0(y,r) &= r^3(36-15r+25r^2-57r^3+59r^4-97r^5+23r^6-7r^7+r^8) \\ &\quad +(-164r^3+54r^4+80r^5-34r^6+344r^7-2r^8+12r^9-2r^{10})y \\ &\quad +(-82r^2+274r^3-374r^4-46r^5-746r^6+26r^7-14r^8+2r^9)y^2 \\ &\quad +(-4r+488r^2+88r^3+652r^4+824r^5-564r^6-108r^7)y^3 \\ &\quad +(1+33r-1277r^2-637r^3-877r^4+1947r^5+553r^6+r^7)y^4 \\ &\quad +(2-160r+1734r^2+488r^3-2794r^4-1032r^5+66r^6)y^5 \end{aligned}$$

$$
\begin{aligned}
&+(-28+356r-1144r^2+2232r^3+644r^4-396r^5)y^6+(136-352r-352r^2+400r^3+968r^4)y^7\\
&+(-336+80r-1136r^2-1264r^3)y^8+(448+736r+992r^2)y^9+(-384-448r)y^{10}+128y^{11}\,, \qquad (18)\\
f_1(y,r) &= -2yf_2(y,r)\,, \qquad (19)\\
f_2(y,r) &= 2\big[r^2(6+8r-47r^2+33r^3-24r^4+46r^5-7r^6+r^7)\\
&+(-16r^2+96r^3+56r^4+2r^5-206r^6-10r^7-2r^8)y\\
&+(-16r-148r^2-248r^3-74r^4+502r^5+110r^6+2r^7)y^2\\
&+(124r+470r^2+286r^3-614r^4-234r^5+16r^6)y^3\\
&+(-7-285r-592r^2+320r^3+151r^4-99r^5)y^4+(34+336r+204r^2+128r^3+242r^4)y^5\\
&+(-84-220r-340r^2-316r^3)y^6+(112+232r+248r^2)y^7+(-96-112r)y^8+32y^9\big]\,, \qquad (20)\\
g_0(y,r) &= 2\big[r^4(-9+r-8r^2-8r^3+r^4-r^5-8r^6)+(46r^4+10r^5+71r^6+20r^7+4r^8+66r^9+7r^{10})y\\
&+(28r^3-111r^4-94r^5-148r^6-34r^7-213r^8-20r^9)y^2\\
&+(-148r^3+193r^4+146r^5+150r^6+356r^7-111r^8-26r^9)y^3\\
&+(-28r^2+297r^3-232r^4-120r^5-330r^6+695r^7+182r^8)y^4\\
&+(192r^2-166r^3+452r^4+152r^5-1604r^6-498r^7+16r^8)y^5\\
&+(-608r^2-590r^3-662r^4+1930r^5+614r^6-124r^7)y^6\\
&+(1160r^2+1152r^3-896r^4-112r^5+408r^6)y^7\\
&+(8r-1152r^2-216r^3-696r^4-744r^5)y^8+(-104r+360r^2+864r^3+816r^4)y^9\\
&+(8+216r-376r^2-520r^3)y^{10}+(-16-48r+160r^2)y^{11}\big]\,, \qquad (21)\\
g_1(y,r) &= -2yg_2(y,r)\,, \qquad (22)\\
g_2(y,r) &= 2\big[r^3(-3-5r+8r^2+3r^4+13r^5+16r^6)-(-10r^3-14r^4+11r^5+4r^6+84r^7+138r^8+11r^9)y\\
&-(-10r^2+11r^3+114r^4+60r^5-196r^6-495r^7-76r^8)y^2\\
&-(16r^2-183r^3-492r^4+86r^5+940r^6+201r^7-8r^8)y^3\\
&-(16r+175r^2+796r^3+640r^4-914r^5-215r^6+62r^7)y^4\\
&-(-96r-688r^2-1172r^3+108r^4-76r^5-204r^6)y^5\\
&-(218r+922r^2+562r^3+502r^4+372r^5)y^6+(200r+472r^2+568r^3+408r^4)y^7\\
&-(-4+36r+268r^2+260r^3)y^8-(8-8r-80r^2)y^9\,. \qquad (23)
\end{aligned}
$$

References

1. G.T. Bodwin, E. Braaten, T.-C. Yuan, and G.P. Lepage, Phys. Rev. D**46**, R3703(1992).
2. E. Braaten and S. Fleming, Phys. Rev. Lett. **74**, 3327(1995).
3. T.A. DeGrand and D. Toussiant, Phys. Lett. **B89**, 256(1980).
4. M. Wise, Phys. Lett. **B89**, 229(1980).
5. J.H. Kuhn, S. Nussinov, and R.Z. Ruckle, Z. Phys. C**5**, 117(1980).
6. C.H. Chang, Nucl. Phys. **B172**, 425(1980).
7. E.L. Berger and D.L. Jones, Phys. Lett. B121, 61(1983); ibid, Phys. Rev. D**23**, 1521(1981).
8. P.L. Cho and A.K. Leibovich, Phys. Rev. D **53**, 150(1996); Phys. Rev. D**53**, 53(1996).
9. M. Mangano and A. Petrelli, Phys. Lett. **B352**, 445(1995).
10. CTEQ Collaboration, H.L. Lai *et al.*, Eur. Phys. J. C**12**, 375(2000).
11. Cong-Feng Qiao, De-Long Ren and Peng Sun, Phys. Lett. B680, 159 (2009).
12. E. Braaten and T.C. Yuan, Phys. Rev. Lett. **71**, 1673 (1993).
13. E. Braaten and T.C. Yuan, Phys. Rev. D**50**, 3176 (1994).
14. E. Braaten and T.C. Yuan, Phys. Rev. D**52**, 6627 (1995).
15. G.T. Bodwin, E. Braaten and G.P. Lepage, Phys. Rev. D**51**, 1125(1995), Erratum-ibid. D**55**, 5853 (1997).
16. Gouranga C. Nayak, Jian-Wei Qiu, and George Sterman, Phys. Lett. **B613**, 45 (2005).
17. Gouranga C. Nayak, Jian-Wei Qiu, and George Sterman, Phys. Rev. D**72**, 114012 (2005).
18. C.-F. Qiao and C.Z. Yuan, Phys. Rev. D**63**, 014007(2001).

Quarkonia production in PHENIX/RHIC in 200 GeV p-p collisions

Denis Jouan
Institut de physique nucléaire, IN2P3/CNRS et Université Paris Sud XI, Orsay, France

Quarkonia production is a favoured tool both for studying production mechanisms and hot matter properties. An overview of the quarkonia production measured in pp collisions at $\sqrt{s} = 200GeV$ is presented. J/ψ ψ' χ_c and Υ are observed in dilepton measurements taken in 2006 with improved statistics.

Quarkonia are well know particles and usual elements in the landscape of high energy physics. But for about 15 years, their production have been challenging the model predictions. The color singlet model (CSM) failed to predict the cross section at TEVATRON [1], the color octet model (COM) seemed to solve the question, but failed on the polarization side[2]. Production in Nucleus-Nucleus (A+A) collisions also displayed unexpected features with a similar J/ψ suppression at SPS and RHIC energies. At the moment there is then no definite interpretation of the quarkonia production in p+p , p+A and A+A , but the extension of the measurements and of their precision in a wide energy domain is increasingly constraining the models. The advent of detectors like PHENIX, measuring many quarkonia on a wide kinematical range and with a variety of beams, joining separated areas of research , could allow to reach new observables, as the first tentative measurement of J/ψ production asymmetry with transversely polarized proton beams suggests.

This talk will concentrate on p+p production. d+Au and Au+Au are adressed in [3]. The PHENIX collaboration at RHIC collected data in p+p collisions at $\sqrt{s}$=200 GeV, allowing measurement of quarkonia states with a rapidity coverage of $|\eta| < 0.35$ (electrons pairs) and $1.2 < |\eta| < 2.4$ (muons pairs). Results are extracted from the 2006 run, with three time more luminosity than the 2005 [4] run.

When measuring pairs, there is a contribution of pairs coming from random combinations. This contribution is estimated from same sign pairs spectra or from mixed events. The remaining mass spectrum contains correlated pairs from $b\bar{b}$ and $c\bar{c}$ semi leptonic decays, and pairs from Drell Yan process and from resonances decays. These distributions are simulated, using PYTHIA generator and the simulation of the detector, and used in a fit.

In this new results, the Υ production is extracted separately from the continuum. The 1S, 2S and 3S states of the Υ are extracted together, and presented as a function of rapidity in Figure 1. The shape of this rapidity distribution is consistent with the prediction of the Color Evaporation Model [5]. A calculation in the Color Singlet NLO approximation [6] reproduces also very well the shape. This agreement is improved in this new extraction. The values of the Υ cross section are $BR * d\sigma/dy = 28.2 \pm 9.4(stat) \pm 4.8(syst)pb$ $(-2.2 < y < -1.2)$ and $BR * d\sigma/dy = 31.1 \pm 8.7(stat) \pm 6.2(syst)pb$ $(1.2 < y < 2.2)$.

Charmonia have a higher production rate, and also the same interesting properties than Υ :

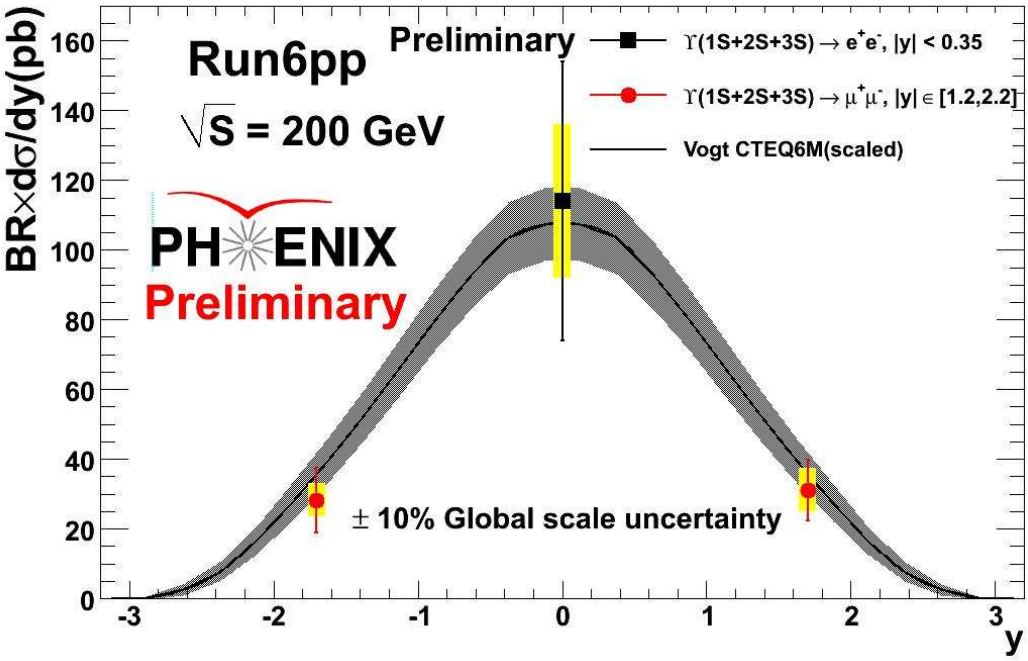

Figure 1: Rapidity distribution of the Υ resonances.

rare production, weak coupling with light mesons, a variety of states and binding energies, they can also be treated in the non relativistic approximation, which makes them attractive probes for studies of production or destruction (QGP melting) mechanisms. One complication arises from the side feeding from quarkonia higher states or from higher masses particles, which should imply to consider all these productions simultaneously. For instance an important fraction of the J/ψ comes from decays of χ_c , ψ' , and bottom quarks, and the J/ψ suppression pattern measured at SPS and RHIC could be due essentially to the melting of χ_c and ψ' states [7].

The Figure 2 displays the first p_T distribution of an excited charmonium state measured at RHIC. The ratio between ψ' and J/ψ agrees with that from other experiments [8,9]. The overall preliminary J/ψ feed down fraction from ψ' is $8.6 \pm 2.4\%$. This value is very consistent with the one deduced from p-A data around SPS energies 8.1 ± 0.3 % [10].

Feed-down fraction from χ_c is studied by looking at dielectron pairs in the J/ψ peak in coincidence with a photon in the electromagnetic calorimeter. Contribution of χ_{c1} and χ_{c2} lead to a gaussian contribution in the spectrum which must be separated from an underlying continuous component.

Preliminary studies at central rapidity led to an upper limit of 42 % (at 90% C.L.) for the fraction of inclusive J/ψ production originating from χ_c decay. This value is consistent with measurement from other experiments, mostly at lower energy, displayed in Figure 3, and with a recent selected average [10] leading to 25 ± 5 % . Mean value and uncertainties are on the way, together with estimates at forward rapidity.

As observed in CDF results previously mentionned, The J/ψ rapidity and transverse momentum distributions [11] have been found consistent with predictions from Color Octet Model [12]. They can be reproduced also by the Color Singlet Model, either through S-channel cut [13] alternative approach, either when additional contributions are taken into account: NLO contributions and charm initiated processes [14] or NNLO [15].

Such good agreement has been proved in the past [2] not to imply the agreement of the predictions regarding the polarization. In the helicity frame, the polarization characterizes the

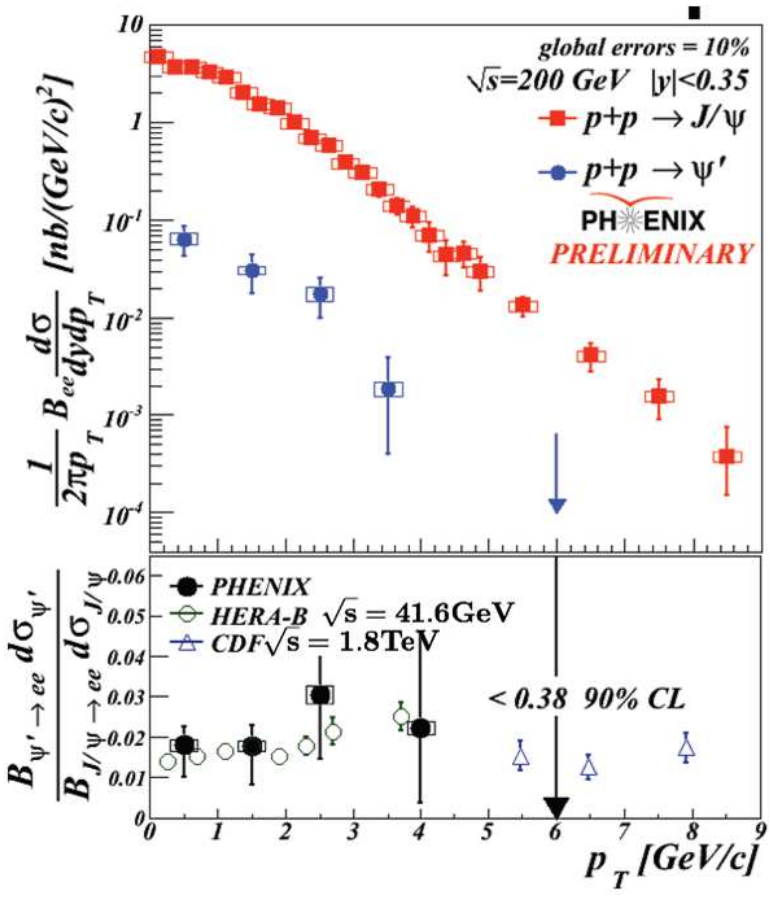

Figure 2: J/ψ and ψ' transverse momentum distributions and their ratio

distribution of the angle, in J/ψ rest frame, between the positive lepton and the axis defined by the J/ψ momentum in colliding hadrons center of mass [16]. This distribution is parameterized by $dN/dcos\theta \propto 1+\lambda cos^2\theta$, where λ is the polarization parameter. In the central rapidity region, the figure 4 displays the values of the λ obtained [16] as a function of the transverse momentum. It is suggesting a trend similar to the one expected by CSM s-channel cut calculations [17]. Extraction in the forward rapidity region in under way, and, as suggested by this model should bring sensitive informations. CSM calculation to next to leading order approximation and inclusion of charm-gluon production [18] lead to a smaller variation with respect to p_T but is still compatible with these data and keeps a difference between central and forward rapidity domains. Might this later feature turn out later to be the ultimate discriminating tool between models since the COM calculation [19] is also consistent with available datas, in the higher p_T part where all calculations are more reliable ?

PHENIX is also performing a program with polarized protons beams. Recently the first measurement [20] of W longitudinal asymmetry has been obtained. These beams also open new perspectives for the quarkonia. The single transverse-spin asymmetry of J/ψ , using measurement in collisions between beams with different polarization, is tentatively explored [21]. This new observable should be sensitive to the production mode: a vanishing asymmetry is predicted [22] in e+p collisions in CSM, and p+p collisions in COM. More data in p+p and also e+p is needed. In it final remarks D. Kharzeev [23] underlined the interest, on top of the separation between color octet and color singlet mechanisms with unpolarized beams, of measuring the quarkonia angular distribution of the spin asymmetry [24] with polarized beams to get access to the gluon helicity distribution in the proton.

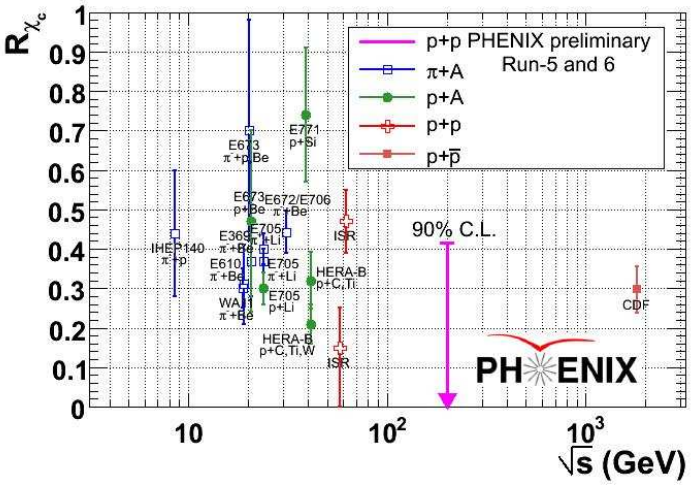

Figure 3: J/ψ feed -down fraction from χ_c in various experiment as a function of the collision energy

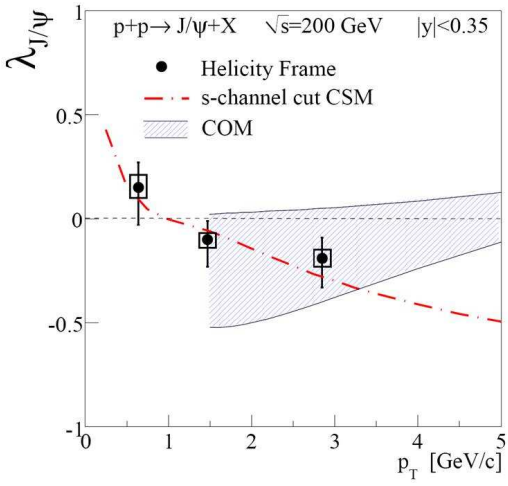

Figure 4: J/ψ polarization as a function of the transverse momentum, compared to theoretical predictions (see text)

References

1. F. Abe et al. *Phys. Rev. Lett.* **79**, 578 (1997).
2. A. Abulencia et al. *Phys. Rev. Lett.* **99**, 132001 (2007).
3. H.Pereira Da Costa, [PHENIX Collaboration], Proceedings in this volume.
4. A. Adare et al. [PHENIX Collaboration],*Phys. Rev. Lett.* **98**, 232002 (2007)
5. R.Vogt, private communication, see *Phys. Rev.* C **81**, 044903 (2010)
6. S.J. Brodsky and J.P. Lansberg *Phys. Rev.* D **81**, 051502(R) (2010)
7. F. Karsch, D. Kharzeev and H. Satz *Phys. Lett.* B **637**, 75 (2006)
8. Calculated from F.Abe et al. *Phys. Rev. Lett.* **79**, 572 (1997)
9. I. Abt et al. *Eur. Phys. J* C **49**, 545 (2007)
10. P. Faccioli, C. Lourenço, J. Seixas and H.K. Wöhri, JHEP **10**, 004 (2008)
11. C.L. da Silva for the PHENIX Collaboration, *Nucl. Phys.* A **830**, 227c-230c (2009)
12. F. Cooper, M. X. Liu, G. C. Nayak, *Phys. Rev. Lett.* **93**, 171801 (2004)
13. H.Haberzettl and J.P. Lansberg, *Phys. Rev. Lett.* **100**, 032006 (2008)
14. J.P. Lansberg, these proceedings, and reference [6]
15. V.A. Khoze, A.D. Martin, M.G. Ryskin, W.J. Stirling, *Eur. Phys. J* C **39**, 163 (2005)
16. A.Adare et al. Transverse momentum dependence of J/ψ polarization at midrapidity in $p+p$ collisions at $\sqrt{s} = 200$ GeV, arXiv:0912.2082, to be published in Physical Review D
17. J.P. Lansberg and H.Haberzettl ,archiv 0806.4901.v1, *AIP Conf. Proc.* **1038**, 83 (2008)
18. J.P. Lansberg, arXiv1003.4319v1, 23 march 2010
19. H. S. Chung, S. Kim, J. Lee, and C. Yu, *Phys. Rev.* D **81**, 014020 (2010)
20. K. Okada , [PHENIX Collaboration], arXiv1006.1106v1
21. C.Aidala, Single-Spin-Asymmetries and Transverse-Momentum-Dependent Distributions at RHIC, Electromagnetic Interactions with Nucleons and Nuclei, Milos Island, Greece, September 27-October 2, 2009
22. F. Yuan *Phys. Rev.* D **78**, 014024 (2008)
23. D.Kharzeev, these proceedings
24. R.L. Jaffe and D. Kharzeev *Phys. Lett.* B **455**, 306 (1999)

Heavy Quarkonia Production in Relativistic d+A and A+A collisions at RHIC, as Measured by the PHENIX Experiment

H. Pereira Da Costa, for the PHENIX collaboration
IRFU/Sphn, CEA Saclay,
F-91191, Gif-sur-Yvette, France

This contribution presents the latest results on heavy quarkonia (J/ψ and Υ) production in $d+\mathrm{A}$ and $\mathrm{A}+\mathrm{A}$ at RHIC at a center of mass energy per nucleon-nucleon collision $\sqrt{s_{\mathrm{NN}}} =$ 200 GeV, measured by the PHENIX experiment, as well as their implications in terms of understanding cold nuclear matter effects and the possible formation of a quark gluon plasma in central $\mathrm{Au}+\mathrm{Au}$ collisions.

Heavy quarkonia have long been considered a favored probe to study the formation of a Quark Gluon Plasma (QGP) in heavy ion collisions for the following reasons: 1) due to their large masses, they are hard probes produced during the first instants of the collision via hard scattering of partons (dominantly gluons, at RHIC); 2) their large binding energy makes them harder to dissociate via interactions with the surrounding hadrons; 3) their production was predicted to be affected by the formation of a QGP, provided that the temperature is high enough, via a color screening mechanism similar to the Debye screening in QED [1].

However their production is also affected by other mechanism that do not necessitate the formation of a QGP, and are therefore referred to as Cold Nuclear Matter (CNM) effects. Such effects include: 1) the modification of the Parton Distribution Functions (PDF) in the nuclei, which relates to the fact that the number of partons at a given momentum fraction x inside a nucleon is different whether the nucleon is isolated or inside a nucleus, thus affecting the momentum distribution of quarkonia formed via the hard scattering of these partons [2,3,4] (note that a qualitatively similar effect exists at small x in the so-called *gluon saturation* region, which can be described in the Color Glass Condensate framework [5]); 2) the energy loss (via inelastic scattering) of the projectile parton inside the target nucleus before the hard scattering leading to the quarkonia formation, denoted as *initial state energy loss* [6]; 3) the broadening of the quarkonia transverse momentum distribution due to elastic scattering of its parent partons inside the nucleus, denoted as Cronin effect [7]; 4) the dissociation of the quarkonia bound state (or its precursors) by scattering off the surrounding hadrons [2]. These effects can be quantified by studying the production of heavy quarkonia in $p+\mathrm{A}$ (or rather $d+\mathrm{A}$, at RHIC) collisions.

Two quantities are used in this presentation to characterize changes to heavy quarkonia production in $d+\mathrm{A}$ and $\mathrm{A}+\mathrm{A}$ collisions:

- the nuclear modification factor $R_{d\mathrm{A}}$ (or R_{AA}), obtained by forming the ratio of the heavy quarkonia yield measured in $d+\mathrm{A}$ ($\mathrm{A}+\mathrm{A}$) collisions, to the yield measured in $p+p$ collisions, normalized by the number of binary ($p+p$) collisions, N_{col}, corresponding to one $d+\mathrm{A}$ collision. This factor does not depend on the heavy quarkonia production

mechanism (provided that this mechanism is a hard process), and is equal to unity if $d+\mathrm{A}$ collisions can effectively be considered as an incoherent superposition of independent $p+p$ collisions, as far as heavy quarkonia production is concerned. $R_{d\mathrm{A}}$ can be evaluated in bins of the heavy quarkonia rapidity (y) and transverse momentum, but also as a function of the collision centrality, which is related to the distance between the target and the projectile nuclei centers (also called *impact parameter*, b). Central collisions correspond to small values of b, whereas peripheral collisions correspond to large values of b. Note that b can never be measured directly, and that depending on how the centrality is actually measured, its correlation to b can be rather lose (especially in the $d+\mathrm{A}$ case).

- the central to peripheral ratio R_{CP}, obtained by forming the ratio of the heavy quarkonia yields between central collisions (for which maximum modifications are expected) and peripheral collisions (which should be more similar to the $p+p$ case), properly normalized by the corresponding N_{col} values. The advantage of R_{CP} over $R_{d\mathrm{A}}$ is that most experimental systematic uncertainties are canceled, since the same data set can be used for the numerator and the denominator. On the other hand, the quantitative interpretation of R_{CP} deviations from unity is more ambiguous due to the fact that peripheral collisions cannot be strictly considered identical to $p+p$.

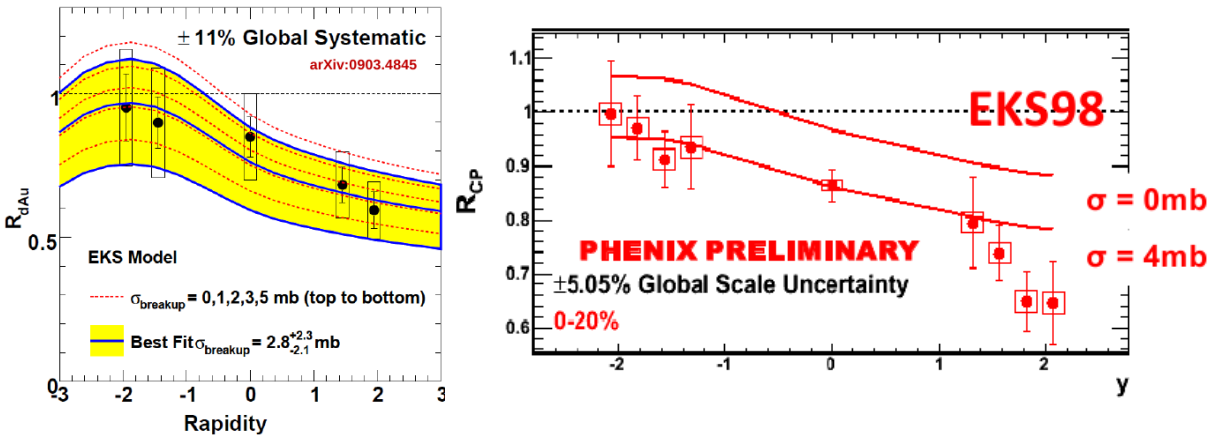

Figure 1: Left: J/ψ $R_{d\mathrm{Au}}$ as a function of rapidity using 2003 $d+\mathrm{Au}$ minimum bias collisions. Right: J/ψ R_{CP} as a function of rapidity using 2008 $d+\mathrm{Au}$ central ($0-20$ %) and peripheral ($60-88$ %) collisions. Solid lines correspond to calculations from R. Vogt based on the EKS shadowing model convoluted to different values for the J/ψ breakup cross-section $\sigma_{\mathrm{breakup}}$.

Figure 1 (left) shows the published J/ψ $R_{d\mathrm{Au}}$ measured by PHENIX using RHIC 2003 $d+\mathrm{Au}$ minimum bias data as a function of the J/ψ rapidity [8]. J/ψ produced at negative rapidity (the gold going side) originate from gluons of rather large x in the gold nuclei, with x being the fraction of the nucleon momentum carried by the gluon. On the contrary, J/ψ produced at positive rapidity originate from gluons of rather small x in the gold nuclei. A J/ψ suppression is observed at positive rapidity, which is consistent with gluon shadowing (and/or saturation) in the small x regime inside the gold nuclei. The various curves shown on the figure correspond to model calculations that include a parametrization of the gluon shadowing (here EKS [3]) together with a J/ψ break-up cross-section $\sigma_{\mathrm{breakup}}$ that varies from 0 to 5 mb. These curves can be used to fit the data and extract the most probable value for $\sigma_{\mathrm{breakup}}$. The shape obtained using this most probable value describes the data reasonably well, within the large statistical and systematic uncertainties.

Figure 1 (right) shows the preliminary J/ψ R_{CP} measured by PHENIX using RHIC 2008 $d+\mathrm{Au}$ data. This data set corresponds to an integrated luminosity of ~ 55 nb^{-1}, which represents an increase of about a factor 40 with respect to the 2003 data set, thus allowing to have

more experimental points as a function of rapidity and use several centrality bins. The curves shown on the figure have been obtained using a similar approach to that of the left panel. Due to the reduced uncertainties and the larger number of experimental points, it appears that this approach (shadowing + $\sigma_{\rm breakup}$) is unable to properly describe the data, especially at the most forward rapidity, and that additional effects, such as initial state energy loss, must be accounted for in the calculation. Alternatively, one can parametrize the difference between the shadowing calculation (obtained with $\sigma_{\rm breakup} = 0$) and the data by a phenomenological rapidity dependent cross-section. Such a cross-section naturally increases for positive rapidity. A qualitatively similar trend has also been observed for lower energy J/ψ measurements [9].

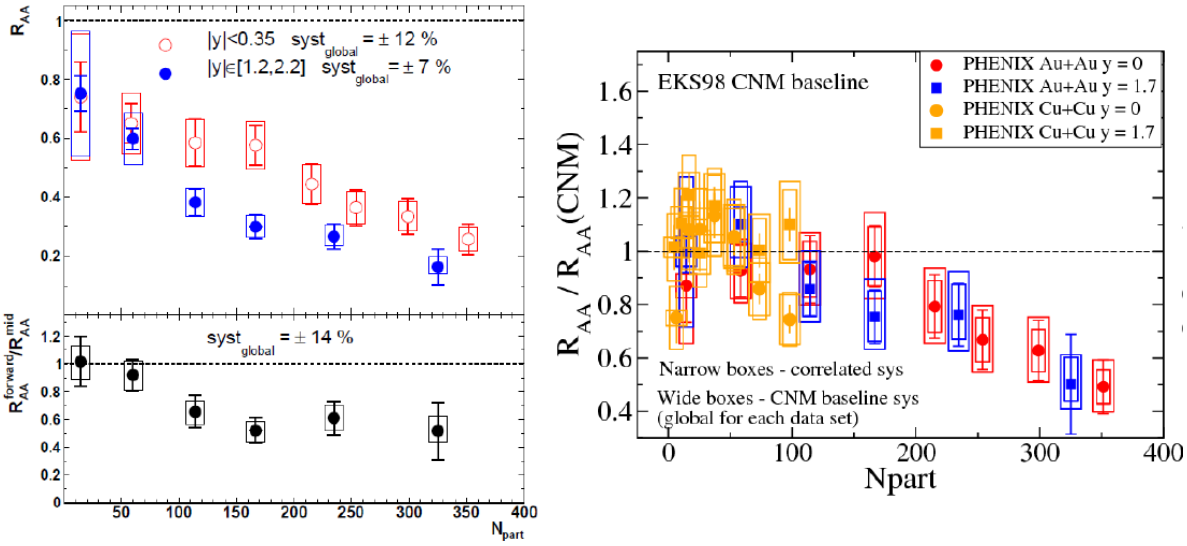

Figure 2: Left: J/ψ $R_{\rm AA}$ as a function of centrality in 2004 Au + Au collisions, for two rapidity bins. Right: J/ψ $R_{\rm AA}$ divided by extrapolated cold nuclear matter effects based on 2008 d + Au data set and using different values for $\sigma_{\rm breakup}$ as a function of rapidity.

A significant J/ψ suppression has also been measured in Au + Au collisions as illustrated as a function of centrality (here $N_{\rm part}$, the average number of nucleons that participate to Au + Au collisions at a given centrality) in figure 2 (left) for two rapidity regions [10]. It appears that the suppression is larger at forward rapidity than at mid-rapidity. It is important to quantify which fraction of this suppression is due to CNM effects alone, in order to single out the effect of the possible formation of a QGP. This is achieved by using a parametrization of the observed d + Au suppression (using a shadowing model and a rapidity dependent $\sigma_{\rm breakup}$) and extrapolating it to the Au + Au case. The measured $R_{\rm AA}$ can then be divided by this CNM-only expected suppression, as shown in figure 2 (right) [11]. A significant J/ψ suppression remains for central enough collisions (large values of $N_{\rm part}$) even after CNM effects have been removed. This indicates that additional effects (for instance due to the formation of a QGP) must be accounted for to be able to describe the J/ψ suppression observed in central Au + Au collisions. Besides, this remaining suppression is now similar between the two rapidity domains, meaning that the differences observed in figure 2 (left) can be entirely accounted for by CNM effects. Also shown on the figure are the results obtained in Cu + Cu collisions [12] and for which no significant suppression beyond CNM effects is observed.

Finally, Υ resonances have been measured by PHENIX in both $p + p$ (using 2006 data set) and d + Au collisions (using the 2008 data set), allowing one to form the first Υ $R_{d\rm A}$ at this energy. Figure 3 (left) shows the di-muon invariant mass distribution at the Υ mass, measured in one of PHENIX muon arms in d + Au collisions. The various coloured bands correspond to the different contributions to this spectra, and are fitted to the data in order to evaluate the

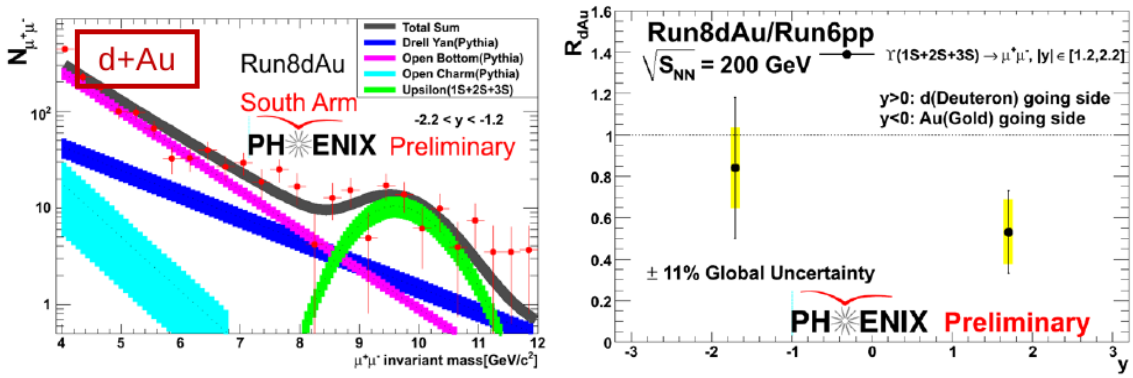

Figure 3: Left: di-muon invariant mass distribution at the Υ mass measured using 2008 $d+$Au collisions. Coloured area correspond to the different contribution to the di-muon spectra. Right: Υ R_{dA} as a function of rapidity.

number of produced Υ resonances. Figure 3 (right) shows the Υ $R_{d\mathrm{A}}$ obtained by combining these data to yields measured in $p+p$ collisions. A suppression is observed at forward rapidity, similarly to the J/ψ case, which has yet to be compared to theoretical calculations.

Υ resonances have also been measured in Au + Au collisions at mid-rapidity by the PHENIX experiment. However, due to the limited statistics, only a 90 % Confidence Level (CL) could be evaluated so far for R_{AA} and the contributions to the di-lepton invariant mass spectrum from other (background) sources in the Υ mass region have not been accounted for. The resulting value is $R_{\mathrm{AA}} < 0.64$ at 90 % CL for all di-leptons produced at mid-rapidity ($|y| < 0.35$) with mass $M \in [8.5, 11.5]$ GeV/c^2.

To summarize, a significant J/ψ suppression has been observed by PHENIX in both 2003 and 2008 $d+$Au data sets at positive rapidity (in the gluon shadowing/saturation region for the gold nuclei), with an increased statistics of about a factor 40 for the 2008 data. This suppression can be attributed to CNM effects, but cannot be properly described (for the 2008 data) with a simple model that considers only PDF modifications and a (rapidity independent) J/ψ break-up cross section. Phenomenologically parametrized CNM effects can be extrapolated to Au + Au collisions and compared to the J/ψ suppression measured in these conditions. It appears that an additional suppression (not attributed to CNM effects) remains for central Au + Au collisions, which is largely rapidity independent. Concerning the Υ resonance, a suppression similar to that of the J/ψ has also been observed for the first time in $d+$Au collisions and a 90 % confidence level for high mass di-lepton pairs (dominantly Υ mesons) R_{AA} has measured.

1. T. Matsui and H. Satz,*Phys. Lett.* B **178** 416 (1986).
2. R. Vogt, *Phys. Rev.* C **71**, 054902 (2005).
3. K. J. Eskola, V. J. Kolhinen, and R. Vogt, *Nucl. Phys.* A **696**, 729 (2001).
4. K. J. Eskola, H. Paukkunen, C. A. Salgado, JHEP **0904**, 065 (2009).
5. L. McLerran and R. Venugopalan, *Phys. Rev.* D **49**, 2233 (1994).
6. R. Vogt, *Phys. Rev.* C **61**, 035203 (2000).
7. D. Antreasyan *et al.*, *Phys. Rev.* D **19**, 764 (1979).
8. A. Adare *et al.*, PHENIX Collaboration, *Phys. Rev.* C **77**, 024912 (2008) and erratum: *Phys. Rev.* C **77**, 024912 (2008).
9. C. Lourenco, R. Vogt, H. K. Woehri, JHEP **0902**, 014 (2009).
10. A. Adare *et al.*, PHENIX Collaboration, *Phys. Rev. Lett.* **98**, 232301 (2007).
11. A. D. Frawley, private communication and CATHIE, INT workshop (2009).
12. A. Adare *et al.*, PHENIX Collaboration, *Phys. Rev. Lett.* **101**, 122301 (2008).

Total J/ψ production cross section at the LHC

J.P. Lansberg
Centre de Physique Théorique, École Polytechnique, CNRS, 91128 Palaiseau, France

We evaluate the production cross section for direct J/ψ integrated in P_T for various collision energies of the LHC in the QCD-based Colour-Singlet Model. We consider the LO contributions from gluon fusion as well as the one from a fusion of a gluon and a charm quark from the colliding protons. The rapidity distribution of the yield is evaluated in the central region relevant for the ATLAS and CMS detectors, as well as in the more forward region relevant for the ALICE and LHC-b detectors. The results obtained here are compatible with those of other approaches within the range of the theoretical uncertainties which are admittedly very large. This suggests that the "mere" measurements of the yield at the LHC will not help disentangle between the different possible quarkonium production mechanisms.

1 Introduction

In 2007, the first evaluations of QCD corrections to quarkonium-production rates at hadron colliders became available. It is now widely accepted – and understood– that α_s^4 and α_s^5 corrections to the CSM [1] are fundamental for understanding the P_T spectrum of J/ψ and Υ produced in high-energy hadron collisions, [2,3,4,5,6,7] while the difficulties of predicting these observables had been initially attributed to non-perturbative effects associated with channels in which the heavy quark and antiquark are produced in a colour-octet state [8,9,10,11]. Further, the effect of QCD corrections is also manifest in the polarisation predictions. While the J/ψ and Υ produced inclusively or in association with a photon are predicted to be transversally polarised at LO, it has been recently emphasised that their polarisation at NLO is increasingly longitudinal when P_T gets larger. [4,5,12,13,14]

In a recent work,[15] we have also shown that hard subprocesses based on colour singlet $Q\bar{Q}$ configurations alone are sufficient to account for the observed magnitude of the P_T-integrated cross section. In particular, the predictions at LO [1] (Fig. 1 (left)) and NLO [2,3,4] accuracy are both compatible with the measurements by the PHENIX collaboration at RHIC [20] within the present uncertainties.[a] The compatibility between the LO and NLO yields provided some indications that the computations are carried in a proper perturbative regime, at least at RHIC energies. The agreement with the data is improved when hard subprocesses involving the charm-quark distribution of the colliding protons are taken into consideration. These constitute part of the LO (α_S^3) rate (Fig. 1 (right)) and are responsible for a significant fraction of the observed yield.[15]

We proceed here to the evaluation the P_T-integrated yield at higher energies both in the central and forward rapidity regions. While we find a good agreement with CDF data,[18] our study

[a] As recently noted, [15] this points at a reduced impact of the s-channel cut contributions[16] as well as of the colour-octet mediated channels relevant for the low P_T region. The latter are anyway very srongly constrained by very important recent e^+e^- analyses [17] which leave in some cases no room at all for colour octets of any kind.

shows that the theoretical uncertainties become very large –close to one decade– reminiscent of the case of total charm production.[19] Besides, the yield coming from gluon-charm fusion is shown to remain a visible fraction of the direct yield at the LHC energies. Finally, we shortly discuss the impact of higher QCD corrections and the comparison with other approaches.

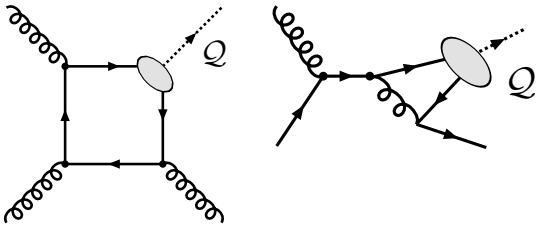

Figure 1: Representative diagrams contributing to ${}^3S_1$ charmonium hadroproduction at high energies in the CSM by gluon fusion (left) and initiated by a charm quark at order α_S^3.

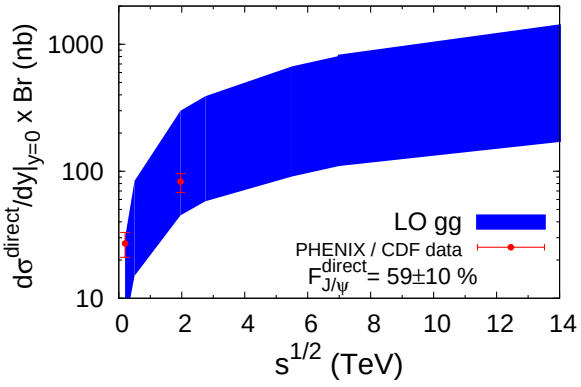

Figure 2: $d\sigma^{direct}_{J/\psi}/dy|_{y=0} \times$ Br from gg fusion in pp collisions for $\sqrt{s}$ from 200 GeV up to 14 GeV compared to the PHENIX [20] and the CDF [18] data multiplied by the direct fraction.

2 Total J/ψ cross section at the LHC

The P_T integrated cross sections obtained here have been evaluated along the same lines as our previous study.[15] The uncertainty bands have been evaluated following exactly the same procedure using the same values for m_c, μ_R and μ_F.

In Fig. 2, we show $d\sigma^{direct}_{J/\psi}/dy|_{y=0} \times$ Br from gg contributions as function of $\sqrt{s}$ from 200 GeV up to 14 TeV compared to the PHENIX [20] and the CDF [18] data multiplied by the direct fraction[b]. We have found a good agreement. At larger energies, these results at 7 TeV (100 to 800 nb) and at 14 TeV (200 to 1400 nb) are in the same range as those of the Colour Evaporation Model [24] with central (upper) values of 140 nb (400 nb) at 7 TeV and 200 nb (550 nb) at 14 TeV. They are also compatible with the results of the "gluon tower model" (GTM) [21], 300 nb at 7 TeV and 480 nb at 14 TeV, which takes into account some NNLO contributions shown to be enhanced by $\log(s)$. Quoting the authors, [21] "the expected accuracy of the prediction is about a factor of 2-3 in either direction or even worse."

In Fig. 3, one shows the differential cross section in rapidity from both gg and cg contributions (separately and then summed) at $\sqrt{s} = 7$ TeV. One sees that the contribution from cg is not negligible. To be more quantitative, we have computed the ratio $(d\sigma^{cg}_{J/\psi}/dy)/(d\sigma^{cg+gg}_{J/\psi}/dy)$ for $m_c = 1.4$ GeV using 3 choices of the charm distribution in the proton [22] and taking uncorrelated values for μ_R and μ_F for both contributions. At large rapidity, one starts to see the enhancement of BHPS [23] $c(x, Q^2)$ for $x > 0.1$. Fig. 5 and Fig. 6 show the same contributions at $\sqrt{s} = 2.75$ TeV and $\sqrt{s} = 14$ TeV.

[b] Note that the measurement of the prompt yield by CDF went only down to $P_T = 1.25$ GeV. We have assumed a fraction of non-prompt J/ψ of 10% below.

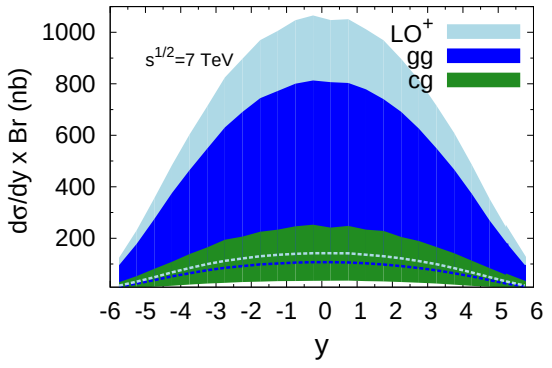

Figure 3: $d\sigma^{direct}_{J/\psi}/dy \times$ Br from gg fusion (dark blue), from cg fusion (green) and from all the LO contributions (light blue) in pp collisions at $\sqrt{s} = 7$ TeV.

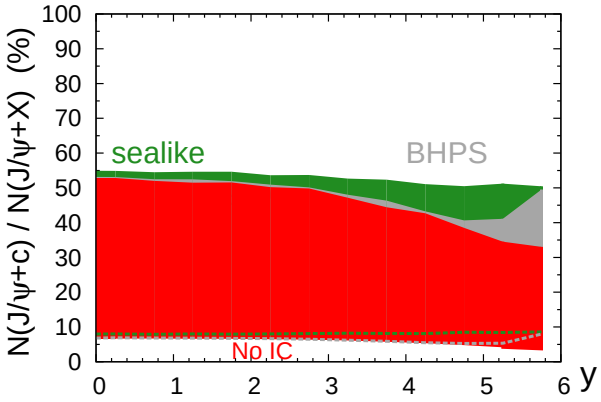

Figure 4: Ratio $(d\sigma^{cg}_{J/\psi}/dy)/(d\sigma^{cg+gg}_{J/\psi}/dy)$ at $\sqrt{s} = 7$ TeV for $m_c = 1.4$ GeV for uncorrelated values of μ_R and μ_F for gg and cg contributions and for 3 $c(x, Q^2)$: NoIC (red), sealike (green) and BHPS (gray)

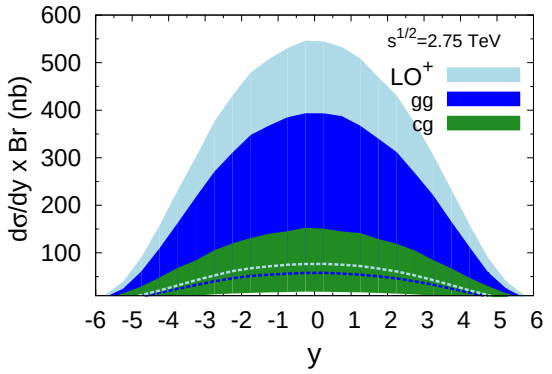

Figure 5: $d\sigma^{direct}_{J/\psi}/dy \times$ Br from gg fusion (dark blue), from cg fusion (green) and from all the LO contributions (light blue) in pp collisions at $\sqrt{s} = 2.75$ TeV, i.e. the $\sqrt{s_{NN}}$ planned for Pb+Pb collisions in 2010.

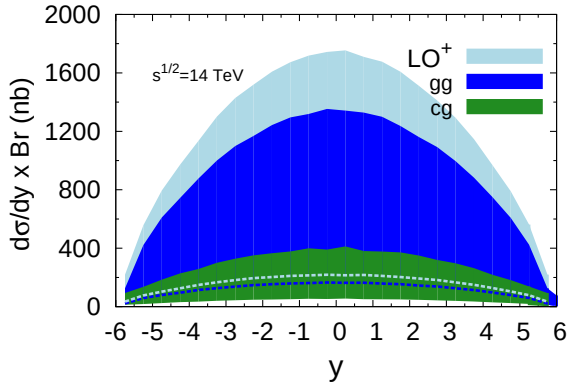

Figure 6: $d\sigma^{direct}_{J/\psi}/dy \times$ Br from gg fusion (dark blue), from cg fusion (green) and from all the LO contributions (light blue) in pp collisions at $\sqrt{s} = 14$ TeV.

3 Discussion and conclusion

Let us now discuss briefly the expectations for the results when QCD corrections are taken into account. First, we would like to stress that, although NLO results [2] are perfectly well behaved in nearly all of the phase space region at RHIC energies, [15] it seems not to be so for larger s. One observes that the region where the differential cross section in P_T and/or y is negative (i.e. very low P_T and large y) widens for increasing s. Negative differential cross section at low P_T is a known issue. Nonetheless, for $\sqrt{s}$ above a couple of TeV, and for some (common) choices of μ_F and μ_R, the P_T-integrated "yield" happens to become negative, even in the central region. This can of course be explained by a larger contribution from the virtual corrections at α_S^4 –which can be negative– compared to the real emission contributions –which are positive–. Naturally, such results cannot be compared to experimental ones. This also points at likely large virtual NNLO contributions at low P_T; these are not presently known. Yet, as already mentioned, specific NNLO contributions were shown [21] to be enhanced by $\log(s)$.

As we have discussed above, one may try compare the LO CSM with other theoretical approaches such as the CEM [24] and the GTM [21]. They all qualitatively agree, as well as with

PHENIX and CDF measurements. For all approaches, one expects a significant spread –up to a factor of ten – of the results when the scales and the mass are varied.

Owing to these uncertainties, it will be difficult to discriminate between different mechanisms by only relying on the yield integrated in P_T and even, to a less extent, on its P_T dependent counterpart. This is a clear motivation to study at the LHC other observables related to the production of J/ψ such as its production in association with a single charm (or lepton),[15], with a prompt isolated photon [12,13] or even with a pair of $c\bar{c}$. [3]

Acknowledgments

I would like to thank the organisers for inviting me to their lively conference. I thank V.Khoze, A. Kraan, M. Ryskin, G. Smbat, R. Vogt for correspondences and F. Fleuret for useful discussions.

References

1. C-H. Chang, Nucl. Phys. B **172** (1980) 425; R. Baier and R. Rückl, Phys. Lett. B **102** (1981) 364; E. L. Berger and D. L. Jones, Phys. Rev. D **23** (1981) 1521; R. Baier and R. Rückl, Z. Phys. C **19** (1983) 251; V. G. Kartvelishvili, A. K. Likhoded and S. R. Slabospitsky, Sov. J. Nucl. Phys. **28** (1978) 678 [Yad. Fiz. **28** (1978) 1315].
2. J. Campbell, F. Maltoni and F. Tramontano, Phys. Rev. Lett. **98**, 252002 (2007)
3. P. Artoisenet, J. P. Lansberg and F. Maltoni, Phys. Lett. B **653**, 60 (2007)
4. B. Gong and J. X. Wang, Phys. Rev. Lett. **100** (2008) 232001; Phys. Rev. D **78** (2008) 074011.
5. P. Artoisenet, J. Campbell, J. P. Lansberg, F. Maltoni and F. Tramontano, Phys. Rev. Lett. **101** (2008) 152001.
6. P. Artoisenet, AIP Conf. Proc. **1038**, 55 (2008);
7. J. P. Lansberg, Eur. Phys. J. C **61**, 693 (2009);
8. J. P. Lansberg, Int. J. Mod. Phys. A **21**, 3857 (2006)
9. N.Brambilla *et al.*, CERN Yellow Report 2005-005,hep-ph/0412158
10. M. Kramer, Prog. Part. Nucl. Phys. **47**, 141 (2001)
11. J. P. Lansberg *et al.*, AIP Conf. Proc. **1038** (2008) 15 [arXiv:0807.3666 [hep-ph]].
12. R. Li and J. X. Wang, Phys. Lett. B **672** (2009) 51.
13. J. P. Lansberg, Phys. Lett. B **679** (2009) 340.
14. J. P. Lansberg, arXiv:1003.4319 [hep-ph].
15. S. J. Brodsky and J. P. Lansberg, Phys. Rev. D **81** 051502(R) (2010).
16. H. Haberzettl and J. P. Lansberg, Phys. Rev. Lett. **100** (2008) 032006. J. P. Lansberg, J. R. Cudell and Yu. L. Kalinovsky, Phys. Lett. B **633** (2006) 301.
17. Z. G. He, Y. Fan and K. T. Chao, Phys. Rev. D **81** (2010) 054036; Y. J. Zhang, Y. Q. Ma, K. Wang and K. T. Chao, Phys. Rev. D **81** (2010) 034015; Y. Q. Ma, Y. J. Zhang and K. T. Chao, Phys. Rev. Lett. **102** (2009) 162002; B. Gong and J. X. Wang, Phys. Rev. Lett. **102** (2009) 162003.
18. D. E. Acosta *et al.* [CDF Collaboration], Phys. Rev. D **71** (2005) 032001.
19. R. Vogt, Eur. Phys. J. C **61** (2009) 793.
20. A. Adare *et al.*, Phys. Rev. Lett. **98** (2007) 232002. C. L. da Silva,Nucl. Phys. A **830** (2009) 227C; L. Linden Levy, Nucl. Phys. A **830** (2009) 353C
21. V. A. Khoze, *et al.* Eur. Phys. J. C **39** (2005) 163.
22. J. Pumplin, H. L. Lai and W. K. Tung, Phys. Rev. D **75** (2007) 054029.
23. S. J. Brodsky, P. Hoyer, C. Peterson and N. Sakai, Phys. Lett. B **93** (1980) 451.
24. M. Bedjidian *et al.*, CERN-2004-009-C, arXiv:hep-ph/0311048. R. Vogt, private communication.

3.
QCD

LATEST JET RESULTS FROM THE TEVATRON

DARREN D. PRICE
on behalf of the CDF and DØ Collaborations
Department of Physics, Indiana University,
Bloomington, IN 47405, USA

A brief overview of the latest status of jet physics studies at the Tevatron in proton-antiproton collisions at $\sqrt{s} = 1.96$ TeV are presented. In particular, measurements of the inclusive jet production cross-section, dijet production and searches for new physics, the ratio of the 3-jet to 2-jet production cross-sections, and the three-jet mass are discussed.

The measurement of inclusive jet rates in Tevatron data at $\sqrt{s} = 1.96$ TeV has allowed for tests of perturbative QCD (pQCD) and searches for new physics at jet transverse momenta of up to 700 GeV and over eight orders of magnitude in cross-section. Much work went into understanding the calorimeter response in both experiments, using a single particle response technique[1] in the case of CDF and a data-driven photon-plus-jet event calibration method at DØ. Both extended the calorimeter response to non-optimal calorimeter regions using dijet p_T balancing techniques. The result of such studies and accurate simulation was to minimise the experimental systematics and these inclusive measurements are thus dominated by theoretical uncertainties. As a result, the Tevatron has been able to make significant contributions to the understanding of the proton structure and the strong force and improve sensitivity to new physics effects. The understanding gained by these measurements are important not just for QCD analyses, but also have relevance to any analyses which have jets as a feature of interest.

CDF's measurement of the inclusive jet cross-section was performed[2] using the midpoint cone algorithm[3] with a cone size of $R = 0.7$ in five bins of jet rapidity up to $|y| < 2.1$ and, as in all studies described here, was fully corrected for efficiencies and bin-to-bin migrations caused by the p_T resolution of the detector. The corrected spectrum was compared to NLO pQCD from FastNLO[4] based on the NLOJet++[5] program, using CTEQ6.1M[6]. NLO calculations are provided at the parton-level whilst cross-sections are corrected back to the particle-level, so in all comparisons to NLO a parton-to-particle non-perturbative correction is derived from parton-shower Monte Carlo to place the corrected data and the NLO theory on an equal footing. Such corrections are largest at low jet p_T, where underlying event corrections to the jet area can be significant (of order $10 - 20\%$). After this correction, the measured cross-sections were found to be lower than but in agreement with NLO within the uncertainties. CDF also measured[7] the inclusive jet cross-section using the k_T clustering algorithm[8] for three jet size parameter choices $D = 0.4$, 0.7 and 1.0. An advantage of this jet algorithm is its infrared and collinear safety to all orders in perturbation theory, and measurement using both k_T and midpoint is an important validation test of the use of different jet algorithms at hadron colliders. The data with k_T and midpoint were found to agree across a wide range of rapidity and p_T. NLO theory and data were also in good agreement apart from in the highest rapidity bin where the data is

lower than NLO prediction (but within uncertainties), with the measurements using different distance parameters showing similar behaviours. From this one may conclude that the cone and k_T clustering algorithms can be used to retrieve consistent results at hadron-hadron machines.

DØ's measurement[9] of the inclusive jet cross-section made use of the midpoint cone algorithm with $R = 0.7$, analysed data in six rapidity bins up to $|y| < 2.4$ and is the most precise measurement to-date. A comparison was also made to NLO theory with NLOJet++ and FastNLO using the CTEQ6.5M PDFs, and whilst in agreement, the data prefers the lower bound of the theoretical prediction. The jet energy scale (JES) uncertainty of $1.2 - 2\%$ (compared to CDF's $2-3\%$) dominates the experimental error. Due to the steeply falling cross-section this translates into a large error on the final results, leading to total errors on the measurement of $15-30\%$ for DØ and $15-50\%$ for CDF. These uncertainties still generally smaller than those from theory (largely coming from PDF uncertainties), and has enabled (along with the CDF inclusive jet data) constraints of the gluon PDF at high x and high Q^2, now used in the MSTW2008[10] fits.

Utilising this well-understood dataset it is possible to extract many other jet results. Both CDF[11] and DØ[12] measured the dijet mass spectrum (see Figure 1), not only as a test of theoretical calculations but as a search for new physics in models that predict the existence of a particle that decays into two high p_T jets. DØ made a measurement of the dijet mass in the

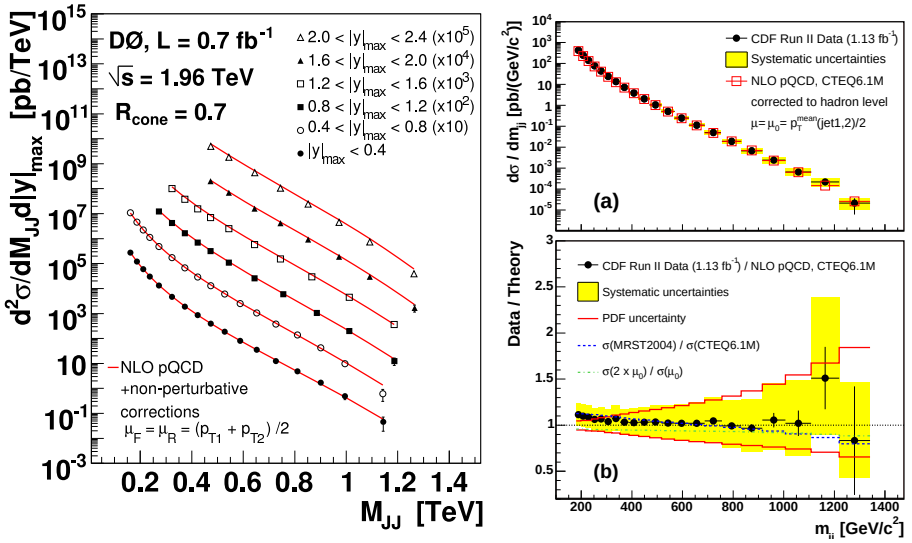

Figure 1: Measured dijet mass cross-section from DØ (in bins of the highest rapidity jet) *(left)* and from CDF for jets in $|y| < 1.0$ *(right)* compared to NLO calculations. In both cases the theoretical uncertainty from the PDF is comparable to the systematic uncertainties (largely from the jet energy scale uncertainty).

six rapidity bins of the inclusive cross-section measurement and compared the results to NLO predictions from FastNLO with MSTW2008NLO PDFs. Bin sizes in m_{JJ} are chosen to give a bin purity and efficiency[a] of about 50%; experimental corrections vary between 0.5% and 12%, NLO non-perturbative corrections are between $5-20\%$ in size. Systematic uncertainties on the measurement are similar to those from PDF and scale uncertainties, suggesting the measurement can be used to constrain future predictions. CDF restricted itself to a central jet ($|y| < 1.0$) measurement (also shown in Figure 1) where jets from new physics are most likely to be produced. The data were consistent with NLO predictions. From this data, CDF searched for narrow dijet resonances by fitting the data before bin-by-bin unfolding corrections (to avoid any resultant degradation in a possible signal) to a smooth functional form and looking for significant data excesses from the fit. Figure 2 shows the expected signals in the presence of

[a] Determined from a parameterised detector model. Efficiency [purity] is defined as the ratio of Monte Carlo events reconstructed [generated] to those generated [reconstructed] in a particular bin.

excited quarks at various masses, and in the absence of any resonant structure, exclusion limits for various new physics models and in particular the most stringent limits on excited quark, axigluon, flavour-universal coloron, E_6 diquark and colour-octet techni-ρ models.

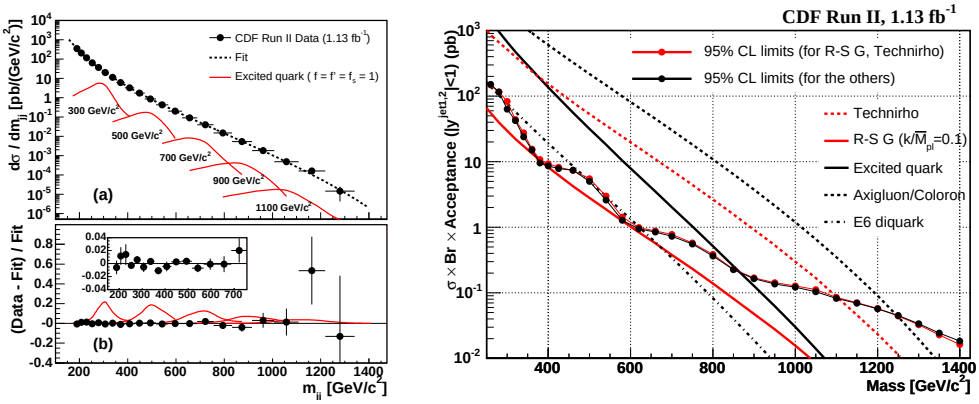

Figure 2: Measured dijet mass spectrum before bin-by-bin unfolding (a) and ratio (b) compared to excited quark signals expected at various masses *(left)*, and resultant 95% C.L limits for various BSM predictions *(right)*.

DØ has made the first measurement of the three-jet cross-section in RunII data from the Tevatron (see also a previous result[13] from CDF using RunI data) in three rapidity regions ($|y| < 0.8, < 1.6, < 2.4$) and three bins ($p_{T3} > 40, 70, 100$ GeV) of third jet transverse momentum (shown in Figure 3) as a function of three-jet mass. A leading jet requirement of $p_{T1} > 150$ GeV, in conjunction with the third jet p_T requirement ensures the trigger for selected events is 100% efficient. Any pair ij of jets is required to have a $y - \phi$ spatial separation of $\Delta R_{ij} > 1.4$ to avoid jet overlap reliant on the split-merge procedure of the midpoint jet cone algorithm. The SHERPA[14] Monte Carlo generator with MSTW2008LO PDFs were used to perform the event simulation and correct for various detector effects after determining the generator performed well at describing the data distributions. There is agreement with NLO calculations, with the data preferring the lower range of the predictions.

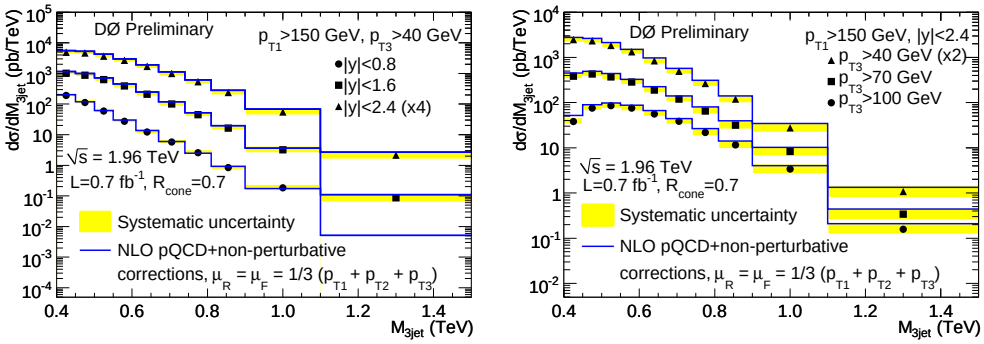

Figure 3: Three-jet mass cross-section in bins of jet rapidity *(left)* and third jet p_T *(right)* and systematic uncertainties (up to $20 - 30\%$) compared to NLO calculations using NLOJet++ and MSTW2008LO PDFs.

Using the same dataset at DØ and again using simulation with SHERPA, the first measurement of the ratio of the three to two-jet cross-section at the Tevatron has been made corrected for all detector effects and measured as a function of two momentum scales: $p_{T\mathrm{max}}$ the leading jet p_T and $p_{T\mathrm{min}}$ the scale at which the other jets are resolved. This is a test of pQCD largely independent of PDFs, and many other uncertainties cancel in the ratio making this measurement particularly sensitive. The results are shown in Figure 4 over a range

$p_{T\min} + 30$ GeV$< p_{T\max} < 500$ GeV to allow sufficient phase space for jets to be resolved and experimental corrections to be small (0.9−1.2 in the ratio). A jet $\Delta R_{ij} > 1.4$ requirement is again used to ensure good separation of the jets. Despite the relatively small integrated luminosity, the measurement is dominated by systematic uncertainties ($< 5\%$) for $p_{T\max} < 250 - 300$ GeV.

This ratio can be interpreted as the conditional probability for an inclusive dijet event at $p_{T\max}$ to contain a third jet. SHERPA predictions using MSTW2008LO (with matrix element matching for up to 4-jet production) are compatible with data within 20%, but PYTHIA comparisons (which rely on the parton shower for more than two jet emissions) are generally unable to describe the data. Tune BW has a reasonable description, but not as good as that of SHERPA, and is incompatible with DØ measurement of dijet azimuthal decorrelations.

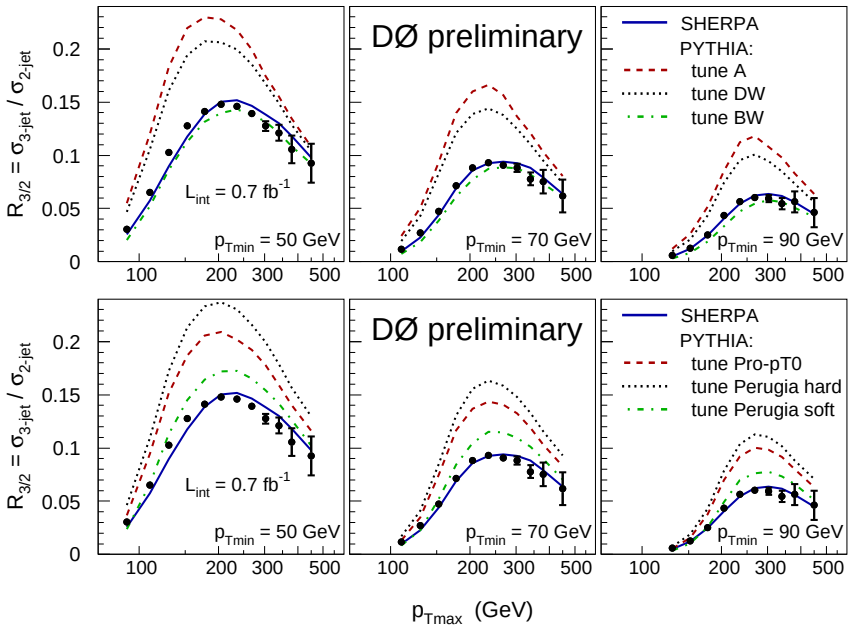

Figure 4: Ratio of trijet to dijet cross-section with hardest jet p_T in bins of $p_{T\min}$ of the other jets and predictions of SHERPA and of PYTHIA for three tunes with virtuality-ordered showers *(top)* and p_T-ordered showers *(bottom)*.

References

1. A. Bhatti *et al.*, Nucl. Inst. Meth. Phys. Res. Sect. A **566** (2006) 375.
2. T. Aaltonen *et al.* [CDF Collaboration], Phys. Rev. D **78** (2008) 052006 [Erratum-ibid. D **79** (2009) 119902] [arXiv:0807.2204 [hep-ex]];
3. G. C. Blazey *et al.*, "Run II jet physics," arXiv:hep-ex/0005012.
4. T. Kluge, K. Rabbertz and M. Wobisch, arXiv:hep-ph/0609285.
5. Z. Nagy, Phys. Rev. D **68** (2003) 094002 [arXiv:hep-ph/0307268].
6. D. Stump *et al.*, J. High Energy Phys. 10 (2003) 046.
7. A. Abulencia *et al.* [CDF Collaboration], Phys. Rev. D **75** (2007) 092006;
8. S. Catani, Y. L. Dokshitzer, M. H. Seymour and B. R. Webber, Nucl. Phys. B **406** (1993) 187; S. D. Ellis and D. E. Soper, Phys. Rev. D **48** (1993) 3160 [arXiv:hep-ph/9305266].
9. V. M. Abazov *et al.* [D0 Collaboration], Phys. Rev. Lett. **101** (2008) 062001.
10. A. D. Martin, W. J. Stirling, R. S. Thorne and G. Watt, Eur. Phys. J. C **63** (2009) 189.
11. T. Aaltonen *et al.* [CDF Collaboration], Phys. Rev. D **79** (2009) 112002 [arXiv:0812.4036].
12. V. M. Abazov *et al.* [D0 Collaboration], Submitted to Phys. Lett. B, arXiv:1002.4594.
13. D. E. Acosta *et al.* [CDF Collaboration], Phys. Rev. D **71** (2005) 032002.
14. T. Gleisberg, S. Hoche, F. Krauss, M. Schonherr, S. Schumann, F. Siegert and J. Winter, JHEP **0902** (2009) 007 [arXiv:0811.4622 [hep-ph]].

Higher-twist contributions to large $p_\perp$ hadron production in hadronic collisions

François Arleo
LAPTH[a], BP 110, 74941 Annecy-le-Vieux cedex, France

Stanley J. Brodsky
SLAC National Accelerator Laboratory, Stanford University, Stanford, California 94309, USA
& CP3-Origins, University of Southern Denmark, Odense 5230 M, Denmark

Dae Sung Hwang
Department of Physics, Sejong University, Seoul 143–747, Korea

Anne M. Sickles
Brookhaven National Laboratory, Upton, New York 11973, USA

The scaling behavior of large-$p_\perp$ hadron production in hadronic collisions is investigated. A significant deviation from the NLO QCD predictions is reported, especially at high values of $x_\perp = 2p_\perp/\sqrt{s}$. In contrast, the prompt photon and jet production data prove in agreement with leading-twist expectations. These results are interpreted as coming from a non-negligible contribution of higher-twist processes, where the hadron is produced directly in the hard subprocess. Predictions for scaling exponents at RHIC are successfully compared to PHENIX preliminary measurements. We suggest to trigger on *isolated* large-$p_\perp$ hadron production to enhance higher-twist processes, and point that the use of isolated hadrons as a signal for new physics at colliders can be affected by the presence of direct hadron production processes.

1 Introduction

The most important discriminant of the twist of a perturbative QCD subprocess in a hard hadronic collision is the scaling of the inclusive invariant cross section [?],

$$\sigma^{\rm inv} \equiv E\,\frac{{\rm d}\sigma}{{\rm d}^3p}(A\;B\;\to C\;{\rm X}) = \frac{F(x_\perp,\vartheta)}{p_\perp^n}, \tag{1}$$

at fixed $x_\perp = 2p_\perp/\sqrt{s}$ and center-of-mass (CM) angle ϑ. In the original parton model the power fall-off is simply $n = 4$ since the underlying $2 \to 2$ subprocess amplitude for point-like partons is scale invariant, and there is no dimensionful parameter as in a conformal theory. However, in general additional higher-twist (HT) contributions involving a larger number of elementary fields contributing to the hard subprocess, $n_{\rm active} > 4$, are also expected. For example, the detected hadron C can be produced directly in the hard subprocess as in an exclusive reaction. Unlike quark or gluon fragmentation, the direct processes do not waste same-side energy, thus involving minimal values of the momentum fractions x_1 and x_2 where parton distributions are maximal. Neglecting scaling violations in QCD, the scaling exponent n is given by $n = 2n_{\rm active} - 4$.

[a] Laboratoire d'Annecy-le-Vieux de Physique Théorique, UMR5108, Université de Savoie, CNRS

The idea of direct hadron production was considered in the 1970's to explain the large fixed $x_{\perp}$ scaling exponents reported at ISR and fixed target FNAL energies [?]. However, there has been no comprehensive and quantitative analysis of the data up to now which could bring compelling evidence for such higher-twist effects. In these proceedings, we summarize the novel aspects discussed in our recent analysis [?], namely:

(i) a dedicated analysis of the most recent FNAL, RHIC and Tevatron data on large-$p_{\perp}$ hadrons, prompt photons and jets;

(ii) the systematic comparison of the experimental scaling exponents with NLO QCD expectations;

(iii) predictions for the top RHIC energy and at the LHC.

2 Analysis

The exponent $n^{\rm NLO}$ of mid-rapidity particle production has been computed in QCD at next-to-leading order (NLO) accuracy from Ref. [?]. The $x_{\perp}$-dependence of $n^{\rm NLO}$ at fixed $p_{\perp}$ has been determined for various hadron species (π, K, $p/\bar{p}$). At $p_{\perp} = 10$ GeV the exponents increase slowly from $n^{\rm NLO} \simeq 5$ at small values of $x_{\perp}$ ($x_{\perp} = 10^{-2}$) up to $n^{\rm NLO} \simeq 6$ at $x_{\perp} = 0.5$ with almost no dependence on the specific hadron species. Remarkably, the exponent extracted in the prompt photon channel is below those of hadrons, by roughly one unit, close to the conformal limit, $n = 4$, at the smallest values of $x_{\perp}$. This observation is understood from the (relative) absence of fragmentation processes and one less power in α_s, leading to less scaling violation in this channel.

On the experimental side, the exponent $n^{\rm exp}$ has been systematically extracted from measurements in hadronic collisions, from fixed-target to collider experiments. It is deduced from the comparison of $x_{\perp}$-spectra at different CM energies,

$$n^{\rm exp}(x_{\perp}) \equiv -\frac{\ln\left(\sigma^{\rm inv}(x_{\perp},\sqrt{s_1})/\sigma^{\rm inv}(x_{\perp},\sqrt{s_2})\right)}{\ln\left(\sqrt{s_1}/\sqrt{s_2}\right)} \qquad (2)$$

which is equivalent to (**??**) at fixed $x_{\perp}$. The data sets include π^0 measurements by the E706 at FNAL [?] and by the PHENIX collaboration at RHIC [?]. At higher energies, the measurements of charged hadrons (or charged tracks) in p–$\bar{p}$ collisions at $\sqrt{s} = 630,\ 1800$ GeV by CDF [?] and $\sqrt{s} = 500,\ 900$ GeV by UA1 [?] are included in the analysis. Also considered are prompt photon [?] and jet [?] data obtained by CDF and D0 at $\sqrt{s} = 546,\ 630,\ 1800$ GeV.

3 Results

The hadron exponents plotted in Fig. **??** (left) exhibit a clear trend, with a significant rise of $n^{\rm exp}$ as a function of $x_{\perp}$. Typical values of $n^{\rm exp}$ are $n^{\rm exp} \simeq$ 5–6 at small $x_{\perp} \simeq 10^{-2}$ while PHENIX data point to a mean value $n^{\rm exp} \simeq 6.7$ at an intermediate $x_{\perp} \simeq 10^{-1}$. At higher values of $x_{\perp}$, the measurements by PHENIX and E706 reveal an exponent even larger, $n^{\rm exp} \simeq 8$, confirming the results reported long ago at the ISR. The exponents obtained in the photon and jet channels are strikingly different, showing almost no dependence on $x_{\perp}$. Importantly enough, the values obtained lie only slightly above the conformal limit, $n_{\gamma}^{\rm exp} \simeq 4.6$ and $n_{\rm jets}^{\rm exp} \simeq 4.4$, i.e. several units smaller than the exponents observed for hadrons.

In order to compare properly data and theory, the *difference* between experimental and theoretical exponents, $\Delta(x_{\perp}) \equiv n^{\rm exp} - n^{\rm NLO}$, is plotted in the right panel of Fig. **??** for hadrons and photons/jets. Note that the error bars include both experimental *as well as* theoretical

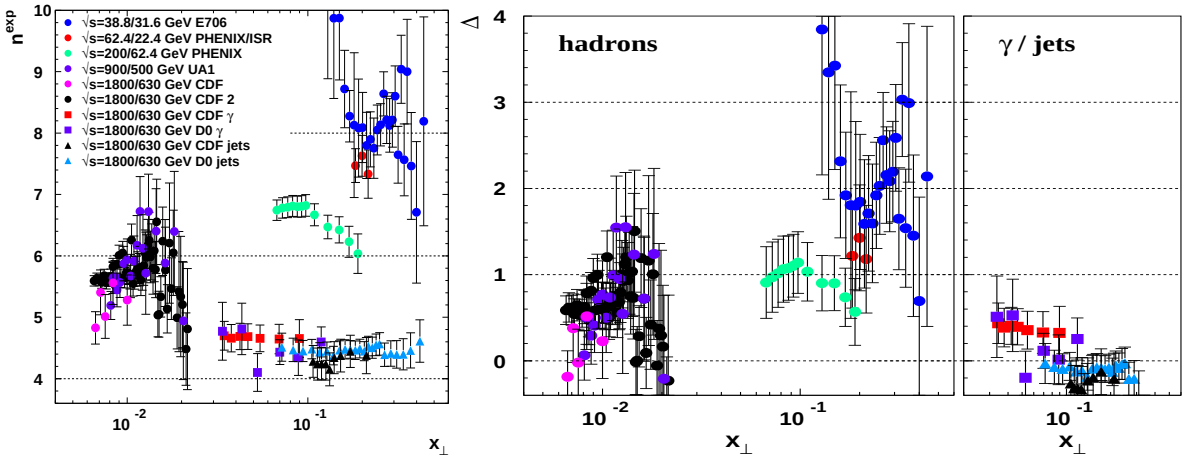

Figure 1: *Left:* Values of $n^{\rm exp}$ as a function of $x_\perp$ for $h^\pm/\pi^0$ (circles), γ (squares) and jets (triangles). *Right:* $\Delta \equiv n^{\rm exp} - n^{\rm NLO}$ vs. $x_\perp$, error bars include the experimental and the theoretical uncertainties added in quadrature.

errors, added in quadrature. The theoretical uncertainty is estimated from the variation of renormalization/factorization scales from $p_\perp/2$ to $2p_\perp$. Fig. **??** (right) indicates that the hadronic exponents extracted experimentally prove significantly above the leading-twist (LT) predictions. The discrepancy is moderate at small $x_\perp \sim 10^{-2}$, $\Delta \simeq 0.5$, but becomes increasingly larger at higher values of $x_\perp$: $\Delta \simeq 1$ at $x_\perp = 10^{-1}$ and up to $\Delta \simeq 2$ in the largest $x_\perp$ region. In contrast, the scaling behavior observed for photons and jets are in very good agreement with the NLO predictions ($\Delta \simeq 0$).

4 Discussion

Part of the discrepancy reported in hadron production data at large $x_\perp \sim 1$ could occur because of the appearance of large threshold logarithms, $\ln(1 - x_\perp)$, which should be resummed to all orders in perturbation theory [?]. It would therefore be most interesting to investigate whether or not threshold resummation might bring data and theory in agreement. Note however that the discrepancy is also observed at small values of $x_\perp \sim 10^{-2}$, where such effects are usually expected to be small.

A natural explanation for the large exponents observed in the hadron channel is the presence of important HT contributions from processes in which the detected hadron is produced directly in the hard subprocess, because of the dimension of the hadron distribution amplitude. In contrast, particles having no hadronic structure like isolated photons and jets are much less sensitive to such HT contributions and should behave closer to LT expectations, as observed. Another piece of evidence for HT effects is the larger exponents for protons than for pions observed at the ISR. As discussed in [?], the difference between the *direct* proton and pion scaling exponent is $n_p - n_\pi = 2$ ($n_p = 8$, $n_\pi = 6$) instead of $n_p - n_\pi \simeq 0$ at LT. The experimental value obtained from the ISR, $n_p - n_\pi \simeq 1$, thus reflects the mixture of LT and HT contributions to the total cross section. It has also been noted [?] that the presence of color-transparent HT subprocesses can account for anomalous features of proton production in heavy ion collisions [?].

Finally, we discuss the phenomenological consequences of possible HT contributions to hadron production in p–p collisions at RHIC and LHC. In order to obtain qualitative predictions, the difference Δ between the experimental and the NLO exponent has been fitted to the hadron data currently analyzed. The typical values of $\Delta^{\rm fit}$ expected at RHIC (taking $\sqrt{s} = 200, 500$ GeV) and at LHC ($\sqrt{s} = 7$ TeV, compared to $\sqrt{s} = 1.8$ TeV at Tevatron) are

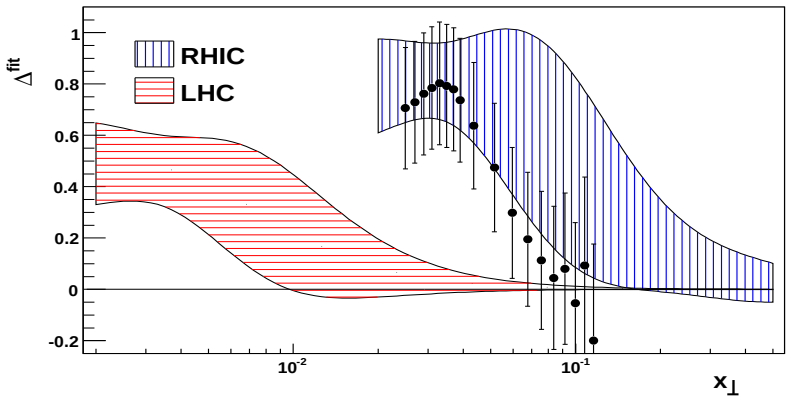

Figure 2: Predicted difference between the experimental and NLO scaling exponent at RHIC ($\sqrt{s} = 200, 500$ GeV) and the LHC ($\sqrt{s} = 7$ TeV as compared to $\sqrt{s} = 1.8$ TeV), compared to PHENIX preliminary measurements.

plotted as a function of $x_\perp$ in Fig. **??**. At RHIC, $\Delta^{\rm fit}$ is slightly below 1 at small $x_\perp \lesssim 5.10^{-2}$ but decreases towards zero at larger $x_\perp$. The predictions turn out to be in very good agremment, both in shape and magnitude, with the PHENIX preliminary measurements[?] performed at $\sqrt{s} = 500$ GeV. At LHC, smaller deviations with NLO expectations are expected because of the large values of $\langle p_\perp \rangle$ probed at high energy: $\Delta^{\rm fit} \simeq 0.5$ below $x_\perp = 5 \times 10^{-3}$ and smaller above. In order to enhance the HT contribution to hadron production, we suggest to trigger on *isolated* hadrons, i.e. with small hadronic activity in their vicinity. We also point that the use of isolation cuts, usually applied for prompt photons, will strongly suppress LT processes. Consequently, the scaling exponents of isolated hadrons are expected to be somewhat larger than those in the inclusive channel. The use of isolated hadrons as a signal for Higgs production or new physics scenarios[?] might be confused by the presence of direct hadron production processes.

We thank A. Bazilevsky for providing us with Fig. **??**. FA thanks CERN-TH for hospitality. SJB was supported by the Department of Energy under contract DE-AC02-76SF00515. DSH was supported by the International Cooperation Program of the KICOS and the Korea Research Foundation Grant (KRF-2008-313-C00166). AMS was supported by the Department of Energy under contract DE-AC02-98CH10886.

1. See e.g. S. J. Brodsky, G. R. Farrar, Phys. Rev. Lett. **31** (1973) 1153
2. F. Arleo, S. J. Brodsky, D.S. Hwang, A. M. Sickles, arXiv:0911.4604, to appear in PRL
3. P. Aurenche *et al.*, Eur. Phys. J. C **9** (1999) 107; *ibid.*, Eur. Phys. J. C **13** (2000) 347; Z. Kunszt and D. E. Soper, Phys. Rev. D **46** (1992) 192
4. L. Apanasevich *et al.*, Phys. Rev. D **68** (2003) 052001
5. A. Adare *et al.*, Phys. Rev. D **76** (2007) 051106; *ibid.*, **79** (2009) 012003
6. F. Abe *et al.*, Phys. Rev. Lett. **61** (1988) 1819; D. E. Acosta *et al.*, Phys. Rev. D **65** (2002) 072005
7. C. Albajar *et al.*, Nucl. Phys. **B335** (1990) 261
8. D. E. Acosta *et al.*, Phys. Rev. D **65** (2002) 112003; B. Abbott *et al.*, Phys. Rev. Lett. **84** (2000) 2786; V. M. Abazov *et al.*, Phys. Rev. Lett. **87** (2001) 251805
9. F. Abe *et al.*, Phys. Rev. Lett. **70** (1993) 1376; B. Abbott *et al.*, Phys. Rev. D **64** (2001) 032003
10. See e.g. D. de Florian and W. Vogelsang, Phys. Rev. D **71** (2005) 114004.
11. S. J. Brodsky, A. Sickles, Phys. Lett. B **668** (2008) 111
12. S. S. Adler *et al.*, Phys. Rev. Lett. **91** (2003) 172301
13. A. Bazilevsky, talk at APS Meeting 2010, `http://meetings.aps.org/Meeting/APR10`
14. A. Nisati (ATLAS), and Y. Sirois (CMS), private communication.

PRODUCING HARD PROCESSES REGARDING THE COMPLETE EVENT: THE EPOS EVENT GENERATOR

S.Porteboeuf *, T.Pierog †, K.Werner
SUBATECH, University of Nantes - IN2P3/CNRS - EMN, Nantes, France

Jet cross sections can be in principle compared to simple pQCD calculations, based on the hypothesis of factorization. But often it is useful or even necessary to not only compute the production rate of the very high pt jets, but in addition the "rest of the event". The proposed talk is based on recent work, where we try to construct an event generator – fully compatible with pQCD – which allows to compute complete events, consisting of high pt jets plus all the other low pt particles produced at the same time. Whereas in "generators of inclusive spectra" like Pythia one may easily trigger on high pt phenomena, this is not so obvious for "generators of physical events", where in principle one has to generate a very large number of events in order to finally obtain rare events (like those with a very high pt jet). We recently developped an independnat block method which allow us ta have a direct access to dedicated variables [1]. We will present latest results concerning this approach.

1 Motivation : Jet production

High-p_T Jets are rare processes which provide useful informations on the medium via jet-quenching [2]. Usually, when one wants to compute jets (hard processes), one uses the parton model, assuming factorization. But, one has to keep in mind here one only computes inclusive cross sections: P+P $\rightarrow$ Jet +X, with no possibility to investigate the "X-part". One cannot obtain partial cross sections, neither exclusive ones. In addition, the jet production is uncoupled from the rest of the event (soft production). As a consequence, event generators based on this approach could not compute complete event, they only compute jets, which may be supplemented by soft events from a different source.

The parton model hides multiples scatterings, which occur even in pp collisions. The importance of multiple scatterings was shown by [3], where the authors plotted the total cross section and the jet cross section as a function of the collision energy. For higher energies $\sigma_{jet} > \sigma_{Total}$. It means that there is more than one jet produced in a pp collisions, and therefore there is more than one interaction. As a consequence, if one wants to reproduce a complete event, an event that match the best what occurs in reality, one needs to consider multiples scattering.

In [4], the authors studied $p\bar{p}$ collisions at Tevatron energies, and they plotted the average p_T as a function of the charged multiplicity. When the charged multiplicity increase, on get an events with increasing multiple interaction. What they observed is that the usual event generators where not able to reproduce the data. There is a real need of an event generator with a careful treatment of multiple scatterings. EPOS is actually such an generator of complete

*now at LLR, École polytechnique, Palaiseau, France
†Forschungszentrum Karlsruhe, Institut fuer Kernphysik, Karlsruhe, Germany

events, which generates hard scatterings in the context of multiple scattering. As a test, our approach must follow pQCD calculations for inclusive spectra at SPS and Tevatron energies. Some LHC prediction on our preliminary work can be found in [5].

By computing jets in a complete event, we will have a real event generator. We want to do a correspondence :

$$1 \text{ experimental event } = 1 \text{ generator event} \tag{1}$$

As a consequence, we will have a control over the underlying event. In other events generators, jets and soft part are computed in different manner : there is no connection between the two. Our approach gives us a better understanding of the event : jet regarding to the corresponding underlying event. Finally, a parallel work is done to implement an event generator with hydrodynamics [6]. For the future, on can expect an event generator with jet quenching, event by event.

2 Event generator : EPOS

EPOS stands for **E**nergy conserving quantum mechanical approach, based on **P**artons, parton ladders, strings, **O**ff-shell remnants, and **S**plitting of parton ladders). A compact description can be found in [7], many technical details about the physical basis of EPOS are described in [8], where we also discuss in detail the parameters of the model and how they are fixed. Concerning the basic features of this approach: EPOS is a consistent quantum mechanical multiple scattering approach based on partons and strings, where cross sections and the particle production are calculated consistently, taking into account energy conservation in both cases (unlike other models where energy conservation is not considered for cross section calculations). Motivated by the very nice data obtained by the RHIC experiments, nuclear effects related to Cronin transverse momentum broadening, parton saturation, and screening have been introduced into EPOS. Furthermore, high density effects leading to collective behavior in heavy ion collisions are also taken into account. It appears that EPOS does very well compared to RHIC data [9,10], and also all other available data from high energy particle physic experiments (ISR,CDF and especially SPS experiments at CERN). As a result, EPOS is the only model used both for Extensive Air Shower simulations and accelerator physic which is able to reproduce consistently almost all data from 100 GeV lab to 1.8 TeV center of mass energy, including anti-baryons, multi-strange particles, ratios and pt distributions.

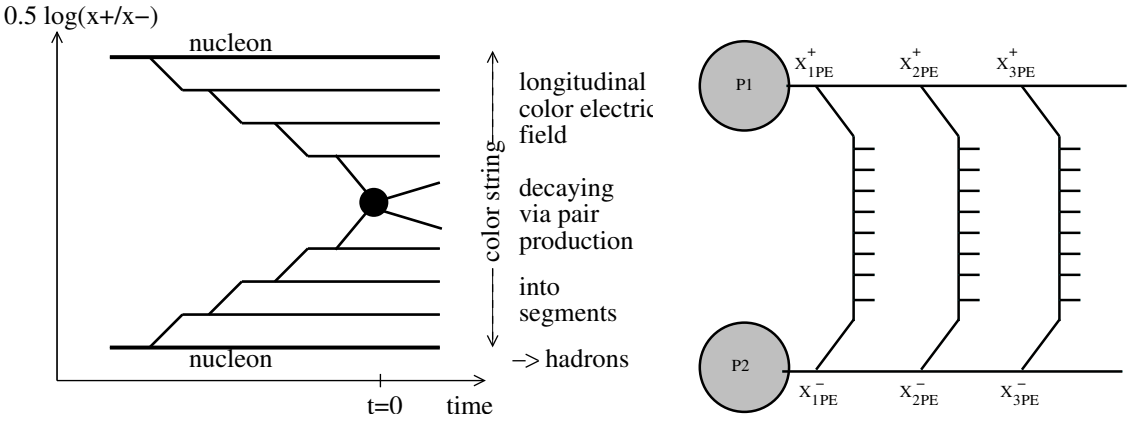

Figure 1: (left) Elementary Interaction. (right) Multiple Interaction : exchange of ladders in parallel, energy is shared between ladders.

The elementary interaction in EPOS is a parton ladder, see Fig.2 (left). The whole ladder could be seen as a longitudinal color electric field that decays via pair productions into seg-

ments. Those segments are then identified as hadrons. Particle production follows the Lund String Model. In the initial stage of proton-proton collisions or heavy ion collisions, multiples interactions occur in parallel. This phenomenon represents in EPOS an exchange of parton ladder in parallel, see Fig.2 (right). In the two limits, a parton ladder could either be soft or hard. This representation allows us to consider semi-hard cases. What is important to remark is that both, hard and semi-hard interactions are computed in the same formalism. Finally, this picture produces hard scattering regarding the complete event.

One can see on Fig.2 (right) a scheme of an event with multiple interaction. Several ladders are exchanged in parallel. All ladders exist at the same time. The total energy is shared between ladders. This means that it's impossible to have an infinite number of ladder. The total energy is conserved. x_{PE} refers to the fraction of light cone momentum of the parton which enter the ladder.

3 Hard process in a complete event

We now zoom on one ladder. This ladder can be soft – with a parametrization in regge fashion – or it can be be semi-hard, as shown in Fig.2. In the semi-hard case, there is a soft pre-evolution, followed by a DGLAP evolution. In Fig.2, the two evolutions are contained in the central blob. Finally, in the center of the ladder, there is a hard process $2 \to 2$ (green part of Fig. 2).

Once the Monte Carlo procedure has determined how many ladders there are, and the x_{PE} values at the ladder ends, we employ an iterative procedure to compute emission up to the hard scattering $2 \to 2$. We define x_{IB} as the light cone momentum entering the hard process, while x_{PE} refers to the light cone momentum entering the ladder. For complete definition of variables, sea section **??**. One first generates all resolvable partons emitted at one side of the ladder before the hardest process. At each step one decides whether there is any resolvable emission at the forward end of the ladder before the hardest process. In case of no forward emission, the generation of all resolvable parton emissions at the forward side of the ladder has been completed. One then proceeds to generate all resolvable parton emissions for the backward side of the ladder by using a corresponding recursive algorithm. For more details about probability of forward and backward emission and the probability distribution of the light cone momentum and momentum transfer squared for the current parton branching, see [8].

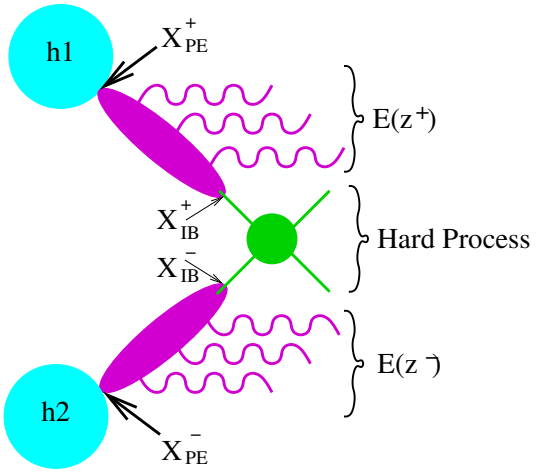

Figure 2: A semi-hard ladder

In the usual event generators based on parton model are generators of inclusive spectra, as discussed earlier. In such generators, one can easly work with cuts, in order to look at rare

event such as very high p_T jets. In our case of a generator of "complete events" this is more complicated. An inconvenience is that, like in experiments, if one wants rare event, one needs a a large number of simulations. The question is now : How to compute hard partons, in a generator with multiple scattering, with cuts (to look at rare events)?

In[1], we presented the selection cut method based on a two-step procedure, where the internal part of the ladder is rewritten with independant block. A detailed description of the independant block method can be found in[11]. We will now present the latest results concerning this approach.

4 Computation of hard parton cross section

In this section, we will describe observables from the EPOS framework that can be compared to measurment, the inclusive jet cross section. To do so, we need to express the internal quantity $n_{\rm semi}$, which represents the number of semi-hard ladder (ladders describe by Fig. 2), as a function of p_T. This expression is expressed here in for the case of factorisation, which araise naturally in the EPOS framework[8]. This limit describe inclusive spectrum such as the inclusive jet cross section. This observable is a good first test for the independant block method in the limit of factorisation. The independnat block method can then be used to construct a new Monte Carlo with the implementation of cuts.

$$\frac{dn_{\rm semi}}{dtdu} = \int dx^+_{\rm IB} dx^-_{\rm IB} \sum_{ij} f^{M,i}_+(x^+_{\rm IB}) f^{M,j}_-(x^-_{\rm IB}) K_{ij}(x^+_{\rm IB} x^-_{\rm IB} s,t,u) \tag{2}$$

In eq.2, $n_{\rm semi}$ is expressed as a function of the internal variables of the ladder, described in Fig. 2. K represents the internal block of the $2 \to 2$ process and f the evolution of the parton from the proton to $2 \to 2$ process. A more complete description can be found in [1,11].

With:

$$dtdu = |\frac{\partial(t,u)}{\partial(y,p_\perp)}| dydp_\perp = \frac{2tu}{p_\perp} dydp_\perp = sdydp^2_\perp \tag{3}$$

we obtain:

$$\begin{aligned}
\frac{dn_{\rm semi}}{dydp^2_\perp} &= \int dx^+_{\rm IB} dx^-_{\rm IB} \sum_{ij} f^{M,i}_+(x^+_{\rm IB}) f^{M,j}_-(x^-_{\rm IB}) \\
&\quad \times s K_{ij}(x^+_{\rm IB} x^-_{\rm IB} s,t) \delta(x^+_{\rm IB} x^-_{\rm IB} s - x^+_{\rm IB} p_\perp \sqrt{s} e^{-y} - x^-_{\rm IB} p_\perp \sqrt{s} e^{y}) \\
\frac{dn_{\rm semi}}{dydp^2_\perp} &= \frac{1}{\sigma_{\rm inel}} \int dx^+_{\rm IB} \sum_{ij} f^{M,i}_+(x^+_{\rm IB}) f^{M,j}_-(\tilde{x}^-_{\rm IB}) s \frac{d\sigma_{ij}}{dt}(s,t) \frac{s^{-1}_{hh}}{x^+_{\rm IB} - x_\perp e^y/2}
\end{aligned} \tag{4}$$

with:

$$s = x^+_{\rm IB} x^-_{\rm IB} s_{hh},\ \tilde{x}^-_{\rm IB} = \frac{x^+_{\rm IB} x_\perp e^{-y}/2}{x^+_{\rm IB} - x_\perp e^y/2},\ x_\perp = \frac{2p_\perp}{\sqrt{s_{hh}}}$$

Finally, if one wants to compute the number of outborn partons (partons from the $2 \to 2$ process that initiate jets), one need to multiply by two the formula, each ladder gives two hard partons: $n_{\rm ptn} = 2n_{\rm semi}$.

5 Results

The test of the approach is presented in Fig.5, where we compare EPOS analytic (facorization case) results from section 4 to experimental data for the inclusive jet spectrum in proton-proton

collision at $\sqrt{s} = 200$ GeV. On the left hand-side the spectrum is presented and compare with results from cross-section compiled with PDF (GRV and CTEQ6) and an NLO computation with variable cone radius of the jet. Data are exctracted from [12]. There is two data sets, each one being a combination of 2003 and 2004 runs. Empty square refers to a minimum bias selection and full point refers to a high tower trigger selection: event where there is an energetic jet with an energetic leading particle. Jet are identified with a cone jet-finder algorithm with a cone radius of $R = 0.4$, chosen in regards of the acceptance of the detector, according to the author, 95% of the total energy of the jet is expected to be in a cone of a radius of 0.4.

We can see that EPOS is close to STAR data with less than a factor two over nine orders of magnitude. This is also shown an the right hand-side of Fig. 5, upper plot, where ratio of STAR over EPOS computation is plotted.At high p_T EPOS is in between the two PDF sets. Data are also compared with NLO QCD computation from [13]. This specific contribution is able ta take into account the variation of the cone radius of the jet. Here we want to point out the fact that in this EPOS compuation, we compute the production of a hard parton, which is, in practise, not exaclty the same observable as a reconstructed jet. To go furter into details, one should compare event produced inside the event generator with this independant block method. This work is in progress. Finaly this NLO QCD computation should be in better agreement with the data than the 3 other computation, the ratio of STAR/NLO is shown on the right-hand side, middle plot. The lower plot shows ratio of EPOS over NLO, which is, at first order, in good agreement. Finally, it appears that the comparison to data is a first good test fo the independant block method.

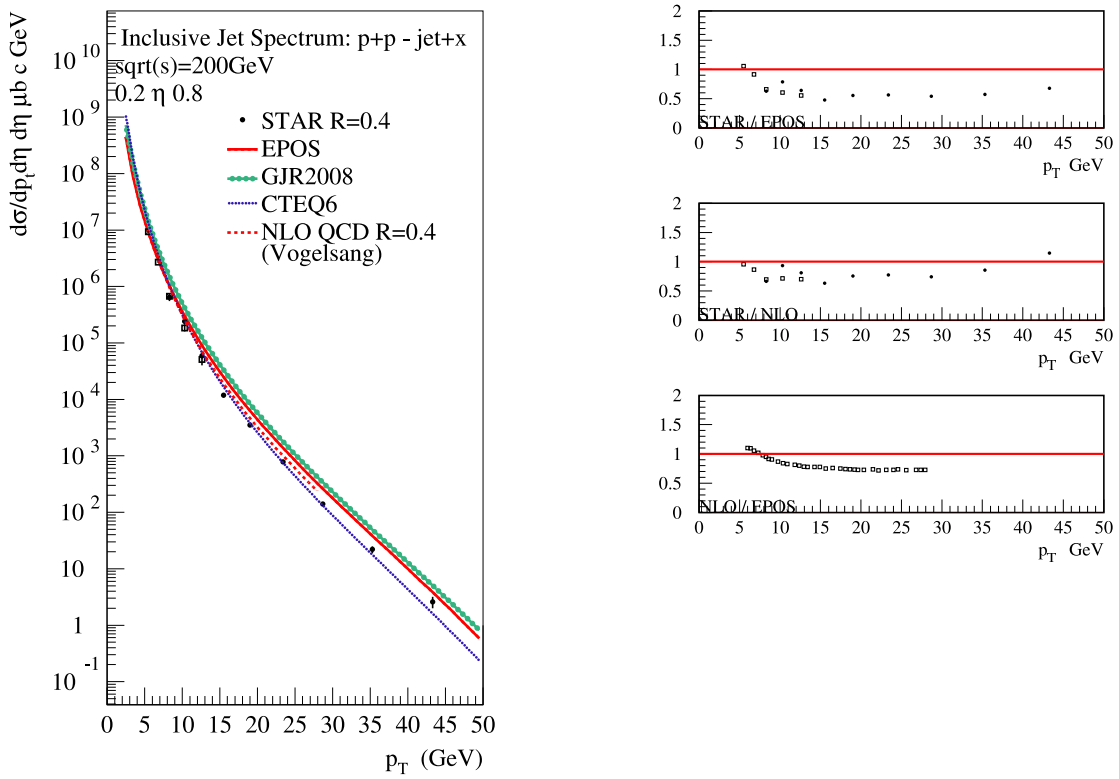

Figure 3: Inclusive jet cross section for pp → Jet+X for $\sqrt{s} = 200$GeV. (left) Spectrum for Star data, EPOS, computation cross section with PDF set, GJR2008 and CTEQ6 and NLO QCD from. (right) ratios : upper plot STAR/EPOS, middle plot: STAR/NLO, lower plot: NLO/EPOS.

6 Conclusion

EPOS has been constructed as an event generator of complete events, very close to an experimental event, with soft and hard parts in the same formalism. To produce complete event, we consider multiple scattering with energy conservation, and we compute hard partons in this context. We are able to produce a jet connected to its event. One benefit is to control the underlying event and to connect an underlying event to the production of a jet. The price to pay is that – as in experiments – high p_T jets are rare and one needs many simulations to observe one. Therfore we present a procedure to produce hard partons by making use of cuts, to reasonable statistics in a reasonable time. The method as describe earlier is to change the procedure for computing the internal part of the ladder. A validation of the method is shown by the comparison of EPOS computation with STAR data for the inclusive jet spectrum for proton-proton scatering at $\sqrt{s} = 200$ GeV. This comparison validate the independant block method, and encourage the developement of the new approach into the compete event procedure. This work is in progress.

References

1. S. Porteboeuf and K. Werner. Generation of complete events containing very high-p(T) jets. *Eur. Phys. J.*, C62:145–150, 2009.
2. (ed.) Alessandro, B. et al. ALICE: Physics performance report, volume II. *J. Phys.*, G32:1295–2040, 2006.
3. Xin-Nian Wang and Miklos Gyulassy. A Systematic study of particle production in p + p (anti- p) collisions via the HIJING model. *Phys. Rev.*, D45:844–856, 1992.
4. Darin E. Acosta et al. Soft and hard interactions in $p\bar{p}$ collisions at $\sqrt{s} = 1800$-GeV and 630-GeV. *Phys. Rev.*, D65:072005, 2002.
5. (ed.) Armesto, N. et al. Heavy Ion Collisions at the LHC - Last Call for Predictions. *J. Phys.*, G35:054001, 2008.
6. Klaus Werner. Core-Corona Separation in Ultra-Relativistic Heavy Ion Collisions. *Phys. Rev. Lett.*, 98:152301, 2007.
7. Klaus Werner, Fu-Ming Liu, and Tanguy Pierog. Parton ladder splitting and the rapidity dependence of transverse momentum spectra in deuteron gold collisions at RHIC. *Phys. Rev.*, C74:044902, 2006.
8. S.Ostapchenko T.Pierog K.Werner H.J.Drescher, M.Haldik. Parton-based gribov-regge theory. *Phys. Rep*, 350, 2001.
9. R.Bellwied. Strange particle production mechanisms in proton-proton collisions at rhic. *Acta Phys. Hung*, A27:201–204, 2006.
10. B. I. Abelev et al. Rapidity and species dependence of particle production at large transverse momentum for d + Au collisions at s(NN)**(1/2) = 200-GeV. *Phys. Rev.*, C76:054903, 2007.
11. Porteboeuf Sarah. *Étude des processus durs dnas les collisions proton-prton et ions lourds aux énergies LHC.* PhD thesis, Université de Nantes, 2009.
12. B. I. Abelev et al. Longitudinal double-spin asymmetry and cross section for inclusive jet production in polarized proton collisions at s**(1/2) = 200-GeV. *Phys. Rev. Lett.*, 97:252001, 2006.
13. B. Jager, M. Stratmann, and W. Vogelsang. Single inclusive jet production in polarized pp collisions at $O(alpha_s^3)$. *Phys. Rev.*, D70:034010, 2004.

Collective flow in (anti)proton-proton collision at Tevatron and LHC

Tanguy Pierog[(1)], S. Porteboeuf[(2)], Iu. Karpenko[(3,4)], K. Werner[(4)]
[(1)] *Karlsruhe Institut of Technology, Institut für Kernphysik, Postfach 3640, 76021 Karlsruhe Germany*
[(2)] *LLR, Ecole Polytechnique, Palaiseau, France*
[(3)] *Bogolyubov Institute for Theoretical Physics, Kiev 143, 03680, Ukraine*
[(4)] *SUBATECH, University of Nantes – IN2P3/CNRS– EMN, Nantes, France*

Collective flow as a consequence of hydrodynamical evolution in heavy ion collisions is intensively studied by theorists and experimentalists to understand the behavior of hot quark matter. Due to their large mass, heavy ions suffer collective effects even at low (SPS) or intermediate energies (RHIC). In case of light systems such as (anti)proton-proton interactions, collective effects was not expected. Within a global model such as EPOS, where light and heavy systems are treated using the same physics, it appears that Tevatron data are better described if a flow is introduced. Then the extrapolation to LHC can easily be done and we can compare to first data from ATLAS experiment.

1 Introduction

There seems to be little doubt that heavy ion collisions at RHIC energies produce matter which expands as an almost ideal fluid [1,2]. This observation is mainly based on the studies of azimuthal anisotropies, which can be explained on the basis of ideal hydrodynamics [3]. A big success of this approach was the correct description of the so-called mass splitting, which refers to quite different transverse momentum dependencies of the asymmetries for the different hadrons, depending on their masses.

As it was pointing out already in 2007 in [4], a model which describe properly these effects for heavy ion interactions will predict the same mechanism already for (anti)proton-proton interactions when the "centrality" is large enough (high multiplicity in the central region). And it can be compared to Tevatron data [5] where such effects are clearly visible in the dependence of the average transverse momentum with central multiplicity (including mass splitting) as shown fig. 1.

After a short introduction on the EPOS model section 2, we will compare its results to the latest ATLAS data at 900 GeV and show section 3 that the same effect is already visible event at this relatively "low" energy. In the section 4, we will present how a correct calculation of collective effects can be done in the framework of the EPOS model.

2 EPOS Model

One may consider the simple parton model to be the basis of high energy hadron-hadron interaction models, which can be seen as an exchange of a "parton ladder" between the two hadrons.

In additions to the parton ladder, hadronized using strings (flux-tube), there is another source of particle production: the two off-shell remnants.

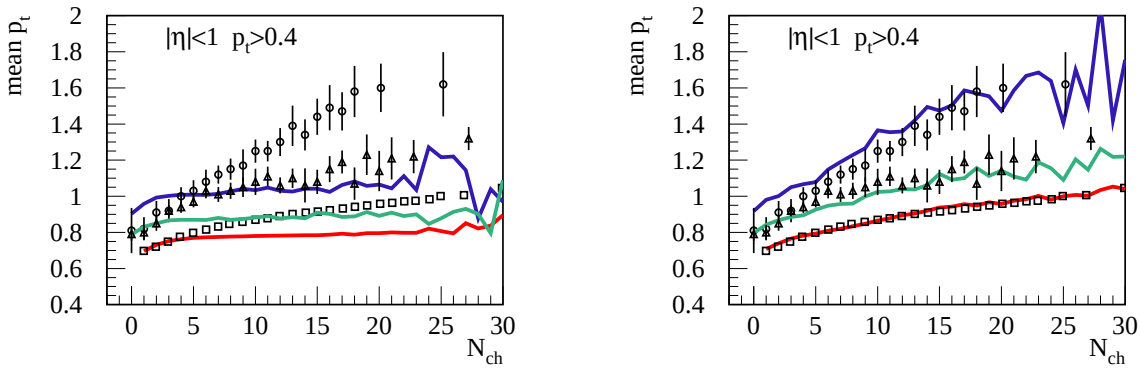

Figure 1: Average transverse momentum $\langle p_t \rangle$ as a function of central multiplicity of charged particles for different particle types (from top to bottom : lambdas, kaons short and charged particles). Points are data from CDF experiment [5]. Line are simulations with EPOS without hydro (left hand-side) and with hydro (right hand-side).

EPOS [6] is a consistent quantum mechanical multiple scattering approach based on partons and strings, where cross sections and the particle production are calculated consistently, taking into account energy conservation in both cases. Nuclear effects related to Cronin transverse momentum broadening, parton saturation, and screening have been introduced into EPOS. Furthermore, high density effects leading to collective behavior in heavy ion collisions are also taken into account. In next section preliminary results are shown using an effective treatment using a parameterized flow (not using LHC data). The full hydrodynamic treatment described in section 4 applied to (anti)proton-proton will be shown in a paper in preparation.

3 Comparison to LHC data

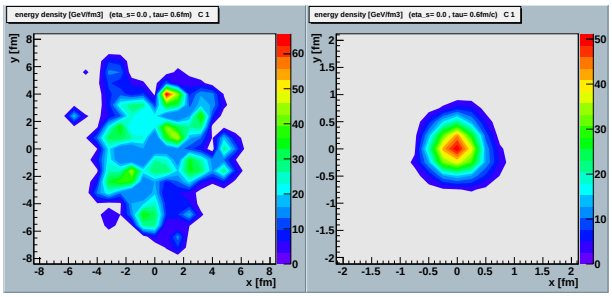

Figure 2: Energy density in central Au-Au (L) and pp (R) scattering at 200 GeV resp. 7ŤeV.

Let us consider the energy density at an early time in a Au-Au scattering at RHIC, as obtained from an EPOS simulation [6]. In the left hand-side of fig. 2, we plot the energy density at the space-time rapidity $\eta_s = 0$, as a function of the transverse coordinates x and y . We observe a very bumpy structure concerning the $x-y-$dependence. There are in particular peaks in the $x-y-$plane which are sub-flux-tubes which exhibit a long range structure in the longitudinal variable η_s.

In fig. 2 , we clearly identify several sub-flux-tubes, with a typical width of the order of a fermi. This is exactly the width we obtain if we compute the initial energy density in proton scattering at the LHC (fig. 2 right hand-side). This means, if a hydrodynamic treatment is justified for Au-Au collisions at RHIC, it is equally justified for pp scattering at the LHC, provided the energy densities are high enough. This latter condition can easily be satisfied,

since in proton-proton scattering on has the possibility to trigger on high multiplicity events, with ten or twenty times the multiplicity compared to an average event.

If collective effects are possible in light system, how can it be observed ? Besides correlations between particles, one of the striking consequence of a collective hadronization is the creation of a radial velocity. In case of heavy ion collisions, the asymmetry created by the impact parameter allows the measurement of the v_2 parameter of the flow to quantify this effect. In case of anti(proton)-proton scattering, it is experimentally difficult to define a "collision plane" and actually it was never done or even foreseen to measure v_2 in that case. But the radial flow increase the transverse momentum of the particles, so that this effect should change the mean transverse momentum $\langle p_t \rangle$. A measure of the energy density is given by the multiplicity of charged particles N_{ch} event-by-event. As a consequence the variation of the $\langle p_t \rangle$ as a function of N_{ch} has to be sensitive to the collective effects in a very light system.

The effect shown in fig. 1 for Tevatron at 1.8 TeV is actually confirmed at 900 GeV by the ATLAS experiment [8]. In fig. 3 we can see the difference between simulation with (full line) or without (dashed line) hydrodynamic evolution of the high density region. This effect has only little influence on the total multiplicity has shown in fig. 4.

4 Hydrodynamics in EPOS

In future version of EPOS, we are going to employ a new tool for treating the hydrodynamic evolution, based on the following features (see [7] for details and tests with AuAu data):

- initial conditions obtained from a flux tube approach (EPOS), compatible with the string model used since many years for elementary collisions (electron-positron, proton proton), and the color glass condensate picture;
- consideration of the possibility to have a (moderate) initial collective transverse flow;
- event-by-event procedure, taking into the account the highly irregular space structure of single events, being experimentally visible via so-called ridge structures in two-particle correlations;
- core-corona separation, considering the fact that only a part of the matter thermalizes;
- use of an efficient code for solving the hydrodynamic equations in 3+1 dimensions, including the conservation of baryon number, strangeness, and electric charge;
- employment of a realistic equation-of-state, compatible with lattice gauge results – with a cross-over transition from the hadronic to the plasma phase;
- use of a complete hadron resonance table, making our calculations compatible with the results from statistical models;
- hadronic cascade procedure after hadronization from the thermal system at an early stage.

5 Summary

EPOS is an interaction model constructed on a solid theoretical basis. It has been tested very carefully against all existing hadronic data. Designed to be compared to heavy ion collisions, the collective effects are being implemented in a very sophisticated way. Based on a realistic event-by-event energy density with large fluctuations, a 3D hydrodynamical calculation is performed until chemical freeze-out followed by a hadron cascade until thermal freeze-out. Applying the

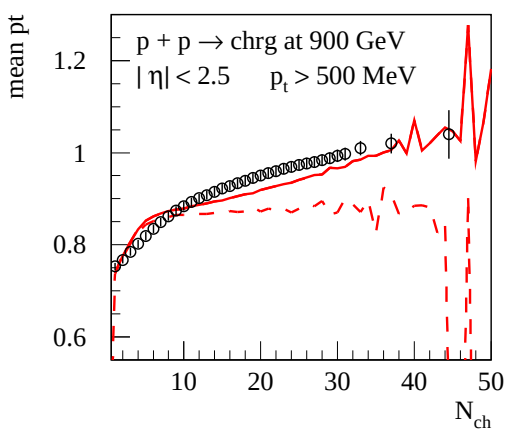

Figure 3: $\langle p_t \rangle$ as a function of multiplicity of charged particles for proton-proton collisions at 900 GeV. ATLAS data points [8] are compared to EPOS simulations with (full line) or without (dashed line) hydro evolution.

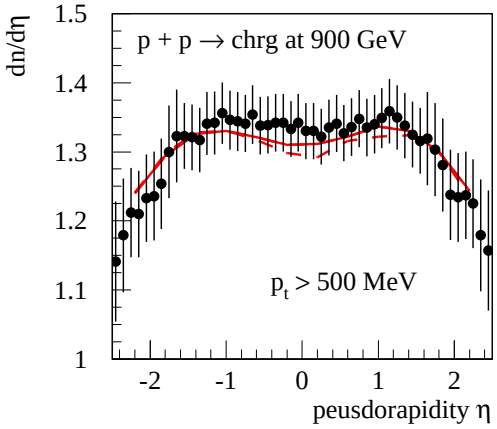

Figure 4: Pseudorapidity distribution of charged particles with $p_t > 500$ MeV for proton-proton collisions at 900 GeV. ATLAS data points [8] are compared to EPOS simulations with (full line) or without (dashed line) hydro evolution.

same scheme for (anti)proton-proton scattering at high energy, the most inelastic collisions will actually satisfy the conditions to create a small thermalized system which will hadronized statistically and with a non-negligible radial velocity. We showed that this effect is visible in the dependence of the $\langle p_t \rangle$ with the particle multiplicity of each event at Tevatron or LHC energies, especially if we look at the dependence with the mass of the particles. Further detailed measurements at LHC (correlations) will allow us to actually test the space-time evolution of the energy density of hadronic interactions.

Acknowledgments

This research has been carried out within the scope of the ERG (GDRE) "Heavy ions at ultra-relativistic energies", a European Research Group comprising IN2P3/CNRS, Ecole des Mines de Nantes, Université de Nantes, Warsaw University of Technology, JINR Dubna, ITEP Moscow, and Bogolyubov Institute for Theoretical Physics NAS of Ukraine. Iu. K. acknowledges partial support by the MESU of Ukraine, and Fundamental Research State Fund of Ukraine, agreement No F33/461-2009. Iu.K. and K.W. acknowledge partial support by the Ukrainian-French grant "DNIPRO", an agreement with MESU of Ukraine No M/4-2009. T.P. and K.W. acknowledge partial support by a PICS (CNRS) with KIT (Karlsruhe).

References

1. STAR Collaboration, J. Adams, *et al*, *Nucl. Phys.* A **757**, 102 (2005)
2. PHOBOS Collaboration, B.B. Back *et al.*, *Nucl. Phys.* A **757**, 28-101 (2005)
3. Quark-Gluon Plasma 3, eds. R. C. Hwa and X. N. Wang (World Scientific, Singapore, 2004)
4. N. Armesto *et al.*, *J. Phys.* G **35**, 054001 (2008).
5. CDF Collaboration, D. E. Acosta *et al.*, *Phys. Rev.* D **72**, 052001 (2005).
6. K. Werner *et al.*, *Phys. Rev.* C **74**, 044902 (2006).
7. K. Werner *et al.*,arXiv:1004.0805, submitted to *Phys. Rev.* **C**.
8. ATLAS Collaboration, G. Aad *et al.*, *Phys. Lett.* B **688**, 21 (2010).

JET RECONSTRUCTION AT RHIC

Sevil Salur for the STAR Collaboration
Department of Physics, University of California, One Shields Avenue, Davis, CA 95616 USA

Full jet reconstruction in heavy-ion collisions is expected to provide more sensitive measurements of jet quenching in hot QCD matter at RHIC. In this paper we review recent studies of jets utilizing modern jet reconstruction algorithms and their corresponding background subtraction techniques.

1 Introduction

Jets can be used to probe the properties of the high energy density matter created in the collisions at the Relativistic Heavy Ion Collider (RHIC). Strong suppression of inclusive hadron distributions and di-hadron correlations at high p_T have provided evidence for partonic energy loss in an indirect way [1,2]. These measurements however suffer from well-known geometric biases due to the competition of fragmentation and energy loss. It is possible to avoid the geometric biases if the jets are reconstructed independent of their fragmentation details whether they are quenched or unquenched. In this paper, we discuss the current status of the jet reconstruction in heavy ion collisions and the implication of the results.

2 Jet Reconstruction Techniques

During the last several decades, many algorithms were developed to combine measured particles into jets in leptonic and hadronic colliders. For a detailed overview of jet algorithms in high energy collisions, see [3,4,5,6,7,8] and references therein. Measuring jets above the complex heavy ion background however is a challenging task. For a long time, it has thought to be not possible due to the large underlying high multiplicity heavy ion event background. The expected increase in Large Hadron Collider (LHC) luminosities (20 to 200 collisions in a detector) leading to p+p pile up events requires that the traditional jet algorithms are to be improved with underlying event subtraction techniques. These improved techniques can be also used to reconstruct and separate jets from the underlying heavy ion background [9].

The minimum requirement for an unbiased jet reconstruction in heavy ion collisions is that the signal and the background must be separable. With the assumption that it can be, the background correction can be estimated by following three steps. The first step is measuring the jet area for the infrared safe algorithms. An active area of each jet is estimated by filling an event with many very soft particles and then counting how many are clustered into a given jet. The second step is measuring the diffuse noise (mean p_T per unit area in the remainder of the event) and noise fluctuations. These fluctuations in the background can distort the jet spectrum towards larger p_T which can be corrected through an unfolding procedure (i.e., deconvolution).

So the final step is the deconvolution of signal from the background using parameters that are extracted from measurable quantities.

3 Results

The transverse momentum dependence of the inclusive differential cross sections for $p + p \rightarrow jet + X$ at $\sqrt{s}$ =200 GeV are shown in Figure 1. The sequential recombination algorithm jets shown as circles using FastJet suite of algorithms are compared to jets reconstructed with a cone algorithm as shown as blue stars [10,11,12]. Both resolution parameters for k_T and anti-k_T algorithms and the cone radius are selected to be 0.4. These jet cross-sections agree well with each other within their statistical and systematic uncertainties. The comparison of cone jets to NLO pQCD cross-section using the CTEQ6M parton distributions is presented in the inset of Figure 1 [10,13]. A satisfactory agreement for cross-sections over 7 orders of magnitude shows that jets in p+p collisions at RHIC energies are also theoretically well understood like the jets that are produced at the Tevatron energies [14].

The nuclear modification factor (R_{AA}) for the reconstructed jet spectra with a resolution parameter of 0.4 from k_T and anti-k_T can be calculated after jets are reconstructed and corrected in Au+Au collisions. The preliminary version of the jet spectra in Au+Au collisions can be found in other publications [11,15]. Figure 2 shows the R_{AA} of jets in Au+Au collisions. The envelopes represent the one sigma uncertainty of the deconvolution of the heavy ion background. The total systematic uncertainty due the jet energy scale is around 50%, shown as the gray bar. The jet R_{AA} is compared to the one from the charged $\pi^{\pm}$ mesons [16].

In the case of full jet reconstruction, N_{Binary} scaling as calculated by a Glauber model [17] ($R_{AA} = 1$) is expected if the reconstruction is unbiased, i.e. if the jet energy is recovered fully independent of the fragmentation details, even in the presence of strong jet quenching. This scaling is analogous to the cross section scaling of high p_T direct photon production in heavy ion collisions observed by the PHENIX experiment [18]. While the experimental uncertainties are large, a trend towards a much less suppression than that of single particle suppression is observed with the implication that a large fraction of jets are reconstructed. However a hint of a suppression of jet R_{AA} above 30 GeV can be observed.

The ratio of jet spectra reconstructed with R=0.2 and 0.4 for p+p and Au+Au systems for k_T and anti-k_T is presented in Figure 3. A suppression in the Au+Au ratio with respect to p+p is observed. For a smaller resolution parameter due to possible additional jet broadening effects in Au+Au collisions, a larger fraction of the jet energy is not recovered unlike the jets reconstructed in p+p events. The jet broadening effects can be investigated by selecting a biased sample of recoil jets in di-jet coincidence measurements. The ratio of the spectra from the recoil jets in 0-20% central Au+Au to p+p collisions [19] is presented in Figure 4. The recoil jets are selected when the triggered jets have p_T greater than 10 GeV. Before taking the ratio, the recoil jet spectra in p+p and Au+Au collisions are normalized to the number of triggered jets. When a population of recoil jets biased towards the ones that are interacting with the medium are selected, the effects of jet broadening can be observed to be much more comparable to the measurement of π meson R_{AA}. This is in contrast to the inclusive jet measurements yielding a much smaller nuclear modification suppression as seen in Figure 2.

4 Conclusions

It is possible to reconstruct jets up to a large transverse momentum in heavy ion collisions. A large fraction of the jet energy can be measured as seen by the closeness of nuclear modification factors to 1. However new physics effects such as momentum dependence of relative quark and gluon sub-processes to inclusive jet production in the presence of quark and gluon plasma and

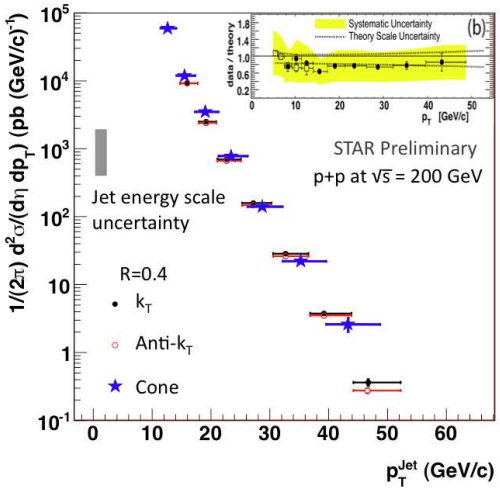

Figure 1: Inclusive jet cross-section vs transverse jet energy for the p+p collisions obtained by the sequential recombination (k_T and anti-k_T) algorithm (shown as circles) and the previously published cone jets (shown as stars). Gray band is the jet energy scale uncertainty. Inset shows the comparison of the STAR cone jets with the NLO pQCD cross-section calculations.

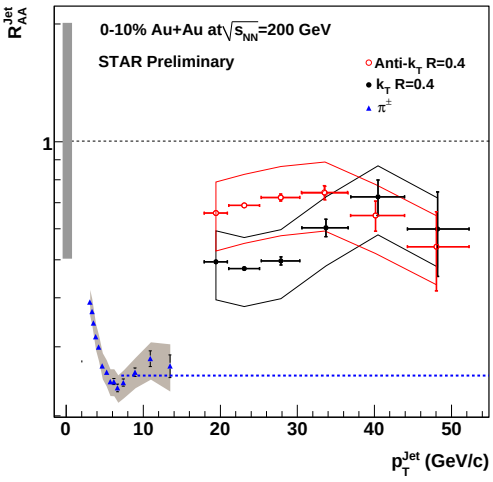

Figure 2: Momentum dependence of the nuclear modification factors of jet spectra reconstructed with k_T and anti-k_T algorithms with R=0.4 (0-10% most central Au+Au divided by N_{Binary} scaled p+p collisions) compared to $\pi^{\pm}$ R_{AA}. The systematic uncertainty of the π measurement is shown as the gray band and the gray bar centered at 1 is the jet energy scale uncertainty. The dashed lines are to guide the eye for $R_{AA} = 1$ and single particle R_{AA}.

the initial state effects should be considered when interpreting and comparing these results with model calculations[20]. Some other contributions like the EMC effect might be playing a major role in the relative suppression or enhancement of nuclear modification factors at large momentum[21]. Implication of jet broadening is observed when comparing different jet definitions with various resolution parameters and recoil jets of the di-jet coincidence measurements in p+p and Au+Au systems. In order to study the effects of jet quenching quantitatively, model calculations are required. Monte-Carlo based simulations of partonic level jet quenching in medium such as Jewel [22], Q-Pythia [23] and YaJEM [24] and complementary analytic calculations [25,26] recently became available. New robust QCD jet observables that are unaffected by the treatment of hadronization resulting into additional uncertainities need to be explored experimentally to confront these calculations.

References

1. J. Adams et. al. *Phys. Rev. Lett.* 91 072304 (2003).
2. S. S. Adler et. al. *Phys. Rev. Lett.* 96 202301 (2006).
3. S.D Drell, D. J. Levy and T.M. Yan, *Phys. Rev.* 187, 2159 (1969); N. Cabibbo, G. Parisi and M. Testa, Lett. Nuovo Cimento 4,35 (1970); J.D. Bjorken and S.D. Brodsky, *Phys. Rev.* D 1, 1416 (1970); G. Sterman and S. Weinberg, *Phys. Rev. Lett.* 39, 1436 (1977) .
4. M. H. Seymour, CERN-TH/95-176, hep-ph/9506421 (1995).
5. B. Flaugher and K. Meier. FERMILAB-CONF-90-248-E, Dec (1990).
6. G. C. Blazey et al. FERMILAB-CONF-00-092-E, hep-ex/0005012 (2000).
7. N. Brown, W. J. Stirling *Z.Phys.* C 53:629-636 (1992).
8. S. Catani, Y. L. Dokshitzer, M. Olsson, G. Turnock and B. R. Webber, *Phys. Lett.* B 269, 432 (1991); S. Catani, Y. L. Dokshitzer, M. H. Seymour and B. R. Webber, *Nucl. Phys.* B 406, 187 (1993); S. D. Ellis and D. E. Soper, *Phys. Rev.* D 48, 3160 (1993).
9. M. Cacciari, G. P. Salam, G. Soyez, *JHEP* 0804:005 (2008), arXiv:0802.1188; and references

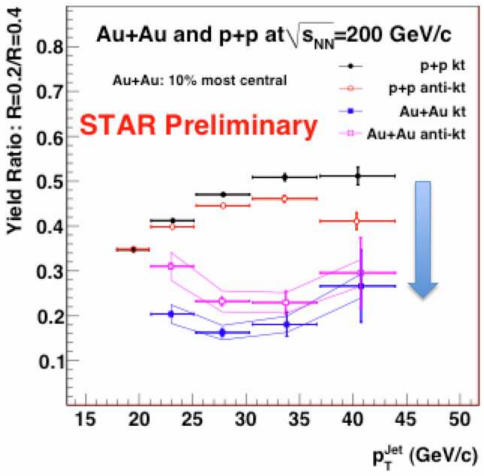

Figure 3: Momentum dependence of the ratio of inclusive jet cross-sections (R(0.2)/R(0.4)) reconstructed by k_T and anti-k_T recombination algorithms for p+p and Au+Au collisions.

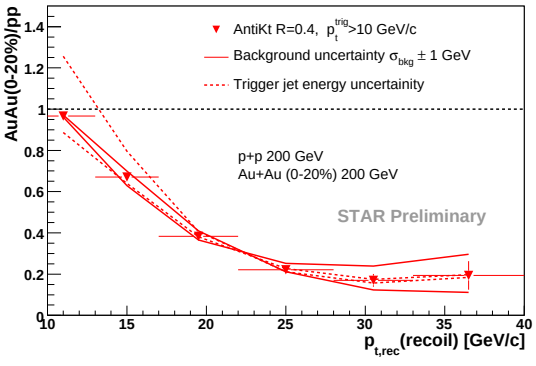

Figure 4: Momentum dependence of the ratio of the spectra of the recoil jets in 0-20% central Au+Au to p+p collisions utillizing the HT trigger events. The systematic uncertainties in the estimation of the background fluctuations and the triggered jet energy are shown as the solid and the dashed lines.

therein.

10. B. I. Abelev, et. al. STAR Collaboration *Phys. Rev. Lett.* 97 252001 (2006).
11. M. Ploskon for the STAR Collaboration, *Nucl. Phys.* A830:255C-258C (2009), arXiv:0908.1799.
12. M. Cacciari, G. P. Salam, G. Soyez, http://www.lpthe.jussieu.fr/~salam/fastjet.
13. B. Jäger et. al., *Phys. Rev. D* 70, 034010 (2004).
14. A. Abulencia et al. CDF Collaboration Phys.Rev.D75:092006 (2007), hep-ex/0701051; Erratum-ibid.D75:119901 (2007).
15. S. Salur for the STAR Collaboration, Eur. Phys. J. C61:761-767 (2009), arXiv:0809.1609.
16. Y. Xu for the STAR Collaboration, Nucl.Phys.A830:701C-704C (2009), arXiv:0907.4644.
17. R. J. Glauber, *Phys. Rev.* 100,242 (1955).
18. PHENIX Collaboration, S. S Adler et al. *Phys. Rev. Lett* 96 202301 (2006), nucl-ex/0601037.
19. E. Bruna for the STAR Collaboration, *Nucl. Phys.* A830:267C-270C (2009), arXiv:0907.4788.
20. S. Salur, *Nucl. Phys.* A830:139C-146C (2009), arXiv:0907.4536.
21. J. Gomez et al., SLACPUB5813 June 7, (2001); D.F. Geesaman et al., Ann. Rev. Nucl. Part. Sci. 45, 337 (1995);
22. K. Zapp, G. Ingelman, J. Rathsman, J. Stachel, U. A. Wiedemann arXiv:0805.4759 (2008); K. Zapp, G. Ingelman, J. Rathsman, J. Stachel, U. A. Wiedmann, Eur. Phys. J. C60:617-632 (2009), arXiv:0804.3568.
23. N. Armesto, L. Cunqueiro and C. A. Salgado Eur. Phys. J. C 61:775-778 (2009), arXiv:0809.4433; N. Armesto, L. Cunqueiro, C.A. Salgado, arXiv:0907.1014 (2009).
24. T. Renk, *Phys. Rev.* C80:044904 (2009), arXiv:0906.3397; T. Renk, arXiv:0808.1803 (2008).
25. I. Vitev, B. W. Zhang, *Phys. Rev. Lett.* 104:132001 (2010), arXiv:0910.1090.
26. N. Borghini *Phys. Lett.* B 678:82-85, (2009), arXiv:0902.2951.

Jet Energy Loss at RHIC

N. Grau
Columbia University, Nevis Laboratories,
PO Box 137, Irvington, NY 10533

One of the most well-known results from BNL-RHIC heavy ion collisions is the experimental confirmation of the energy loss of partons traversing a colored medium, *i.e.* jet energy loss. This has resulted from much study both experimentally and theoretically over the last decade during heavy ion collisions at RHIC. In this talk, the brief history of attempts to understand energy loss is given with an eye towards future experiments at both RHIC and the LHC.

One of the interests in studying jets in nuclear collisions is to answer a fundamental, non-trivial problem in QCD. The problem: how does a parton lose energy via interactions with an extended colored medium. This is analogous to the problem in QED of a charged particle losing energy in (charged) matter. This was studied extensively by Bethe.[1] He showed that the energy lost by the charged particle per unit path length, dE/dx depends on the density of scattering centers in the medium and the energy of the charged particle. Important for the discussion that follows is that the rate of energy lost is independent of length that particle has traveled in the medium. The problem has been analyzed in QCD. Because of the Albelian nature of QCD, not only are there diagrams where the parton directly interacts with the medium and emits a gluon, but the radiated gluon also interacts with the medium. This increases the rate of energy lost by the colored parton in the colored medium. A pQCD analysis, that is, weak coupling between the incoming parton (jet) and the medium, with a particular model of the scattering centers yields an energy loss rate that is proportional to the length the parton traverses in the medium, $dE/dx \sim x$.[2]

To study this experimentally, partons must be moving through an extended colored medium. Performing heavy ion collisions at an appropriate center-of-mass energy would achieve both. At high enough energy density and temperatures, evidence from the lattice indicates, a phase transition occurs in QCD where partons are not bound within color singlet states. This state is known as the quark-gluon plasma. This phase of matter could be created in relativistic heavy ion collisions to produce a colored medium much larger than the size of the proton. [a] Also at collider energies, hard-scattered partons, which will subsequently fragment into jets, are simultaneously produced in these events. Therefore, hard partons are auto-generated and lose energy as they traverse the quark-gluon plasma produced in heavy ion collisions.

Ideally the jets produced from these quenched partons would be measured. But the large detectors at RHIC, PHENIX and STAR, were not initially designed to perform full jet reconstruction measurements. Furthermore, the luminosity in heavy ion collisions is much lower than in e^+e^- annihilation and $p+p$ collisions, so obtaining statistics on jets above about 10 GeV has

[a] Indeed parton energy loss was first discussed by Bjorken in terms of $p+\bar{p}$ collisions at the Tevatron.[3]

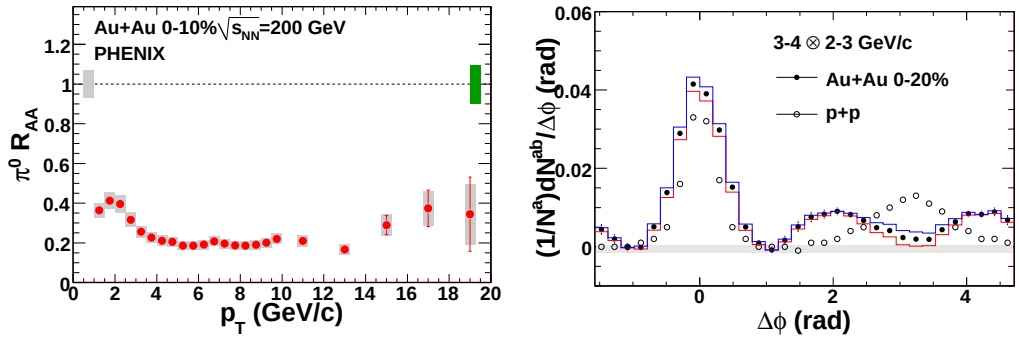

Figure 1: *Left:* Single high-p_T π^0 R_{AA}. *Right:* Relative azimuthal correlations between pairs of hadrons in $p+p$ (open) and $Au+Au$ (closed) collisions.

taken time to amass. As a first measurement, the rate of single, high-p_T particles, those that are the leading jet fragments, have been measured. This rate, for example, of π^0s in A+A collisions is compared to p+p collisions and quantified by R_{AA}, defined as

$$R_{AA} = \frac{1/N_{evt} dN^{AA\to\pi^0 X}/dp_T^{\pi^0}}{\langle N_{bin}\rangle\, 1/N_{evt} dN^{AA\to\pi^0 X}/dp_T^{\pi^0}} \tag{1}$$

Here the $p+p$ rate is scaled by the number of nucleon-nucleon scatterings that occur in the overlap region of the nuclear collision, N_{bin}. So, if nuclear collisions were simply a sum of multiple $p+p$ collisions, $R_{AA}=1$. Deviations from unity would indicate nuclear effects. Figure 1 shows the most recent π^0 R_{AA} from PHENIX [4]. Clearly, a factor of five fewer particles are produced at a given p_T in Au+Au compared to $p+p$ at the same energy. What is implicit are the particle invariant p_T spectra that have been measured over many orders of magnitude. The $p+p$ spectrum compares to NLO calculations down to 2 GeV, lending support to the fact that these are QCD jets that are contributing. R_{AA} <1 indicates that those $p+p$ jets, when created in Au+Au collisions, lose energy and resulting in a softer leading particle.

The next measurements to extract information about jets and their modifications from energy loss was to look at two-particle azimuthal correlations. Here, the event-averaged distribution of the relative azimuthal angle ($\Delta\phi$) between all pairs of particles in particular p_T ranges are constructed. In this way two particles fragmenting from a jet have $\Delta\phi \sim 0$. Particles which fragment from each of a di-jet pair have $\Delta\phi \sim \pi$. The right panel of Figure 1 shows these azimuthal correlations between unidentified charged hadrons with one p_T ranges from 3-4 GeV and 2-3 GeV in both $p+p$ and Au+Au.[5] The distribution in p+p looks as expected, i.e. peaks at 0 and π. But in Au+Au has a qualitatively different shape, especially at these p_T. There is a large yield of particles away from π not observed in p+p. This structure could indicate that energy loss modifies the angular distribution of fragments in a jet. Others have speculated that the supersonic parton would produces a Mach cone. [6] It is possible that this structure could arise from Cerenkov gluons from superluminal partons.[7] This has opened up a rich avenue of study both theoretically and experimentally in studying these aspects of QCD.

There are obvious, measurable effects on high-p_T particle production due to the medium. However, there is little quantitative information at this time due to a number of complications. These issues range from the level of understanding of the medium produced at RHIC to energy-loss biases in the measurements. Energy-loss biases result from the fact that, by requiring a high-p_T particle in the event with bias those particles to have lost little energy either due to fluctuations in the energy loss mechanism or that they have traversed little medium. Currently and in the future both at RHIC and the LHC, a program of quantitative and precision studies of energy loss is being planned and implemented. Some initial results are presented here.

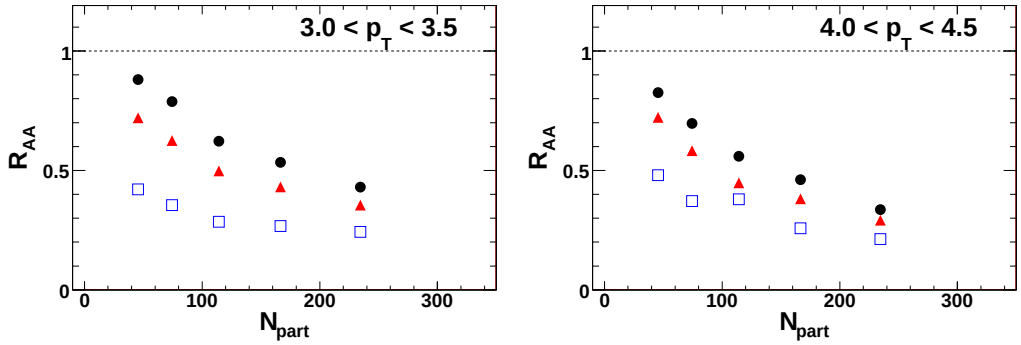

Figure 2: Th R_{AA} as a function of the number of participating nucleons (N_{part}) in the nuclear overlap regions, i.e. the centrality, for 3-3.5 GeV (left) and 4-4.5 GeV (right) π^0s emitted in the reaction plane (0-15 degrees,), out of the reaction plane (75-90 degrees,), and between (30-45 degrees,).

Initially it was presented that the Bjorken-like formula for QCD has a path-length dependence. Ideally, we would like to determine the exponent on $dE/dx \sim x^n$. An experimental observable that is sensitive to the path-length dependent energy loss is by measuring R_{AA} as a function of the particle's angle with respect to the reaction plane. The reaction plane is the plane defined by the impact parameter in the collisions. In moderately large impact parameter collisions, the overlap region is shorter along the reaction plane than perpendicular to it. Consequently, particles emitted in the reaction plane traverse less medium than perpendicular to it. Figure 2 shows the π^0 R_{AA} for two different p_T selections as a function of centrality (impact parameter) for those along the reaction plane (0-15 degrees), out of the reaction plane (75-90 degrees), and in between (30-45 degrees).[8] Qualitatively we see that the R_{AA} decreases from in-plane to out-of-plane, consistent with the path-length dependence of energy loss. However, a single exponent has not been extracted from this data.

One complication from single- and two-particle observables is that, to compare to theory, one must integrate over jet energies. Ideally, the jet energy would be experimentally measured via jet reconstruction. An alternative approach is to use direct photon-charged hadron correlations. Here the direct photon is isolated and the charged hadron fragments from the opposing jet. To leading order the photon measures the jet energy. Figure 3 shows the number of correlated unidentified charged hadron pairs per direct photon as a function of $z_T = \left\langle p_T^h \right\rangle / \langle p_T^\gamma \rangle$, essentially the fragmentation function, in p+p and Au+Au for several different direct photon p_T ranges[9]. One would expect a softening of the fragmentation functions in Au+Au as energy is transported from high-z to low-z fragments. The current statistics are suggestive but insufficient to claim that this is indeed the case.

Recently, the study of fully reconstructed jets at RHIC has been undertaken. In PHENIX, the Gaussian filter algorithm [10], a IR and colinearly safe extension of the cone algorithm, is used. Because of the large underlying event background that has little to no correlation with the jet, additional care must be taken to reconstruct jets. For example, correlated fluctuations in the background can produce a jet signal which are not from an underlying hard scattering process[11]. These must be removed from the sample of total measured jets. However, removing these jets can result in a bias. For example, PHENIX makes a cut on a combination of the p_T and R distribution of the fragments which rejects soft and wide jets from the sample. These jets that are rejected could, however, be those modified jets that are of interest in studying energy loss. The R_{AA} of jets in Cu+Cu after rejection of the fake jets is shown in Figure 3. For the more central collisions, $R_{AA} < 1$. While one might expect the jet R_{AA} ~1 because of energy conservation, loses could be due to radiation that has leaked outside the jet area. Another interpretation, being explicit of the use of the fake jet rejection condition, is that about 50% of

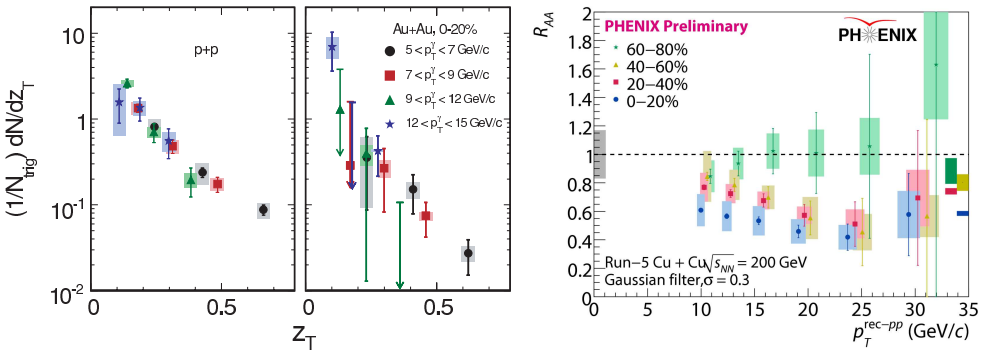

Figure 3: *Left panels:* The rate of correlated unidentified charged hadrons to a direct photon as a function of z_T (see text), which is the effective fragmentation function, measured in $p+p$ and Au+Au for various direct photon p_T ranges. *Right:* The R_{AA} of fully reconstructed jets in Cu+Cu collisions using the Gaussian filter algorithm (see text) and with fake jet rejection.

the jets are $p+p$-like. In the future it will be important to loosen the fake jet cuts to study those jets which are not $p+p$-like in order to reduce the energy-loss bias introduced by this cut.

At the end of the year, another exciting milestone will be reached at the LHC: nuclear collisions. At the LHC jets with energy well above 50 GeV will be reached, which is much higher than the current statistics at RHIC. Furthermore, the experiments, especially ATLAS and CMS are ideally suited to calorimetrically measure jets over a wide pseudo-rapidity range. The large increase in center-of-mass energy may well mean a qualitatively different medium will be produced and produce different effects on the jets at the LHC. Studying jets at both RHIC and the LHC simultaneously will ultimately help us to have a broad understanding of the effects of an interesting problem in QCD, how a parton loses energy in as it traverses an extended colored medium.

References

1. Bethe, H. and J. Ashkin "Experimental Nuclear Physics", ed. E. Segre, J. Wiley, New York, 1953
2. Baier, R. *et al.* Nucl. Phys. B **483**, 291 (1997)
3. Bjorken, J. D. n.d. FERMILAB-PUB-82-059-THY
4. Adare, A. *et al.* (PHENIX collaborator) Phys. Rev. Let. **101**, 232301 (2008)
5. Adare, A. *et al.* (PHENIX collaborator) Phys. Rev. **C78**, 014901 (2008)
6. Stoecker, H. Nucl. Phys. **A750**, 121 (2005)
   Casalderrey-Solana, J., E. V. Shuryak and D. Teaney Nucl. Phys. **A774**, 557 (2006)
7. Koch, V., A. Majumder and X. N. Wang Phys. Rev. Lett. **96**, 172302 (2006)
   Dremin, I. M. Eur. Phys. J. **C56**, 81 (2008)
8. Afanasiev S. *et al.* (PHENIX collaborator) Phys. Rev. **C80**, 054907 (2009)
9. Adare, A. *et al.* (PHENIX collaborator) Phys. Rev. **C80**, 024908 (2009)
10. Lai, Y.-S. and B. A. Cole **arXiv:0806.1499**
11. Grau, N. Eur. Phys. J. **C62**, 191 (2009)

W/Z+JET AND W/Z+HEAVY FLAVOR JET PRODUCTION AT THE TEVATRON

S. GRINSTEIN
ICREA/Institut de Física d'Altes Energies. Barcelona, 01893-E, Spain.

In this contribution recent measurements of the associated production of jets and vector bosons in Run II at the Tevatron are presented. Results which additionally require the presence of heavy-flavor are also discussed. The data cover wide regions of jet transverse momentum and jet rapidity. The measurements are compared to predictions from various theoretical models.

1 Introduction

The associated production of vector bosons and jets (W/Z+jets) presents a valuable analysis sample in hadron colliders. Production cross sections and kinematic distributions measurements of W/Z+jets provide a stringent test of perturbative QCD predictions. Furthermore, W/Z+jets processes constitute a significant source of background in many measurements and searches at the Tevatron and the LHC, like top-quark measurements and Higgs boson and super-symmetric particles searches. Because of the phenomenological importance of W/Z+jets processes, improved theoretical predictions became available in recent years, both in the form of parton-level NLO calculations and particle-level predictions which combine a tree-level matrix element calculation with a parton shower evolution. These predictions have to be validated against experimental measurements. In the last years both CDF and D0 experiments have made numerous W/Z+jets production measurements, the most recent ones are presented below. The inclusive results are discussed first, followed by the measurement which require heavy-flavor jets.

2 Inclusive Z+jets Measurements

The CDF experiment presented measurements of Z+jets production cross sections[1] as a function of $p_T^{\rm jet}$, $|y^{\rm jet}|$, and jet multiplicity, for jets in the region $p_T^{\rm jet} \geq 30$ GeV and $|y^{\rm jet}| < 2.1$, using data corresponding to an integrated luminosity of 2.4 fb^{-1}. Events are required to have two opposite signed muons with a reconstructed invariant mass in the range $66 < M_{\mu\mu} < 116$ GeV around the Z boson mass. Jets are defined using the mid-point algorithm with a cone of radius $R = 0.7$, and their momentum corrected for for instrumental effects and contributions from additional $p\overline{p}$ collisions. The cross sections are corrected for acceptance and smearing effects back to particle level employing an unfolding procedure using PYTHIA event samples. Figure 1 (left) shows the measured inclusive differential cross section in $Z/\gamma^*+ \geq 1$ jet events. The data is compared to NLO pQCD predictions obtained using the MCFM program. The theoretical predictions include parton-to-particle correction factors that account for the non-perturbative underlying event and fragmentation effects, estimated with PYTHIA Monte Carlo simulations. The corrected NLO predictions agree with the data within experimental and systematic uncertainties over the full

$p_T^{\rm jet}$ range. Also shown in Fig. 1 is the measured total cross in $Z/\gamma^* \to \mu^-\mu^+$+jets events as a function of the number of jets ($N_{\rm jet}$) compared to LO and NLO pQCD predictions. The LO predictions underestimate the measured cross section, while a good description is obtain with the NLO calculation for the $N_{\rm jet} \geq 1$ and $N_{\rm jet} \geq 2$. These results complement previous ones [2], based on a data sample corresponding to an integrated luminosity of 2.5 fb^{-1}, in which the boson is selected via its decay into an electron pair.

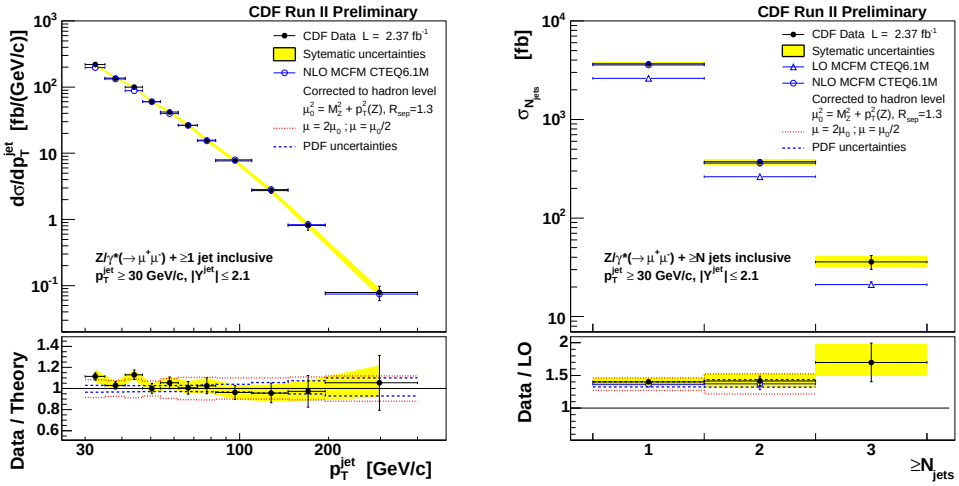

Figure 1: The plot on the left shows the measured inclusive jet differential cross section as a function of $p_T^{\rm jet}$ in $Z/\gamma^*+\geq 1$ jet events compared the NLO pQCD predictions (left). The shaded bands show the total systematic uncertainty, except for the luminosity uncertainty (5.8%). The plot on the right shows the measured total cross in $Z/\gamma^* \to \mu^-\mu^+$+jets events as a function of the number of jets ($N_{\rm jet}$) compared to LO and NLO pQCD predictions.

The D0 experiment presented first measurements of the angular correlations between the Z and leading jet in Z+jet+X production [3], using events in which the Z boson decays into a muon pair and data corresponding to an integrated luminosity of 0.97 fb^{-1}. The event selection is similar to the one implemented in the CDF analysis, though jets are reconstructed with a mid-point algorithm with a cone of radius $R = 0.5$ and a minimum transverse momentum of $p_T > 20$ GeV. The differential cross sections are normalized to the measured inclusive Z cross section, canceling many systematic uncertainties. The angular distributions are sensitive to QCD radiation and do not require more jets to be observed in the event, thus avoiding some systematics associated to jet calibrations. The normalized differential cross section binned in $\Delta\phi(Z,{\rm jet})$ is presented in Fig. 2. The data is compared to NLO pQCD predictions from MCFM, PYTHIA with tunes QW and Perugia*, ALPGEN interfaced to PYTHIA with the same tunes, HERWIG (with JIMMY for multiple interactions) and SHERPA. The ratios in Fig. 2 are shown only with respect to the prediction of SHERPA and the shaded band indicates the corresponding scale uncertainty. The NLO pQCD prediction, in the $\Delta\phi(Z,{\rm jet})$ range where it is available, provides a reasonable description of the data. Of the event generators, SHERPA provides the best description of the shape of the data, but shows a normalization difference. These studies of the kinematics of inclusive Z production at D0 complement previous cross section measurements in which the boson decays into electron and muon pairs [4,5].

3 W/Z+Heavy Flavor Jet Production

The measurement of vector boson production with associated heavy-flavor jets provides an important test of pQCD predictions. Understanding these processes is also critical in many searches for new particles, like low-mass Higgs boson and super-symmetric particles, which

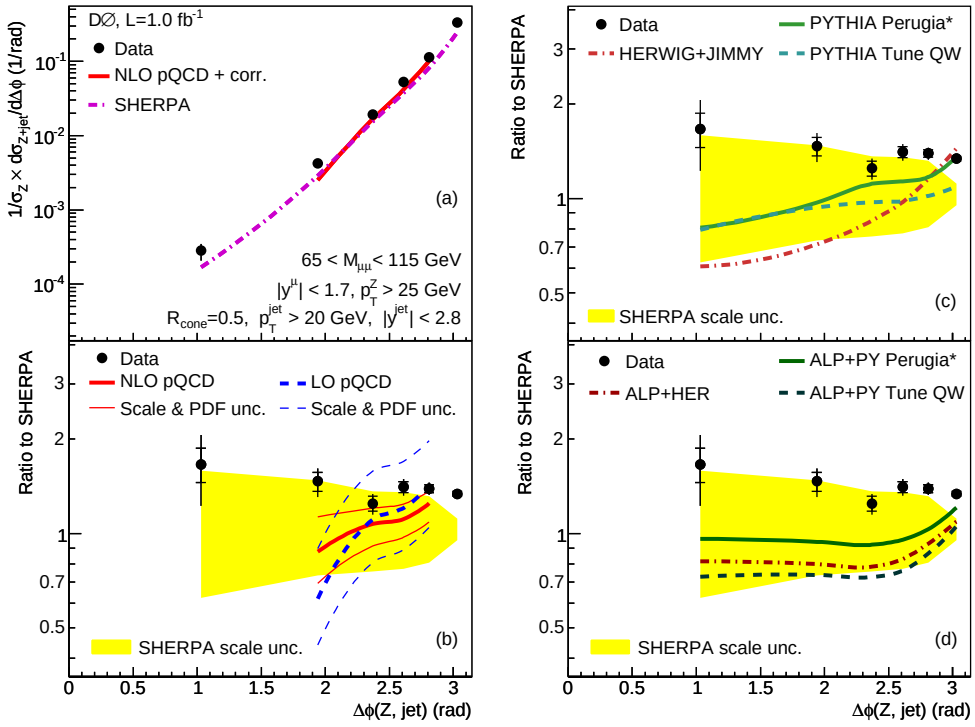

Figure 2: Measured cross section as a function of $\Delta\phi(Z,\text{jet})$ for Z+jet+X events for $p_T^Z > 25$ GeV normalized to the inclusive $Z(\rightarrow \mu^+\mu^-)$ cross section (a). The data is compared to fixed order calculations (b), and parton shower generators (c and d), see text for details.

usually require the presence of heavy-flavor jets (b-tagging) in order to improve the signal purity.

The CDF experiment presented a measurement of the cross section for jets from b-quarks produced with a W boson [6] using data corresponding to an integrated luminosity of 1.9 fb^{-1}. Events that are consistent with the electronic and muonic W boson decay and contain one or two jets ($E_T > 20$ GeV and $|\eta| < 2.0$) are selected. A b-tagging algorithm, based on displaced secondary vertices, is used to enhance the presence of b-jets in the selected sample. The flavor composition of the tagged jets is determined through a maximum likelihood template fit of the distribution of the vertex mass in the data. The simulation model is tested using a high purity ($\approx 99\%$) sample of b-jets from double tagged events in a non-isolated low-E_T lepton filtered di-jet sample. After removing the background contribution to the b-jets sample (mainly from top and single top production) the measured cross section is $\sigma_{b-\text{jets}} \times \text{BR} = 2.74 \pm 0.27(\text{stat.}) \pm 0.42(\text{syst.})$ pb. This result cannot be accommodated by different available theoretical predictions. The PYTHIA prediction is 1.10 pb, while ALPGEN predicts 0.78 pb, a factor 2.5-3.5 lower than the measurement. A recent NLO calculation predicts $1.22 \pm 0.14(\text{syst.})$ pb [7], also significantly lower than the measurement.

The CDF experiment also presented a measurement of the production cross section of a W boson with a single charm quark [8], using data corresponding to an integrated luminosity of 1.8 fb^{-1}. In addition to being an important component of the $W + 1, 2$ jet samples (a dataset used, for example, in Higgs boson searches), Wc production is also sensitive to the s-quark content of the proton at large Q^2. The W boson is selected via a high-p_T lepton (either e or μ), and large missing E_T. Charm jets are identified from their semi-leptonic decay by looking for a muon within the jet (*soft muon tagging*). The measurement exploits the charge correlation between the W boson and the muon from the semi-leptonic decay, extracting the signal from a background-dominated sample using the excess of oppositely charged over same charge events. Figure 3 (left) shows the tagged muon p_T relative to the beam axis. The measurement of

$\sigma_{Wc} \times \mathrm{BR} = 9.8 \pm 3.2$ pb is in agreement with the NLO prediction of $11.0^{+1.4}_{-3.0}$ pb [9]. Following a similar strategy, but for a larger phase space and using soft electron tagging, CDF presented a preliminary measurement of $\sigma_{Wc} \times \mathrm{BR} = 33.7 \pm 11.4(\mathrm{stat.}) \pm 4.7(\mathrm{syst.})$ pb [10]. This result, with large uncertainties, is consistent with the NLO prediction of 17.8 ± 1.7 pb [9].

The D0 experiment presented a measurement of the fraction of inclusive W+jets events produced with a single charm quark [11], using data corresponding to an integrated luminosity of approximately 1 fb^{-1}. The analysis uses soft muons within a jet as described above to measure a cross section ratio of $\sigma(W + c\text{–jet})/\sigma(W + \mathrm{jets}) = 0.074 \pm 0.019(\mathrm{stat.})^{+0.012}_{-0.014}(\mathrm{syst.})$, which is in agreement within uncertainties with the ALPGEN+PYTHIA prediction of 0.044 ± 0.003. Figure 3 shows the differential Wc fraction compared to the ALPGEN+PYTHIA prediction.

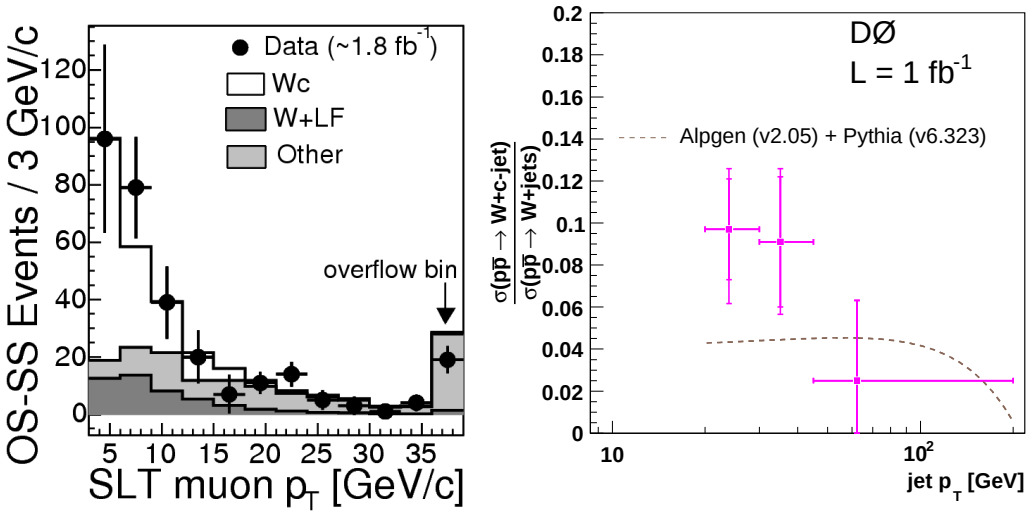

Figure 3: Tagged muon p_T relative to the beam axis, with the Wc contribution normalized to the measurement (left). Measured cross section ratio of $W + c$–jet$/W +$ jets for jet $p_T > 20$ GeV and $|\eta| < 2.5$. The inner error bars around the data points show the statistical only uncertainties and the full bars include the systematic uncertainties.

Acknowledgments

I would like to thank the organizers and my colleagues of the CDF and D0 experiments.

References

1. The CDF Collaboration, CDF Conference Note 10113 (2010).
2. The CDF Collaboration, T. Aaltonen *et al.*, Phys. Rev. Lett. **100**, 102001 (2008).
3. The D0 Collaboration, V. M. Abazov *et al.*, Phys. Lett. B **682**, 370 (2010).
4. The D0 Collaboration, V. M. Abazov *et al.*, Phys. Lett. B **678**, 45 (2009).
5. The D0 Collaboration, V. M. Abazov *et al.*, Phys. Lett. B **669**, 278 (2008).
6. The CDF Collaboration, T. Aaltonen *et al.*, Phys. Rev. Lett. **104**, 131801 (2010).
7. J. Campbell, F. Febres Cordero, L. Reina, private communication (2009).
8. The CDF Collaboration, T. Aaltonen *et al.*, Phys. Rev. Lett. **100**, 091803 (2008).
9. J. Campbell, R. K. Ellis and R. Mahbubani, private communication.
10. The CDF Collaboration, CDF Public Note 10089 (2010).
11. The D0 Collaboration, V. M. Abazov *et al.*, Phys. Lett. B **666**, 23 (2008).

W Boson Production in Polarized p+p Collisions at RHIC

J.R. Stevens for the STAR Collaboration
Department of Physics and CEEM, Indiana University, Bloomington, IN 47408 USA

The production of $W^{\pm}$ bosons in longitudinally polarized $\vec{p}+\vec{p}$ collisions at RHIC provides a new means of studying the spin-flavor asymmetries of the proton sea quark distributions. Details of the $W^{\pm}$ event selection in the $e^{\pm}$ decay channel at mid-rapidity are presented, along with preliminary results for the production cross section and parity-violating single-spin asymmetry, A_L, from the STAR Collaboration's 2009 data at $\sqrt{s} = 500$ GeV.

1 Introduction

The high-energy polarized $\vec{p}+\vec{p}$ collisions at $\sqrt{s} = 500$ GeV at RHIC provide a unique way to study one of the unresolved questions in Quantum Chromodynamics (QCD), namely the spin structure of the nucleon. Polarized deep-inelastic scattering (DIS) experiments have shown that the contribution of quark spins to that of the proton is surprisingly small, at the level of $\sim 25\%$. [1] Inclusive DIS measurements sum over quark flavor and are only sensitive to the combined contributions of quarks and anti-quarks. Semi-inclusive DIS measurements, however, can achieve separation of the quark and anti-quark spin contributions by flavor and have been included, along with RHIC data constraining the gluon spin contribution, in a recent global analysis. [2] The extracted anti-quark polarized Parton Distribution Functions (PDFs) have sizable uncertainties compared to the well-constrained quark + anti-quark sums.

$W^{-(+)}$ bosons are produced at leading order through $\bar{u}+d\,(\bar{d}+u)$ interactions at the partonic level, and can be detected through their leptonic decays. The parity-violating nature of the weak production process gives rise to large longitudinal single-spin asymmetries, A_L, which yield a direct and independent probe of the quark and anti-quark polarized PDFs. The asymmetry is defined as $A_L = (\sigma^+ - \sigma^-)/(\sigma^+ + \sigma^-)$, where $\sigma^{+(-)}$ refer to the cross section when the helicity of the polarized proton beam is positive (negative). Theoretical frameworks have been developed to describe the production of W bosons and their decay leptons in polarized $\vec{p}+\vec{p}$ collisions. [3,4]

2 Experimental Details

The STAR [5] detector systems used in this measurement are the Time Projection Chamber (TPC), which provides tracking of charged particles in a 0.5 T solenoidal magnetic field for pseudorapidities of $|\eta| < 1.3$, and the Barrel and Endcap Electromagnetic Calorimeters (BEMC, EEMC), which are lead-scintillator sampling calorimeters covering $|\eta| < 1$ and $1.09 < \eta < 2$, respectively. Each of these detectors provides 2π coverage in the azimuthal angle, ϕ.

The data presented in this contribution were accumulated in 2009 when, for the first time, a significant dataset was collected for polarized proton collisions at a center of mass energy of $\sqrt{s} = 500$ GeV. The beam polarizations, measured with Coulomb-Nuclear Interference (CNI)

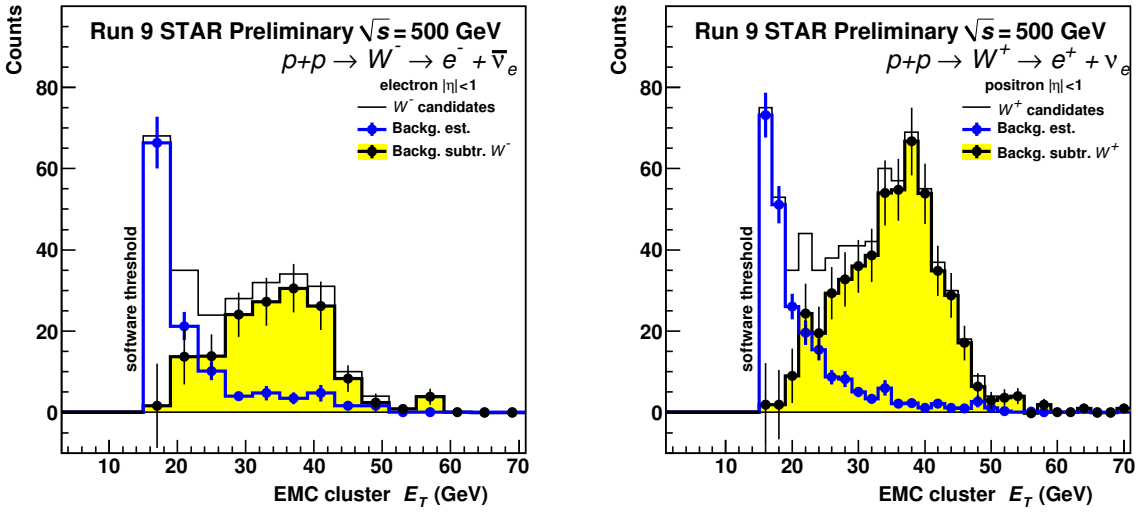

Figure 1: Candidate $e^{\pm}$ BEMC cluster E_T for W^- (left) and W^+ (right).

proton-carbon polarimeters[6] and calibrated with a polarized hydrogen gas-jet target,[7] averaged $(38 \pm 8.3)\%$ and $(40 \pm 12.1)\%$ for the two beams. The trigger condition used to select events online for this measurment involved a two-stage energy requirement in the BEMC. Electrons and positrons from W decays at mid-rapidity are characterized by a large transverse energy, E_T, peaked at $\sim M_W/2$ (Jacobian peak). To pass the trigger, an event must satisfy a hardware threshold of $E_T > 7.3$ GeV in a single BEMC tower. Additionally a software level trigger searched for a seed tower with $E_T > 5$ GeV and required that the maximum 2×2 tower cluster including that seed have an E_T sum larger than 13 GeV. The cross section for the hardware level trigger was measured using the vernier scan technique[8] to be 481 ± 10 (stat.) $\pm$ 110 (syst.) nb, which yields an integrated luminosity of 13.7 ± 0.3 (stat.) $\pm$ 3.1 (syst.) pb^{-1} for this data set. The systematic uncertainty in the luminosity is dominated by possible non-gaussian components of the beam profile seen in the vernier scan data.

W candidate events were selected offline based on kinematical and topological differences between leptonic $W^{\pm}$ decay, and QCD background events. $W^{\pm} \rightarrow e^{\pm} + \nu$ decay events contain a nearly isolated $e^{\pm}$ and an undetected neutrino opposite in azimuth, leading to a large missing E_T, characterized by a large imbalance in the vector p_T sum of all reconstructed final-state objects. Background QCD (e.g., di-jet) events, however, typically have a small imbalance in the vector p_T sum. An $e^{\pm}$ candidate is thus defined to be any TPC track with $p_T > 10$ GeV which originated from a primary vertex with $|z| < 100$ cm, where z is the direction along the beamline from the nominal interaction point. The candidate track is required to point to a 2×2 BEMC tower cluster with an E_T sum, E_T^e, larger than 15 GeV and whose centroid is less than 7 cm from the extrapolated track. Furthermore, two isolation cuts are imposed on the candidate: a) a requirement that the excess E_T in the surrounding 4×4 tower cluster be less than 5% of E_T^e, and b) that the excess EMC tower + TPC track E_T sum within a cone radius $R = 0.7$ of the cadidate in η-ϕ space be less than 12% of E_T^e. The final two selection criteria are based on cuts on the 'away-side' E_T and the vector p_T sum, whose meaning and construction are as follows. The away-side E_T is the EMC + TPC E_T sum over the full η range and $\phi \in [\phi_e + \pi + 0.7, \phi_e + \pi - 0.7]$. The vector p_T sum is defined as the sum of the $e^{\pm}$ candidate p_T vector and the p_T vectors of all the reconstructed jets with thrust axes outside the $R = 0.7$ cone around the candidate. Jets were reconstructed using the standard mid-point cone algorithm used in previous STAR jet measurements.[9] The final W candidate events are selected

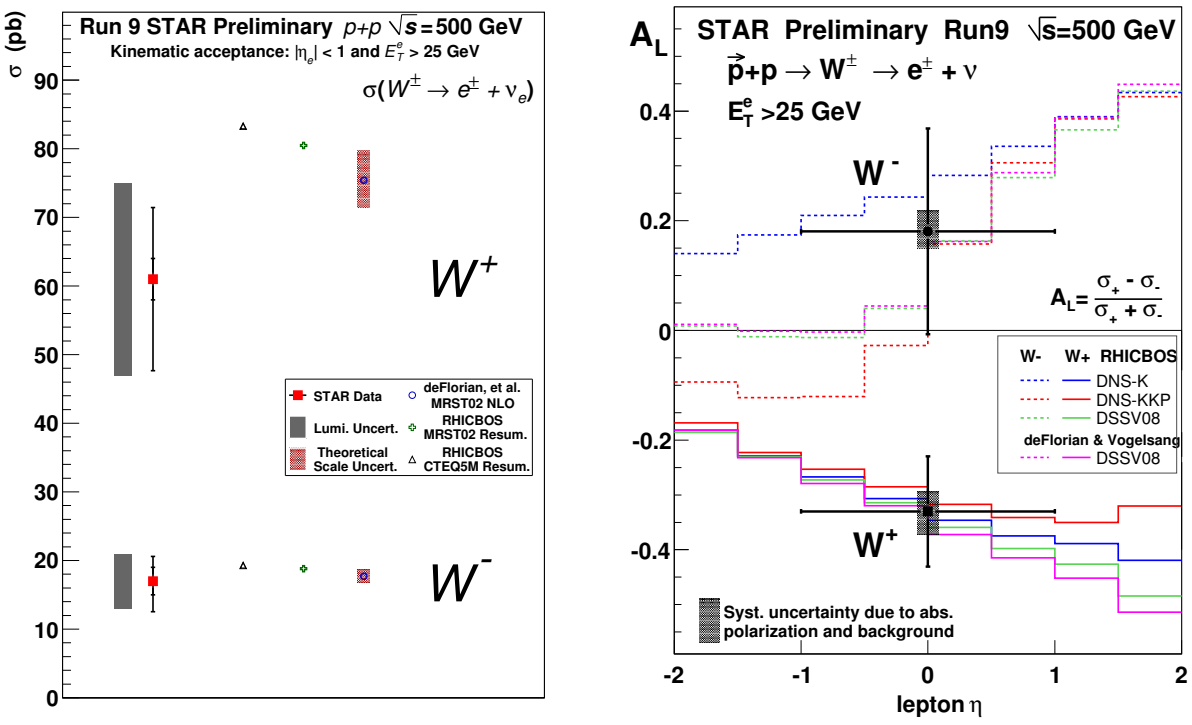

Figure 2: Measured cross section (left) and longitudinal single-spin asymmetry, A_L, (right) for $W^{\pm}$ production.

by requiring the away-side E_T to be less than 30 GeV and the magnitude of the vector p_T sum to be larger than 15 GeV.

Figure 1 shows the charge-separated yield as a function of the candidate 2×2 BEMC tower cluster E_T, or E_T^e, for events satisfying the selection criteria above. The W candidates show the characteristic Jacobian peak at $E_T^e \sim M_W/2$. The efficiency for reconstructing $W^{\pm} \rightarrow e^{\pm} + \nu$ events was evaluated using PYTHIA Monte-Carlo with full GEANT simulation of the detector response. Within the imposed kinematic acceptance of the decay $e^{\pm}$, $|\eta_e| < 1$ and $E_T^e > 25$ GeV, the overall reconstruction efficiency was estimated to be 56%.

The amount of background remaining in the W candidate sample, after applying the selection criteria described above, is estimated from three contributions. The first contribution is from $W^{\pm} \rightarrow \tau^{\pm} + \nu$ decay where the $\tau^{\pm}$ decays semi-leptonically to an $e^{\pm}$. This background was estimated using a similar Monte-Carlo simulation as was used for the efficiency. Another contribution estimates the impact of the missing calorimetric coverage for $-2 < \eta < -1.09$. To determine this contribution to the background, the analysis was performed a second time with the EEMC not used as an active detector. The difference in the W candidate E_T^e distribution with and without the EEMC included in the analysis is taken to be the estimate for the missing calorimetric coverage. The final contribution is estimated by normalizing a data-driven background shape to the remaining W candidate signal, in the E_T^e range below 19 GeV, after the first two background contributions are removed. This data-driven background shape is obtained by inverting the last two requirements in the W candidate selection, namely requiring that the away-side E_T be greater than 30 GeV or the magnitude of the vector p_T sum be less than 15 GeV. The total background and the remaining background-subtracted spectra are shown in Figure 1 in the blue and yellow histograms, respectively. A systematic uncertainty for the background estimation was determined by varying the inverted cuts used to obtain the data-driven

background shape and by varying the range where the background shape is normalized to the remaining W candidate signal.

3 Results

Preliminary results for the production cross section of $W^{\pm} \rightarrow e^{\pm} + \nu$ from candidate events with $|\eta_e| < 1$ and $E_T^e > 25$ GeV are shown in Figure 2 (left). The measured values are $\sigma(W^+ \rightarrow e^+ + \nu) = 61 \pm 3$ (stat.) $^{+10}_{-13}$ (syst.) ± 14 (lumi.) pb and $\sigma(W^- \rightarrow e^- + \bar{\nu}) = 17 \pm 2$ (stat.) $^{+3}_{-4}$ (syst.) ± 4 (lumi.) pb. The statistical and systematic uncertainties are shown as the error bars on the red data points. The systematic uncertainty of the measured luminosity, shown separately as the grey bands in Figure 2 (left), is dominated by the uncertainty in the vernier scan measurement mentioned previously. The measured cross sections are consistent with predictions based on full resummed [3] and NLO [4] calculations, which are also shown in Figure 2 (left).

Figure 2 (right) presents preliminary results for the single-spin asymmetry A_L for candidate events with $|\eta_e| < 1$ and $E_T^e > 25$ GeV. The measured asymmetries are $A_L^{W^+}$ = -0.33 $\pm$ 0.10 (stat.) $\pm$ 0.04 (syst.) and $A_L^{W^-} = 0.18 \pm 0.19$ (stat.) $^{+0.04}_{-0.03}$ (syst.). The systematic uncertainties, shown as the grey bands in figure 2 (right), are dominated by the absolute uncertainties of the beam polarization. The four curves shown are predictions based on full resummed [3] and NLO [4] calculations for two polarized PDFs, [2,10] which are constrained by inclusive and semi-inclusive DIS measurements. Our results are consistent with the theoretical expectations.

4 Summary and Outlook

The study of parity-violating single-spin asymmetries for $W^{\pm}$ bosons produced in polarized $\vec{p} + \vec{p}$ collisions offers a clean and unique approach to probe the flavor and spin structure of the proton. Presented in this contribution are the first measurements of $W^{\pm}$ single-spin asymmetries, A_L, and production cross sections by the STAR Collaboration, both of which are consistent with resummed and NLO calculations. Future planned STAR measurements at mid-rapidity and forward rapidity with increased luminosity and beam polarization are expected to provide significant constraints on the polarized QCD sea.

References

1. B.W. Filippone and X.D. Ji, *Adv. Nucl. Phys.* **26**, 1 (2001).
2. D. de Florian, R.sassot, M. Stratmann, and W.Vogelsang, *Phys. Rev. Lett.* **101**, 072001 (2008).
3. P.M. Nadolsky and C.P. Yuan, *Nucl. Phys.* B **666**, 31 (2003).
4. D. de Florian and W. Vogelsang, arXiv:1003.4533.
5. K.H. Ackermann *et al* (STAR), *Nucl. Instrum. Methods* A **499**, 624 (2003).
6. I. Nakagawa *et al*, *AIP Conf. Proc.* **915**, 912 (2007).
7. Y.I. Makdisi *et al*, *AIP Conf. Proc.* **915**, 975 (2007).
8. A. Drees and Z. Xu, *Proceedings of the Particle Accelerator Conference, Chicago,* p. 3120 (2001).
9. B.I. Abelev *et al* (STAR) *Phys. Rev. Lett.* **100**, 232003 (2008)
10. D. de Florian, G.A. Navarro, R. Sassot, *Phys. Rev.* D **71**, 094018 (2005)

LEPTON CHARGE ASYMMETRY FROM W DECAYS AT HADRON COLLIDERS IN NNLO QCD

G. FERRERA
Dipartimento di Fisica e Astronomia, Università di Firenze
and INFN, Sezione di Firenze,
I-50019 Sesto Fiorentino, Florence, Italy

We present the next-to-next-to-leading order (NNLO) QCD computation of the charged leptons asymmetry from $W^{\pm}$ boson decays in hadron collisions. Our calculation includes the dependence on the lepton kinematical cuts applied in actual experimental analyses. We compare numerical results on the charge asymmetry in $p\bar{p}$ collisions with some of the available Tevatron data. We show illustrative results for the asymmetry in pp collisions at LHC energy.

1 Introduction

The asymmetry in the rapidity distribution of charged leptons from $W^{\pm}$ decay is an important observable at hadron colliders [a]. In $p\bar{p}$ collisions, the W^+ and W^- bosons are produced with equal rates; however, the W^+ tends to be produced along the proton beam direction (i.e. at positive rapidity) and the W^- along the antiproton direction (i.e. at negative rapidity). In pp collisions, W production is forward–backward symmetric; however, the W^- production rate is smaller than the W^+ production rate and, moreover, the W^- is mostly produced at central rapidities, while the W^+ is mostly produced at larger rapidities.

These W^+/W^- asymmetries are related to the proton content of u and d quarks and, in particular, to the fact that u quarks carry, on average, a larger fraction of the proton's momentum than d quarks. Therefore the W boson charge asymmetries provide important quantitative information on the u and d quark momentum distribution in the proton [1].

At hadron colliders, the produced W bosons are identified by their leptonic decay $W \to l\nu_l$. Since the longitudinal component of the neutrino momentum is unmeasured, what is actually measured is the rapidity of the charged lepton and the corresponding lepton charge asymmetry [b], which is defined as

$$A_{h_1h_2}(y_l) = \frac{d\sigma_{h_1h_2}(l^+)/dy_l \;-\; d\sigma_{h_1h_2}(l^-)/dy_l}{d\sigma_{h_1h_2}(l^+)/dy_l \;+\; d\sigma_{h_1h_2}(l^-)/dy_l} \quad , \tag{1}$$

where h_1 and h_2 label the two incoming hadrons and $d\sigma_{h_1h_2}(l^{\pm})/dy_l$ is the charged lepton ($l^{\pm}$) rapidity (y_l) distribution.

In actual experimental determinations, the measured rapidity cross sections and charge asymmetries depend on the kinematical cuts and variables that are used to identify and select the observed $W \to l\nu_l$ events. Our computation of the lepton charge asymmetry is carried

[a] We consider the charged leptons in the massless approximation, thus the lepton rapidity y_l coincides with the pseudorapidity η_l.

[b] A direct determination of the W charge asymmetry has recently been presented by the CDF collaboration [2].

out by using the partonic Monte Carlo program DYNNLO [3], which encodes the NNLO radiative corrections to the Drell-Yan process at the fully-differential level[c]. This allows us to compute the lepton charge asymmetry by including the kinematical cuts applied in experimental analyses [5].

Our N^{n}LO (with $n = 0, 1, 2$) computation uses the expression of $\alpha_S(\mu_R^2)$ at the n-th order (i.e., we use the μ_R dependence at the level of $(n+1)$ loops), and it is consistently convoluted with parton densities at each corresponding order. The reference value of $\alpha_S(M_Z)$ is fixed at the actual value used in the corresponding set of parton densities. We consider finite-width effects, treating the W boson off shell, and we include the spin correlations of the W leptonic decay. The values of the electroweak parameters used in our computation can be found in Ref. [5].

Since our main purpose is the study of asymmetries up to NNLO QCD, we consider only the parton distribution function (PDF) sets of Refs. [6], [7] and [8] which include NNLO parton densities with $N_f = 5$ (effectively) massless quarks. Among these PDFs sets only the global fit of Ref. [6] includes some data on the lepton charge asymmetry at the Tevatron: the ensuing parton densities are thus expected to produce better agreement with available measurements of charge asymmetries.

2 Charged lepton asymmetry at the Tevatron

In the following we present our perturbative QCD calculations up to NNLO, and their comparison with some of the published Tevatron data. We note that our calculation is invariant under CP transformations. Therefore, in $p\bar{p}$ collisions, the charge asymmetry fulfils $A_{p\bar{p}}(-y) = -A_{p\bar{p}}(y)$.

We first consider the electron charge asymmetry in the experimental configuration of the CDF data at the Tevatron Run II [9]. The events are required to have a missing transverse energy $E_T^\nu > 25$ GeV and a transverse mass 50 GeV $< M_T <$ 100 GeV. The charged lepton must be in the central rapidity region ($|y_l| \leq 2.45$) and must be isolated[d] i.e. $E_T^{\rm iso}/E_T < 0.1$, where $E_T^{\rm iso}$ is the hadronic (partonic) transverse energy in a cone of radius $R = 0.4$ (in pseudorapidity–azimuth space) along the lepton momentum and E_T is the electron transverse energy. Following the experimental analysis we consider two kinematical region of the electron transverse energy: 25 GeV $< E_T <$ 35 GeV (low-E_T) and 35 GeV $< E_T <$ 45 GeV (high-E_T).

In Fig. 1(a) we report the CDF data and present the results of our LO, NLO and NNLO results using the corresponding parton densities from the MSTW2008 Collaboration [6], which include the CDF data [9] in their fit. At small values of η_e, the radiative corrections lead to little effects. In the low-E_T bin, as η_e increases, both the NLO and NNLO effects slightly increase the value of the asymmetry. In the high-E_T bin, as η_e increases, the NLO and NNLO effects are negative and the asymmetry slightly decreases. The NNLO effects are not yet quantitatively relevant in comparison with the size of the experimental uncertainties. The data are well fitted by the MSTW2008 NNLO partons, especially in the low-E_T region, this is confirmed by the values of χ^2 from the comparison of the data with the QCD calculations reported in Fig. 1(a).

We then consider the D0 data for the electron charge asymmetry [10] at the Tevatron Run II. The D0 measurement extends to high rapidities, $|\eta_e| \leq 3.2$, the missing transverse energy is required to be $E_T^\nu > 25$ GeV and the transverse mass to be $M_T > 50$ GeV. As for lepton isolation the D0 procedure is similar to the CDF one, with the requirement $E_T^{\rm iso}/E_T < 0.15$. We examine two regions of electron transverse energy: $E_T > 25$ GeV (wide E_T region) and $E_T > 35$ GeV (high-E_T region). Let us note that the D0 electron asymmetry data [10] are not included in the MSTW PDF fit [6]: their inclusion in the global analysis does not permit to obtain a good quality fit, with significant tension between the D0 electron asymmetry data and other data.

[c] This Monte Carlo program is based on the NNLO subtraction method introduced in Ref. [4].

[d] The charged lepton isolation has a small impact on our results, since it is not effective at the leading order and the radiative corrections are not large.

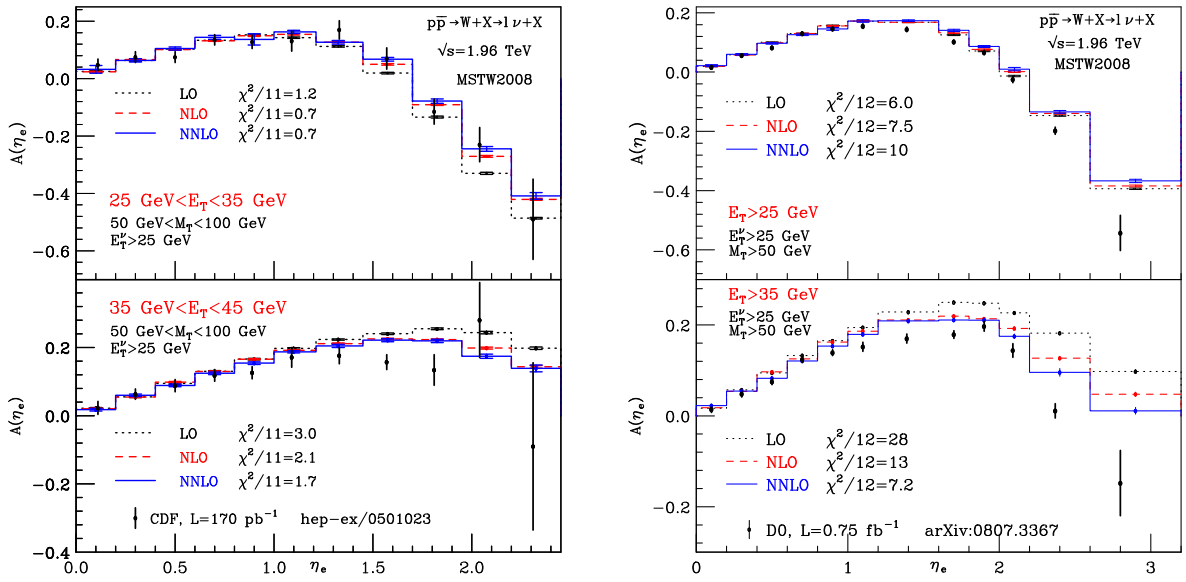

(a) (b)

Figure 1: Electron charge asymmetry up to NNLO compared to a) CDF data in the lower E_T region (upper panel) and higher E_T region (lower panel); b) D0 data in the wide E_T region (upper panel) and (high-E_T) region.

In Fig. 1(b) we display the D0 electron data and present the corresponding QCD results at LO, NLO and NNLO using the corresponding MSTW2008 PDFs. In the wide E_T region at high values of the electron rapidity, the effect of the NLO and NNLO corrections is positive and increases the deviation of the QCD results from the D0 data. We see that the agreement between the QCD calculations and the data is poor. This is quantitatively confirmed by the values of χ^2 reported in Fig. 1(b). We note that the value of χ^2 increases in going from LO to NLO and to NNLO. In the high-E_T region (as in the case of the high-E_T bin in Fig. 1(a)) the effect of the NLO and NNLO corrections is negative as the lepton rapidity increases toward high values. This effect reduces the difference between the QCD calculations and the D0 data, although a substantial disagreement between them still persists at the NNLO. The value of χ^2 decreases in going from LO to NLO and to NNLO.

The NNLO results of Fig. 1(b) are reported in Fig. 2(a) by including the PDF errors (68% C.L.) from the MSTW2008 [6], ABKM09 [7] and JR09VF [8] set of PDFs. The ABKM09 PDF errors are slightly smaller than the errors of the MSTW2008 set and the ABKM09 result tends to overshoot the MSTW2008 result. The JR09VF PDF errors are larger than the PDF errors of the MSTW2008 set and the JR09VF result tends to undershoot the MSTW2008 result in most of the rapidity bins. The PDF errors are comparable to (or, larger than) the D0 experimental errors; the inclusion of the PDF errors thus reduces the differences between the NNLO results and the D0 electron data, although a substantial disagreement can be noticed from the value of χ^2 for different sets of PDFs reported in Fig. 2(a).

3 Charged lepton asymmetry at the LHC

We now consider pp collisions and we present results of our QCD calculations at the centre–of–mass energy $\sqrt{s} = 7$ TeV. The lepton charge asymmetry at the LHC is sensitive to parton densities with momentum fractions that are smaller than those probed at the Tevatron. To the purpose of presenting some quantitative, though illustrative, results on the lepton asymmetry at the LHC, we refer to the framework considered in a recent 'Physics Analysis' [11] of the CMS Collaboration. The study of Ref. [11], based on data sets from Monte Carlo simulations, regards

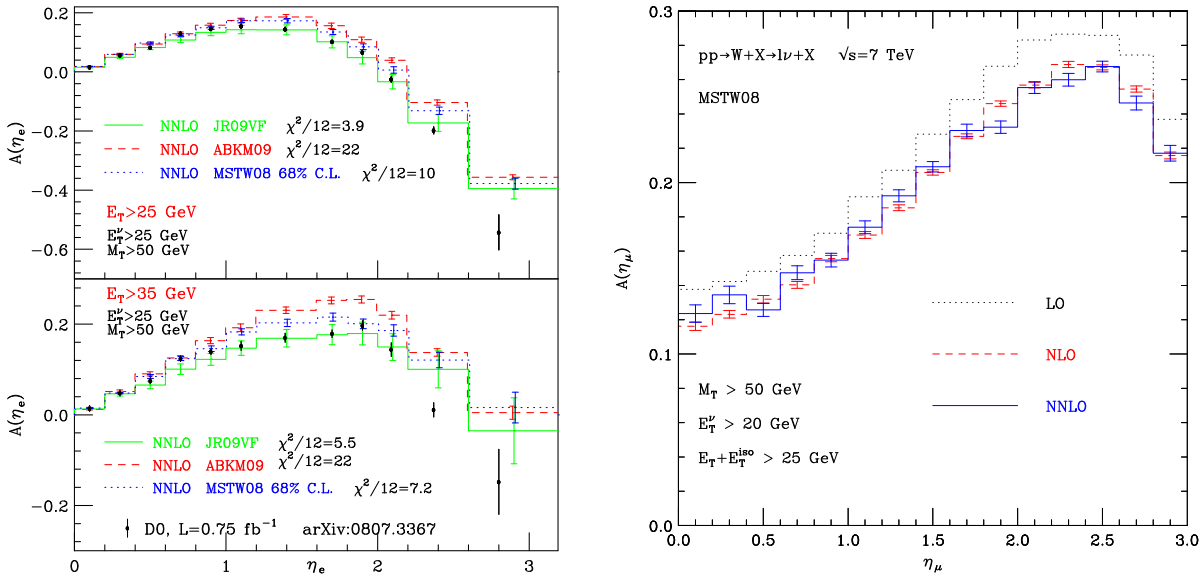

(a) (b)

Figure 2: a) Electron charge asymmetry at NNLO with PDF uncertainties compared to D0 data in the lower E_T region (upper panel) and higher E_T region (lower panel); b) Muon charge asymmetry up to NNLO at the LHC.

the muon rapidity cross sections and charge asymmetry that can be measured with the CMS detector at the LHC. The lepton selection cuts applied in Ref.[11] require the transverse mass and the missing transverse energy to be $M_T > 50$ GeV and $E_T^\nu > 20$ GeV, respectively. The muons are isolated: the hadronic (partonic) transverse energy $E_T^{\rm iso}$ in a cone of radius $R = 0.3$ is required to fulfil the constraints $E_T^{\rm iso}/E_T < z/(1-z)$ with $z = 0.05$, and $E_T + E_T^{\rm iso} > E_T^{\rm max} = 25$ GeV.

The results for the lepton charge asymmetry at $\sqrt{s} = 7$ TeV are presented in Fig. 2(b). The three histograms show the LO, NLO and NNLO results of our calculation with the MSTW2008 parton densities. Considering the effect of the QCD radiative corrections, we see that, the NLO corrections tend to decrease the asymmetry, and the NNLO corrections do not significantly change the NLO result thus indicating a very good quantitative convergence of the truncated perturbative expansion.

References

1. E. L. Berger, F. Halzen, C. S. Kim and S. Willenbrock, Phys. Rev. D **40** (1989) 83 [Erratum-ibid. D **40** (1989) 3789]; A. D. Martin, R. G. Roberts and W. J. Stirling, Mod. Phys. Lett. A **4** (1989) 1135.
2. T. Aaltonen *et al.* [CDF Collaboration], Phys. Rev. Lett. **102** (2009) 181801.
3. S. Catani, L. Cieri, G. Ferrera, D. de Florian and M. Grazzini, Phys. Rev. Lett. **103** (2009) 082001.
4. S. Catani and M. Grazzini, Phys. Rev. Lett. **98** (2007) 222002.
5. S. Catani, G. Ferrera and M. Grazzini, JHEP **1005** (2010) 006 [arXiv:1002.3115 [hep-ph]].
6. A. D. Martin, W. J. Stirling, R. S. Thorne and G. Watt, Eur. Phys. J. C **63** (2009) 189.
7. S. Alekhin, J. Blumlein, S. Klein and S. Moch, report DESY 09-102 (arXiv:0908.2766 [hep-ph]).
8. P. Jimenez-Delgado and E. Reya, report DOTH-0913 (arXiv:0909.1711 [hep-ph]).
9. D. E. Acosta *et al.* [CDF Collaboration], Phys. Rev. D **71** (2005) 051104.
10. V. M. Abazov *et al.* [D0 Collaboration], Phys. Rev. Lett. **101** (2008) 211801.
11. CMS Collaboration, report CMS PAS Note EWK-09-003 (2009).

Direct photon pair measurement at DØ

L. HAN
Department of Modern Physics, University of Science and Technology of China (USTC), Hefei, Anhui 230026, P.R.China

We present a measurement of direct photon pair production cross sections using $4.2fb^{-1}$ of data collected with the D0 detector at the Fermilab Tevatron $p\bar{p}$ Collider. We measure single differential cross sections as a function of the diphoton mass, the transverse momentum of the diphoton system, the azimuthal angle between the photons and the polar scattering angle of the photons, and double differential cross sections considering the last three kinematic variables in three diphoton mass bins. The results are compared with different perturbative QCD predictions and event generators.

The direct photon pair (DPP) production with large invariant mass at hadron colliders is of special interesting. It constitutes large irreducible background for Higgs decaying into diphoton mode, and new heavy resonances and extra dimensions searches. Thus, precise measurements of the diphoton differential production cross sections for various kinematic variables and their theoretical understanding are extremely important for future Higgs and new phenomena searches. On the other hand, providing opportunity of verifying the validity of the predictions of perturbative quantum chromodynamics (pQCD) and soft-gluon resummation methods implemented in theoretical calculations, diphoton production itself is interesting. In this letter, we present a brief report on the precise measurements of DDP production at the D0 experiment in $p\bar{p}$ collisions at $\sqrt{s} = 1.96\ TeV$ at the Tevatron Collider. With large integrated luminosity, the double differential cross sections of this process are measured for the first time, detail can be found in [1].

The dominant $p\bar{p} \to \gamma\gamma + X$ production mode is via quark scattering $q\bar{q} \to \gamma\gamma$, then followed by gluon fusion as $gg \to \gamma\gamma$. Although the gluon fusion contribution is governed by quark-loop diagrams at leading order (LO) and suppressed by a factor of α_s^2 compared to the quark scattering processes, it would be significantly enhanced by gluon patron density in low invariant mass $M_{\gamma\gamma}$ region. For example, the expected fraction of gluon fusion to the total DPP rate can reach more than 10% when $M_{\gamma\gamma} < 100\ GeV$, predicted by by the PYTHIA [2] Monte Carlo (MC) event generator with the CTEQ6.1L [3] parton distribution function (PDF) set. In addition, direct photons may be produced from single or double parton-to-photon fragmentation processes of the partons produced in the hard scattering [4,5]. There are two next-to-leading order (NLO) theoretical predictions on DPP production in pQCD, namely RESBOS [4] and DIPHOX [5]. In DIPHOX, gluon fusion contribution is considered only at LO, but the explicit fragmentation effects are included up to NLO, while in RESBOS an approximate NLO fragmentation function is adopted. Also, only in RESBOS, the resummation of initial state gluon soft and collinear emissions is taken into account to all orders.

The DPP production cross sections are measured by using $4.2fb^{-1}$ data collected by D0

experiment from August 2006 to June 2009. The cross sections are measured differentially as a function of the diphoton invariant mass $M_{\gamma\gamma}$ and transverse momentum $p_T^{\gamma\gamma}$, the azimuthal angle between the photons $\Delta\phi_{\gamma\gamma}$, and the cosine of the polar scattering angle of the photon in the frame with no net transverse momentum of the diphoton system. These kinematic variables probe different aspects of the DPP production mechanism, for example, the shapes of the $p_T^{\gamma\gamma}$ and $\Delta\phi_{\gamma\gamma}$ distributions are mostly affected by initial state gluon radiation and fragmentation effects. The invariant mass $M_{\gamma\gamma}$ spectrum is particularly sensitive to potential contributions from new phenomena.

The D0 detector is discussed in detail elsewhere [6]. Events are selected by requiring two photon candidates with transverse momentum $p_T > 21(20)\ GeV$ for the leading(trailing) p_T photon and pseudorapidity $|\eta| < 0.9$. The photon p_T is computed with respected to the reconstructed primary vertex with the highest number of associated tracks in the event. The asymmetry p_T cuts for the two photon candidates are required to suppress the impact of kinematic region $p_T^{\gamma\gamma} \to 0(\Delta\phi_{\gamma\gamma} \to \pi)$, where the NLO pQCD calculation diverges. The photon candidates are selected by requiring to deposit most of its energy in the electromagnetic (EM) calorimeter layers, and the energy weighted EM shower shape be consistent with that expected for an electromagnetic shower. The EM cluster energy must be isolated in the calorimeter, $[E_{tot}(0.4) - E_{EM}(0.2)]/E_{EM}(0.2) < 0.1$, where $E_{tot}(R)$ and $E_{EM}(R)$ are the total energy and the energy in the EM section, respectively, within a cone of radius $R = \sqrt{(\Delta\eta)^2 + (\Delta\phi)^2} = 0.2$ around the photon direction. To minimize electrons misidentified as photons, the EM candidates are required to not be spatially matched to significant tracker activity. This track-match veto suppress background contributions from Drell-Yan events $Z/\gamma^* \to e^+e^-$, where both electrons are misidentified as photons. To further suppress a jet misidentified as a single photon resulting from fluctuations in the parton fragmentation into a well-isolated neutral meson (π^0 or η) decay into a final state with two or more photons, an artificial neural network discriminant O_{NN} is developed by exploiting differences in the tracker activity and energy deposits in the EM calorimeter and the central preshower detector between photons and jets. The O_{NN} is trained using single photon and jet PYTHIA MC samples and the performance is verified using a data event sample consisting of photons radiated from charged leptons in Z boson decays ($Z \to l^+l^-\gamma, l = e, \mu$). A loose $O_{NN} > 0.3$ cut is required, which offers nearly full efficiency for photons and rejects 40% of the jet faked photons. Finally, the two photon candidates are required to be spatially separated as $\Delta R > 0.4$ and satisfy invariant mass cut as $M_{\gamma\gamma} > p_T\gamma\gamma$. The mass requirement, together with photon isolation cut, significantly remove the component of fragmentation contribution in DPP events, therefore restricting the data-to-theory comparison to the region where the theoretical calculations should have smaller uncertainties.

After imposing all above requirements, the selected data sample includes Drell-Yan and QCD γ+jet and dijet instrumental background. The contribution from Drell-Yan events is estimated using the MC simulation with PYTHIA, normalized to the NNLO cross section. The charge misidentification rate determined from the MC simulation are corrected to those measured in the data. Backgrounds due to γ+jet and dijet events are estimated from data by using a 4×4 matrix background estimation method [7]. A tighter $O_{NN} > 0.6$ is employed to divide the data events into four orthogonal categories, depending on whether the leading/trailing p_T photon candidates pass (p) or fail (f) this requirement. The corresponding number of events, after subtracting the estimated Drell-Yan contribution, compose a 4-component vector $(N_{pp}, N_{pf}, N_{fp}, N_{ff})$. The difference in relative efficiencies of the $O_{NN} > 0.6$ between photons and jets allows estimation of the sample composition by solving a linear system of equations: $(N_{pp}, N_{pf}, N_{fp}, N_{ff})^T = \epsilon \times (N_{\gamma\gamma}, N_{\gamma j}, N_{j\gamma}, N_{jj})^T$, where $N_{\gamma\gamma}(N_{jj})$ is the number of DPP (dijet) events and $N_{\gamma j}(N_{j\gamma})$ is the number of γ+jet events with the leading(trailing) p_T photon candidate being a real photon. The 4×4 matrix ϵ contains the photon ϵ_γ and jet ϵ_j efficiencies, estimated using photon and jet MC samples and validated in data.

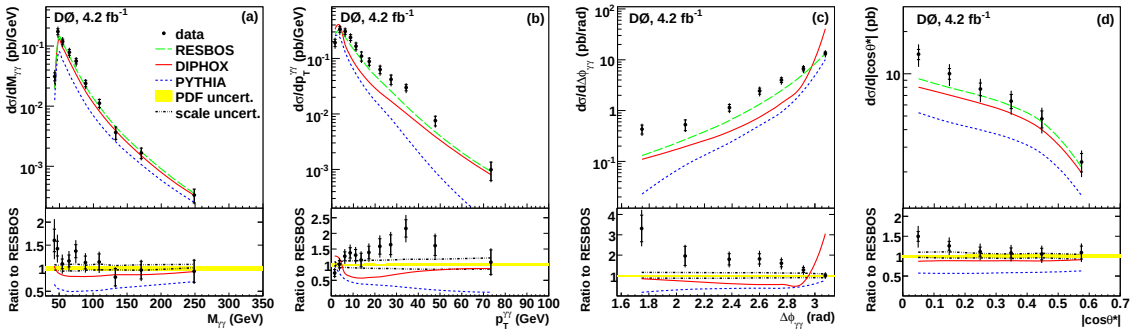

Figure 1: The measured differential diphoton production cross sections as functions of (a)$M_{\gamma\gamma}$, (b)$p_T^{\gamma\gamma}$, (c) $\Delta\phi_{\gamma\gamma}$ and (d) $|\cos\theta^*|$. The data are compared to the theoretical predictions from RESBOS, DIPHOX, and PYTHIA. The ratio of differential cross sections between data and RESBOS are displayed as black points with uncertainties in the bottom plots. The inner line for the uncertainties in data points shows the statistical uncertainty, while the outer line shows the total uncertainty. The solid (dashed) line shows the ratio of the predictions from DIPHOX (PYTHIA) to those from RESBOS. In the bottom plots, the scale uncertainties are shown by dash-dotted lines and the PDF uncertainties by shaded regions.

The estimated number of DPP events $N_{\gamma\gamma}$ in each kinematic bin is corrected for the DPP event selection efficiency and acceptance. The event efficiency is calculated using PYTHIA MC and processed through a GEANT-based simulation of the D0 detector. Differences between data and MC in the per-photon selection efficiencies are corrected for with suitable scale factors derived using control samples of electrons from Z boson and its radiative decays. The acceptance is calculated using DPP events generated with RESBOS. The differential cross sections $d\sigma/dM_{\gamma\gamma}$, $d\sigma/dp_T^{\gamma\gamma}$, $d\sigma/d\Delta\phi_{\gamma\gamma}$ and $d\sigma/d|\cos\theta^*|$ are obtained from the number of data events corrected for the background contribution, divided by the trigger, vertex and diphoton selection efficiencies, acceptance, integrated luminosity, and the bin width for each kinematic variable. The dominant systematic uncertainties include γ+jet and dijet background substraction resulting from the uncertainties on ϵ_γ and ϵ_j and typically varying within (11-15)%, the common uncertainties of photon selection criteria (4.3%) and luminosity (6.1%).The measured differential cross sections, compared to the theoretical predictions from RESBOS, DIPHOX and PYTHIA, are depicted in Fig. 1

The results obtained show that none of the theoretical predictions considered is able to describe the data well in all kinematic regions of the four variables. RESBOS shows the best agreement with data, although systematic discrepancies are observed at low $M_{\gamma\gamma}$, high $p_T^{\gamma\gamma}$ and low $\Delta\phi_{\gamma\gamma}$, the agreement is fair at intermediate $50 < M_{\gamma\gamma} < 80\ GeV$ and good at high $M_{\gamma\gamma} > 80\ GeV$. The large discrepancy between RESBOS and DIPHOX in some regions of the phase space is due to absence of all-order soft-gluon resummation and accounting $gg \to \gamma\gamma$ contribution only at LO in DIPHOX.

Further insight on the dependence of the $p_T^{\gamma\gamma}$, $\Delta\phi_{\gamma\gamma}$ and $|\cos\theta^*|$ kinematic distributions on the mass scale can be gained through the measurement of double differential cross sections. For instance, the differential cross sections as functions of $p_T^{\gamma\gamma}$ are measured in three $M_{\gamma\gamma}$ bins: $30-50\ GeV$, $50-80\ GeV$ and $80-350\ GeV$. The results are presented in Fig.2 , corresponding to each of the three $M_{\gamma\gamma}$ intervals. These results confirm that the discrepancies between data and RESBOS originate are largest in the lowest mass region $M_{\gamma\gamma} < 50\ GeV$, where the contribution from gluon fusion is expected to be largest, while are reduced in the intermediate region, and good description of all kinematic variables can be achieved for the $M_{\gamma\gamma} > 80\ GeV$ high mass region, the relevant region for the Higgs boson and new phenomena searches. It should be noticed that at the Tevatron, DPP production at high masses is strongly dominated by $q\bar{q}$ annihilation, in contrast with the LHC, where the contribution from gg and qg initiated

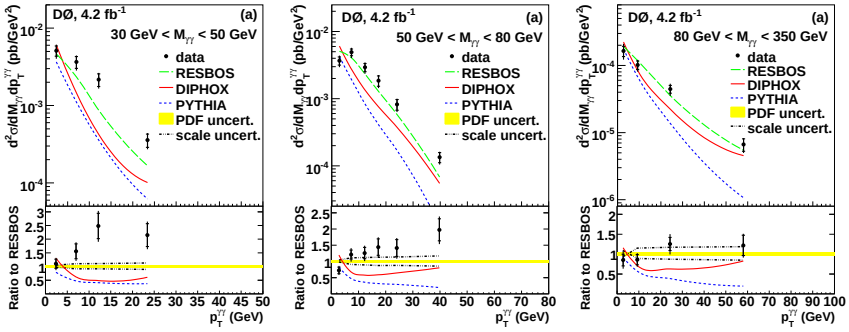

Figure 2: The measured double differential diphoton production cross sections as functions of $p_T^{\gamma\gamma}$ in three $M_{\gamma\gamma}$ intervals. The notations for points, lines and shaded regions are the same as in Fig. 1.

process will be significant. It would be interesting to see if the addition of NNLO corrections to RESBOS, as done in[8], will improve the description of the high $p_T^{\gamma\gamma}$ spectrum at low $M_{\gamma\gamma}$ region.

In summary, we present measurements of single and double differential cross sections for DPP production in $p\bar{p}$ collisions at $\sqrt{s} = 1.96\ TeV$. The analysis uses 4.2 fb^{-1} data accumulated at D0 experiment. The measured cross sections are compared to theoretical predictions from RESBOS, DIPHOX and PYTHIA, showing the necessity of including higher order corrections beyond NLO as well as the resummation to all orders of soft and collinear initial state gluons. These results allow the tuning of the theoretical predictions for this process, which is of great relevance for improving the sensitivity of searches for the Higgs boson and other new phenomena at the Tevatron and the LHC.

References

1. V.M. Abazov *et al* (D0 Collaboration), Phys. Rev. Lett. **102**, 231801 (2009)
2. T. Sjostrand *et al*, JHEP **0605**, 026(2006).
3. W.K. Tung *et al*, JHEP **0702**, 052(2007).
4. C. Balazs, E.L. Berger, S. Mrenna, and C.-P. Yuan, *Phys. Rev.* D **57**, 6934 (1998); C. Balazs, E.L. Berger, P. Nadolsky, and C.-P. Yuan, *Phys. Rev.* D **76**, 013009 (2007).
5. T. Binoth, J.P.Guillet, E.Pilon, and M. Werlen, Eur. Phys. J. C **16**, 311 (2000).
6. V.M. Abazov *et al* (D0 Collaboration), Nucl. Instrum. Methods in Phys. Res. A **565**, 463 (2006);
7. V.M. Abazov *et al* (D0 Collaboration), Phys. Rev. Lett. **102**, 231801 (2009).
8. Q.-H. Cao, C.-R. Chen, C. Schmidt, and C.-P. Yuan, arXiv:0909.2305 [hep-ph] (2009).

On strategies for determination and characterization of the underlying event

S. SAPETA
LPTHE, UPMC Univ. Paris 6 and CNRS UMR 7589
Paris, France

We discuss the problem of the separation and description of the underlying event (UE) within two existing approaches to UE measurement: the "traditional" method, widely used at Tevatron, and a recently proposed jet-area/median method. A simple toy model of UE is developed in order to understand how these approaches perform. We find that both methods are comparably good for measuring average properties of the UE but the jet-area/median approach is favorable for determining fluctuations. We also use the latter method to study the UE from several existing Monte Carlo generator tunes. We investigate which characteristics of the underlying event might be useful to measure in order to improve understanding of its properties and to simulate it well. These include transverse momentum density per area, intra- and inter-event fluctuations and correlations.

1 Introduction

The hard processes studied at hadron collider are nearly always accompanied by the *underlying event* (UE). This predominantly soft activity affects a wide variety of high-p_t measurements, e.g. by introducing a bias or by degrading kinematic jet reconstruction. Therefore, a good understanding and precise theoretical control over the underlying event is of great importance in order to fully exploit the potential of LHC.

Study of the UE, both experimental and theoretical, faces, however, a number of problems. The first of them appears already at the level of definition since the very concept of the underlying event is ambiguous. This is because none of the events measured at hadron colliders has a clear boundary between the hard part and the UE. Also modeling of the UE is difficult. Most successful and widely used Monte Carlo models generate the majority of the underlying activity via the mechanism of multiple parton interactions. There are however other conceivable mechanisms which could contribute to the UE and which have not been given as thorough study. Questions include e.g. the role of correlations as well as the effects of possible contributions from the BFKL type radiation.

Given the above difficulties, one can ask the question if, at least, it would be possible to measure the UE in, admittedly always to some extent arbitrary, but well defined and well controlled way.

This leads us to addressing the following two questions: [1] What do we really measure with existing methods of UE determination and which observables are interesting to measure? To answer the first question we develop a simple toy model and use it as a testing ground for two existing methods of UE measurement. To address the second question we study the UE from Monte Carlo models and identify a set of quantities which could serve as valuable characteristics of the UE.

2 Relevant characteristics and measuring methods of the UE

We concentrate on quantities related to energy flow. Those involve the main observable called ρ, which is defined as the amount of transverse momentum of UE per unit area. We will be also interested in rapidity dependence of ρ, its point-to-point fluctuations within a single event, σ, and its fluctuations from event to event as well as the point-to-point correlations.

Two methods exist which allow one to study the underlying event: the traditional approach,[2,3] widely used at Tevatron, and the more recent area/median based approach.[4,5] Certain freedom is present in each of the methods. Below, we describe the version used in our study.

In the traditional method all particles within a certain rapidity range are first clustered into jets. Then, four regions in the transverse plane are defined based on the position of the leading jet, whose direction defines $\phi = 0$: the "towards" region, $|\phi| < \pi/3$, an away region, $2\pi/3 < |\phi| < \pi$, and two transverse regions. The characteristic p_t of the UE is defined as p_t in one or both of those transverse regions. To further reduce the contamination from the perturbative radiation, the transverse regions are labeled, on an event-by-event basis, as TransMin and TransMax depending on their relative value of p_t. The contribution of perturbative radiation to the average p_t in TransMin should be suppressed by an additional α_s with respect to the average result from both regions TransAv.

The area/median method is jet-based, exploits the concept of jet areas[5] and can be carried out using the `FastJet` package.[6,7] It starts by adding a dense set of infinitely soft particles, *ghosts*, to an event. Then, all particles (real and ghosts) are clustered with the C/A algorithm[8,9] leading to a set of jets ranging from hard to soft. The typical UE scale in the event is defined as

$$\rho = \underset{j\in\text{jets}}{\text{median}} \left[\left\{ \frac{p_{tj}}{A_j} \right\} \right] , \tag{1}$$

where A_j is a jet area, designed to measure susceptibility of a jet to soft radiation. In a similar manner, a quantity measuring the intra-event fluctuations, denoted as σ, is determined from the sorted list $\{p_{tj}/A_j\}$. It is given by the value for which 15.86% of jets have smaller p_{tj}/A_j.

3 Understanding systematic effects: a toy model study

It is not guaranteed a priori that the methods described above will give a sensible result for the characteristic momentum scale of UE. Therefore, to better understand how those methods perform, we have tested them against a simple toy model.

The model involves two components: a soft one, which we identify with genuine UE, and a hard one, which comes from perturbative contamination. The main parameters of the soft component are: the average density of particles per unit area, ν, and the average p_t of a particle, μ. Therefore, the true value of $\rho = \nu\mu$ by definition. The number of particles is governed by the Poisson distribution and the p_t of a single particle by the exponential distribution. The hard contamination is modeled as coming from the initial state radiation of soft and collinear primary emissions. We assume this radiation to be independent of rapidity and ϕ for $1 \lesssim p_t \lesssim Q$, where Q is a hard scale of the process (e.g. half of the hardest jet's p_t for the dijet event).

One of the results of the toy model study are the biases for ρ and σ extraction.[1] For instance, the hard radiation introduces the bias for ρ determined in the traditional approach, $\delta\rho \sim \alpha_s^2 Q$, which depends linearly on the hard scale of the process. The corresponding bias in the area/median approach has only log(log) dependence $\delta\rho \sim \sigma\,(n_b/A_{\text{tot}} + \text{const} \cdot \log\log Q)$, where n_b is the number of final state born particles and A_{tot} is the total used area of the event.

Another important outcome of the study with the toy model concerns fluctuations. The extracted values of ρ vary from one event to another, even if the same ρ distribution is used to generate all events. This is because, usually, one works only with limited part of an event

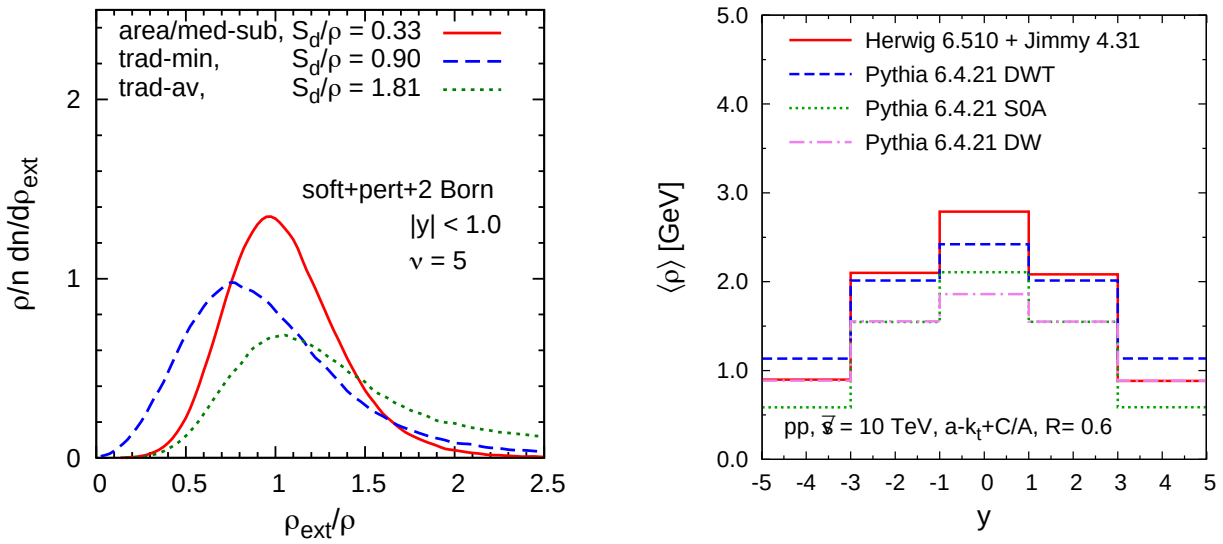

Figure 1: Left: Distribution of $\rho_{\rm ext}$ from toy model. Right: Rapidity dependence of $\langle\rho\rangle$ from series of MC model.

(y and ϕ cuts) and a finite number of objects (particles, jets). The magnitude of these intrinsic event-to-event fluctuations is an important characteristic of a method.

Fig. 1 (left) shows the histograms of ρ from the toy dijet events extracted with the traditional method in its TransMin and TransAv variants and with the area/median method. The latter was used after removing the two hardest jets from the list of jets. We see that using the area/median based method results in the peak which is better both in terms of position and the width. The real difference is seen, however, in the values of the standard deviation. In the traditional method, it comes out as big as the value of ρ itself, while staying moderately small for the area/median method. The reason for this is again related to the difference in the sensitivity to the hard radiation between average and median (linear vs log(log) as discussed above for ρ).

4 Approaching real life: Monte Carlo study

The weak sensitivity of the area/median method to the hard radiation makes it advantageous for event-by-event studies and for measuring fluctuations. Therefore, we have used this method to examine the underlying event from a series of Monte Carlo generators and tunes. [1] We have carried out the study for dijet events at $\sqrt{s} = 10\,\text{TeV}$. The leading and next to leading jets, found with the anti-k_t algorithm [10] with $R = 0.6$, were required to lie in the rapidity window $|y| < 4$ and to have p_t greater than 100 GeV and 80 GeV, respectively. For the study of the UE we used the C/A algorithm with $R = 0.6$.

As a first step, we verified that the more realistic UE from MC models shows a number of characteristic features found in our study of the toy UE. Then, we have examined a series of observables of potential interest for measuring at the LHC.

The main quantity, $\langle\rho\rangle$, is show in Fig. 1 (right) as a function of y. We note that the rapidity dependence is quite strong and the exact level of the UE extrapolated for the LHC depends on the MC model/tune. UE may fluctuate both from point to point within a single event and from one event to another. The first kind of fluctuation is measured by $\langle\sigma\rangle$ and is shown in Fig. 2 (left). We see that all the models predict large intra-event fluctuations. Another interesting thing to note is that in Herwig they are nearly 40% smaller than in Pythia. This difference is consistent with the correlation coefficients shown in Fig. 2 (right) as a function of y_2 for a single y_1 bin. Altogether, the results from Figs. 1 and 2 illustrate the potential gain to be had from studying wider variety of observables.

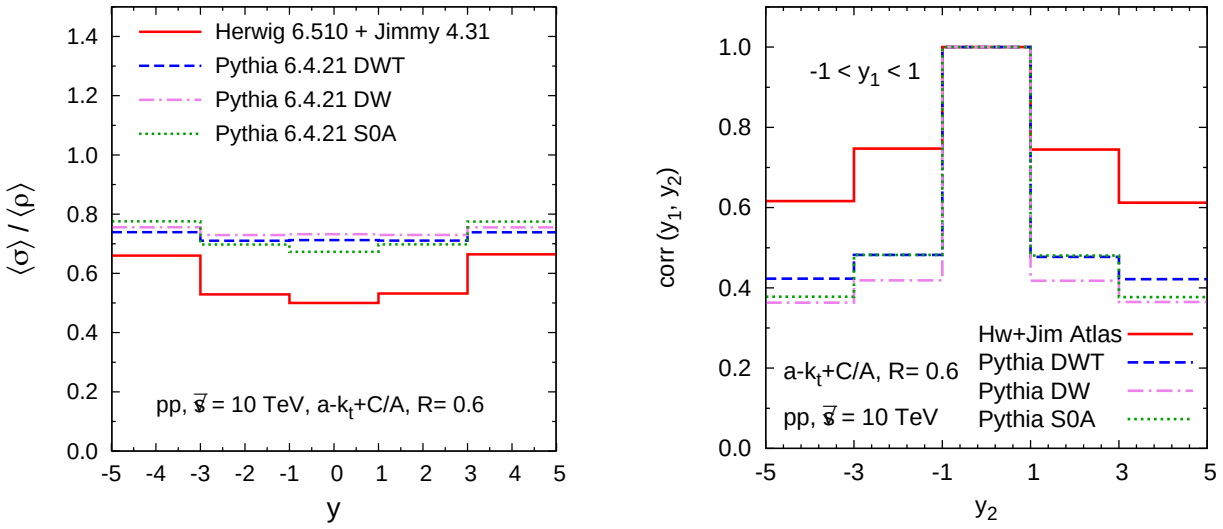

Figure 2: Left: Average intra-event fluctuation $\langle\sigma\rangle$ from series of MC models as function of rapidity. Right: Correlations of $\rho(y_2)$ with $\rho(y_1)$, as function of y_2 for y_1 in the bin $-1 < y < 1$.

5 Conclusions

We have carried out a twofold study devoted to the problem of measuring the underlying event. Using a simple toy model of UE, we have examined the methods of its determination. Subsequently, by studying the events simulated with MC generators, we have identified a range of important characteristics of the UE.

One conclusion from the toy model study is that for determinations of averaged quantities, like $\langle\rho\rangle$, both the traditional and the area/median measurement methods give comparably good results. In contrast, for event-by-event measurements and determinations of fluctuations of the soft component, the traditional approach is affected significantly more by the hard radiation.

Therefore, we chose the area/median method to examine more realistic UE from the MC models. We found noticeable differences between predictions of different generators/tunes extrapolated to LHC energy. For this reason we advocate measuring a broader range of observables including rapidity dependence of ρ, intra- and inter-event fluctuations and correlations.

Acknowledgments

The original results presented here were obtained with Matteo Cacciari and Gavin Salam. The work was supported in part by the French ANR under contract ANR-09-BLAN-0060.

References

1. M. Cacciari, G. P. Salam and S. Sapeta, JHEP **1004**, 065 (2010).
2. M. G. Albrow *et al.* [TeV4LHC QCD Working Group], arXiv:hep-ph/0610012.
3. D. Kar and R. Field (CDF collaboration), CDF/PUB/CDF/PUBLIC/9531, July (2008).
4. M. Cacciari and G. P. Salam, *Phys. Lett.* B **659**, 119 (2008).
5. M. Cacciari, G. P. Salam and G. Soyez, *JHEP* **0804**, 005 (2008).
6. M. Cacciari and G. P. Salam, *Phys. Lett.* B **641**, 57 (2006).
7. M. Cacciari, G. P. Salam and G. Soyez, FastJet, http://fastjet.fr
8. Y. L. Dokshitzer, G. D. Leder, S. Moretti and B. R. Webber, JHEP **9708**, 001 (1997).
9. M. Wobisch and T. Wengler, arXiv:hep-ph/9907280.
10. M. Cacciari, G. P. Salam and G. Soyez, JHEP **0804**, 063 (2008).

DETERMINATION OF THE STRONG COUPLING CONSTANT USING THE INCLUSIVE JET CROSS SECTION IN $p\bar{p}$ COLLISIONS at $\sqrt{s} = 1.96\,\mathbf{TeV}$

Robert J. Hirosky
Department of Physics, University of Virginia,
Charlottesville, Virginia

This talk presents a determination of the strong coupling constant α_s using a measurement of the inclusive jet cross section in $p\bar{p}$ collisions at $\sqrt{s} = 1.96\,\text{TeV}$ by the DØ Experiment. The energy dependence of the strong coupling constant is determined using jet measurements in the transverse momentum range $50 < p_T < 145\,\text{GeV}/c$. Comparing data with perturbative QCD calculations to order $O(\alpha_s^3)$ plus threshold corrections at $O(\alpha_s^4)$, we obtain the result $\alpha_s(M_Z) = 0.1161^{+0.0041}_{-0.0048}$. This is the most precise result obtained at a hadron-hadron collider

1 Introduction

The theory of quantum chromodynamics (QCD) has proven successful at describing the phenomenology of strong interactions over enormous ranges of interaction energies, from scales slightly higher than the mass of the proton upwards to the most energetic collisions so far observed. Although the value of the strong coupling constant α_s is not predicted at any finite scale, its energy dependence is calculable to high accuracy using perturbative QCD. A dramatic consequence of this energy dependence is that the strong force between quarks and gluons weakens when it is probed at increasingly small distance scales, leading to asymptotic freedom. The renormalization group equation (RGE) describes the dependence of α_s on the renormalization scale μ_r, or equivalently, on the momentum transfer q^2 in a strong interaction. Therefore, the determination of $\alpha_s(\mu_r)$ over a large range of momentum transfer serves as a powerful test of the RGE and asymptotic freedom. A variety of processes have been used to determine α_s, including measures of hadronic jet production rates in ep and e^+e^- collisions, precise measures of the hadronic branching fraction in τ decays, and calculations on the lattice with constrains from data on quarkonia states [1]. A previous determination of a_s in hadron-hadron collisions, presented by the CDF Collaboration and based on the inclusive jet cross section in $p\bar{p}$ collisions at $\sqrt{s} = 1.8\,\text{TeV}$, reported the value $a_s(M_Z) = 0.1178^{+0.0081}_{-0.0095}(\text{exp.})^{+0.0071}_{-0.0047}(\text{scale}) \pm 0.0059(\text{PDF})$ [2]. Taking advantage of improvements in experimental uncertainties, advances in perturbative QCD calculations, and progress in modeling of parton distributions, we present a new determination [3] of α_s and its q^2 dependence using data from the measurement of the inclusive jet cross section [4,5] with the DØ detector [6] in $p\bar{p}$ collisions at $\sqrt{s} = 1.96\,\text{TeV}$ at the Fermilab Tevatron Collider.

The D0 measurement of the inclusive jet cross section $d^2\sigma_{jet}/dp_T d|y|$ is the most precise measure of differential jet production rates at a hadron collider. Jets are reconstructed using the Run II iterative cone algorithm [7] with cone radius of 0.7 in rapidity and azimuthal angle (y, ϕ). Data are corrected to the particle level [8] for jet transverse momenta from 50 GeV to $600\,\text{GeV}/c$ in six regions of $|y|$. Uncertainties are smaller than those from parton distribution

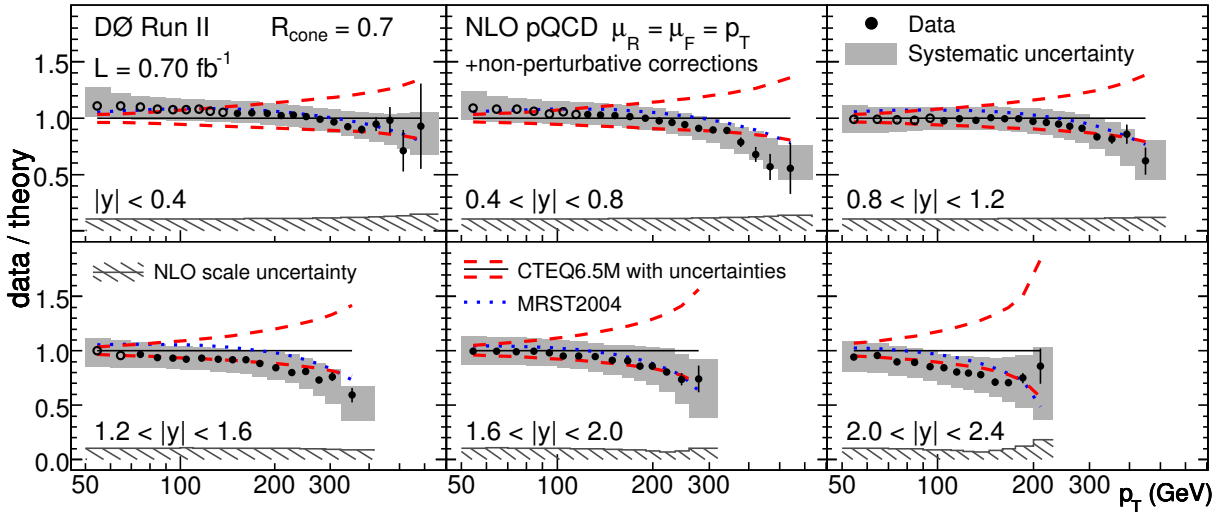

Figure 1: Data divided by theory for the D0 inclusive jet cross section as a function of jet p_T in six $|y|$ bins. Systematic uncertainties on data are shown by the shaded band. NLO pQCD calculations using the CTEQ6.5M PDFs and including non-perturbative corrections are compared to the data. The CTEQ6.5 PDF uncertainties are shown as long dashed lines and the predictions with MRST2004 PDFs as short dashed lines. The scale uncertainty at NLO is $\approx 10-15\%$. Open circles mark the points used in the determination of α_s.

functions (PDFs) and scale dependence in NLO pQCD over a wide kinematic range as illustrated in Fig. 1. These data probe momentum scales in common with ep data and also scales well beyond those accessible in $ep \to$ jets and other determinations of α_s.

2 Analysis Method

The calculation of the inclusive jet cross section in hadron collisions using pQCD depends on α_s, a series of perturbative coefficients c_n, and parton distribution functions with parametrizations also depending on α_s. Thus the cross section can be written as:

$$\sigma^{jet}_{pert}(\alpha_s) = \left(\sum_n \alpha_s^n c_n\right) \otimes f_1(\alpha_s, x_1) \otimes f_2(\alpha_s, x_2) \tag{1}$$

where the sum is over all powers n of α_s. $f_{1,2}$ denote PDFs for the initial state hadrons with convolution over the momentum fractions x_1, x_2 of the partons. The dependence of α_s and the PDFs on the momentum scale is implicit. Each point in the inclusive jet cross section is sensitive to $\alpha_s(p_T)$ and hence the running of α_s.

We use a combined fit of selected data points along with the RGE to determine the value of $\alpha_s(M_Z)$. The method is summarized in Eqn. 2:

$$\chi^2(\xi, \vec{\epsilon}, \vec{\alpha}) = \sum_{i=1}^{npoints} \frac{\left[d_i - t_i(\xi, \vec{\alpha})\left(1 + \sum_j \delta_{ij}(\epsilon_j)\right)\right]^2}{\sigma^2_{i,stat.} + \sigma^2_{i,uncorr.}} + \sum_j \epsilon_j^2 + \sum_k \alpha_k^2 \tag{2}$$

A χ^2 is minimized with respect to the fit parameter $\xi = \alpha_s(M_Z)$. The data are represented by d_i and t_i is the pQCD theory including non-perturbative corrections for hadronization and the underlying event. The theory term contains the matrix element and depends on the PDFs. The symbols $\sigma^{stat.}$ and $\sigma^{uncorr.}$ represent statistical uncertainties on the data and systematic uncertainties that are uncorrelated between individual points. Both the data and theory are allowed to vary according to their correlated systematic uncertainties, $\vec{\epsilon}$ and $\vec{\alpha}$, respectively, where these

are constrained by prior knowledge of systematics (via the two terms on the right). The theory fitted to the data is calculated at $O(\alpha_s^3)$ next-to-leading order (NLO) with additional $O(\alpha_s^4)$ 2-loop terms from threshold resummation corrections [9], significantly reducing dependencies on renormalization and factorization (μ_f) scales in the calculation. The PDFs are parameterized at next-to-next-to-leading order (NNLO) using the distributions given by MSTW2008 [10,11]. This NNLO PDF set is determined for 21 different values of $\alpha_s(M_Z)$ in the range 0.107 - 0.127 in steps of 0.001, allowing for accurate interpolation to arbitrary values of $\alpha_s(M_Z)$ within the range provided. The calculations are performed using the program fastNLO [12]. Combining pQCD calculations from NLOJET++ [13,14] and corrections from Ref. [9], fastNLO allows fast recalculations of jet cross sections for arbitrary PDFs. Calculations are performed using $\mu_f = \mu_r = p_T^{\rm jet}$ and uncertainties from scale dependence in the theory are estimated by varying the scales by factors 0.5 and 2.0.

The MSTW2008 PDFs include the D0 inclusive jet data and these data provide dominant constraints on the parameterization of the momentum fractions carried by gluons at large-x. In the absence of having full documentation of the correlations between experimental and PDF uncertainties, the analysis is restricted to kinematic regions where the Tevatron jet data do not provide significant constraints to the PDFs. This corresponds to gluon momentum fractions $\lesssim 0.3$. At leading order the parton x values may be determined in di-jet events via $x_1 = x_T(e^{y_1} + e^{y_2})/2$ and $x_2 = x_T(e^{y_1} - e^{y_2})/2$ with $x_T = 2p_T/\sqrt{s}$. Because the inclusive jet cross section is binned according to the p_T of the leading jet only, it is not possible to define a unique mapping for a given bin in p_T and $|y|$. An approximation is based on the variable $\tilde{x} = x_T \cdot (e^{|y|} + 1)/2$ that represents the maximum of the values x_1, x_2 if all sub-leading jets in the event are treated as single jet with rapidity $|y| = 0$. Requiring $\tilde{x} < 0.15$ restricts the data points to those where a majority of events satisfy $x_{max} < 0.25$. This leaves 22 of 110 data points to use in the measurement of α_s, these points are shown as open circles in Fig. 1. Since this requirement is somewhat arbitrary, variations in the cut value are used to determine an additional systematic uncertainty on the measurement.

3 Results

Data with similar p_T from different $|y|$ intervals are grouped into nine transverse momentum intervals to determine $\alpha_s(M_Z)$ and $\alpha_s(p_T)$. A combined fit to the data points and inclusion of all systematic uncertainties yields $\alpha_s(M_Z) = 0.1161^{+0.0041}_{-0.0048}$. The results for the combined p_T values in the range of $50 < p_T < 145\,\mathrm{GeV}/c$ are given in Fig. 2(a). The full uncertainties shown for each value are largely correlated among the data points. Figure 2(b) displays the same data plotted as a function of $1/log(p_T)$, showing consistency with asymptotic freedom. The largest contribution to the uncertainties is due to the correlated experimental uncertainty, dominated by jet energy calibration, jet transverse momentum resolution, and normalization by the integrated luminosity. Scaling the non-perturbative corrections by factors of 0.5 and 2.0 changes the central result by $^{+0.0003}_{-0.0010}$. Replacing the MSTW2008 NNLO PDFs by the CTEQ 6.6 PDFs leads to an increase of 0.5%, this is significantly less than the PDF uncertainty of $^{+0.0012}_{-0.0011}$. Removing the 2-loop threshold corrections and using NLO pQCD together with the MSTW2008 NLO PDFs and the 2-loop solution to the RGE yields $\alpha_s(M_Z) = 0.1201^{+0.0072}_{-0.0059}$. This increase in the central value, originating from the missing $O(\alpha_s^4)$ contributions, is well within the scale uncertainty of the NLO result.

The results obtained for $\alpha_s(p_T)$ are consistent with the energy dependence predicted by the RGE and extend the results based on the HERA jet data [15]. The value obtained for $\alpha_s(M_Z)$ is consistent with the the world average value [1] and are of similar precision to those obtained in $ep \to$ jets. This is the most precise measure of the strong coupling constant at a hadron collider and provides the highest momentum scale test of the running of α_s.

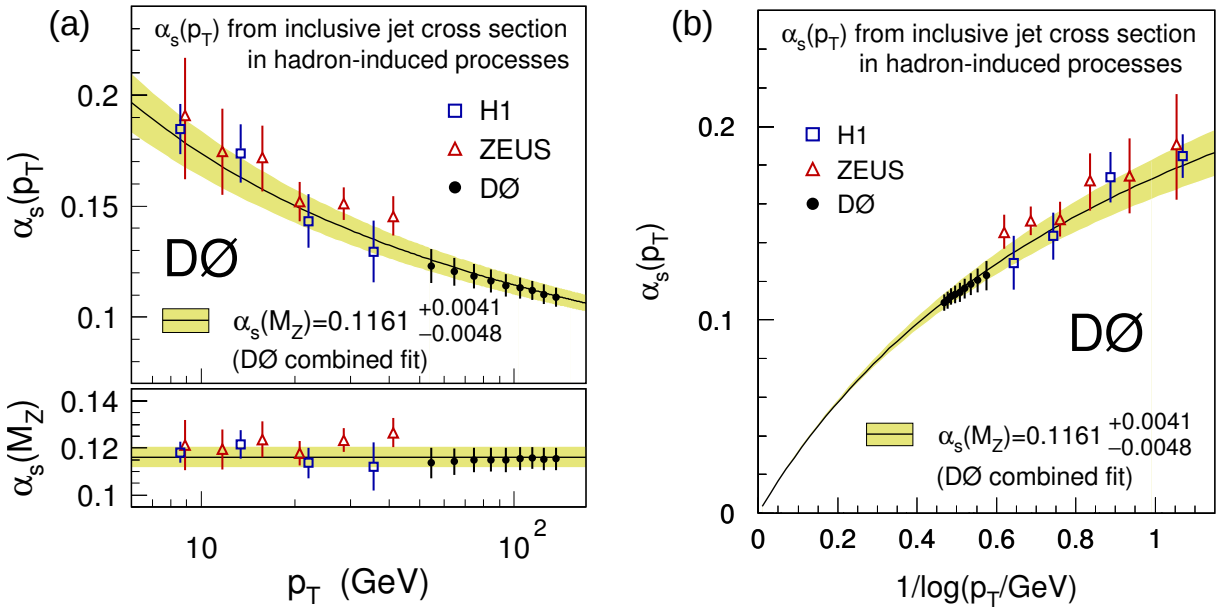

Figure 2: (a) Measurement of $\alpha_s(p_T)$ (top) and $\alpha_s(M_Z)$ (bottom). Data points are shown with their total uncertainties. (b) The same plotted as a function of $1/log(p_T)$ showing consistency with asymptotic freedom.

References

1. S. Bethke, Eur. Phys. J. C **64**, 689-703 (2009).
2. T. Affolder et al. (CDF Collaboration), Phys. Rev. Lett. **88**, 042001 (2002).
3. V. M. Abazov et al. (D0 Collaboration), Phys. Rev. D **80**, 111107 (2009).
4. V. M. Abazov et al. (D0 Collaboration), Phys. Rev. Lett. **101**, 062001 (2008).
5. Tables of the inclusive jet cross section results and the uncertainties are available from EPAPS Document No. E-PRLTAO-101-033833, http://www.aip.org/pubservs/epaps.html.
6. V. M. Abazov et al. (D0 Collaboration), Nucl. Instrum. Methods Phys. Res. A **565**, 463 (2006).
7. G. C. Blazey et al., FERMILAB Report No. FERMILAB-PUB-00-297
8. C. Buttar et al., arXiv:0803.0678, Sec. 9.
9. N. Kidonakis and J. F. Owens, Phys. Rev D **63**, 054019 (2001).
10. A. D. Martin, W. J. Stirling, R. S. Thorne and G. Watt, Eur. Phys. J. C **63**, 189 (2009).
11. A. D. Martin, W. J. Stirling, R. S. Thorne and G. Watt, Eur. Phys. J. C **64**, 653 (2009).
12. T. Kluge, K. Rabbertz and M. Wobisch, DESY-06-186, FERMILAB-CONF-06-352-E, arXiv:hep-ph/0609285 (2006).
13. Z. Nagy, Phys. Rev. D **68**, 094002 (2003).
14. Z. Nagy, Phys. Rev. Lett. **68**, 122003 (2002).
15. C. Glasman, (H1 and ZEUS Collaborations), J. Phys. Conf. Ser. **110**, 022013 (2008).

TAKING $D \neq 4$ SERIOUSLY: NUMERICAL REAL−VIRTUAL CANCELLATIONS IN MELLIN SPACE

Nicolas HOUDEAU[a] and Matteo CACCIARI[a,b]
[a] *LPTHE - CNRS et UPMC, Paris, France*
[b] *Université Paris Diderot, Paris, France*

We propose a method to combine the various, separately divergent, contributions of a differential cross section in a purely numerical way. We show how performing an integral transform allows one to perform a numerical cancellation of the regularized divergences, both in the total cross section and in the differental distributions case, and obtain an accurate and finite result. As a proof of principle, we apply the method to a simple example, $e^+e^- \to q\,\bar{q}$ hard cross section at first order in α_S.

1 Introduction

The Large Hadron Collider (LHC) has started producing pp collisions at 7 TeV centre-of-mass energy, and the experimental collaborations are now performing their first analyses. Their results will be compared to theoretical predictions which have been obtained in the past several years by the phenomenology community, and to others that must still be calculated to even higher order in perturbation theory before they can meet the experimentalists' necessities [1].

The phenomenologists' Grail would be a fully automated method of calculation. However, the available procedures often require extensive work to be adapted to each specific processes, a number of steps in cross section calculations involving non-systematic procedures. For instance, even analytic continuation has to be worked out independently for many different functions, and this limits a method's automatization: the processes it can be applied to can only involve functions whose analytic continuations are already known.

In this work we wish to propose a method that makes it potentially simpler to automate one of the many operations that must be performed in order to evaluate a physical cross section, namely the combination of virtual and real contributions. Our aim will be to perform in a purely numerical way the cancellation of their singularities appearing as poles in powers of $1/\epsilon$ in dimensional regularization. This operation can of course already be performed in a number of different ways, for instance during the integration over phase space using the slicing [2] or the subtraction method [3,4]. However, we speculate that our new method may be fruitfully employed as one of the building blocks of a different approach to automated cross sections calculations.

2 Numerical combination

We consider the combination of the different contributions of a differential hard cross-section: virtual and real terms, and possibly a collinear counter-term. In the standard procedure, this combination is performed by first expanding in power series of ϵ the various terms. A certain

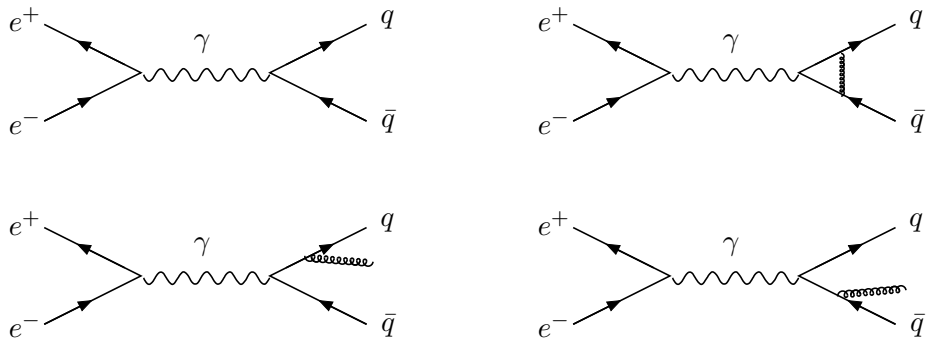

Figure 1: Born (top left), virtual (top right) and real (bottom) Feynman diagrams contributing to the first α_S order of the $e^+e^- \to q\,\bar{q}(g)$ hard cross section.

amount of analytical manipulation is necessary, though it can be automated to a large extent. We propose instead to combine the various contributions in a fully numerical way. In order to do so we use an integral transform, the Mellin one:

$$\mathcal{M}(f)(n) = \tilde{f}(n) = \int_0^1 f(x)x^{n-1}dx \qquad \mathcal{M}^{-1}(\tilde{f})(x) = f(x) = \frac{1}{2\pi i}\int_{c-i\infty}^{c+i\infty} x^{-n}\tilde{f}(n)dn \tag{1}$$

The reason for doing so is that the distributions that typically appear in the process of performing the series expansion in powers of ϵ will now be represented by standard functions, susceptible of immediate numerical evaluation. Denoting $\sigma_\epsilon^{(r)}(n)$, $\sigma_\epsilon^{(v)}(n)$ and $\sigma_\epsilon^{(c)}(n)$ the Mellin transforms of the real and virtual parts, and of the collinear counterterm respectively, we can write the full observable cross section as

$$\sigma(n) = \lim_{\epsilon\to 0}\left[\sigma_\epsilon^{(r)}(n) + \sigma_\epsilon^{(v)}(n) + \sigma_\epsilon^{(c)}(n)\right] \tag{2}$$

where both the sum and the $\epsilon \to 0$ limit will be performed numerically. No series expansion of the separate terms in series of ϵ will be necessary either. One can of course then recover the differential cross section $d\sigma/dx$ by numerical inverse Mellin transform, see eq. (1).

3 Proof of principle: the $e^+e^- \to \gamma^* \to q\,\bar{q}(g)$ hard process

3.1 Differential cross section contributions

As a proof of principle, we investigate the case of the $e^+e^- \to \gamma^* \to q\,\bar{q}(g)$ hard process (Fig 1). More precisely, we consider its one-particle inclusive differential cross-section to order α_S in the Björken variable : $x = 2p.q/q^2$, with p and q being the final state quark and the virtual photon four-momentum respectively.

The full results in dimensional regularization for the the differential cross-section contributions' expressions (real, virtual and $\overline{MS}$ counter-term) in x-space are

$$\begin{aligned}
\frac{d\sigma_\epsilon^{(r)}}{dx} &= \frac{C_F\alpha^2\alpha_S}{W^2}\left(\frac{W^2}{4\pi\mu^2}\right)^{-2\epsilon}\frac{\Gamma(2-\epsilon)^2x^{-2\epsilon}}{(3-2\epsilon)\Gamma(2-2\epsilon)^2}\Big((\epsilon^2-7\epsilon+2)x^2-4\epsilon(\epsilon-2)x+(4\epsilon^2-6\epsilon+2)\Big)\frac{[1-x]^{-1-\epsilon}}{-\epsilon}\\
\frac{d\sigma_\epsilon^{(v)}}{dx} &= \left(\frac{4-2\epsilon}{3-2\epsilon}-2\epsilon\right)\frac{\pi\alpha^2}{W^2}\left[\left(\frac{W^2}{4\pi\mu^2}\right)^{-\epsilon}2^{2\epsilon}\frac{\sqrt{\pi}/2}{\Gamma(\frac{3}{2}-2\epsilon)}\right]\left[1-\left(\frac{W^2}{4\pi\mu^2}\right)^{-\epsilon}\frac{C_F\alpha_S}{\pi}\cos(\epsilon\pi)F_\epsilon\right]\delta(1-x)\\
\frac{d\sigma_\epsilon^{(c)}}{dx} &= \left(\frac{4-2\epsilon}{3-2\epsilon}-2\epsilon\right)\frac{C_F\alpha^2\alpha_S}{2W^2}\left[\left(\frac{W^2}{4\pi\mu^2}\right)^{-\epsilon}2^{2\epsilon}\frac{\sqrt{\pi}/2}{\Gamma(\frac{3}{2}-2\epsilon)}\right]\frac{1}{\Gamma(1-\epsilon)}\frac{1}{\epsilon}\left[\frac{1+x^2}{1-x}\right]_+
\end{aligned} \tag{3}$$

with

$$F_\epsilon = 1 + \Gamma(-\epsilon)\frac{\Gamma(1+\epsilon)}{\Gamma(2-2\epsilon)}\left(\Gamma(-\epsilon)+\frac{1}{2}\Gamma(1-\epsilon)\right) \tag{4}$$

These expressions can be Mellin-transformed exactly, and yield

$$\begin{aligned}
\sigma_\epsilon^{(r)}(n) &= \left(\frac{2-2\epsilon}{3-2\epsilon}\right)\frac{C_F\alpha^2\alpha_S}{W^2}\left[\left(\frac{W^2}{4\pi\mu^2}\right)^{-2\epsilon}\frac{\Gamma(2-\epsilon)}{\Gamma(2-2\epsilon)^2}\right]\frac{\Gamma(-\epsilon)^2\ \Gamma(n-2\epsilon)}{\Gamma(2+n-3\epsilon)}\times \\
&\qquad\qquad \times\left[2n(1+n)-5(1+\frac{n}{2}(5+n))\epsilon+(21+\frac{n}{2}(25+n))\epsilon^3+8\epsilon^4\right] \\
\sigma_\epsilon^{(v)}(n) &= \left(\frac{4-2\epsilon}{3-2\epsilon}-2\epsilon\right)\frac{\pi\alpha^2}{W^2}\left[\left(\frac{W^2}{4\pi\mu^2}\right)^{-\epsilon}2^{2\epsilon}\frac{\sqrt{\pi}/2}{\Gamma(\frac{3}{2}-2\epsilon)}\right]\left[1-\left(\frac{W^2}{4\pi\mu^2}\right)^{-\epsilon}\frac{C_F\alpha_S}{\pi}\cos(\epsilon\pi)F_\epsilon\right] \\
\sigma_\epsilon^{(c)}(n) &= \left(\frac{4-2\epsilon}{3-2\epsilon}-2\epsilon\right)\frac{C_F\alpha^2\alpha_S}{2W^2}\left[\left(\frac{W^2}{4\pi\mu^2}\right)^{-\epsilon}2^{2\epsilon}\frac{\sqrt{\pi}/2}{\Gamma(3/2-2\epsilon)}\right]\frac{1}{\epsilon\Gamma(1-\epsilon)}\left[-2\sum_{i=1}^{n+1}\frac{1}{i}+\frac{2n+1}{n(n+1)}+\frac{3}{2}\right]
\end{aligned} \tag{5}$$

3.2 Combination

As mentioned above, the standard analytical procedure would consist in expanding each x-space expression in powers of ϵ and summing the results order by order. The singularities must cancel for all the terms with negative powers of ϵ, and one then simply takes the limit for ϵ going to zero of the remainder. The result being finite, this is equivalent to taking the sum of the zeroth order coefficients. The automatization of this procedure is straightforward as long as as one knows the expansions of the different functions of ϵ. However, the appearance of distributions at this stage prevents a straightforward numerical approach.

In n-space, the contributions' expressions are standard functions. This means that we can perform their sum and the limit numerically, without any analytical manipulation. The limit $\epsilon \to 0$ can be evaluated in different ways. Two methods are presented in figure 2, where the cross section as a function of ϵ, $\sigma_\epsilon(n)$, is presented divided by its 'exact' result, i.e. the analytical limit $\sigma(n) = \lim_{\epsilon\to 0}\sigma_\epsilon(n)$ (of course, $\sigma(n)$ can also be thought of as the Mellin transform of the cross section calculated with more standard techniques).

In the left plot, the numerical calculation of $\sigma_\epsilon(n=1)$ has been performed for ϵ values small enough to reach a precision which is sufficient for phenomenology applications. The limit can be approximated by the value of $\sigma_\epsilon(n=1)$ for a small ϵ. In fact, one can see that in a large region $10^{-3} > |\epsilon| > 10^{-6}$ the calculation is numerically stable and its result well within a few per mille of the exact value. In the right plot, the Mellin transforms have been performed numerically in order to simulate a more demanding calculation. In this situation, the numerical precision limits the calculation of $\sigma_\epsilon(n)$ to larger values of $|\epsilon|$, and one cannot anymore approximate the limit by taking ϵ small. In such cases, one can instead use a fit in the region near $\epsilon = 0$ and approximate the limit of $\sigma_\epsilon(n)$ with the value of the fitting function at $\epsilon = 0$. Any precision requirement can be met by properly choosing the value of ϵ in the first method, or the position of the fitted points and the order of the fit in the second. In fact, the first method corresponds to a zeroth order fit.

4 Conclusions and perspectives

We have proposed the use of integral transforms as a way to allow for an easy numerical approach to the problem of combining virtual and real contributions in cross section evaluations. We have shown that the simple case of $e^+e^- \to q\bar{q}(g)$ one-particle inclusive differential hard cross-section

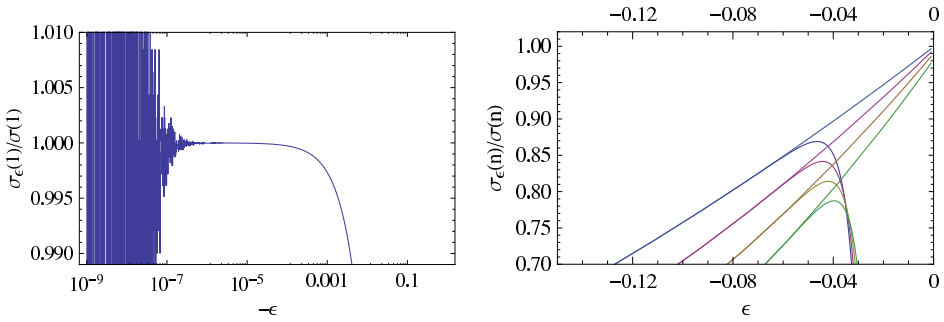

Figure 2: Ratio of the calculated cross section $\sigma_\epsilon(n)$ for $\epsilon \neq 0$ and its exact value for $n = 1$ on the left, and $n = 1$, 10, 10^2 and 10^3 (top to bottom) on the right, as functions of ϵ. In the left plot, $\sigma_\epsilon(1)$ is the sum of the numerical values of the different contributions directly obtained from their analytical expressions in Mellin space. In the right plot, the contributions' values are calculated with a numerical Mellin transform of their analytical expression in x space, and the limits for $\epsilon \to 0$ are evaluated by extrapolating to $\epsilon = 0$ the quadratic fits shown in the plot.

can be treated straightforwardly using a Mellin transform. One advantage of this method is that it does not rely in any way on the knowledge of the soft-collinear limit of the matrix elements: it can therefore used immediately and identically at any order in perturbation theory.

Of course, the burden of the analytical manipulation has been, in first instance, only shifted from the series expansion of the dimensional-regularized expression to the calculation of the Mellin transform. This is straightforwardly done in the simple case that we have treated, but will in general be much harder or even impossible. A possible avenue is to perform the transform numerically, but as we have seen this has a cost in terms of numerical accuracy. An alternative approach is to follow the method proposed in ref. [5], and perform the Mellin transform before the integration over phase space.

Other possible roadblocks concern the extension to more than one variable, in order to obtain fully exclusive distributions. While the problem of performing a multi-dimensional Mellin transform does not appear daunting, their numerical inversion seems instead much more complex than the mono-dimensional case, and we have not yet seriously tackled it. This extension, as well as different approaches to the calculation of the Mellin transforms themselves, will be the subject of future investigations.

References

1. J. R. Andersen *et al.*, arXiv:1003.1241 [hep-ph]
2. K. Fabricius, G. Kramer, G. Schierholz and I. Schmitt, *Z. Phys.* C **11**, 315 (1981); G. Kramer and B. Lampe, *Fortschr. Phys.* **37**, 161 (1989).
3. R.K. Ellis, D.A. Ross and A.E. Terrano, *Nucl. Phys.* B **178**, 421 (1981)
4. S. Catani, and M. H. Seymour, *Nucl. Phys.* B **485**, 291 (1997) [hep-ph/9605323v3]
5. A. Mitov, *Phys. Lett.* B **643**, 366 (2006) [hep-ph/0511340]

CALCULATION OF QCD LOOPS USING TREE-LEVEL MATRIX ELEMENTS

JAN WINTER [a]
Theoretical Physics Department,
Fermi National Accelerator Laboratory, P.O. Box 500, Batavia, IL 60510, USA

The possibility of treating colour in one-loop amplitude calculations alike the other quantum numbers is briefly discussed for semi-numerical algorithms based on generalized unitarity and parametric integration techniques. Numerical results are presented for the calculation of virtual corrections in multi-gluon scattering.

1 An algorithmic solution based on generalized unitarity for the evaluation of colour-dressed one-loop amplitudes

The evaluation of QCD higher-order corrections in particular for multi-particle processes is indispensable for a good understanding of total and differential cross sections at hadron colliders such as the Tevatron or the LHC. The automation of these calculations at the next-to-leading order (NLO) in the strong coupling constant has been a very appealing goal ever since the Monte Carlo tools dealing with the computation of tree-level cross sections have matured and been greatly optimized. Over the past few years a number of subtraction codes has been developed handling the cancellations of singularities occurring in NLO calculations in a general way. Accordingly a standard interface has lately been agreed on between Monte Carlo tools and one-loop matrix-element programs [1,2]. Recently these programs have also shown a remarkable advancement. New techniques based on combining generalized unitarity and parametric integration methods have become available and made the computation of multi-leg one-loop corrections feasible. Prominent examples are given by the vector boson plus 3 jet NLO predictions provided by the BlackHat and Rocket groups [3,4,5,6] and the $t\bar{t}$ plus 1 jet NLO result [7]. These calculations separate the treatment of the colour quantum numbers from the other degrees of freedom, which makes it harder to fully automatize these approaches. In a recent publication [8] it has been shown that the Ellis–Giele–Kunszt–Melnikov algorithm [9] can be extended to treat colour along the same line with the other quantum numbers. Given the implementation for ordered gluon one-loop amplitudes [10], the important changes are: the sums over ordered cuts present in the decomposition of the one-loop integrands and amplitudes are replaced by sums over unordered partitions including their non-cyclic and non-reflective permutations. Gluon bubble contributions now come with a symmetry factor of 1/2!. The integrand's residues are calculated through products of colour-dressed tree-level amplitudes obtained from dressed recursion relations where internal colour degrees of freedom are summed over. Finally, to extract the lower-point coefficients, the subtraction terms due to higher-cut contributions are identified by a de-pinching procedure that may involve loop-momentum shifts by external momenta.

[a] Talk presented at the 45th Rencontres de Moriond, Workshop on QCD and High Energy Interactions, March 13-20, 2010 at La Thuile, Italy.

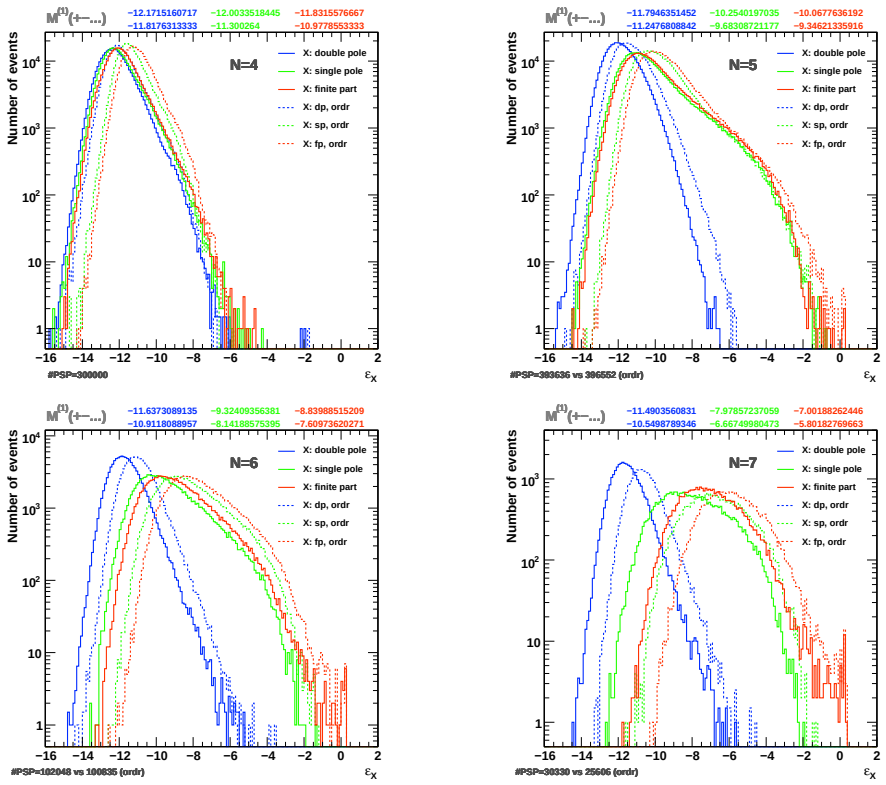

Figure 1: Double-, single-pole and finite-part accuracy distributions obtained from double-precision computations of one-loop amplitudes for $N = 4, 5, 6, 7$ gluons with polarizations $\lambda_k = + - + - \ldots$ and randomly chosen non-vanishing colour configurations. Results from the colour-dressed algorithm are compared to those of the colour-ordered method (labeled "ordr") indicated by dashed curves. The mean accuracies and the number of randomly picked phase-space points (subject to the cuts detailed in the text) are displayed at the top and bottom left of the plots, respectively. Phase-space points required to be calculated at higher precision were vetoed.

2 Numerical calculation of multi-gluon one-loop corrections

Taking the example of multi-gluon scattering, the performance and major results of the algorithm briefly introduced in Section 1 are discussed below. A more comprehensive description of the outcomes of these numerical calculations can be found in the original paper [8].

The convenient way to cross-check the results of the colour-dressed algorithm for the full one-loop amplitudes for N gluons is to make use of the colour decomposition approach. Given the polarization states $\lambda_k \in \{+, -\}$ of the $k = 1, \ldots, N$ gluons and their colours $(ij)_k$ using the colour-flow notation $i_k, j_k \in \{1, 2, 3\}$, one sums up all relevant ordered amplitudes after having multiplied them by their corresponding colour factors. The colour-ordered N-gluon one-loop amplitudes are computed with the algorithm [10] based on the original Ellis–Giele–Kunszt–Melnikov method. The quality of the one-loop amplitude determination can be analyzed by means of the logarithmic relative deviations of the double (dp) and single poles (sp) and the finite part (fp). They are defined as follows:

$$\varepsilon_{\rm dp} \;=\; \log_{10} \frac{|\mathcal{M}^{(1)[1]}_{\rm dp,num} - \mathcal{M}^{(1)}_{\rm dp,th}|}{|\mathcal{M}^{(1)}_{\rm dp,th}|}\,, \qquad \varepsilon_{\rm s/fp} \;=\; \log_{10} \frac{2\,|\mathcal{M}^{(1)[1]}_{\rm s/fp,num} - \mathcal{M}^{(1)[2]}_{\rm s/fp,num}|}{|\mathcal{M}^{(1)[1]}_{\rm s/fp,num}| + |\mathcal{M}^{(1)[2]}_{\rm s/fp,num}|}\,, \tag{1}$$

Two independent solutions denoted by [1] and [2] are used to test the accuracies of the single poles and finite parts. The analytic structure of the double poles is particularly simple and proportional to the Born amplitudes, $\mathcal{M}^{(1)}_{\rm dp,th} = -(c_\Gamma/\epsilon^2)\, N\, N_{\rm C}\, \mathcal{M}^{(0)}$ where $N_{\rm C}$ denotes the number of colours. This allows for a direct comparison with the semi-numerical results. Figure 1 shows

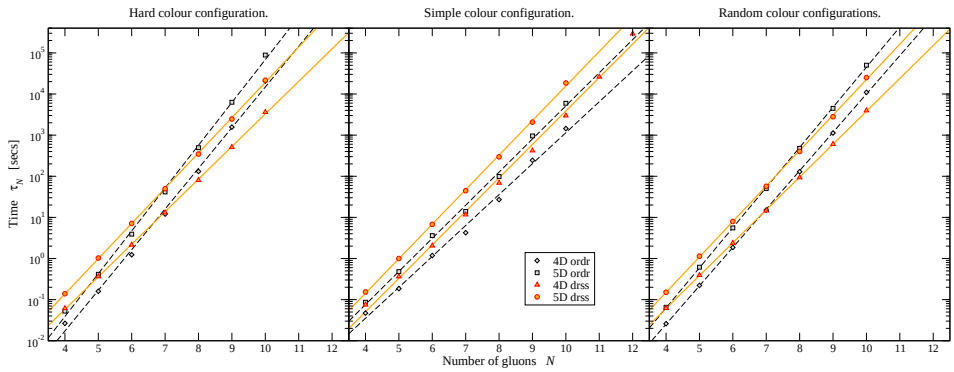

Figure 2: Times τ_N to compute two N-gluon one-loop amplitudes for a hard, a simple and random colour configurations using 3.0 and 2.66 GHz Intel Core2 Duo processors. The solid and dashed curves represent fit results for the colour-dressed (drss) and colour-ordered (ordr) approach, respectively. The times to compute the cut-constructible part of the amplitudes using the 4-dimensional (4D) versions of the algorithms are also shown.

the ε-distributions in absolute normalization obtained by using double-precision computations for various numbers of external gluons with alternating polarization states. The phase-space points are accepted if the generated momenta satisfy the cuts: $|\eta_n| < 2\,,\ p_{\perp,n} > 0.1\,|E_1 + E_2|$ and $\Delta R_{kn} > 0.7$ where η_n and $p_{\perp,n}$ respectively denote the pseudo-rapidity and transverse momentum of the n-th outgoing gluon ($n = 3, \ldots, N$); the ΔR_{kn} describe the pairwise geometric separations in η and azimuthal-angle space of gluons k and n. For $N \geq 5$ gluons, a small fraction of events requires higher than double precision calculations to reliably determine the master-integral coefficients.[b] These phase-space points can be identified by a simple procedure testing the stability of the solutions for the bubble coefficients that contribute to the cut-constructible part. As seen in the plots of Figure 1 the gluon one-loop amplitudes can be determined quite accurately for the bulk of the events. The tails are sufficiently under control and fall off more steeply for larger ε-values owing to the veto on points that yield unstable solutions in double-precision calculations. The distributions and peak positions of the double poles are rather stable while those of the single poles and finite parts noticeably shift to larger ε with an increasing number N of gluons. In all cases the dressed approach is seen to provide more accurate results than the method relying on the colour decomposition.

The complexity of the colour-dressed tree-level recursion relations and the asymptotic behaviour of the Stirling numbers of the second kind that govern the growth of the number of the unitarity cuts both follow an exponential scaling law when more legs are added. The colour-dressed algorithm is hence expected to scale similarly with N, i.e. the computing time τ_N is proportional to x^N where x is an attribute of the implemented algorithm. Relying on the colour decomposition, the ordered one-loop amplitude calculations exhibit polynomial complexity while the number of orderings that need be evaluated for one colour configuration grows factorially. The effective growth however will be determined by the increase in the number of non-vanishing orderings. Figure 2 depicts how the N-gluon one-loop amplitude computation times scale with increasing N for different examples of assigning the gluons' colour states. Amplitudes with a small number of gluons, $N \leq 6$, can always be calculated faster using the colour decomposition. This remains true as long as there is a sufficient number of vanishing orderings, i.e. one deals with simple colour configurations only. In all other cases – for random colour assignments most importantly – the colour-dressed method takes over for $N \geq 7$ owing to its milder exponential growth. The curve fitting for the general case indicates base-values of $x = 7.3(1)$ for the dressed algorithm versus $x = 9.5(1)$ when using the colour decomposition. One notices that the factorial growth caused by the sum over orderings has been tamed to become effectively exponential.

[b] For $N = 6$ and 7 gluons, about 3% and 10% of the events need be treated in higher precision, respectively.

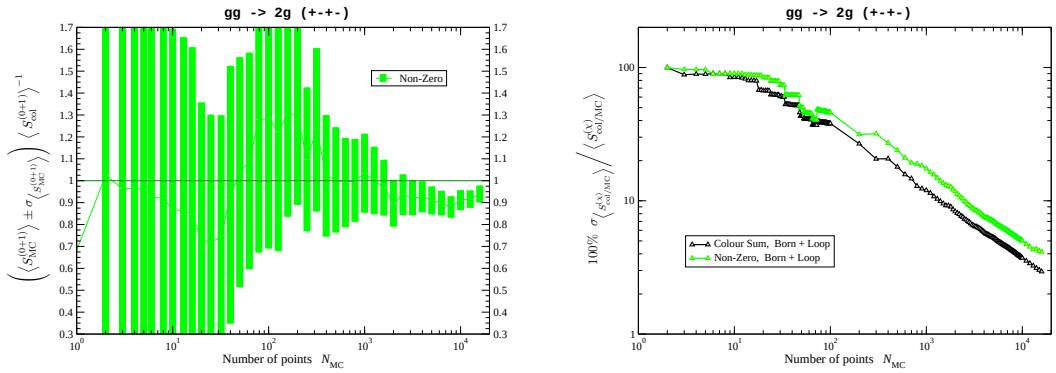

Figure 3: Consistency check for and relative errors of the phase-space integrations of colour-summed and colour-sampled amplitudes at the Born plus virtual-correction level. The distributions are given as functions of the number of generated uniform phase-space points; cuts are specified in the text. After 15900 events one obtains $\langle S_{\rm MC}^{(0+1)}\rangle/\langle S_{\rm col}^{(0+1)}\rangle = 0.939 \pm 0.039({\rm MC}) \pm 0.028({\rm col})$ with the left plot showing errors due to colour sampling only.

Utilizing the ability of calculating the full one-loop amplitudes for multiple gluons, one can study the effect of the Monte Carlo sampling over non-vanishing ("Non-Zero") colour configurations on the performance of phase-space integrations for the Born plus virtual contributions. Figure 3 shows the simplest example of $2 \to 2$ gluon scattering. The colour-sampled and colour-summed integrals are defined as $S_{\rm MC}^{(0+1)} = W_{\rm col} \times \mathcal{K}$ and $S_{\rm col}^{(0+1)} = \sum_{\rm col} \mathcal{K}$, respectively, where the colour weight $W_{\rm col}$ depends on the actual colour configuration ("col") and the kernel is given by

$$\mathcal{K} \;=\; \left|\mathcal{M}^{(0)}\right|^2 + \frac{\widehat{\alpha}_s}{2\,\pi}\,\Re\left(\mathcal{M}_{\rm fp}^{(1)}\,\mathcal{M}^{(0)\,\dagger}\right) \qquad \text{with} \quad \widehat{\alpha}_s \equiv 0.12\;. \tag{2}$$

In the left panel of Figure 3 the sampled and summed integrations are shown to converge after about 10^3 Monte Carlo steps, $N_{\rm MC}$, while in the right panel their relative errors are displayed as a function of $N_{\rm MC}$. One finds that the colour sampling only introduces an additional integration uncertainty, which can be reduced more easily than the full colour sum can be carried out.

Acknowledgments

I thank the organizers for creating a fantastic atmosphere during the course of the workshop. I also would like to acknowledge my collaborators Walter Giele and Zoltan Kunszt for many exciting and important discussions while working on this subject. Fermilab is operated by the Fermi Research Alliance under CN DE-AC02-07CH11359 with the U.S. Department of Energy.

References

1. T. Binoth *et al.*, arXiv:1001.1307 [hep-ph].
2. J. R. Andersen *et al.* [SM and NLO Multileg Working Group], arXiv:1003.1241 [hep-ph].
3. C. F. Berger *et al.*, Phys. Rev. D **80** (2009) 074036 [arXiv:0907.1984 [hep-ph]].
4. C. F. Berger *et al.*, arXiv:1004.1659 [hep-ph].
5. R. K. Ellis, K. Melnikov, G. Zanderighi, Phys. Rev. D **80** (2009) 094002 [arXiv:0906.1445].
6. K. Melnikov and G. Zanderighi, Phys. Rev. D **81** (2010) 074025 [arXiv:0910.3671 [hep-ph]].
7. K. Melnikov and M. Schulze, arXiv:1004.3284 [hep-ph].
8. W. T. Giele, Z. Kunszt and J. Winter, arXiv:0911.1962 [hep-ph].
9. R. K. Ellis, W. T. Giele, Z. Kunszt, JHEP **0803** (2008) 003 [arXiv:0708.2398 [hep-ph]]; W. T. Giele, Z. Kunszt, K. Melnikov, JHEP **0804** (2008) 049 [arXiv:0801.2237 [hep-ph]].
10. J. Winter and W. T. Giele, arXiv:0902.0094 [hep-ph].

$e^+e^- \to$ HADRONS IN INITIAL STATE RADIATION AND TWO-PHOTON REACTIONS WITH BELLE AND BABAR

F. ANULLI
INFN, Sezione di Roma,
P.le Aldo Moro, 2 00185 Rome, Italy

We report on recent results of a variety of Belle and *BABAR* measurements of hadron production involving e^+e^- initial state radiation and two photon production. These include the precision measurement of the cross section of $e^+e^- \to \pi^+\pi^-$ and its implication for the hadronic vacuum polarization correction to the anomalous magnetic moment of the muon; search for new states in open-charm production; two-photon production of pairs of light pseudoscalar mesons and measurement of pseudoscalar meson transition form factors.

1 Introduction

Several aspects about the nature and production mechanisms of many hadronic states are still poorly known or controversial. Study of exclusive final states at the B-factories, thanks to the huge statistics and the clean experimental environment, can help on shedding light to that open questions. We provide here a short review of the most recent results obtained using Initial State Radiation (ISR) or two-photon fusion ($\gamma\gamma$) events, with Belle and *BABAR*, the two experiments that have operated for about ten years at the B-factories KEKB and PEP-II, respectively. Due to the limited space, we give a description of the light hadrons production only, and provide the proper references to the other results presented at the conference, namely, open-charm production with ISR ($e^+e^- \to D^{(*)}\bar{D}^{(*)}$ [1,2], $e^+e^- \to D\bar{D}^{(*)}\pi$ [3]), and the process $\gamma\gamma \to D\bar{D}$ [4].

2 Hadronic cross sections and the $(g-2)_\mu$

Precise measurements of the $e^+e^- \to$ hadrons cross section are necessary to evaluate the dispersion integrals for calculation of a_μ^{had}, the hadronic contribution to the theoretical prediction of $a_\mu = (g-2)_\mu$. Comparison of the theoretical and measured [5] values shows a discrepancy of more than three standard deviations when current e^+e^- data [6,7,8] are used, possibly hinting at new physics. The *BABAR* Collaboration [9] has an intensive program to study the e^+e^- cross section at low center-of-mass (CM) energy using ISR [10], with e^+e^- events collected at the peak of the $\Upsilon(4S)$ resonance. A number of multi-hadron processes have been measured with unprecedented accuracy, providing a major contribution to the calculation of a_μ^{had}. Among them, the recent measurement of the process $e^+e^- \to \pi^+\pi^-$ [11], which contribute for approximately 73% to a_μ^{had}, and is also the leading contributor to the uncertainty of a_μ.

The $e^+e^- \to X$ cross section, is deduced from a measurement of the radiative process $e^+e^- \to X\gamma$, where the photon is emitted by the e^+ or the e^- with a CM energy E_γ^*, and X can be any final state produced at the reduced CM energy $\sqrt{s'} = m_X$, with $s' = s(1-2E_\gamma^*/\sqrt{s})$.

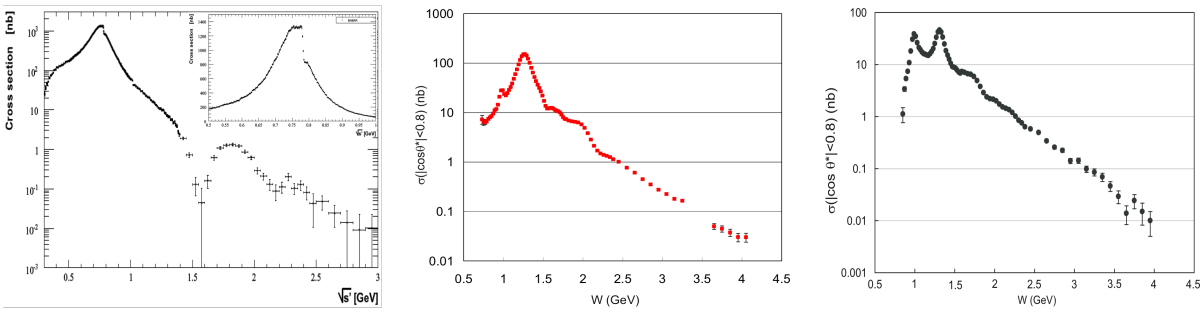

Figure 1: (Left) $e^+e^- \to \pi^+\pi^-(\gamma)$ cross section *vs* $\sqrt{s}$; in the inset, a detail of the region near the ρ peak is shown. (Center) the $\gamma\gamma \to \pi^0\pi^0$ and (right) $\gamma\gamma \to \eta\pi^0$ cross sections, shown as a function of the $\gamma\gamma$ invariant mass.

In this analysis, $X = \pi^+\pi^-(\gamma)$ and $X = \mu^+\mu^-(\gamma)$ are measured, with the charged pair possibly accompanied by a final state radiation (FSR) photon. The ISR photon is detected at large angle; the $\pi^+\pi^-$ cross section are obtained from the ratio of pion to muon yield. In this way the main systematic uncertainties cancel (e^+e^- integrated luminosity, ISR photon efficiency, additional ISR). The measured $\pi^+\pi^-(\gamma)$ bare cross section, including FSR, $\sigma^0_{\pi\pi(\gamma)}(\sqrt{s'})$, is shown in Fig. 1(left). Systematic uncertainties are about 0.5% in the region dominated by the ρ peak, and do not exceed the statistical errors over the full measured spectrum. The leading-order contribution to a_μ is obtained integrating the measured cross section (up to $1.8\,GeV$) and amounts to

$$a_\mu^{\pi^+\pi^-(\gamma),LO} = \frac{1}{4\pi^3}\int_{4m_\pi^2}^{\infty} ds'\, K(s')\,\sigma^0_{\pi\pi(\gamma)}(\sqrt{s'}) = (514.1 \pm 2.2 \pm 3.1)\times 10^{-10}, \qquad (1)$$

where $K(s')$ is a known kernel [12], and the errors are statistical and systematic, respectively. This value is larger than from a combination of previous e^+e^- data, $(503.5 \pm 3.5)\times 10^{-10}$, while it is in good agreement with the updated value extracted from τ spectral functions [13].

Combining *BABAR* result with the previous e^+e^- data and including all other contributions, the discrepancy between the Standard Model prediction and the experimental value of a_μ is reduced to $a_\mu^{exp} - a_\mu^{SM} = (25.5 \pm 8.0)\times 10^{-10}$, still above three standard deviations [13].

3 $\gamma\gamma$ in no-tag mode

Studies of exclusive final states in two-photon fusion processes, $e^+e^- \to e^+e^-\gamma^\star\gamma^\star \to e^+e^-X$, provide valuable information concerning the physics of light- and heavy-quark hadrons, perturbative and non perturbative QCD, and hadron production mechanism. The beam particles are generally scattered at small angles, most of the times escaping undetected along the beam-line. In such a case (no-tag mode) two *quasi-real* photons are produced with $q^2 = (p - p')^2 \simeq 0$, where p and p' are the electron's initial and final four momenta. At a B-factory, $\gamma\gamma$ invariant masses up to $W \sim 5\,GeV$ can be effectively studied; the final states are produced with even C-parity and angular momentum $J \neq 1$. The Belle Collaboration [14] measured the production cross section for several pairs of light mesons. Both experiments have also measured a number of final states in the charm and charmonium sector.

The $\gamma\gamma \to \pi^0\pi^0$ and $\gamma\gamma \to \eta\pi^0$ [15], extracted from the corresponding $e^+e^- \to e^+e^-X$ cross sections, and integrated over a CM angular range $|cos\theta^*_{\gamma\gamma}| < 0.8$, are shown as a function of W in Fig. 1. For $W < 2\,GeV$ the production is dominated by intermediate resonances with even angular momentum and $I^G = 0^+$ (that is $f_0, f_2...$) in the $\pi^0\pi^0$, and $I^G = 1^-$ (that is $a_0, a_2...$) in the $\eta\pi^0$ final state. Full partial wave analyses have been performed to disentangle the different contributions and extract information on these states. The cross section at higher energies can be compared to perturbative QCD predictions. At leading order, the $\pi^0\pi^0$ cross section is predicted

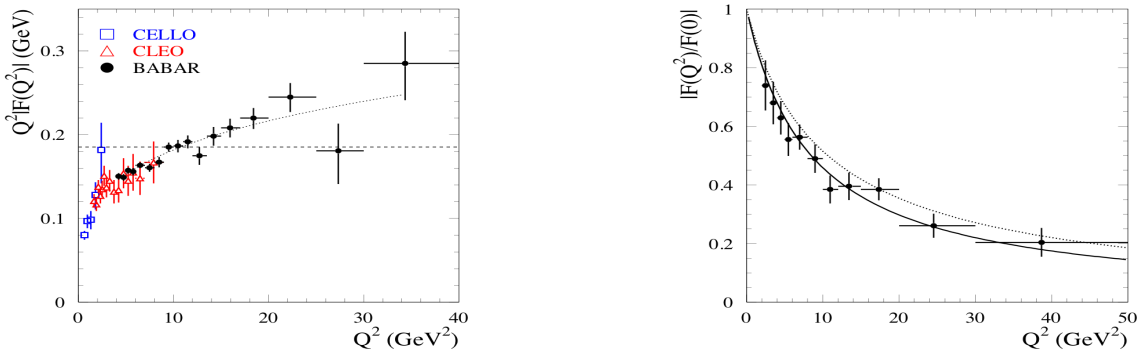

Figure 2: (Left) $\gamma^\star\gamma \to \pi^0$ TFF shown as a function of Q^2; the horizontal dashed line refers to the asymptotic value predicted by pQCD. (Right) $\gamma^\star\gamma \to \eta_c$ TFF normalized to the FF for zero transferred momentum; the solid line is the result of the fit described in the text, while the dotted line refer to a LO pQCD prediction.

to be much smaller than of $\pi^+\pi^-$, and the ratio of $\pi^0\pi^0$ to $\pi^+\pi^-$ to be in the range $0.03 - 0.06$. The observed ratio shows a fast decrease for $W < 3\,GeV$, and then flatten to a roughly constant value of 0.3, which is significantly higher than the LO pQCD prediction, while it is not far from the value of 0.5 as expected if the amplitudes for the two processes are the same. A prediction of this kind is provided for example by the handbag model [16]. A fit to a power law, W^{-n}, of the $\gamma\gamma \to \pi^0$ differential cross section integrated over the polar angle $|cos\theta^*_{\gamma\gamma}| < 0.6$, in the CM energy region $3.1 < W < 4.1\,GeV$, gives a value of $n = 6.9 \pm 0.6 \pm 0.7$, which is compatible with the results found for the $\pi^+\pi^-$ and K^+K^- channels, while a significantly higher value is found for the $\eta\pi^0$ channel.

4 $\gamma\gamma$ in single-tag mode

If one of the electron is scattered at large angle and detected, the emitted photon is highly off-shell, and the momentum transfer $q_1^2 = -Q^2$ is large. The cross section for pseudoscalar meson (P) production depends on only one form factor, $F(Q^2)$, which describe the $\gamma^\star\gamma \to P$ transition [17]. At large enough Q^2, the form factor can be represented as a convolution of a calculable hard scattering $\gamma^\star\gamma \to q\bar{q}$, with a non perturbative meson distribution amplitude (DA), $\phi_P(x, Q^2)$ [18], which describe the transition of the meson into two quarks, carrying a fraction x and $(1 - x)$ of the meson momentum. Measurements of the transition form factors (TFF) can be used to determine its dependence on x. The *BABAR* Collaboration has measured the TFF for the neutral pion and the η_c.

The π^0 is reconstructed from its decay into two photons. A total of about 14000 $\gamma\gamma \to \pi^0$ events are selected in 442 fb^{-1} of data, and divided in 17 Q^2 bins of different width, from 4 to 40 GeV^2. The TFF extracted from the measured cross section is shown in Fig. 2(left). The *BABAR* results [19] are in agreement with a previous measurement by the CLEO Collaboration [20] in the Q^2 range from 4 to 9 GeV^2, but have significantly better precision. The horizontal dashed line shown in the plot indicates the asymptotic limit $Q^2F(Q^2) = \sqrt{2}f_\pi \approx 0.185\,GeV$ for $Q^2 \to \infty$, as predicted by pQCD [18]. The measured TFF exceeds the limit for $Q^2 > 10\ GeV^2$, contradicting most models for the pion DA which predict form factors approaching the asymptotic limit from below.

A similar analysis has been performed to measure the $\gamma^\star\gamma \to \eta_c$ TFF, with η_c reconstructed through the decay $\eta_c \to K_S K^\pm\pi^\mp$. This channel has been studied also in no-tag mode, in order to measure the parameters of the resonance, in particular the product of the two-photon width times the branching fraction, and normalize $F(Q^2)$ to $F(Q^2 = 0)$. The $\gamma^\star\gamma \to \eta_c$ TFF measured [21] in the single-tag analysis is shown in Fig. 2(right). Experimental data are well described by the monopole form $|F(Q^2)/F(0)| = 1/(1 + Q^2/\Lambda)$. The fitted value for the pole is

$\Lambda = (8.5 \pm 0.6 \pm 0.7)$ GeV^2, consistent with that expected from vector dominance, $\Lambda = m^2_{J/\psi} =$ 9.6 GeV^2, and with a lattice QCD calculation [22]. The data lie instead systematically below a calculation at leading-order pQCD [23], but within the quoted theoretical uncertainties.

5 Conclusions

ISR and $\gamma\gamma$ processes have proved to be very effective tools for studying hadronic interactions at low energies, when combined with the high statistics provided by the modern B-factories. Here, we have reported about a small fraction of the numerous measurements performed, with unprecedented accuracy, by the Belle and *BABAR* experiments.

Acknowledgments

I wish to thank the Organizing Committee of the Conference for the warm hospitality. I am also grateful to the colleagues from the *BABAR* and Belle collaborations for the fruitful discussions during the preparation of the talk, with particular thanks to Galina Pakhlova, Sadaharu Uehara and Pavel Pakhlov.

References

1. G. Pakhlova *et al*, Belle Collaboration, *Phys. Rev.* D **77**, 011103 (2008); *Phys. Rev.* D **98**, 092001 (2007).
2. B. Aubert *et al*, *BABAR* Collaboration, *Phys. Rev.* D **76**, 111105(R) (2007); *Phys. Rev.* D **79**, 092001 (2009).
3. G. Pakhlova *et al*, Belle Collaboration, arXiv:0908.0231 [hep-ex] (2009).
4. S. Uehara *et al*, Belle Collaboration, *Phys. Rev. Lett.* **78**, 082003 (2006); B. Aubert *et al*, *BABAR* Collaboration, *Phys. Rev.* D **81**, 092003 (2010).
5. G.W. Bennet *et al*, *Phys. Rev.* D **73**, 072003 (2006).
6. R.R. Akhmetshin *et al*, CMD-2 Collaboration, *Phys. Lett.* B **648**, 28 (2007).
7. M.N. Achasov *et al*, SND Collaboration, JETP Lett. 2006, **103**, 380.
8. F. Ambrosino *et al*, KLOE Collaboration, *Phys. Lett.* B **670**, 285 (2009).
9. B. Aubert *et al*, *BABAR* Collaboration, *Nucl. Instrum. Methods* A **479**, 1 (2002).
10. A.B. Arbuzov *et al*, J. High Energy Phys., **9812**, 009 (1998); S. Binner, J.H. Kuhn, and K. Melnikov, *Phys. Lett.* B **459**, 279 (1999).
11. B. Aubert *et al*, *BABAR* Collaboration, *Phys. Rev. Lett.* **103**, 231801 (2009).
12. S.J. Brodsky and E. de Rafael, *Phys. Rev.* **168**, 1620 (1968).
13. M. Davier *et al*, arXiv:0908.4300 (2010),
14. A. Abashian *et al*, Belle Collaboration, *Nucl. Instrum. Methods* A **479**, 117 (2002).
15. S. Uehara *et al*, Belle Collaboration, *Phys. Rev.* D **78**, 052004 (2008); *Phys. Rev.* D **79**, 052009 (2009); *Phys. Rev.* D **80**, 032001 (2009).
16. M. Diehl, P. kroll, and C. Vogt, *Phys. Lett.* B **532**, 99 (2002).
17. S.J. Brodsky, T. Kinoshita, and H. Terazawa, *Phys. Rev.* D **4**, 1532 (1971).
18. G.P. Lepage and S.J. Brodsky, *Phys. Rev.* D **22**, 2157 (1980).
19. B. Aubert *et al*, *BABAR* Collaboration, *Phys. Rev.* D **80**, 052002 (2009).
20. J. Gronberg *et al*, CLEO Collaboration, *Phys. Rev.* D **57**, 33 (1998).
21. J.P.Lees *et al*, *BABAR* Collaboration, *Phys. Rev.* D **81**, 052010 (2010).
22. J.J. Dudek and R.G. Edwards, *Phys. Rev.* D **97**, 172001 (2006).
23. T. feldmann and P. Kroll, *Phys. Lett.* B **413**, 410 (1997).

4.
Higgs

Searches for High-Mass Standard Model Higgs Boson at the Tevatron

Ralf Bernhard
on behalf of the DØ and CDF collaborations
Physikalisches Institut, Albert-Ludwigs Universität Freiburg, Germany

Searches for the Standard Model Higgs boson at a center-of-mass energy of $\sqrt{s}$ =1.96 TeV, using up to 5.4 fb^{-1} of data collected with the CDF and DØ detectors at the Fermilab Tevatron collider in the mass range around 160 GeV/c^2 are presented. As no significant excess is observed, limits on standard-model Higgs boson production are set.

1 Introduction

In the standard-model of particle physics the Higgs mechanism is responsible for breaking electroweak symmetry, thereby giving mass to the W and Z bosons. It predicts the existence of a heavy scalar boson, the Higgs boson, with a mass that can not be predicted by the standard-model . Direct searches for the Higgs Boson were performed at the LEP experiments and yielded a direct mass limit of $m_H > 114.4$ GeV/c^2 [1] at the 95% confidence level (CL) [a].

Indirect limits have been placed on the Higgs boson mass by the LEP, SLD and Tevatron experiments from electroweak precision measurements [2]. The main contribution to these indirect constraints from the Tevatron experiments are the measurements of the W Boson and top quark masses [2]. The standard-model fit yields a best value of $m_H = 87^{+35}_{-26}$ GeV/c^2 [3]. The upper limit on the Higgs mass at 95% CL is $m_H < 157$ GeV/c^2. If the direct mass limit is also taken into account this limit is increased to $m_H < 186$ GeV/c^2.

At the Tevatron CDF and DØ search for direct Higgs boson production in the mass range above the LEP limit using $p\bar{p}$ collisions at $\sqrt{s} = 1.96$ TeV. The relevant processes at these energies are associated Higgs production ($q\bar{q}' \rightarrow WH$, $q\bar{q} \rightarrow ZH$) and gluon fusion ($gg \rightarrow H$).

The main focus here is for masses above $m_H = 140$ GeV/c^2 (high mass region) where the Higgs boson will predominantly decay into WW boson pairs. Leptons from the decays of the W bosons and the missing transverse energy are used to reject background. In order to take

[a] All limits given in this paper are at 95% CL

advantage of the maximum potential signal acceptance, also the associated production with a W or Z boson and Higgs boson production via vector boson fusion is considered.

2 $H \to WW^{(*)} \to \ell\nu\ell'\nu'$

The dominant decay mode for higher Higgs boson masses is $H \to WW^{(*)}$. The leptonic decays of the W bosons are used to suppress the QCD background. The signature of the $gg \to H \to WW^{(*)}$ channel is two high-p_T opposite signed isolated leptons with a small azimuthal separation, $\Delta\phi_{\ell\ell}$, due to the spin-correlation between the final-state leptons in the decay of the spin-0 Higgs boson. In contrast, the lepton pairs from background events, mainly WW events, are predominantly back-to-back in $\Delta\phi_{\ell\ell}$. This is shown in Figure 1 (left) for a preselected CDF data sample with zero reconstructed jets. An additional selection requires $E_T^{\rm miss} > 25$ GeV for CDF and

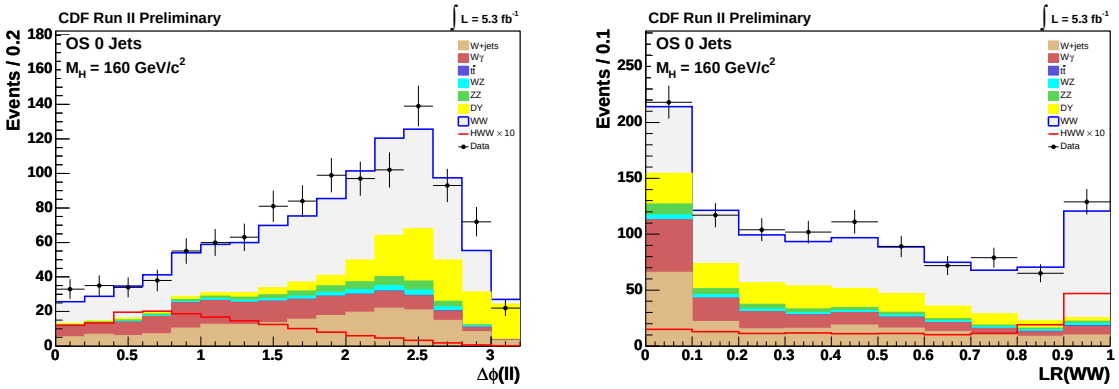

Figure 1: CDF $H \to WW^{(*)}$ channel: The azimuthal angle between the two leptons in the $H \to WW^{(*)}$ search. Due to spin correlations, the signal is at low $\Delta\phi_{\ell\ell}$, whereas the background is at high $\Delta\phi_{\ell\ell}$.

$E_T^{\rm miss} > 20$ GeV for DØ to account for the neutrinos in the final state. DØ defines three final states (e^+e^-, $e^\pm\mu^\mp$, and $\mu^+\mu^-$) [4]. CDF separates the $H \to WW^{(*)}$ events into five non-overlapping samples, first by separating the events by jet multiplicity (0, 1 or 2), then subdviding the 0 and 1 jet samples in two, one having a low signal/background (S/B) ratio, the other having a higher one. In these analyses, the final discriminants are neural-network outputs based on several kinematic variables. These include likelihoods constructed from matrix-element probabilities as input to the neural network for CDF and is shown on the right side of Figure 1. The NN distribution for DØ is shown in Figure 2 on the left side and the background subtracted NN distribution in the center of Figure 2. The expected yields for CDF in this five channels are

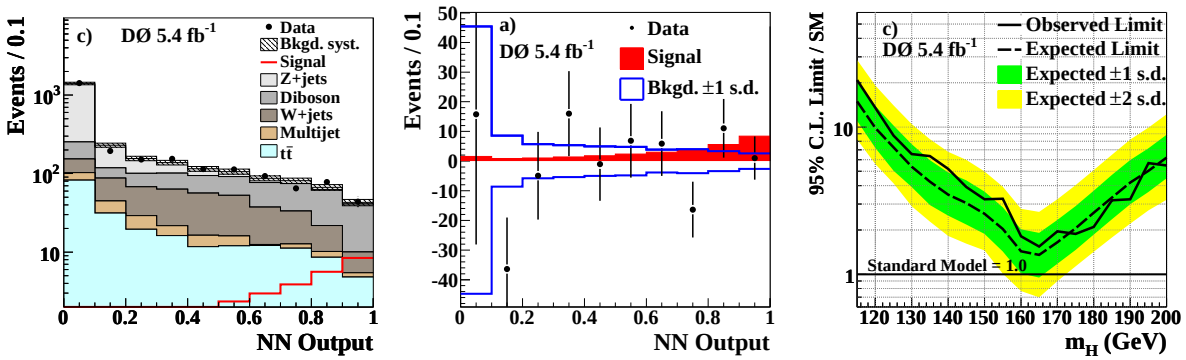

Figure 2: DØ $H \to WW^{(*)}$ channel: The NN distribution (left) and background subtracted distribution of the NN (center) and the obtained median observed and expected limits on the production cross-section (right).

32 signal events and 1840 background events in 5.3 fb^{-1} of data and for DØ in the three search channels 30 signal events and 2445 background events in 5.4 fb^{-1} of data.

3 Additional Acceptance

Additional signal acceptance is gained by including events with low dilepton invariant mass as a separate search region and the search for associated Higgs production in events with same-sign dileptons and trileptons in the final state. For each of the search channels a neural network is trained on a weighted combination of known signal and background events from Monte Carlo independently for each of the Higgs mass hypothesis.

3.1 Low Dilepton Invariant Mass

To increase signal acceptance, events with low dilepton invariant mass ($M_{ll} < 16$ GeV/c^2) of the opposite-sign signal region selection are analyzed at CDF separately. In this case only events with zero or one jets are considered. Heavy flavor contributions (J/ψ, Υ) are effectively removed by the missing transverse energy requirements. The primary background in this selection region are Wγ events, where the photon is misidentified as a lepton. The modeling of this background is tested with a control sample of the same selection but two same-sign leptons which is composed primarily of Wγ events. The expected yield of this selection is about one signal event and 100 background events.

3.2 Same-Sign Dileptons

To further increase the sensitivity, also searches for Higgs signal in like sign, or same-sign (SS), dileptons are performed. These occur naturally in VH $\rightarrow$ VWW production, when the vector boson (Z or W) and one of the W bosons from the Higgs decay leptonically. The primary backgrounds in this search are from charge misidentification of a real lepton and misidentification of a photon or jet as a lepton. At DØ the rate of charge mis-measurements for muons is determined by comparing the independent charge measurements within the solenoidal and in the toroidal fields of the detector. For electrons the charge mis-measurement rate is determined by comparing the charge measurement from the solenoid with the azimuthal offset between the track and the calorimeter cluster associated to the electron. The additional expected acceptance for CDF in this channel is 2.1 signal events and 81 background events in 5.3 fb^{-1} of data and for DØ 1.1 events and 118 background events in 2.5 fb^{-1} of data.

3.3 Trileptons

CDF searches in addition for a potential Higgs signal in the trilepton final state. Trilepton events occur naturally in WH $\rightarrow$ WWW production, in the case where all three W bosons decay leptonically, and in ZH $\rightarrow$ ZWW production, where the Z boson and one of the W bosons from the Higgs decay leptonically while the second W boson decays hadronically. The gluon fusion and vector boson fusion production modes contribute to the trilepton final state only in cases where a photon or jet is misidentified as a lepton and are therefore not considered. The primary background in this search is WZ production. To allow better discrimination against the dominant WZ background, events are separated into two channels depending on whether or not there are two same-flavor opposite-sign leptons with an invariant mass of the Z-boson.

Trilepton events with a same-flavor opposite-sign dilepton pair in the Z-mass peak have a Higgs signal contribution predominantly from ZH production. These events are required to have missing transverse energy larger than 10 GeV only since ZH trilepton events will in most cases contain a single neutrino. The decay of the second W boson in ZH trilepton events most often

results in the production of additional jets, so one or more reconstructed jets are required. The expected yields of this selection are 0.6 signal events and 24 background events in 5.3 fb^{-1} of data. The output of the NN classifier is shown in Figure 3 on the left.

Trilepton events without a same-flavor opposite-sign dilepton pair in the Z-mass peak have a Higgs signal contribution predominantly from WH production. Because most WH trilepton events contain three neutrinos, they typically have high values of missing transverse energy (center of Figure 3), and these events are required to have missing transverse energy larger than 20 GeV. The expected yields of this selection are 0.8 signal events and 15 background events in 5.3 fb^{-1} of data.

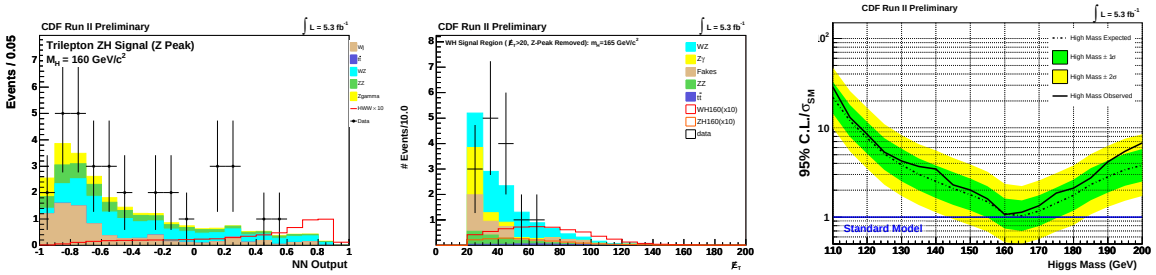

Figure 3: CDF: NN output classifier for the ZH trilepton events (left) and missing transverse energy for the WH trilepton search (center).

4 Results

No excess above the background expectation have been found neither by the CDF experiment nor the DØ experiment, therefore limits on the production cross-section of the Higgs boson can be set. The obtained limits of the combination of the orthogonal search channels for CDF on the production cross-section as a function of the Higgs boson mass are shown in Figure 3 on the right side. The best sensitivity is reached for a Higgs boson mass of 165 GeV/c^2 with an extracted median observed (expected) limit on the production cross-section of $\sigma_{95}/\sigma_{SM} = 1.13\,(1.03)$.

DØ uses the NN distribution (Figure 2 on the left) to extract median observed (expected) limits on the production cross-section of $\sigma_{95}/\sigma_{SM} = 1.55\,(1.36)$ for $m_H = 165$ GeV/c^2. The obtained limits on the production cross-section as a function of the Higgs boson mass are shown in Figure 2 on the right side.

A recent combination of the limits on Higgs boson production from the two Tevatron experiments excluded at the 95% CL a standard-model Higgs boson in the mass range 162–166 GeV [6,7].

References

1. R. Barate *et al*, *Phys. Lett.* B **565**, 61 (2003).
2. Tevatron Electroweak Working Group, August 2009, `http://tevewwg.fnal.gov/`.
3. LEP Electroweak Working Group, August 2009, `http://lepewwg.web.cern.ch/LEPEWWG/`.
4. V. M. Abazov *et al.*, *Phys. Rev. Lett.* **104**, 061804 (2010)
5. T. Aaltonen *et al.*, CDF note 10102 (2010)
6. T. Aaltonen *et al.*, *Phys. Rev. Lett.* **104**, 061802 (2010)
7. W. Yao, this proceedings.

Combinations of Searches for SM Higgs at the Tevatron

Wei-Ming Yao
Physics MS-50B-5239, Lawrence Berkeley National Lab, 1 Cyclotron Road, Berkeley, CA 94720, USA

We present the recent results from combinations of searches for a standard model (SM) Higgs boson (H) by the CDF and D0 experiments at the Tevatron $p\bar{p}$ collider at $\sqrt{s} = 1.96$ TeV. The data correspond to an integrated total luminosity of 2.0-4.8 (CDF) and 2.1-5.4 (D0) fb^{-1} of $p\bar{p}$ collisions. No excess is observed above background expectation, and resulting limits on Higgs boson production exclude a standard-model Higgs boson in the mass range 162–166 GeV/c^2 at the 95% C.L. The absence of $gg \to H \to WW$ also constrains some new physics such as 4^{th} generation models. Assuming the presence of a fourth sequential generation of fermions with very large masses, we exclude a standard-model-like Higgs boson with a mass between 131 and 204 GeV/c^2.

1 Introduction

The search for the standard model(SM) Higgs boson has been a major goal of HEP for many years, and is a central part of Tevatron physics program. Recent observations of single top production [1] and diboson production [2] in semileptonic decayss have paved the way for Tevatron to probe the production process with cross section at sub-pb level. Direct search from LEP and global fit of precision electroweak data constrains the Higgs mass between 114.4 GeV/c^2 and 186 GeV/c^2 at 95% C.L., which therefore places the SM Higgs boson within the Tevatron reach. In this note, we present the recent results from the combination of multiple direct searches for the SM Higgs boson at the Tevatron [3]. The analyses that are combined seek signals of Higgs bosons produced in associated with vector bosons ($q\bar{q} \to W/ZH$), through gluon-gluon fusion ($gg \to H$), and through vector boson fusion (VBF) ($q\bar{q} \to q'\bar{q}'H$) corresponding to integrated luminosities ranging from 2.0 to 4.8 fb^{-1} at CDF and 2.1 to 5.4 fb^{-1} at D0.

1.1 Higgs Search Strategies

The Higgs search strategies are quite similar for the corresponding CDF and D0 analyses. Based on Higgs decay, we divide the searches into many different channels. The Higgs signature can be either $H \to b\bar{b}$ at low mass, $H \to W^+W^-$ at high mass, $H \to \tau^+\tau^-$, or $H \to \gamma\gamma$. Both CDF and D0 empolyed "no channel too small" strategies to gain signal acceptances while reducing the background with advanced multivariate analysis techniques, such as neural network(NN), matrix element(ME), and boosted decision tree(BDT). There are in total 90 mutually exclusive final states, 54 channels from D0 and 36 channels from CDF. All analyses provide binned histograms of the final discriminant for signal and background predictions itemized separately for each source, and the data. More details for the low and high-mass SM Higgs searches can be found in these talks [4].

We use the most recent high-order calculations of the SM Higgs production cross section and decay branching ratio to normalize the signal event yield in each individual channel. So we can combine them statistically.

1.2 Combination Procedures

To gain confidence that the final result does not depend on the details of statistical method, we perform two types of combinations, using Bayesian and Modified Frequentist approaches, which yield results that agree within 10%. Both methods rely on distributions of final discriminants, not just on events counts. Systematic uncertainties are treated as nuisance parameters with truncated Gaussian. Both methods use likelihood calculations based on Poisson probabilities. There are two types of systematic uncertainties that affect the rate and shape of estimated signal and background in a correlated way. The rate systematic only affects overall normalization while the shape systematic is changing differential distribution due to the jet energy scale(JES) and Monte Carlo(MC) modeling.

CDF and D0 share common systematic uncertainties on luminosity, the theoretical cross sections, and some scale and PDF veriations, which are treated as correlated. Other sources of systematic are experiment dependent, treated uncorrelated between experiments, but correlated within the experiment, such as lepton identification, b-tagging efficiency, JES, detector effects and instrumental backgrounds.

In order to check the consistency between data and expectations, we rebin the final discriminant from each channel in terms of signal to background ratio (s/b) and the data with similar s/b may be added without loss in sensitivity. Figure 1 show the data after background subtraction, compared to the expected signal as function of log(s/b) for m_H = 115 and 165 GeV/c^2, respectively. There is no significant excess of events observed in the higest s/b bins.

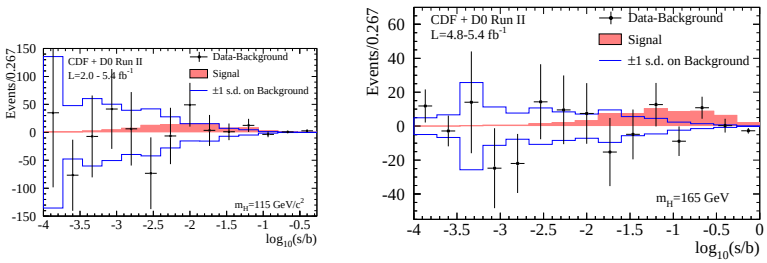

Figure 1: Background-subtracted data distributions for the discriminant histograms, summed for bins with similar s/b, for $m_H = 115$ GeV/c^2 (left) and $m_H = 165$ GeV/c^2 (right).

2 Combined Tevatron Searches for SM Higgs

Before extracting the combined results, we check the search sensitivity using log-likelihood ratio(LLR) for different hypotheses to quantify the expected sensitivity across the mass range tested. Figure 2 (left) shows the combined distributions of the log-likelihood ratio as function of Higgs mass. The black dot curve is for the background-only hypothesis, the red dot curve is for signal-plus-background hypothesis, and the solid curve is for the observed data. The sizes of one and two sigma bands indicate the width of the LLR background-only distribution. The separation between the background-only and signal-plus-background hypotheses provides a measure of the search sensitivity, which is about one sigma at low mass and slightly more than 2 sigma at $m_H = 165$ GeV/c^2.

Figure 2 (middle) shows the ratio of the 95% C.L. expected and observed limit to the SM Higgs cross section times branching ratio at the Tevatron after combining CDF and D0 searches

together using the results presented at HCP 09 [3]. We obtain the observed limit of 2.70 with expected 1.78 for $m_H = 115$ GeV/c^2 and 0.94 with expected 0.89 for $m_H = 165$ GeV/c^2.

Since then we have combined searches using $H \to W^+W^-$ only and have published the first joint CDF and D0 publication [5]. For the first time, the Tevatron set mass exclusion in the mass range between 162 and 166 GeV/c^2 with expected $159 < m_H < 169$ GeV/c^2 at 95% C.L. as shown in Figure 2(right).

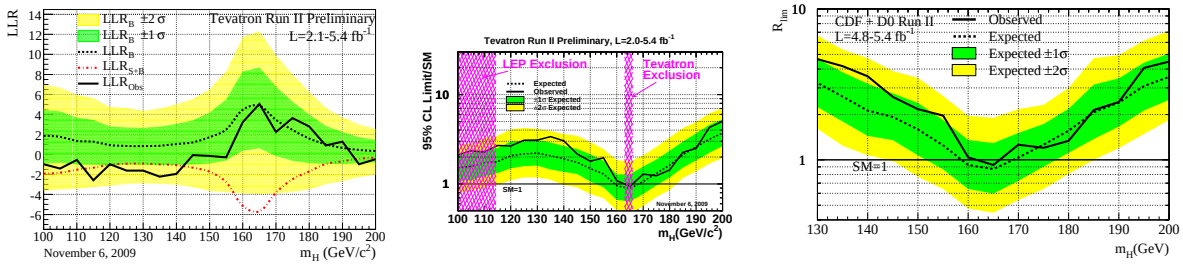

Figure 2: Distributions of the log-likelihood ratio (left), observed and expected 95% C.L. upper limits on the ratio to the SM prediction for the full Higgs mass range (middle), and the corresponding observed and expected limits in the $H \to W^+W^-$ decay (right). The bands indicate the 68% and 95% probability regions where the limits can fluctuate, in the absence of signal.

3 Constraints on Fourth-Generation Fermion Models

With the absence of $H \to WW$ signal, we can constrain some new physics models such as 4^{th} generation, which may exist in nature if the masses are much higher than the current experiment limit. In this scenario $gg \to H$ coupling is enhanced by a factor of $K = 3$ with additional heavy quarks in the triangle loop. The production cross section then is enhanced by a factor of K^2 and K for the heavy quark and the electro-weak contributions, respectively. The Higgs decay is also modified due to the presence of 4^{th} generation, in particular, the partial decay width for $H \to gg$ is enhanced by the same factor as production cross section. Two 4^{th} generation scenarios are considered in this study:

- high-mass scenario: set $m_{\nu_4} = m_{l_4} = 1$ TeV/c^2;
- low-mass scenario: set $m_{\nu_4} = 80$ GeV/c^2, $m_{l_4} = 100$ GeV/c^2, just above the current limit.

The analysis strategy [6] is similar to the one used in the SM Higgs case, except we consider $gg \to H \to WW$ signal only by ignoring contributions from WH, ZH, and VBF; loosen the $\delta\phi < 2.5$ cuts for D0 analysis to gain acceptance for large m_H; extending the Higgs mass from 110 to 300 GeV/c^2.

Keeping the same background predictions, we use the same combination procedure to set the limit on $\sigma(p\bar{p} \to H) \times B(H \to W^+W^-)$ as function of Higgs mass. The combined limit is shown in Figure 3(left) along with the 4^{th} generation theory predictions [7] for the high-mass scenario, as well as for the low-mass scenario.

In order to set limits on m_H in these two scenrios, we perform a second combination on the limit relative to the model prediction, including the uncertainties on the prediction due to scale and pdf uncertainties at each Higgs mass tested.

Figure 3 (right) shows the 95% C.L. limit over the model prediction as a function of Higgs mass. In the low-mass scenario, we exclude a SM-like Higgs boson with a mass in the range 130-210 GeV/c^2, with an expected exclusion of 125-218 GeV/c^2.

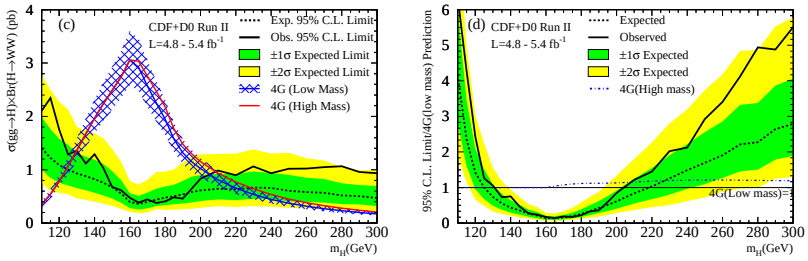

Figure 3: The combined observed (solid black lines) and expected (dashed black lines) 95% C.L. upper limit on $\sigma(p\bar{p} \to H) \times B(H \to W^+W^-)$ are shown(left) and the ratio of 95% C.L. combined limit relative to the theoretical predictions(right).

4 Conclusions and Future Prospects

We present recent results from combinations of searches for a standard model (SM) Higgs boson (H) by the CDF and D0 experiments at the Tevatron $p\bar{p}$ collider at $\sqrt{s} = 1.96$ TeV. The data correspond to an integrated total luminosity of 2.0-4.8 (CDF) and 2.1-5.4 (D0) fb^{-1} of $p\bar{p}$ collisions. No excess is observed above background expectation, and resulting limits on Higgs boson production exclude a standard-model Higgs boson in the mass range 162–166 GeV at the 95% C.L. The absence of $gg \to H \to WW$ can also constrain some new physics such as 4^{th} generation models. Assuming the presence of a fourth sequential generation of fermions with very large masses, we exclude a standard-model-like Higgs boson with a mass between 131 and 204 GeV/c^2.

The Tevatron is doing remarkably well and has delivered an integrated luminosity close to 9 fb^{-1}. Both CDF and D0 continue to add additional Higgs sensitivity with "no channel too small" strategies. By this summer, we aim to publish the combined searches in full mass region and each experiment should reach individual exclusion sensitivity near $m_H = 165$ GeV. With 12 fb^{-1} by 2012, the Tevatron would either find some evidence for the SM Higgs boson or exclude it up to $m_H < 180$ GeV/c^2 at 95% conference level.

Acknowledgments

We would like to thank the organizers of the XLVth Rencontres de Moriond for a wonderful conference with excellent presentations and wish to thank the CDF and D0 collaborations for the results presented at this conference.

References

1. V.M. Abazov *et al.*, The D0 Collaboration, *Phys. Rev. Lett.* **98**, 181802 (2007); T. Aaltonen *et al.*, The CDF Collaboration, *Phys. Rev. Lett.* **103**, 092002 (2009).
2. V.M. Abazov *et al.*, The D0 Collaboration, *Phys. Rev. Lett.* **102**, 161801 (2009); T. Aaltonen *et al.*, The CDF Collaboration, *Phys. Rev. Lett.* **103**, 091803 (2009).
3. The CDF and D0 Collaborations, arXiv:0911.3930(2009).
4. S. Shalhout, "Searches for Low-Mass SM Higgs at the Tevatron", this proceeding; R. Bernhard, "Searches for High-Mass SM Higgs at the Tevatron", this proceeding.
5. T. Aaltonen *et al.*, The CDF and D0 Collaborations, *Phys. Rev. Lett.* **104**, 061802 (2010).
6. T. Aaltonen *et al.*, The CDF and D0 Collaborations, "Combined Tevatron upper limit on $gg \to H \to W^+W^-$ and constraints on the Higgs boson mass in fourth-generation fermion models", Submitted to *Phys. Rev.* DRapid Communications.
7. C. Anastasiou, R. Boughezal, and E. Furlan, arXiv:1003.4677[hep-ph] (2010).

HADRONIC PRODUCTION OF A HIGGS BOSON AND TWO JETS AT NEXT TO LEADING ORDER.

John M. Campbell[‡], R. Keith Ellis[‡], Ciaran Williams[♭]
[‡] *Fermilab, Batavia, IL 60510, USA*
[♭] *Department of Physics, University of Durham, Durham, DH1 3LE, UK*

We present an update on the next-to-leading order calculation of the rate for Higgs boson production in association with two jets. Our new calculation incorporates the full analytic result for the one-loop virtual amplitude. Results are presented for the Tevatron, where implications for the Higgs search are sketched, and for the LHC at $\sqrt{s} = 7$ TeV.

1 Higgs-Gluon coupling in the large m_t limit

In this talk we present results for the production of a Higgs boson in association with two jets which has recently been implemented in MCFM [1]. Our calculation is performed at next-to-leading order (NLO) using an effective Lagrangian to express the coupling of gluons to the Higgs field,

$$\mathcal{L}_H^{\rm int} = \frac{C}{2} H \ {\rm tr}\, G_{\mu\nu} G^{\mu\nu}. \tag{1}$$

This Lagrangian replaces the full one-loop coupling of the Higgs boson to the gluons via an intermediate top quark loop by an effective local operator. The effective Lagrangian approximation is valid in the limit $m_H < 2m_t$ and, in the presence of additional jets, when the transverse momenta of the jets is not much larger than the top mass m_t. A commonly used improvement of the effective Lagrangian approximation is to multiply the resulting differential jet cross section by a ratio R given by,

$$R = \frac{\sigma_{\text{finite } m_t}(gg \to H)}{\sigma_{m_t \to \infty}(gg \to H)} \ , \tag{2}$$

where $\sigma(gg \to H)$ is the total cross section.

This rescaling is known to be an excellent approximation for the LO Higgs + 2 jet rate [2]. Our numerical results for the Higgs cross section will not include the rescaling of Eq. (2). The phenomenology of the production of a Higgs boson in association with two jets has been presented [3] for the LHC operating at $\sqrt{s} = 14$ TeV. Over the last few years a great deal of effort has been devoted to the *analytic* calculation of one-loop corrections to Higgs + n-parton amplitudes, with particular emphasis on the $n = 4$ amplitudes which are relevant for this study. The complete set of one-loop amplitudes for all Higgs + 4 parton processes are now available [4,5,6,7,8,9,10]. The values of the amplitudes calculated by the new analytic code and the previous semi-numerical code [3] are in full numerical agreement for all amplitudes.

To define the jets we perform clustering according to the k_T algorithm, with jet definitions detailed further below.

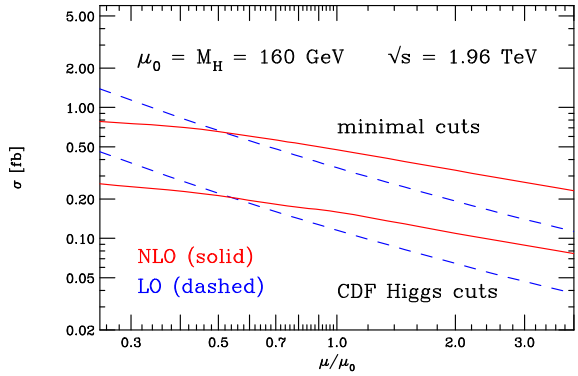

Figure 1: Scale dependence for the Higgs + 2 jet cross section, with the Higgs decay into $W^-(\to \mu^-\bar{\nu})W^+(\to \nu e^+)$, at the Tevatron and using the a central scale $\mu_0 = M_H$. Results are shown for the minimal set of cuts in Eq. (3) (upper curves) and for cuts that mimic the latest CDF $H \to WW^\star$ analysis (lower curves).

2 Tevatron results

We have checked the scale dependence of the NLO cross section using both a very simple set of inclusive cuts, with no requirements on the Higgs boson decay products,

$$p_t(\text{jet}) > 15 \text{ GeV}, \qquad |\eta_{\text{jet}}| < 2.5, \qquad R_{\text{jet,jet}} > 0.4 \,, \tag{3}$$

and cuts which more closely resemble the experimental setup of CDF. The results are shown in Fig. 1, the overall shape of the scale variation is not sensitive to the cuts on the decay products of the Higgs. At the Tevatron the search for the Higgs boson has been divided into jet bins. As such it has been argued [11] that one should estimate the overall scale uncertainty by using the appropriate PDF's and α_s running for the order in perturbation theory to which the Higgs plus number of jets amplitudes are known. Anastasiou *et al.* [11] use NNLO results for the 0-jet bin, NLO results for the 1-jet bin and LO results for the 2-jet bin, which dominates the overall scale uncertainty. However, with our NLO result we can update Anastasiou *et al*'s Eq. (4.3).

$$\frac{\Delta N_{\text{signal}}(\text{scale})}{N_{\text{signal}}} = 60\% \cdot \binom{+5\%}{-9\%} + 29\% \cdot \binom{+24\%}{-23\%} + 11\% \cdot \binom{+35\%}{-31\%} = \binom{+13.8\%}{-15.5\%} \tag{4}$$

The result in Eq. (4) updates the Anastasiou *et al.* [11] result $(+20\%, -16.9\%)$, reducing the overall scale uncertainty.

3 LHC results

In order to study the impact of the NLO corrections at the LHC, we adopt a different set of cuts to define the jets. The rapidity range of the detectors is expected to be much broader, allowing for a larger jet separation too, and we choose a somewhat higher minimum transverse momentum,

$$p_t(\text{jet}) > 40 \text{ GeV}, \qquad |\eta_{\text{jet}}| < 4.5, \qquad R_{\text{jet,jet}} > 0.8 \,. \tag{5}$$

In this section we do not consider the decay of the Higgs boson for the sake of simplicity.

Since results for this scenario have already been discussed at some length [3], we restrict ourselves to a short survey of the essential elements of the phenomenology at the lower centre-of-mass energy, $\sqrt{s} = 7$ TeV. We present the scale dependence of the LHC cross section for Higgs + 2 jets ($m_H = 160$ GeV) in Figure 2. As noted in the earlier paper [3], the corrections are quite modest using our central scale choice, $\mu_0 = \mu_H$, increasing the cross section by approximately 21%. Once again, although the scale dependence is much reduced it is still substantial.

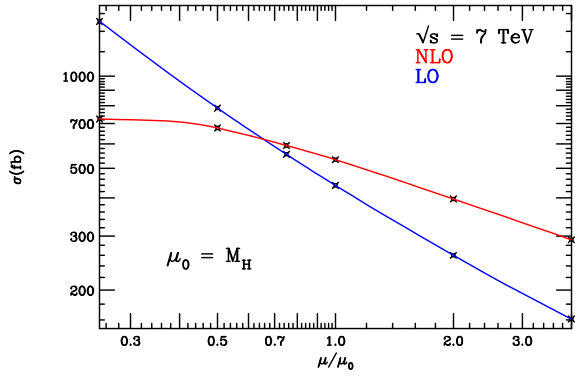

Figure 2: Scale dependence for the Higgs boson + 2 jet cross section, using the basic set of cuts in Eq. (5) and a central scale choice $\mu_0 = m_H$.

3.1 Weak boson fusion

The Higgs plus two jet process produces the same final state as expected from Higgs production via weak boson fusion (WBF). Therefore the contribution from gluon fusion must be taken into account when considering measurements of the Higgs coupling to W and Z bosons.

To address this issue, in this section we present a study of the rate of events expected using typical WBF search cuts. In addition to the cuts already imposed (Eq. (5)), these correspond to,

$$|\eta_{j_1} - \eta_{j_2}| > 4.2 \,, \qquad \eta_{j_1} \cdot \eta_{j_2} < 0 \,, \tag{6}$$

where j_1 and j_2 are the two jets with the highest transverse momenta. These cuts pick out the distinctive signature of two hard jets in opposite hemispheres separated by a large distance in pseudorapidity.

In Fig 3 we show the dependence of the cross section on the c.o.m. energy, from $\sqrt{s} = 7$ TeV to $\sqrt{s} = 14$ TeV.

We show the cross section both before and after application of the additional WBF search cuts given in Eq. (6), together with the corresponding results for the WBF process. The QCD corrections to both processes decrease slightly as $\sqrt{s}$ is increased, whilst the ratio of the gluon fusion to WBF cross sections after the search cuts are applied increases from 20% at 7 TeV to 35% at 14 TeV. This indicates that, viewed as a background to the weak boson fusion process, the hadronic Higgs + 2 jet process is less troublesome at energies below the nominal design value.

4 Conclusions

We have presented phenomenological predictions for the production of a Higgs boson and two jets through gluon fusion. These predictions have been made possible through the implementation of recent compact analytic results for the relevant 1-loop amplitudes [4,5,6,7,8,9,10]. The speed with which these amplitudes can be evaluated has enabled us to improve upon an existing semi-numerical implementation of the same process [3], with various decays of the Higgs boson now included.

We have investigated the behaviour of the NLO cross section at the Tevatron, where contributions from this channel form part of the event sample for the latest Higgs searches. We find that corrections to the event rate in the Higgs + ≥ 2 jet bin are modest and that the scale variation is reduced from $\approx (+90\%, -44\%)$ at LO to $\approx (+37\%, -30\%)$ at NLO.

For the LHC we have provided a brief study of the behaviour of our predictions for collisions at $\sqrt{s} = 7$ TeV. We have also performed an analysis of this channel in the context of detecting a

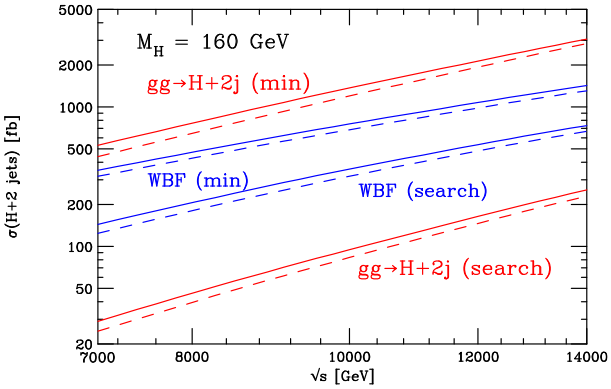

Figure 3: The $\sqrt{s}$ dependence of the cross section for $m_H = 160$ GeV at LO (dashed) and NLO (solid). Results are shown for the minimal set of cuts in Eq. (5) (two upper red curves) and after application of the additional WBF Higgs search cuts given in Eq. (6) (two lower red curves). The cross section for the weak boson fusion process is also shown for comparison (four central blue curves).

Higgs boson via weak boson fusion, where the improved theoretical prediction presented in this paper is essential in the long-term for making a measurement of the Higgs boson couplings to W and Z bosons.

Acknowledgments

We would like to thank Babis Anastasiou, Massimiliano Grazzini and Giulia Zanderighi for useful discussions. CW acknowledges the award of an STFC studentship. Fermilab is operated by Fermi Research Alliance, LLC under Contract No. DE-AC02-07CH11359 with the United States Department of Energy.

References

1. J.M. Campbell, R.K. Ellis and C. Williams *Phys. Rev.* D **81**, 074023 (2010) [arXiv:1001.4495].
2. V. Del Duca, W. Kilgore, C. Oleari, C. Schmidt and D. Zeppenfeld, Nucl. Phys. B **616**, 367 (2001) [arXiv:hep-ph/0108030].
3. J. M. Campbell, R. K. Ellis and G. Zanderighi, JHEP **0610**, 028 (2006) [arXiv:hep-ph/0608194].
4. C. F. Berger, V. Del Duca and L. J. Dixon, Phys. Rev. D **74**, 094021 (2006) [Erratum-ibid. D **76**, 099901 (2007)] [arXiv:hep-ph/0608180].
5. S. D. Badger and E. W. N. Glover, Nucl. Phys. Proc. Suppl. **160**, 71 (2006) [arXiv:hep-ph/0607139].
6. S. D. Badger, E. W. N. Glover and K. Risager, JHEP **0707**, 066 (2007) [arXiv:0704.3914 [hep-ph]].
7. E. W. N. Glover, P. Mastrolia and C. Williams, JHEP **0808**, 017 (2008) [arXiv:0804.4149 [hep-ph]].
8. S. Badger, E. W. N. Glover, P. Mastrolia and C. Williams, JHEP **1001**, 036 (2010) [arXiv:0909.4475 [hep-ph]].
9. L. J. Dixon and Y. Sofianatos, JHEP **0908**, 058 (2009) [arXiv:0906.0008 [hep-ph]].
10. S. Badger, J. M. Campbell, R. K. Ellis and C. Williams, JHEP **0912**, 035 (2009) arXiv:0910.4481 [hep-ph].
11. C. Anastasiou, G. Dissertori, M. Grazzini, F. Stockli and B. R. Webber, JHEP **0908**, 099 (2009) [arXiv:0905.3529 [hep-ph]].

BEYOND HEAVY TOP LIMIT IN HIGGS BOSON PRODUCTION AT LHC

Alexey Pak, Mikhail Rogal, and Matthias Steinhauser
Institut für Theoretische Teilchenphysik (TTP), KIT Karlsruhe

QCD corrections to inclusive Higgs boson production at the LHC are evaluated at next-to-next-to leading order. By performing asymptotic expansion of the cross section near the limit of infinitely heavy top quark we obtained a few first top mass-suppressed terms. The corrections to the hadronic cross sections are found to be small compared to the scale uncertainty, thus justifying the use of heavy top quark approximation in many published results.

1 Introduction

The Large Hadron Collider (LHC) at CERN is expected to provide insights on the mechanism of electroweak symmetry breaking, possibly by discovering the elusive Higgs boson. In the Standard Model, the dominant process of the Higgs boson production is the gluon fusion, $gg \to H$, mediated by a top quark loop. Predictions of Higgs boson production in gluon fusion both at the Tevatron and the LHC [1,2] include electroweak effects and results beyond the fixed-order perturbation theory, but QCD corrections have the greatest numerical effect. Since 1977, when the leading order (LO) calculation appeared [3], also next-to-leading order (NLO) [4,5,6], and more recently next-to-next-to-leading order (NNLO) [7,8,9,10] QCD corrections have been evaluated.

While the NLO results are exact in the top quark and Higgs boson masses, the NNLO results rely on the effective theory built in the limit of the large top quark mass (for a review see e.g. Ref. [11]). At NLO, this approximation results in $< 2\%$ deviations from the exact result for $M_H < 2M_t$ [12,13]. NNLO effects of the finite top quark mass have been first indirectly addressed in Ref. [14], where the asymptotics in the opposite limit of large center-of-mass energy $\sqrt{\hat{s}}$ were considered. Recently, two independent groups [15,16,17] performed an expansion of the inclusive Higgs production cross-section in $\rho = M_H^2/M_t^2$. In this contribution we summarize those results and provide some details of our calculation [16].

2 Calculation of partonic cross-sections

The QCD corrections to the cross-sections of partons are:

$$\hat{\sigma}_{ij\to H+X} \;=\; \hat{A}_{\rm LO}\left(\Delta_{ij}^{(0)} + \frac{\alpha_s}{\pi}\,\Delta_{ij}^{(1)} + \left(\frac{\alpha_s}{\pi}\right)^2\Delta_{ij}^{(2)} + \dots\right), \quad \hat{A}_{\rm LO} = \frac{G_F\,\alpha_s^2}{288\sqrt{2}\pi} f_0(\rho,0). \quad (1)$$

Here ij denote one of the possible initial states: gg, qg, $q\bar{q}$, qq, or qq', and q and q' stand for (different) massless quark flavours. At the leading order, the only non-zero contribution is $\Delta_{gg}^{(0)} = \delta(1-x)$, and the function $f_0(\rho,0)$ [18] describes the mass dependence. We focus on the

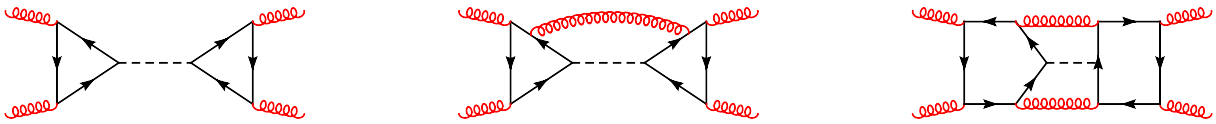

Figure 1: Sample forward scattering diagrams whose cuts correspond to the LO, NLO and NNLO corrections to $gg \to H$. Dashed, curly and solid lines represent Higgs bosons, gluons and top quarks, respectively.

x- and ρ-dependence of $\Delta_{ij}^{(1)}$ and $\Delta_{ij}^{(2)}$. As is common in the literature, by "infinite top quark mass approximation" we assume that $\Delta_{ij}^{(k)}$ are evaluated for $M_t \to \infty$, but $\hat{A}_{\rm LO}$ is exact in M_t.

To account for the real and virtual corrections we employ the optical theorem and compute imaginary parts of the four-point forward-scattering amplitudes such as in Fig. 1. After the asymptotic expansion in the limit $M_t^2 \gg \hat{s}, M_H^2$ the loop integrals factorize. The most non-trivial cases are two-loop four-point functions dependent on both $\hat{s}$ and M_H. Reducing them with IBP's [19] we obtain around 30 master integrals. The latter are available [10], however, we re-computed them with the combination of soft expansion and differential equation methods. Finally, we add renormalization terms and obtain a few first terms in the expansion of $\Delta_{ij}^{(k)}$ in powers of ρ, where coefficients are functions of x.

3 NLO and NNLO results

In Fig. 2 we compare the x-dependence of the exact NLO results [4,5,6] (evaluated for $M_H = 130$ GeV and $M_t = 173.1$ GeV) to the $\mathcal{O}(\rho^n)$ approximations for successive n. The leading term in ρ is smooth and demonstrates a reasonably good agreement with the exact curve for $x \to 1$. However, the higher order terms in ρ introduce divergences at $x \to 0$ which are the most obvious for the $q\bar{q}$ channel. This signifies the breakdown of the assumption that $M_t^2 \gg \hat{s}$ for large $\hat{s}$. Note, however, the decent convergence above the threshold for the top quark pair production (in Fig. 2, $x_{\rm th} \approx 0.14$). To recover the proper $x \to 0$ behaviour, we utilize $\hat{s} \to \infty$ asymptotics [14,17]. Interpolation between the $\mathcal{O}(\rho^n)$ result and the value at $x \to 0$ (dots in Fig. 2) agrees well with the exact curve for the gg channel. For the quark channels, the introduced error in hadronic contributions does not exceed 50%, which, if also true at NNLO, translates to a shift less than the total scale uncertainty of the full NNLO cross-section.

The NNLO diagrams require considerably more effort. Using the known virtual corrections [17,18] we were able to evaluate three terms in the expansion of $\Delta_{gg}^{(2)}$ and four terms in the other channels. Our analytic results are in full agreement with the $M_t \to \infty$ results [10] and the mass corrections expanded in $(1-x)$ (soft expansion) [15,17]. In Fig. 3 we present x-dependence of the functions $\Delta_{gg}^{(2)}$, $\Delta_{qg}^{(2)}$, and $\Delta_{g\bar{q}}^{(2)}$, with interpolations constructed similarly to the NLO case.

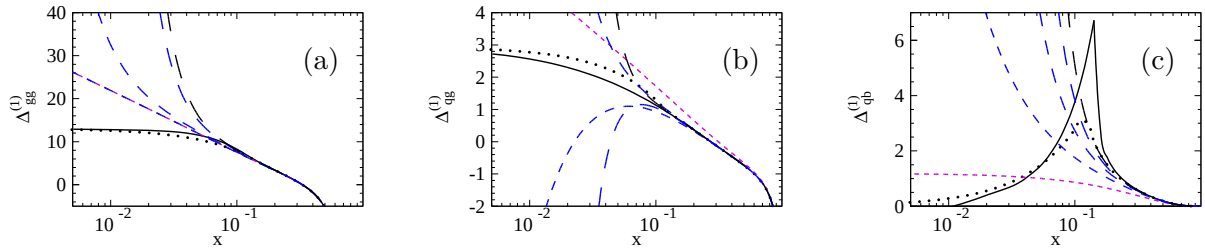

Figure 2: NLO partonic cross sections for the (a) gg, (b) qg and (c) $q\bar{q}$ channel as functions of x for $M_H = 130$ GeV. The expansion in $\rho \to 0$ (dashed lines) is compared with the exact result (solid lines). Lines with longer dashes include higher order terms in ρ. The interpolation (see text) is shown as a dotted line.

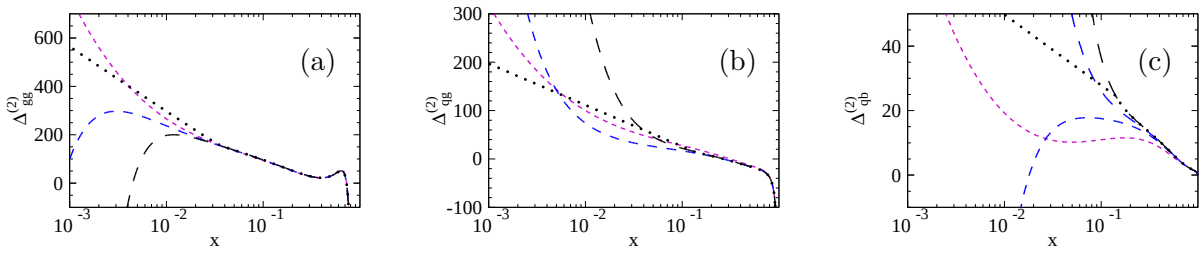

Figure 3: Partonic NNLO cross sections for the (a) gg, (b) qg, (c) $q\bar{q}$ channels for $M_H = 130$ GeV. Lines with longer dashes include higher order terms in ρ. Dotted lines corresponds to interpolation.

4 Hadronic results

The hadronic cross sections are given by the convolution of $\hat{\sigma}_{ij\to H+X}$ with the corresponding parton distribution functions (PDFs). We decompose it into LO, NLO, and NNLO contributions: $\sigma_{pp'\to H+X}(s) = \sigma^{\rm LO} + \delta\sigma^{\rm NLO} + \delta\sigma^{\rm NNLO}$. In Fig. 4 we show the M_H-dependence of $\delta^{(2)}_{qg}$, $\delta^{(2)}_{q\bar{q}}$, and $\delta^{(2)}_{qq}$ normalized to the infinte top quark mass result, labeled with subscript ∞. In all cases the power-suppressed terms lead to an increase of the cross section between 4% and 10% for the quark-gluon and up to 25% for the quark-anti-quark channel in our range of Higgs boson masses. For the qq and qq' channels we observe rapid convergence beyond $1/M_t^2$.

NNLO corrections to the gg channel are shown in Fig. 5(a). Finally, in Fig. 5(b) we present the gluon-induced cross-section including exact LO and NLO contributions. Minor differences with the left panel of Fig. 7 in Ref. [15] can be attributed to the different matching procedure. As one can see, the effects of matching near $x = 0$ and M_t-suppressed corrections nearly cancel and the final deviation from the heavy top mass result is below 1% (when exact LO mass dependence is factored out).

5 Conclusion

We present the NNLO production cross section of the Standard Model Higgs boson including the finite top quark mass effects. To improve $x \to 0$ behaviour for the gluon-gluon channel we match our results to the $\hat{s} \to \infty$ limit. The numerical impact of the top quark mass suppressed terms is below 1% and thus about a factor of ten smaller than the scale variation uncertainty. Our calculation justifies the use of the heavy top quark mass approximation in NNLO cross section calculations. In addition, we independently confirm the analytic results in the heavy top limit [10] and the soft expansion of M_t-suppressed terms [15].

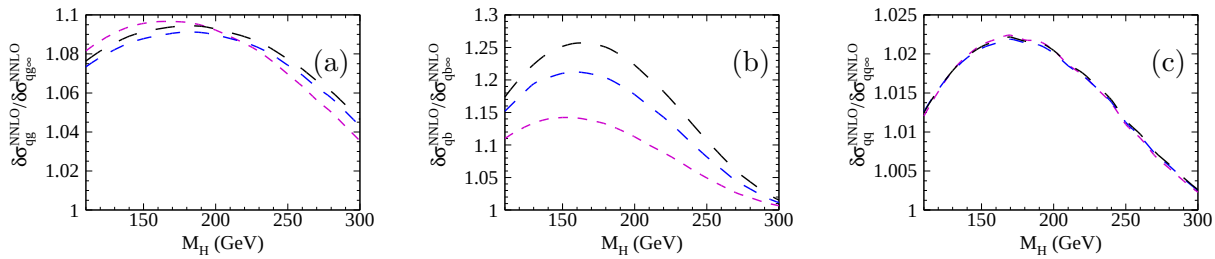

Figure 4: NNLO contributions to hadronic cross section with higher orders in $1/M_t$ (from short to long dashes) normalized to the heave top quark mass result, (a) qg, (b) $q\bar{q}$, (c) qq. Channels qq' and qq are almost identical.

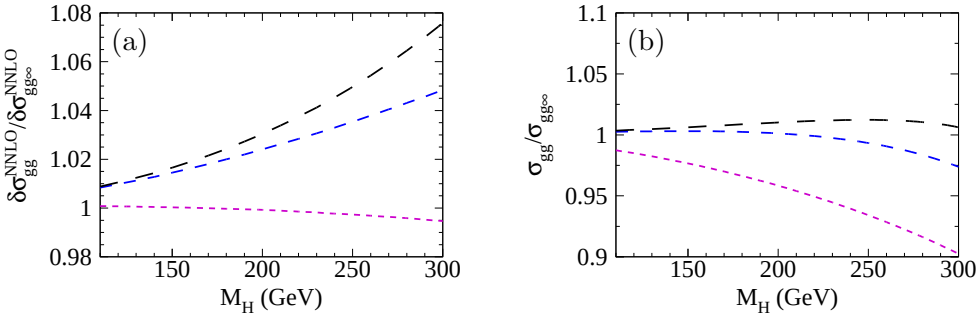

Figure 5: (a) Ratio of the NNLO hadronic cross section (gg contribution) including successive higher orders in $1/M_t$ normalized to the infinite top quark mass result. (b) Prediction for the gluon-induced inclusive Higgs production cross section up to NNLO normalized to the heavy top limit.

Acknowledgements. This work was supported by the DFG through the SFB/TR 9 "Computational Particle Physics". M.R. was supported by the Helmholtz Alliance "Physics at the Terascale".

References

1. D. de Florian and M. Grazzini, Phys. Lett. B **674** (2009) 291, arXiv:0901.2427 [hep-ph].
2. C. Anastasiou, R. Boughezal, and F. Petriello, JHEP **04** (2009) 003, arXiv:0811.3458 [hep-ph].
3. F. Wilczek, Phys. Rev. Lett. **39** (1977) 1304; J. R. Ellis, M. K. Gaillard, D. V. Nanopoulos and C. T. Sachrajda, Phys. Lett. B **83** (1979) 339; H. M. Georgi, S. L. Glashow, M. E. Machacek and D. V. Nanopoulos, Phys. Rev. Lett. **40** (1978) 692; T. G. Rizzo, Phys. Rev. D **22** (1980) 178 [Addendum-ibid. D **22** (1980) 1824].
4. S. Dawson, Nucl. Phys. B **359** (1991) 283;
5. M. Spira, A. Djouadi, D. Graudenz and P. M. Zerwas, Nucl. Phys. B **453** (1995) 17; arXiv:hep-ph/9504378;
6. A. Djouadi, M. Spira and P. M. Zerwas, Phys. Lett. B **264** (1991) 440.
7. R. V. Harlander, Phys. Lett. B **492** (2000) 74, arXiv:hep-ph/0007289;
8. R. V. Harlander and W. B. Kilgore, Phys. Rev. Lett. **88** (2002) 201801, arXiv:hep-ph/0201206;
9. V. Ravindran, J. Smith and W. L. van Neerven, Nucl. Phys. B **665** (2003) 325, arXiv:hep-ph/0302135.
10. C. Anastasiou and K. Melnikov, Nucl. Phys. B **646** (2002) 220, arXiv:hep-ph/0207004.
11. M. Steinhauser, Phys. Rept. **364** (2002) 247, arXiv:hep-ph/0201075.
12. R. Harlander, Eur. Phys. J. C **33** (2004) S454 arXiv:hep-ph/0311005.
13. M. Kramer, E. Laenen, M. Michael, Nucl. Phys. B **B511** (1998) 523-549, arXiv:hep-ph/9611272;
14. S. Marzani, R. D. Ball, V. Del Duca, S. Forte and A. Vicini, Nucl. Phys. B **800** (2008) 127 arXiv:0801.2544 [hep-ph].
15. R. V. Harlander and K. J. Ozeren, arXiv:0909.3420 [hep-ph].
16. A. Pak, M. Rogal and M. Steinhauser, arXiv:0911.4662 [hep-ph].
17. R. V. Harlander and K. J. Ozeren, Phys. Lett. B **679** (2009) 467 arXiv:0907.2997 [hep-ph].
18. A. Pak, M. Rogal and M. Steinhauser, Phys. Lett. B **679** (2009) 473 arXiv:0907.2998 [hep-ph].
19. S. Laporta, Int. J. Mod. Phys. A **15** (2000) 5087, arXiv:hep-ph/0102033.
20. R. V. Harlander, H. Mantler, S. Marzani and K. J. Ozeren, arXiv:0912.2104 [hep-ph].

HIGGS TO FOUR TAUS AT ALEPH

JAMES BEACHAM,
on behalf of the ALEPH Collaboration

Department of Physics, New York University, 4 Washington Place, New York, NY, USA

A search has been performed on 683 pb^{-1} of data collected by the ALEPH detector at the Large Electron-Positron (LEP), collider at centre-of-mass energies from 183 to 209 GeV looking for a Higgs boson decaying into four τ leptons via intermediate pseudoscalar a particles, for a Higgs mass range of 70 to 114 GeV/c^2 and an a mass range of 4 to 12 GeV/c^2. No excess above background is seen and a limit is placed on $\xi^2 = \frac{\sigma(e^+e^- \to Z+h)}{\sigma_{SM}(e^+e^- \to Z+h)} \times (h \to aa) \times (a \to \tau^+\tau^-)^2$ in the m_h, m_a plane. For $m_h < 107$ GeV/c^2 and $m_a < 10$ GeV/c^2, $\xi^2 > 1$ can be excluded at the 95% confidence level.

1 Introduction

Direct searches at LEP2 for the standard model (SM) Higgs boson, h, decaying into $b\bar{b}$ or $\tau^+\tau^-$ placed a lower bound of 114 GeV/c^2 on the Higgs mass [1]. However, fits of the SM to electroweak precision data suggest a Higgs with a mass within the kinematic limit of LEP. Additionally, a small, non-SM-like excess observed at a Higgs mass of around 100 GeV/c^2 in the $b\bar{b}$ final state at LEP and the fine-tuning needed in the minimal supersymmetric standard model (MSSM) have led to the consideration of models, such as the next-to minimal supersymmetric standard model (NMSSM) [2], that feature exotic Higgs boson decays and naturally light pseudoscalar particles, a. In these models, new decay channels, such as $h \to aa$, can dominate over $h \to b\bar{b}$ and render the Higgs boson "invisible" to conventional searches. In particular, the Higgs can decay into four SM particles instead of two, via two intermediate a particles. Several of these possible final states, such as $h \to 2a \to 4b$, are already highly constrained by existing analyses; see Ref. [3], for example. For $m_a < 2m_b$, however, the decay $a \to \tau^+\tau^-$ is expected; this process, with the Higgs decaying into $\tau^+\tau^-\tau^+\tau^-$ for a Higgs mass range of 86 to 114 GeV/c^2, is not covered by existing analyses. To investigate this range, the ALEPH data has been revisited. The present analysis is described in detail in Ref. [4].

2 The ALEPH Detector

A detailed description of the ALEPH detector can be found in Ref. [5] and of its performance in Ref. [6]. High momentum resolution is achieved via a large tracking volume immersed in a 1.5 T magnetic field. An energy-flow reconstruction algorithm measures total visible energy in the event by combining measurements from the tracking sub-detectors and the electromagnetic and hadronic calorimeters, and provides a list of reconstructed objects (*energy-flow objects*) which

are classified as charged particles (which correspond to charged particle tracks, here called *tracks*), photons, and neutral hadrons. These energy-flow objects are the basic entities used in the present analysis.

During LEP2 the machine operated at centre-of-mass energies from 183 to 209 GeV and collected data corresponding to a total integrated luminosity of 683 pb^{-1}.

3 Signal and Background Samples

We revived all steps of the ALEPH analysis framework, including the ability to generate simulated samples of standard model background and data. We produced 3000 simulated signal events (with $h \to aa$ followed by $a \to \tau^+\tau^-$) for each of the three Z decay channels considered and for each combination of Higgs boson and pseudoscalar masses in the ranges $70 < m_h < 114$ GeV/c^2 and $4 < m_a < 12$ GeV/c^2 in steps of 2 GeV/c^2. For the relevant background processes, our samples were either 10-30 or 300-1000 times larger than the data, depending upon the process.

4 Event Selection

For the mass range considered, the Higgs is produced approximately at rest, and thus the decay $h \to 2a \to 4\tau$ results in a pair of taus recoiling against another pair of taus. For the a mass range considered, the decay products of each 2τ system will be observed as a highly-collimated jet of charged particles. Due to this high level of collimation, individual identification of taus, via standard algorithms, would fail. Instead, we used the fact that each tau decays into either one charged particle or three charged particles, and we would thus expect each a jet to contain two, four or six tracks. We used the JADE algorithm to form jets with a y_{cut} chosen to merge proto-jets up to a mass of $m_{jet} = 15$ GeV/c^2.

We considered three possible decays of the Z boson, namely $\mathrm{Z} \to e^+e^-$, $\mathrm{Z} \to \mu^+\mu^-$, and $\mathrm{Z} \to \nu\bar{\nu}$, and formulated a set of *loose* selection criteria (convenient to allow comparison of data and simulation at an intermediate stage without compromising the blind nature of the analysis) and *final* selection criteria for each of the two Z decay classes considered: $\mathrm{Z} \to l^+l^-$ (where $l = e$ or μ) and $\mathrm{Z} \to \nu\bar{\nu}$.

4.1 $Z \to l^+l^-$

For the $\mathrm{Z} \to l^+l^-$ channel, four-fermion background processes are prominent. We used ALEPH lepton identification algorithms to mask the two most energetic leptons in the event from the list of objects clustered by the JADE jet-finding algorithm. The loose selection consisted of the following requirements: Two oppositely-charged, isolated leptons; two jets, well-contained within the tracking volume ($|\cos\theta_j| < 0.9$); and the jets and leptons sufficiently isolated from each other ($|\cos\theta_{jl}^{min}| < 0.95$). The final selection consisted of the following requirements: The invariant mass of the lepton pair near the Z mass ($80 < m_{l^+l^-(\gamma)} < 120$ GeV/c^2, where γ indicates an isolated photon that may have been radiated from one of the leptons and which is added to the di-lepton system if doing so corresponds to an invariant mass closer to the Z mass than the di-lepton pair alone); missing energy due to neutrinos from tau decays ($\not{E} > 20$ GeV); jets sufficiently separated ($|\cos\theta_{jj}| < 0$); and a signal-like track multiplicity, i.e., each jet must contain either two or four tracks.

4.2 $Z \to \nu\bar{\nu}$

The $\mathrm{Z} \to \nu\bar{\nu}$ channel represents a larger branching ratio of the Z than the lepton channel, and thus drives the analysis. A major background contribution arises from $\gamma\gamma$ events. The

loose selection consisted of the following requirements: Modest missing energy and missing mass ($\not\!\!E > 30$ GeV and $\not\!\!m > 20$ GeV/c^2); exactly two jets, well-contained in the tracking volume, with a modest invariant mass cut on the dijet system ($|\cos\theta_j| < 0.85$ and $m_{jj} > 10$ GeV/c^2); requirements on the angle of the missing momentum vector with the beam axis and the total visible energy in the event, to reject substantial portions of two-photon-initiated and beam background events ($|\cos\theta_{miss}| < 0.9$ and $E_{vis} > 0.05\ E_{CM}$); and modest requirements on the most energetic jet ($E_{j_1} > 25$ GeV and containing either two or four tracks). The final selection consisted of the following requirements: Less than 5 GeV within 30° of the beam axis, to reject events with energy deposits in the forward region of the detector; consistency with the Z boson decaying to neutrinos ($\not\!\!E > 60$ GeV and $\not\!\!m > 90$ GeV/c^2); small aplanarity (< 0.05), consistent with two back-to-back, highly collimated jets; and a signal-like track multiplicity, i.e., each jet must contain either two or four tracks.

5 Results

Based upon these selection criteria, our signal efficiency ranged from ∼25% to ∼50%, depending on Z decay channel, Higgs mass, and a mass. We determined that, for the $Z \to l^+l^-$ channel, we should expect ∼3 signal events versus < 0.2 background events, and for the $Z \to \nu\bar{\nu}$ channel our expectation was ∼11 signal events versus ∼6 background events.

Systematic uncertainties in our Monte Carlo simulation were estimated to be 5% for all signal and 10% for background in the $Z \to l^+l^-$ channel versus 30% for background in the $Z \to \nu\bar{\nu}$ channel. We found that the background estimate and the number of events seen in data at the loose selection agreed within the systematic and statistical uncertainty for all Z channels.

For the $Z \to l^+l^-$ channels, we observed zero events after applying all selection criteria, while for the $Z \to \nu\bar{\nu}$ channel we observed two events. These observations are consistent with background.

We place limits on the cross section times branching ratio of our signal process with respect to the SM Higgsstrahlung production cross section, $\xi^2 = \frac{\sigma(e^+e^- \to Z+h)}{\sigma_{SM}(e^+e^- \to Z+h)} \times (h \to aa) \times (a \to \tau^+\tau^-)^2$. The limits are based upon event counts in three separate track multiplicity bins (corresponding to events with two jets where 1) each jet contains two tracks, 2) each jet contains four tracks, or 3) one jet contains two tracks while the other contains four tracks) times each of the three Z decay channels considered, resulting in nine categories. The resulting joint probability density for the event counts is then used to construct confidence intervals using a generalized version of the Feldman-Cousins technique [7], which incorporates systematic uncertainties in a frequentist way [8] [9]. Results are shown, for the 95% confidence level, as a function of m_h (for $m_a = 10$ GeV/c^2) on the left in Fig. 1 and as contours within the m_h, m_a plane on the right in Fig. 1. Note that our selection criteria do not depend on m_h or m_a, and thus our upper limits are fully correlated. The observed number of events is consistent with a downward fluctuation of the background and, as such, our limits on ξ^2 are stronger than expected.

Also shown on the left in Fig. 1 is the effect of these results upon some possible favored scenarios in the NMSSM; see Ref. [10], Figures 17 and 21 therein. Our limits highly constrain scenarios with $\tan\beta \geq 3$, while scenarios with $\tan\beta \leq 2$, where there is a larger branching ratio of the Z boson into jets, remain unconstrained.

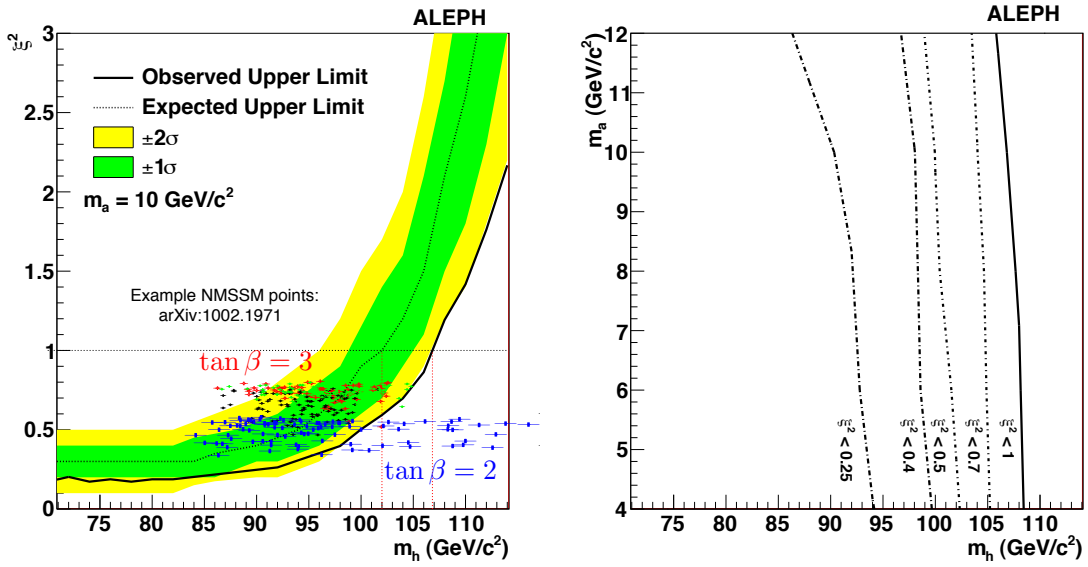

Figure 1: Left: Observed and expected 95% CL limit on ξ^2 as a function of m_h for $m_a = 10$ GeV/c^2. Also shown are some favored points in the parameter space of the NMSSM. Right: Contours of observed 95% CL limit on ξ^2 in the m_h, m_a plane.

6 Conclusions

We have performed a search for a Higgs decaying into four taus via Higgstrahlung at LEP2, for the process $h \to 2a \to 4\tau$ and Z $\to e^+e^-$, $\mu^+\mu^-$, or $\nu\bar{\nu}$, using ALEPH data. We observed no excess above background, and for $m_h < 107$ GeV/c^2 and $m_a < 10$ GeV/c^2, $\xi^2 > 1$ can be excluded at the 95% CL, where $\xi^2 = \frac{\sigma(e^+e^- \to Z+h)}{\sigma_{SM}(e^+e^- \to Z+h)} \times (h \to aa) \times (a \to \tau^+\tau^-)^2$. This analysis covers a region of parameter space previously unexplored and further constrains models that feature light pseudoscalar Higgs particles and non-standard Higgs decays, such as the NMSSM.

Acknowledgments

The author would like to thank K. Cranmer, I. Yavin and P. Spagnolo for their fruitful collaboration, as well as all members of the ALEPH collaboration for the successful design, construction and operation of the ALEPH detector.

References

1. LEP Working Group for Higgs Boson Searches, *Phys. Lett.* B **565**, 61–75 (2003), [hep-ex/0306033]
2. R. Dermisek and J.F. Gunion, *Phys. Rev. Lett.* **95**, 041801 (2005), [hep-ph/0502105]
3. LEP Working Group for Higgs Boson Searches, *Eur. Phys. J.* **C47**, 547–587 (2006), [hep-ex/0602042]
4. ALEPH Collaboration, *JHEP* **05**, 049 (2010), [arXiv:1003.0705]
5. ALEPH Collaboration, *Nucl. Instrum. Meth.* **A294**, 121–178 (1990)
6. ALEPH Collaboration, *Nucl. Instrum. Meth.* **A360**, 481–506 (1995)
7. G.F. Feldman and R.D. Cousins, *Phys. Rev.* D **57**, 3873 (1998)
8. T.L. Chuang, C-S Lai, *Biometrika* **85(2)**, 317–332 (1998)
9. K. Cranmer, *Proc. of PhyStat05* , [SPIRES 6994415] (2005)
10. R. Dermisek and J.F. Gunion, *Phys. Rev.* D **81**, 075003 (2010), [arXiv:1002.1971]

CP-properties of the Higgs-boson couplings from H + dijets through gluon fusion

Jeppe R. Andersen
Theory Division, Physics Department, CERN, CH-1211 Geneva 23, Switzerland

At lowest order in perturbation theory, the production of a Higgs boson in association with dijets displays a strong correlation in the azimuthal angle between the dijets, induced by the CP-properties of the Higgs Boson coupling. However, the phase space cuts necessary for a clean extraction of the CP-properties in the gluon fusion channel simultaneously induce large corrections from emissions of hard radiation and thus formation of additional jets. This contribution discusses how the CP-properties of the Higgs boson coupling can be cleanly extracted from events with more than two jets, based on a technique developed from insight into the high energy limit of hard scattering matrix elements.

1 Introduction

One of the primary goals of experiments at the CERN Large Hadron Collider (LHC) is the search for the Higgs boson(s) which, within the Standard Model (SM) and many of its extensions, provide direct access to the dynamics of electroweak symmetry breaking. Once discovered, the focus of Higgs physics will turn to the study of Higgs boson properties, like its mass, spin, CP parity and the strength and structure of Higgs boson couplings to heavy fermions and gauge bosons.

Among the various Higgs channels at the LHC, the production of a Higgs boson in association with two energetic jets has emerged as particularly promising in providing information on the dynamics of the Higgs sector. This is true in particular for the gluon fusion channel, where the CP-properties of the Higgs boson couplings to the fermions in the loop-induced coupling can be extracted[1]: Tree-level considerations lead to the expectations of a strong azimuthal correlation between the two jets, with a phase depending on the relative weight of a CP-even (SM-like) and CP-odd coupling. The azimuthal angle modulations get particularly pronounced when the two jets are widely separated in rapidity. Equivalent effects are expected in vector boson fusion and have been discussed in Ref.[2,3] for the idealised situation of parton level events at leading order.

The extraction of the CP-properties of the Higgs boson couplings in gluon fusion will require some cut on the rapidity separation between the two hard (e.g. $p_\perp > 40$GeV) jets; typically, they are required to be at least 3 units apart in rapidity[1], or alternatively[4] the Higgs boson is required to be produced between the dijets in rapidity, with a minimum distance of .5-1 units of rapidity between the Higgs boson and the hard jets.

2 Hard Radiative Corrections

The tree-level observations leading to the expectation of the azimuthal correlation are jeopardised by the requirement of a size-able rapidity separation between the jets. For the gluon fusion channel, this requirement increases the hard radiative corrections leading to the formation of additional jets; and therefore one must address the problem of how to extract the CP-properties of the Higgs boson couplings from events with strictly more than two jets, where one might think it is not so clear how to generalise the azimuthal angle studied for events of pure Higgs-boson plus dijet. It is clear that the study of just the azimuthal angle between any two jets (e.g. the two hardest) will necessarily be less correlated once real radiative corrections are taken into account. This contribution discusses how to form an observable, so that the extraction of the CP-properties is stable against radiative corrections[4].

First, we will briefly discuss the reason for the increasing weight of real, hard radiative corrections as the rapidity span between the dijets is increased. This is caused by two effects.

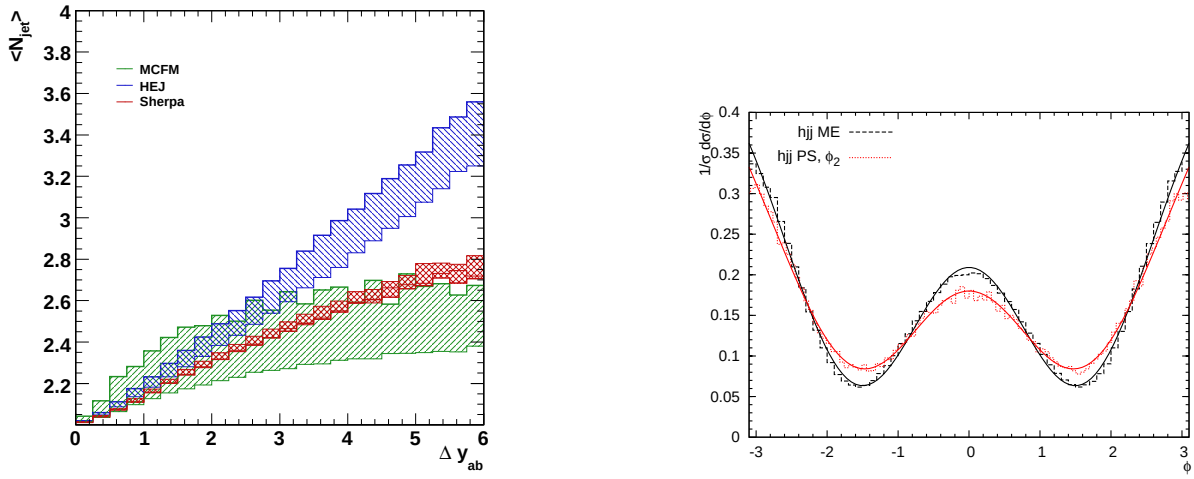

Figure 1: Left: The average number of hard jets ($p_\perp > 40$GeV) in Higgs-boson production in association with dijets as a function of the rapidity difference between the most forward and most backward hard jet. Figure taken from Ref.[6] Right: The differential cross section on the azimuthal angle discussed in the text for the tree-level calculation (black) and for showered and hadronised events (red). Figure taken from Ref.[6]

First, two widely separated (in rapidity) jets will dominate the contribution to the light-cone momentum fraction of the partons extracted from the proton, so the relative impact of extracting a little extra energy from the proton in order to form an additional central jet is small (the details will obviously depend on just how steeply the parton density functions are falling with increasing x). Secondly, the phase space for the emission of additional radiation increases as the rapidity span between the most forward and most backward jet is increased. These kinematic considerations are shared of course by all processes, and by all models for the these (e.g. shower MC, fixed order perturbation theory). The amount of hard radiation generated obviously differs between different processes (e.g. Higgs boson+dijets through weak boson fusion or gluon fusion[5]), and between different models of a given process (e.g. shower MC, NLO, resummation). To illustrate this last effect, Figure 1 (taken from Ref.[6]) displays the average number of jets in events (at a pp-machine with $\sqrt{s} = 10$TeV) with a Higgs-boson in association with at least two hard jets (of transverse momentum greater than 40GeV) as a function of the rapidity span between the most forward and most backward hard jet, as calculated at fixed next-to-leading order[7] (green), `Sherpa`[8] with tree-level matching up to Higgs-boson plus four partons using `Comix`[9] (red), and finally an all-order sum of the leading radiative corrections for widely separated emissions[10,11,12,13] (blue). The width of the bands indicate the scale variation, but the initial choice is different and the range of variation is smaller in `Sherpa` than in the two other models. We see that all models for this process predicts a strong correlation between the rapidity span between the most forward and most backward hard jet, and the average number of hard jets (all above 40GeV in transverse momentum) in the event. In fact, the increasing relevance of the high-multiplicity states with growing rapidity span is a central motivation for the BFKL[14,15] resummation programme for hard processes. Indeed, the strong correlation between the rapidity span of the event and the average number of hard jets were observed in variants[16,17] on the BFKL formalism also for pure jets[18] and W+dijets[19]. While the BFKL formalism reproduces the limit of the full QCD amplitudes for infinite rapidity separation between all (hard) particles, the formalism developed in Ref.[10,11,12,13] obeys also other constraints (e.g. gauge-invariance) in all of phase space (i.e. also for sub-leading kinematics).

Figure 1 also indicates that for the rapidity spans of interest for the extraction of the CP-properties, the average number of jets is significantly larger than 2. For the NLO calculation,

the exclusive 2-jet and 3-jet rates have to be equal, in order to get an average number of hard jets of 2.5. It is clear that understanding the pattern of multi-jet radiation will be important for a stable extraction of the CP-properties of the Higgs-boson couplings.

3 Lessons From The High Energy Limit

In order to generalise the lowest order study of the azimuthal angle between the dijets to the case of multiple hard jets we start by studying the (colour and helicity summed and averaged) square of the matrix element for $gg \to g\cdots ghg\cdots g$ in the limit of infinite rapidity separation between each produced particle (the so-called multi-Regge-kinematic (MRK) limit):

$$|\overline{\mathcal{M}}_{gg\to g\cdots ghg\cdots g}|^2 \to \frac{4\hat{s}^2}{N_C^2-1}\left(\prod_{i=1}^{j}\frac{C_A\ g_s^2}{\mathbf{p}_{i\perp}^2}\right)\frac{|C^H(\mathbf{q}_{a\perp},\mathbf{q}_{b\perp})|^2}{\mathbf{q}_{a\perp}^2\ \mathbf{q}_{b\perp}^2}\left(\prod_{i=j+1}^{n}\frac{C_A\ g_s^2}{\mathbf{p}_{i\perp}^2}\right), \tag{1}$$

where $\mathbf{q}_{a\perp} = -\sum_{i=1}^{j}\ \mathbf{p}_{i\perp}$, where j is the number of gluons with rapidity smaller than that of the Higgs boson, and $\mathbf{q}_{b\perp} = \mathbf{q}_{a\perp} - \mathbf{p}_{h\perp}$. In this limit, the contribution from quark-initiated processes is found by just a change of one colour factor $C_A \to C_F$ for each incoming gluon replaced by a quark. The effective vertex for the coupling of a SM Higgs boson to two off-shell gluons through a top loop is in the combined large-m_t and MRK limit[20]

$$\begin{aligned} C^H(\mathbf{q}_{a\perp},\mathbf{q}_{b\perp}) &= i\,\frac{A}{2}\,\left(|\mathbf{p}_{h\perp}|^2 - |\mathbf{q}_{a\perp}|^2 - |\mathbf{q}_{b\perp}|^2\right) = -iA\ \mathbf{q}_{a\perp}\cdot\mathbf{q}_{b\perp}, \\ A &= \frac{\alpha_s}{3\pi v}, \quad v = 246\ \text{GeV}. \end{aligned} \tag{2}$$

In the simple case of hjj at tree level in the SM we recover from Eq. (2) a cosine modulation in the azimuthal angle between the two jets, which is indeed the correct limiting behaviour seen in the full tree-level matrix element. A CP-odd contribution to the coupling would introduce a sinus-component, and a phase-shift in the angular distributions discussed later. However, Eq. (2) also hints how to recover this azimuthal modulation in events with more than two jets[4]: simply divide the jets into two sets according to whether their rapidities are smaller or greater than that of the Higgs boson; then calculate the azimuthal angle between the transverse sum of vectors from each set. This angle will in the MRK limit display the same behaviour as that of the azimuthal angle between the two partons in the lowest order analysis.

4 Results

In Ref.[4] we checked the stability of the angle as defined above against several corrections beyond the tree-level description, and will here present just a few of the findings. The first thing one could worry about is the stability against the effects, both perturbative and non-perturbative, included in a general-purpose Monte Carlo generator. In Fig. 1 (right) we compare the azimuthal modulation using the definition discussed in the previous section found at tree-level with that found after showering and hadronisation of these states with HERWIG++[21]. We see that the azimuthal modulation survives the effects of hadronisation etc., and also that the real emission from the shower, which does not end up in hard jets (and is thus not included in the construction of the azimuthal angle), does not spoil the positions of the peaks and troughs of the distribution.

While the shower-formalism correctly resums the soft- and collinear radiation from the tree-level hjj-configuration, the pure shower-formalism underestimates the amount of hard radiation, which can lead to further decorrelation. In order to check the stability of the azimuthal distribution, against such radiation, we analyse the constructed azimuthal observable on a set of hjj-events generated in the all-order formalism discussed earlier[10,11,12,13]. In Fig. 2 we show on

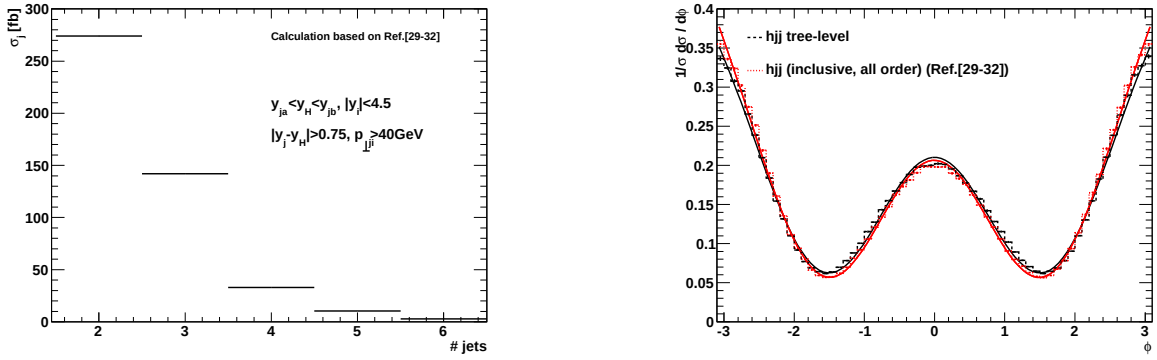

Figure 2: Left: The jet rates in the inclusive all-order sample generated with the method discussed in Ref.[10,11,12,13]. The exclusive 2-jet rate accounts for only roughly 60% of the inclusive 2-jet sample. Right: The distribution on the azimuthal angle discussed in the text as calculated at tree-level (black) and in the all-order sample. Figure taken from Ref.[4]

the left the distribution of the number of hard jets in the event sample within the cuts mentioned in the figure. The exclusive 2-jet rate accounts for around 60% of the inclusive two-jet rate, so it is clearly necessary with a strategy for a stable extraction of the CP-properties of the Higgs boson couplings for events with strictly more than two jets. In Fig. 2 (right) we have used the same event sample as used for the plot on the left, and show the differential distribution on the azimuthal angle constructed as discussed. Furthermore, we compare this to the result obtained at lowest order.

In conclusion, the constructed azimuthal observable is clearly very stable against higher order perturbative corrections, allowing for a stable extraction of the CP-properties of the Higgs boson couplings in gluon fusion.

References

1. G. Klamke and D. Zeppenfeld, JHEP **0704**, 052 (2007).
2. T. Plehn, D. L. Rainwater and D. Zeppenfeld, Phys. Rev. Lett. **88** (2002) 051801.
3. V. Hankele, G. Klamke, D. Zeppenfeld and T. Figy, Phys. Rev. D **74**, 095001 (2006).
4. J. R. Andersen, K. Arnold and D. Zeppenfeld, arXiv:1001.3822.
5. Y. L. Dokshitzer, V. A. Khoze, T. Sjostrand, Phys. Lett. **B274** (1992) 116-121.
6. J. R. Andersen *et al.* [SM and NLO Multileg Working Group], [arXiv:1003.1241 [hep-ph]].
7. J. M. Campbell, R. K. Ellis, C. Williams, [arXiv:1005.3733 [hep-ph]].
8. T. Gleisberg, S. Höche, F. Krauss *et al.*, JHEP **0902** (2009) 007.
9. T. Gleisberg, S. Höche, JHEP **0812**, 039 (2008).
10. J. R. Andersen, C. D. White, Phys. Rev. **D78** (2008) 051501.
11. J. R. Andersen, V. Del Duca, C. D. White, JHEP **0902** (2009) 015.
12. J. R. Andersen, J. M. Smillie, JHEP **1001** (2010) 039.
13. J. R. Andersen, J. M. Smillie, Phys. Rev. D **81**, 114021 (2010).
14. E. A. Kuraev, L. N. Lipatov and V. S. Fadin, Sov. Phys. JETP **45** (1977) 199.
15. I. I. Balitsky and L. N. Lipatov, Sov. J. Nucl. Phys. **28** (1978) 822.
16. L. H. Orr and W. J. Stirling, Phys. Rev. D **56** (1997) 5875.
17. J. R. Andersen, V. Del Duca, S. Frixione, W. J. Stirling, JHEP **0102** (2001) 007.
18. J. R. Andersen, W. J. Stirling, JHEP **0302** (2003) 018.
19. J. R. Andersen, V. Del Duca, F. Maltoni, W. J. Stirling, JHEP **0105** (2001) 048.
20. V. Del Duca, W. Kilgore, C. Oleari *et al.*, Phys. Rev. **D67** (2003) 073003.
21. M. Bahr *et al.*, Eur. Phys. J. C **58** (2008) 639.

5.
Top

TOP QUARK PAIR PRODUCTION AT THE TEVATRON

M. BEGEL
for the CDF & DØ Collaborations
Department of Physics, Brookhaven National Laboratory,
Upton, New York 11973, United States

Recent innovations in the measurement of the inclusive $t\bar{t}$ production cross section at the Fermilab Tevatron collider have improved the precision of the results. Two recent measurements that apply these techniques, in the ℓ+jets and dilepton decay channels, are presented. The CDF and D0 collaborations have also begun making differential measurements of $t\bar{t}$ production. The first measurement of $t\bar{t}$+jet production and of $d\sigma/dp_T$ binned in top-quark p_T are presented. In all cases, expectations from next-to-leading order perturbative QCD agree with the measurements from the CDF and D0 collaborations.

There were two recent innovations that improved the uncertainty of the inclusive $t\bar{t}$ cross section at $\sqrt{s} = 1.96$ TeV. The first, implemented by the CDF collaboration, normalized the $t\bar{t}$ cross section to the production of Z bosons. This swapped the systematic uncertainty associated with the experimentally measured luminosity (dominated by the inelastic $p\bar{p}$ cross section at $\sqrt{s} = 1.8$ TeV) with the smaller uncertainty associated with the perturbative QCD (pQCD) prediction for Z boson production. Measuring the ratio also allowed for reduction of common systematic uncertainties, such as those related to lepton efficiencies. CDF used this technique to measure the inclusive $t\bar{t}$ cross section in the ℓ+jets decay channel.[1] The measurement was performed as both a template fit to the output of an artificial neural network (ANN) trained to separate $t\bar{t}$ signal from background and as a counting experiment using b-tagging to suppress background contributions (Fig. 1). The total uncertainty in each measurement improved by approximately 20% by normalizing to the Z boson. The two measurements were combined yielding $\sigma_{t\bar{t}} = 7.70 \pm 0.52$ pb for a top quark mass $m_t = 172.5$ GeV. The result is consistent with the standard model next-to-leading order pQCD (NLO pQCD) prediction $\sigma_{t\bar{t}} = 7.45^{+0.72}_{-0.63}$ pb.[2]

The second improvement came from further investment in multi-variate analysis techniques such as ANN (used in the CDF ℓ+jets result above) and boosted decision trees (BDT). The latter was used by the D0 collaboration in a recent measurement of the inclusive $t\bar{t}$ cross section in the dilepton decay channel.[3] The BDT was trained on $t\bar{t}$ signal and the $Z/\gamma^\star$ and diboson backgrounds. A cut, optimized on $S/\sqrt{S+B}$, was placed on the BDT discriminant output for the e^+e^- and $\mu^+\mu^-$ decay channels. The resulting cross section, shown in Fig. 2, was $\sigma_{t\bar{t}} = 8.8 \pm 1.4$ pb at $m_t = 172.5$ GeV. This result, measured with $\int \mathcal{L} = 4.3$ fb^{-1}, was combined with an earlier 1 fb^{-1} measurement yielding $\sigma_{t\bar{t}} = 8.4 \pm 1.2$ pb which is in good agreement with the NLO pQCD expectation.[2]

Results on the inclusive $t\bar{t}$ cross section, in several decay channels, from the CDF and D0 collaborations are summarized in Fig. 3. The measurements are consistent with each other and with expectations from NLO pQCD.[2,4,5]

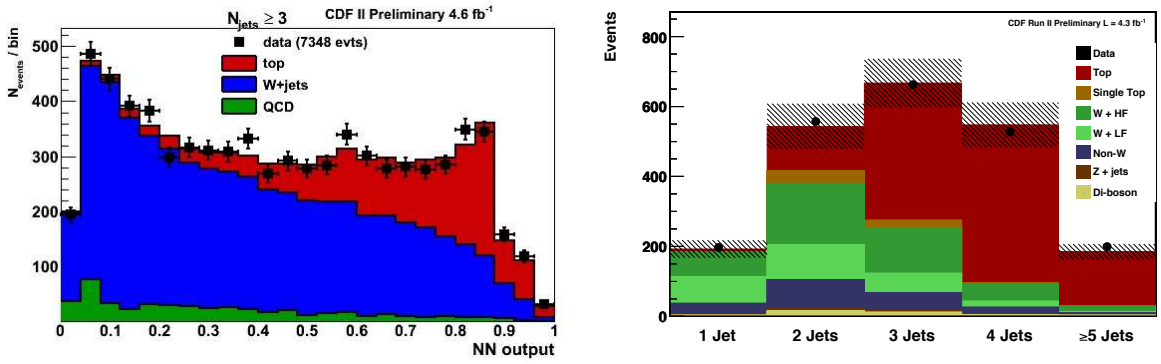

Figure 1: Meaurement of the $t\bar{t}$ cross section in the ℓ+jets decay channel from the CDF collaboration. Left: output of ANN trained to distinguish $t\bar{t}$ from background. The $t\bar{t}$ cross section was extracted from a fit of templates (colored regions) to the data (points). Right: number of data and predicted background events as a function of jet multiplicity, with the $t\bar{t}$ normalized to the measured cross section.

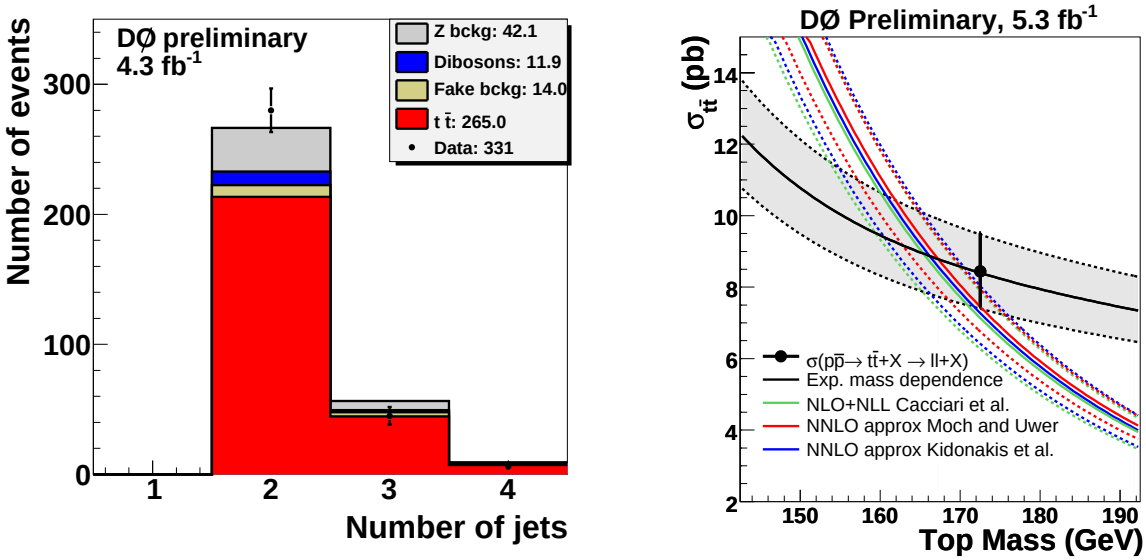

Figure 2: Left: observed and predicted jet multiplicity for various backgrounds and the signal after the final D0 dilepton selection requirements. The $t\bar{t}$ signal was normalized to the measured cross section. Right: variation of the combined $t\bar{t}$ production cross section (points) as a function of top quark mass. The colored lines show several theoretical predictions.[2,4,5]

In addition to the inclusive $t\bar{t}$ cross section results summarized above, both collaborations have recently begun measuring differential cross sections. CDF has made the first measurement of the cross section for jet production associated with the $t\bar{t}$. The jet multiplicity distribution and p_T spectrum of the fifth jet in ℓ+jet events are shown in Fig. 4. The theoretical cross section for this process, known to LO for many years, has been recently calculated to NLO.[7] This was a very difficult calculation and is an important step towards the full NNLO pQCD calculation for $t\bar{t}$ production. The theoretical expectation of $\sigma_{t\bar{t}j} = 1.79^{+0.16}_{-0.31}$ pb agrees with the measurement of $1.6 \pm 0.2 \pm 0.5$ pb.

Comparisons between measurements of the inclusive jet cross section binned in jet p_T and pQCD calculations are used to extract information about partons and the strong force. These comparisons are, however, obscured by the non-abelian nature of QCD through the fragmentation and hadronization processes. The top quark, with its exceptionally large mass, has a

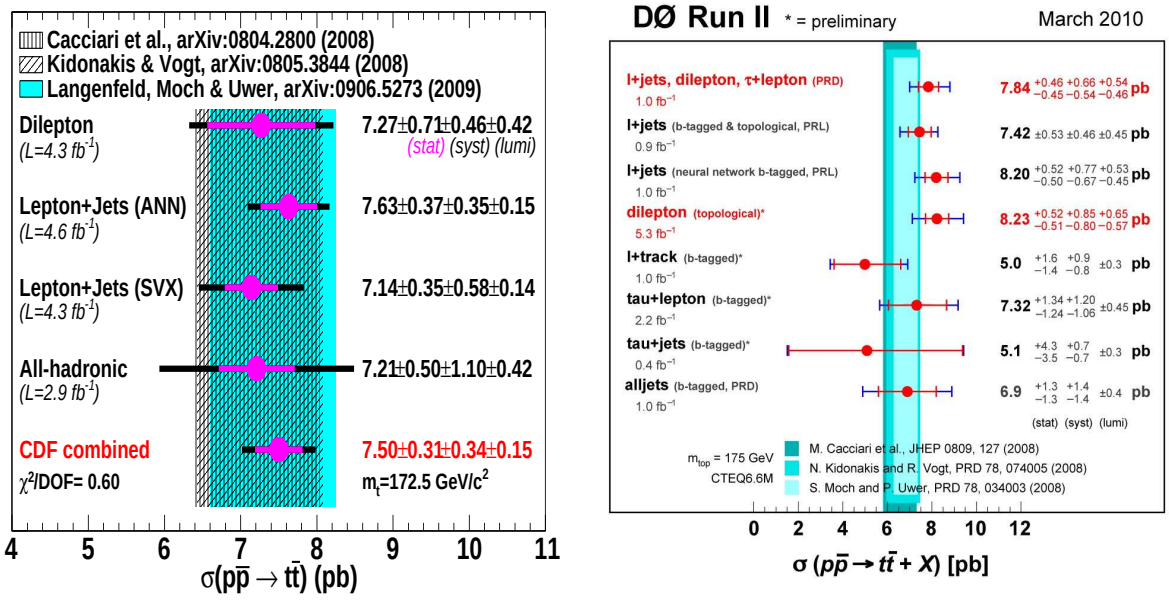

Figure 3: Summary of recent $t\bar{t}$ cross section measurements by the CDF (left) and D0 (right) collaborations. The results are compared with expectations from three NLO pQCD calculations.[2,4,5]

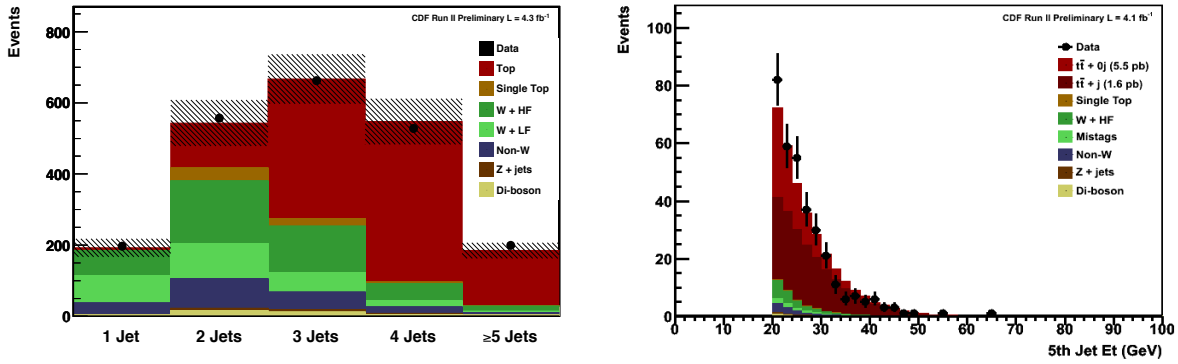

Figure 4: Measurement of the $t\bar{t}$+jet cross section in the ℓ+jets decay channel from the CDF collaboration. Left: distribution of events as a function of the number of reconstructed jets. Right: distribution of the p_T of the fifth jet. Data are represented by the points; results from simulation as the colored regions. The $t\bar{t}$ and $t\bar{t}$+jet contributions are indicated by the brown regions.

shorter lifetime than the characteristic hadron-formation time, so top quarks typically decay before interacting via the strong force. Measurements of top quark kinematics essentially access the properties of a bare quark. The D0 collaboration has recently measured the differential cross section for $t\bar{t}$ production binned in the top-quark p_T.[8] The cross section is shown in ratio to NLO pQCD[9] in Fig. 5. Expectations from an approximate NNLO pQCD calculation[5] and from three event generators[10,11,12] are also shown. The LO pQCD results disagree in normalization with the measurement; all the calculations agree with the shape of the cross section.

In summary, recent innovations in the measurement of the inclusive $t\bar{t}$ production cross section have allowed significant improvements in precision. Two recent measurements, in the ℓ+jets and dilepton decay channels, were presented. The CDF and D0 collaborations are also measuring differential $t\bar{t}$ production. The first measurement of $t\bar{t}$+jet production and of $d\sigma/dp_T$ binned in top-quark p_T were presented. In all cases, expectations from NLO pQCD agreed with the measurements from the CDF and D0 collaborations.

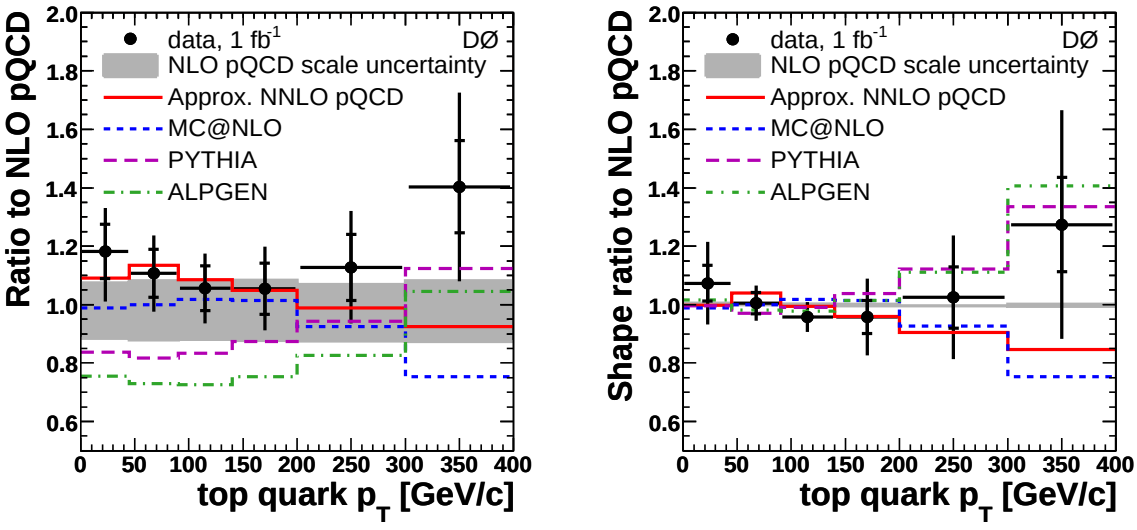

Figure 5: Inclusive differential $t\bar{t}$ cross section binned in top-quark p_T from the D0 collaboration. Left: ratio of $\mathrm{d}\sigma/\mathrm{d}p_T$ to the expectation from NLO pQCD.[9] Right: ratio of $(1/\sigma)\mathrm{d}\sigma/\mathrm{d}p_T$ to the expectation from NLO pQCD. There are two entries for each event. Also shown are ratios relative to NLO pQCD for an approximate NNLO pQCD calculation[5] and of predictions for several event generators.[10,11,12]

1. T. Aaltonen *et al.* [CDF Collaboration], arXiv:1004.3224 [hep-ex].
2. S. Moch and P. Uwer, Nucl. Phys. Proc. Suppl. **183**, 75 (2008); *ibid.* Phys. Rev. D**78**, 034003 (2008).
3. D0 Note 6038-CONF (2010).
4. M. Cacciari *et al.*, JHEP **09**, 127 (2008).
5. N. Kidonakis, R. Vogt, Phys. Rev. D**78**, 074005 (2008).
6. CDF Conf. Note 9850 (2009).
7. S. Dittmaier, P. Uwer, and S. Weinzierl, arXiv:0810.0452 [hep-ph].
8. V. M. Abazov *et al.* [D0 Collaboration], arXiv:1001.1900 [hep-ex].
9. M. Mangano, P. Nason, and G. Ridolfi, Nucl. Phys. B**373**, 295 (1992); P. Nason, S. Dawson, and R. K. Ellis, Nucl. Phys. B**327**, 49 (1989) [*Erratum-ibid.* B**335**, 260 (1990)].
10. S. Frixione and B. R. Webber, J. High Energy Phys. **0206**, 029 (2002); S. Frixione, P. Nason, and B. R. Webber, J. High Energy Phys. **0308**, 007 (2003).
11. M. L. Mangano, *et al.*, J. High Energy Phys. **0307**, 001 (2003).
12. T. Sjöstrand *et al.*, Comput. Phys. Commun. **135**, 238 (2001); R. Field and R. C. Group, arXiv:hep-ph/0510198.

Top Quark Mass Measurements

Hyun Su Lee on behalf of CDF and D0 Collaborations
Enrico Fermi Institute, University of Chicago,
Chicago, IL 60637, USA

The top quark mass is a fundamental parameter of the Standard Model (SM). The precision measurement of its mass combined with W boson mass measurement can constrain the mass range of the SM Higgs boson, which is the only unobserved SM particle. In this letter we present updated results of selected analyses using data up to 4 8 fb ^{1} of pp collisions at Tevatron Fermilab obtained by the CDF and D0 detector.

1 Introduction

The top quark, observed by both the CDF and D0 experiments in 1995 [1,2], is by far the heaviest known elementary particle and its mass is almost 40 times heavier than its isospin partner, the bottom (b) quark [3]. Due to the heavy mass, the top quark plays an important role in electroweak radiative corrections. Therefore, top quark mass (M_{top}) measurements are important tests of the Standard Model (SM) and provide constraints on the Higgs boson mass. For these reasons, the CDF and D0 collaborations have measured M_{top} in all possible ways, and with continuous improvement.

2 Top quark production and decay

Top quarks at the Tevatron are predominantly produced in pairs, and decay almost always to a W boson and a b quark in the SM. The topology of tt events depends on the di erent decay of the two W bosons. In the dilepton channel, each W boson decay to charged lepton (electron and muon) and neutrino. Events in this channel thus contain two leptons, two b-quark jets, and two undetected neutrino. Because of the presence of two leptons, this channel has the lowest background. However the dilepton channel has the smallest branching fraction. In the all-jets channel, each W boson decays to two jets so that this channel contains two b quark jets and four light quark jets. This channel has the largest branching fraction but also the largest background from QCD multijet production. The lepton+jets channel has one W boson decaying leptonically and the other hadronically so that we have one charged lepton, two b-quark jets, two light quark jets, and one undetected neutrino. Because of the relatively large branching fraction with manageable background levels, we made the most precise $M_{\rm top}$ measurements using events in the lepton+jets decay topology.

To improvement the $M_{\rm top}$ measurement, CDF and D0 collaborations identify b quarks using the properties of the longer lifetime of metastable B hadrons [4,5]. Therefore jets arising from b quarks have secondary vertices that are displayed from the primary collision vertex. b-tagging

signi cantly improve not only background fraction but also the combinatorics of jet-to-parton assignments, improving M_{top} resolution.

In the lepton+jets and all-jets channels, we have at least one W boson decaying hadronically (W decaying to two jets). Therefore we use the reconstructed dijet mass from W boson decay to constrain, *in situ*, the largest systematic in M_{top} measurements, the jet energy scale (JES), which is the calibration between jets energies and parton level energies, because of the narrow decay width and well known mass of the W boson.

3 Top quark mass measurement

For the M_{top} measurements, two primary techniques have been established. The template method (TM) uses the distributions of variables (templates) which are strongly correlated with the top quark mass and JES. In the building of a probability, only a few variables (usually less than two) are used, for instance reconstructed top quark mass and dijet mass in the lepton+jets channel. The Matrix Element Method (ME) uses event's probability to be a combinates signals and background. ME exploit all the information in the event by using a leading order matrix element calculation convoluted with parton distribution function and transfer functions (TFs) making connection between detector response and parton level particle. Because we can use all the information in principle, ME usually provide better precision of M_{top} than TM. Both techniques employ a likelihood to compare data to the modeling of signals and background to extract M_{top}.

D0 has a ME measurement in the lepton+jets channel using 3.6 fb^{-1}. D0 employed neural network (NN) based b-tagging [5] to improve signal to background ratio and also reduce jets to partons assignments. The TF factorizes into contributions from the individual top pair decay products. One can assume that the angles are well measured while their energy and momentum resolutions are determined from MC simulations. D0 estimates TF for four di erent η regions and for b jets, light jets, and leptons. A W+jets ME is used to estimate background probabilities. *In situ* JES calibration is performed using dijet mass from hadronically decaying W bosons. D0 measure $M_{top} = 173.7 \pm 1.8$ GeV/c^2 [6].

CDF also has a ME based measurement in the lepton+jets channel using 4.8 fb^{-1}. This analysis integrates over more than 19 variables using a quasi-MC integration technique to account imperfect assumptions about perfectly measured angles and intermediate particle masses. TF is parameterized as a function of η and p_T separately for b-jets and light jets. This analysis also makes a cut using a NN to reject not only background contribution but also poorly modeled signal events where the objects in the detector do not match the assumed partons at the matrix element level. In this measurement, we increase muon acceptance by using missing energy plus two jets trigger which give almost 30% more candidate events with a similar signal to background ratio. With *in situ* JES calibration, we measure $M_{top} = 172.8 \pm 1.3$ GeV/c^2 [7]. This measurement is the most precise top quark mass measurement in the world to date.

CDF has another lepton+jets channel measurement using TM. We uses exactly the same data as the ME analysis, including missing energy plus two jets trigger to increase muon acceptance. In this measurement, three variables are used to estimate probabilities of events. The rst two variables are the reconstructed top quark mass from the kinematic tter and dijet mass from hadronically decaying W boson used to make the M_{top} measurement with *in situ* JES calibration in the same channel [8]. In addition, a 3rd variable is introduced: the 2nd best reconstructed top quark mass by choosing 2nd jets to parton assignment based on the kinematic t. To take into account correlation between the variables and build probabilities without parameterization, kernel density estimation (KDE) [8,9] was employed. This revisit in a measured $M_{top} = 172.0 \pm 1.5$ GeV/c^2 [10]. This measurement use a technique complementary to the ME based measurement and gives a consistent result.

CDF has a dilepton channel measurement using TM. Two variables sensitive to M_{top} are used by taking into account the correlations using KDE. One variable is the reconstructed top quark mass using the neutrino weighting algorithm (NWA) [11,12] in the underconstrained system from two neutrinos. The unknown pseudorapidities of the two neutrinos are integrated over. The solutions for a given top quark mass are weighted by using measured missing transverse energy. The other variable is m_{T2} [13,14] which is a measure of transverse mass in two missing particles nal states. It provides a measured M_{top} in the dilepton channel [15] and is the rst use of this technique. The simultaneous measurement with the two variables gives $M_{top} = 170.6 \pm 3.8$ GeV/c^2 [10].

Because two TM measurements share the same machinery, a simultaneous measurement can be made using the lepton+jets and dilepton channels [8]. The correlation of systematic uncertainties is intrinsically taken into account. The combined measurement both lepton+jets and dilepton channels using 4.8 fb^{-1} data gives $M_{top} = 171.9 \pm 1.5$ GeV/c^2 [10].

D0 makes a dilepton channel measurement using a rather di erent idea with 1 fb^{-1} of data. The basic idea is to use the measured $t\bar{t}$ production cross section as a function of top quark mass and compare with predictions from theoretical calculations. In general, the di erent theoretical prediction gives di erent results but all the measurements are consistent with results from the direct measurement [16].

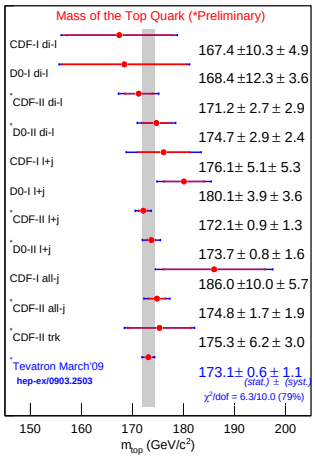

Figure 1: World average top quark mass and comparison with individual measurements from CDF and D0 experiments.

The measurements from di erent channels and di erent experiments can be combined using the best linear unbiased estimation technique, as shown in Fig. 1. In such combinations correlations among uncertainties for di erent results are properly taken into account. As a world average, we have $M_{top} = 173.1 \pm 1.3$ GeV/c^2 [17] with a good agreement between di erent channels and methods. However, this combination does not re ect recent updates. Especially CDF ME measurement in the lepton+jets channel has approximately same precision with this world average due to improvements of machinery, using more data, and increasing muon acceptance etc. The combination re ecting all the updated measurements will give much better precision of M_{top} .

3.1 Top and anti-top quark mass di erence measurement

The precision determination of M_{top} allows us to measure the mass di erence between top quark and anti-top quark to a few GeV. In the CPT theorem, which is fundamental to any local Lorentz-invariant quantum eld theory, the quark mass should be same as its anti-quark

partner. Despite the fact that no violations have ever been observed in the meson and baryon sectors, it is important to test CPT violation in all sectors such as quarks and high mass particles. D0 collaboration has a rst direct measurement of top quark and anti-top quark mass di erence (δM_{top}) in the lepton+jets channel using the ME technique. In the ME calculation, one assumes SM-like tt production and decay, where identical particle and antiparticle masses are assumed for b quarks and W bosons but not for top quarks. Using 1 fb^{-1} of pp collisions data, they measure $\delta M_{top} = 3.8 \pm 3.7$ GeV/c^2 [18].

4 Conclusion

The CDF and D0 collaborations have performed a robust set of analyses using many techniques and improvements to have better understand the important fundamental parameter of the SM. As a result, CDF ME measurement gives $M_{top} = 172.8 \pm 1.3$ GeV/c^2 which has consistent result and similar uncertainty with a year ago world average, $M_{top} = 173.1 \pm 1.3$ GeV/c^2 . The new world average considering the most recent updated analyses will be available soon to give much better precision of M_{top} . By end of Run II, we expect 8$\sim$12 fb^{-1} of data delivered by the Tevatron which could be almost a double the data sample used in this letter for both CDF and D0. An ultimate precision of about 1 GeV/c^2 or below on the mass of the top quark is expected to be reached.

Acknowledgments

I would like to thank for the CDF and D0 colleagues for their e orts to carry out these challenging physics analyses. I also thank for the conference organizers for a very rich week of physics.

References

1. F. Abe *et al.* (CDF Collaboration), *Phys. Rev. Lett.* **74**, 2626 (1995).
2. S. Abachi *et al.* (D0 Collaboration), *Phys. Rev. Lett.* **74**, 2632 (1995).
3. C. Amsler *et al.* (Particle Data Group), *Phys. Lett.* B **667**, 551 (2008).
4. D. Acosta *et al.* (CDF Collaboration), *Phys. Rev.* D **71**, 052003 (2005).
5. T. Scanlon, Ph.D. thesis, Imperial College London (FERMILAB-THESIS-2006-43,2006).
6. D0 Collaboration, *D0 Conference note* 5877 (2009).
7. CDF Collaboration, *CDF Conference note* 10077 (2010).
8. T. Aaltonen *et al.* (CDF Collaboration), *Phys. Rev.* D **79**, 092005 (2009).
9. K. Cranmer, Comput. Phys. Commun. **136**, 198 (2001), arXiv:hep-ex/0011057v1.
10. CDF Collaboration, *CDF Conference note* 10033 (2010).
11. B. Abbott *et al.* (D0 Collaboration), *Phys. Rev.* D **60**, 052001 (1999).
12. A. Abulencia *et al.* (CDF Collaboration), *Phys. Rev.* D **73**, 112006 (2006).
13. C. Lester and D. Summers, *Phys. Lett.* B **463**, 99 (1999).
14. A. Barr, C Lester, and P. Stephens, J. Phys. G **29**, 2343 (2003).
15. T. Aaltonen *el al* (CDF Collaboration), PRD **81**, 031102 (2010).
16. V. M. Abazov *el al* (D0 Collaboration), *Phys. Rev.* D **80**, 071102 (2009).
17. CDF and D0 Collaboration, FERMILAB-TM-2427-E (2009), *CDF Conference note* 9717 (2009), *D0 Conference note* 5899 (2009), arXiv:0903.2503v1.
18. V. M. Abazov *el al* (D0 Collaboration), *Phys. Rev. Lett.* **103**, 132001 (2009).

Top quark properties at the Tevatron

V. Sorin
(On behalf of the CDF and DØ Collaborations)
Instituto de Física de Altas Energías
Universidad Autónoma de Barcelona, Spain

Recent results in top quark properties from the CDF and DØ collaborations are presented. With close to 5 fb^{-1} of data, new and precise measurements are being performed at the Tevatron, probing the Standard Model predictions and improving our understanding of the intriguing top quark.

1 Introduction

At the Tevatron, a $p\bar{p}$ collider with $\sqrt{s} = 1.96$ TeV, the SM top quark is mostly produced in pairs with a theoretical cross section prediction of $7.5^{+0.66}_{-0.8}$ pb [1] for a top mass of 172.5 GeV/c^2. It decays almost 100% of the time to a W boson and a b quark and therefore the final states are defined based on the decay channel of the W boson. Cases in which both W's decay to a lepton-neutrino pair are classified as "dilepton", while "lepton+jets" events are those where only one W decays leptonically. Dilepton and lepton+jets represent 5% and 30% of the $t\bar{t}$ decays, respectively. In the following sections the most recent results in these two decay channels are presented.

2 Top quark properties

The latest measurement of the top quark mass [2] from the Tevatron corresponds to a value of $173.1 \pm 0.6(stat) \pm 1.1(syst)$ GeV/c^2. Given its large mass, it is expected the top quark to have a large decay width and a lifetime less than 10^{-24} seconds, therefore decaying before hadronizating. This is an important characteristic as many of its properties can thus be studied through its decay products.

2.1 Spin Correlations

Though at the Tevatron, the top and antitop are produced unpolarized, their spins are correlated. Because, as mentioned above, the top quarks are expected to decay before they fragment, their spin correlation (C) can be study through correlations between flight directions of their decay products. The correlation factor depends on the choice of spin basis. At the Tevatron optimal choices are the beam and the off-diagonal basis for which the coefficient C is expected to be ~ 0.78 [3]. Both DØ [4] and CDF [5] have measured the spin correlation in the dilepton channel by means of a fit to the joint lepton angular distributions, as shown in Fig 1. CDF also adds the

angular information from the b quarks. DØ finds a correlation of $C = -0.17^{+0.64}_{-0.53}$ while CDF measures $C = 0.32^{+0.55}_{-0.78}$. Both results are consistent with the NLO QCD expectation.

In the lepton+jets channel, the CDF collaboration studies the spin correlation using the helicity angles of the lepton and the down and bottom quark from the hadronically decaying top. Shown in Fig 1 is the $cos(\theta_{lep})cos(\theta_{down})$ distribution for data and simulation. A 2D fit to the angle bilinears $cos(\theta_{lep})cos(\theta_{down})$ and $cos(\theta_{lep})cos(\theta_b)$ is performed for a data sample of 4.3 fb^{-1} and a coefficient $C = 0.60 \pm 0.50(stat) \pm 0.16(syst)$ is found [6], consistent with the expected value ($C = 0.4$) in the helicity basis.

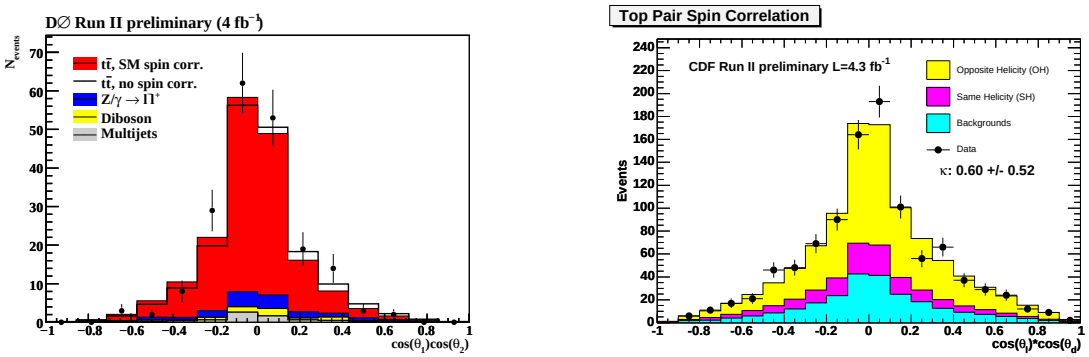

Figure 1: Left: The joint lepton angular distribution $cos(\theta_1)cos(\theta_2)$ for the full dilepton event sample. The sum of $t\bar{t}$ signal including NLO QCD spin correlation (C=0.777) (red) and multijet (grey), diboson (yellow) and Drell-Yan (blue) background is compared to data. The open black histogram shows the prediction without $t\bar{t}$ spin correlation (C=0). Right: Distribution of the $cos(\theta_{lep})cos(\theta_{down})$ variable in data compared to the sum of the background model, the SH template and the OH template. The measured value of the spin correlation coefficient is shown in the figure.

2.2 Top quark Width

As mentioned above, the top quark has a large decay width, which is expected to be of the order of 1 GeV. The first direct bound from the Tevatron was $\Gamma < 13.1$ GeV [7]. The latest measurement from CDF uses a 2D template fitting technique in a lepton+jets sample with 1 or more b-tagged jets. In this case, one of the variables corresponds to the reconstructed top quark mass, sensitive to different values of top width. The second variable, the dijet mass (or that closest to the W boson mass for 1-tagged events), was chosen in order to reduce the systematics from the Jet Energy Scale uncertainties. From the fit, a value of $0.4 < \Gamma < 4.4$ GeV and an upper limit of $\Gamma < 7.5$ GeV at 95% CL were determined [8].

2.3 Top quark Charge

The electric charge is one of the fundamental quantities that characterize the top quark. Due to the ambiguity in the assignment of the b quark and W boson to which the top decays, it is possible to reconstruct an object of charge -4/3, instead of the 2/3 top quark charge that the SM predicts. In fact, such an hypothesis has been proposed [9], in which this new particle would correspond to an exotic quark, part of a fourth generation of quarks and leptons. Thus, determining whether the top quark ($\bar{t}$) decays into a W^+ and a b quark ($W^-\bar{b}$) would indirectly indicate that the top charge is indeed 2/3. Both CDF [10] and DØ [11] have performed such a measurement. A key element of these analyses is the b-jet flavor determination. Previous measurements used a Jet Charge Algorithm that sums up the charge of the tracks assigned to the jet, each weighted by its momentum along the jet axis, calibrated in $b\bar{b}$ data events. The latest result from CDF identifies the b-jets by the presence of a soft lepton (from a semileptonic

b decay) and therefore its flavor is derived based on the charge of this lepton. The analysis used a data sample of 2.7 fb^{-1} and found, in agreement with previous measurements, the result to be consistent with the SM excluding the exotic interpretation with 95% CL.

3 Top quark decay

In the SM, top quark decays into a W boson and a b quark with a branching ratio close to 100%. The V-A coupling of the tWb vertex only allows the W boson to have longitudinal or left-handed polarizations while the right-handed polarization is suppressed. The fraction of decays to longitudinal and left-handed W bosons is expected to be $F_0^{SM} \sim 0.7$ [12] and $F_- \sim 0.3$, respectively. Thus, measuring the W helicity provides a direct test of the V-A nature of the tWb coupling and a probe of new physics beyond the SM.

3.1 W helicity

DØ and CDF collaborations have measured F_0 and the right-handed F_+ fractions in both the lepton+jets and dilepton channels. The latest result from DØ reports a simultaneous measurement of F_0 and F_+ as a result of a fit to the $cos\theta^*$ distribution (angle between the down-type fermion in W boson rest frame and the top quark direction) in both decay channels. Using up to 2.7 fb^{-1} of data the values obtained [13] are $F_0 = 0.49 \pm 0.106(stat) \pm 0.085(syst)$ and $F_+ = 0.110 \pm 0.059(stat) \pm 0.052(syst)$. In a data sample of similar size, but only the lepton+jets channel, CDF performs as well a model independent analysis based on a matrix element method and obtains [14] $F_0 = 0.88 \pm 0.11(stat) \pm 0.06(syst)$ and $F_+ = -0.15 \pm 0.07(stat) \pm 0.06(syst)$. Both results are consistent with Standard Model expectations.

3.2 Anomalous Couplings

If a more general form for the Wtb coupling is considered, the Lagrangian describing the interaction can be written in terms of the form factors f_1^L, f_2^L, f_1^R and f_2^R. In the SM, all are equal to zero except $f_1^L = 1$. Variations in the coupling form factors can arise from new physics and may manifest by changing the rate and kinematcs of distributions of electroweak single top production and by altering the W helicity fractions. Combining information from the single top quark production and the analysis described in previous section, DØ observes no anomalous contributions as shown in Fig 2 and results favor the left-handed hypothesis [15].

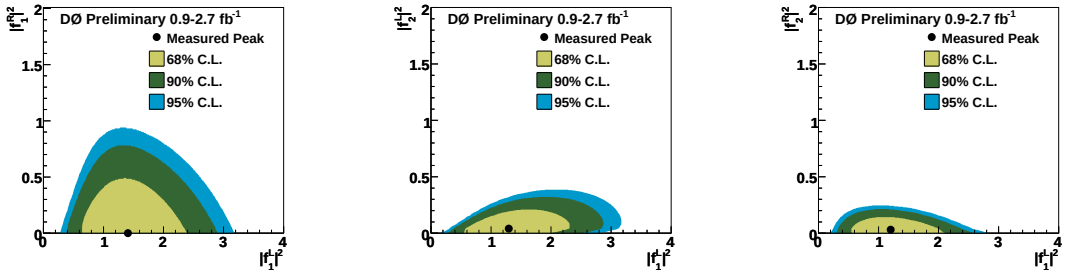

Figure 2: Final posterior densities for right- vs left-handed vector coupling (left),left-handed tensor vs left-handed vector coupling (center), and right-handed tensor vs left-handed vector coupling (right).The posterior density is shown in terms of contours of equal probability density.

4 Forward-Backward Asymmetry

Both CDF [16] and DØ [17] Collaborations have performed measurements of the forward-backward asymmetry in top pair production. From NLO QCD predictions, a non-zero asymmetry is expected in $q\bar{q} \to t\bar{t}$, therefore it is particularly interesting to study this at the Tevatron since at LHC top quark production is dominated by gluon fusion. The latest measurement [18] from CDF finds an asymmetry in the laboratory frame of $A_{fb} = 19.3 \pm 6.5(stat) \pm 2.4(syst)\%$, in $3.2\,\mathrm{fb}^{-1}$, to compare with the SM prediction of 5%.

5 Conclusions

Measurements of top quark properties provide important tests of the Standard Model predictions and could potentially be sensitive to new physics. In this report, recent results from the Tevatron have been presented. A more detailed description of these and other related measurements can be found at the CDF and DØ collaboration web pages [19].

Acknowledgments

I thank the organizers for an excellent conference and specially my CDF and DØ colleagues for their efforts to achieve the results presented in this work.

References

1. U. Langerfeld, S. Moch and P. Uwer, arXiv:0906.5273(2009); S. Moch and P. Uwer arXiv:0807.2794, and arXiv:0804.1476 (2008).
2. Top quark mass, Tevatron Combination, hep-ex 0903.2503
3. W. Bernreuther et al., *Nucl. Phys.* B **690**, 81 (2004)
4. The DØ Collaboration, DØ Conference Note 5950 (2009)
5. The CDF Collaboration, CDF Conference Note 9824 (2009)
6. The CDF Collaboration, CDF Conference Note 10048 (2010)
7. T. Aaltonen *et al*, The CDF Collaboration *Phys. Rev. Lett.* **102**, 042001 (2009).
8. The CDF Collaboration, CDF Conference Note 10035 (2010)
9. D. Chang *et al* , *Phys. Rev.* D **59**, 091503 (1999)
10. The CDF Collaboration, CDF Conference Notes 8782 (2007) and 9939 (2010).
11. V.M. Abazov *et al* , The DØ Collaboration, *Phys. Rev. Lett.* **98**, 041801 (2007)
12. G.L. Kane *et al* , *Phys. Rev.* D **45**, 124 (1992)
13. The DØ Collaboration, *Phys. Rev. Lett.* **100**, 062004 (2008)
14. The CDF Collaboration, arXiv:1003.0224v1.
15. The DØ Collaboration, Conference Note 5838, *Phys. Rev. Lett.* **102**, 092002 (2009)
16. CDF Collaboration *Phys. Rev. Lett.* **100**, 202001 (()2008)
17. DØ Collaboration *Phys. Rev. Lett.* **100**, 142002 (()2008)
18. CDF Conference Note 9724 (2009)
19. CDF Collaboration public web page: http://www-cdf.fnal.gov/physics/new/top/top.html; DØ Collaboration public web page: http://www-d0.fnal.gov/Run2Physics/top/top_public_web_pages/top_public.html.

Single top quark production at the Tevatron

Arán García-Bellido
Department of Physics and Astronomy, University of Rochester, 500 Wilson Blvd., Rochester, NY 14627

The observation of single top quark production by the CDF and D0 collaborations is one of the flagship measurements of the Run II of the Tevatron. The Tevatron combined single top quark cross section is measured to be: $\sigma(tb+X,\ tqb+X) = 2.8^{+0.6}_{-0.5}$ pb for a top quark mass of 170 GeV. This result is in agreement with the standard model production of a single top quark together with a jet in $p\bar{p}$ collisions at $\sqrt{s}$=1.96 TeV and allows to measure the CKM matrix element $|V_{tb}|$ without assumptions about the number of quark families. Other analyses involving tau leptons have been performed, and several properties, like the top quark width or the polarization have been measured.

1 Introduction

The production of top quarks at the Tevatron occurs mainly in $t\bar{t}$ pairs through the strong interaction with a cross section of 7.91 ± 0.91 pb [1], but top quarks can also be produced singly via the electroweak interaction with a cross section of 3.46 ± 0.14 pb [2] for $m_t = 170$ GeV. Two production modes are dominant at the Tevatron, categorized by how the W boson is exchanged: the s-channel $p\bar{p} \to tb+X$ and the t-channel $p\bar{p} \to tqb+X$.[3] This note describes the two analysis by CDF and D0 that observe for the first time the combined $s+t$ single top quark production, a D0 analysis that measures separately the s- and t-channels cross section, a CDF measurement of the single top cross section in the missing transverse energy (MET) and jets final state and another one from D0 that reconstructs the tau+jets final state, the first determination of the top quark width by D0 using the singletop, and finally the first measurement of the top quark polarization in single top events by CDF.

2 Single top quark observation

The final state consists of one high p_T lepton (electron or muon), missing energy, and at least two jets, one or two of them originating from b-quarks. Loose selections are employed by both

CDF and D0 to select events with this final state. The main background is W+jets, specially $Wb\bar{b}$, $Wc\bar{c}$ and Wcj, which are normalized to data before b-tagging. Good agreement is achieved after b-tagging between the data and the predicted backgrounds. D0 selects 4,519 events in data, with 4,652±352 expected events (including 223±30 s+t expected signal events) in 2.3 fb^{-1} of data. CDF selects 3,315 events in data, with 3,377±505 expected events (including 191±28 s+t expected signal events) in 3.2 fb^{-1} of data. Since there is no single variable that differentiates the signal from the large backgrounds, several multivariate techniques are employed and then combined by each experiment, separately for each channel: electron or muon, two, three (or four) jets, and 1 or 2 b-tagged jets. D0 uses three multivariate techniques: Boosted Decision Trees (BDT), Bayesian Neural Networks (BNN) and a Matrix Elements (ME) probability based calculation. Similarly, CDF uses BDTs, Neural Networks, ME, and likelihood functions. These different discriminants are run over the same data sample and since they are not 100% correlated, but rather 60-90%, the combination improves the sensitivity of any single discriminant.

By combining their individual multivariate methods, both CDF and D0 have established separately the presence of single top quark production in their data with 5σ in 3.2 fb^{-1} and 2.3 fb^{-1} respectively.[4] Additionally, the Tevatron collaborations have combined their analyses following the standard procedures of the Tevatron Electroweak Working Group.[5] The result is a measured $s+t$ cross section of $2.76^{+0.58}_{-0.47}$ pb, which is converted in a measurement of the CKM matrix element: $|V_{tb}| = 0.88 \pm 0.07$, equivalent to 8% relative uncertainty on $|V_{tb}|$. Figure 1 shows the summary of the individual CDF and D0 results and the combined measurement.

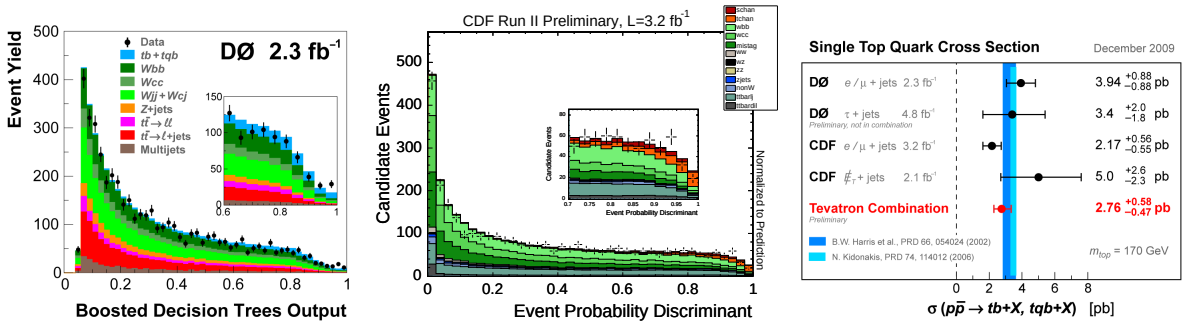

Figure 1: Left: D0 BDT output. Middle: CDF ME output. Right: individual CDF and D0 results and Tevatron combination of the $s+t$ single top quark production cross section.

3 Single top quarks in $W \to \tau\nu$ decays

D0 has searched in the τ final state with 4.8 fb^{-1} of integrated luminosity, directly reconstructing the hadronic τ candidates.[6] The selection requires one hadronic tau candidate, missing transverse energy, and two or three jets with one or two b-tags. This analysis developed a new BDT technique to identify hadronic taus, it improved efficiency by $\approx$ 5% with respect the Neural Network usually employed by D0, for the same rejection rate of 98%. In this final state, the main background is multijet production, which is derived from data. A final BDT is trained to discriminate against multijet background and its output used as discriminant to measure the single top cross section. The BDT output is shown in Figure 2. The result from this analysis is a cross section of 3.4 ± 2.0 pb, or an upper limit of 7.3 pb at 95% C.L. This result was not part of the Tevatron combination described above. When combined with the D0 electron and muon final states, it yields the most precise measurement of the cross section of $3.84^{+0.89}_{-0.83}$ pb.

CDF has published a similar search[7], also looking at the tau final state, but not reconstructing the hadronic tau candidates directly nor electrons nor muons. The sample used consists of 2.1 fb^{-1} with MET and jets, so it is enriched in $W \to \tau\nu$ decays. Using two Neural Net-

works, one trained against the dominant QCD background, and another against the remaining backgrounds, the measured cross section is $4.9^{+2.5}_{-2.2}$ pb. This result was included in the CDF observation paper and is part of the Tevatron combination.

4 Separate s- and t-channel search

Using the same dataset of 2.3 fb^{-1} as for the observation, D0 has published a separate search for s and t-channels.[8] The motivation for this search lies in the fact that the observation analyses assumed the SM ratio for the relative contributions of s and t channels in the $s+t$ signal. That assumption is relaxed here, to probe possible new physics in each different channel. In general, new physics affect the s and t-channel differently: new heavy bosons would enhance the s-channel production cross section, while anomalous couplings like flavor changing neutral currents, and CP violating or tensor couplings would affect the t-channel production cross section.[9] D0 employs the same multivariate techniques as in the observation, but now trained with s-channel as signal and t-channel as background, and viceversa. The outputs from the BDT, BNN and ME outputs are then combined with a Neural Network. The results are $3.14^{+0.94}_{-0.80}$ pb for the t-channel and 1.05 ± 0.81 pb for the s-channel. The measured t-channel result is found to have a significance of 4.8 standard deviations and is consistent with the standard model prediction. Figure 2 shows the two-dimensional plane of the s- and t-channels cross section, with possible new physics signatures. This result is still not sensitive enough to exclude new physics models, but with more data and improved selections it will be important to tell apart possible sources of new physics.

5 Top width from single top quarks

Direct measurements of the top quark width from the invariant mass distribution are limited by the experimental resolution and statistics. D0 has performed an indirect measurement [10], utilizing the t-channel single top cross section measurement [8] to extract the partial width $\Gamma(t \to Wb)$, and using the measurement of the ratio of branching fractions $R = \mathcal{B}(t \to Wb)/\mathcal{B}(t \to Wq)$ in $t\bar{t}$ decays to extract the branching fraction $\mathcal{B}(t \to Wb)$.[11] The total width is then derived from the two separate measurements: $\Gamma_t = \Gamma(t \to Wb)/\mathcal{B}(t \to Wb)$. This method yields the most precise determination of the total width: $\Gamma_t = 2.1 \pm 0.6$ GeV, or a lifetime of $\tau_t = (3 \pm 1)10^{-25}$ s, for $m_t = 170$ GeV. This result can be used to exclude some models of non-SM helicity amplitudes of the top quark, and constrain the coupling of a fourth generation heavy b' quark with the W boson and the top quark.

6 Top quark polarization

Single top quark production offers a nice sample of 100% polarized top quarks along the accompanying down-type quark axis. Non-SM contributions, such as W' bosons, charged Higgs bosons, or flavor changing neutral currents, can change the polarization of top quarks. CDF has performed the first analysis [12] to measure the polarization assuming right-handed couplings in the production vertices and SM left-handed couplings in the decay, a model denoted by RRLL. The most discriminant variable is the angle between the lepton and the b-quark in the top rest frame. This variable has been added to the existing likelihood function from the observation: two discriminants were trained separately one for the SM production and another for the assumed RRLL production and decay. As seen in Fig. 2, the best fit in the two dimensional plane of the measured cross sections is in agreement with the SM: $\sigma_{s+t}(\mathrm{SM}) = 1.72$ pb and $\sigma_{s+t}(\mathrm{RRLL}) = 0$ pb. This can be translated into a measurement of the polarization: $\mathcal{P} = \frac{\sigma_{s+t}(\mathrm{RRLL}) - \sigma_{s+t}(\mathrm{SM})}{\sigma_{s+t}(\mathrm{RRLL}) + \sigma_{s+t}(\mathrm{SM})} = -1.0^{+1.5}_{-0}$.

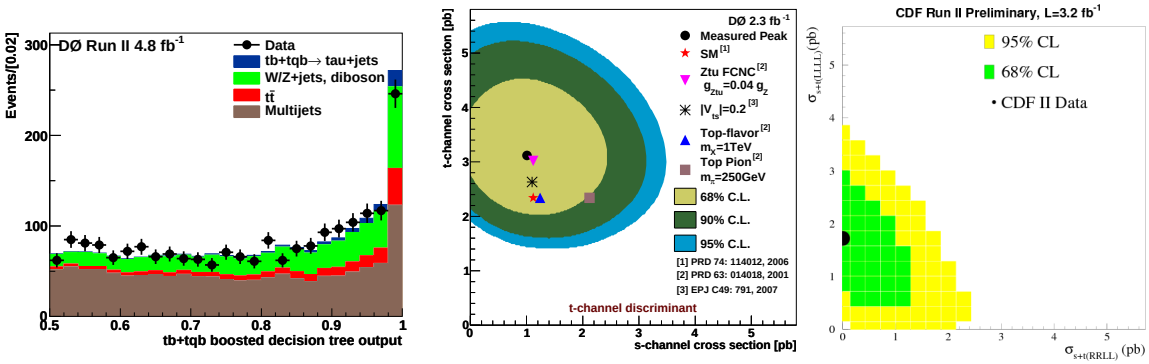

Figure 2: Left: BDT output in the D0 τ channel measurement. Middle: s vs. t-channel plane, with the separate D0 measurement and contributions from new physics. Right: CDF's measurement of the SM and the RRLL cross sections for the polarization.

7 Conclusions

The observation in 2009 of single top quark production is a very significant milestone of the Tevatron program. This flagship measurement of Run II has opened the door to further studies of the properties of top quarks and searches beyond the standard model. We have presented here only a fraction of them, namely the measurements in hadronic τ final states, the extraction of the top quark width, and a measurement of the top quark polarization. More analyses can be found in the top group webpages from CDF and D0.[13]

Acknowledgments

The author thanks the organizers of the Rencontres de Moriond for the enjoyable and fruitful atmosphere of the meeting. His accommodation for this conference was funded by an NSF grant through Brown University.

References

1. N. Kidonakis and R. Vogt, Phys. Rev. **D 68**, 114014 (2003).
2. N. Kidonakis, Phys. Rev. **D 74**, 114012 (2006).
3. S. S. D. Willenbrock and D.A. Dicus, Phys. Rev. D **34**, 155 (1986); C.-P. Yuan, *ibid.* **41**, 42 (1990); S. Cortese and R. Petronzio, Phys. Lett. B **253**, 494 (1991).
4. V. M. Abazov *et al.* [D0 Collaboration], Phys. Rev. Lett. **103**, 092001 (2009). T. Aaltonen *et al.* [CDF Collaboration], Phys. Rev. Lett. **103**, 092002 (2009).
5. T. E. W. Group [CDF Collaboration and D0 Collaboration], arXiv:0908.2171 [hep-ex].
6. V. M. Abazov *et al.* [D0 Collaboration], Phys. Lett. B **690**, 5 (2010).
7. T. Aaltonen *et al.* [The CDF Collaboration], Phys. Rev. D **81**, 072003 (2010).
8. V. M. Abazov *et al.* [D0 Collaboration], Phys. Lett. B **682**, 363 (2010).
9. T. M. P. Tait and C. P. P. Yuan, Phys. Rev. D **63**, 014018 (2001).
10. V. M. Abazov *et al.* [D0 Collaboration], D0 Note 6034-CONF, `http://www-d0.fnal.gov/Run2Physics/WWW/results/prelim/TOP/T87`
11. V. M. Abazov *et al.* (D0 Collaboration), Phys. Rev. Lett. **100**, 192003 (2008).
12. T. Aaltonen *et al.* [The CDF Collaboration], CDF Note 9920, `http://www-cdf.fnal.gov/physics/new/top/2009/singletop/polarization/Public_pol_32.html`
13. `http://www-cdf.fnal.gov/physics/new/top/public_singletop.html` `http://www-d0.fnal.gov/Run2Physics/top/top_public_web_pages/top_public.html`

Spin Correlation Effects in Top Quark Pair Production

Stephen J. Parke
Theoretical Physics Department
Fermi National Accelerator Laboratory
P.O. Box 500, Batavia, IL 60510, USA
parke@fnal.gov

An analysis of the spin correlation effects in top quark pair production at hadron colliders is presented with special emphasis for the Large Hadron Collider (LHC). At the LHC top quark pair production is dominated by gluon-gluon fusion. For gluon-gluon fusion at high energies the production is dominated by *unlike* helicity gluon fusion which has the same spin correlations as quark-antiquark annihilation. At low energies the production is dominated by *like* helicity gluon fusion which imparts very strong azimuthal correlations on the di-lepton decay products in top quark pair decay. This production process is studied in detail and this suggest a new way to look for spin correlations in top quark pair production at the LHC.

1 Spin Correlations in Top Quark Pair Production

At a 14 TeV proton-proton collider, the Large Hadron Collider (LHC), top quark pairs are produced 85% of the time by gluon-gluon fusion and 15% of the time by quark-antiquark annihilation. Thus, to understand spin correlation effects at the LHC one needs to understand top quark pair production via gluon-gluon fusion [1]. To facilitate this understanding it is natural to separate the gluon-gluon fusion process into the contribution from *unlike* helicity gluons ($g_L g_R + g_R g_L$) and *like* helicity gluons ($g_L g_L + g_R g_R$).

For top quark pair production by *unlike* helicity gluons and also via quark-antiquark annihilation [2], top quark pairs are always in an UD or DU configuration, if the off-diagonal basis [3] is used. In this basis, the spin axis of the top quark makes an angle, Ω, with respect to the top quark direction in the ZMF. This angle is given by

$$\tan\Omega = (1-\beta^2)\tan\theta, \tag{1}$$

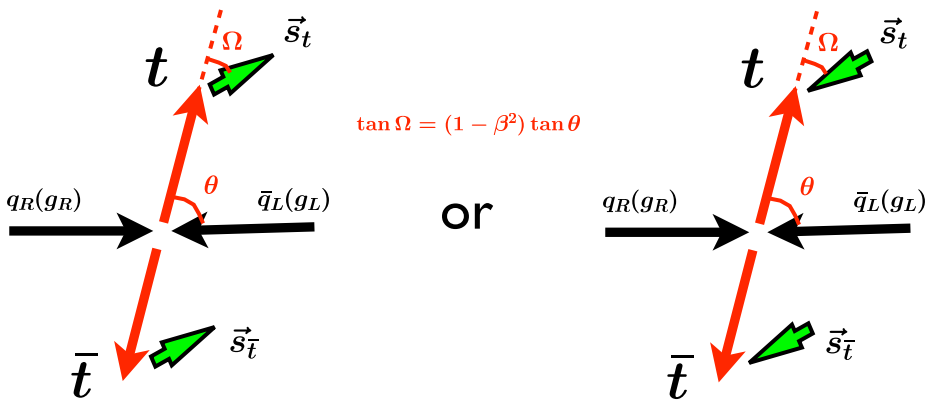

Figure 1: The non-zero spin configurations for top quark pair production via quark-antiquark annihilation ($q_R\bar{q}_L \to t\bar{t}$) or *unlike* helicity gluon fusion ($g_R g_L \to t\bar{t}$) in the off-diagonal basis. This basis interpolates between the beam line at threshold, $\Omega = \theta$, and the helicity basis at ultra-relativistic energies, $\Omega = 0$. For general β, $\tan\Omega = (1-\beta^2)\tan\theta$ and the relative weight of the left ($t_U\bar{t}_D$) contribution to the right ($t_D\bar{t}_U$) contribution is given by $\left(1+\sqrt{1-\beta^2\sin^2\theta}\right)^2$ to $\left(1-\sqrt{1-\beta^2\sin^2\theta}\right)^2$.

where β is the speed of the top quarks in the zero momentum frame (ZMF) and θ is the scattering angle in this frame. Thus, at threshold, the top quark spin is aligned along the beam line, $\Omega = \theta$, and at high energy the top quark spin is aligned along the direction of the top quark motion (helicity), $\Omega = 0$; the off-diagonal basis smoothly interpolates between these two extremes. The axis for the anti-top quark is always taken anti-parallel to the spin axis for the top quark, see Fig 1.

CDF and D0 at the Tevatron have attempted to measure the spin correlations from quark-antiquark annihilation and have found it to be very challenging. Since top quark pairs from *unlike* helicity gluon fusion have the same spin correlations as quark-antiquark annihilation, this does not seem like a fruitful way to proceed as the top quarks will be more highly boosted at the LHC.

So, what about top quark pairs from *like* helicity gluons which possibly have different spin correlations? The contribution from *like* helicity gluons dominates at low invariant mass of the top quark pair whereas the *unlike* helicity process dominates at high invariant mass. In particular, if

$$\beta^2 < \frac{1}{(2-\cos^2\theta)}, \tag{2}$$

then the *like* helicity contribution dominates. In fact the *like* helicity contribution to $gg \to t\bar{t}$ is 65% of the total contribution for top quark pair production via gluon-gluon fusion, i.e. 55% of the total top quark pair production.

For the production of top quark pairs from *like* helicity gluons, the most appropriate basis is the helicity basis, where the top quark pairs are always produced in a LL or RR helicity spin state, see Fig 2.

The fully correlated, total matrix element squared for top quark production and decay from *like* helicity gluons,

$$g_R g_R + g_L g_L \quad \to \quad t + \bar{t} \quad \to \quad (b + \bar{e} + \nu) + (\bar{b} + \mu + \bar{\nu}), \tag{3}$$

is given by

$$(|\mathcal{A}|^2_{RR} + |\mathcal{A}|^2_{LL})_{corr} \;\sim\; m_t^2\{(t\cdot\bar{e})(t\cdot\mu) + (\bar{t}\cdot\bar{e})(\bar{t}\cdot\mu) - m_t^2(\bar{e}\cdot\mu)\}. \tag{4}$$

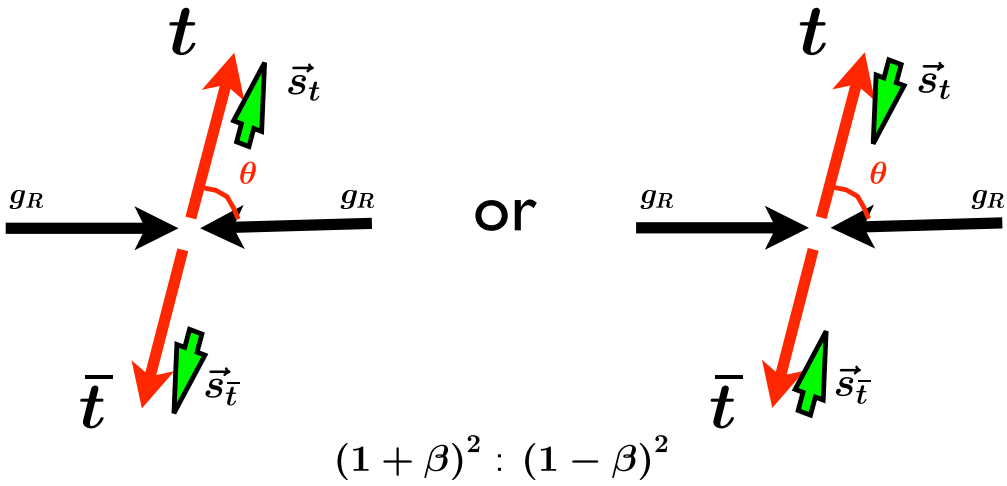

Figure 2: The non-zero spin configurations for top quark pair production via *like* helicity gluon fusion ($g_R g_R \to t\bar{t}$) in the helicity basis. This is the best basis for this process. the relative weight of the left ($t_R\bar{t}_R$) contribution to the right ($t_L\bar{t}_L$) contribution is given by $(1+\beta)^2$ to $(1-\beta)^2$.

where, for example, $(t \cdot \bar{e})$ is shorthand for $(p_t \cdot p_{\bar{e}})$, the dot product of the four momentum of the top quark, p_t, and that for the positron.

For comparison, we define the decay of a top or anti-top quark into a W-boson and b-quark uncorrelated if this decay is spherical in the top quark rest frame and thus independent of the top quark spin. The W-boson is then assumed to decay in the usual (fully correlated) manner. The uncorrelated matrix element squared is then simple given by

$$(|\mathcal{A}|^2_{RR} + |\mathcal{A}|^2_{LL})_{uncorr} \sim \ (t \cdot \bar{e})(\bar{t} \cdot \mu)(t \cdot \bar{t}). \tag{5}$$

The ratio of the correlated to uncorrelated matrix elements squared, $\mathcal{S}$, for like-helicity gluons is given by

$$\begin{aligned} \mathcal{S} \equiv \frac{(|\mathcal{A}|^2_{RR} + |\mathcal{A}|^2_{LL})_{corr}}{(|\mathcal{A}|^2_{RR} + |\mathcal{A}|^2_{LL})_{uncorr}} &= \frac{m_t^2\{(t \cdot \bar{e})(t \cdot \mu) + (\bar{t} \cdot \bar{e})(\bar{t} \cdot \mu) - m_t^2(\bar{e} \cdot \mu)\}}{(t \cdot \bar{e})(\bar{t} \cdot \mu)(t \cdot \bar{t})} \\ &= \left(\frac{1-\beta^2}{1+\beta^2}\right)\left(\frac{(1+\beta^2) + (1-\beta^2)c_{\bar{e}\mu} - 2\beta^2 c_{t\bar{e}}c_{\bar{t}\mu}}{(1-\beta c_{t\bar{e}})(1-\beta c_{\bar{t}\mu})}\right), \end{aligned} \tag{6}$$

where the last line is given in the ZMF in terms of the cosine of the angles between t and $\bar{e}$ ($c_{t\bar{e}}$), $\bar{t}$ and μ ($c_{\bar{t}\mu}$) and $\bar{e}$ and μ ($c_{\bar{e}\mu}$). The range of $\mathcal{S}$ is between (2,0). At threshold, $\beta \to 0$, the maximum of $\mathcal{S}$ occurs when the charged leptons are parallel, $c_{\bar{e}\mu} = +1$, whereas the minimum occurs when the charged leptons are back-to-back, $c_{\bar{e}\mu} = -1$, independent of their correlation with the top-antitop axis.

For non-zero β, the maximum (minimum) still occurs when the charged leptons are parallel (back-to-back), but they are now correlated with the top-antitop axis. The fact that the charged leptons are more likely to have their momenta being parallel rather than back-to-back is what is expected for top quark pairs that have spins which are anti-aligned, *i.e.* LL or RR. However, here the enhancement is even stronger than what one would naïvely expect because the interference between LL and RR strengthens the correlation between the momenta of the two charged leptons. This argument suggests looking at the ΔR, $\Delta\eta$ and $\Delta\phi$ distributions of the two charged leptons with a cut on the invariant mass of the top-antitop system. However, only the $\Delta\phi$ distribution shows significant differences between the correlated and uncorrelated cases.

In Fig. 3 we give the distribution $(1/\sigma_T)\ d\sigma/d(\Delta\phi)$ verses $\Delta\phi$ for the case where we have constrained the invariant mass of the top quark pair to be less than 400 GeV (left) and where the

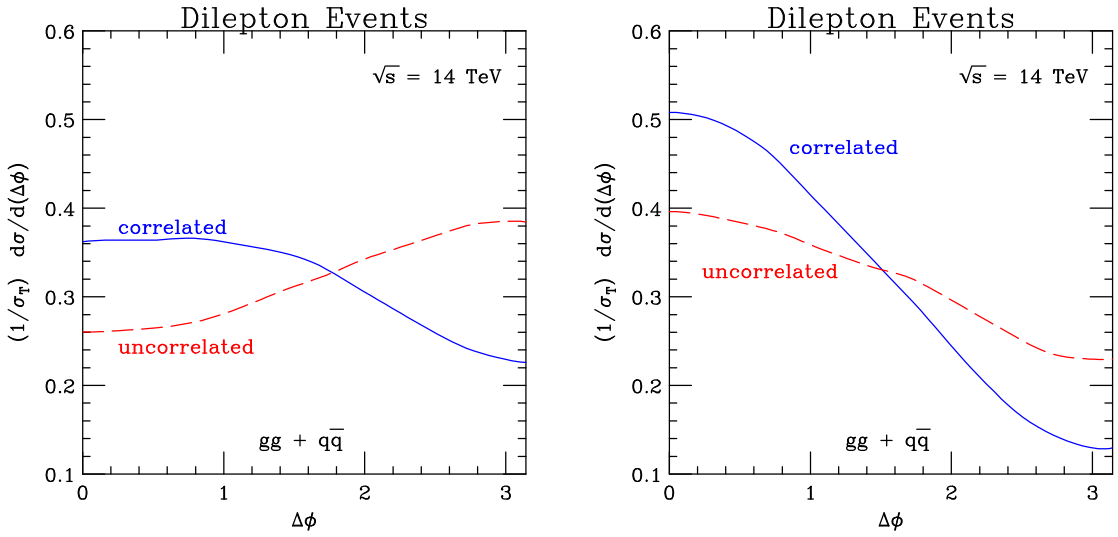

Figure 3: The differential distribution of $\Delta\phi$, $(1/\sigma_T)\ d\sigma/d(\Delta\phi)$. The solid curve is for the fully correlated case whereas the dashed curve assumes that the top quarks decay spherically in their respective rest frames. Left: A cut restricting the invariant mass of the $t\bar{t}$ pairs to a maximum of 400 GeV has been applied to these distributions. Right: A cut restricting the average reconstructed invariant mass of the $t\bar{t}$ pairs to a maximum of 400 GeV has been applied to these distributions.

constraint is on the average reconstructed mass of the top quark pair (right). Clearly, there is a difference between the correlated and uncorrelated cases using both methods of constraining the top quark pair invariant mass. Unfortunately, the shape of the curves changes as you go from the true invariant mass constraint to the average reconstructed mass constraint, suggesting that this mass cut needs to be studied at NLO to properly understand these shape change effects.

In summary, a new way to investigate spin correlations in top quark production and decay is presented for the LHC. The essences of this method is to look at the azimuthal angles between the two charged leptons in a sample of di-lepton quark pair events where the invariant mass of the $t\bar{t}$ system is constrained to be less than 400 GeV. Given the large top quark pair cross section at the LHC, it is estimated that there will be 1000 such events per fb^{-1} at 14 TeV.

Acknowledgments

I would like to thank the organizers for a fantastic workshop and especially Vera de Sa-Varanda for making everything run so smoothly. I would like to also acknowledge my collaborator Greg Mahlon for many important discussions on this subject. I, also, dedicate this proceedings to the memory of my friend and collaborator Jiro Kodaira (1951-2006) with whom I had many wonderful discussions on top quark physics as well as many other topics. Fermilab is operated by the Fermi Research Alliance under contract no. DE-AC02-07CH11359 with the U.S. Department of Energy.

References

1. G. Mahlon and S. J. Parke, arXiv:1001.3422 [hep-ph].
2. G. Mahlon and S. J. Parke, Phys. Rev. **D53**, 4886 (1996) [arXiv:hep-ph/9512264], T. Stelzer and S. Willenbrock, Phys. Lett. B **374**, 169 (1996) [arXiv:hep-ph/9512292].
3. S. J. Parke and Y. Shadmi, Phys. Lett. B **387**, 199 (1996) [arXiv:hep-ph/9606419], G. Mahlon and S. J. Parke, Phys. Lett. B **411**, 173 (1997) [arXiv:hep-ph/9706304].

NEXT-TO-LEADING ORDER $t\bar{t}$ PLUS JETS PHYSICS WITH HELAC-NLO

MAŁGORZATA WOREK [a]
Fachbereich C Physik, Bergische Universität Wuppertal, D-42097 Wuppertal

A report on the recent next-to-leading order QCD calculations to $t\bar{t}b\bar{b}$ and $t\bar{t}jj$ processes at the CERN Large Hardon Collider is presented. Results for integrated and differential cross sections are given. A significant reduction of the scale dependence is observed in both cases, which indicates that the perturbative expansion is well under control. The results are obtained in the framework of the HELAC-NLO system.

1 Introduction

For a light Higgs boson, with mass $m_H \leq 135$ GeV the highest decay rate mode is $H \to b\bar{b}$. In the dominant Higgs boson production channel at the CERN Large Hardon Collider (LHC), i.e. in gluon fusion, this decay mode is not very highly considered because of its overwhelming QCD background. On the other hand, the associated production of a top quark pair with a Higgs boson includes more distinctive signature, which should provide a unique opportunity of independent direct measurement of Higgs boson Yukawa couplings to tops and bottoms. Whether or not it will also provide a discovery channel, depends very much on the ratio between this signal and the main QCD backgrounds. Early studies at ATLAS and CMS even suggested discovery potential, however, analyses with more realistic calculations of background processes, still only based on leading-order (LO) matrix elements, show problems if the latter are not very well controlled [1,2]. A careful and detailed examination of the backgrounds shows that the most relevant are the direct production of the final state $t\bar{t}b\bar{b}$ (irreducible background) and the production of a top quark pair in association with two jets, $t\bar{t}jj$ (reducible background). The latter needs to be taken into account due to the finite efficiency in identifying b-quarks in jets (b-tagging). The calculation of the next-to-leading-order (NLO) QCD corrections to both background processes can be regarded as a major step forward towards the observability of the $t\bar{t}H \to t\bar{t}b\bar{b}$ signal at the LHC.

The calculations of the NLO QCD corrections to the $pp \to t\bar{t}b\bar{b}$ process have been first presented last year [3] and subsequently confirmed by our group at the permille level [4]. Very recently, the NLO QCD corrections to $pp \to t\bar{t}jj$ background process have been performed [5]. In this contribution, a brief report on these computations is given.

2 Details of the next-to-leading order calculation

The next-lo-leading order results are obtained in the framework of HELAC-NLO based on the HELAC-PHEGAS leading-order event generator for all parton level processes [6,7,8]. The NLO

[a] Presented at the XLVth Rencontres de Moriond on QCD and High Energy Interactions, La Thuile (Aosta), Italy, March 13-20, 2010.

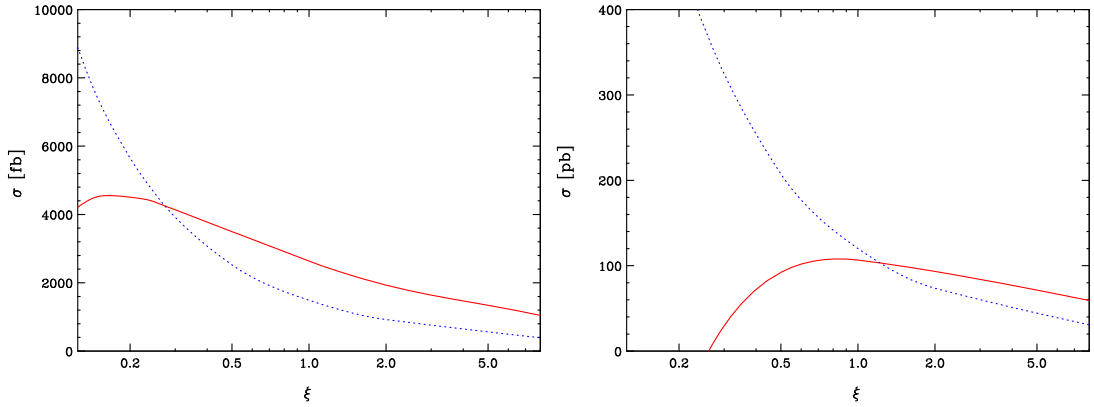

Figure 1: Scale dependence of the total cross section for $pp \to t\bar{t}b\bar{b} + X$ (left panel) and for $pp \to t\bar{t}jj + X$ (right panel) at the LHC with $\mu_R = \mu_F = \xi \cdot \mu_0$ where $\mu_0 = m_t = 172.6$ GeV. The blue dotted curve corresponds to the LO whereas the red solid to the NLO one.

system consists of: 1) CutTools [9], for the OPP reduction of tensor integrals with a given numerator to a basis of scalar functions and for the rational parts [10,11,12]; 2) Helac-1Loop [13] for the evaluation of one loop amplitude, more specifically for the evaluation of the numerator functions for given loop momentum (fixed by CutTools); 3) OneLOop [13], a library of scalar functions, which provides the actual numerical values of the integrals. 4) Helac-Dipoles [14], automatic implementation of Catani-Seymour dipole subtraction [15], for the calculation of the real emission part.

Let us emphasize that all parts are calculated fully numerically in a completely automatic manner.

3 Numerical results

Proton-proton collisions at the LHC with a center of mass energy of $\sqrt{s} = 14$ TeV are considered. The mass of the top quark is set to be $m_t = 172.6$ GeV. We leave it on-shell with unrestricted kinematics. The jets are defined by at most two partons using the k_T algorithm with a separation $\Delta R = 0.8$, where $\Delta R = \sqrt{(y_1 - y_2)^2 + (\phi_1 - \phi_2)^2}$, $y_i = 1/2 \ln(E_i - p_{i,z})/(E_i + p_{i,z})$ being the rapidity and ϕ_i the azimuthal angle of parton i. Moreover, the recombination is only performed if both partons satisfy $|y_i| < 5$ (approximate detector bounds). We further assume for $t\bar{t}b\bar{b}$ ($t\bar{t}jj$) processes, that the jets are separated by $\Delta R = 0.8$ (1.0) and have $|y_{\rm jet}| < 2.5$ (4.5). Their transverse momentum is required to be larger than 20 (50) GeV respectively. We consistently use the CTEQ6 set of parton distribution functions, i.e. we take CTEQ6L1 PDFs with a 1-loop running α_s in LO and CTEQ6M PDFs with a 2-loop running α_s at NLO.

We begin our presentation of the final results of our analysis with a discussion of the total cross section. At the central value of the scale, $\mu_R = \mu_F = \mu_0 = m_t$, we have obtained

$$\sigma^{\rm LO}_{pp\to t\bar{t}b\bar{b}+X} = 1489.2\ ^{+1036.8(70\%)}_{-\ 565.8(38\%)}\ \text{fb}\,, \qquad \sigma^{\rm NLO}_{pp\to t\bar{t}b\bar{b}+X} = 2636\ ^{+862(33\%)}_{-703(27\%)}\ \text{fb}\,,$$

$$\sigma^{\rm LO}_{pp\to t\bar{t}jj+X} = 120.17\ ^{+87.14(72\%)}_{-46.64(39\%)}\ \text{pb}\,, \qquad \sigma^{\rm NLO}_{\rm pp\to t\bar{t}jj+X} = 106.94\ ^{-14.30(13\%)}_{-13.28(12\%)}\ \text{pb}\,,$$

where the error comes from varying the scale up and down by a factor 2. From the above result one can obtain K factors

$$K_{pp\to t\bar{t}b\bar{b}+X} = 1.77\,, \qquad K_{pp\to t\bar{t}jj+X} = 0.89\,.$$

In case of $pp \to t\bar{t}b\bar{b} + X$ corrections are large of the order of 77%. However, they can be reduced substantially, even down to -11%, either by applying additional cuts or by a better choice of

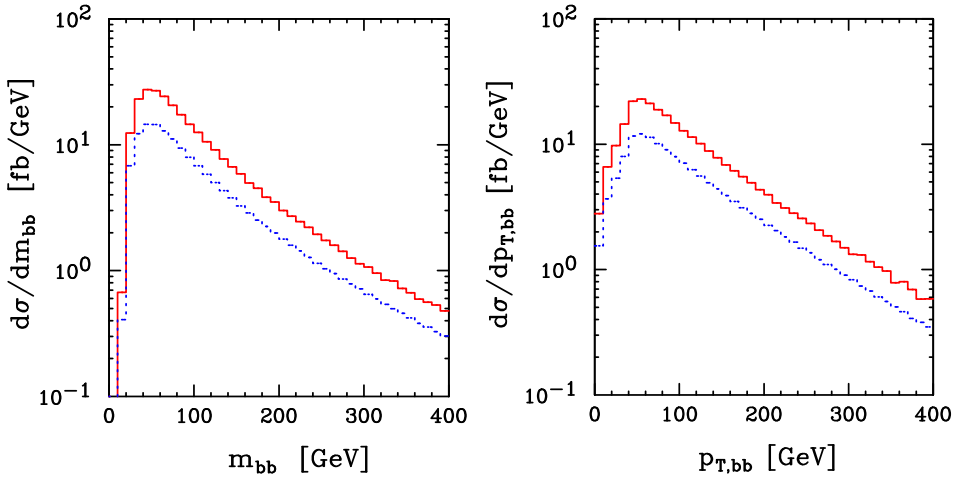

Figure 2: Distribution of the invariant mass $m_{b\bar{b}}$ (left panel) and the distribution in the transverse momentum $p_{T_{b\bar{b}}}$ (right panel) of the bottom-anti-bottom pair for $pp \to t\bar{t}b\bar{b} + X$ at the LHC. The blue dotted curve corresponds to the LO whereas the red solid to the NLO one.

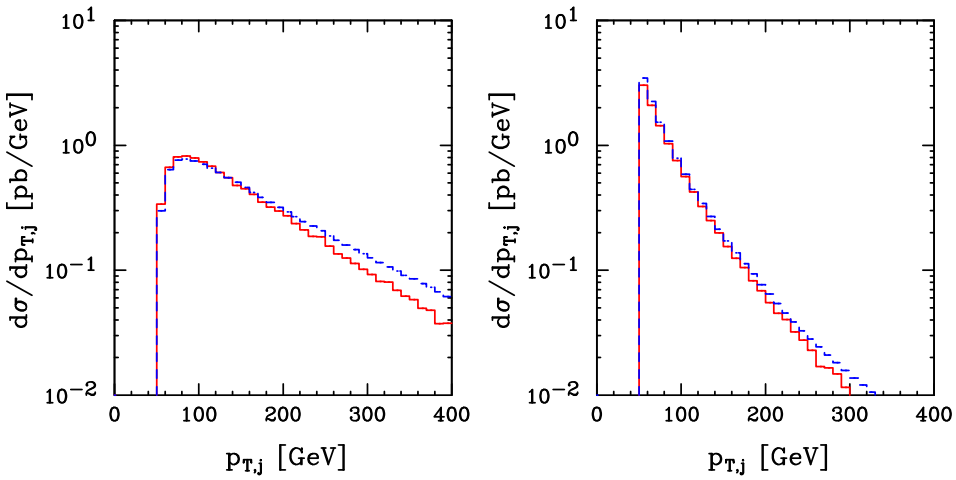

Figure 3: Distribution in the transverse momentum p_{T_j} of the 1st hardest jet (left panel) and the 2nd hardest jet (right panel) for $pp \to t\bar{t}jj + X$ at the LHC. The blue dotted curve corresponds to the LO whereas the red solid to the NLO one.

factorization and renormalization scales as already suggested by Bredenstein et al. [16]. In case of $pp \to t\bar{t}jj + X$ we have obtained negative corrections of the order of 11%. In both cases a dramatic reduction of the scale uncertainty is observed while going from LO to NLO. The scale dependence of the corrections for both processes is graphically presented in Fig. 1.

While the size of the corrections to the total cross section is certainly interesting, it is crucial to study the corrections to the distributions. In Fig. 2 the differential distributions for two observables, namely the invariant mass and transverse momentum of the two-b-jet system are depicted for the $pp \to t\bar{t}b\bar{b} + X$ process. Clearly, the distributions show the same large corrections, which turn out to be relatively constant contrary to the quark induced case [17]. In Fig. 3 the transverse momentum distributions of the hardest and second hardest jet are shown for the $pp \to t\bar{t}jj + X$ process. Distributions demonstrate tiny corrections up to at least 200 GeV, which means that the size of the corrections to the cross section is transmitted to the distributions. On the other hand, strongly altered shapes are visible at high p_T especially in case of the first hardest jet. Let us underline here, that corrections to the high p_T region can

only be correctly described by higher order calculations and are not altered by soft-collinear emissions simulated by parton showers.

Conclusions

A brief summary of the calculations of NLO QCD corrections to the background processes $pp \to t\bar{t}b\bar{b} + X$ and $pp \to t\bar{t}jj + X$ at the LHC has been presented. They have been calculated with the help of the HELAC-NLO system.

The QCD corrections to the integrated cross section for the irreducible background are found to be very large, changing the LO results by about 77%. The distributions show the same large corrections which are relatively constant. The residual scale uncertainties of the NLO predictions are at the 33% level. On the other hand, the corrections to the reducible background with respect to LO are negative and small, reaching 11%. The error obtained by scale variation is of the same order. The size of the corrections to the cross section is transmitted to the distributions at least for the low p_T region. However, the shapes change appreciably at high p_T.

Acknowledgments

I would like to thank the organizers of Recontres de Moriond for the kind invitation and the very pleasant atmosphere during the conference. The work presented here was funded by the Initiative and Networking Fund of the Helmholtz Association, contract HA-101 ("Physics at the Terascale") and by the RTN European Programme MRTN-CT-2006-035505 HEPTOOLS - Tools and Precision Calculations for Physics Discoveries at Colliders.

References

1. G. L. Bayatian *et al.* [CMS Collaboration], *J. Phys.* G **34**, 995 (2007).
2. G. Aad *et al.* [The ATLAS Collaboration], arXiv:0901.0512 [hep-ex].
3. A. Bredenstein, A. Denner, S. Dittmaier and S. Pozzorini, *Phys. Rev. Lett.* **103**, 012002 (2009).
4. G. Bevilacqua, M. Czakon, C. G. Papadopoulos, R. Pittau and M. Worek, *J. High Energy Phys.* **0909**, 109 (2009).
5. G. Bevilacqua, M. Czakon, C. G. Papadopoulos and M. Worek, arXiv:1002.4009 [hep-ph].
6. A. Kanaki and C. G. Papadopoulos, *Comput. Phys. Commun.* **132**, 306 (2000).
7. C. G. Papadopoulos, *Comput. Phys. Commun.* **137**, 247 (2001).
8. A. Cafarella, C. G. Papadopoulos and M. Worek, *Comput. Phys. Commun.* **180**, 1941 (2009).
9. G. Ossola, C. G. Papadopoulos and R. Pittau, *J. High Energy Phys.* **0803**, 042 (2008).
10. G. Ossola, C. G. Papadopoulos and R. Pittau, *Nucl. Phys.* B **763**, 147 (2007).
11. G. Ossola, C. G. Papadopoulos and R. Pittau, *J. High Energy Phys.* **0805**, 004 (2008).
12. P. Draggiotis, M. V. Garzelli, C. G. Papadopoulos and R. Pittau, *J. High Energy Phys.* **0904**, 072 (2009).
13. A. van Hameren, C. G. Papadopoulos and R. Pittau, *J. High Energy Phys.* **0909**, 106 (2009).
14. M. Czakon, C. G. Papadopoulos and M. Worek, *J. High Energy Phys.* **0908**, 085 (2009).
15. S. Catani, S. Dittmaier, M. H. Seymour and Z. Trocsanyi, *Nucl. Phys.* B **627**, 189 (2002).
16. A. Bredenstein, A. Denner, S. Dittmaier and S. Pozzorini, arXiv:1001.4006 [hep-ph].
17. A. Bredenstein, A. Denner, S. Dittmaier and S. Pozzorini, *J. High Energy Phys.* **0808**, 108 (2008).

6.
New Phenomena

SUSY SEARCHES AT TEVATRON

GIANLUCA DE LORENZO
Institut de Fisica d'Altes Energies (IFAE), Edifici Cn. Facultat Ciencies, Universitat Autonoma de Barcelona, E-08193 Bellaterra (Barcelona), Spain

This contribution provides a review of the latest results of searches for Supersymmetry (SUSY) by the CDF and DØ experiments with integrated luminosities up to 4.1 fb^{-1}. No evidence of new physics has been found and results were translated into exclusion limits on the investigated SUSY phase space parameters.

1 Direct Searches for Squarks and Gluinos

1.1 Inclusive Search for Squarks and Gluinos

The inclusive search for squarks ($\tilde{q}$) and gluinos ($\tilde{g}$) has been developed within the framework of minimal supergravity (mSUGRA) characterized by only five free parameters: M_0, $M_{1/2}$, A_0, tanβ, and sign(μ). The assumption of R-parity conservation implies that squarks and gluinos are produced in pairs and ultimately decay into energetic jets and large $\not\!\!E_T$ due to the LSP neutralinos ($\tilde{\chi}_1^0$) in the final state. Depending on the masses of squarks ($M_{\tilde{q}}$) and gluinos ($M_{\tilde{g}}$), different event topologies are expected. CDF [5] and DØ [6] collaborations performed several analyses with different jet requirements and optimizing the final selection cuts to enhance the signal over background separation for different gluino and squark mass configurations. No significant deviation from SM predictions has been found by CDF and DØ in 2 and 2.1 fb^{-1} of data, respectively. The results have been translated into 95% C.L. limits on the squark/gluino production cross section as a function of their masses. Figure 1 (left) shows the CDF 95% C.L. excluded region in the squark-gluino mass plane. Masses up to 392 GeV/c^2 are excluded in the region where $M_{\tilde{q}} \sim M_{\tilde{g}}$, and $M_{\tilde{g}} > 280$ GeV/c^2 for any $M_{\tilde{q}}$. Similar exclusion limits have been found by the DØ collaboration.

1.2 Searches for Scalar Bottom Quarks

In a constraint MSSM scenario, large values of tanβ lead to large mixing between the chiral states of the sbottom squark and result in a significant mass difference between mass eigenstates in the sbottom squark sector with a rather light $\tilde{b}_1$ mass state. Assuming a SUSY particle mass hierarchy such that the sbottom decays exclusively as $\tilde{b}_1 \to b\tilde{\chi}_1^0$, the expected signal for direct sbottom pair production contains two b-jets and large missing transverse energy $\not\!\!E_T$ from the two LSPs in the final state. The DØ [10] experiment searched for direct sbottom pair production in 4.0 fb^{-1} of data. Specific cuts were implemented to reject contamination from beam-halo and cosmic particles as well as SM processes. Events with b-jets in the final state were selected with a NN based b-tagging algorithm. The dominant source of background in the analysis is due to events with a light-flavor jet which is misidentified as a b-jet (mistags). Other backgrounds with

heavy-flavor jets in the final state come from SM QCD multijet processes, W and Z production in association with jets, $t\bar{t}$, single top, and diboson decays. All the background contributions have been estimated with MC simulation, except for mistags and QCD modelled with data driven techniques. Final selection cuts were optimized to enhance the signal over background separation for different values of the sbottom mass $M_{\tilde{b}_1}$. CDF[9] performed a very similar analysis in 2.65 fb^{-1} of data. None of the two experiments observed any significant deviation from the background predictions and the results have been translated into 95% exclusion limits on sbottom pair production cross section and sbottom-neutralino masses. Figure 1 (right) shows the DØ exclusion limit on the neutralino/sbottom mass plane and compares the latest results with previous limits from CDF and DØ in Run I and Run II. DØ excludes sbottom masses up to 250 GeV/c^2 with the $M_{\tilde{\chi}_1^0} < 70$ GeV; in the same range of neutralino masses CDF excludes sbottom masses below 232 GeV/c^2.

1.3 Searches for Scalar Top Quarks

In a constraint MSSM scenario, the large top quark mass leads to a substantial splitting between the masses of the two stop states, allowing $\tilde{t}_1$ to be the lightest squark. Due to the conservation of R-parity, scalar tops are pair produced and can decay into a neutralino and a charm quark. CDF[7] searched for the production of stop pairs decaying into a final state of two c-jets and large missing transverse energy coming from the LSP neutralinos. The heavy flavour tagging efficiency was enhanced with a NN-based flavour separator and the final selection was optimized for best sensitivity at different stop masses. Good agreement has been found between the number of events observed in 2.6 fb^{-1} of data and the SM predictions, and CDF set exclusion limits on the production cross sections for different values of the neutralino-stop masses. With the assumption that $\tilde{t}_1$ decays 100% of the times into a charm quark and a neutralino, CDF excludes stop masses up to 180 GeV/c^2 for $M_{\tilde{\chi}_1^0} \sim 90$ GeV/c^2. DØ[8] searched for stop in 3.1 fb^{-1} of data and assuming a different MSSM scenario, with $BR(\tilde{t}_1 \to b\tilde{\nu}\ell) = 100\%$. In this case, the sneutrino $\tilde{\nu}$ is the LSP and generates $\not\!\!E_T$ in the final state with two opposite sign leptons and two jets coming from the hadronization of the bottom quarks. No evidence of SUSY has been found and the extracted 95% C.L. limit excludes stop masses up to 200 GeV/c^2 for sneutrino masses below 100 GeV/c^2.

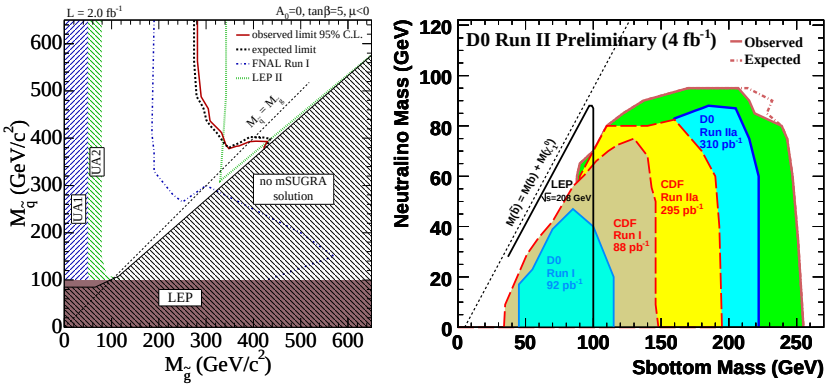

Figure 1: LEFT: CDF 95%C.L. exclusion limit on the gluino-squark production in the squark-gluino mass plane. RIGHT: The DØ 95%C.L. sbottom pair production exclusion contour in $(M_{\tilde{b}_1}, M_{\tilde{\chi}_1^0})$ mass plane.

2 Searches for Charginos and Neutralinos

2.1 Search for Charginos and Neutralinos in Trilepton Decays

After the Supersymmetry breaking, charginos and neutralinos can have low mass and a no negligible cross section at Tevatron. In a scenario with light enough sleptons, the two leptonic decays $\tilde{\chi}^{\pm} \rightarrow \ell\nu\tilde{\chi}_1^0$ and $\tilde{\chi}_2^0 \rightarrow \ell^+\ell^-\tilde{\chi}_1^0$ are enhanced, and the final state contains three isolated leptons and large missing $\not\!\!E_T$. CDF [12] and DØ [11] searched for charginos and neutralinos in events with three identified leptons in the final state, and accepting also events with only two identified leptons plus an isolated track. The observed data were found to be consistent with SM predictions and 95%C.L. exclusion limits on the production cross section and leptonic branching fraction have been extracted. Results have been interpreted within the framework of mSUGRA, where exclusion limits on the stop production cross section lead to the exclusion of a range of M_0 and $M_{1/2}$ values. Figure 2 (left) shows the DØ excluded region on the M_0-$M_{1/2}$ plane.

2.2 Search for GMSB Charginos and Neutralinos

When the SUSY breaking mechanism is gauge mediated (GMSB), the LSP is the gravitino $\tilde{G}$ with a very low mass of just few KeV. At Tevatron, analyses developed in a GMSB framework focus on the search for gauginos pair production with the assumption that the neutralino is the NLSP and decays as $\tilde{\chi}_1^0 \rightarrow \gamma\tilde{G}$. Depending on the value of their lifetime, neutralinos might decay with a signature of one or two photons and large $\not\!\!E_T$ due to the presence of gravitinos in the final state. The latest results from CDF [13] collaboration include a search for short-lived neutralinos in the di-photon final state, using 2.6 fb^{-1} of data. No event survived the analysis cuts and the null observation was consistent with the prediction of 1.2 ± 2.6 events from SM background. A specific set of GMSB parameters, the one that corresponds to the *Snowmass Slope* constraint SPS8 [14], has been set as a benchmark for the optimization of the final thresholds and the interpretation of the results Considering neutralino lifetimes up to 2 ns 95%C.L. limits on production cross section and masses have been set, with neutralinos lighter than 149 GeV/c^2 excluded for lifetimes below 1 ns .

3 Search for SUSY Hidden Valley

DØ [18] performed a search for a new light gauge boson called dark photon (γ_D) within a SUSY hidden valley framework [17] in which particles are produced in pairs and decay into SM particles and the lightest neutralino $\tilde{\chi}_1^0$. In this scenario $\tilde{\chi}_1^0$ is not the LSP and can further decay into a so called darkino $\tilde{\text{X}}$ (the hidden sector state) plus a photon or a dark photon. γ_D ultimately decays into a pair of spatially closed fermions and, if $BR(\tilde{\chi}_1^0 \rightarrow \gamma_D\tilde{\text{X}})$ is small enough, the final state signature is analogous as in GMSB models with jets or leptons plus $\not\!\!E_T$ in the final state. Since the expected backgrounds from SM jets is enormous, the search was optimized for a signature with spatially closed lepton pairs, opposite charged electrons or muons. No evidence of dark photon signal has been found in the 4.1 fb^{-1} of data analyzed and the resulting 95%C.L. limit on production cross section excludes chargino masses up to 230 GeV/c^2 for M_{γ_D} below 0.5 GeV/c^2.

4 Search for RPV Scalar Neutrinos

In some SUSY scenarios the R-parity is not conserved and the LSP can decay into SM particles, no longer providing a valid cold dark matter candidate. Tevatron analyses developed in RPV scenarios focus on the search for resonant scalar particles decaying into a pair of leptons of different flavors. The latest searches from CDF [16] and DØ [15] were optimized for a dilepton final state coming from the decay of a heavy sneutrino. CDF results are based on 1 fb^{-1} and assume

a signal of $e\mu$, $e\tau$, and $\mu\tau$. DØ used 4.1 fb^{-1} of data and assumed a final state with only $e\mu$ from $\tilde{\nu}_t$ decay. Results were found to be consistent with SM predictions and with no evidence of SUSY, 95%C.L. exclusion limits on the production cross section times branching ratio (see Figure 2 (right) for DØ) have been extracted.

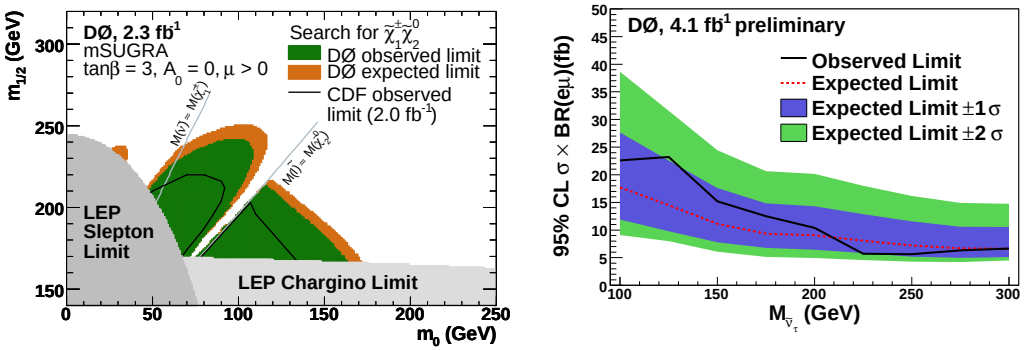

Figure 2: LEFT: DØ chargino-neutralino excluded region as a function of M_0-$M_{1/2}$ mSUGRA parameters (green). RIGHT: DØ limits on RPV sneutrino production cross section times branching ratio ($\sigma \times$ BR).

5 Summary

This contribution reports on the most recent results of searches for Supersymmetry at the Tevatron. The review includes analyses performed by the CDF and DØ collaborations using up to 4.1 fb^{-1} of data. None of the searches have found hints of new physics and the results have been translated into 95%C.L. exclusion limits on the free parameters of several SUSY scenario.

References

1. J. Wess and B. Zumino, *Nucl. Phys.* B **70**, 39 (1974).
2. J. R. Ellis, S. Kelley, and D.V. Nanopolous, *Phys. Lett.* B **260**, 131 (1991).
3. A.H. Chamseddine, R. Arnowitt, and P. Nath, *Phys. Rev. Lett.* **49**, 970 (1982).
4. S. Ambrosiano, G.L. Kane, G.D. Kribs, S.P. Martin and S. Mrenna, *Phys. Rev.* D **54**, 5395 (1996).
5. CDF Collaboration, T. Aaltonen et al, *Phys. Rev. Lett.* **102**, 121801 (2009).
6. DØ Collaboration, V.M. Abazov et al, *Phys. Lett.* B **660**, 449 (2008).
7. DØ Collaboration, V.M. Abazov et al, *Phys. Lett.* B **665**, 1 (2008).
8. DØ Collaboration, V.M. Abazov et al, *Phys. Lett.* B **665**, 1 (2008).
9. CDF Collaboration, *Public Note* **9834**, (2009)
10. DØ Collaboration, *Conference Note* **5931**, (2009)
11. DØ Collaboration, V.M. Abazov et al, *Phys. Lett.* B **680**, 34 (2009).
12. CDF Collaboration, *Public Note* **9817**, (2009)
13. CDF Collaboration, *Public Note* **9625**, (2009)
14. B.C. Allanach et al., *European Physical Journal* C **25**, 1 (2002)
15. DØ Collaboration, *Conference Note* **5894**, (2009)
16. CDF Collaboration, *Public Note* **9430**, (2009)
17. T. Han, Z. Si, K. Zurek, and M. Strassler, JHEP 0807, 008 (2008); M. Strassler and K. Zurek, *Phys. Rev. Lett.* **B**, 651 (374)2007.
18. DØ Collaboration, V.M. Abazov et al, *Phys. Rev. Lett.* **103**, 081802 (2009).

NON-SUSY SEARCHES AT THE TEVATRON

LIDIJA ŽIVKOVIĆ
Columbia University, 538 West 120th Street, New York, NY 10027

We present results from several new searches for physics beyond the Standard Model using up to 5.4 fb^{-1} of data collected with CDF and DØ experiments at the Fermilab Tevatron.

1 Search for Randall Sundrum Graviton

The Standard Model (SM) is a very successful description of particle physics up to the weak scale. One of the remaining puzzles, known as gauge hierarchy, is the large disparity between the Planck scale, $M_{Pl} = 10^{16}$ TeV and the weak scale of the order of 1 TeV. Solution was proposed by Randall and Sundrum (RS) [1] in which a fifth dimension with a warped spacetime metric exists, bounded by two three-dimensional branes, the SM brane and the Planck brane. We assumed the simplest RS model, in which the SM fields are localized on the SM brane and gravity originates on the Planck brane with the graviton wave function exponentially suppressed away from the brane along the extra dimension. In this model, TeV scales are naturally generated from the Planck scale due to a geometrical exponential factor (the warp factor), $\Lambda_\pi = \overline{M_{Pl}} e^{-k\pi r_c}$, where $\overline{M_{Pl}} = M_{Pl}/\sqrt{8}\pi$ is the reduced Planck scale, k and r_c are the curvature scale and compactification radius of the extra dimension respectively.

We searched with a DØ detector for the first Klauza Klein (KK) graviton in the simplest RS model, where graviton decays to a pair of electrons or photons in a 5.4 fb^{-1} of data [2]. We select events with two electromagnetic clusters, each with transverse momentum $p_T > 25$ GeV and we search for narrow mass resonance in dielectron or diphoton final state. Figure 1 shows dielectron (left) and diphoton (right) invariant mass for data (black points), total background (white area with a blue line), and graviton signals with masses 300, 450 and 600 GeV and $k/\overline{M_{Pl}} = 0.02$.

Since we did not observe any signal above SM prediction we set an upper limit on the production of KK gravitons times the branching fraction into the ee final state using a Poisson log-likelihood ratio (LLR) test. Figure 2 (left) shows the resulting limits for several values of $k/\overline{M_{Pl}}$. Figure 2 (right) shows 95% C.L. upper limit on $k/\overline{M_{Pl}}$ versus graviton mass M_1 compared with the expected limit and the previously published exclusion.

2 Heavy Gauge Bosons decaying to dileptons

Many models predict new heavy gauge boson that will decay into two leptons [3]. The E6 Z's are examples of specific new particles decaying to a lepton-antilepton final state. The Z'_ψ, Z'_χ, Z'_η, Z'_I, Z'_{sec} and Z'_N are chosen to test the E6 model. We searched for a heavy resonances that decay into two electrons with CDF detector [4] in a 2.5 fb^{-1}, and with DØ detector [5] in a 3.6 fb^{-1}. We selected two isolated electrons with $p_T > 25$ GeV at both experiments. The

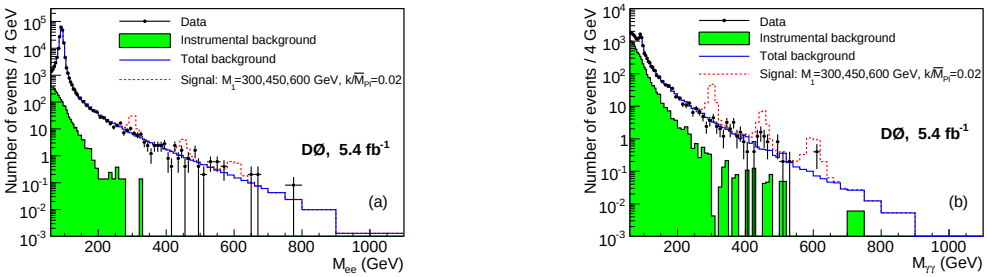

Figure 1: Invariant mass of ee (left) and $\gamma\gamma$ (right).

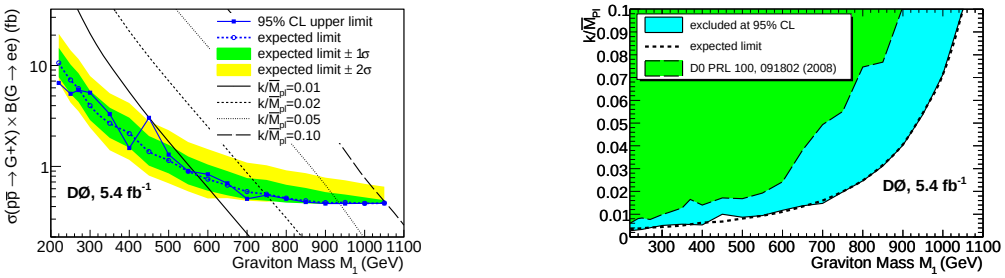

Figure 2: Upper limit on $\sigma(p\bar{p} \rightarrow G + X) \times BR(G \rightarrow ee)$ compared with the expected limit and the theoretical predictions for different couplings$k/\bar{M}_{Pl}$ (left) and an upper limit on $k/\bar{M}_{Pl}$ versus graviton mass M_1 (right).

main irreducible background is Drell Yan production. Other backgrounds include instrumental backgrounds where one or both electrons were missidentified, and smaller SM processes.

Figure 3 (left) shows the observed dielectron invariant mass spectrum from 2.5 fb^{-1} of data collected with CDF detector together with the expected backgrounds. The most significant region of excess of data over background occurs for a dielectron invariant mass window of 240 GeV, and is 3.8 standard deviations above the SM prediction. Figure 3 (right) shows the observed upper limits from data and the expected limits from background-only simulated events for spin 1 particles as a function of the e+e invariant mass, together with the expected cross sections for Z'.

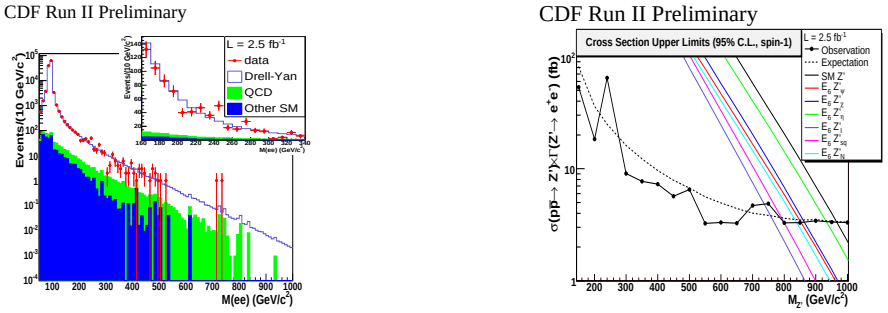

Figure 3: Dielectron invariant mass (left) and an upper limit on cross section for various Z' models.

Figure 4 (left) shows the observed dielectron invariant mass spectrum from 3.6 fb^1 of data collected with DØ detector together with the expected backgrounds. At DØ we did not observe any excess in a mass region around 240 GeV, as shown in Figure 4 (middle). In the absence of any significant signal, we set upper limits on the production cross section. Figure 4 (right) shows the expected and observed 95% confidence-level upper limits on $\sigma(p\bar{p} \rightarrow Z') \times BR(Z' \rightarrow ee)$ for Z_{SSM} and E6 Z' models as a function of Z' mass.

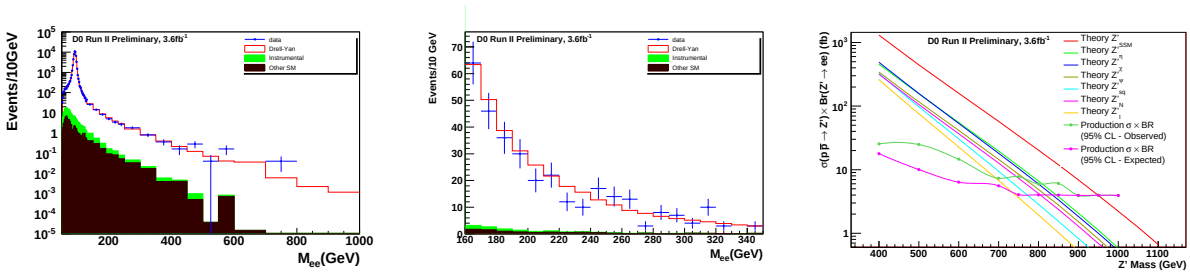

Figure 4: Dielectron invariant mass (left), also shown zoomed around 240 GeV (right), and an upper limit on cross section for various Z' models..

3 Search for diboson resonances

Many extensions of the SM predict new heavy gauge boson that will decay into pair of SM gauge bosons. We searched for such resonances in electron, missing E_T and two jets final state, with CDF detector[6] in 2.9 fb^{-1} of data. This final state has the advantage of searching for two types of diboson resonances, $W^{\pm}W^{\mp}$ and $W^{\pm}Z$, with the same final state. We select events with an isolated electron with $E_T > 30$ GeV, a missing $E_T > 30$ GeV, 2 or 3 jets with $E_T > 30$ GeV, and an overall $H_T > 150$ GeV, where H_T is defined as the sum of the electron E_T , the missing E_T and the jet E_T of all jets with raw $E_T > 8$ GeV. Since the real missing E_T in the event is coming only from one neutrino fro the W decay, we used energy and momentum conservation to calculate E_Z component, and thus to reconstruct the invariant mass of the resonance. We further optimized cuts on object p_T to be greater than 40-120 depending on signal mass. Figure 5 shows invariant mass of WW(Z) system in a three scenarios that we investigated, W' (left), Z' (middle) and RS graviton (right).

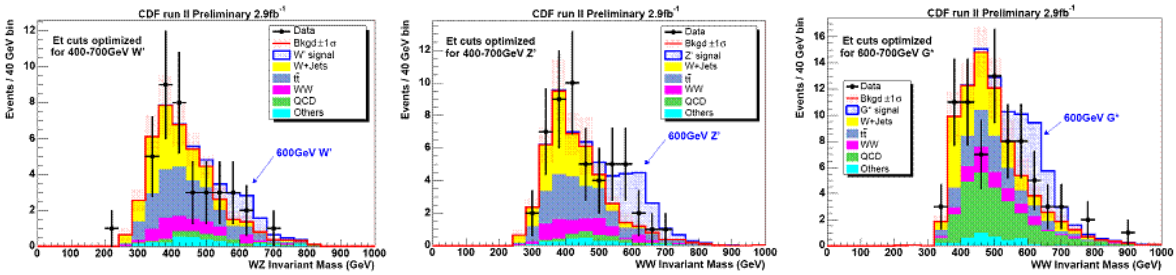

Figure 5: Diboson invariant mass for W' (left), Z' (middle) and RS graviton (right).

In the absence of signal we set an upper limit on the cross section of the resonance decaying to two gauge bosons decaying further to electron, missing E_T and two jets, where resonance is W' (see Figure 6 (left)), Z' (see Figure 6 (middle)) and RS graviton (see Figure 6 (right))

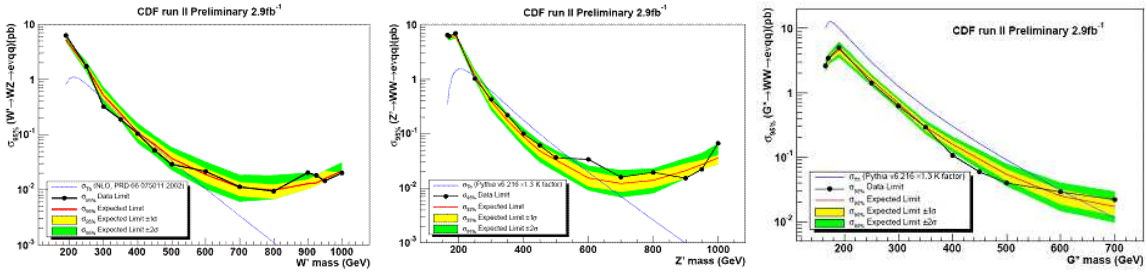

Figure 6: An upper limit on cross section for heavy resonance, W' (left), Z' (middle) and RS graviton (right) decaying to two bosons.

With DØ detector[7], we searched for a heavy charged boson decaying to WZ that further

decay to three leptons and missing E_T in 4.1 fb^{-1} of data. The events are required to have missing transverse energy greater than 30 GeV and at least three charged leptons with transverse momenta $p_T > 20$ GeV satisfying the electron or muon identification criteria. We require the presence of a candidate Z boson by selecting the electron pairs and muon pairs with opposite electric charges that have invariant mass nearest to the mass of the Z boson. Then, we select the highest transverse momentum lepton among the remaining lepton candidates in the event as the lepton from the W boson decay. The WZ transverse mass shown in Figure 7 (left) is used to discriminate between the W' signal and the backgrounds in the limit setting procedure. Since we did not observe any excess in a data over SM background we set upper limit on the $\sigma \times BR(W' \to WZ)$ in Sequential Standard Model (see Figure 7). We also studied the sensitivity to other models that predict heavy charged boson. We interpreted the results in terms of the $W'WZ$ trilinear coupling normalized to the SSM value as function of the W' mass (see Figure 7).

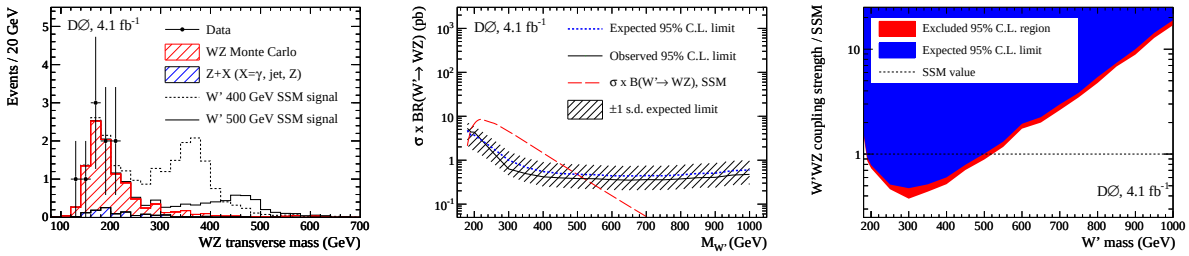

Figure 7: Transverse mass of WZ system (left), an upper limit on cross section for W' in SSM (middle), and expected and excluded area of the $W'WZ$ coupling strength normalized to the SSM value as a function of the W' mass (right).

Acknowledgments

We thank the staffs at Fermilab and collaborating institutions, and acknowledge support from the DOE and NSF (USA); CEA and CNRS/IN2P3 (France); FASI, Rosatom and RFBR (Russia); CNPq, FAPERJ, FAPESP and FUNDUNESP (Brazil); DAE and DST (India); Colciencias (Colombia); CONACyT (Mexico); KRF and KOSEF (Korea); CONICET and UBACyT (Argentina); FOM (The Netherlands); STFC and the Royal Society (United Kingdom); MSMT and GACR (Czech Republic); CRC Program and NSERC (Canada); BMBF and DFG (Germany); SFI (Ireland); The Swedish Research Council (Sweden); and CAS and CNSF (China).

I would also like to thank organizers of the Recontre de Moriond for financial supportthat was provided for me. In addition, I would like to thank NSF and professors Chung-I Tan and Greg Landsberg for the grant that cover part of my costs.

References

1. L. Randall and R. Sundrum, Phys. Rev. Lett. **83**, 3370 (1999)
2. V. M. Abazov *et al.* [The DØ Collaboration], Phys. Rev. Lett. **104**, 241802 (2010)
3. P. Langacker, Rev. Mod. Phys. **81**, 1199 (2008)
4. T. Aaltonen *et al.* [CDF Collaboration], Phys. Rev. Lett. **102**, 031801 (2009)
5. DØ Collaboration, Conference Note **5923**, (2009)
6. T. Aaltonen *et al.* [The CDF Collaboration], Phys. Rev. Lett. **104**, 241801 (2010)
7. V. M. Abazov *et al.* [DØ Collaboration], Phys. Rev. Lett. **104**, 061801 (2010)

THRESHOLD AND TRANSVERSE-MOMENTUM RESUMMATIONS FOR GAUGINO-PAIR HADROPRODUCTION

Jonathan Debove

Laboratoire de Physique Subatomique et de Cosmologie, Université Joseph Fourier/CNRS-IN2P3/INPG, 53 Avenue des Martyrs, F-38026 Grenoble, France

We present precision calculations of the invariant-mass and transverse-momentum distributions of gaugino pairs produced at hadron colliders. We implement the threshold and transverse-momentum resummation formalisms at next-to-leading order accuracy and match the obtained result to the perturbative prediction at $\mathcal{O}(\alpha_s)$. We compare the various resummed cross sections with the perturbative results and Monte Carlo predictions. The theoretical uncertainties coming from renormalisation and factorisation scale variations are also discussed.

1 Introduction

The Minimal Supersymmetric Standard Model (MSSM) continues to be a very attractive extension of the Standard Model of particle physics.[1,2] If R-parity is conserved, it provides a convincing candidate for the dark matter observed in the universe. In the MSSM, this is generally the lightest neutralino, one of the fermionic partners of the electroweak gauge and Higgs bosons which mix to give four neutral (charged) mass eigenstates, namely the neutralinos (charginos). Light enough to be produced at current hadron colliders, these particles have been studied extensively, and the cross sections for the production of gaugino-pairs are known at leading order [3,4,5] and next-to-leading order of perturbative QCD.[6]

In this paper, we extend this last work and resum the soft-gluon contributions which appear in both the invariant-mass (M) and transverse-momentum (p_T) distributions of the gaugino pairs. Indeed, starting at $\mathcal{O}(\alpha_s)$, logarithmic terms of the forms $[\alpha_s \ln(1-z)/(1-z)]_+$ and $\alpha_s \ln(M^2/p_T^2)/p_T^2$ appear where $z = M^2/s$ and $\sqrt{s}$ is the partonic centre-of-mass energy. These terms become large close to the production threshold and in the small-p_T region, thus possibly spoiling the convergence of the usual perturbative calculations. In order to gain control over these terms, they must be resummed to all order in α_s.

2 Resummation formalisms

The methods to systematically perform all-order resummation of classes of enhanced logarithms are well known and are generally performed in conjugate spaces.[7,8,9,10] Working with the Mellin moments of the differential partonic cross sections, the resummed contributions take the fac-

torised forms

$$M^2 \frac{d\sigma^{(\mathrm{res})}}{dM^2}(N) = H(M) \exp[G(N)] \quad \text{and} \tag{1}$$

$$\frac{M^2 d\sigma^{(\mathrm{res})}}{dM^2 dp_T^2}(N) = \int \frac{d^2b}{4\pi} e^{i\mathbf{b}\cdot\mathbf{p_T}} \mathcal{H}(M,N) \exp[\mathcal{G}(N,Mb)] \tag{2}$$

for M- and p_T-distributions respectively. The Mellin variable N and the impact parameter b are the conjugate variables of z and p_T. In these factorised expressions, all the potentially large logarithmic terms are embodied and resummed in the exponential form factors $\exp[G]$ and $\exp[\mathcal{G}]$. The process-dependent functions H and $\mathcal{H}$ do not depend on the relevant conjugate variables and can thus be computed perturbatively. The general expressions for the functions H, G and $\mathcal{H}$, $\mathcal{G}$ can be found in Refs. [11,13] and Refs. [10,12], respectively.

Once the large logarithms have been resummed in N- and b-space, we have to switch back to the physical spaces in order to achieve a phenomenological study. Special attention has to be paid to the singularities in the exponents G and $\mathcal{G}$. They are related to the presence of the Landau pole in the perturbative running of α_s, and a prescription is needed. In our numerical study, we follow Refs. [14,15] and deform the integration contour in the complex N- and b-planes. Finally, in order to conserve the full information contained in the fixed-order calculation, the $\mathcal{O}(\alpha_s)$ and the resummed calculations are matched by subtracting from their sum the expansion of the resummed cross section truncated at $\mathcal{O}(\alpha_s)$

$$d\sigma = d\sigma^{(\mathrm{f.o})} + d\sigma^{(\mathrm{res})} - d\sigma^{(\mathrm{exp})}, \tag{3}$$

thus avoiding possible double counting of the logarithmically enhanced contributions.

3 Numerical results

We now present numerical results for the production of gaugino pairs at the Tevatron and at the LHC. Unless stated otherwise, the parton densities are evaluated in the most recent parametrisation of the CTEQ collaboration `CTEQ6.6M`[16] with α_s evaluated at two-loop accuracy. In the following, we choose the minimal supergravity benchmark point SPS1a' [17] and obtain the weak-scale supersymmetric parameters through the computer code `SuSpect2.3`.[18] The obtained gaugino masses are $m_{\tilde{\chi}_1^0} = 61$ GeV and $m_{\tilde{\chi}_2^0} = m_{\tilde{\chi}_1^\pm} = 183$ GeV.

In Fig. 1, we show the invariant mass spectrum of neutralino-chargino pairs at the Tevatron with centre-of-mass energy of $\sqrt{S} = 1.96$ TeV. Here, the $\mathcal{O}(\alpha_s^0)$ cross section (LO) is evaluated with the leading-order parton distribution functions `CTEQ6L1`. While the $\mathcal{O}(\alpha_s)$ corrections (NLO) are large and positive, they do not clearly improve the scale uncertainties obtained by varying the factorisation and renormalisation scales (μ) in the range $[M/2, 2M]$. However once they are matched to the resummed cross section at next-to-leading logarithmic accuracy, the resulting prediction (NLL+NLO) is found to be very stable and precise.

The impact of the resummation of the threshold-enhanced terms is shown for several gaugino pairs in Fig. 2. Setting $\mu = M$ and defining the NLL K-factor by

$$K^{NLL} = \frac{d\sigma^{\mathrm{NLL+NLO}}}{d\sigma^{\mathrm{NLO}}}, \tag{4}$$

we see that the NLL contributions increase the NLO predictions by a few percent in the low-M region and can reach 20 % for large invariant masses. Note that threshold resummation has already been applied to the associated production of neutralino and chargino in Ref. [19]. A careful comparison between their results and ours can be found in Ref. [13].

In Fig. 3, we show the p_T-spectrum of chargino-neutralino pairs produced at the LHC with a hadronic centre-of-mass energy of $\sqrt{S} = 10$ GeV. The $\mathcal{O}(\alpha_s)$ calculation (LO) diverges at low

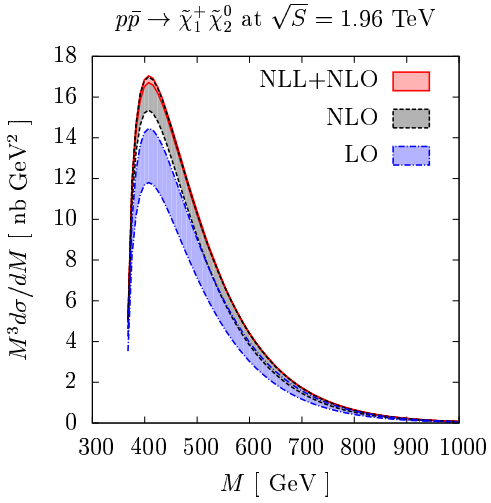

Figure 1: Invariant-mass distribution of chargino-neutralino pairs at the Tevatron. The LO calculation (dot-dashed) is compared to the resummation prediction (full) matched to the NLO calculation (dashed). The scale uncertainties are shown as shaded bands.

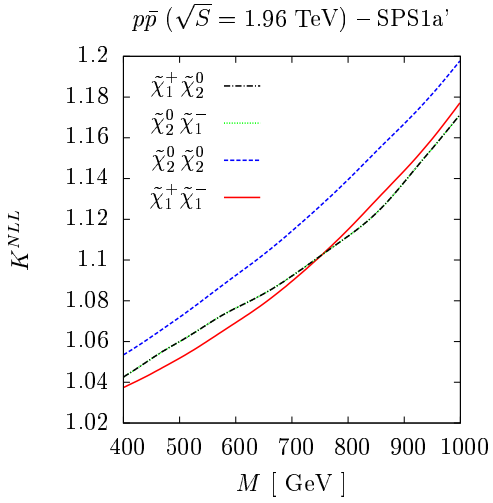

Figure 2: NLL K-factor, as defined in Eq. (4), for the associated production of charginos and neutralinos (dotted and dot-dashed) as well as chargino (full) and neutralino (dashed) pairs at the Tevatron.

p_T due to the logarithmic terms of the form $\alpha_s \ln(M^2/p_T^2)/p_T^2$, thus being totally unreliable. However, it becomes finite after having been matched to the resummed prediction at next-to-leading logarithmic (NLL+LO) accuracy. We also evaluate the uncertainties coming from scale variations in the range $[m_{\tilde{\chi}}/2, 2m_{\tilde{\chi}}]$. The scale dependence of the NLL+LO prediction is clearly improved with respect to the LO result. For comparison, the NLL+LO prediction for the 14 TeV design energy of the LHC is also presented.

In Fig. 4, we compare our NLL+LO prediction with our resummed result at leading-logarithmic (LL) accuracy and two different setups for the `PYTHIA6.4` [20] Monte Carlo (MC) generator. We see that the default (STD) MC simulation is clearly improved beyond the LL approximation and approaches our NLL+LO result, but peaks at slightly smaller values of p_T. This behaviour can be improved by tuning the intrinsic p_T of the partons in the hadron (AW'),[12] but both simulations underestimate the intermediate p_T-region. Results for the transverse-momentum distributions of neutralino and chargino pairs can be foud in Ref. [12].

4 Conclusion

In this work, threshold and transverse-momentum resummations have been presented for gaugino pair hadroproduction. We found that the NLL contributions are important especially for the p_T-distributions which are not even finite using standard perturbation theory. Our resummed predictions show a better stability under unphysical scale variations than the fixed-order calculations. Finally we have demonstrated that our results modify considerably the commonly used MC predictions. All these features will possibly lead to improvements for the experimental determination of the gaugino parameters.

Acknowledgements

We thank M. Klasen for useful discussions and comments.

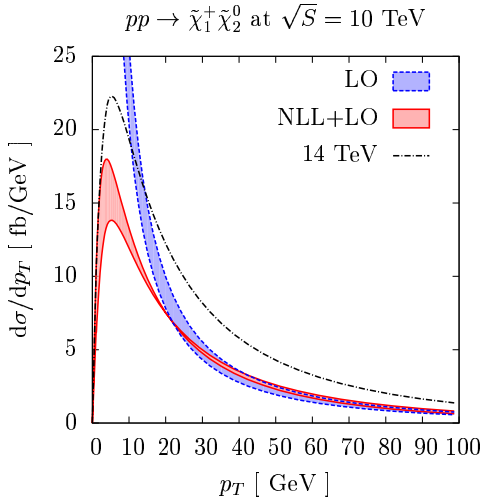

Figure 3: Transverse-momentum distributions of chargino-neutralino pairs at the LHC. The LO calculation (dashed) is matched to the resummed calculation (full). The scale uncertainty is shown as a shaded band and the matched result for the LHC design energy of 14 TeV as a dot-dashed line.

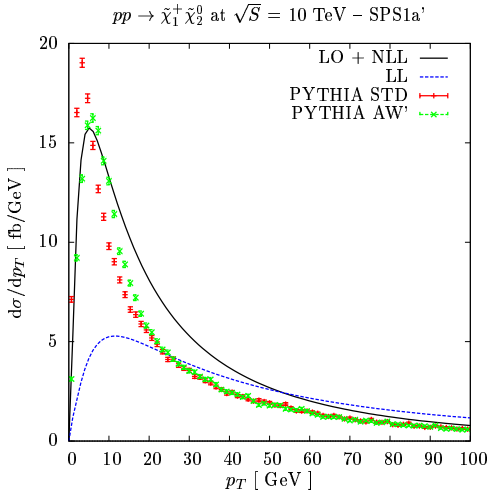

Figure 4: Transverse-momentum distributions of chargino-neutralino pairs at the LHC. The matched LO+NLL (full) and the LL (dashed) results are compared with the predictions of the PYTHIA parton shower with default (bars) and tuned (crosses) parameters.

References

1. H. P. Nilles, *Phys. Rept.* **110** (1984) 1–162.
2. H. E. Haber and G. L. Kane, *Phys. Rept.* **117** (1985) 75–263.
3. V. D. Barger, R. W. Robinett, W.-Y. Keung and R. J. N. Phillips, *Phys. Lett.* **B131** (1983) 372.
4. S. Dawson, E. Eichten and C. Quigg, *Phys. Rev.* **D31** (1985) 1581.
5. J. Debove, B. Fuks and M. Klasen, *Phys. Rev.* **D78** (2008) 074020.
6. W. Beenakker *et. al.*, *Phys. Rev. Lett.* **83** (1999) 3780–3783.
7. G. Sterman, *Nucl. Phys.* **B281** (1987) 310.
8. S. Catani and L. Trentadue, *Nucl. Phys.* **B327** (1989) 323.
9. J. C. Collins, D. E. Soper and G. Sterman, *Nucl. Phys.* **B250** (1985) 199.
10. G. Bozzi, S. Catani, D. de Florian and M. Grazzini, *Nucl. Phys.* **B737** (2006) 73–120.
11. A. Vogt, *Phys. Lett.* **B497** (2001) 228–234.
12. J. Debove, B. Fuks and M. Klasen, *Phys. Lett.* **B688** (2010) 208–211.
13. J. Debove, B. Fuks and M. Klasen, `arXiv:1005.2909 [hep-ph]`.
14. S. Catani, M. L. Mangano, P. Nason and L. Trentadue, *Nucl. Phys.* **B478** (1996) 273–310.
15. E. Laenen, G. Sterman and W. Vogelsang, *Phys. Rev. Lett.* **84** (2000) 4296–4299.
16. P. M. Nadolsky *et. al.*, *Phys. Rev.* **D78** (2008) 013004.
17. J. A. Aguilar-Saavedra *et. al.*, *Eur. Phys. J.* **C46** (2006) 43–60.
18. A. Djouadi, J.-L. Kneur and G. Moultaka, *Comput. Phys. Commun.* **176** (2007) 426–455.
19. C. S. Li, Z. Li, R. J. Oakes and L. L. Yang, *Phys. Rev.* **D77** (2008) 034010.
20. T. Sjostrand, S. Mrenna and P. Z. Skands, *JHEP* **05** (2006) 026.

The electroweak fit and constraints on new physics

Johannes Haller[a]
Institut für Experimentalphysik,
Universität Hamburg, Germany

The global electroweak fit of the Standard Model (SM) with *Gfitter* can be used to constrain yet unknown SM parameters, such as the Higgs mass, but also physics beyond the SM (BSM) via the formalism of oblique parameters. This paper presents updated results of the *Gfitter* SM fit using the latest available electroweak precision measurements and the recent combination of direct Higgs searches at the Tevatron. In addition newly obtained constraints on BSM models, such as models with extra dimensions, little Higgs and a fourth fermion generation, are presented. While a light Higgs mass is preferred by the fit in the SM, significantly larger Higgs masses are allowed in these new physics models.

1 Introduction

By exploiting contributions from quantum loops precise measurements can be used to obtain insights into physics at much higher energy scales than the masses of the particles directly involved in the experimental reactions. In combination with accurate theoretical prediction the experimental data allow us to constrain the free parameters of the physics model in question. Using this principle, in particular the yet unknown mass of the Higgs boson M_H, can be constrained in the Standard Model (SM) using the electroweak precision measurements and state-of-the-art SM predictions since M_H enters logarithmically the prediction of radiative corrections in the SM. Furthermore, in models describing physics beyond the SM (BSM) new effects, *e.g.* from additional heavy particles entering the loops, can influence the prediction of the raditive corrections of the electroweak observables. The formalism of *oblique* parameters, which parametrize the new physics contribution to the radiative corrections, can then be used to probe the new physics models and constrain their free parameters.

In this paper we present updated results of the global electroweak fit with the *Gfitter* framework [1] taking into account the latest experimental precision measurements and the results of direct Higgs searches from LEP and Tevatron. In addition, we present newly obtained constraints on BSM models with extra dimensions, little Higgs and a fourth fermion generation using the oblique parameters.

2 The global electroweak fit of the SM with Gfitter

A detailed discussion of the statistical methods, the experimental data, the theoretical calculations and the results of the global electroweak fit with *Gfitter* can be found in our reference paper [1]. Since its publication the fit has been continuously maintained and kept in line with

[a] for the *Gfitter* group (www.cern.ch/gfitter)

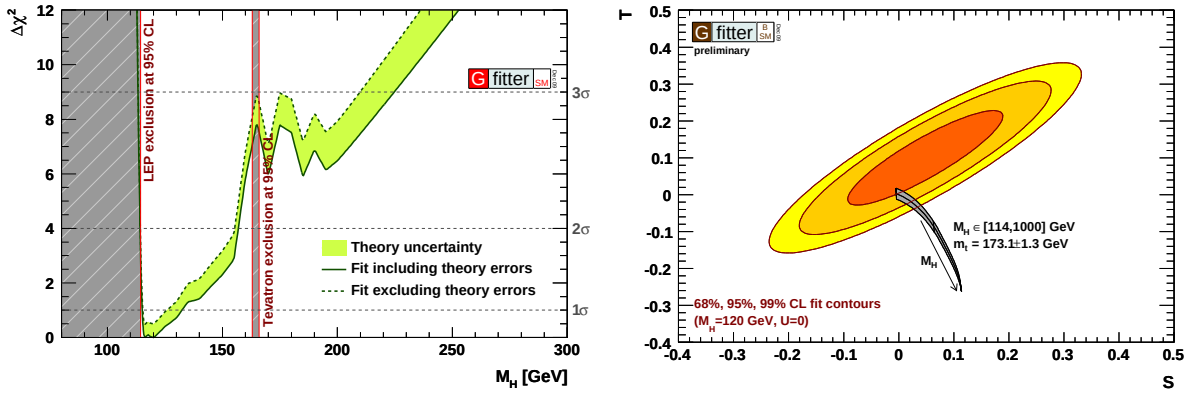

Figure 1: (left) $\Delta\chi^2$ profile as a function of M_H for the global fit of the electroweak SM with *Gfitter* including the results of the direct Higgs searches at LEP and Tevatron. The regions currently excluded with 95 % CL by LEP and Tevatron are indicated by the shaded areas. (right) Fit result of the oblique parameters: Shown are the 68 %, 95 % and 99 % CL allowed regions in the (S,T)-plane with $U = 0$ for a reference SM with $M_H = 120\,\text{GeV}$ and $m_t = 173.2\,\text{GeV}$. The gray/dark area illustrates the prediction in the SM for various values of M_H and m_t.

experimental and theoretical progress. In the following the most important aspects of the fit are quickly repeated and the results of recent changes – mainly updates of the experimental data used in the fit, e.g. M_W, m_t and the direct Higgs searches at the Tevatron – are reported.

The SM predictions for the electroweak precision observables measured by the LEP, SLC, and Tevatron experiments are fully implemented in *Gfitter*. State-of-the-art calculations have been used, in particular the full two-loop and the leading beyond-two-loop corrections for the prediction of the W mass and the effective weak mixing angle [2], which exhibit the strongest constraints on the Higgs mass. In the *Gfitter* SM library the fourth-order (3NLO) perturbative calculation of the massless QCD Adler function [3] is included which allows to fit the strong coupling constant with unique theoretical uncertainty.

The experimental data used in the fit include the electroweak precision data measured at the Z pole [4], the latest world average [5] of the W mass, $M_W = (80.399 \pm 0.023)\,\text{GeV}$, and width, $\Gamma_W = (2.098 \pm 0.048)\,\text{GeV}$, which include the recent run-2 mass measurement reported by D0, and the newest average [6] of the Tevatron top mass measurements, $m_t = (173.1 \pm 1.3)\,\text{GeV}$. For the electromagnetic coupling strength at M_Z we use the $\Delta\alpha^{(5)}_{\text{had}}$ value reported in [7] which does not include the recent measurements of the cross-section $e^+e^- \to \pi^+\pi^-$ from Babar and Kloe using the ISR method since an updated $\Delta\alpha^{(5)}_{\text{had}}$ value including both measurements is not yet available. Also included in the fit is the information from the direct Higgs searches at LEP [8] and Tevatron [9], where we use the latest combination. [b]

The free fit parameters are M_Z, M_H, m_t, m_b, m_c, $\Delta\alpha^{(5)}_{\text{had}}$ and $\alpha_S(M_Z^2)$ where only the latter parameter is fully unconstrained since no direct experimental measurement of $\alpha_S(M_Z^2)$ is used. The minimum χ^2 value of the fit with (without) using the information from the direct Higgs searches amounts to 17.8 (16.4) which corresponds to a p-value for wrongly rejecting the SM of 0.22 (0.23). None of the pull values exceeds 3σ. The 3NLO result of $\alpha_S(M_Z^2)$ obtained from the fit is given by $\alpha_S(M_Z^2) = 0.1193 \pm 0.0028 \pm 0.0001$, where the first error is the experimental fit error and the second is due to missing QCD orders. Among the most important outcomes of the fit is the estimation of the mass of the Higgs boson. Without using the information from the direct Higgs searches we obtain a χ^2 minimum at $M_H = 82.8^{+30.2}_{-23.3}\,\text{GeV}$ with a 2σ

[b] For the purpose of combination with the electroweak fit we transform the one-sided confidence level $\text{CL}_{\text{s+b}}$ reported by the experiments into a two-sided confidence level $\text{CL}^{2-\text{sided}}_{\text{s+b}}$ and calculate the contribution to the χ^2 estimator via $\delta\chi^2 = 2 \cdot [\text{Erf}^{-1}(1 - \text{CL}^{2-\text{sided}}_{\text{s+b}})]^2$. A more detailed discussion of the combination method can be found in [1]. The alternative direct use of the test statistics $-2\ln Q$ in the fit leads to similar results.

interval of [41, 158] GeV. The combination of the indirect fit with the direct Higgs searches can be used to significantly reduce the allowed regions for M_H in the SM. The resulting $\Delta\chi^2$ profile as a function of M_H is shown in Fig. 1 (left). The expected strong increase at the LEP 95% CL exclusion limit and the contribution of the Tevatron searches at higher masses are clearly visible. We obtain a χ^2 minimum at $M_H = 119.4^{+13.4}_{-4.0}$ GeV with a 2σ interval of [114, 157] GeV.

3 Constraints on new physics models

A common approach to constrain physics beyond the SM using the global electroweak fit is the formalism of oblique parameters. Assuming that the contribution of new physics models only appears through vacuum polarization most of the BSM effects on the electroweak precision observables can be parametrized by three gauge boson self-energy parameters (S, T, U) introduced by Peskin and Takeuchi [10]. In this approach the prediction of a certain electroweak observable O is given by the sum of the prediction of a reference SM ($\mathrm{SM_{ref}}$, defined by fixing the values for M_H and m_t) and the new physics effects parametrized by STU, *i.e.* $O = O_{\mathrm{SM,ref}}(M_H, m_t) + c_S S + c_T T + c_U U$. The parameters STU hence measure deviations of the data from the chosen $\mathrm{SM_{ref}}$ and are zero if the data are equal to the $\mathrm{SM_{ref}}$ prediction. S ($S + U$) is sensitive to BSM contributions to neutral (charged) current processes at different energy scales, while T is sensitive to isospin violation effects. The parameter U is small in most BSM models. Further generalizations like additional corrections to the Zbb coupling [11] are also taken into account in *Gfitter*.

Following this approach we have determined the oblique parameters from the electroweak fit. For a $\mathrm{SM_{ref}}$ with $M_H = 120\,\mathrm{GeV}$ and $m_t = 173.2\,\mathrm{GeV}$ we obtain

$$S = 0.02 \pm 0.11, \qquad T = 0.05 \pm 0.12; \qquad U = 0.07 \pm 0.12 \quad . \tag{1}$$

The correlation between S and T is strong and positive (+0.879) while the correlation between S and U and between T and U is negative (−0.469 and −0.716, respectively). Figure 1 (right) shows the 68%, 95% and 99% CL allowed contours in the (S, T)-plane for $U = 0$, together with the SM prediction featuring a logarithmic dependence on M_H. Apart from the trivial fact that the prediction for our $\mathrm{SM_{ref}}$ ($M_H = 120\,\mathrm{GeV}$, $m_t = 173.2\,\mathrm{GeV}$) is indeed $S = T = U = 0$, it can be seen that the data are compatible with the SM prediction for small values of M_H. Hence, no actual need for new physics can be derived from this study.

However, certain BSM models feature a similar agreement with the data. The prediction of these models can cover large regions in the ST-plane due to the allowed variation of the additional free model parameters which in turn can be constrained by comparing the experimental data and the model prediction. As shown in the following, in some BSM models large values of M_H are allowed due to a possible compensation of BSM and Higgs effects.

3.1 Universal Extra Dimensions

As a first example we discuss a model with additional space dimensions accessible for all SM particles [12] (UED). In these models the conservation of a Kaluza-Klein (KK) parity leads to a phenomenology similar to supersymmetry with a stable lightest KK state, which is a candidate particle for the cold dark matter in the universe. The free parameters of the model are the number of extra dimensions d_{ED} and the compactification scale R^{-1}. The contribution to the electroweak precision observables via vacuum polarisation effects in these models, *i.e.* the prediction of the STU parameters, have been calculated in [12]. The main contribution results from additional KK-top/bottom and KK-Higgs loops. For $d_{ED} = 1$, as assumed in the following, the prediction of the oblique parameters mainly depends on R^{-1} and M_H.

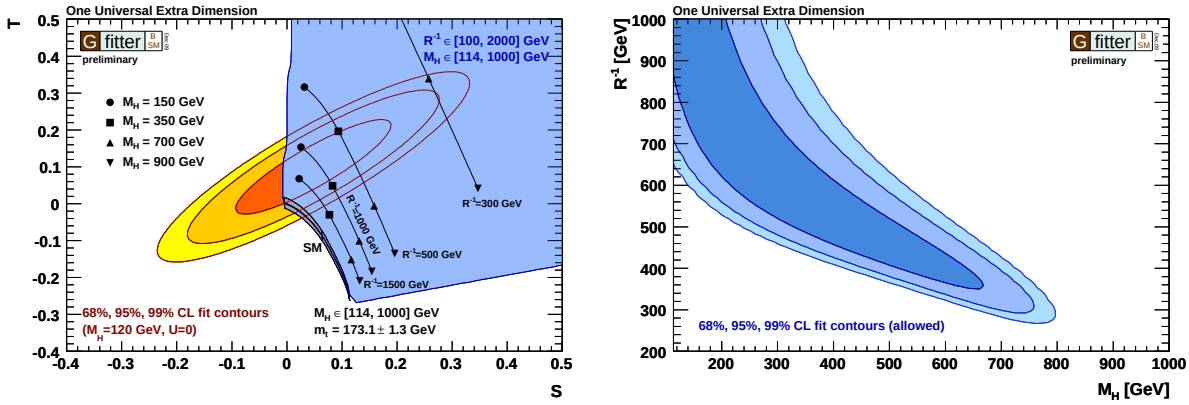

Figure 2: Example results for a model with one Universal Extra Dimension: (left) Comparison of the *STU*-fit result with the prediction in the UED model for various values of the compactification scale R^{-1} and the Higgs mass M_H. (right) The 68 %, 95 % and 99 % CL allowed regions in the (M_H, R^{-1})-plane as derived from the fit.

In Fig. 2 (left) the experimental fit result in the (S, T)-plane is compared to the UED prediction for various values of R^{-1} and M_H. It can be seen that for high values of R^{-1} the UED prediction approaches the SM expectation while for smaller R^{-1} values a significant deviation from the SM prediction is expected. The same behavior can be observed in Fig. 2 (right) where the resulting 68%, 95% and 99% CL allowed regions in the (M_H, R^{-1})-plane are shown. For high R^{-1} values the constraint on M_H approaches the SM result, *i.e.* small M_H are preferred, while for small R^{-1} values, significantly larger M_H values are still allowed since the UED contribution is compensated by a heavier Higgs boson. The latter parameter region is well within the direct discovery reach of the LHC since R^{-1} indicates the expected mass region of the additional KK states. The region $R^{-1} < 300\,\text{GeV}$ and $M_H > 800\,\text{GeV}$ can be excluded. These findings are in agreement with previous publications [12].

3.2 Littlest Higgs model with T-parity conservation

Little Higgs theories tackle the SM hierarchy problem by introducing a new global symmetry broken at a scale $f \sim 1\,\text{TeV}$ where new SM-like fermions and bosons exist canceling the one-loop quadratic divergengies of M_H in the SM. The Littlest Higgs (LH) Model [13] is based on a non-linear 1σ model describing an SU(5)/SO(5) symmetry breaking. Similar to R-parity conservation in supersymmetry, T-parity conservation provides a possible candidate for the cold dark matter in the universe and, important for the current discussion, it forbids tree-level contribution from heavy gauge bosons to the electroweak observables. In this case the dominant oblique corrections [14] rather result from loops involving the two new heavy top states (T-even and T-odd). The corrections depend on the scale f, the ratio of the top state masses $s_\lambda = m_{T^-}/m_{T^+}$, M_H and a coefficient δ_c whose exact value depends on details of the UV physics. [c]

In Fig. 3 (left) the experimental fit result in the (S, T)-plane is compared to the LH prediction for example values of f, s_λ and M_H. It can be seen that for certain parameter settings the LH model with T-conservation is indeed in agreement with the data. In Fig. 3 (right) the fit results for $s_\lambda = 0.45$ are illustrated as 68%, 95% and 99% CL allowed regions in the (M_H, f)-plane. As expected, for high values of f the M_H-constraint in the LH model approaches the M_H-constraint of the SM, while for smaller f values significantly larger values of M_H are allowed than in the SM. Although the allowed regions in the (M_H, f)-plane are strongly dependent on s_λ and no absolute exclusion limit on one of the parameters alone can be derived, the above statements are true for all values of s_λ.

[c] The latter parameter is treated as theory uncertainty in the *Gfitter* fit with $\delta_c = [-5, 5]$.

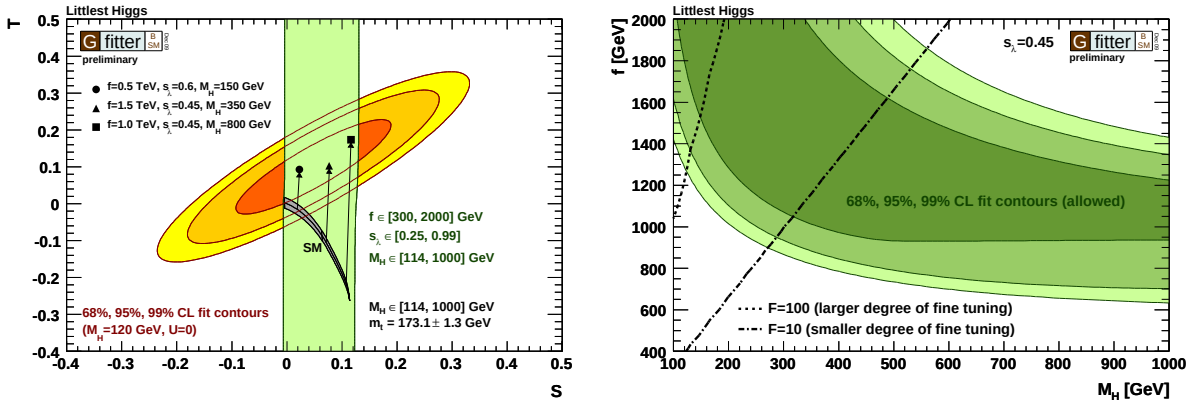

Figure 3: Example results for the Littlest Higgs model with T-parity conservation: (left) Comparison of the STU-fit result with the prediction in the LH model. The symbols illustrate the LH predictions for three example settings of the parameters f, s_λ and M_H. The light green area illustrates the predicted region when varying the free parameters in the ranges indicated in the figure. (right) The allowed region in the (M_H, f)-plane as derived from the fit for $s_\lambda = 0.45$.

3.3 Models with a fourth fermion generation

While the fermion sector of the Standard Model is composed of three generations of leptons and quarks without explanation of this number, several SM extensions suggest extra matter families. In a simple, generic model with only one extra family two new fermions (Ψ_1, Ψ_2) are added to both the quark and lepton sector, *i.e.* a left-handed isospin doublet $\Psi_L = (\Psi_1, \Psi_2)_L$ and two right-handed isospin singlet states $\Psi_{1,R}$ and $\Psi_{2,R}$ with charges equal to the three SM generations. The free model parameters are the masses of the new quarks and leptons m_{u_4}, m_{d_4}, m_{e_4} and m_{ν_4} respectively. Assuming no mixing of the extra families among themselves and with the SM fermions the additional one-loop fermionic contributions to the oblique corrections have been calculated in [15]. In particular, the importance of an appropriate mass splitting of the up-type and down-type fermions has been highlighted.

In Fig. 4 (left) our experimental fit result in the (S, T)-plane is compared to the prediction of the fourth generation model for example values of the masses of the additional fermions and M_H. It can be seen that for some parameter settings the fourth generation model is indeed in agreement with the data and high values of M_H could in principle be allowed. Since the oblique parameters are mainly sensitive to the mass differences of the up-type and down-type fermions and rather insensitive to the absolute mass values of the additional fermions, we have calculated the 68%, 95% and 99% CL allowed regions in the $(m_{u_4} - m_{d_4}, m_{l_4} - m_{\nu_4})$-plane for various values of M_H. The example results for $M_H = 600\,\text{GeV}$, shown in Fig. 4 (right), demonstrate that a high Higgs mass is indeed in agreement with the data for a range of new fermion masses. In general, the data prefer a heavier charged lepton.

4 Conclusion and outlook

Using the *Gfitter* package, the reimplementation of the global fit to the electroweak precision data and its combination with the recent results of the direct Higgs searches allows an exclusion of the SM Higgs mass above 158 GeV at 95% CL. However, contributions from new physics may change this result significantly. The effects on the gauge boson self-energy graphs, called oblique corrections, are known for most of the BSM models and must be continuously confronted with the latest experimental data. Newly obtained results of a few example BSM models implemented in *Gfitter* have been reported in this paper, demonstrating that larger M_H values are in agreement with the electroweak precision data in these models. Apart from an continuous maintenance of

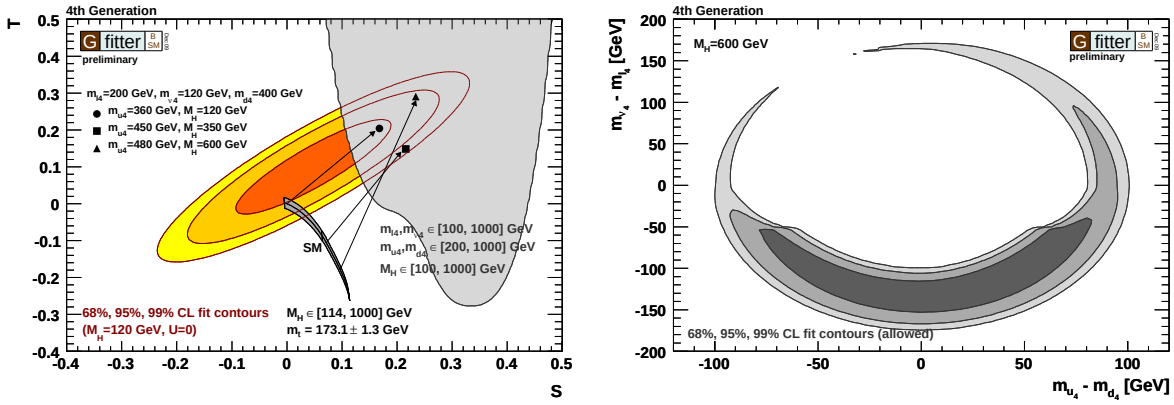

Figure 4: Example results for the model with a fourth fermion generation: (left) Comparison of the *STU*-fit result with the prediction in the fourth generation model. The symbols illustrate the predictions for three example settings of the parameters m_{U_4}, m_{d_4}, m_{ν_4}, m_{l_4} and M_H. The light gray area illustrates the predicted region when varying the free parameters in the ranges indicated in the figure. (right) The allowed regions in the $(m_{u_4} - m_{d_4}, m_{l_4} - m_{\nu_4})$-plane as derived from the fit for $M_H = 600\,\text{GeV}$.

the results reported here, an important future objective of *Gfitter* will be a further diversification of the latter analysis towards more BSM models.

Acknowledgments

This work funded by the German Research Foundation (DFG) in the Collaborative Research Centre (SFB) 676 "Particles, Strings and the Early Universe" located in Hamburg.

References

1. H. Flächer *et al*, *Eur. Phys. J.* C **60**, 543 (2009), [arXiv:0811.0009], updates and newly obtained results available at www.cern.ch/gfitter.
2. M. Awramik *et al.*, *Phys. Rev.* D **69**, 053006 (2004); M. Awramik *et al.*, *JHEP* 11, 048 (2006).
3. P. A. Baikov *et al.*, *Phys. Rev. Lett.* **101**, 012022 (2008).
4. ADLO + SLD collaborations, *Phys. Rept.* 427, 257 (2006).
5. ADLO collaborations, [hep-ex/0612034]; CDF collabroation, *Phys. Rev.* D **77**, 112001 (2008); D0 collabroation, *Phys. Rev. Lett.* **103**, 141801 (2009); D0 collaboration, *Phys. Rev. Lett.* **103**, 141801 (2009); Tevatron Elektroweak Working Group, [arXiv:0808.0147]; Tevatron Elektroweak Working Group, [arXiv:0908.1374].
6. Tevatron Elektroweak Working Group, [arXiv:0903.2503].
7. K. Hagiwara *et al.*, *Phys. Lett.* B **649**, 173 (2007).
8. ADLO collaborations, *Phys. Lett.* B **565**, 61 (2003).
9. Tevatron New Physics Higgs Working Group, [arXiv:0911.3930].
10. M. E. Peskin and T. Takeuchi, *Phys. Rev.* D **46**, 381 (1991).
11. C. P. Burgess *et al.*, *Phys. Lett.* B **326**, 276 (1994); C. P. Burgess *et al.*, *Phys. Rev.* D **49**, 6115 (1994).
12. T. Appelquist *et al.*, *Phys. Rev.* D **67**, 055002 (2003); I. Gogoladze *et al.*, *Phys. Rev.* D **74**, 093012 (2006).
13. N. Arkani-Hamed *et al.*, *JHEP* 0207:034 (2002).
14. J. Hubisz *et al.*, *JHEP* 0601:135 (2006).
15. H. He *et al.*, *Phys. Rev.* D **64**, 053004 (2001).

7.
Light mesons

KLOE RESULTS ON HADRONIC PHYSICS

S. GIOVANNELLA

Laboratori Nazionali di Frascati dell'INFN, via Enrico Fermi 40, 00044 Roma, Italy

on behalf of the KLOE Collaboration

The KLOE experiment collected 2.5 fb^{-1} of e^+e^- collisions at the ϕ peak and about 240 pb^{-1} below the ϕ resonance ($\sqrt{s}$ = 1 GeV). Preliminary results on light meson spectroscopy and the new measurement of the pion form factor are presented.

1 Study of η decays

In the $\eta \to \pi^+\pi^-\gamma$ decay a significant contribution from the chiral anomaly is expected [1]. The chiral anomaly predicts the values of the amplitudes for the non-resonant coupling at the chiral limit, however, the momentum dependence is not predicted and is modeled by many theoretical approaches. The distribution of the two pions invariant mass was pointed out as an important observable in the effort to disentangle possible resonant contributions, e.g. from the ρ-meson. Several theoretical approaches have been developed to treat the contributions of the anomalies to the decay [2] [3] [4]. This decay has been measured in the 1970s with data samples of the order of 10^4 events [5] [6]. However the theoretical papers which tried to combine the two data sets reported discrepancy in data treatment and, as a consequence, difficulty in obtaining consistent results. Therefore, to clarify the situation, results from experiments with large statistics are really needed [7]. Recently the CLEO collaboration published their results on the ratio of charged decays branching ratios $\Gamma_{\eta \to \pi^+\pi^-\gamma}\,/\Gamma_{\eta \to \pi^+\pi^-\pi^0} = 0.175 \pm 0.007 \pm 0.006$ which differ more than $3\,\sigma$'s from old results. From the analysis of 1.2 fb^{-1}, the preliminary KLOE measurement of ratio of branching ratios is: $\Gamma_{\eta \to \pi^+\pi^-\gamma}\,/\Gamma_{\eta \to \pi^+\pi^-\pi^0} = 0.2014 \pm 0.0004_{\rm stat}$. The systematic error, under evaluation, is expected to be less than 1%. Our number is in agreement with the old results from Thaler and Gormley and differs significantly from recent CLEO results as shown in Tab. 1.

Table 1: Comparison of the existing results for the ratio $\Gamma_{\eta \to \pi^+\pi^-\gamma}\,/\Gamma_{\eta \to \pi^+\pi^-\pi^0}$.

PDG08 Average		0.203 ± 0.008
LOPEZ (CLEO) 2007	859 events	$0.175 \pm 0.007 \pm 0.006$
THALER 1973	18k events	0.209 ± 0.004
GORMLEY 1970	7250 events	0.201 ± 0.006
KLOE Preliminary	611k events	0.2014 ± 0.0004

Recently KLOE has started studying the $\eta \to e^+e^-e^+e^-$ decay. This decay, together with

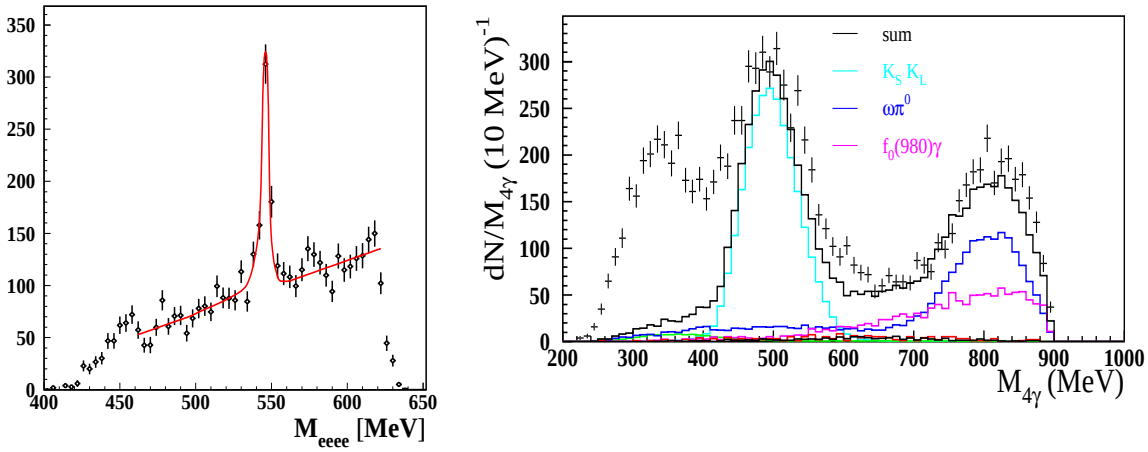

Figure 1: Left: $\eta \to e^+e^-e^+e^-$ analysis, fit of the four electron invariant mass. Right: spectrum of the four-photon invariant mass for data taken at 1 GeV (crosses) compared with the sum of the expected backgrounds (black solid line). The main background contributions are shown in colors.

the $\eta \to \mu^+\mu^-e^+e^-$ channel, is interesting for the η meson form factor measurement because there are only leptons in the final state. Events with four electrons are selected using time of flight information provided by the calorimeter. Backgrounds from $\eta \to \gamma\gamma/e^+e^-\gamma$ with photon conversion are rejected by reconstructing the conversion point on the beam pipe or drift chamber walls. Most of the residual background comes from continuum events and a small contribution is due to ϕ decays. The latter is subtracted from data using the MC spectrum. The number of signal events is obtained by fitting the data distribution of the four electron invariant mass, M_{eeee}, with signal and background shapes (Fig. 1-left). From the fit we extract $N_{\eta\to e^+e^-e^+e^-} = 413 \pm 31$. This constitutes the first observation of this decay.

2 $\gamma\gamma$ physics

The study of the reaction $e^+e^- \to e^+e^-\gamma^*\gamma^* \to e^+e^-X$, where X is some arbitrary final state resulting from fusion of two photons, gives access to states with $J^{PC} = 0^{\pm+}$, $2^{\pm+}$. In the low-energy region covered by the KLOE detector, $m_{\pi^0} < W_{\gamma\gamma} < 700$ MeV, existing measurements [9] are affected by large statistical and systematic uncertanties. At KLOE, where there is no tagging of the outgoing e^+e^-, $\gamma\gamma$ interactions have been studied using off-peak data (240 pb^{-1} collected at $\sqrt{s} = 1$ GeV), as the main source of background comes from ϕ decays.

The study of the $e^+e^- \to e^+e^-\pi^0\pi^0$ process is interesting because of a possible contribution from the controversial σ scalar meson. In Fig. 1-right, the preliminary spectrum of the four-photon invariant mass, $M_{4\gamma}$, is compared with accountable background yields. An excess of about 4000 events is evident at low $M_{4\gamma}$ values, where the σ contribution is expected. Detailed studies of the background contamination and the extraction of the $\sigma \to \pi^0\pi^0$ contribution are in progress.

The η radiative width, $\Gamma_{\eta\gamma\gamma}$, is usually extracted from the measurement of the $e^+e^- \to e^+e^-\eta$ cross section. The KLOE analysis is performed using the $\eta \to \pi^+\pi^-\pi^0$ decay channel. After background rejection, distributions of longitudinal momentum (p_L) and recoil missing mass (M^2_{miss}) are independently fitted with the superposition of MC shapes for signal and background (Fig. 2). More than 600 $e^+e^- \to e^+e^-\eta \to e^+e^-\pi^+\pi^-\pi^0$ events are obtained. Determination of $\sigma(e^+e^- \to e^+e^-\eta)$ and $\Gamma_{\eta\gamma\gamma}$ are under way.

These results are encouraging in view of the forthcoming data taking campaign of the KLOE-2 project [10], when both low and high energy $e^\pm$ tagging devices will be available.

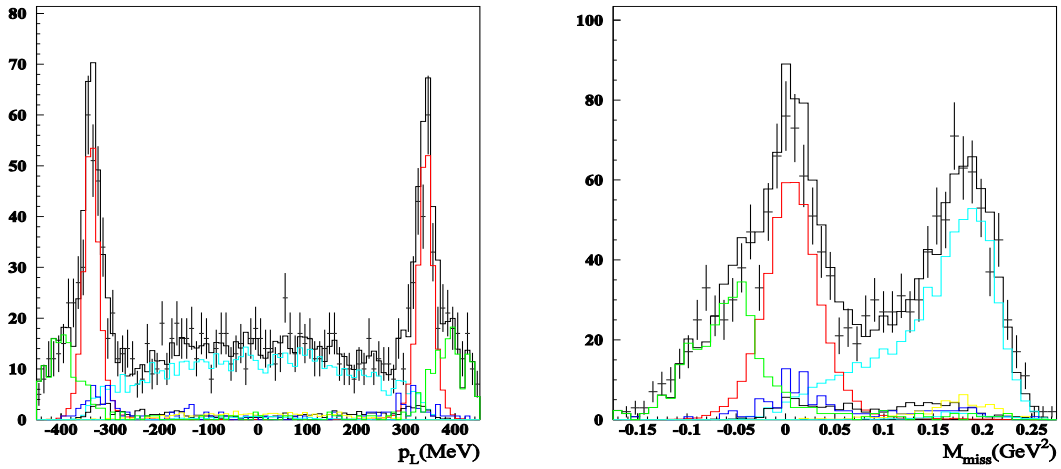

Figure 2: Fit to the p_L (left) and M^2_{miss} (right) distributions for $\gamma\gamma \to \eta$ events. Signal (cyan), $\phi \to \eta\gamma$ (red) and radiative Bhabha events (green) contributions are also shown.

3 The measurement of the hadronic cross section

The published KLOE measurements [8,11] of the hadronic cross section for the process $e^+e^- \to \pi^+\pi^-$ used initial state radiation (ISR) events with photon emitted at small angle to the beam line, resulting in a kinematical suppression of events with $M^2_{\pi\pi} < 0.35$ GeV^2. To access the two pion threshold, a new analysis has been performed requiring events with photon at large polar angles ($50^\circ < \theta_\gamma < 130^\circ$), in the same angular region of the pions. The drawback using such acceptance cuts is a reduction in statistics of about a factor 5, as well as an increase of events with final state radiation and from ϕ radiative decays. The uncertainty on the model dependence of the ϕ radiative decays to the scalars $f_0(980)$ and $f_0(600)$ together with $\phi \to \rho\pi \to (\pi\gamma)\pi$ has a pontentially strong impact on the measurement [13]. For this reason, the present analysis uses the data taken by the KLOE experiment in 2006 at a value of $\sqrt{s} = 1$ GeV, about 5 Γ_ϕ outside the narrow peak of the ϕ resonance. This reduces the effect due to contributions from $f_0\gamma$ and $\varrho\pi$ decays of the ϕ-meson to $\sim 1\%$. Contaminations from the processes $\phi \to \pi^+\pi^-\pi^0$ and $e^+e^- \to \mu^+\mu^-\gamma$ are rejected using kinematical variables. A particle ID estimator based on calorimeter information and time-of-flight is used to efficiently suppress the high rate of radiative Bhabhas. The radiative differential cross section is then obtained subtracting the residual background events and dividing by the selection efficiencies and the integrated luminosity. The total cross section $\sigma_{\pi\pi}$ is obtained using the formula [12]:

$$s\,\frac{\mathrm{d}\sigma_{\pi\pi\gamma}}{\mathrm{d}M^2_{\pi\pi}} = \sigma_{\pi\pi}(M^2_{\pi\pi})\; H(M^2_{\pi\pi})\;, \tag{1}$$

where H is the radiator function, describing the photon emission at the initial state. This formula omits Final State Radiation (FSR) terms, which are however properly taken into account in the analysis. From $\sigma_{\pi\pi}$ the squared modulus of the pion form factor $|F_\pi|^2$ can be derived. Fig. 3 shows $|F_\pi|^2$ as a function of $(M^0_{\pi\pi})^2$ for the new KLOE09 measurement compared with the previous KLOE publication (KLOE08) and with results from CMD-2 [14,15] and SND [16] experiments. On the ρ-peak and above, the new analysis confirms KLOE08 data being smaller than the Novosibirsk results, below the ρ-peak the three experiments show good agreement.

The cross section corrected for the running of α_{em} and inclusive of FSR is used to determine the dipion contribution to the muon anomalous magnetic moment, $\Delta a_\mu^{\pi\pi}$:

$$\Delta a_\mu^{\pi\pi}(0.1 - 0.85\ \mathrm{GeV}^2) = (478.5 \pm 2.0_{\mathrm{stat}} \pm 4.8_{\mathrm{exp}} \pm 2.9_{\mathrm{theo}}) \cdot 10^{-10}. \tag{2}$$

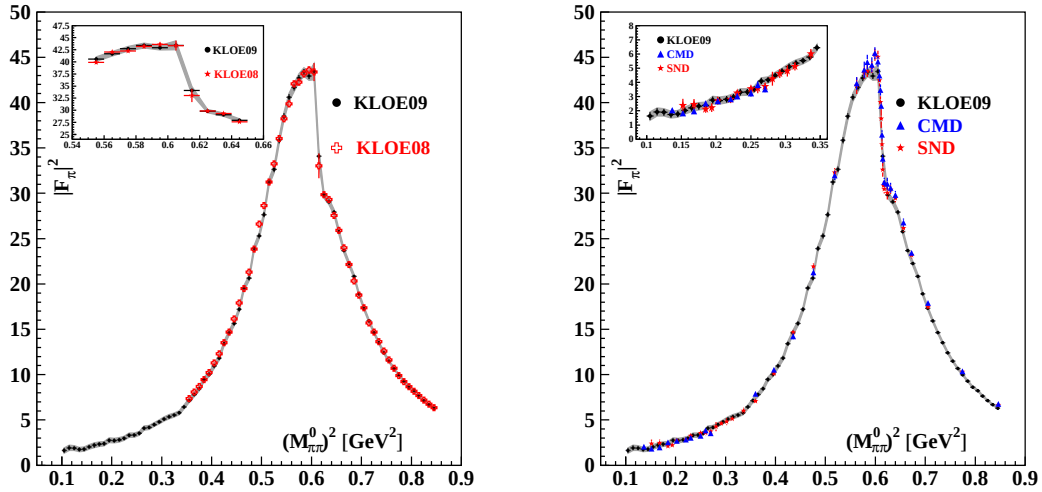

Figure 3: Pion form factor $|F_\pi^2|$ obtained in the present analysis (KLOE09) compared with the previous KLOE result (left) and results from the CMD and SND experiments (right). KLOE09 data points have statistical error attached, the grey band gives the statistical and systematic uncertainty (added in quadrature). Errors on KLOE08, CMD2 and SND points contain the combined statistical and systematic uncertainty.

Table 2: a_μ evaluation from different KLOE analyses.

KLOE Analysis	$\Delta a_\mu^{\pi\pi}(0.35 - 0.85\ \mathrm{GeV}^2) \times 10^{-10}$
KLOE09	$376.6 \pm 0.9_{\mathrm{stat}} \pm 2.4_{\mathrm{exp}} \pm 2.1_{\mathrm{theo}}$
KLOE08	$379.6 \pm 0.4_{\mathrm{stat}} \pm 2.4_{\mathrm{exp}} \pm 2.2_{\mathrm{theo}}$

The evaluation of $\Delta a_\mu^{\pi\pi}$ in the range between 0.35 and 0.85 GeV^2 allows to compare the result obtained in this new analysis with the previously published result by KLOE [11], as shown in Tab. 2. The two values are in good agreement, therefore the new measurement confirms the $\sim 3\,\sigma$'s discrepancy between the Standard Model prediction and the BNL measurement on a_μ.

References

1. S. L. Adler, *Phys. Rev.* **177**, 2426 (1969).
2. B. R. Holstein, *Phys. Scripta* T **99**, 55 (2002).
3. M. Benayoun *et al*, *Eur. Phys. J.* C **31**, 525 (2003).
4. B. Borasoy and R. Nissler, *Nucl. Phys.* A **740**, 362 (2004).
5. P. Gormley, *Phys. Rev.* D **2**, 501 (1970).
6. J. Layter, *Phys. Rev.* D **7**, 2565 (1973).
7. B. Borasoy and R. Nissler, arXiv:0705.0954 [hep-ph] (2007).
8. A. Aloisio *et al.* [KLOE Coll.], *Phys. Lett.* B **606**, 12 (2005).
9. H. Marsiske *et al.* [Crystal Ball Coll.], *Phys. Rev.* D **41**, 3324 (1990); T. Oest *et al.* [JADE COll.], *Z. Phys.* C **47**, 343 (1990).
10. G. Amelino-Camelia *et al.*, arXiv:1003.386 (2010).
11. F. Ambrosino *et al.* [KLOE Coll.], *Phys. Lett.* B **670**, 285 (2009).
12. S. Binner, J. H. Kühn and K. Melnikov, *Phys. Lett.* B **459**, 279 (1999).
13. D. Leone, PhD thesis, KA-IEKP-2007-7 (2007).
14. R. R. Akhmetshin *et al* [CMD-2 Coll.], *Phys. Lett.* B **648**, 28 (2007).
15. R. R. Akhmetshin *et al* [CMD-2 Coll.], *J. Exp. Theor. Phys. Lett.* **84**, 413 (2006).
16. M. N. Achasov *et al* [SND Coll.], *J. Exp. Theor. Phys.* **45**, 380 (2006).

Hadron spectroscopy with COMPASS – First results

Frank Nerling
Physikalisches Institut, Universität Freiburg,
Hermann-Herder-Str. 3, D-79104 Freiburg, Germany
nerling@cern.ch
for the COMPASS collaboration

The COMPASS experiment at CERN is dedicated to light hadron spectroscopy with emphasis on the detection of new states, in particular the search for spin exotic states and glueballs. After a short pilot run in 2004 (190 GeV/c π^- beam, Pb target) showing significant production strength of an exotic $J^{PC} = 1^{-+}$ state at 1.66 GeV/c^2, we have collected data with 190 GeV/c hadron beams on a liquid hydrogen target in 2008/09. The spectrometer features good coverage by calorimetry and our data provide excellent opportunity for simultaneous observation of new states in different decay modes. The diffractively produced $(3\pi)^-$ system for example can be studied in both modes $\pi^- p \to \pi^-\pi^+\pi^- p$ and $\pi^-\ p \to \pi^-\pi^0\pi^0\ p$. Reconstruction of charged and neutral mode rely on completely different parts of the apparatus. Observation of new states in both modes provides important checks. The results on diffractive dissociation into 3π final states from the 2004 data recently published are discussed as well as the first comparison of neutral vs. charged mode based on a first partial wave analysis of 2008 data.

1 Introduction

The COMPASS fixed-target experiment [1] at CERN SPS is dedicated to the study of structure and dynamics of hadrons, both aspects of non-perturbative QCD. In a first phase (2002-2007) COMPASS studied the nucleon spin structure by deep inelastic scattering of 160 GeV/c polarised muons off polarised ^{6}LiD and NH_3 targets. During a second phase in 2008/09, measurements with 190 GeV/c hadron beams on a liquid hydrogen and nuclear targets were performed, mainly dedicated to hadron spectroscopy. Of particular interest is the search for non-$q\bar{q}$ mesons, like hybrids, glueballs or tetra-quarks, which do not fit into the Constituent Quark Model (CQM), but are allowed within QCD. Such objects, however, would mix with ordinary $q\bar{q}$ states of same J^{PC} quantum numbers, making it difficult to disentangle the different contributions. The observation of spin-exotic states with quantum numbers forbidden in the CQM, like $J^{PC} = 0^{--},\ 0^{+-},\ 1^{-+},\ \ldots$, would provide clear evidence for physics beyond the CQM and thus a fundamental confirmation of QCD. The lowest mass hybrid candidate, means a meson consisting of a colour octet $q\bar{q}$ pair neutralised in colour by an excited gluon, is predicted [2] to have exotic $J^{PC} = 1^{-+}$, and a mass between 1.3 and 2.2 GeV/c^2. Two experimental candidates for a 1^{-+} hybrid in the light quark sector have been reported in the past, the $\pi_1(1400)$ and the $\pi_1(1600)$. The latter was observed in diffractive production by different experiments, decaying – among others, like $\eta'\pi$, $f_1(1285)\pi$ and $\omega\pi\pi$ – into $\rho\pi$ [3,4]. Especially the resonance nature of both candidates, is still heavily disputed [5,6]. To improve our understanding, new experiments have to be performed at high statistics, extending the spectrum to masses beyond 2.2 GeV/c^2. COMPASS has just started to shed new light on the puzzle [7], as discussed in this paper.

2 The COMPASS experiment

A detailed description of the COMPASS two-stage spectrometer, Fig. 1 (left), dedicated to a variety of fixed-target physics programmes can be found in [1]. For the measurements with hadron beams started in 2008, a 40 cm long liquid hydrogen target, and simple disks of solid material (part of 2009 run) have been used. The spectrometer features electromagnetic and hadronic calorimetry in both stages (E/HCAL in Fig. 1). Photon detection in a wide angular range with high resolution is crucial for decay channels involving π^0, η or η'. Nearly 4π coverage is achieved for charged and neutral particles in the final states with forward kinematics. A Recoil Proton Detector (RPD) consisting of two concentric barrels of scintillator slats was introduced to trigger on interactions inside the target It detects the recoil particle to ensure exclusivity by a time-of-flight measurement at high accuracy of $\sim$350 ps.

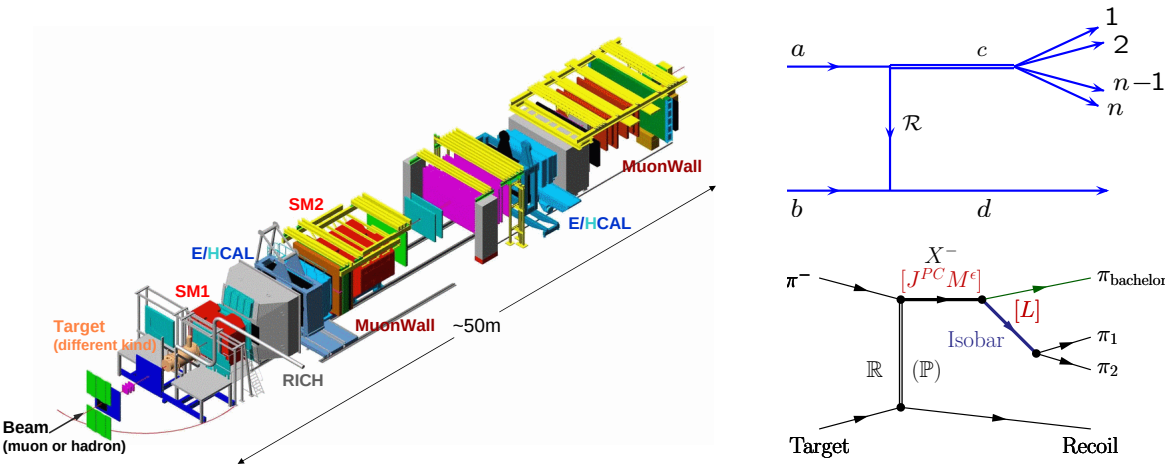

Figure 1: Left: Sketch of the two-stage COMPASS spectrometer. Right: *(top)* Diffractive meson production via t-channel Reggeon exchange: The beam particle a is excited to a resonance c subsequently decaying into n mesons, the target stays intact. *(bottom)* Diffractive dissociation into 3π final states as described in the isobar model: The produced resonance X^- with quantum numbers $J^{PC}M^{\epsilon}$ decays into an isobar with spin S and relative orbital angular momentum L with respect to the π_{bachelor}. The isobar subsequently decays into two pions. At high energies, the Pomeron is the dominant Regge-trajectory.

3 Analysis of 3π final states from diffractive dissociation

Consider the reaction $a+b \to c+d$, with $c \to 1+2+...+n$, where a is the incoming beam particle, b the target, c the diffractively produced object decaying into n particles, and d the target recoil particle staying intact, see Fig. 1 *(right/top)*. The reaction is described by two kinematic variables, the square of the total centre of mass energy $s = (p_a + p_b)^2$ and $t' = |t| - |t|_{\text{min}} \geq 0$, with $t = (p_a - p_c)^2$ the squared momentum transfer from the target to the beam particle, and $|t|_{\text{min}}$ is the minimum absolute value of t allowed by kinematics for a given mass m_c. The basic selection of diffractive 3π events common to all analyses discussed in this paper requires exactly one primary vertex within the target volumes. One incoming beam particle plus three outgoing charged tracks (charged mode) and one outgoing negatively charged track plus exactly 4 clusters detected in the ECALs (neutral mode) are requested, respectively, both with total charge -1. An exclusivity cut, taking into account the momentum transfer t' to the target, ensures that the total energy of the three outgoing pions add up to the beam energy. The partial wave analysis (PWA) is performed in the range of $0.1 < t' < 1.0\,\text{GeV}^2/\text{c}^2$ in order to stay above hardware thresholds and to ensure diffractive processes. In case of 2008 data, a cut on the collinearity of the recoil proton and the outgoing pion system further suppresses non-exclusive background.

3.1 Observation of a $J^{PC} = 1^{-+}$ exotic resonance – 2004 pilot run data

The PWA is based on the isobar model, see Fig.1 *(right/bottom)*. A partial waves is defined by a set of quantum numbers $J^{PC}M^{\epsilon}[isobar]L$, with spin J, parity P and C-parity of the resonance X^-. M and ϵ (reflectivity) define the spin projection. The resonance decays via an intermediate di-pion resonance (the isobar) accompanied by a so-called bachelor pion, with relative orbital angular momentum L. We perform our PWA in two steps, a mass-independent fit and a subsequent mass-dependent fit. The former is performed on the data binned into $40\,\text{MeV}/\text{c}^2$ wide mass intervals, so that no assumption on the resonance structure of the 3π system is made. A total set of 42 waves including a flat background wave is fitted to the data using an extended maximum likelihood method, which comprises acceptance corrections. The mass-dependent fit is applied to the six main waves, which result from the first step, and uses a χ^2 minimisation. The mass dependence is parameterised by relativistic Breit-Wigners (BW) and coherent background if present. The employed parameterisation of the spin density matrix has a rank of two, accounting for spin-flip and spin-non-flip amplitudes at the baryon vertex. Fig. 2

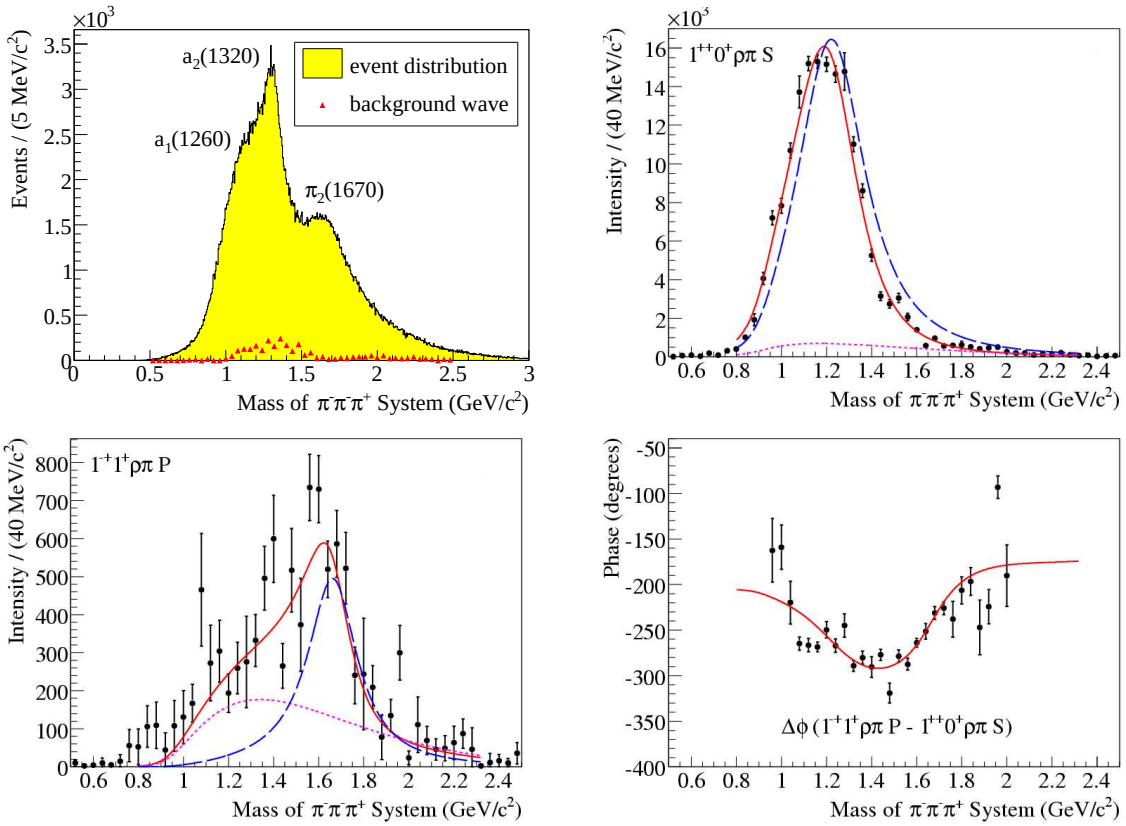

Figure 2: Top: *(Left)* Invariant mass of $\pi^-\pi^+\pi^-$ showing the most prominent resonances (2004 data). *(Right)* Example PWA fit for $a_1(1260)$: Intensity of $1^{++}0^+[\rho^-\pi]S$ wave. Bottom: *(Left)* Fitted intensity of the exotic $1^{-+}1^+[\rho\pi]P$ wave. *(Right)* Phase differences of the exotic $1^{-+}1^+$ and the $1^{++}0^+$ wave – for details see text.

shows the intensity of the 1^{++} wave with the well-established $a_1(1260)$ and that of the spin-exotic 1^{-+} wave as well as the phase difference $\Delta\Phi$ between the two, for the fits of all six waves, see [7]. The black data points represent the mass-independent fit, whereas the mass-independent one is overlayed as red solid line, the separation into background (purple) and BW (blue) is plotted where applicable. In previous observations, especially the resonant nature of the exotic $1^{-+}1^+[\rho\pi]P$ wave is questioned, whereas our data shows a clear and rapid phase motion. Our result of a mass of $1660 \pm 10^{+0}_{-64}\,\mathrm{MeV/c^2}$ and a width of $269 \pm 21^{+42}_{-64}\,\mathrm{MeV/c^2}$ is consistent with the famous $\pi_1(1600)$ [7] already reported by previous experiments but still controversially discussed.

3.2 First comparison of neutral versus charged mode – 2008 data

The event selections have been discussed more detailed [8,9]. The resultant invariant mass spectra for charged and neutral mode are shown in Fig. 3 *(top)*, exhibiting the same prominent resonances as in Fig. 2. In this first analysis, we apply the same PWA model as for the 2004 data. The mass-independent fit results are compared in Fig. 3 *(bottom)*, normalised using the $a_2(1320)$ to account for different statistics. Even though acceptance corrections have not yet been applied (estimated effect up to 20%), the comparison is already quite promising. From simple isospin symmetry consideration, we expect for all isobars decaying into $\rho\pi$ the same intensities for both modes, whereas for those going to $f_2\pi$, a suppression factor of two is expected for the neutral mode, simply due to Clebsch-Gordon coefficients. Indeed Bose-Symmetrisation with the bachelor pion might modify the picture. We checked, however, that the effect is the same for $\rho\pi$ decays and thus cancels out, whereas for $f_{0,2}\pi$ channels, the effects can be large in general, but no effect was found for the one chosen here. Indeed similar intensities are found for the $1^{++}0^+[\rho(770)\pi]S$ wave in both modes, and about half intensity in the $2^{-+}0^+[f_2(1270)\pi]S$ wave for the neutral mode – as expected. Such kind of isospin-symmetry checks will validate independent confirmation in

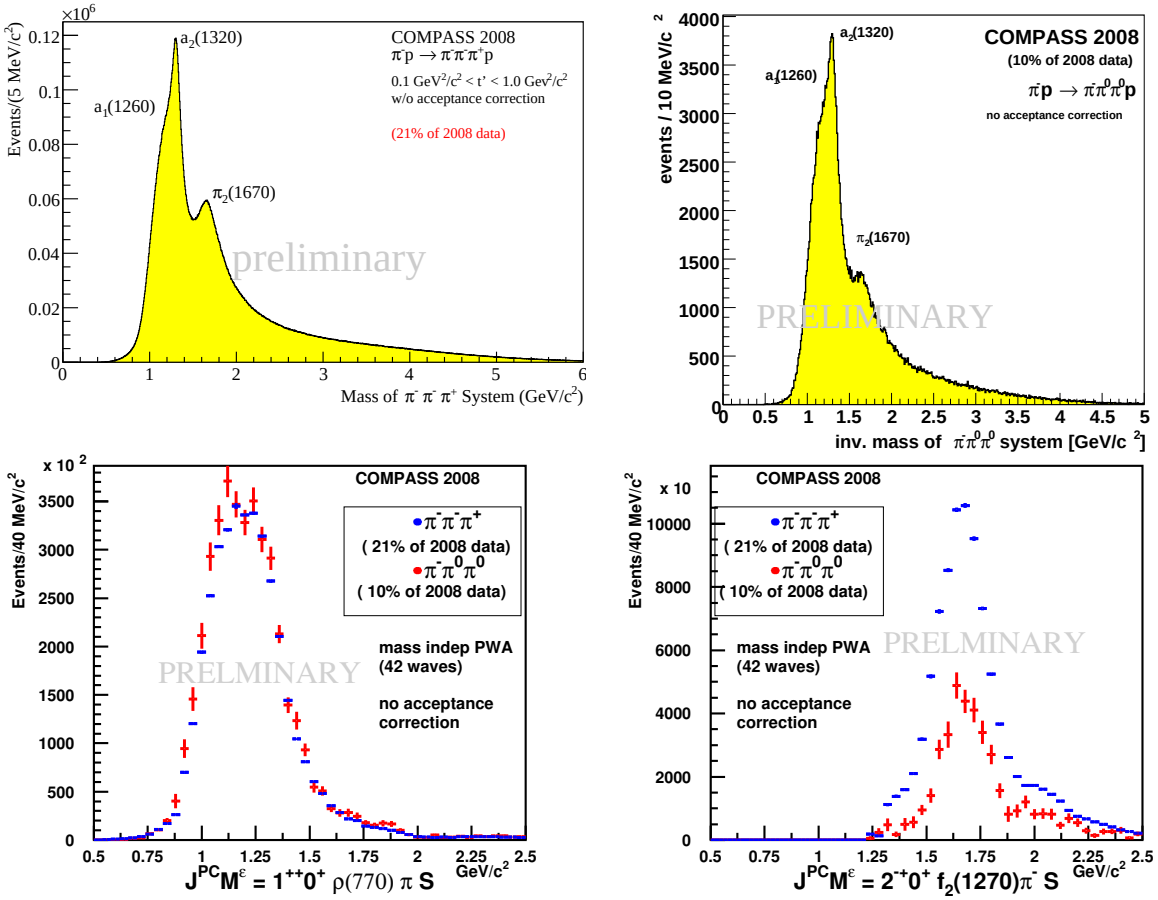

Figure 3: Comparison of 3π analyses neutral vs. charged mode (2008 data). Top: Invariant mass of $\pi^-\pi^+\pi^-$ and $\pi^-\pi^0\pi^0$ showing the most prominent resonances. Bottom: Exemplary intensities of main waves, for comparison, neutral and charge mode intensities were normalised to the well-established $a_2(1320)$: $2^{++}1^+[\rho\pi]D$ wave. *(Left)* $a_1(1260)$: $1^{++}0^+[\rho\pi]S$ wave, *(Right)* $\pi_2(1670)$: $2^{-+}0^+[f_2(1270)\pi]S$ wave.

case of new states, like e.g. the $\pi_1(1600)$, simultaneously observed in different decay modes.

Summary

First results on the COMPASS hadron data show the high potential for meson spectroscopy. Our 2004 pilot run data show a significant spin exotic signal consistent with the controversially discussed $\pi_1(1600)$. The data collected in 2008/09 exceeds the world statistics by up to two orders of magnitude. One advantage of COMPASS as compared to previous fixed-target experiments is the ability for detecting final states involving charged and neutral particles. COMPASS has not only access to many decay channels but also to higher masses exceeding 3.5 GeV/c^2.

Acknowledgements

This work is supported by the BMBF (Germany), particularly the "Nutzungsinitiative CERN".

References

1. P. Abbon *et al.*, COMPASS collaboration, Nucl. Instrum. Meth. **A577**, 455 (2007).
2. K.J. Juge, J. Kuti, C. Morningstar, AIP Conf. Proc. **688**, 193 (2004).
3. G.S. Adams *et al.*, Phys. Rev. Lett. **81**, 5760 (1998).
4. Y. Khokhlov, Nucl. Phys. A **663**, 596 (2000).
5. D.V. Amelin *et al.*, Phys. Atom. Nucl. **68**, 359 (2005).
6. A.R. Dzierba *et al.*, Phys. Rev. D **73**, 072001 (2006).
7. M. Alekseev *et al.*, COMPASS collab., subm. to Phys. Rev. Lett, arXiv:0910.5842v2 (2010).
8. F. Nerling *et al.*, COMPASS collab., AIP Conf. Proc. (2009), to be published.
9. F. Haas *et al.*, COMPASS collab., AIP Conf. Proc. (2009), to be published.

Recents results by the NA48/2 experiment

S. Venditti on behalf of the NA48/2 collaboration
Università di Pisa, L.go B. Pontecorvo 3, 56127 Pisa(Italy)

The NA48/2 experiment at CERN[?] collected ~$18{\cdot}10^9$ charged kaon decays during the years 2003/4. Along with the primary goals of the collaboration, i.e. the measurement of the CP-violating asymmetry in the $K^\pm \to \pi^\pm\pi^+\pi^-$ and $K^\pm \to \pi^\pm\pi^0\pi^0$ decays, the collected data allowed to perform many other interesting analyses. In this paper the results obtained for the $K^\pm \to e^\pm\nu\pi^+\pi^-$ (Ke4), $K^\pm \to \pi^\pm\pi^0\gamma$ (Kpi2g) and the $K^\pm \to \pi^\pm\gamma\gamma$ decays will be reviewed.

1 The NA48/2 experiment

A sketch of the NA48/2 beamline is shown in fig.**??**. Kaons are produced by impinging 400 GeV protons from the SPS on a Beryllium target and selected through an achromat system in a 60 GeV/c and 3.8% r.m.s. momentum band; afterwards they decay in the ~113 m long fiducial region, downstream of which the following detectors are placed (fig.**??**):

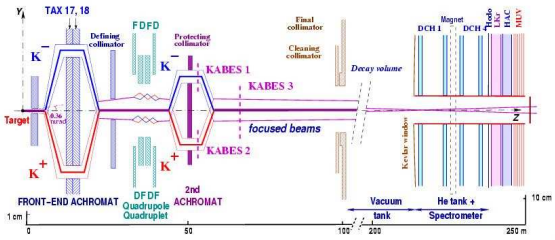

Figure 1: Sketch of the NA48/2 beamline.

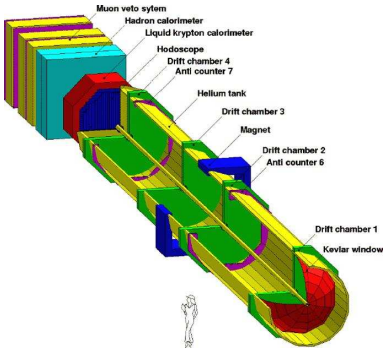

Figure 2: Layout of the NA48/2 detectors.

- the drift chamber (DCH) system, made of 4 octagonal DCHs. Each chamber is made of 4 views of 2 wire planes, staggered by half wire pitch. A magnet, placed between DCH 2 and 3, gives the charged particles a 120 MeV/c transverse momentum kick. The position and momentum resolutions are ~100μm and $\frac{\sigma(P)}{P} = 1.0\% \oplus 0.044 \cdot P(GeV/c)\%$ respectively.
- the charged hodoscope, made of two planes of 64 plastic scintillator strips. It provides fast trigger conditions ($T_{res} \sim 150$ ps) and yields the time measurement for charged tracks.
- the liquid krypton calorimeter (LKr), made of 13248 2×2 cm^2 cells, defined by Cu-Be-Co 127 cm long ribbons. The 27 radiation lengths and small Molière radius allow an excellent

energy resolution: $\frac{\sigma_E}{E} = \frac{0.032}{\sqrt{E(GeV)}} \oplus \frac{0.09}{E(GeV)} \oplus 0.0042$.

Other detectors include: a TPC detector aiming at measuring the kaons' momentum and direction, a neutral hodoscope made of scintillating fibers, a veto system of 7 rings of iron and scintillator placed along the decay region, a hadronic calorimeter and a muon veto.

2 Ke4 form factors and phase shift

2.1 Theory and analysis

The Ke4 is a four body decay, which implies five independent variables; the Cabibbo-Maksymowicz variables S_e, S_π, θ_e, θ_π, ϕ [?] are commonly used. The hadronic part of the amplitude can be written as:

$$< \pi^+\pi^-|A^\lambda|K^+ >= \frac{1}{M_K}(F(p_{\pi^+} + p_{\pi^-})^\lambda + G(p_{\pi^+} - p_{\pi^-})^\lambda + R(p_e + p_\nu)^\lambda +$$

$$+\frac{H}{{M^2}_K}\epsilon^{\lambda\mu\rho\sigma}(p_{\pi^+} + p_{\pi^-} + p_e + p_\nu)_\mu(p_{\pi^+} + p_{\pi^-})_\rho(p_{\pi^+} - p_{\pi^-})_\sigma)$$

The form factors F, G and H can be expanded in partial waves:

$$F = F_s e^{i\delta_s} + F_p e^{i\delta_p}\cos\theta_\pi + ... \qquad G = G_p e^{i\delta_g} + ... \qquad H = H_p e^{i\delta_h} + ... \tag{1}$$

The form factor R is suppressed in Ke4 decays (but is relevant in Kμ4). Neglecting d wave terms and assuming the same phase for every coefficient, four coefficients (F_s, F_p, G_p, H_p) are left, which can in turn be expanded in powers of $q^2 = (\frac{S_\pi}{4{m_\pi}^2} - 1)$ and $\frac{S_e}{4{m_\pi}^2}$:

$$F_s = f_s + f'_s q^2 + f''_s q^4 + f'_e \frac{S_e}{4m_\pi^2} + ... \tag{2}$$

$$F_p = f_p + f'_p q^2 + ... \qquad G_p = g_p + g'_p q^2 + ... \qquad H_p = h_p + h'_p q^2 + ... \tag{3}$$

The selection of the events was performed requiring two opposite sign pions (E/p<0.8, p_π >5 GeV/c[a]) and one electron or positron (0.9<E/p<1.1, p_e >3 GeV/c). Time cuts, as well as minimum distance cuts among tracks and clusters, were applied. The background (from $K^\pm \to \pi^\pm\pi^+\pi^-$ followed by a $\pi \to e\nu$ decay or with a misidentified pion, or from $K^\pm \to \pi^\pm\pi^0(\pi^0)$ with a Dalitz decay $\pi^0 \to e^+e^-\gamma$ and photon(s) lost) has been checked directly on data, using the so called wrong-sign events and so avoiding to heavily rely on the MC.

2.2 Fitting procedure and form factor extraction

15000 iso-populated bins were used in the five-dimensional phase space, the average number of events/bin being 48 for the K^+ and 27 for the K^- sample. Form factor values are extracted by minimizing an estimator well suited for small numbers. Since no branching fraction has been measured in this analysis, only relative form factors $\frac{F_p}{F_s}, \frac{G_p}{F_s}, \frac{H_p}{F_s}$ and the phase shift $\delta = \delta_s - \delta_p$ are accessible. The F_s^2 dependence from $M_{\pi\pi}$ and $M_{e\nu}$ is extracted using the relative normalization data/MC and then deconvoluted from the other relative form factors, whose residual dependence by $M_{\pi\pi}$, $M_{e\nu}$ is finally investigated. The results of the form factor fits are (value$\pm$stat$\pm$syst):

$$f'_s/f_s = 0.152\pm0.007\pm0.005 \quad f''_s/f_s = -0.073\pm0.007\pm0.006 \quad f'_e/f_s = 0.068\pm0.006\pm0.007 \tag{4}$$

$$f_p/f_s = -0.048\pm0.003\pm0.004 \quad g_p/f_s = 0.868\pm0.010\pm0.010 \quad g'_p/f_s = 0.089\pm0.017\pm0.013 \tag{5}$$

$$h_p/f_s = -0.398 \pm 0.015 \pm 0.008 \tag{6}$$

[a] E/p is the ratio between the energy in the EM calorimeter and the momentum measured by the spectrometer.

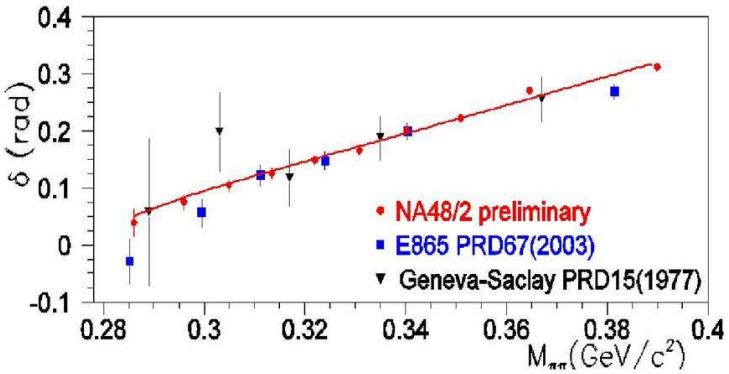

Figure 3: Phase shift δ from NA48/2 compared to the measurements of other experiments [??].

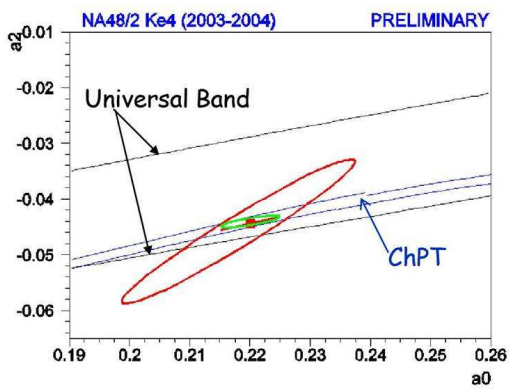

Figure 4: The a_2-a_0 plane.

2.3 The δ phase shift and scattering length extraction

The extraction of pion scattering lengths from δ requires the use of Roy equations [?] and data at intermediate energies [?]. Besides performing a 2 parameter fit on a_0^0 and a_2^0, the Universal Band approach, corresponding to a 1-dimensional fit of δ with a fixed relation between a_0^0 and a_2^0, is also used, while an additional constraint comes from ChPT [?], see fig. **??**. Isospin breaking and radiative corrections are included. The phase shift fit is shown in fig. **??**; the estimation of pion scattering lengths yields:

$$a_0 = 0.2199 \pm 0.0215_{exp} \pm 0.003 t_{th} \qquad a_2 = -0.0430 \pm 0.0083_{exp} \pm 0.0028 t_{th} \tag{7}$$

$$a_0 = 0.2206 \pm 0.0049_{exp} \pm 0.0018_{syst} \pm 0.0064_{th} \quad \text{(ChPT constraint)} \tag{8}$$

3 $K^{\pm} \to \pi^{\pm}\pi^0\gamma$ (Kpi2g) decay

The decay rate as a function of W=$\sqrt{(P_K \cdot P_\gamma)/(M_K M_{\pi^+})}$ can be written as:

$$\frac{d\Gamma}{dW} \simeq (\frac{d\Gamma}{dW})_{IB}[1 + 2(\frac{m_\pi}{m_K})^2 W^2 |E| \cos((\delta_1 - \delta_0) \pm \phi) + (\frac{m_{\pi^+}}{m_K})^4 W^4 (|E|^2 + |M|^2)] \tag{9}$$

where three contributions, respectively representing the inner bremsstrahlung (IB), the direct emission (DE) and the interference (INT) part of the decay, can be distinguished; the estimation of the INT and DE part represents the main goal of this analysis. The selection of the $K^{\pm} \to \pi^{\pm}\pi^0\gamma$ decay requires at least 1 track with E/p <0.85 and 3 clusters in the final state. Several BG channels were analyzed and reduced, the most important being the $K^{\pm} \to \pi^{\pm}\pi^0\pi^0$ decay; the probability of photon mistagging was seen to be at 1% level, while the residual BG is at 0.1% level of the DE part. The estimation of the DE and INT part is performed using the variable W=$\sqrt{(P_K \cdot P_\gamma)/(M_K M_\pi)}$ in the interval 0.2<W<0.9, where events from the IB, DE and INT parts distribute differently. The relative weights minimizing the DATA/MC ratio are determined, the fit function being W_{DATA}=(1-A-B)·W_{IB}+A·W_{DE}+B·W_{INT} with A,B free parameters (see fig. **??**). The final results on 2003/4 data are:

$$A_{DE}(0 < W < 1) = (3.32 \pm 0.15_{stat} \pm 0.14_{syst})\%, \tag{10}$$

$$A_{INT}(0 < W < 1) = (-2.35 \pm 0.35_{stat} \pm 0.39_{syst})\% \tag{11}$$

where the systematics are dominated by trigger efficiency. This represents the first measurement of the INT component of the decay so far. Two tests of CP violation using $K^{\pm} \to \pi^{\pm}\pi^0\gamma$ data were also performed, the first computing the difference in the decay rate between positive and negative events (and using $K^{\pm} \to \pi^{\pm}\pi^0\pi^0$ events to compute the kaon flux) and the second fitting the W spectrum. Both of them yielded results compatible with no CPV.

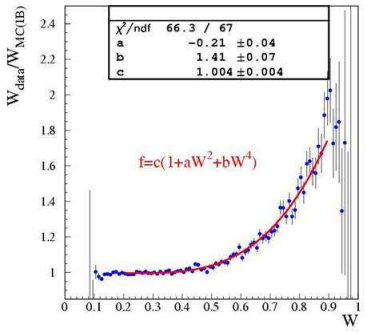

Figure 5: Fit of the W variable allowing the determination of INT and DE parts in Kpi2g decay.

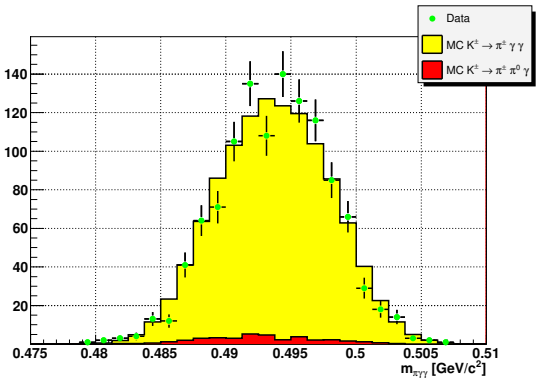

Figure 6: Distribution of reconstructed kaon mass for $K^{\pm} \to \pi^{\pm}\gamma\gamma$ events.

4 $K^{\pm} \to \pi^{\pm}\gamma\gamma$ decay

The differential decay rate of the $K^{\pm} \to \pi^{\pm}\gamma\gamma$ channel can be written as:

$$\frac{d^2\Gamma}{dydz} = \frac{m_{K^+}}{(8\pi)^3}[z^2(|A+B|^2+|C|^2)+(y^2-\frac{1}{4}\lambda(1,r_\pi^2,z))^2(|B|^2+|D|^2) \quad (12)$$

where y=P·(q_1-q_2)/M_K^2, z=(q_1+q_2)/M_K^2=$M_{\gamma\gamma}^2$/M_K^2 and P, q_1, q_2 are respectively the pion and the two photon four-momenta. A, B, C and D only depend on z and on the free parameter ĉ, which is a function of several strong and weak coupling constants. Depending on the ĉ value, the BR theoretical estimation and the shape of the $m_{\gamma\gamma}$ distribution sizably change. Corrections at $\mathcal{O}(p^6)$ order in ChPT can increase BR by 30-40%, depending on the ĉ value [?].

The event selection is performed by requiring at least one track with E/p<0.8 and two LKr clusters. The reconstructed kaon mass, shown in fig. **??**, is required to be within ±0.02 GeV/c^2 from its PDG value. 1164 events are selected, with ∼3% estimated BG, mostly from $K^{\pm} \to \pi^{\pm}\pi^0\gamma$ decays. The ĉ value used for the MC generation is 2.0, which yields a good agreement with data. The preliminary BR result, using $K^{\pm} \to \pi^{\pm}\pi^0$ as normalization, is:

$$BR(K^{\pm} \to \pi^{\pm}\gamma\gamma)/BR(K^{\pm} \to \pi^{\pm}\pi^0) = (1.07 \pm 0.04_{stat} \pm 0.08_{syst}) \cdot 10^{-6} \quad (13)$$

Future tasks include the ĉ measurement using a model-independent BR estimation.

1. V. Fanti *et al.*, *Nucl.Instrum.Meth.* **A574** 433-471 (2007).
2. N. Cabibbo, and A. Maksymowicz, *Phys.Rev.* **B438** 137 (1965).
3. S. Roy, *Phys. Lett.* **353** (1971).
4. B. Ananthanarayan *et al.*, *Phys.Rept.* **353** (2001).
5. Colangelo *et al.*, *Nucl. Phys. B* **603** (2001).
6. S. Pislak et al., *Phys Rev. Lett.* **87** 221801 (2001).
7. L. Rosselet *et al.*, *Phys.Rev.* **D15** 574 (1977).
8. F. Gabbiani, *Phys.Rev.D* **59** (1999) 094022.

RECENT RESULTS ON LIGHT HADRON SPECTROSCOPY AT BES

H.X. YANG (for BES COLLABORATION)
Institute of High Energy Physics,CAS,19B YuquanLu,
Shijingshan District Beijing, PR China

BESII has reported a $p\bar{p}$ near-threshold enhancement in $J/\psi \to \gamma p\bar{p}$ and a new particle as X(1835) in $J/\psi \to \gamma\pi^+\pi^-\eta'$. The κ particle were also found in $J/\psi \to K^+K^-\pi^+\pi^-$(neutral one) and $J/\psi \to K^\pm K_s^0\pi^\mp\pi^0$(charged one). BESIII has collected more than 100M ψ' events and 220M J/ψ events. With these data samples, $p\bar{p}$ near-threshold enhancement and X(1835) are analyzed carefully and the BESII result are confirmed.

1 Introduction of BES at BEPC

The BES detector is a large solid-angle magnetic spectrometer at the Beijing Electron Positron Collider(BEPC). 58M J/ψ events were collected at BESII [1]. BESIII [2] is upgraded from BESII, it begins physics run since March 2009. There are more than 100M ψ' and 220M J/ψ events have been collected. The $p\bar{p}$ mass threshold structure and X(1835) were first observed and measured at BESII, the evidence for the existence of κ was also reported. Here we report the observation of κ at BESII and the confirmation of $p\bar{p}$ mass threshold structure and X(1835) at BESIII.

2 Analysis of charged κ at BESII

σ and κ are first found in the analysis of $\pi\pi$ and πK scattering data, which can not be filled into any nonets of ordinary $q\bar{q}$ mesons. Evidences for the κ have been reported recently by the E791 experiment [3] and the FOCUS experiment [4]. In 2006, BESII reported the existence of κ particle in the analysis of $J/\psi \to \bar{K}^*(892)^0K^+\pi^- \to K^+K^-\pi^+\pi^-$ [5]. Because of the isospin symmetry, there should be charged κ particle. Here, we try to find the charged κ in $J/\psi \to \bar{K}^*(892)^\pm\kappa^\pm \to K^\pm K_s^0\pi^\mp\pi^0$ with 58M J/ψ data collected with BESII [6]. A partial wave analysis, which is based on the covariant helicity amplitude analysis, is performed for the charged κ analysis. The final fit of $K\pi$ spectrum is shown in Fig. 1(a), where points with error bars are data, and the light shaded histogram is the final fit. In the figure, the dark shaded histogram shows the contribution of the charged κ. Fig. 1(b) shows the final fit for the $K^*(892)\pi$ spectrum. Three different parameterizations are used to fit the κ. They are

$$BW_\kappa = \frac{1}{m_\kappa^2 - s - im_\kappa\Gamma_\kappa}, \Gamma_\kappa = cons., \tag{1}$$

$$BW_\kappa = \frac{1}{m_\kappa^2 - s - i\sqrt{s}\Gamma_\kappa(s)}, \Gamma_\kappa(s) = \frac{g_\kappa^2.k_\kappa}{8\pi s}, \tag{2}$$

$$BW_\kappa = \frac{1}{m_\kappa^2 - s - i\sqrt{s}\Gamma_\kappa(s)}, \Gamma_\kappa(s) = \alpha.k_\kappa, \tag{3}$$

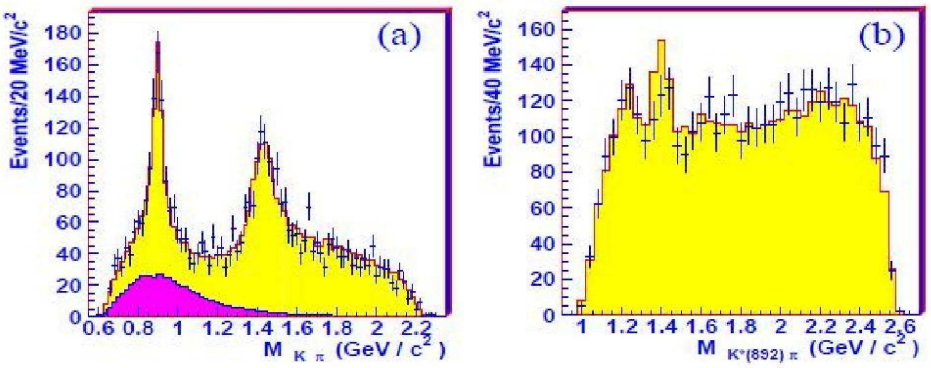

Figure 1: (a) Final fit results for the $K\pi$ spectrum. Points with error bars are data, the light shaded histogram is the final global fit, and the dark shaded histogram is the contribution of the kappa. (b) Final fit of $K^*(892)\pi$ spectrum. Points with error bars are data, the light shaded histogram is the final global fit. The two peaks in the lower mass region are fitted by $K_1(1270)$(lower one) and $K_1(1400)$(higher one) seperately.

Table 1: Masses, widths and pole positions of the charged κ. In the table, the first errors are statistical, and the second are systematic. BW (1) means equation (1) in the fit, BW (2) and BW (3) have similar meanings.

	BW(1)	BW(2)	BW (3)
Mass (MeV/c^2)	$810 \pm 68^{+15}_{-24}$	$884 \pm 40^{+11}_{-22}$	$1165 \pm 58^{+120}_{-41}$
Width (MeV/c^2)	$536 \pm 87^{+106}_{-47}$	$478 \pm 77^{+71}_{-41}$	$1349 \pm 500^{+472}_{-176}$
pole (MeV/c^2)	$(849 \pm 77^{+18}_{-14})$ $-i(256 \pm 40^{+46}_{-22})$	$(849 \pm 51^{+14}_{-28})$ $-i(288 \pm 101^{+64}_{-30})$	$(839 \pm 145^{+24}_{-7})$ $-i(297 \pm 51^{+50}_{-18})$

where k_κ is the magnitude of the momentum of the K in the $K\pi$, or the κ center of mass system, and α is a constant which will be determined by fit. Parameters in the Breit-Wigner function are determined by mass and width scans. The final results are listed in the Table 1, where the first errors are statistical, and the second are systematic. The mass and width parameters obtained by different parameterizations are quite different, but their poles are almost the same. This situation is quite similar to what we found in the study of the neutral κ. The corresponding results for the neutral κ [5] are shown in Table 2. The results for the charged κ are consistent with those of the neutral κ.

3 Conformation of $p\bar{p}$ mass threshold structure at BESIII

An anomalously strong $p\bar{p}$ mass threshold enhancement was observed by the BESII experiment in the radiative decay process $J/\psi \to \gamma p\bar{p}$ [7]. An interesting feature of this enhancement is that corresponding structures are not observed in near-threshold $p\bar{p}$ cross section measurements, in

Table 2: Masses, widths and pole positions of the neutral κ. BW (1) means equation (1) in the fit, BW (2) and BW (3) have similar meaning

	BW(1)	BW(2)	BW (3)
Mass (MeV/c^2)	$745 \pm 26^{+14}_{-91}$	$874 \pm 25^{+12}_{-55}$	$1140 \pm 39^{+47}_{-80}$
Width (MeV/c^2)	$622 \pm 77^{+61}_{-78}$	$518 \pm 65^{+27}_{-87}$	$1370 \pm 156^{+406}_{-148}$
pole (MeV/c^2)	$(799 \pm 37^{+16}_{-90})$ $-i(290 \pm 33^{+25}_{-38})$	$(836 \pm 38^{+18}_{-87})$ $-i(329 \pm 66^{+28}_{-46})$	$(811 \pm 74^{+17}_{-83})$ $-i(285 \pm 20^{+18}_{-42})$

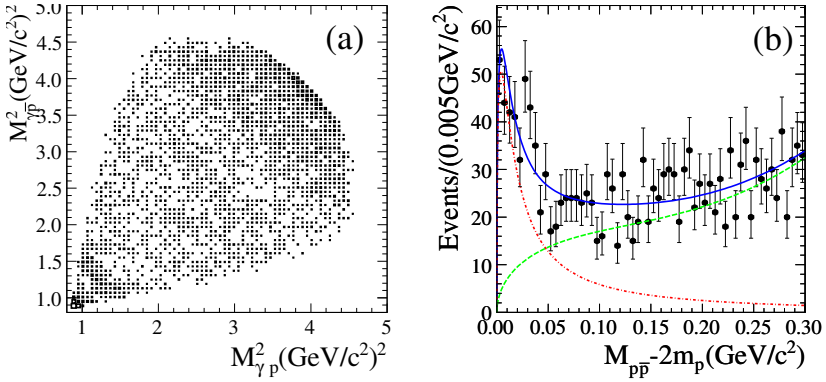

Figure 2: Analysis of ψ' $\pi^+\pi^- J/\psi$,J/ψ $\gamma p\bar{p}$ at BESIII (a)Dalitz plot. (b)Fitting of $p\bar{p}$ near-threshold structure, the solid curve is the fit result; the dashed curve shows the fitted background function.

B-meson decays [8,9], in radiative ψ' or $\Upsilon \to \gamma p\bar{p}$ decays [10,11]. This experimental observation stimulated a number of theoretical speculations. One of these is the intriguing suggestion that it is an example of a $p\bar{p}$ bound state, sometimes called baryonium, which has a long history and has been the subject of many experimental searches.

With 100M ψ' data collected at BESIII, $\psi' \to \pi^+\pi^- J/\psi(J/\psi \to \gamma p\bar{p})$ is used to study the $p\bar{p}$ mass threshold structure. Fig. 2(a) shows the Dalitz plot. There is obvious structure near the threshold of the $p\bar{p}$ mass spectrum. The enhancement is fitted with an acceptance weighted Breit-Wigner function of the form $BW(M) \propto \frac{q^{2L+1}k^3}{(M^2-M_0^2)^2+M_0^2\Gamma^2}$(Fig. 2(b)), where Γ is a constant(determined from fit), q is the proton momentum in the $p\bar{p}$ rest-frame, L is the $p\bar{p}$ orbital angular momentum, and k is the photon momentum. The fitting gives the mass and width as $m = 1861^{+6}_{-13}(stat)^{+7}_{-26}(syst)MeV/c^2$ and $\Gamma < 38MeV/c^2(90\%C.L.)$. The result is consistent with BESII. $\psi' \to \gamma p\bar{p}$ is also studied and no such an enhancement observed, which indicated pure FSI interpretation of the narrow and strong $p\bar{p}$ threshold enhancement in J/ψ radiative decay is disfavored.

4 Confirmation of X(1835) at BESIII

X(1835) was observed in the $\pi^+\pi^-\eta'$ invariant-mass spectrum with a statistical significance of 7.7σ at BESII [12]. A fit with a Breit-Wigner function yields a mass $M = 1833.7 \pm 6.1(stat) \pm 2.7(syst)MeV/c^2$, a width $\Gamma = 67.7 \pm 20.3(stat) \pm 7.7(syst)MeV/c^2$, and a production branching fraction $B(J/\psi \to \gamma X) \times B(X \to \pi^+\pi^-\eta') = [2.2 \pm 0.4(stat) \pm 0.4(syst)] \times 10^{-4}$. The mass and width of X(1835) are not compatible with any known meson resonance.

With 220M J/ψ events collected at BESIII, $J/\psi \to \gamma\pi^+\pi^-\eta'(\eta' \to \gamma\rho, \eta\pi^+\pi^-)$ is studied to verify the BESII observation. Fig. 3(a) shows the invariant mass spectrum of $\pi^+\pi^-\eta'$ for $J/\psi \to \gamma\pi^+\pi^-\eta'(\eta' \to \gamma\rho)$. A significant peak at $M \sim 1835$ MeV/c^2 is observed. If it is fitted with one resonance plus a polynomial background shape, the statistical significance of the resonance is about 18σ. Fig. 3(b) is the invariant mass spectrum of $\pi^+\pi^-\eta'$ for $J/\psi \to \gamma\pi^+\pi^-\eta'(\eta' \to \eta\pi^+\pi^-)$. There is also a significant peak at $M \sim 1835$ MeV/c^2. The fitting shows the statistical significance is about 9σ. Extensive studies of potential background processes using both data and MC is made, none can produce a peak around 1835 MeV/c^2 in the $\pi^+\pi^-\eta'$ mass spectrum. Fig.3(c) shows the $\pi^+\pi^-\eta'$ invariant-mass spectrum for the combined $J/\psi \to \gamma\pi^+\pi^-\eta'(\eta' \to \gamma\rho)$ and $J/\psi \to \gamma\pi^+\pi^-\eta'(\eta' \to \pi^+\pi^-\eta)$. This spectrum is fitted with a Breit-Wigner function convolved with a Gaussian mass resolution function. The mass and width obtained from the fit are $M = 1842.4 \pm 2.8(stat)$ MeV/c^2 and $\Gamma = 99.2 \pm 9.2$ (stat) MeV/c^2 with a statistical significance of 21σ. These values are consistent with the published BESII results [12]. More

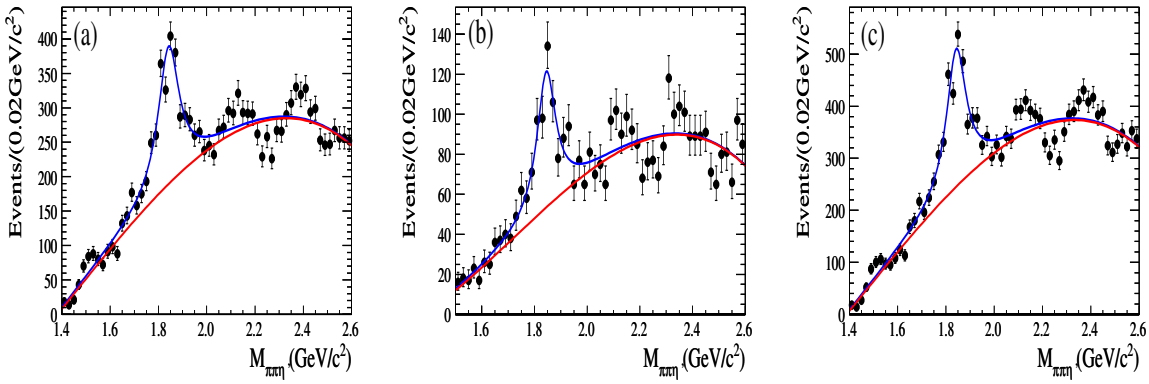

Figure 3: Fitting the invariant mass spectrum of $\pi^+\pi^-\eta'$ in $J/\psi \to \gamma\pi^+\pi^-\eta'$ at BESIII. (a)$\eta' \to \gamma\rho$; (b)$\eta' \to \pi^+\pi^-\eta$;(c)The combined invariant mass spectrum of $\eta' \to \gamma\rho$ and $\eta' \to \pi^+\pi^-\eta$. The mass spectrum is fitted with a resonance plus polynomial background shape.

studies will be performed on the high $\pi^+\pi^-\eta'$ mass region of $2.1 \sim 2.5$ GeV/c^2.

5 Summary

Charged κ is observed at BESII with $J/\psi \to K^\pm K_s^0 \pi^\mp \pi^0$. Partial Wave Analysis has been performed on the charge κ, and the mass and width are measured. An anomalous strong, near-threshold enhancement in the $p\bar{p}$ invariant mass distribution is observed in the decay process of $\psi' \to \pi^+\pi^- J/\psi(J/\psi \to \gamma p\bar{p})$. If it is fitted with an S-wave Breit-Wigner resonance function, the peak mass is $M = 1865 \pm 5$ (stat) MeV/c^2 and the width is $\Gamma < 33$ MeV/c^2 at the 90% confidence level. The resonance, $X(1835)$ is confirmed in two decay modes of η' for $J/\psi \to \pi^+\pi^-\eta'$. The BESIII results are consistent with those published by BESII.

References

1. J.Z. Bai *et al*, *Nucl. Instrum. Methods* A **458**, 627 (2001)
2. M. Ablikim *et al*, arXiv:0911.4960
3. E.M. Aitala *et al*, *Phys. Rev. Lett.* **89**, 121801 (2002)
4. J.M. Link *et al*, *Phys. Lett.* B **535**, 430 (2002)
5. M. Ablikim *et al*, *Phys. Lett.* B **633**, 681 (2006)
6. M. Ablikim *et al*, arXiv:1002.0893.
7. J.Z. Bai *et al*, *Phys. Rev. Lett.* **91**, 022001 (2003)
8. M.Z. Wang *et al*, *Phys. Rev. Lett.* **92**, 138101 (2004)
9. S. Jin, Int.J.Mod.Phys.A **20**, 5145 (2005)
10. M. Ablikim *et al*, *Phys. Rev. Lett.* **99**, 011802 (2007)
11. S.B. Athar *et al*, *Phys. Rev.* D **73**, 032001 (2006)
12. M. Ablikim *et al*, *Phys. Rev. Lett.* **95**, 262001 (2005)

Study light scalar meson property from heavy meson decays

Cai-Dian Lü[a] and Wei Wang[b]
[a] *Institute of High Energy Physics, Chinese Academy of Sciences, Beijing 100049, PR China*
[b] *Istituto Nazionale di Fisica Nucleare, Sezione di Bari, Bari 70126, Italy*

In the SU(3) symmetry limit, the ratio $R \equiv \frac{\mathcal{B}(D^+ \to f_0 l^+ \nu) + \mathcal{B}(D^+ \to \sigma l^+ \nu)}{\mathcal{B}(D^+ \to a_0^0 l^+ \nu)}$ is equal to 1 if the scalar mesons are $\bar{q}q$ states, while it is 3 if these mesons are tentraquark states. This ratio provides a model-independent way to distinguish the descriptions for light scalar mesons . It also applies to the $B^- \to S l^- \bar{\nu}$ and $\bar{B}^0 \to J/\psi(\eta_c) S$ decays. The SU(3) symmetry breaking effect is found to be under control, which will not spoil our method. The branching fractions of the $D^+ \to S l^+ \nu$, $B^- \to S l^- \bar{\nu}$ and $\bar{B}^0 \to J/\psi(\eta_c) S$ decays roughly have the order 10^{-4}, 10^{-5} and 10^{-6}, respectively. The B factory experiments and ongoing BEPC-II experiments are able to measure these channels and accordingly to provide the detailed information of the scalar meson inner structure.

In spite of the striking success of QCD theory for strong interaction, the underlying structure of the light scalar mesons is still under controversy.[1,2,3] To understand the internal structure of scalar mesons is one of the most interesting topics in hadron physics for several decades. Irrespective of the dispute on the existence of σ and κ mesons, scalar mesons have been identified as ordinary $\bar{q}q$ states, four-quark states or meson-meson bound states or even those supplemented with a scalar glueball. Due to the unknown nonperturbative properties of QCD, there is almost no model-independent way to effectively solve these old puzzles.

Most of the studies up to now, concentrated on the decay property of scalar mesons. It is interesting to study the production property of the scalar mesons, especially the production from heavy meson decays. At present, there are many experimental studies on the production of scalar mesons in nonleptonic D decays. For example, branching ratios of $D^+ \to \sigma\pi^+$ and $D^+ \to f_0\pi^+$ have the order of 10^{-3} and 10^{-4}, respectively.[4] On the theoretical side compared with nonleptonic D decays, semileptonic $D^+(B^+) \to S l^+ \nu$ decays only contain one scalar meson in the final state, where the heavy quark effective theory can be used. This could be the better candidate to probe different structure scenarios of scalar mesons.

In this work, we will only focus on the two-quark and the four-quark scenarios for scalar mesons. We propose a model-independent way to distinguish these two descriptions through the semileptonic $B^- \to S l \bar{\nu}$ and/or $D^+ \to S l^+ \nu$ decays, where S denotes a scalar meson among $a_0(980)$, $f_0(980)$ and σ.[5] These two kinds of decays are clean as they do not receive much pollution from the strong interactions. In B decays, the lepton pair can also be replaced by a charmonium state since they share the same properties in the flavor SU(3) space. For example, the $\bar{B}^0 \to J/\psi(\eta_c) S$ decays are probably much easier for the experiments to observe.

A number of scalar mesons have been discovered experimentally. Among them, there are 9 mesons below or near 1 GeV, which form a nonet consisting of $\sigma, \kappa, f_0(980)$ and $a_0(980)$. Hereafter we will use f_0 and a_0 to abbreviate $f_0(980)$ and $a_0(980)$ for simplicity. In the $\bar{q}q$

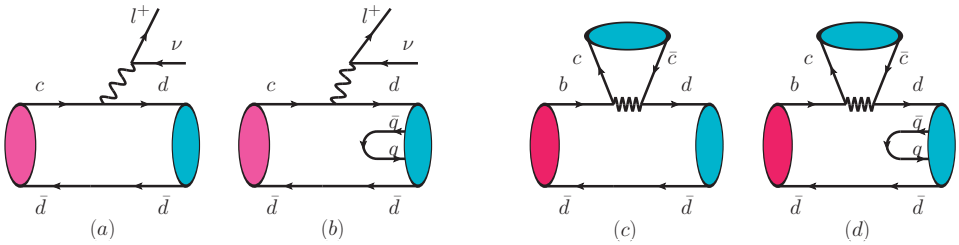

Figure 1: Feynman diagrams for D^+ decays into a scalar meson and $B \to J/\psi(\eta_c)S$ decays. The diagrams (a,c) are for two-quark picture, while the diagrams (b,d) are for the four-quark mesons.

picture, scalar mesons are viewed as P-wave states,[6] whose flavor wave functions are given by

$$|\sigma\rangle = \tfrac{1}{\sqrt{2}}(|\bar{u}u\rangle + |\bar{d}d\rangle) \equiv |\bar{n}n\rangle, \quad |f_0\rangle = |\bar{s}s\rangle, \quad |a_0^0\rangle = \tfrac{1}{\sqrt{2}}(|\bar{u}u\rangle - |\bar{d}d\rangle), \quad |a_0^-\rangle = |\bar{u}d\rangle, \quad |a_0^+\rangle = |\bar{d}u\rangle.$$
$$|\kappa^-\rangle = |\bar{u}s\rangle, \quad |\bar{\kappa}^0\rangle = |\bar{d}s\rangle, \quad |\kappa^0\rangle = |\bar{s}d\rangle, \quad |\kappa^+\rangle = |\bar{s}u\rangle. \tag{1}$$

In this picture, f_0 is mainly made up of $\bar{s}s$, which is supported by the large production rates in $J/\psi \to \phi f_0$ and $\phi \to f_0\gamma$ decays.[4] Meanwhile, the experimental data also indicate the nonstrange component of f_0: the branching fraction of $J/\psi \to \omega f_0$ is comparable with that of $J/\psi \to \phi f_0$. To accommodate with the experimental data, f_0 is supposed to be the mixture of $\bar{n}n$ and $\bar{s}s$ as

$$|f_0\rangle = |\bar{s}s\rangle\cos\theta + |\bar{n}n\rangle\sin\theta, \quad |\sigma\rangle = -|\bar{s}s\rangle\sin\theta + |\bar{n}n\rangle\cos\theta.$$

With various available experimental data, the mixing angle θ is constrained as $25^\circ < \theta < 40^\circ, 140^\circ < \theta < 165^\circ$.[7]

The classical $\bar{q}q$ picture meets with several difficulties. In particular it is difficult to explain the fact that the strange meson κ is lighter than the isotriplet mesons a_0, and the isosinglet meson f_0 has a degenerate mass with a_0, since s quark is expected to be heavier than u/d quark. Inspired by these difficulties, other candidate scenarios are proposed. In Ref. [8], scalar mesons are identified as diquark-diquark states. In the SU(3) flavor space, the two quarks can form two multiplets as $3 \otimes 3 = \bar{3} \oplus 6$, while the other two antiquarks reside in 3 or $\bar{6}$ multiplets. The diquark in a scalar meson is taken to be totally antisymmetric for all quantum numbers, color antitriplet, flavor antitriplet, spin 0. The lightest $q^2(\bar{q})^2$ states make a flavor nonet, whose internal structure is given as:

$$|\sigma\rangle = \bar{u}u\bar{d}d, \quad |f_0\rangle = |\bar{n}n\bar{s}s\rangle, \quad |a_0^0\rangle = \tfrac{1}{\sqrt{2}}(\bar{u}u - \bar{d}d)\bar{s}s, \quad |a_0^+\rangle = |\bar{d}u\bar{s}s\rangle, \quad |a_0^-\rangle = |\bar{u}d\bar{s}s\rangle.$$
$$|\kappa^+\rangle = |\bar{s}u\bar{d}d\rangle, \quad |\kappa^0\rangle = |\bar{s}d\bar{u}u\rangle, \quad |\bar{\kappa}^0\rangle = |\bar{d}s\bar{u}u\rangle, \quad |\kappa^-\rangle = |\bar{u}s\bar{d}d\rangle. \tag{2}$$

Taking the mixing into account, the isosinglet mesons are expressed as

$$|f_0\rangle = |\bar{n}n\bar{s}s\rangle\cos\phi + |\bar{u}u\bar{d}d\rangle\sin\phi, \quad |\sigma\rangle = -|\bar{n}n\bar{s}s\rangle\sin\phi + |\bar{u}u\bar{d}d\rangle\cos\phi,$$

where the ϕ between f_0 and σ meson is constrained as$\phi = (174.6^{+3.4}_{-3.2})^\circ$.[9]

The Feynman diagrams for $D^+ \to Sl^+\nu$ decays and $B \to J/\psi(\eta_c)S$ decays in two different pictures are given in Fig. 1. The diagrams (a,c) are for the two-quark scenario, while the diagrams are for the four-quark scenario. If a scalar meson is made of $\bar{q}q$, the light quark is generated from the electroweak vertex and the antiquark $\bar{d}$ serves as a spectator. Thus only the component $\bar{d}d$ contributes to semileptonic D decays. In the SU(3) symmetry limit, decay amplitudes of $D \to f_0(\sigma)l\nu$ channels under the $q\bar{q}$ picture have the following relation

$$\mathcal{A}(D^+ \to f_0 l^+\nu) = -\sin\theta\hat{\mathcal{A}}, \quad \mathcal{A}(D^+ \to \sigma l^+\nu) = -\cos\theta\hat{\mathcal{A}}, \tag{3}$$

where the transition amplitude $\hat{\mathcal{A}}$ is defined as $\hat{\mathcal{A}} \equiv \mathcal{A}(D^+ \to a_0^0 l^+ \nu)$. This leads to

$$\mathcal{B}(D^+ \to a_0^0 l^+ \nu) = \mathcal{B}(D^+ \to f_0 l^+ \nu) + \mathcal{B}(D^+ \to \sigma l^+ \nu). \tag{4}$$

One may worry about the accuracy of our results because of the possible large QCD scattering effect. However if we use the hadron picture, we can still get the same result. The $d\bar{d}$ pair produced from the weak interaction in Fig.1(a) can form isospin 0 and isospin 1 states with the ratio of 1:1. Although the scattering can mix between states, the non-perturbative QCD interactions conserve the isospin. Therefore the sum of production rates of isospin 0 states on the right hand side of eq.(4) is always equal to production rates of the isospin 1 states on the left hand side of eq.(4). The isospin breaking effect in strong interaction is negligible.

If a scalar meson is composed of four quarks, besides the light quark from the electroweak vertex and the spectator, another $\bar{q}q$ pair is generated from the QCD vacuum. The decay amplitudes are given as

$$\mathcal{A}(D^+ \to f_0 l^+ \nu) = -(\cos\phi + \sqrt{2}\sin\phi)\hat{\mathcal{A}}, \quad \mathcal{A}(D^+ \to \sigma l^+ \nu) = (\sin\phi - \sqrt{2}\cos\phi)\hat{\mathcal{A}}, \tag{5}$$

which gives

$$\mathcal{B}(D^+ \to a_0^0 l^+ \nu) = \frac{1}{3}[\mathcal{B}(D^+ \to f_0 l^+ \nu) + \mathcal{B}(D^+ \to \sigma l^+ \nu)].$$

It is meaningful to define the ratio of partial decay widths

$$R \equiv \frac{\mathcal{B}(D^+ \to f_0 l^+ \nu) + \mathcal{B}(D^+ \to \sigma l^+ \nu)}{\mathcal{B}(D^+ \to a_0^0 l^+ \nu)}. \tag{6}$$

Clearly, the ratio is 1 for the two-quark description, while it is 3 for the four-quark description of scalar mesons. Similarly for semileptonic $B \to S l \bar{\nu}$ decays, the charm quark in Fig.1 is replaced by a bottom quark and the $\bar{d}$ quark is replaced by a $\bar{u}$ quark, while leptons are replaced by their charge conjugates. We have the same sum rules

$$R \;=\; \frac{\mathcal{B}(B^- \to f_0 l^- \bar{\nu}) + \mathcal{B}(B^- \to \sigma l^- \bar{\nu})}{\mathcal{B}(B^- \to a_0^0 l^- \bar{\nu})} \;=\; \begin{cases} 1 & \text{two quark} \\ 3 & \text{tetra-quark} \end{cases}. \tag{7}$$

The semileptonic D/B decays are clean, which do not receive much pollution from the strong interaction. But since the neutrino is identified as missing energy, the efficiency to detect these channels may be limited. The lepton pair can also be replaced by some other SU(3) singlet systems such as a J/ψ or η_c meson. Replacing the lepton pair by the J/ψ and replacing B^- by a $\bar{B}^0$ state (a different spectator antiquark will not change the relation) in Eq. (7), one can easily obtain the similar sum rules for the branching fractions

$$R \;=\; \frac{\mathcal{B}(\bar{B}^0 \to f_0 J/\psi(\eta_c)) + \mathcal{B}(\bar{B}^0 \to \sigma J/\psi(\eta_c))}{\mathcal{B}(\bar{B}^0 \to a_0^0 J/\psi(\eta_c))} \;=\; \begin{cases} 1 & \text{two quark} \\ 3 & \text{tetra-quark} \end{cases}. \tag{8}$$

Since we used SU(3) symmetry to obtain these relations, it is necessary to estimate the size of SU(3) symmetry breaking effects. For example, the isospin singlet scalar mesons have different masses, which can change the phase space in the semileptonic D/B decays. Fortunately, this SU(3) breaking effect can be well studied, which almost does not depend on the internal structure of scalar mesons or the strong interactions. The mass of f_0 is well measured but the mass of σ meson has large uncertainties $m_\sigma = (0.4 - 1.2)$ GeV. This big range of masses indeed induces large differences to D decays, since the D meson mass is only 1.87GeV. The branching ratio of the semileptonic decay is affected by a factor of $(0.31 - 5.4)$ depending on the mass of the σ meson. Therefore the sum rule in eq.(6) is not good unless the σ meson mass is well

measured. But in B meson decays, the sum rule in eq.(6) will not be affected sizably, since the σ meson mass is negligible compared with the large B meson mass. Numerically, this correction factor in B decays is $(0.9 - 1.1)$.

Another SU(3) breaking effect comes from the decay form factors of various scalar mesons. In the two-quark scenario, only the $\bar{d}d$ component contributes to the form factors shown in the diagram (a) of Fig.1. The SU(3) symmetry breaking effect to the form factors is thus negligible. In the four-quark scenario, there are $\bar{u}u\bar{d}d$ component in f_0 and σ meson state, which is different from the internal structure of a_0 (with a pair of $\bar{s}s$). From the diagram (b) of Fig.1, one can see that it would be easier to produce the $\bar{u}u$ quark pair from the vacuum than the $\bar{s}s$ quark pair since the $\bar{u}u$ quark pair is lighter. The SU(3) symmetry breaking effects may make the form factor of $D/B \to \sigma$ and $D/B \to f_0$ larger than that of $D/B \to a_0$. It will make the ratio R larger than 3 in the four-quark scenario. Thus this SU(3) symmetry breaking effects in the form factors will not spoil our method but it will instead improve its applicability.

In heavy meson D/B decays, there is an advantage to apply heavy quark effective theory. Unlike non-leptonic decays, the SU(3) breaking effects in semi-leptonic heavy meson decays is quite small, which is guaranteed by the heavy quark symmetry. The size of the SU(3) breaking effect could be roughly estimated by the mass difference between u/d and s quarks, whose magnitude is

$$\frac{m_s - m_{u/d}}{\sqrt{m_{D/B}\Lambda}} \sim \begin{cases} 0.3 \text{ for D} \\ 0.1 \text{ for B} \end{cases}, \tag{9}$$

where $\sqrt{m_{D/H}\Lambda}$ denotes the typical scale in the form factors, and Λ is hadronic scale. Clearly, the B decays suffer less pollution from the SU(3) symmetry breaking effect. Even if in the D meson case, the SU(3) breaking effect of 30% can not pollute the clear difference between 1 and 3 of ratio R in eq.(7).

If the mixing angle is close to $\theta = 0^\circ$ or $\theta = 90^\circ$ in the two-quark picture ($\phi = 54.7^\circ$ or $\phi = 144.7^\circ$ in four-quark scenario), either σ or f_0 meson has small production rates but the other one should have large production rates. Neglecting the highly suppressed channel, the ratio defined in eq.(6,7) can still distinguish the two different scenarios for scalar mesons. If the mixing angle is modest, i.e. it is not close to the values discussed in the above paragraph, all three $D^+ \to Sl^+\nu$ channels would have similar branching ratios in magnitude. The branching ratio of the semileptonic $D_s \to f_0$ decay is measured as[10] $\mathcal{B}(D_s \to f_0 l\bar{\nu}) \times \mathcal{B}(f_0 \to \pi^+\pi^-) = (2.0 \pm 0.3 \pm 0.1) \times 10^{-3}$.Thus as an estimation, branching ratios for the cascade $D^+ \to Sl^+\nu$ decays are expected to have the order $\frac{V_{cd}^2}{V_{cs}^2} \times 2 \times 10^{-3} \sim 1 \times 10^{-4}$. The luminosity of BES-III experiment at BEPC II in Beijing is designed as $3 \times 10^{32}\text{cm}^{-2}\text{s}^{-1}$. This experiment, starting running since summer 2008, will accumulate 30 million $D\bar{D}$ pair per running year.[11] Even we assume the detect efficiency is only 20%, there will be 600 events per running year. It is very likely to observe these decay channels.

As for the B decays, the branching ratio of $B \to Sl\bar{\nu}$ can be estimated utilizing the $B \to \rho l\bar{\nu}$ and $D_s^+ \to \phi l^+\nu$ decays. If the mixing angle is moderate, the branching ratio can be estimated using heavy quark symmetry as

$$\mathcal{B}(B \to f_0 l\bar{\nu}) \sim \mathcal{B}(B \to \rho l\bar{\nu}) \frac{\mathcal{B}(D_s \to f_0 l\bar{\nu})}{\mathcal{B}(D_s \to \phi l\bar{\nu})} \sim 10^{-4} \times \frac{10^{-3}}{10^{-2}} = 10^{-5}. \tag{10}$$

Such a large branching fraction offers a great opportunity for distinguishing the descriptions. Even if the present B factory does not observe these channels, it is easy for the forthcoming Super B factory to measure these channels. Although $\bar{B} \to J/\psi S$ are hadronic decays, the hadronic uncertainties are mostly canceled in the sum rule of ratios. The branching fraction is

expected to have the order

$$\mathcal{B}(B \to f_0 J/\psi) \sim \mathcal{B}(\bar{B}^0 \to \rho^0 J/\psi)\frac{\mathcal{B}(D_s \to f_0 l\bar{\nu})}{\mathcal{B}(D_s \to \phi l\bar{\nu})} \sim 10^{-5} \times \frac{10^{-3}}{10^{-2}} = 10^{-6}. \qquad (11)$$

On experimental side, the J/ψ is easily detected through a lepton pair l^+l^- and thus this mode may be more useful.

In conclusion, we have investigated the possibility to distinguish the two-quark and four-quark picture for light scalar mesons. The semileptonic $D/B \to Sl\bar{\nu}$ decays and the nonleptonic $B \to J/\psi(\eta_c)S$ decays are discussed in detail. These decay channels have a large potential to be measured on the ongoing BES-III and the forthcoming Super B experiments. With the same quantum number as the vacuum, the lightest scalar mesons are very complicated in nature. It is likely that these scalar mesons are neither pure 2-quark nor 4-quark states. However, our method is at least helpful to rule out one of the possibility. If the ratio R were 1, the pure 4-quark picture is likely to be ruled out but if the ratio R were 3 the pure 2-quark picture is likely to be excluded. Our proposed method provides a unique role to uncover the internal structures of scalar mesons and help to solve the old puzzles.

Acknowledgments

This work is partially supported by National Natural Science Foundation of China under the Grant No. 10735080, and 10625525. W. Wang would like to acknowledge Pietro Colangelo for warm hospitality and useful discussions.

References

1. S. Spanier, N. A. Tornqvist and C. Amsler, "Note on Scalar Mesons," Review published on Particle Data Group.
2. S. Godfrey and J. Napolitano, Rev. Mod. Phys. **71**, 1411 (1999).
3. F. E. Close and N. A. Tornqvist, J. Phys. G **28**, R249 (2002).
4. C. Amsler *et al.* [Particle Data Group], Phys. Lett. B **667**, 1 (2008).
5. W. Wang, C.D. Lu, e-Print: arXiv:0910.0613 [hep-ph]
6. N. A. Tornqvist, Z. Phys. C **68**, 647 (1995).
7. H. Y. Cheng, C. K. Chua and K. C. Yang, Phys. Rev. D **73**, 014017 (2006); and references therein.
8. R. L. Jaffe, Phys. Rev. D **15**, 267 (1977); Phys. Rev. D **15**, 281 (1977).
9. L. Maiani, F. Piccinini, A. D. Polosa and V. Riquer, Phys. Rev. Lett. **93**, 212002 (2004).
10. K. M. Ecklund *et al.* [CLEO Collaboration], Phys. Rev. D **80**, 052009 (2009) [arXiv:0907.3201 [hep-ex]].
11. D. M. Asner *et al.*, arXiv:0809.1869 [hep-ex].

8. Structure function, Spin, Diffraction, Forward physics

NOVEL MEASUREMENTS OF PROTON STRUCTURE AT HERA

K.R. OLIVER (on behalf of the H1 and ZEUS collaborations)
Department of Physics, Denys Wilkinson Building, Keble Road, Oxford OX1 3RH, England

ZEUS and H1 are multi-purpose detectors located on the HERA *ep* collider at DESY, Hamburg. Recent measurements of proton structure from both collaborations are presented, including the combination of early HERA data and associated PDF fit, measurement of high Q^2 cross-sections and direct measurement of the structure function F_L.

1 HERA Combined Inclusive Cross Sections & QCD Fit

1.1 HERA Combined Cross Sections

Inclusive neutral current (NC) and charged current (CC) deep inelastic scattering (DIS) reduced cross sections were measured for unpolarised $e^{\pm}p$ scattering by both collaborations during 1994-2000 [1]. The kinematic range of the NC data in negative four-momentum-transfer squared, Q^2 , and in Bjorken x was $6 \cdot 10^{-7} \leq x \leq 0.65$ and $0.045 \leq Q^2 \leq 30000$ GeV^2 for values of inelasticity, y, between 0.005 and 0.95. The kinematic range of the CC data was $1.3 \cdot 10^{-2} \leq x \leq 0.40$ and $300 \leq Q^2 \leq 30000$ GeV^2 for y between 0.037 and 0.76. Each experiment took about 115pb^{-1} of integrated luminosity.

In order to combine the measurements from each collaboration, the measured reduced cross-sections were moved to a common Q^2-x grid. Those points which were measured at p-beam energy of 820 GeV were moved to 920 GeV. Average values and uncertainties were then calculated. The combination method used was a χ^2 minimisation procedure which took into account the correlations of systematic uncertainties, resulting in an improved accuracy above that expected by doubling the statistics of the measurement. As two different detectors and different reconstruction methods were used, cross-calibration was possible. Similar systematic sources influenced the measured cross section differently as a function of x and Q^2. Therefore, requiring the cross sections to agree at all x and Q^2 constrained the systematics efficiently. In total 1402 data points were combined to 741 cross-section measurements. The combination gave $\chi^2/\text{NDF} = 637/656$, showing that the data are consistent. Figure 1 shows the improvement in the uncertainties on the combined points relative to the uncertainties on the separate ZEUS and H1 measurements.

1.2 HERA QCD Fit

The combined data were the sole input in a NLO QCD analysis which determined a new set of parton distributions: HERAPDF1.0 [1]. The low Q^2 NC e^+p data determined the low-x sea quark and gluon distributions. The high-Q^2 CC data, together with the difference between NC e^+p and e^-p cross sections at high Q^2, constrained the valence quark distributions. The use of the

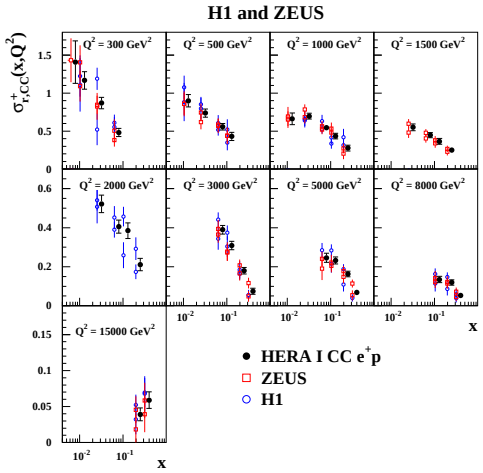

Figure 1: HERA combined CC e^+p reduced cross section (filled circles) as a function of x for 9 Q^2-bins compared to the separate H1 (open circles) and ZEUS (open squares) data input to the averaging procedure.

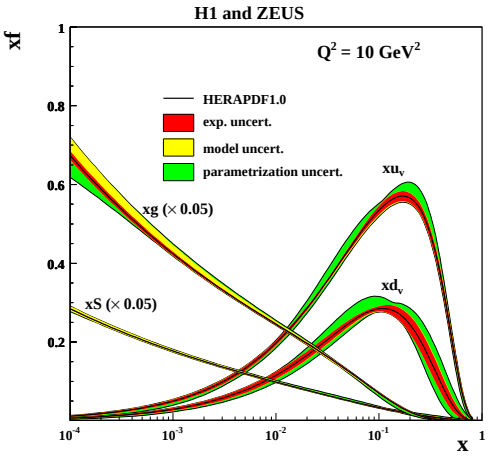

Figure 2: The HERAPDF1.0 PDFs (with experimental, model and parameterisation uncertainties) at $Q^2 = 10$ GeV^2: xu_v, xd_v, xg and $xS = 2x(\overline{u}+\overline{c}+\overline{d}+\overline{s}+\overline{b})$. xg and xS are scaled down by a factor 20.

CC data allowed the down quark distribution in the proton to be determined without assuming isospin symmetry. In addition, the use of HERA data alone for the determination of parton distribution functions (PDFs) eliminated the need for heavy target corrections, which must be applied to DIS data from nuclear targets. The PDFs have small experimental uncertainties; an estimate of the model and parameterisation uncertainties of the fit result was also evaluated. A summary plot of the PDFs is shown in Figure 2. From Figure 3 it is clear that the HERA-I data used in deriving the fits had good sensitivity at low Q^2 but limited statistical precision at high Q^2. Since HERA-II data is not yet included, further improvement is possible.

2 High-Q^2 Cross Sections

H1 recently made preliminary high-Q^2 CC [2] and NC [3] analyses using the complete HERA-II data set (collisions of unpolarised protons with polarised electron and positron beams in left and right helicity states).

The CC analysis includes measurement of the following polarised cross-sections: total cross-section; single differential cross-section in Q^2; and the reduced cross-section. All were measured at two values of polarisation for each of the e^+p and e^-p data sets. The polarisation dependence of the charged current cross section has thus been established, extending previous tests of the chiral structure of the charged current interaction to high Q^2. The measurements are consistent with the absence of right handed charged currents.

The NC analysis includes measurement of the inclusive single differential cross section $d\sigma/dQ^2$ and the reduced double differential cross section for the process $e^\pm p \to e^\pm X$ for interactions with longitudinally polarised lepton beams. The data are consistent with the expected Q^2 dependence of polarised cross sections. A measurement of the polarisation asymmetry as a function of Q^2 was also made and agreed with the expectation. The cross sections were combined with previously published data from H1 to obtain the most precise unpolarised measurements. These were used to extract the structure function $xF_3^{\gamma Z}$.

Figure 4 shows the measurement of CC and NC single differential cross-sections in Q^2 for

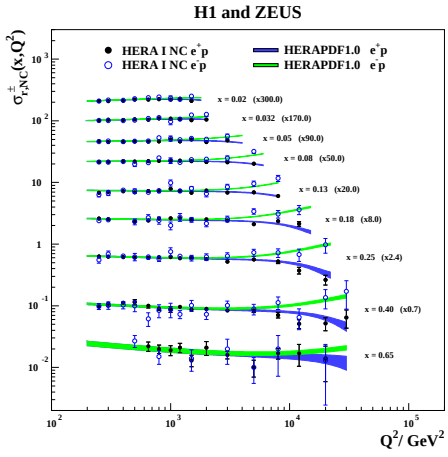

Figure 3: HERA combined NC e^+p reduced cross sections at high Q^2. The HERAPDF1.0 fit is superimposed. The bands represent the total uncertainty of the fit.

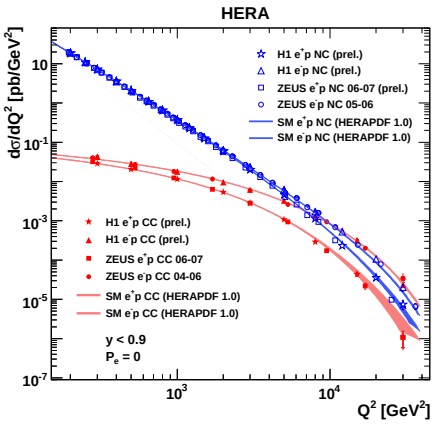

Figure 4: The unpolarised NC and CC cross sections $d\sigma/dQ^2$, shown for e^+p (open points) and e^-p (solid points) data from H1 and ZEUS. The inner (outer) error bars represent the statistical (total) errors.

e^+p and e^-p data made by the ZEUS and H1 collaborations, including recently published data from ZEUS [4,5].

3 HERA Combined Measurement of F_L

At low Q^2 , the NC DIS reduced cross-section includes contributions from the structure functions F_2 and F_L such that $\sigma_r\left(x,Q^2\right) = F_2\left(x,Q^2\right) - y^2/\left(1+(1-y)^2\right)F_L$. F_L is only visible at high y. Direct measurement of F_L requires measurement of the reduced cross-sections at the same x and Q^2 but different y, therefore cross-sections must be measured at different beam energies. H1[6] and ZEUS [7] measured the NC reduced cross-sections at low-x and low-Q^2 at proton beam energies of 920 GeV (21.6 pb^{-1}), 575 GeV (6.2pb^{-1}) and 460 GeV (12.4 pb^{-1}). The two collaborations have recently combined their separate measurements [8,9] to give the best-yet measurement of F_L from HERA. The combination procedure was based on that described in Section 1.1.

Figure 5 shows measurement of the cross-sections at the fixed x and Q^2 at different beam energies. In Figure 6 these points are plotted as a function of $y^2/\left(1+(1-y)^2\right)$. When plotted this way for given x and Q^2, F_2 is the intercept at the y-axis and F_L is the negative slope. The extraction of F_L in the region $2.5 < Q^2 < 800$ GeV^2 is shown in Figure 7. The measurement is a new and important input to QCD fits because at NLO, $F_L \propto \alpha_S xg\left(x,Q^2\right)$ and so the F_L measurement provides information about the gluon density of the proton.

Acknowledgments

I am grateful to Hertford College, Oxford, and the Particle Physics sub-department at the University of Oxford for providing the financial support which enabled me to participate in the QCD and High Energy Interactions Session of the 2010 Recontres de Moriond.

References

1. F. D. Aaron *et al.* H1 Collaboration and ZEUS Collaboration, JHEP **1001** (2010) 109 [arXiv:0911.0884].

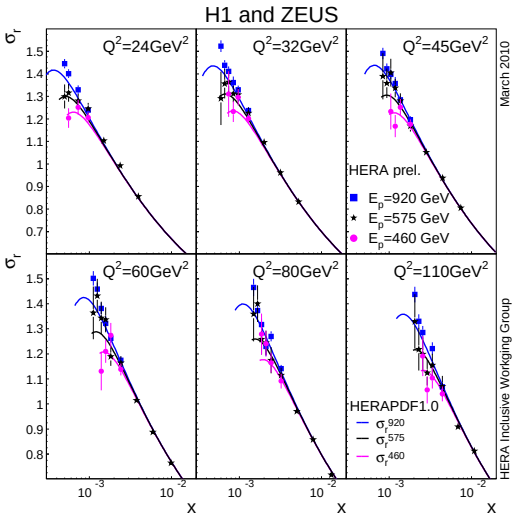

Figure 5: H1 and ZEUS average reduced cross section taken at proton beam energies, E_p, of 920 GeV (squares), 575 GeV (stars) and 460 GeV (circles). The error bars show total experimental uncertainties. Theoretical predictions from HERAPDF1.0 PDFs are shown as solid lines for 920 GeV (blue), 575 GeV (black) and 460 GeV (magenta).

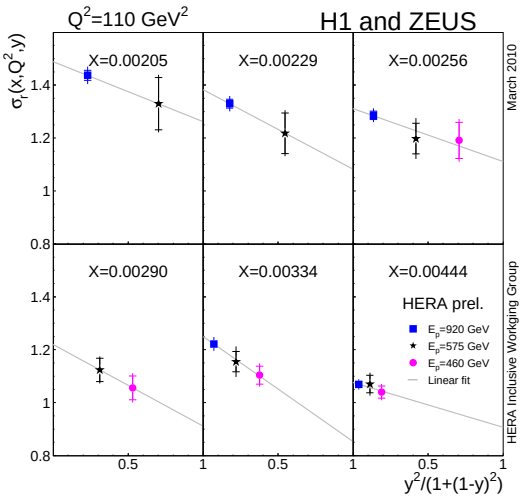

Figure 6: The reduced cross section measured at $Q^2 = 110$ GeV^2 and different x values as a function of $y^2/\left(1+(1-y)^2\right)$. Measurements are taken at proton beam energies, E_p, of 920 GeV (squares), 575 GeV (stars) and 460 GeV (circles). The inner (full) error bars show the statistical (total) uncertainties. The lines show the linear fits used to determine F_L.

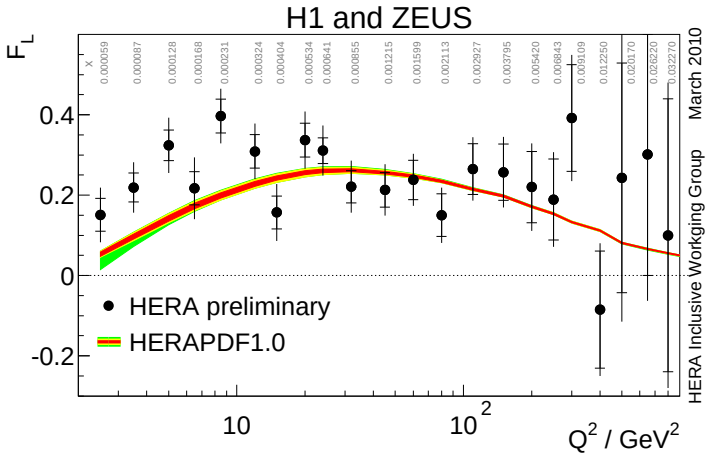

Figure 7: The structure function F_L averaged in x at given values of Q^2 using combined H1 and ZEUS cross-section data. The resulting x values of the averaged F_L measurements are given in the figure for each point in Q^2 . The inner (full) error bars are the statistical (total) uncertainties. The band represents the prediction from HERAPDF1.0 with parameterization (green) model (yellow) and experimental (red) uncertainties.

2. F.D. Aaron *et al.* H1 Collaboration (2009), [H1prelim-09-043].
3. F.D. Aaron *et al.* H1 Collaboration (2009), [H1prelim-09-042].
4. S. Chekanov *et al.* ZEUS Collaboration, Eur. Phys. J. C **61** (2009) 223 [arXiv:0812.4620].
5. S. Chekanov *et al.* ZEUS Collaboration, Eur. Phys. J. C **62** (2009) 625 [arXiv:0901.2385].
6. F. D. Aaron *et al.* H1 Collaboration, Phys. Lett. B **665** (2008) 139 [arXiv:0805.2809].
7. S. Chekanov *et al.* ZEUS Collaboration, Phys. Lett. B **682** (2009) 8 [arXiv:0904.1092].
8. F.D. Aaron *et al.* H1 Collaboration (2010), [H1prelim-10-043].
9. S. Chekanov *et al.* ZEUS Collaboration, (2010), [ZEUS-prel-10-001].

COMBINED PDF AND STRONG COUPLING UNCERTAINTIES AT THE LHC WITH NNPDF2.0

The NNPDF Collaboration:
Maria Ubiali[1,5], Richard D. Ball[1], Luigi Del Debbio[1], Stefano Forte[2],
Alberto Guffanti[3], José I. Latorre[4] and Juan Rojo[2]
[1] *School of Physics and Astronomy, University of Edinburgh, JCMB, KB, Mayfield Rd, Edinburgh EH9 3JZ, Scotland*
[2] *Dipartimento di Fisica, Università di Milano and INFN, Sezione di Milano, Via Celoria 16, I-20133 Milano, Italy*
[3] *Physikalisches Institut, Albert-Ludwigs-Universität Freiburg Hermann-Herder-Straße 3, D-79104 Freiburg i. B., Germany*
[4] *Departament d'Estructura i Constituents de la Matèria, Universitat de Barcelona, Diagonal 647, E-08028 Barcelona, Spain*
[5] *Center for Particle Physics Phenomenology CP3, Universitè Catholique de Louvain Chemin du Cyclotron, 1348 Louvain-la-Neuve, Belgium*

We present predictions for relevant LHC observables obtained with the NNPDF2.0 set. We compute the combined PDF+α_s uncertainties on these observables, and show that combining errors in quadrature yields an excellent approximation to exact error propagation. We then compare the NNPDF2.0 results to the other global PDF fits using a common value of α_s. At LHC 7 TeV, reasonable agreement, both in central values and in uncertainties, is found for NNPDF2.0, CTEQ6.6 and MSTW08.

1 Combined PDF+α_s uncertainties for LHC observables

The determination of the theoretical accuracy in the predictions for LHC observables is one of the most important tasks now that the LHC is producing collisions at $\sqrt{s}$ =7 TeV. QCD uncertainties coming from Parton Distribution Functions (PDFs) and from the strong coupling constant $\alpha_s(M_Z)$ are among the dominant sources of theoretical uncertainties for most relevant LHC cross sections.

In this contribution we present predictions for important LHC observables based on the NNPDF2.0 global PDF analysis [1]. First we will discuss the results for the combined PDF+α_s uncertainty on several LHC observables, and then we compare the NNPDF2.0 predictions with those of the other two global analyses, MSTW2008 and CTEQ6.6. For the latter comparison we use the sets with varying α_s recently presented by these two groups [2,3] in order to use consistently a common value of α_s. The observables have been computed with the MCFM program [4]. We point out that predictions from previous NNPDF sets [5,6,7,8] are consistent with the NNPDF2.0 results, albeit with larger PDF uncertainties due to the reduced dataset used there.

First of all we present results for several LHC observables at 7 TeV computed with the NNPDF2.0 PDF set: W^+ and Z^0 production, $t\bar{t}$ production and Higgs production in gluon–fusion for $m_H = 120$ GeV. We compute predictions for various values of α_s in order to determine the combined PDF+α_s uncertainties for these observables. Our choice for the reference value of α_s and its uncertainty is $\alpha_s(M_Z) = 0.119 \pm 0.002$, where the uncertainty is to be interpreted as a 68% C.L. The combined PDF+α_s uncertainty is computed both adding in quadrature the two uncertainties and using exact error propagation, following the methods presented in Refs. [9,10].

Results are shown in Fig. 1. It is clear that the two methods, quadrature and exact propagation, yield essentially identical results. Indeed, they ought to give exactly the same result [3] if

the combined uncertainty can be obtained as a one–sigma ellipse from a quadratic χ^2. We also note from Fig. 1 that PDF uncertainties are independent of α_s for any reasonable range of α_s.

For processes which depend on α_s at leading order like Higgs or $t\bar{t}$ production, the combined PDF+α_s uncertainty is as expected sizably larger than the PDF uncertainty alone: for such processes, comparing predictions from different PDF sets using a common value of α_s is mandatory to obtain a meaningful comparison.

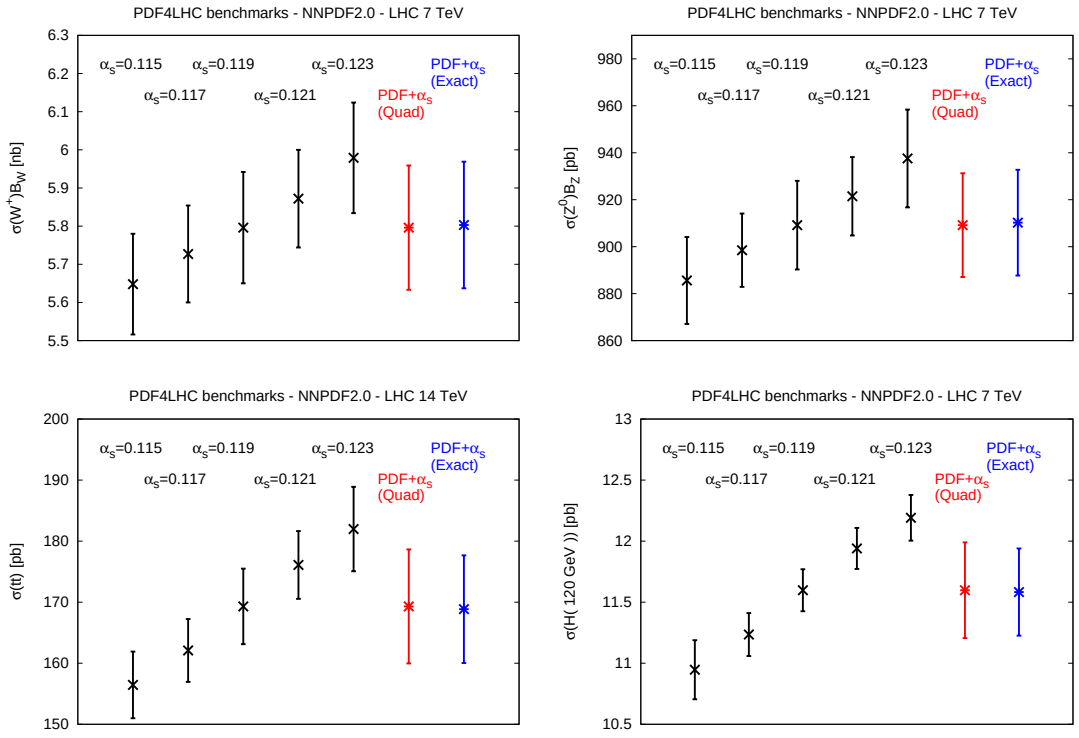

Figure 1: Predictions for some important LHC observables computed at 7 TeV. From top to bottom and from left to right: W^+ and Z production, $t\bar{t}$ production, and Higgs production in gluon-gluon fusion for $m_H = 120$ GeV. Results are shown for different values of $\alpha_s(M_Z)$ as well as for the combined PDF+α_s uncertainties.

2 Comparison between global PDF sets

Now we compare predictions for important LHC observables from the three global PDF fits: NNPDF2.0, MSTW08 [11] and CTEQ6.6 [12] for the LHC 7 TeV run. The comparison is shown in Fig. 2 and in Table 1. For CTEQ and MSTW we show results both at the default value of α_s and for a common value $\alpha_s(M_Z) = 0.119$. For the CTEQ6.6 and MSTW08 predictions with $\alpha_s = 0.119$ the specific sets from Refs. [2,3] have been used. We also assume that the PDF uncertainty for these two PDF sets does not depend in a statistically significant way on the value of α_s when switching from the default to the common value of α_s (which in both cases differ by $\delta\alpha_s = 0.001$). Note that NNPDF2.0 uses as default the value $\alpha_s(M_Z) = 0.119$.

It is clear from Fig. 2 that using a common value of the strong coupling improves the agreement between global PDF sets. If predictions with $\alpha_s = 0.119$ are compared, we observe that the three global PDF sets are in reasonable agreement. From Table 1 is clear that PDF uncertainties extracted from the NNPDF2.0, CTEQ6.6 and MSTW08 global fits are quite similar. We note that a conservative PDF+α_s uncertainty which accounts for the remaining small discrepancies between PDF sets could be obtained using the envelope method discussed in Ref. [10].

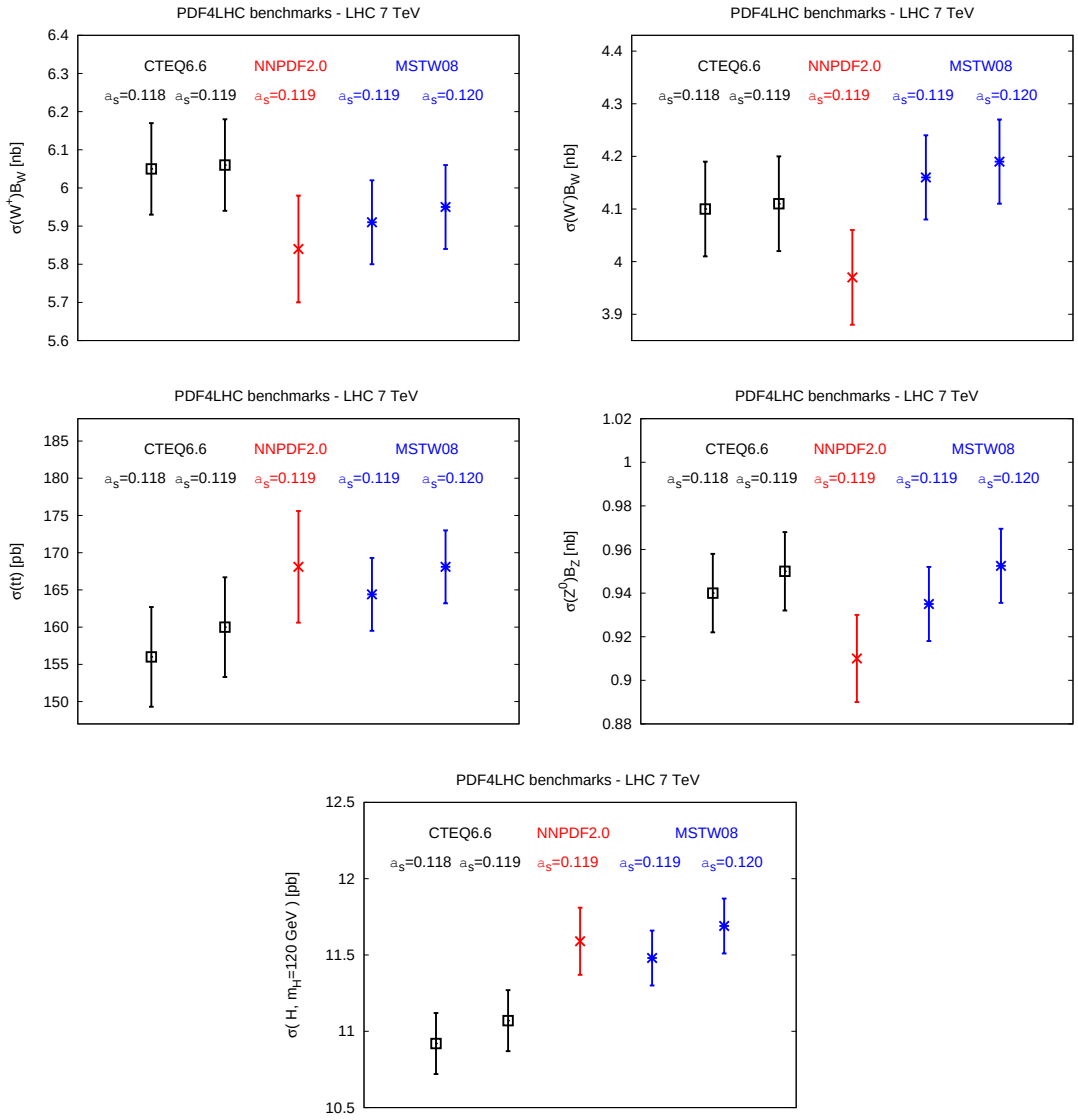

Figure 2: Comparison of predictions for LHC observables for NNPDF2.0, MSTW08 and CTEQ6.6 sets for the LHC at center of mass energy of 7 TeV.

3 Summary

We have presented predictions for important LHC observables obtained with the NNPDF2.0 set. We have computed the combined PDF+α_s uncertainties on these observables, and shown that combining errors in quadrature yields an excellent approximation to exact error propagation. The comparison of the NNPDF2.0 results at the LHC for $\sqrt{s}$ =7 TeV with the other global PDF analyses, CTEQ6.6 and MSTW08, performed using a common value of α_s shows a reasonable agreement both in central values and in uncertainties. To understand the remaining moderate differences between PDF sets a detailed benchmarking on the lines of the HERA-LHC benchmarks [13] would be required.

The NNPDF2.0 PDFs, including sets determined using all values of $0.114 \leq \alpha_s(M_Z) \leq 0.124$ in steps of $\Delta\alpha_s(M_Z) = 0.001$, are available from the NNPDF web site,

`http://sophia.ecm.ub.es/nnpdf .`

They are also available through the LHAPDF interface [14].

	$\sigma(W^+)\text{Br}\left(W^+ \to l^+\nu_l\right)$ [nb]	$\sigma(W^-)\text{Br}\left(W^- \to l^+\nu_l\right)$ [nb]	$\sigma(Z^0)\text{Br}\left(Z^0 \to l^+l^-\right)$ [nb]
NNPDF2.0	5.84 ± 0.14	3.97 ± 0.09	0.91 ± 0.02
CTEQ6.6 - $\alpha_s = 0.118$	6.05 ± 0.12	4.10 ± 0.09	0.94 ± 0.02
CTEQ6.6 - $\alpha_s = 0.119$	6.06 ± 0.12	4.11 ± 0.09	0.95 ± 0.02
MSTW08 - $\alpha_s = 0.119$	5.91 ± 0.11	4.16 ± 0.08	0.94 ± 0.02
MSTW08 - $\alpha_s = 0.120$	5.95 ± 0.11	4.19 ± 0.08	0.95 ± 0.02

	$\sigma(t\bar{t})$ [pb]	$\sigma(H, m_H = 120\,\text{GeV})$ [pb]
NNPDF2.0	168.1 ± 7.5	11.59 ± 0.22
CTEQ6.6 - $\alpha_s = 0.118$	156.0 ± 6.7	10.92 ± 0.20
CTEQ6.6 - $\alpha_s = 0.119$	160.1 ± 6.7	11.07 ± 0.20
MSTW08 - $\alpha_s = 0.119$	164.4 ± 4.9	11.48 ± 0.18
MSTW08 - $\alpha_s = 0.120$	168.1 ± 4.9	11.69 ± 0.18

Table 1: Cross sections for W, Z, $t\bar{t}$ and Higgs production at the LHC at $\sqrt{s} = 7$ TeV and the associated PDF uncertainties. All quantities have been computed at NLO using MCFM for the NNPDF2.0, CTEQ6.6 and MSTW08 PDF sets. All uncertainties shown are one–sigma level. See Fig. 2 for the graphical representation of the results of this table.

References

1. R. D. Ball, L. Del Debbio, S. Forte, A. Guffanti, J. I. Latorre, J. Rojo and M. Ubiali, arXiv:1002.4407 [hep-ph].
2. A. D. Martin, W. J. Stirling, R. S. Thorne and G. Watt, Eur. Phys. J. C **64** (2009) 653 [arXiv:0905.3531 [hep-ph]].
3. H. L. Lai, J. Huston, Z. Li, P. Nadolsky, J. Pumplin, D. Stump and C. P. Yuan, arXiv:1004.4624 [hep-ph].
4. `http://mcfm.fnal.gov/`
5. L. Del Debbio, S. Forte, J. I. Latorre, A. Piccione and J. Rojo [NNPDF Collaboration], JHEP **0703** (2007) 039 [arXiv:hep-ph/0701127].
6. R. D. Ball *et al.* [NNPDF Collaboration], Nucl. Phys. B **809**, 1 (2009) [Erratum-ibid. B **816**, 293 (2009)] [arXiv:0808.1231 [hep-ph]].
7. R. D. Ball *et al.* [The NNPDF Collaboration], Nucl. Phys. B **823**, 195 (2009) [arXiv:0906.1958 [hep-ph]].
8. R. D. Ball, L. Del Debbio, S. Forte, A. Guffanti, J. I. Latorre, J. Rojo and M. Ubiali [NNPDF Collaboration], arXiv:0912.2276 [hep-ph].
9. J. R. Andersen *et al.* [SM and NLO Multileg Working Group], arXiv:1003.1241 [hep-ph].
10. F. Demartin, S. Forte, E. Mariani, J. Rojo and A. Vicini, arXiv:1004.0962 [hep-ph].
11. A. D. Martin, W. J. Stirling, R. S. Thorne and G. Watt, Eur. Phys. J. C **63** (2009) 189 [arXiv:0901.0002 [hep-ph]].
12. P. M. Nadolsky *et al.*, Phys. Rev. D **78**, 013004 (2008) [arXiv:0802.0007 [hep-ph]].
13. M. Dittmar *et al.*, arXiv:0901.2504 [hep-ph].
14. LHAPDF, http://projects.hepforge.org/lhapdf/.

K_T, ANTI$-K_T$ AND SISCONE JETS AND THE STRONG COUPLING α_S AT HERA

Günter Grindhammer (for the H1 and ZEUS collaborations)
Max-Planck-Institute for Physics, Föhringer Ring 6, 80805 Munich, Germany

Recent measurements by the H1 and ZEUS experiments at HERA of inclusive jet and multijet production in deep-inelastic scattering are presented, covering a wide range in the energy scales relevant for the strong interactions. For the first time measurements obtained using the anti$-k_T$ and SISCone jet finders are shown in addition to those using the more traditional k_T jet finder. The measurements are compared to NLO QCD calculations, and the extracted values of the strong coupling α_s as a function of the renormalization scale and at the scale M_Z are shown.

1 Introduction

The HERA *ep*-collider operated with electrons or positrons of 27.6 GeV and protons of 820 or 920 GeV. Each of the two collider experiments H1 and ZEUS collected about 120 pb^{-1} from 1995 to 2000 (HERA-1) and after a luminosity and detector upgrade about 370 pb^{-1} from 2003 to 2007 (HERA-2). Since the results presented here do not depend on whether the incident lepton was an electron or a positron, the term "electron" is used to mean either of them. The kinematic region of deep-inelastic scattering (DIS) is defined by measuring the scattered electron with photon virtualities in the range $5 \leq Q^2 < 20000$ GeV^2. To ensure a well measured hadronic final state, the requirement on the inelasticity $0.2 < y < 0.7$ or on the angle of the scattered quark in the quark-parton model (QPM), $|\cos\gamma_{\rm h}| < 0.65$, measured via the scattered electron and/or the hadronic final state, completes the definition of the DIS phase space.

The n-jet cross sections in DIS can be schematically written as

$$d\sigma_{\rm n-jet} = \sum_{i=q,\bar{q},g} \int dx\, f_i(x,\mu_f) d\hat{\sigma}_i(x,\alpha_s^{n-1}(\mu_r),\mu_r,\mu_f)\ \ (1+\delta_{\rm had})\,, \tag{1}$$

where f_i refers to the parton density function (PDF) of parton i in the proton, $\hat{\sigma}_i$ to the matrix element with parton i, which is calculable in perturbative Quantumchromodynamics (QCD), and $\mu_{\rm F}$ and $\mu_{\rm R}$ to the factorization and renormalization scale respectively. The hadronization correction $(1+\delta_{\rm had})$ needs to applied to the QCD calculation when comparing to data. In jet production in DIS there are two relevant hard scales, i.e. Q $(2-140$ GeV) and $P_{\rm T,jet}$ $(5-80$ GeV), while in photoproduction or hadron-hadron collisions there is only $P_{\rm T,jet}$. In order to have a smooth transition from DIS to photoproduction the scale $\sqrt{(Q^2+P_{\rm T,jet}^2)/2}$ is often used. Furthermore in DIS at HERA we have a more complicated interplay of the two scales. Depending on the kinematic regions in Q and $P_{\rm T,jet}$, either one of them can be larger than the other or they both can have rather similar magnitude.

In the lowest order (QPM) process only one jet is produced, and only the production of two and more jets involves QCD processes. In the Breit [1] frame (or in longitudinally boosted equivalent frames) QCD processes generate jets with transverse momenta in contrast to the QPM process. In order to suppress QPM events this frame or the hadronic center-of-mass frame are used to find jets. Therefore, in this frame jet production depends on α_s already in leading order (LO), in contrast to the totally inclusive measurement, for example F_2, which depends on α_s only at next-to-leading order (NLO). When comparing jet measurements to QCD calculations, a collinear and infrared safe jet algorithm has to be applied in the jet finding. The k_{T}-algorithm [2], which has been used by the HERA experiments for many years already, and the more recent anti$-k_{\mathrm{T}}$ [3] and SISCone [4] algorithms, for which results will be shown for the first time, fulfill this requirement.

The slides of the talk, which include more figures than possible in this written version, can be found in ref. [5].

2 Measurements of k_{T} multijets at low Q^2 by H1

A measurement of multijet cross sections at low Q^2 by H1, corresponding to an integrated luminosity of 44 pb^{-1} of HERA-1 data, has just been published [6]. The DIS phase space of this measurement is defined by $5 < Q^2 < 100$ GeV^2 and $0.2 < y < 0.7$. The jet phase phase space is specified by requiring that inclusive jets, 2-jets and 3-jets have $P_{\mathrm{T,jet}} > 5$ GeV and $-1.0 < \eta_{\mathrm{jet}} < 2.5$ in the Breit and laboratory frame respectively. In addition, for both 2-jet and 3-jet events, the invariant mass of the two leading jets must fulfill $M_{1,2} > 18$ GeV. Single and double differential jet cross sections as well as the 3-jet to 2-jet ratio are measured as a function of Q^2, $P_{\mathrm{T,jet}}$ or $<P_{\mathrm{T,jet}}>$ of the two leading jets and ξ, the fractional momentum at LO of the incident parton in the hard interaction. They are compared to NLO calculations using NLOJET++ [7] for 5 massless quark flavors, using for the proton PDFs the CTEQ6.5M [8] parameterization and $\mu_{\mathrm{F}} = \mu_{\mathrm{R}} = \sqrt{(Q^2 + P^2_{\mathrm{T,jet}})/2}$. In Fig.1 left, the single differential inclusive jet, 2-jet and 3-jet cross sections as a function of Q^2 and $P_{\mathrm{T,jet}}$ or $<P_{\mathrm{T,jet}}>$ and their description by NLO QCD predictions are shown. The main experimental uncertainties are due to the jet

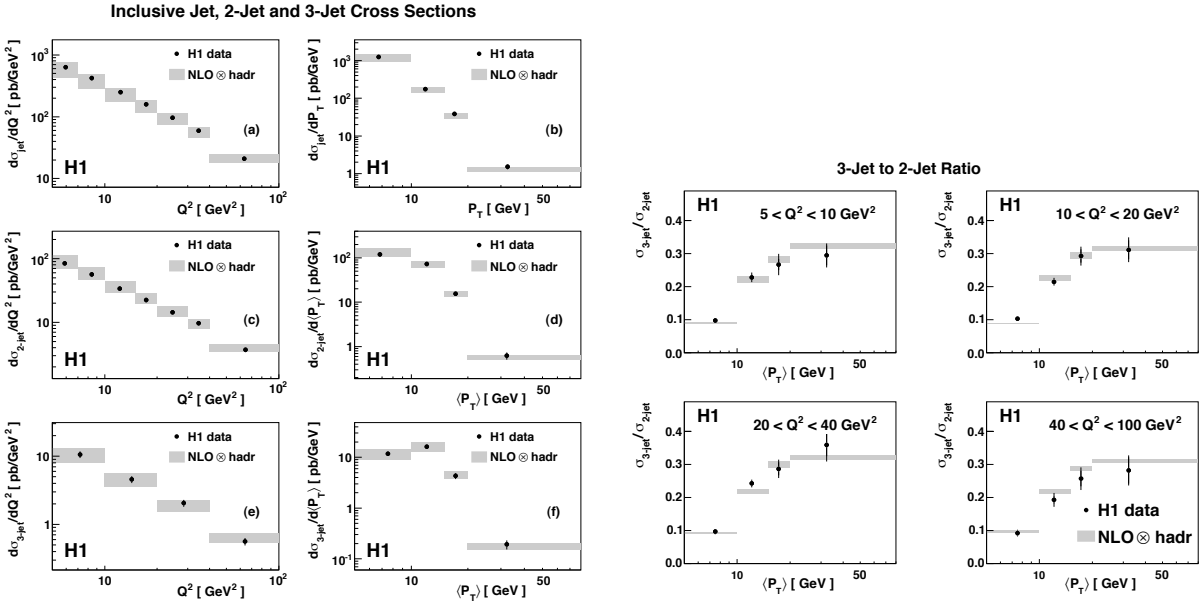

Figure 1: Inclusive jet, 2-jet and 3-jet cross sections (left) and the 3-jet to 2-jet ratio (right) as a function of Q^2 and $P_{\mathrm{T,jet}}$ or $<P_{\mathrm{T,jet}}>$ of the two leading jets compared to NLO calculations corrected for hadronization effects.

energy scale ($\pm 2\%$) and the acceptance, leading to an error on the cross section between $4-10\%$ and $2-15\%$ respectively. In Fig.1 left primarily the theoretical uncertainties are visible. They are dominated by the renormalization scale uncertainty of $\approx 30\%$ ($\approx 10\%$) at lowest Q^2 and $P_{\mathrm{T,jet}}$ (highest Q^2 and $P_{\mathrm{T,jet}}$). The uncertainty due to the PDFs varies from $2-6\%$. With the scale choice for μ_{R} the data are well described by NLO, however, calculations beyond NLO are needed to match the precision of the measurements. Choosing $\mu_{\mathrm{R}} = P_{\mathrm{T,jet}}$ decreases the NLO prediction by $10-20\%$ at lowest Q^2 and $P_{\mathrm{T,jet}}$ and is disfavored by the data.

In Fig.1 right, the double differential 3-jet to 2-jet ratio is shown as a function of the average $P_{\mathrm{T,jet}}$ of the two leading jets in four bins of Q^2. In the ratio the normalization error cancels and other systematic experimental uncertainties are reduced by $\approx 50\%$. Also the sensitivity to the variation of the renormalization scale in the theory is reduced. The ratio is well described by the NLO calculation. For the ratio we find that the experimental errors (dominated by statistical errors) of this HERA-1 data sample are larger than the theoretical ones. With HERA-2 data the statistics will be improved by about a factor of 9.

The extraction of the strong coupling α_s from these measurements on inclusive jet, 2-jet and 3-jet cross section will be discussed in sect.4.

3 Measurements of inclusive k_{T}, anti$-k_{\mathrm{T}}$ and SISCone jets at high Q^2 by ZEUS

A first comparison [9] of inclusive jet cross sections measured using the k_{T}, see [10], and anti$-k_{\mathrm{T}}$ and SISCone jet algorithms, see[9], has been performed by ZEUS. The HERA-1 data analyzed corresponds to an integrated luminosity of 82 pb^{-1}. The DIS phase space is defined by $Q^2 > 125$ GeV^2 and $|\cos\gamma_{\mathrm{h}}| < 0.65$. The jets are reconstructed using the k_{T}, anti$-k_{\mathrm{T}}$ or SISCone jet algorithms, and at least one jet with $E_{\mathrm{T,jet}} > 8$ GeV and $-2 < \eta_{\mathrm{jet}} < 1.5$ in the Breit frame is required. Single and double differential inclusive jet cross sections are measured as a function of Q^2 and $E_{\mathrm{T,jet}}$. The main experimental uncertainties are due to the hadronic jet energy and the acceptance. The former ($\pm 1\%$ for $E^{\mathrm{lab}}_{\mathrm{T,jet}} > 10$ GeV and increasing up to $\pm 3\%$ for lower $E^{\mathrm{lab}}_{\mathrm{T,jet}}$) yields an uncertainty on the cross section of $\approx \pm 5\%$, the latter, determined using different models, leads to an uncertainty of $\approx \pm 4\%$. The NLO predictions for 5 massless quark flavors are calculated using the program DISENT [11] with $\mu_{\mathrm{F}} = Q$ and $\mu_{\mathrm{R}} = E_{\mathrm{T,jet}}$ and the ZEUS-S parameterization [12] for the proton PDFs.

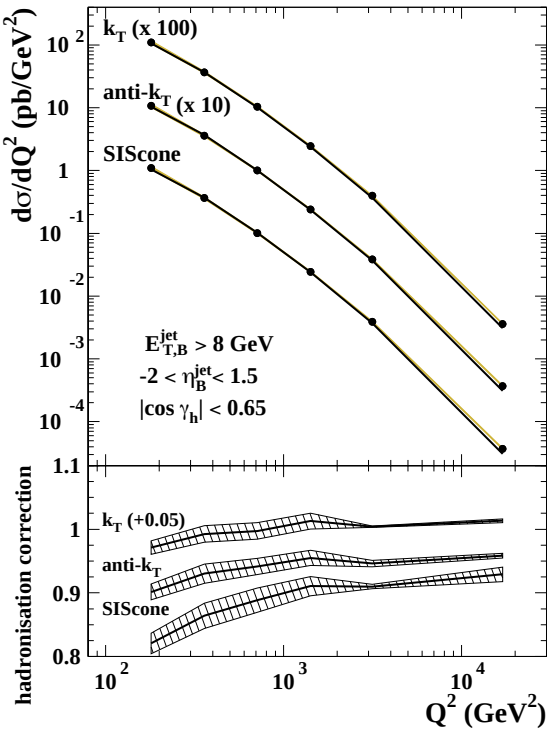

Figure 2: Inclusive jet cross section and NLO prediction (top) and hadronization corrections (bottom) using the k_{T}, anti$-k_{\mathrm{T}}$ and SISCone jet finding algorithms.

In Fig.2 the inclusive jet cross sections as a function of Q^2 are shown for the three different jet algorithms. The measurements are found to be well described by their respective NLO predictions [a]. This also holds for the distributions as a function of $E_{\mathrm{T,jet}}$. As can be also seen in Fig.2 (bottom), the hadronization corrections to

[a] Since the different jet cross sections are very similar, two have been offset by factors of 10 and 100 in Fig.2.

the NLO calculations are smallest for the k_{T} and anti$-k_{\mathrm{T}}$ and somewhat larger for the SISCone algorithm. For all three jet algorithms the parameter R_0 was set to 1.

In a study[9] of the theoretical uncertainties it is found that all three jet algorithms have similar sensitivity to variations of PDFs, $\alpha_s(M_Z)$ and to different models, while SISCone shows slightly larger sensitivity to terms beyond NLO, i.e. to the conventional variations of renormalization and factorization scales. As a function of Q^2 for example, the theoretical uncertainty varies from about $3-7\%$ $(3-10\%)$ for the anti$-k_{\mathrm{T}}$ (SISCone) algorithm.

Calculations of inclusive jet cross sections are currently available up to $\mathcal{O}(\alpha_s^2)$. However, the ratios of inclusive jet cross sections [9] for different jet algorithms, which can be written in terms of differences of jet cross sections, can be calculated up to $\mathcal{O}(\alpha_s^3)$ using NLOJET++. In the ratio the theoretical uncertainty is dominated by the hadronization uncertainty. The data and the QCD predictions are shown in Fig.3 as a function of $E_{\mathrm{T,jet}}$ and Q^2. For the data they differ from unity by less than 3.6%, except at the highest $E_{\mathrm{T,jet}}$ where it is about 10%. The data ratios are well described by calculations including terms up to $\mathcal{O}(\alpha_s^3)$.

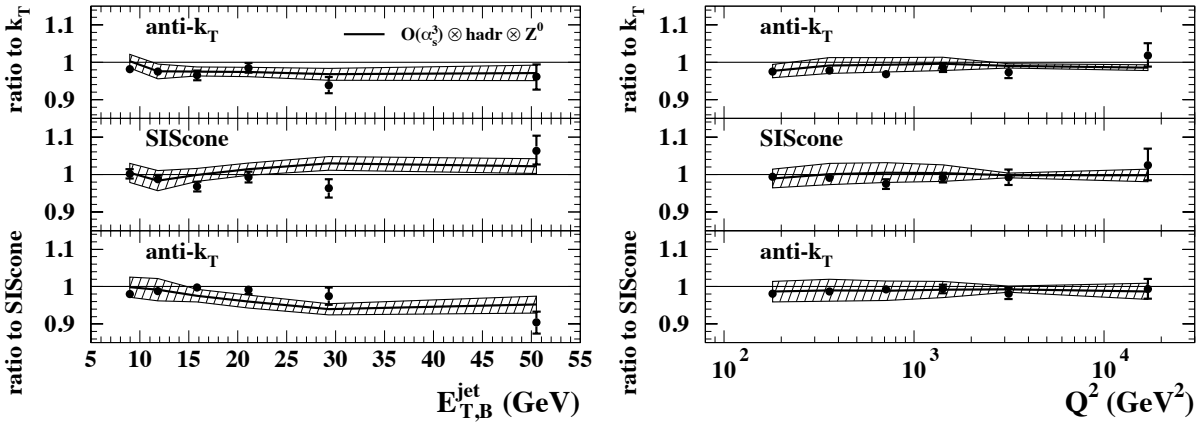

Figure 3: Inclusive jet cross section ratios (anti$-k_{\mathrm{T}}$ to k_{T}, SISCone to k_{T} and anti$-k_{\mathrm{T}}$ to SISCone) for data and QCD calculations including terms up to $\mathcal{O}(\alpha_s^3)$. The hatched band displays the theory uncertainty on the ratio.

4 Extraction of running α_s and $\alpha_s(M_Z)$

The jet cross sections discussed in sections 2 and 3 are used to extract α_s at different values of the renormalization scale μ_{R} and at the Z-boson mass. In the fit procedure the statistical, systematic and correlated uncertainties are taken into account. The dominant theory uncertainty is estimated by a variation of the renormalization and factorization scales by the arbitrary but conventional factor of 1/2 and 2 of the nominal scale. This uncertainty, in the case of H1, is obtained by fitting the changed theory predictions to data. In case of ZEUS it is calculated using a method [13] which does not involve a refit of the data. It leads to smaller theory uncertainties than the H1 method.

The extraction of $\alpha_s(M_Z)$ using the double differential inclusive jet, 2-jet and 3-jet cross sections from H1, using the k_{T} jet finder as discussed in sect.2, yields:

$$k_{\mathrm{T}}: \ \alpha_s(M_Z) = 0.1160 \pm 0.0014\,(\mathrm{exp.})\,^{+0.0093}_{-0.0077}\,(\mathrm{th.}) \pm 0.0016\,(\mathrm{pdfs}) \qquad 5 < Q^2 < 100\ \mathrm{GeV}^2\,.$$

This value can be compared with a value from a recent extraction [14] of α_s from H1 using HERA-1 and HERA-2 data on double differential normalized inclusive jet, 2-jet and 3-jet cross sections in the high Q^2 region, corresponding to an integrated luminosity of 395 pb^{-1}:

$$k_{\mathrm{T}}: \ \alpha_s(M_Z) = 0.1168 \pm 0.0007\,(\mathrm{exp.})\,^{+0.0046}_{-0.0030}\,(\mathrm{th.}) \pm 0.0016\,(\mathrm{pdfs}) \quad 150 < Q^2 < 15000\ \mathrm{GeV}^2\,.$$

The two results are in very good agreement. The higher precision of the latter result is due to full or partial cancelation of a number of systematic uncertainties in normalized jet cross sections (normalized to inclusive events in the Q^2 bins) and reduced theory uncertainty at the higher Q^2. Using the anti$-k_{\mathrm{T}}$ jet finder, H1 finds that the central value of $\alpha_s(M_Z)$ remains within 0.6% [14] of the nominal k_{T} value.

The running of α_s as a function of the renormalization scale is shown in Fig.4 as extracted from the low and high Q^2 data. The $\alpha_s(M_Z)$ value and uncertainties from the high Q^2 extraction are used to extrapolate to lower scales using the two-loop renormalization group equation. The values and experimental uncertainties of α_s in the low Q^2 region (square points) are found to be in very good agreement with the QCD expectation.

The inclusive k_{T}, anti$-k_{\mathrm{T}}$ and SISCone jet cross sections, discussed in sect.3, are used by ZEUS to also extract values for $\alpha_s(M_Z)$. For this purpose the single differential cross sections in Q^2 are used. Only data for $Q^2 > 500$ GeV^2 are taken in order to reduce the theory uncertainty while minimizing the total uncertainty in $\alpha_s(M_Z)$. The following results are obtained:

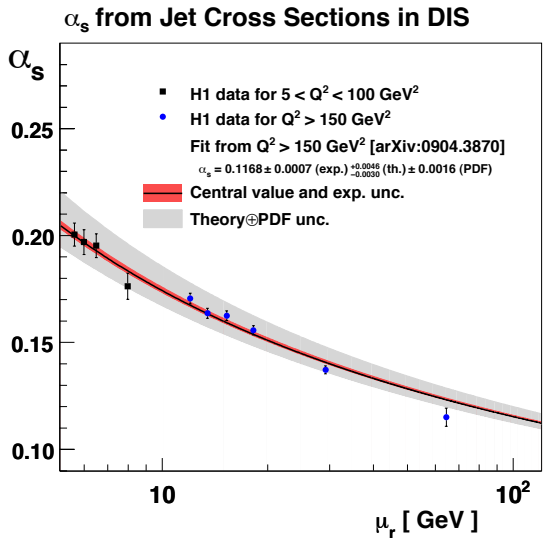

Figure 4: $\alpha_s(\mu_{\mathrm{R}} = \sqrt{(Q^2 + P^2_{\mathrm{T,jet}})/2})$ obtained from inclusive jet, 2-jet and 3-jet cross sections measured at low and high Q^2, compared to the prediction from the renormalization group equation using $\alpha_s(M_Z)$ from the fit of the high Q^2 jet data.

$$
\begin{aligned}
k_{\mathrm{T}}: \quad & \alpha_s(M_Z) = 0.1207 \pm 0.0014\,(\mathrm{stat.})\,^{+0.0035}_{-0.0033}\,(\mathrm{exp.})\,^{+0.0022}_{-0.0023}\,(\mathrm{th.}) \quad Q^2 > 500\ \mathrm{GeV}^2 \\
\text{anti}-k_{\mathrm{T}}: \quad & \alpha_s(M_Z) = 0.1188 \pm 0.0014\,(\mathrm{stat.})\,^{+0.0033}_{-0.0032}\,(\mathrm{exp.})\,^{+0.0022}_{-0.0022}\,(\mathrm{th.}) \quad Q^2 > 500\ \mathrm{GeV}^2 \\
\mathrm{SISCone}: \quad & \alpha_s(M_Z) = 0.1186 \pm 0.0013\,(\mathrm{stat.})\,^{+0.0034}_{-0.0032}\,(\mathrm{exp.})\,^{+0.0025}_{-0.0025}\,(\mathrm{th.}) \quad Q^2 > 500\ \mathrm{GeV}^2\,.
\end{aligned}
$$

These values for $\alpha_s(M_Z)$ are very similar as they should be; the differences observed are comparable to terms beyond NLO.

5 Summary

Recent measurements on multijet cross sections at low Q^2 are found to be in good agreement with NLO calculations and yield a value for $\alpha_s(M_Z)$ consistent with extractions from similar measurements at high Q^2. These and previous jet measurements at HERA have primarily used the k_{T} jet finder. First measurements of inclusive jet cross sections using the anti$-k_{\mathrm{T}}$ and SISCone have been performed. The cross sections have very similar shapes and normalization and are in good agreement with NLO predictions. The theoretical precisions are similar, with the SISCone algorithm leading to slightly less precise results. The k_{T}, anti$-k_{\mathrm{T}}$ and the SISCone jet finder lead to similar values for $\alpha_s(M_Z)$ with similar precision.

The values for $\alpha_s(M_Z)$ at NLO presented here are summarized in Fig.5. Additional values are shown from preliminary jet analyses using deep-inelastic [15] and photoproduction [16] data from ZEUS. The values shown here have become available after the conference. Also displayed are the currently most precise determinations of $\alpha_s(M_Z)$ from the three-jet rate at NNLO [17] in e^+e^- annihilation at LEP and from inclusive jet cross sections [18], at NLO including higher order threshold corrections, obtained by D0 in $p\bar{p}$ collisions at the TEVATRON.

Finally, the 2009 world average [19] is indicated as band in Fig.5. All values shown are consistent with each other and with the world average. One may notice that at HERA the theoretical uncertainties do not yet match the experimental precision, however, calculations of higher orders are expected to improve this situation.

Further experimental progress at HERA, in terms of precision and statistics, is possible by using the final reconstructed data and by performing combined extractions of α_s using H1 and ZEUS jet cross sections.

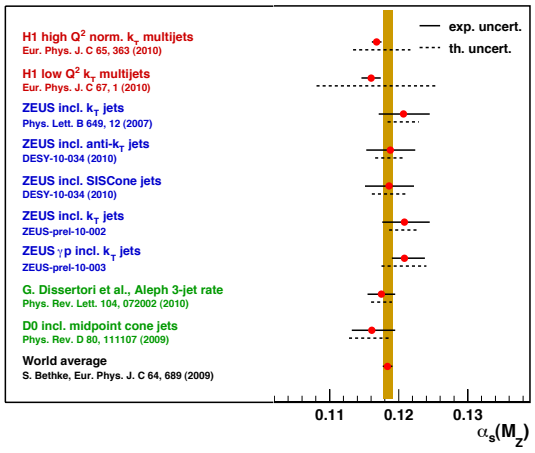

Figure 5: Recent values of $\alpha_s(M_Z)$ from jets and the world average.

Acknowledgments

I want to thank my colleagues in H1 and ZEUS who provided suggestions and help in preparing this talk. Thanks also to the organizers for this interesting conference and the unique atmosphere.

References

1. R.P. Feynman, "*Photon-Hadron Interactions.*" Benjamin, New York, (1972); K.H. Streng, T.F. Walsh and P.M. Zerwas, *Z. Phys.* C **2**, 237 (1979).
2. S. Catani *et al.*, *Nucl. Phys.* B **406**, 187 (1993); S.D. Ellis and D.E. Soper, *Phys. Rev.* D **48**, 3160 (1993).
3. M. Cacciari, G.P. Salam and G. Soyez, *JHEP* **0804**, 063 (2008) [arXiv:0802.1189 [hep-ph]].
4. G.P. Salam and G. Soyez, *JHEP* **0705**, 086 (2007) [arXiv:0704.0292 [hep-ph]].
5. Slides: `http://moriond.in2p3.fr/QCD/2010/FridayMorning/Grindhammer.pdf`
6. F.D. Aaron *et al.* [H1 Collaboration], *Eur. Phys. J.* C **67**, 1 (2010). [arXiv:0911.5678 [hep-ex]].
7. Z. Nagy and Z. Trocsanyi, *Phys. Rev. Lett.* **87**, 082001 (2001). [arXiv:hep-ph/0104315].
8. W.K. Tung *et al.*, *JHEP* **0702**, 053 (2007). [arXiv:hep-ph/0611254].
9. H. Abramowicz *et al.* [ZEUS Collaboration], DESY-10-034, [arXiv:1003.2923 [hep-ex]].
10. S. Chekanov *et al.* [ZEUS Collaboration], *Phys. Lett.* B **649**, 12 (2007). [arXiv:hep-ex/0701039].
11. S. Catani and M.H. Seymour, *Nucl. Phys.* B **485**, 291 (1997) [Erratum-ibid. B **510**, 503 (1998)]. [arXiv:hep-ph/9605323].
12. S. Chekanov *et al.* [ZEUS Collaboration], *Phys. Rev.* D **67**, 012007 (2003). [arXiv:hep-ex/0208023].
13. R.W.L. Jones *et al.*, JHEP **0312**, 007 (2003). [arXiv:hep-ph/0312016].
14. F.D. Aaron *et al.* [H1 Collaboration], *Eur. Phys. J.* C **65**, 363 (2010). [arXiv:0904.3870 [hep-ex]].
15. ZEUS Collaboration, *"Inclusive-jet prod. in NC DIS with HERA II"*, ZEUS-prel-10-002.
16. ZEUS Collaboration, *"Inclusive-jet cross sections in photoproduction"*, ZEUS-prel-10-003.
17. G. Dissertori *et al.*, *Phys. Rev. Lett.* **104**, 072002 (2010). [arXiv:0910.4283 [hep-ph]].
18. V.M. Abazov *et al.* [D0 Collaboration], *Phys. Rev.* D **80**, 111107 (2009). [arXiv:0911.2710 [hep-ex]].
19. S. Bethke, *Eur. Phys. J.* C **64**, 689 (2009). [arXiv:0908.1135 [hep-ph]].

Soft QCD at Tevatron

M. Rangel
on behalf of the D0 and CDF collaborations
Laboratoire de l'Accélérateur Linéaire, Université Paris-Sud 11, Bâtiment 200
91898, Orsay, France

Experimental studies of soft Quantum Chromodynamics (QCD) at Tevatron are reported in this note. Results on inclusive inelastic interactions, underlying events, double parton interaction and exclusive diffractive production and their implications to the Large Hadron Collider (LHC) physics are discussed.

1 Introduction

In hadron collisions, hard interactions are theoretically defined as collisions of two incoming partons along softer interactions from the remaining partons. The soft effects become especially important in very high luminosity enviromments (such as the Large Hadron Collider) and they need to be accounted for in most of experimental measurements. In a particular case, the incoming hadrons stay intact after the collision producing a clean signature, which can be used to search for new physics.

In this note, we review several experimental results related to soft QCD and their implications to LHC physics: inclusive inelastic interactions (section 2), underlying event (section 3), double parton interactions (section 4) and exclusive diffractive production (section 5).

2 Inclusive inelastic interaction

The so-called "minimum-bias" (MB) interactions are defined as data collected with a trigger set up so as events are selected with uniform acceptance from all possible inelastic interactions. Description of inelastic nondiffractive events can only be accomplished by a nonperturbative phenomenological model such as that made available by the PYTHIA Monte Carlo (MC) generator.

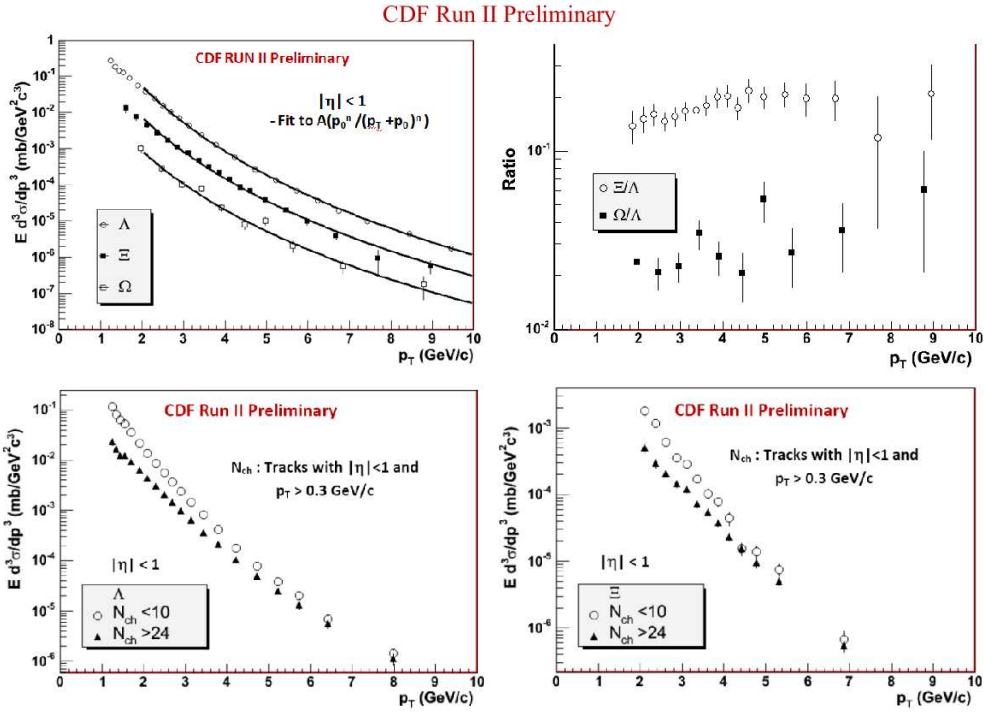

Figure 1: Left upper figure: Inclusive invariant p_T distribution for Λ, Σ and Ω within $|\eta|$ <1. The solid curves are from fit to the functional form $(A)(p0)^n/(pT+p0)^n$ with $p0$ =1.3. Right upper figure: The ratio of Σ/Λ and Ω/Λ as a function of p_T. Two lower figures: The inclusive pT distributions for two different multiplicity regions, number of charged particles < 10 and > 24. Left plot is for lambdas and right plot is for cascades.

Different observables of the final state of antiproton-proton interactions measured with the CDF detector were compared to PYTHIA Tune A [1]. Both the charged and neutral particle activites were studied. In general, poorly agreement is observed between existing MC and data, and the measurements can be used to improve QCD MC.

Measurements of inclusive invariant p_T differential cross section of centrally produced hyperons ($|\eta| < 1$) were performed in minimum biased events [2]. Cascades (Σ), omegas (Ω) and lambdas (Λ) particles are selected and their p_T spectrum measured (Fig. 1). It is observed that the production ratio of the three particles is fairly constant as a function of p_T.

3 Underlying Event

The underlying event (UE) consists of the beam-beam remnants minus the hard-scattering products and is becoming increasingly important to the discovery and precision potential at hadron colliders. CDF has conducted UE studies that exploit jet and Drell-Yan event activity topologies to maximize the sensitivity of UE observables [3]. Several distributions of UE-sensitive observables, corrected to the particle level, suggest the UE may be universal (independent of the hard process) and inform MC tuning and development.

A good agreement between data and PYTHIA Tune AW Monte Carlo predictions was observed, except by a slight excess at transverse region compared to toward region, which is caused by transverse regions receiving contributions from away side jet [3].

4 Double parton interaction

D0 has studied γ+3-jet events to measure double parton scattering (DPS), whereby two pairs of partons undergo hard interactions in a single $p\bar{p}$ collision. DPS is not only a background to many rare processes, especially at higher luminosities, but also provides insight into the spatial distribution of partons in the colliding hadrons. The DPS cross section is expressed as $\sigma_{DPS^{\gamma+3jet}} = \sigma_{jj}\sigma_{\gamma j}/\sigma_{eff}$, where σ_{eff} is the effective interaction region that decreases for less uniform spatial parton distributions. D0 measures a mean of $\sigma_{eff} = 16.4 \pm 2.3$ mb [4], which is consistent with an earlier CDF result [5], and finds σ_{eff} to be independent of jet p_T in the second interaction. More precise studies can reveal a σ_{eff} sensitivity to jet p_T, this could indicate a dynamical departure from the naïve assumption that DPS depends on an uncorrelated product of σ_{jj} and $\sigma_{\gamma j}$.

5 Exclusive Diffractive Production

Exclusive diffrative processes are those where the colliding hadrons emerge intact, but part of their momentum is lost producing central objetcs, with surrounding rapidity regions devoid of particles. CDF recently reported observations of $p\bar{p} \rightarrow p$+dijet+$\bar{p}$, with $p_T^{jet} > 10$ GeV; and $p\bar{p} \rightarrow p$+$[\mu^-\mu^+, J/\Psi, \Psi(2S), \chi_C^0]$+$\bar{p}$ with two oppositely charged central muons and either no other particles or one additional photon detected [6].

D0 recently reported an evidence for diffractive exclusive dijet production with an invariant mass greater than 100 GeV. A discriminant variable (Δ based on calorimeter information was used to demonstrate a significant excess of events with very little energy outside the dijet system (Fig. 2). The probability for the observed excess to be explained by other dijet production processes is 2×10^5 , corresponding to a 4.1 standard deviation significance [7].

Tevatron results support the viability of exclusive Standard Model Higgs production through p+H+p processes at the LHC, which are expected to play an important role in future studies of new physics [8].

6 Conclusion

The Tevatron experiments provide soft QCD physics studies at $\sqrt{s} = 1.96$ TeV. These results are based on less than one third of the anticipated complete Run II sample, therefore more measurements are expected in the coming years to illuminate the Large Hadron Collider physics results.

References

1. T. Aaltonen *et al.* [CDF Collaboration], *Phys. Rev. Lett.* **79**, 112005 (2009).
2. CDF Collaboration, CDF Public Note 10084.
   Web Page: http://www-cdf.fnal.gov/physics/new/qcd/hyperons_10/HyperonWEBV2.htm.
3. CDF Collaboration, CDF Public Note 9351.
   Web Page: http://www-cdf.fnal.gov/physics/new/qcd/run2/ue/chgjet/index.html.
4. V. M. Abazov *et al.* [D0 Collaboration], *Phys. Rev.* D **81**, 052012 (2010).
5. F. Abe *et al.* [CDF Collaboration], *Phys. Rev.* D **56**, 3811 (1997).
6. A. Abulencia *et al.* [CDF Collaboration], *Phys. Rev. Lett.* **98**, 112001 (2007).
   T. Aaltonen *et al.* [CDF Collaboration], *Phys. Rev. Lett.* **99**, 242002 (2007).
   T. Aaltonen *et al.* [CDF Collaboration], *Phys. Rev.* D **77**, 052004 (2008).
   T. Aaltonen *et al.* [CDF Collaboration], *Phys. Rev. Lett.* **102**, 222002 (2009).
   T. Aaltonen *et al.* [CDF Collaboration], *Phys. Rev. Lett.* **102**, 242001 (2009).

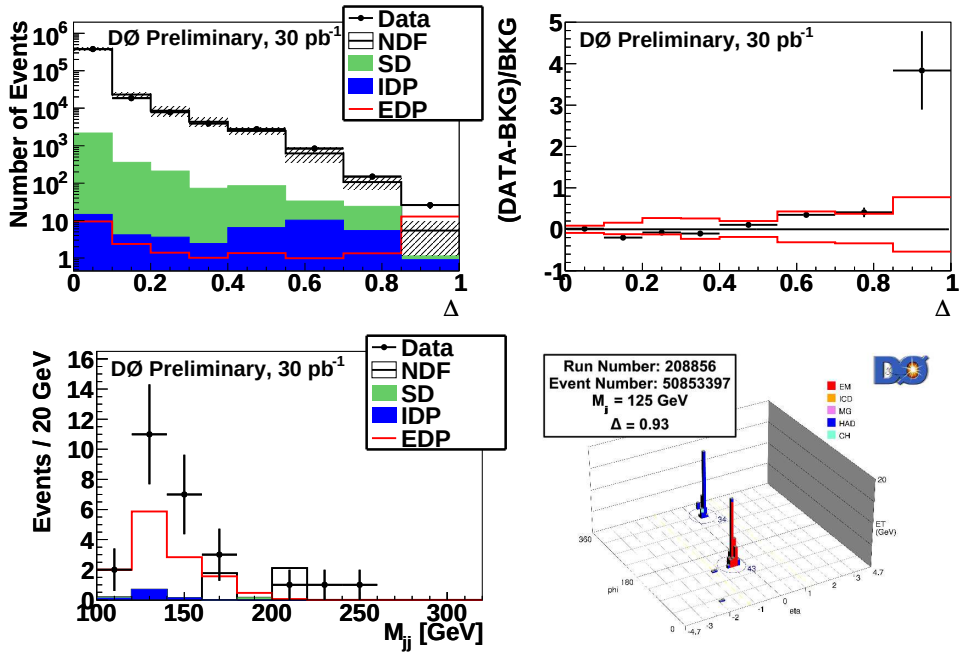

Figure 2: Top Left Figure: Δ distribution for data and background (nondiffractive (NDF), single-diffractive (SD) and inclusive double pomeron (IDP)). A good agreement is observed between data and background except at high values of Δ where exclusive diffracitve production (EDP) dominates. The hatched band indicates the total uncertainty on the background. Top Right Figure: MC background (BKG) subtracted data divided by background. The solid lines are $\pm$ 1 standard deviation systematic uncertainty on the background. Bottom Left Figure: Dijet invariant mass distribution for MC and data after applying the cut on $\Delta \geq 0.85$. The total background prediction is of $5.4\ ^{+4.2}_{-2.9}$ events and 26 signal candidate events are observed in data. Bottom Right Figure: Exclusive diffractive candidate event. No energy deposition is present in the forward regions, only two central jets are observed in the detector

7. D0 Collaboration, DØ Note 6042-CONF.
   Web Page: http://www-d0.fnal.gov/Run2Physics/WWW/results/prelim/QCD/Q17/.
8. V. A. Khoze, A. D. Martin and M. G. Ryskin, Eur. Phys. J. C **23**, 311 (2002).

INCLUSIVE DIFFRACTION AT HERA

V. SOLA
Università di Torino and INFN, Torino, Italy

The H1 and ZEUS Collaborations have measured the inclusive diffractive DIS cross section $ep \to eXp$ with very high precision across a wide kinematic range. Diffractive parton density functions (DPDFs) have been extracted from the data using the DGLAP approach at next-to-leading-order (NLO) of perturbative QCD. Results from diffractive dijets in DIS have also been included in the fit. The first direct measurement of the longitudinal diffractive structure function F_L^D has been compared to the DPDF predictions. Finally, the DPDF predictions have been compared to data on diffractive dijets in photoproduction, where the issue of absorption and gap survival probability in a hadron-hadron environment can be studied.

1 Introduction

Diffractive processes have been studied extensively in deep-inelastic electron-proton scattering (DIS) at the HERA collider. Such interactions are characterised by the presence of a leading proton in the final state carrying most of the initial energy and by the presence of a large gap in rapidity between the proton and the rest of the hadronic system. The kinematic variables used to describe inclusive DIS, $ep \to eX$, are the virtuality of the exchanged boson, Q^2, the Bjorken scaling variable, x, and the inelasticity, y. In addition, the kinematic variables $x_{I\!P}$ and β are specific for diffractive DIS, $ep \to eXp$, with $x_{I\!P}$ the longitudinal fractional momentum of the proton carried by the diffractive exchange and β the longitudinal momentum fraction of the struck parton with respect to the diffractive exchange. They are related by $x = x_{I\!P}\beta$. The inclusive diffractive DIS cross section is usually presented in the form of a diffractive reduced cross section, $\sigma_r^{D(3)}$, integrated over the Mandelstam t variable, here representing the squared four-momentum transferred at the proton vertex, and is related to the experimentally measured differential cross section by

$$\frac{d^3\sigma^{ep\to eXp}}{dx_{I\!P}\,d\beta\,dQ^2} = \frac{2\pi\alpha^2}{\beta Q^2} Y_+ \sigma_r^{D(3)}(x_{I\!P}, \beta, Q^2) \ , \tag{1}$$

where $Y_+ = 1 + (1-y)^2$. The reduced cross section depends at moderate Q^2 on two diffractive structure functions, $F_2^{D(3)}$ and $F_L^{D(3)}$, according to

$$\sigma_r^{D(3)} = F_2^{D(3)} - \frac{y^2}{Y_+} F_L^{D(3)} \ . \tag{2}$$

For y not too close to unity, $\sigma_r^{D(3)} = F_2^{D(3)}$ holds to very good approximation.

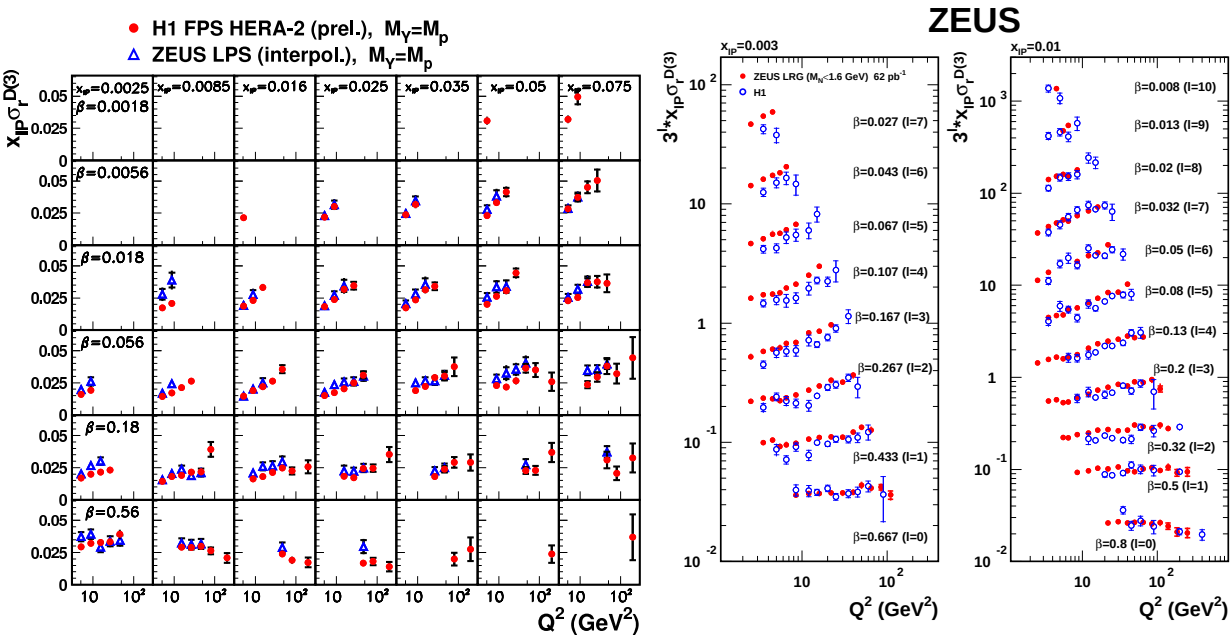

Figure 1: Comparison between the H1 and ZEUS measurements of the diffractive reduced cross section as a function of Q^2, obtained using PS (*left*) or LRG (*right*) samples.

2 Diffractive Cross Section Measurements

Experimentally, diffractive DIS events can be selected by requiring the presence of a large rapidity gap (LRG). A complementary way is the direct measurement of the outgoing proton by using Proton Spectrometers (PS). Whilst the LRG-based techniques yield better statistics than the PS method, they suffer from systematic uncertainties associated with background events due to proton dissociation.

The H1 Collaboration recently released a preliminary proton-tagged measurement using its full available sample from Forward Proton Spectrometer (FPS) data at HERA-II [1]. The measurement agrees in shape and normalization with the previous H1 FPS results from HERA-I [2] and considerably improves the statistical uncertainty and the kinematical coverage, being based on a factor 20 more integrated luminosity than the HERA-I measurement. As shown in Figure 1 (*left*), the new data agree in shape with the recently published final ZEUS results based on Leading Proton Spectrometer (LPS) data from HERA-I [3], but they tend to lie slightly below, still within the combined normalization uncertainty of about 13%.

The recently published ZEUS measurements[3], obtained using the LRG method, substantially improved the statistical precision compared with the older H1 results [4]. Good agreement is observed between the shapes of the H1 and ZEUS cross sections throughout most of the phase space studied, as shown in Figure 1 (*right*). An average 13% normalization difference between the two experiments has been estimated, compatible with the one seen from PS measurements, i.e. the cross sections agree up to a normalization difference between the two Collaborations, independent of experimental method.

3 Diffractive Parton Density Functions

It has been shown by Collins [5] that the NC diffractive DIS process $ep \to eXp$ factorises into diffractive parton density functions (DPDFs) times a term related to the hard-scattering partonic cross section; a useful additional assumption (proton vertex factorisation) is often made

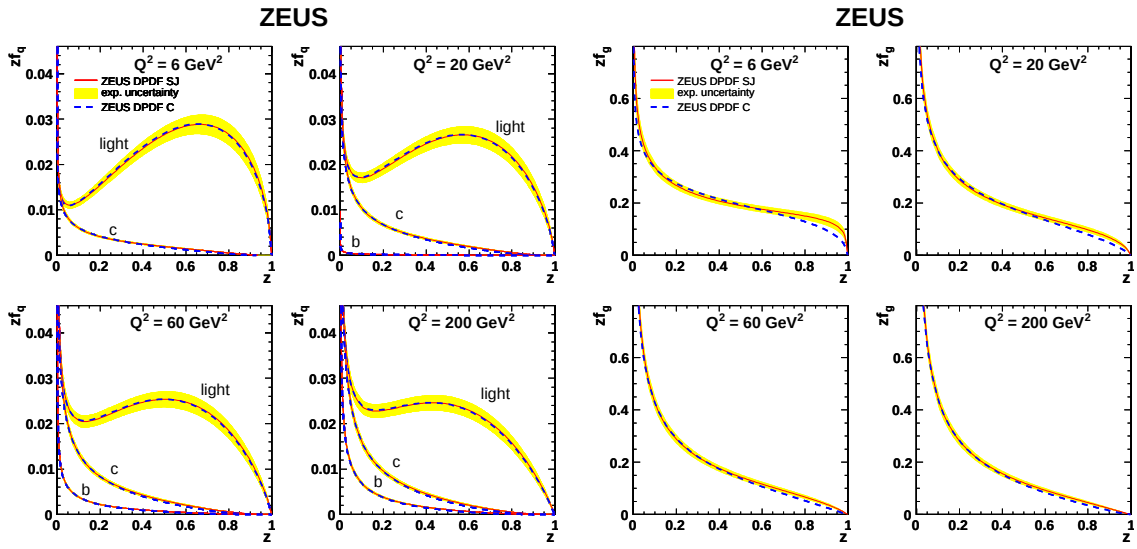

Figure 2: ZEUS singlet (*left*) and gluon (*right*) densities as a function of the momentum fraction, z, for four different values of Q^2. The shaded error bands represent the experimental uncertainty.

whereby the proton vertex dynamics factorise from the vertex of the hard scatter. The β and Q^2 dependences of $\sigma_r^{D(3)}$ may then be subjected to a perturbative QCD analysis based on the DGLAP equations, in order to obtain diffractive PDFs. Whilst F_2^D directly measures the quark density, the gluon density is only indirectly constrained via the scaling violation, $\partial F_2^D/\partial ln Q^2$.

The high statistics ZEUS LRG and LPS data[3] have recently been fitted to extract DPDFs[6]. The method and DPDF parametrisations are similar to the earlier H1 analysis[4], the main difference being in the heavy flavour treatment, which now follows the general mass flavour numbering scheme. In the resulting DPDFs the quark densities are relatively well known throughout the phase space, whilst the theoretical uncertainties on the gluon density are large, in particular at high fractional momentum, z. Indeed, in this region the dominant parton splitting is $q \to qg$ and the sensitivity of $\partial F_2^D/\partial ln Q^2$ to the gluon density becomes poor. Improved large z constraint has been obtained by including in the fit diffractive dijet production data[7], which are directly sensitive to gluons via the boson-gluon fusion process. The resulting quark and gluon densities are presented in Figure 2, showing a comparable precision across the whole z range.

4 The Longitudinal Diffractive Structure Function

At low x and Q^2, the longitudinal diffractive structure function, F_L^D, is closely related to the diffractive gluon density and can thus provide a test of diffractive factorization and of the role of gluons complementarily to jet and charm data. Measurements of F_L^D became possible thanks to the reduced proton beam energy runs at the end of HERA operation.

The H1 Collaboration recently released preliminary F_L^D data[8], shown in Figure 3. When integrated over β, F_L^D is non-zero at 3σ level. It is also clearly incompatible with its maximum possible value, that of F_2^D. The measured F_L^D is in agreement with predictions based on H1 DPDFs[4].

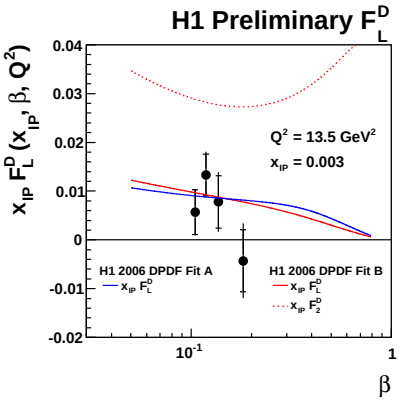

Figure 3: First F_L^D measurement, compared with DPDF predictions.

5 Diffractive Dijets in Photoproduction

DPDFs extracted from inclusive data describe successfully data on dijet in DIS [7,9] and charm [10,11] production. However, predictions obtained with HERA DPDFs grossly overshoot the diffractive dijet cross section at the Tevatron. At HERA, photoproduction events, where $Q^2 \sim 0$, provides an environment similar to a hadron-hadron collider, since the photon can develop an effective partonic structure via $\gamma \to q\bar{q}$ fluctuations and further subsequent splitting. In a simple leading order picture, there are thus two classes of hard photoproduction: 'resolved' interactions, where the photon interacts via its partonic structure, and 'direct' interactions, where the photon behaves as a point-like particle. The variable x_γ is the fraction of the four-momentum of the photon transferred to the hard interaction; the lower the value of x_γ the more hadron-like the photon.

Both H1 [12] and ZEUS [13] have measured diffractive dijets in photoproduction. The ratios of data to theory obtained by both experiments show no dependence on x_γ, which is in constrast with theoretical expectations [14,15]. The data are also suggestive of a weak suppression depending on the transverse energy, E_T, of the jet. More differential studies are required to fully unfold the dynamics.

6 Conclusions

The H1 and ZEUS Collaborations are finalising measurements of the inclusive diffractive DIS cross section, $ep \to eXp$, with the full statistics available from HERA. The DPDFs extracted from NLO QCD fits to inclusive and dijets data result in quark and gluon densities constrained with good precision across the whole kinematic range. The first F_L^D measurement, in agreement with DPDF predictions, provides a unique test of factorization. Comparing the DPDF predictions with diffractive dijets in photoproduction data shows evidence of a small suppression of the cross section which is independent on x_γ and slightly dependent on E_T of the jet, a fact which remains under investigation.

References

1. H1 Coll., *Measurement of diffractive DIS with a leading proton at HERA-2* [H1prelim-09-012].
2. H1 Coll., A. Aktas *et al.*, *Eur. Phys. J.* C **48**, 749 (2006).
3. ZEUS Coll., S. Chekanov *et al.*, *Nucl. Phys.* B **816**, 1 (2009).
4. H1 Coll., A. Aktas *et al.*, *Eur. Phys. J.* C **48**, 715 (2006).
5. J.C. Collins, *Phys. Rev.* D **57**, 3051 (1998).
6. ZEUS Coll., S. Chekanov *et al.*, *Nucl. Phys.* B **831**, 1 (2010).
7. ZEUS Coll., S. Chekanov *et al.*, *Eur. Phys. J.* C **52**, 813 (2007).
8. H1 Coll., *Measurement of the diffractive longitudinal structure function F_L^D at HERA II* [H1prelim-09-011].
9. H1 Coll., A. Aktas *et al.*, *JHEP* **10**, 42 (2007).
10. H1 Coll., A. Aktas *et al.*, *Eur. Phys. J.* C **50**, 1 (2007).
11. ZEUS Coll., S. Chekanov *et al.*, *Eur. Phys. J.* C **51**, 301 (2007).
12. H1 Coll., *Diffractive photoproduction of jets with the H1 detector* [H1prelim-08-012].
13. ZEUS Coll., S. Chekanov *et al.*, *Eur. Phys. J.* C **55**, 177 (2008).
14. A. Kaidalov, V. Khoze, A. Martin, M. Ryskin, *Phys. Lett.* B **567**, 61 (2003).
15. M. Klasen, G. Kramer, *Mod. Phys. Lett* A **23**, 1885 (2008).

PHENOMENOLOGY OF JET PRODUCTION IN FORWARD DIRECTION AT HIGH ENERGY HADRON COLLIDERS

K. Kutak
Department of Physics, University of Antwerp, Groenenborgerlaan 171, B-2020, Belgium

We calculate observables relevant for forward jets at LHC. The simulations are performed using Monte Carlo event generators. In particular we compare results from CASCADE based on high energy factorization and PYTHIA which is based on collinear factorization.

1 Introduction

Experiments at the Large Hadron Collider (LHC) will allow to test the Standard Model at very high energies. Here we are interested in Quantum Chromodynamics (QCD) processes like forward jet production [1,2]. This process is of particular interest since it will allow for better understanding of partonic structure of the proton at extreme energies. The large center of mass energy at the LHC will require application of QCD resummation approaches capable to account for multiple scales in the problem [3,4]. Namely, one has to account for logarithms of type $\alpha_s^n \ln^m p_\perp/\Lambda_{QCD}$ where $\mathrm{p}_\perp$ is a transversal momentum of produced jet and another type of logarithms: $\alpha_s^n \ln^m 1/x$ [5,6] due to the fact that one of the incoming proton will be probed at very small longitudinal momentum fraction. The theoretical framework to resumme consistently both kinds of logarithmic corrections in pQCD is based on high-energy factorization at fixed transverse momentum [7,8,9]. This formulation depends on unintegrated parton distributions, obeying appropriate evolution equations, and short-distance, process-dependent matrix elements. The unintegrated-level evolution is given by evolution equations in rapidity, or angle, parameters. Different forms of the evolution, valid in different kinematic regions, are available, see [10,11,12,13], and references therein. In this article we apply recently obtained [14] results for hard matrix elements relevant for forward jet physics together with parton shower Monte Carlo generator CASCADE [15] for calculating observables related to forward jet phenomenon. The paper is organized as follows. In Sec. 2 we recall elements of high energy factorization framework relevant for our study. In Sec. 3 we present phenomenological results for jet production focusing on transversal momentum spectra and rapidity spectra.

2 Factorization kinematics and matrix elements relevant for forward jets

Forward jet associated with central jet is a process where after collision of two protons one collimated group of high $\mathrm{p}_\perp$ hadrons continues along the direction of one of colliding protons - forward detector region, while another group heads toward central region. The high $\mathrm{p}_\perp$ production at microscopic level can be understood as originating from collision of two partons where one of them which is almost on-shell carries large longitudinal momentum fraction $\xi_1 p_1$ of mother

proton (p_1) while the other one carries small longitudinal momentum fraction $\xi_2 p_2$ of the other proton (p_2) and is off-shell, where k_1, k_2, are the four momenta of initial state partons and p_3 and p_4 are four-momenta of final state partons.
The framework to describe forward jets is provided by high-energy factorization which was derived after observation of gluon exchange dominance at high energies . Similarly to collinear factorization it decomposes cross-section into parton density functions characterizing incoming hadrons $\phi(\xi, k_\perp)$ at fixed transverse momentum, and perturbatively calculable matrix elements $\widehat{\sigma}$. However, it resumes apart from large logarithms of hard scale also large logarithms coming from energy ordering. The formula for high energy factorization while applied to considered here process assumes form:

$$\sigma = \sum_a \int \; d\xi_1 \; d\xi_2 \; d^2k_T \; \phi_{a/A}(\xi_1, \mu^2) \; \widehat{\sigma}(\xi_1 \xi_2 S, Q_T, k_T, \varphi) \; \phi_{g^*/B}(\xi_2, k_T, \mu^2) \tag{1}$$

where as example we took total cross section and where sum runs over quark flavors. In high-energy factorization framework the parton densities are solutions to integro-differential evolution equations summing up perturbative terms with strong ordering condition in rapidity or angle of subsequently emitted partons. Such equations should be supplemented with some nonperturbative input distribution at initial value of ordering parameter which then is evolved with the evolution equation towards larger value of ordering parameter. The matrix elements relevant for high energy factorization describe hard subprocess where at least one of incoming partons is off mass shell. They are calculated by applying to scattering amplitudes $\mathcal{M}$ the high-energy eikonal projectors. In reference [14] matrix elements relevant for forward jets phenomenology have been calculated, in fully exclusive form.

3 Forward jet phenomenology at the LHC

We calculate forward jet cross sections for a typical experimental scenario at LHC. We require at least two jets with $E_\perp > 10$ GeV, where one jet has to be detected in the central region defined by $|\eta_c| < 2$ and the other jet is reconstructed in the forward region defined by $3 < |\eta| < 5$. The jets are reconstructed using the invariant $anti - k_t$-algorithm. We compare predictions from running the CASCADE Monte Carlo event generator with the PYTHIA [16] Monte Carlo event generator running in two modes: with and without multi-parton interactions. Both Monte Carlo generators simulate higher order QCD corrections with parton showers: CASCADE uses parton showers according to the CCFM evolution equation whereas PYTHIA uses DGLAP based parton showers.

3.1 Transverse momentum spectra

In Fig. 1 the prediction of differential cross section $\frac{d\sigma}{dp_\perp}$ is shown as obtained from CASCADE and PYTHIA. The cross sections predicted from both simulations at low momentum are of the similar order, however, at larger transverse momentum the CASCADE predicts a larger cross section what is clearly visible for central jets (Fig. 1 right). This behavior is expected since CASCADE uses matrix elements which are calculated within high energy factorization scheme allowing for harder transversal momentum dependence as compared to collinear factorization. Moreover CASCADE applies CCFM parton shower utilizing angle dependent evolution kernel which at small x does not lead to ordering in transverse momentum, and thus allow for more hard radiations during evolution as compared to based on leading order DGLAP splitting functions Monte Carlo generator PYTHIA. The parton shower has major influence on the side where the small x gluon enters the hard interaction, thus the jets in the central region are mainly affected by the parton shower.

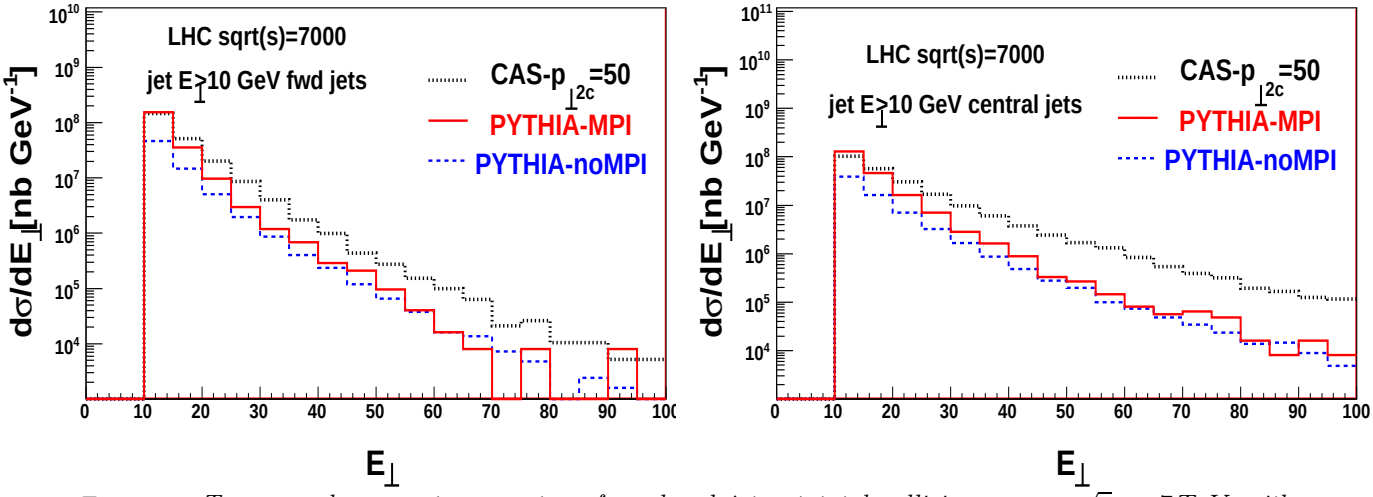

Figure 1: *Transversal momentum spectra of produced jets at total collision energy* $\sqrt{s} = 7\,TeV$ *with requirement that* $p_\perp > 10\,GeV$. *We compare predictions obtained from CASCADE and PYTHIA running in a multiple interactions mode and no multiple interactions mode. Spectrum of forward jets (left); spectrum of central jets (right).*

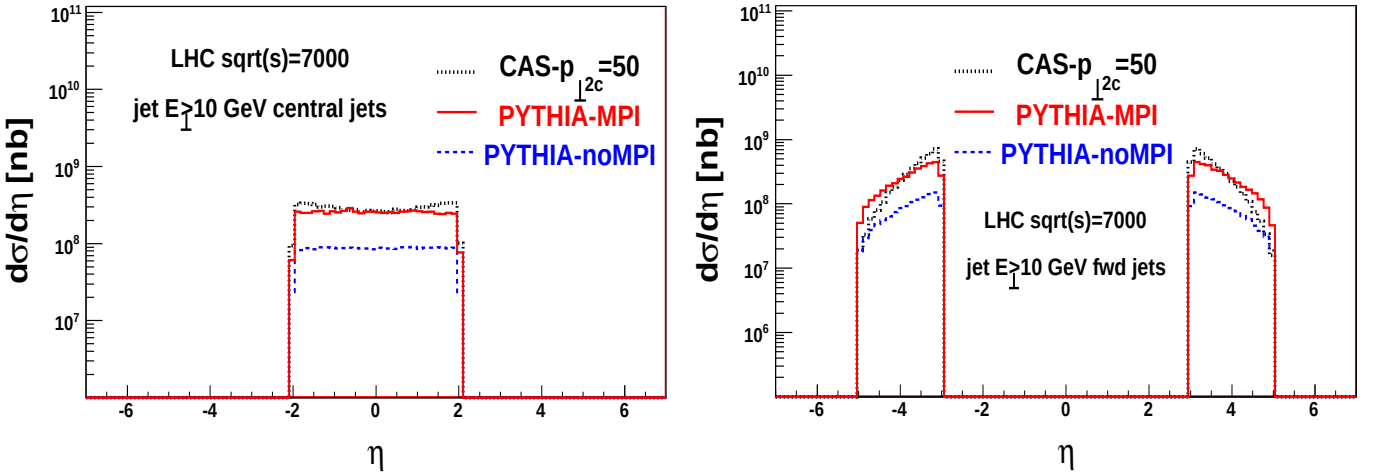

Figure 2: *Pseudorapidity spectra of produced jets at total collision energy* $\sqrt{s} = 7\,TeV$ *with requirement that* $p_T > 10GeV$. *We compare predictions obtained from CASCADE and PYTHIA running in multiple interactions mode and no multiple interactions mode. Spectrum of forward jets (left); spectrum of central jets (right).*

3.2 Rapidity dependence

In fig. 2 we show prediction for pseudorapidity dependence of the cross section in two regions $0 < |\eta| < 2$ and $3 < |\eta| < 5$. We see that results from CASCADE interpolate between PYTHIA with multiple interactions in the central region and PYTHIA without multiple interactions in the forward region. The result is due to the fact that CASCADE (because of angular ordering), and PYTHIA with multiple interactions (because of multi chain exchanges), predict more hadronic activity in the central rapidity region as compared to the collinear shower. In the remaining rapidity region cascade uses collinear parton shower of a similar type as in PYTHIA without

multiple interactions.

Acknowledgements

I would like to thank organizers for a very nice meeting. The results presented in this article have been obtained in collaboration with M. Deák, H. Jung, F. Hautmann.

References

1. X. Aslanoglou *et al.*, "Performance Studies of Prototype II for the CASTOR forward Calorimeter at Eur. Phys. J. C **52**, 495 (2007).
2. Z. J. Ajaltouni *et al.*, "Proceedings of the workshop: HERA and the LHC workshop series on the arXiv:0903.3861 [hep-ph].
3. W. J. Stirling, "Production Of Jet Pairs At Large Relative Rapidity In Hadron Hadron Nucl. Phys. B **423**, 56 (1994).
4. V. Del Duca, M. E. Peskin and W. K. Tang, Phys. Lett. B **306**, 151 (1993).
5. L. N. Lipatov, "Reggeization Of The Vector Meson And The Vacuum Singularity In Non-abelian Sov. J. Nucl. Phys. **23**, 338 (1976) [Yad. Fiz. **23**, 642 (1976)].
6. E. A. Kuraev, L. N. Lipatov and V. S. Fadin, Sov. Phys. JETP **45**, 199 (1977) [Zh. Eksp. Teor. Fiz. **72**, 377 (1977)].
7. S. Catani, M. Ciafaloni and F. Hautmann, Phys. Lett. B **242**, 97 (1990).
8. S. Catani, M. Ciafaloni and F. Hautmann, Nucl. Phys. B **366**, 135 (1991).
9. S. Catani, M. Ciafaloni and F. Hautmann, Phys. Lett. B **307**, 147 (1993).
10. J. Collins, PoS **LC2008**, 028 (2008).
11. F. Hautmann, Acta Phys. Polon. B **40**, 2139 (2009).
12. T. C. Rogers, "Next-to-Leading Order Hard Scattering Using Fully Unintegrated Parton Phys. Rev. D **78**, 074018 (2008) [arXiv:0807.2430 [hep-ph]].
13. F. Hautmann, Phys. Lett. B **655**, 26 (2007) [arXiv:hep-ph/0702196].
14. M. Deak, F. Hautmann, H. Jung and K. Kutak, JHEP **0909** (2009) 121.
15. H. Jung, Comput. Phys. Commun. **143**, 100 (2002).
16. T. Sjostrand, S. Mrenna and P. Z. Skands, JHEP **0605** (2006) 026

DGLAP versus BFKL in hard exclusive diffraction processes with large momentum transfer at HERA and LHC.

B.Blok
Department of Physics, Technion,
Haifa, Israel.

We study the energy dependence of the cross-section of the hard exclusive diffraction processes in QCD with large momentum transfer $-t$ in DGLAP approximation. We show that the results fully explain recent experimental data at HERA. Moreover, such processes at LHC energies and at $-t \geq M_V^2$ can be used as a "golden plate" ones to uncover the existence of perturbative pomeron, not masked by double logs.

1 Introduction.

In this talk [a] (see ref. [1,2] for detailed discussion) we consider the hard inelastic diffractive (HID) processes with large momentum transfer $-t$ and large rapidity gap, like $\gamma + p \to J/\psi +$ rapidity gap $+ X$ (Fig.1), that were studied at HERA recently [3,4,5]. We show that the specific model independent properties of the DGLAP approximation which are absent in the pQCD calculations of Pomeron exchange at large $-t$ (cf. refs. [6,7]) allow to describe the HERA data. In the DGLAP approximation the amplitudes are rapidly increasing with the incident energy since the $\log(x_0/x)$ terms that define the energy dependence of the amplitudes, are multiplied by large logarithms that arise from the integration over parton transverse momenta, leading to double log (DLA) asymptotics of the cross-section. Consider now the diffraction processes with large momentum transfer defined above. It was understood recently [2] that the cross section for diffractive charmonium photoproduction off a parton does not increase with energy for $-t \geq M_{J/\psi}^2$ in striking contrast with a rapid increase of the exclusive charmonium photoproduction at $t = 0$ since logs arising from the integration over parton transverse momenta are $\log(M_V^2/(Q_0^2 - t))$, and thus disappear at $-t \sim M_V^2$. This result is valid in all orders of DGLAP approximation and thus the cross section of diffractive charmonium production off a parton is energy independent at large $-t$.

The dominance of the double logarithmic terms in a wide kinematic region in the two scale processes, shows that the multiRegge dynamics could be revealed only in the very special one scale processes where the Q^2 evolution is suppressed. The large $-t$ ultraperipheral processes at LHC represent an example of such phenomena. In the kinematical range $-t \geq M_{J/\psi}^2$ the double logarithmic (DL) terms are absent. So the HID phenomena represent a golden plated process for uncovering the onset of the pQCD Pomeron. Switching from HERA to ultraperipheral processes at LHC significantly increases the kinematical window allowed for the multiRegge kinematics. In this case there are up to $9 \div 10$ units in rapidity available for the multiRegge gluons. An

[a] The talk is based on recent work with L. Frankfurt and M. Strikman [1,2]

unambiguous signature of these gluons will be a rapid increase of the diffractive cross section with energy in the region where DGLAP predicts the energy independent cross section.

2 DGLAP description of HID processes: theory versus experiment.

The quantative pQCD description of HID processes was recently developed in ref. [2]. The differential cross section in the kinematic range $-t \leq Q^2 + M_V^2$ is given by:

$$\frac{d\sigma}{dtdx_J} = \Phi(t, Q^2, M_V^2)^2 \frac{(4N_c^2 I_1(u))^2}{\pi u^2} G(x_J, t). \tag{1}$$

$$u = \sqrt{16N_c \log(x/x_J)\chi'},\ \chi' = \frac{1}{b}\log(\frac{\log((Q^2+M_V^2)/\Lambda^2)}{\log(-t+Q_0^2)/\Lambda^2}), \tag{2}$$

$$x_J = -t/(M_X^2 - m_p^2 - t), x \sim 3(Q^2+M_V^2)/(2s),\ b = 11 - 2/3N_f, N_c = 3, s = W_{\gamma p}^2$$

The factor $\Phi(t, Q^2, M_V^2)$ in eq.1 is the energy independent function. The second factor corresponds to the distribution of gluons in a parton, calculated in the DL approximation, The last factor in eq. 1 is the gluon structure function of the nucleon that can be calculated using e.g. CTEQ6 data (we neglect small contribution of the quark sea). In this equation M_X^2 is the invariant mass of the hadronic system produced due to the diffractive dissociation of a proton (see Fig. 1), $\Lambda = 300$ MeV, and $-t$ is the transverse momentum transfer. For the photoproduction processes $Q^2 = 0$. Let us stress that a characteristic feature of eq. 1 is the absence of the energy dependence at $-t \geq M_V^2$ (for $Q^2 = 0$).

Let us compare now the theoretical prediction with the recent experimental data. This comparison, as it was first noted in ref. [8], is not straightforward, since the HERA experiments, see e.g. [5], report the integral over invariant masses:

$$\begin{aligned} \frac{d\sigma(s,t)}{dt} &= \int_{B(s)}^{A(s)} \frac{dM_X^2}{(M_X^2 - t)^2} \frac{d^2\sigma}{dtdx_J}(x_J, s, t) \\ A(s) &= 0.05s - t, B(s) = 1\ \text{GeV}^2, \end{aligned} \tag{3}$$

In order to compare the theoretical prediction with the experimental data we calculated the integral 3 numerically for all $-t$. We present the main results of our calculations in Fig. 2. We calculate the logarithmic derivative

$$I(s,t) = \frac{1}{2}\frac{d\log(d\sigma/dt)}{d\log(s)}, \tag{4}$$

for $s = 2 \cdot 10^4$ GeV^2 (we denote this quantity as $\alpha_{I\!P}^{\text{eff}}(t)$), and compare it with the data for $I(s,t)$ presented in Fig. 9 in ref. [5]. It is referred to in ref. [5] as the "Pomeron" trajectory $\alpha_{I\!P}(t) - 1$. In the calculation we use CTEQ6M and CTEQ6L gluon parton distribution functions (pdf) $G(x_J, t)$. For small $-t$ ($-t \sim 2$ GeV^2) the curves for such "effective Pomeron" are given by the dashed lines, since for these $-t$ the integration region includes the range of $x/x_J \sim 0.1 - 1$, where nondiagonal (GPD) effects not included in our treatment may be important. In addition, the gluon pdf's for moderate Q^2 are subject to significant uncertainties. The results are clearly within the experimental errors. For comparison we also depict in Fig. 2 the logarithmic derivative of the double differential cross section, given by eq. 1, which corresponds to the "true" Pomeron in the triple Pomeron limit.

Existing calculations of cross sections of large t diffractive processes within perturbative Pomeron hypothesis, cf [7] predict qualitatively different interplay of t and W dependence compared to DGLAP. They predict that dependence on energy of the gluon pdf of the proton should be independent of Q^2 and perturbative Pomeron trajectory only weakly depends on $-t$,decreasing like $\alpha_s(M_V^2 - t)$, in variance with the HERA data [5].

Let us stress the crucial role of the increase of the rate of energy dependence of $G(x_J, t)$ with the increase of $-t$, that is crucial for the explanation for the HERA data, in particular the increase of $\alpha_{I\!P}$ with $-t$. This property is esily explained by DGLAP, but is absent in BFKL.

Observation that the pQCD Pomeron regime does not set in for the HERA kinematics can be understood as the consequence of the constraints due to the energy-momentum conservation (see refs. [1,2] for references and more detailed discussion). There must be at least $2 \div 2.5$ units in rapidity for each gluon radiation in the multiRegge kinematics. This means that for the radiation of even one such gluon a rapidity window of at least $4 \div 5$ units in rapidity is required. One should add to this interval the 4-5 units of rapidity due to impact-factor and proton fragmentation. Thus it seems that there is no room in the HERA kinematics for the gluon radiation in the multiRegge kinematics.

3 MultiRegge gluons in HID processes with large momentum transfer $-t$ at LHC.

Consider now the ultraperipheral processes at the LHC (for a review see [9]). In this case one may have up to 14 units in rapidity, i.e. up to 9 units in rapidity may be available for a ladder describing gluon-parton scattering. A simple estimate suggests that for small $-t$ most of the kinematic range (even at the LHC) will be dominated by double However, as it is clear from the previous subsection, for $-t \geq M_V^2$ the double logarithmic terms are absent, and the entire increase of the double differential cross section $d^2\sigma/(dtdx_J)$ will be due to multi Regge gluons. In Fig. 3 we show(for illustrative purposes only), the behavior of the $d^2\sigma/(dtdx_J)$ as a function of energy using currently popular pQCD Pomeron models with intercept $\alpha_{I\!P}^{\rm BFKL/resummed}(t) - 1 \sim 0.2$.

4 Conclusion

We have shown that DGLAP predictions are in a good agreement with the behavior of HID processes observed at HERA. We found that the ultraperipheral collisions at LHC are a unique place where the onset of gluon radiation in the multiRegge kinematics may be observed in the near future.

References

1. B. Blok, L. Frankfurt, M. Strikman, arXiv:1002.3048[hep-ph] , Phys. Lett. B, in press
2. B. Blok, L. Frankfurt, M. Strikman,Eur.Phys.J.C67:99-109,2010.
3. S. Chekanov *et al.* [ZEUS Collaboration], Eur. Phys. J. C **26**, 389 (2003).
4. A. Aktas et al [H1 Collaboration] Phys. Lett. B **568**, 205 (2003); ibid B **638**, 422 (2006).
5. S. Chekanov *et al.* [ZEUS Collaboration], arXiv:0910.1235 [hep-ex].
6. L. N. Lipatov, Sov. Phys. JETP **63** (1986) 904.
7. R. Enberg, J. R. Forshaw, L. Motyka and G. Poludniowski, JHEP **0309**, 008 (2003), ibid **0312**, 002 (2003).
8. L. Frankfurt, M. Strikman and M. Zhalov, Phys. Lett. B **670** (2008) 32.
9. K. Hencken *et al.* Phys. Rept. **458** (2008) 1.

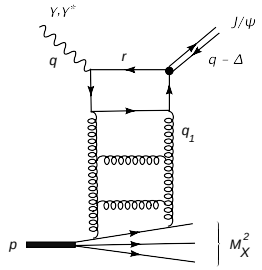

Figure 1: The Feynman diagram describing the double diffractive process in the triple "Pomeron" limit in pQCD (there is also a cross diagram, not depicted explicitly.

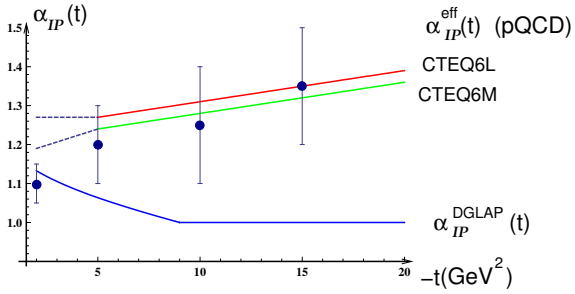

Figure 2: The comparison between the experimental data and theoretical prediction for the HID cross section at HERA for the "effective Pomeron" $\alpha_{I\!P}^{\rm eff}(t)$, i.e. (1/2) logarithmic derivative of the cross section $d\sigma/dt$, obtained after integrating between the energy dependent cuts, as given in the text. The dashed curve means large theoretical uncertainties in the corresponding kinematic region. The values are given at for $W_{\gamma p} = 150$ GeV. In the same figure we depict also "true (DGLAP) "Pomeron", i.e. logarithmic derivative $\alpha_{I\!P}(t)^{\rm DGLAP} = \frac{1}{2}\frac{d(d^2\sigma/(dtdx_J))}{d\log(x/x_J)}$ at this energy. $\Lambda_{\rm QCD} = 300$ MeV.

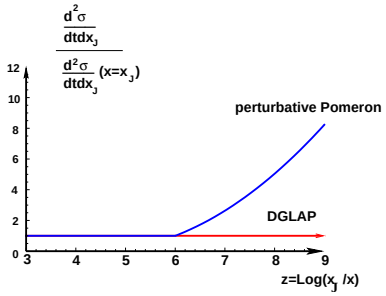

Figure 3: The increase of the cross section $d\sigma/(dtdx_J)$ with energy ($z = Log(x/x_J)$) at LHC in DGLAP and perturbative "Pomeron" scenarios (for fixed x_J)

AdS black disk model for small-x DIS

Lorenzo Cornalba, Miguel S. Costa (a), João Penedones (b)
(a) Centro de Física do Porto e Departamento de Física e Astronomia da Faculdade de Ciências da Universidade do Porto, Rua do Campo Alegre 687, 4169-007 Porto, Portugal
(b) Kavli Institute for Theoretical Physics, University of California, Santa Barbara, CA 93106-4030, USA

Using the approximate conformal invariance of QCD at high energies we consider a simple AdS black disk model to describe saturation in DIS. Deep inside saturation the structure functions have the same power law scaling, $F_T \sim F_L \sim x^{-\omega}$, where ω is related to the expansion rate of the black disk with energy. Furthermore, the ratio F_L/F_T is given by the universal value $\frac{1+\omega}{3+\omega}$, independently of the target.

1 Introduction

Recently, there has been a growing interest in applications of the AdS/CFT duality to Deep Inelastic Scattering (DIS). Here, we shall summarize the main results obtained in [1].

We shall focus on the kinematical limit of fixed Q and $x \ll 1$, which corresponds to the Regge limit of large center of mass energy, $s \approx Q^2/x$, with other kinematical invariants fixed. In this kinematical window one observes a power like growth in $1/x$ of the hadron structure functions [2]. The hadron becomes a dense gluon medium so that the picture of the hadron made of weakly interacting partons is no longer valid. Although the coupling α_s may still be small, say for hard probes with $Q \gtrsim 1\,\mathrm{GeV}$, to understand low x structure functions one needs to include diagrams such as those of order $(\alpha_s \ln(1/x))^n$ due to the kinematical enhancement. Thus, for hard probes, low x DIS is the ideal ground to explore the approximate conformal symmetry of QCD in a situation where the gluon density inside the hadron is so high that non-linear effects are nevertheless important.

2 AdS Black Disk

To define the scattering amplitude of an off-shell photon by a scalar target in a conformal field theory, we consider the momentum space correlation function,

$$(2\pi)^4\,\delta\left(\sum k_j\right)\,i\,T^{ab}(k_j) = \left\langle j^a(k_1)\mathcal{O}(k_2)j^b(k_3)\mathcal{O}(k_4)\right\rangle\,,$$

involving a conserved current j^a and a scalar primary operator $\mathcal{O}$ of dimension Δ. We shall be interested in the limit of large $s = -(k_1+k_2)^2$ with fixed momentum transfer $t = -(k_1+k_3)^2 = -q_\perp^2$ and virtualities k_i^2. As shown in [3,4,5], this limit is conveniently described by the impact parameter representation

$$T^{ab}(k_j) \approx 2is \int dl_\perp\, e^{iq_\perp\cdot l_\perp} \int \frac{dr}{r^3}\,\frac{d\bar{r}}{\bar{r}^3}\,\Psi^{ab}{}_{\mu}{}^{\tau}(r)\;\Phi(\bar{r})\;\left[1-e^{i\chi(S,L)}\right]^{\mu}_{\ \tau}\,, \tag{1}$$

where the phase shift $\chi^{\mu}_{\ \tau}$ is a tensor that encodes all the dynamical information and depends on

$$S = r\bar{r}s \ , \qquad \cosh L = \frac{r^2 + \bar{r}^2 + l_\perp^2}{2r\bar{r}} \, .$$

The scalar function Φ is associated with the operator $\mathcal{O}$ and the tensor function $\Psi^{ab}_{\ \ \mu}{}^{\tau}$ with the current operator j^a. Their explicit form was given in [5]. It is important to note that this representation is valid for any value of the coupling, since it relies only on conformal invariance.

The above conformal representation is quite natural from the view point of the dual AdS scattering process, with transverse space given by the three-dimensional hyperbolic space H_3, whose boundary is the physical transverse space $\mathbb{R}^2$. Using Poincaré coordinates,

$$ds^2(H_3) = \frac{dr^2 + ds^2(\mathbb{R}^2)}{r^2} \ ,$$

we identify L with the geodesic distance between two points that are separated by $l_\perp$ along $\mathbb{R}^2$ and have radial coordinates r and $\bar{r}$. The variable S measures the local energy squared of the scattering process in AdS. The Greek indices μ and τ in (1) label tangent directions to H_3, which are the physical polarizations of the AdS gauge field dual to the conserved current j^a. The functions

$$\Psi^{ab\mu\tau}(r) = \psi^{a\mu}_{in}(r)\, \psi^{b\tau}_{out}(r) \, , \qquad \Phi(\bar{r}) = \phi_{in}(\bar{r})\, \phi_{out}(\bar{r}) \, ,$$

are given by the product of the radial part of the incoming and outgoing dual AdS fields. These functions are non-normalizable because they are produced by a plane wave source created by the dual operator at the boundary.

We shall consider a black disk model defined by a phase shift in the impact parameter representation (1) given by

$$\Big[1 - e^{i\chi(S,L)}\Big]^{\mu}_{\ \tau} = \Theta\big(L_s(S) - L\big)\, \delta^{\mu}_{\ \tau} \ ,$$

where the radius L_s of the disk increases with energy as

$$L_s(S) \approx \omega \log S \ . \tag{2}$$

Note that the size of the disk is independent of the dual AdS gauge field polarization, so that this simple model is characterized by the single parameter $\omega > 0$.

This model appears naturally in the approximation of single Reggeon exchange in a conformal field theory. In this case, the phase shift is given by [5]

$$\chi^{\mu}_{\ \tau} \approx \frac{1}{N^2} \int d\nu \ S^{j(\nu)-1} \left[\beta(\nu)\, \delta^{\mu}_{\ \tau} + \tilde{\beta}(\nu) \left(\nabla^{\mu}\nabla_{\tau} - \frac{1}{3}\, \delta^{\mu}_{\ \tau}\right)\right] \Omega_{i\nu}\,(L) \ , \tag{3}$$

where ∇_μ is the Levi-Civita connection on H_3 and $\Omega_{i\nu}(L) = \nu \sin \nu L/(4\pi^2 \sinh L)$ is a basis of harmonic functions on H_3. The Regge spin $j = j(\nu)$ and the residues $\beta(\nu)$ and $\tilde{\beta}(\nu)$ depend on the 't Hooft coupling $\bar{\alpha}_s = \alpha_s N/\pi$ and are even functions of ν. This is exact in a conformal gauge theory like $\mathcal{N} = 4$ SYM and approximate in QCD at weak coupling.

The explicit form of the Regge residues $\beta(\nu)$ and $\tilde{\beta}(\nu)$ was computed to leading order in perturbation theory in [5]. These residues are purely imaginary and satisfy $\mathrm{Im}\, \chi^{\mu}_{\ \tau} > 0$. For fixed S, the phase shift $\chi(S, L)$ vanishes at large impact parameter $L \to \infty$. As the impact parameter decreases the phase will grow and reach order unity at $L_s(S)$. For impact parameters $L < L_s$ the amplitude will then be that of an absorptive black disk and the details in the form of the phase shift for $L < L_s$ are not important to the computation of the hadronic tensor in (4). To estimate the size L_s of the AdS black disk one can do a saddle point approximation to the ν integral in (3), exactly as in [4]. At weak coupling the Reggeon is the perturbative BFKL hard pomeron [6] and one obtains $\omega \approx 2.44\bar{\alpha}_s$. This value of ω is actually to large to match experiments, and next to leading order correction to the BFKL spin are important.

3 Deep Inelastic Scattering

The total DIS cross section, and corresponding hadron structure functions, are related to the hadronic tensor

$$W^{ab}(k_j) = i \int d^4y\, e^{ik_1\cdot y} \langle k_2 | \mathrm{T}\left\{ j^a(y) j^b(0)\right\} |k_2\rangle\,,$$

where j^a is the electromagnetic current and $|k_2\rangle$ is the target hadron state of momentum k_2. We define the virtuality $Q^2 = k_1^2$, target mass $M^2 = -k_2^2$ and Bjorken

$$x = -\frac{Q^2}{2k_1\cdot k_2} \approx \frac{Q^2}{s}\,.$$

Lorentz invariance and conservation restricts W^{ab} to

$$W^{ab} = \left(\eta^{ab} - \frac{k_1^a k_1^b}{k_1^2}\right)\Pi_1 + \frac{2x}{Q^2}\left(k_2^a + \frac{k_1^a}{2x}\right)\left(k_2^b + \frac{k_1^b}{2x}\right)\Pi_2\,.$$

The structure functions F_i satisfy $2\pi F_i = \mathrm{Im}\,\Pi_i$.

At zero momentum transfer we can use the representation (1) to write the hadronic tensor as

$$W^{ab} \approx 4\pi i s \int \frac{dr}{r^2}\,\frac{d\bar r}{\bar r^2}\,\Psi^{ab}{}_{\mu}{}^{\tau}(r)\;\Phi(\bar r) \int_{|\ln \bar r/r|}^{+\infty} dL \sinh L \left[e^{i\chi(S,L)} - 1\right]^{\mu}_{\ \tau}\,, \tag{4}$$

where we did the angular integral in the impact parameter $l_\perp$ and traded $|l_\perp|$ in the radial integration for the AdS impact parameter L. Note that $\Phi(\bar r) = |\phi(\bar r)|^2$, where now $\phi(\bar r)$ is the radial part of the normalizable AdS wave function dual to the state $|k_2\rangle$. This wave function is localized in the IR around $\bar r \sim 1/M$. Its explicit form in the IR region, where space is no longer AdS, will not be important in what follows, because we shall consider a hard probe localized near the AdS boundary.

The black disk model of the previous section gives

$$W^{ab} \approx -2\pi i s \int \frac{dr}{r^2}\,\frac{d\bar r}{\bar r^2}\,\Psi^{ab}{}_{\mu}{}^{\mu}(r)\;\Phi(\bar r)\left[(sr\bar r)^{\omega} + (sr\bar r)^{-\omega} - \frac{r}{\bar r} - \frac{\bar r}{r}\right]\,. \tag{5}$$

At very low x the first term dominates and we have

$$W^{ab} \approx -2\pi i s^{1+\omega} \int \frac{dr}{r^{2-\omega}}\,\Psi^{ab}{}_{\mu}{}^{\mu}(r) \int \frac{d\bar r}{\bar r^{2-\omega}}\,\Phi(\bar r)\,. \tag{6}$$

To give the explicit form of Ψ it is convenient to write

$$k_1 = \left(\sqrt{s}, -\frac{Q^2}{\sqrt{s}}, 0\right)\,, \qquad k_2 = \left(\frac{M^2}{\sqrt{s}}, \sqrt{s}, 0\right)\,, \tag{7}$$

in light-cone coordinates $(+,-,\perp)$. Then, following [5],

$$\Psi^{ab}{}_{\mu}{}^{\mu}(r) = -\frac{\pi^2}{6} C\, r^2 \int_0^\infty du dv\, e^{-u-v-\frac{Q^2r^2}{4u}-\frac{Q^2r^2}{4v}} \times \begin{pmatrix} \frac{sr^2}{4uv} & \frac{v-1}{u} & 0 \\ \frac{u-1}{v} & \frac{4(u-1)(v-1)}{sr^2} & 0 \\ 0 & 0 & \mathbb{I} \end{pmatrix}\,, \tag{8}$$

where the matrix elements are also ordered by the light-cone coordinates. In particular, we have

$$\Psi^{ij}{}_{\mu}{}^{\mu}(r) = -\delta^{ij}\frac{\pi^2}{6}\,CQ^2r^4K_1^2(Qr)\,, \qquad \Psi^{++}{}_{\mu}{}^{\mu}(r) = -\frac{\pi^2}{6}\,Csr^4K_0^2(Qr)\,,$$

where i, j run over the transverse space $\mathbb{R}^2$ directions and K is the Bessel function of the 2nd kind. The constant C is determined by the conformal two point function

$$\langle j^a(y) j^b(0)\rangle = C\,\frac{y^2\eta^{ab} - 2y^a y^b}{(y^2+i\epsilon)^4}\ .$$

By dimensional analysis the integral over $\bar{r}$ in (6) is

$$\int \frac{d\bar{r}}{\bar{r}^{2-\omega}}\,\Phi(\bar{r}) = \frac{h(\omega)}{M^{1+\omega}}\,,$$

where $h(\omega)$ is a dimensionless function that depends on the details of the IR physics associated to the target hadron wave function but does not affect the small x scaling behavior of the structure functions in the AdS black disk model. Indeed, taking the imaginary part of

$$W^{ij} = \delta^{ij}\Pi_1\ , \qquad W^{++} \approx \frac{1}{2x^2}\left(\Pi_2 - 2x\Pi_1\right)\ ,$$

equation (6) gives

$$F_2 - 2xF_1 \approx x^{-\omega}\,(Q/M)^{1+\omega}\,\frac{\pi^{\frac{5}{2}}\Gamma^3\left(\frac{3+\omega}{2}\right)C\,h(\omega)}{12\Gamma\left(\frac{4+\omega}{2}\right)}\,,$$

$$F_1 \approx \left(\frac{Q}{xM}\right)^{1+\omega}\frac{\pi^{\frac{5}{2}}\Gamma\left(\frac{5+\omega}{2}\right)\Gamma\left(\frac{3+\omega}{2}\right)\Gamma\left(\frac{1+\omega}{2}\right)C\,h(\omega)}{24\,\Gamma\left(\frac{4+\omega}{2}\right)}\ .$$

Moreover, our ignorance about the target hadron wave function drops out from the ratio

$$\frac{F_L}{F_T} = \frac{1+\omega}{3+\omega}\ . \tag{9}$$

We conclude that, in the AdS black disk model and at small x, F_L/F_T attains a universal value uniquely fixed by the exponent ω that controls the growth of the structure functions at small x. We emphasize that this universal value is independent of the nature of the target hadron. Moreover, since the current wave function Ψ localizes in the UV region $r \lesssim 1/Q$, our result should be robust against deviations from conformal symmetry in the IR.

Acknowledgments

This work was partially supported by grants CERN/FP/109306/2009, SFRH/BPD/34052/2006, NSF PHY05-51164 and by the FCT POCI programme.

References

1. L. Cornalba, M. S. Costa and J. Penedones, to appear in Phys. Rev. Lett., arXiv:1001.1157 [hep-ph].
2. L. V. Gribov, E. M. Levin and M. G. Ryskin, Phys. Rept. **100** (1983) 1; L. D. McLerran and R. Venugopalan, Phys. Rev. D **49** (1994) 2233; Phys. Rev. D **49** (1994) 3352.
3. L. Cornalba, M. S. Costa, J. Penedones and R. Schiappa, Nucl. Phys. B **767** (2007) 327.
4. L. Cornalba and M. S. Costa, Phys. Rev. D **78** (2008) 096010.
5. L. Cornalba, M. S. Costa and J. Penedones, *Deep Inelastic Scattering in Conformal QCD*, `0911.0043 [hep-th]`.
6. V. S. Fadin, E. A. Kuraev and L. N. Lipatov, Phys. Lett. **B60** (1975) 50–52; E. A. Kuraev, L. N. Lipatov and V. S. Fadin, Sov. Phys. JETP **45** (1977) 199–204; Ya. Balitsky and L. N. Lipatov, Sov. J. Nucl. Phys. **28** (1978) 822–829.

SEARCH FOR NEW PHYSICS AT HERA USING COMBINED H1 AND ZEUS DATA

S.V. LEVONIAN
on behalf of the H1 and ZEUS Collaborations
Deutsches Elektronen-Synchrotron DESY, Notkestraße 85, 22607 Hamburg, Germany

Two event classes having high sensitivity to New Physics are studied using combined $e^{\pm}p$ data sample collected by H1 and ZEUS experiments at HERA collider in the period 1994 – 2007. The data correspond to an integrated luminosity of about 1 fb^{-1}. Although interesting events are observed at high P_T tails of distributions both for events with at least two high transverse momentum leptons and events containing an isolated lepton and missing transverse momentum, no significant deviations from Standard Model are found. The total single W boson production cross section at $\sqrt{(s)} = 317$ GeV is measured as 1.06 ± 0.16 (stat.) $\pm$ 0.07 (sys.) pb, in agreement with the SM expectation of 1.26 ± 0.19 pb.

1 Introduction

HERA, so far the only *ep* collider in the world, provides a unique opportunity to search for new physics beyond the Standard Model. Promising experimental topologies for this purpose are events with one or more high P_T isolated leptons in the final state, as well as in combination with missing transverse momentum. Such events have clean signature, low Standard Model expectation and hence high sensitivity to novel phenomena. After 15 years of successful data taking two collider experiments, H1 and ZEUS, have collected 0.5 fb^{-1} of data each. In order to fully exploit HERA potential and to benefit from increasing statistical significance combined analyzes of such rare final states were performed in a common phase space, resulting in a total integrated luminosity of about 1 fb^{-1}. Cross sections measured by H1 and ZEUS are combined bin by bin using weighted average.

2 Multi-Lepton Events with High Transverse Momentum

Within the Standard Model (SM) the production of high P_T multi-lepton final states in ep collisions proceeds predominantly via $\gamma\gamma$ interactions. The clean experimental signature together with small and precisely calculable SM cross section provides high sensitivity to possible contributions of physics beyond the SM. Measurements of multi-lepton production at HERA have been performed by the H1 [1] and ZEUS [2] collaborations. A combined analysis of H1 and ZEUS data is performed in a common phase space in which both detectors have high and well understood acceptance, and using full statistics available to both experiments [3].

Electrons are identified in the polar-angle range $5^o < \theta_e < 175^o$, with $E_e > 10$ GeV for $\theta_e < 150^o$ and $E_e > 5$ GeV for $\theta_e > 150^o$. Muons are identified in the range $20^o < \theta_\mu < 160^o$ with $P_T^\mu > 2$ GeV. All lepton candidates are required to be isolated with respect to each other by at least 0.5 units in $\eta - \phi$ plane (where pseudorapidity η is defined as $\eta = -\ln\tan(\theta/2)$). At least two leptons are required in the central region ($20^o < \theta_e < 150^o$): one with $P_T^l > 10$ GeV and the other having $P_T^l > 5$ GeV. Additional leptons identified according to the criteria given above may be present in the event. Selected events are then classified into mutually exclusive samples with different number and flavour of lepton candidates: $ee, \mu\mu, e\mu, eee, e\mu\mu$.

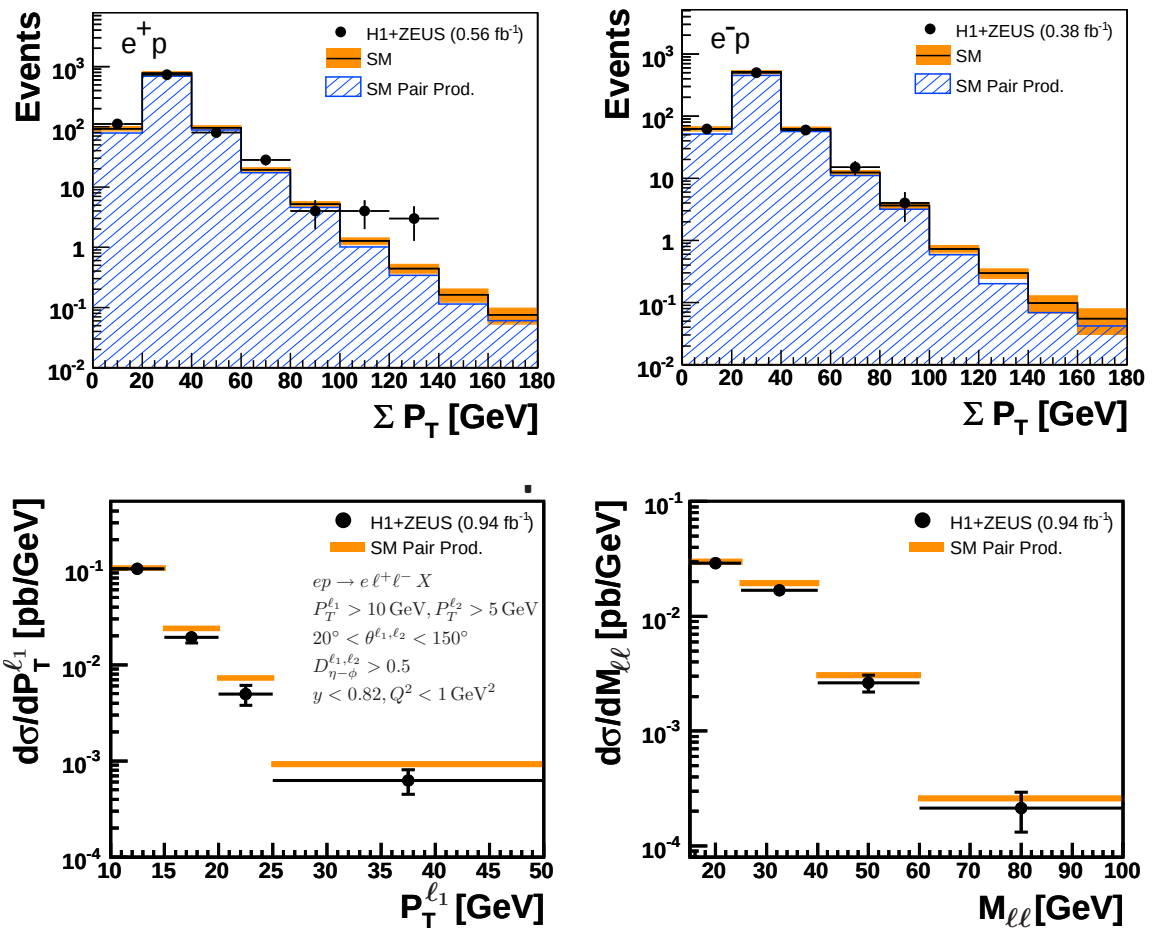

Figure 1: Multi-Lepton events at HERA. Top: the distribution of the scalar sum $\sum P_T$ for combined multi-lepton event topologies in e^+p and e^-p data. Bottom: The cross section for lepton pair photoproduction in a restricted phase space as a function of the leading lepton transverse momentum P_T^{l1} and the invariant mass of the lepton pair M_{ll}. The total error bars represent the statistical and systematic uncertainties added in quadrature. The bands represent the uncertainty in the SM prediction, dominated by the $\gamma\gamma$ process.

Table 1: Observed and predicted multi-lepton event yields for $\sum P_T > 100$ GeV. Di-lepton and tri-lepton events are combined. The uncertainties on the predictions include model uncertainties and experimental systematic uncertainties added in quadrature.

Data sample	Data	SM	Pair Production (GRAPE)	NC DIS + QEDC
e^+p (0.56 fb^{-1})	7	1.94 ± 0.17	1.52 ± 0.14	0.42 ± 0.07
e^-p (0.38 fb^{-1})	0	1.19 ± 0.12	0.90 ± 0.10	0.29 ± 0.05
All (0.94 fb^{-1})	7	3.13 ± 0.26	2.42 ± 0.21	0.71 ± 0.10

A good overall agreement is observed with the SM in all event topologies [3]. Some excess over SM expectation with significance of $\sim 2.6\sigma$ is observed for events with high $\sum P_T^l > 100$ GeV, but only in e^+p data, as can be seen in Table 1 and Figure 1 (top). The lepton pair production cross section of $0.66 \pm 0.03(stat.) \pm 0.03(sys.)$ pb is measured in the phase space dominated by $\gamma\gamma$ interactions, in agreement with the SM prediction of 0.69 ± 0.02 pb. The differential cross sections are also measured as a function of leading lepton $P_T^{l_1}$ and the invariant mass of the lepton pair M_{ll}, as shown in Figure 1 (bottom).

3 Events with Isolated Lepton and Missing Transverse Momentum

Events containing isolated high P_T lepton and large missing transverse momentum, $P_T^{\rm miss}$, is a typical signature in many BSM extensions. In the SM main source of such events in ep collisions is a single W boson production with subsequent decay via leptonic channels. Events of such topology have been observed at HERA by both H1 [4] and ZEUS [5]. In order to increase sensitivity to new physics a combined analysis of the full available data set has been performed in the common phase space [6].

The event selection requires an isolated lepton (e or μ) with $P_T^l > 10$ GeV to be in the central region of the detector $15^o < \theta_e < 120^o$ together with the presence of the hadronic jet reconstructed using k_T algorithm. In addition the event must exhibit significant missing transverse momentum, $P_T^{\rm miss} > 12$ GeV. Further cuts are then applied to minimize SM background [6].

The result of the analysis is summarized in the Table 2. In general, a good agreement is observed between the data and the SM prediction, in which the signal component is dominated by single W production. The lepton-neutrino transverse mass distribution as shown in Figure 2 (left) exhibits a characteristic Jacobean peak around W mass value. A small excess of the data in the region of high transverse momentum of the hadronic final state, $P_T^X > 25$ GeV, which was observed in the H1 analysis [4] almost completely vanishes in the combined HERA data sample. The single W production cross section is measured as 1.06 ± 0.16 (stat.) ± 0.07 (sys.) pb, in

Table 2: Summary of the combined H1 and ZEUS search for events with an isolated electron or muon and missing transverse momentum for the full HERA data set as compared to the SM expectation. The quoted uncertainties contain statistical and systematic errors added in quadrature.

H1+ZEUS 1994–2007 $e^\pm p$ 0.98 fb^{-1}		Data	SM Expectation	SM Signal	Other SM Processes
Electron	Total	61	69.2 ± 8.2	48.3 ± 7.4	20.9 ± 3.2
	$P_T^X > 25$ GeV	16	13.0 ± 1.7	10.0 ± 1.6	3.1 ± 0.7
Muon	Total	20	18.6 ± 2.7	16.4 ± 2.6	2.2 ± 0.5
	$P_T^X > 25$ GeV	13	11.0 ± 1.6	9.8 ± 1.6	1.2 ± 0.3
Combined	Total	81	87.8 ± 11.0	64.7 ± 9.9	23.1 ± 3.3
	$P_T^X > 25$ GeV	29	24.0 ± 3.2	19.7 ± 3.1	4.3 ± 0.8

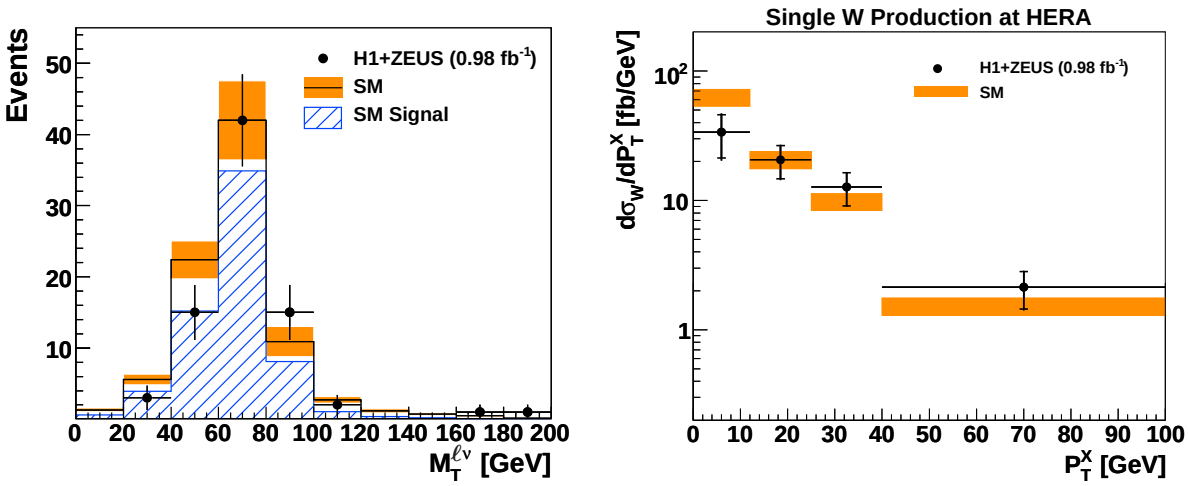

Figure 2: Left: The lepton-neutrino transverse mass $M_T^{l\nu}$ of events with an isolated electron or muon and missing transverse momentum. The data (points) are compared to the SM expectation (open histogram). The signal component of the SM expectation, dominated by single W production, is shown as the hatched histogram. The total uncertainty on the SM expectation is shown as the shaded band. Right: The single W production cross section as a function of the hadronic transverse momentum, P_T^X, measured using the combined H1 and ZEUS data at a centre–of–mass energy of $\sqrt{s} = 317$ GeV. The inner error bar represents the statistical error and the outer error bar indicates the statistical and systematic uncertainties added in quadrature. The shaded band represents the uncertainty on the SM prediction.

agreement with SM prediction of 1.26 ± 0.19 pb. The cross section is also measured as a function of P_T^X, as shown in Fig. 2 (right).

4 Summary

Production of multi-lepton events with high transverse momenta and events containing isolated lepton with $P_T^{\rm miss}$ in ep collisions has been studied. Combined H1 and ZEUS analyzes were performed in a common phase space, to take advantage of complete available HERA high energy data. Good overall agreement is observed with the SM predictions. The cross sections for multi-lepton and single W production in ep collisions at average $\sqrt{s} = 317$ GeV are measured with a greater precision as compared to previously published individual H1 and ZEUS results. A few interesting events are observed by both H1 and ZEUS in e^+p data at high P_T and high mass region where the SM expectation is low.

We thus conclude, that the Standard Model survived full combined HERA data and is now waiting for next challenges expected at the LHC.

References

1. F. D. Aaron *et al*, H1 Collab., *Phys. Lett.* B **668**, 268 (2008).
2. S. Chekanov *et al*, ZEUS Collab., *Phys. Lett.* B **680**, 13 (2009).
3. F. D. Aaron *et al*, H1 and ZEUS Collab., *JHEP* **10**, 013 (2009).
4. F. D. Aaron *et al*, H1 Collab., *Eur. Phys. J.* C **64**,251 (2009).
5. S. Chekanov *et al*, ZEUS Collab., *Phys. Lett.* B **672**, 106 (2009).
6. F. D. Aaron *et al*, H1 and ZEUS Collab., *JHEP* **03**, 035 (2010).

9.
Heavy Ions

Long range phenomena in heavy ion collisions observed by the PHOBOS experiment

Krzysztof Woźniakfor the PHOBOS Collaboration [a]
Institute of Nuclear Physics PAN, Kraków, Poland

The PHOBOS experiment at RHIC has measured large samples of Au+Au and Cu+Cu collisions using a detector with uniquely large angular acceptance. These data enable studies of particle production over a very wide pseudorapidity interval which reveal unexpected features. In the analysis of correlations with a high-p_T trigger particle ($p_T > 2.5$ GeV/c) a ridge extending at least 4 units of pseudorapidity was found. The results on forward-backward and two-particle correlations suggest that particles are produced in very large clusters which are wider in pseudorapidity than is expected for isotropic decays. Explanation of these experimental results requires models in which both short-range and long-range correlations are present.

Since the year 2000 at the Relativistic Heavy Ion Collider (RHIC), collisions of heavy ions at the highest energies have been measured and analysed. Several phenomena found in these studies manifest creation of a new type of matter, strongly interacting Quark-Gluon Plasma (sQGP). Most noticeable are the absorption of partons observed as suppression of high-p_T particles or jets and the collective effects visible as a strong elliptic flow [?]. Better understanding of properties of the matter created in heavy ion collisions and a search for signs of potential phase transition require detailed analysis of many observables and studies of correlations between them.

The PHOBOS experiment measured all types of collisions available at RHIC using a detector optimized for registering charged particles2 in almost full solid angle - with the multiplicity detector covering uniquely wide range $|\eta| < 5.4$. In the spectrometer, momenta of about 1% of charged particles were determined. Using this detector it was possible to measure the yields of particles with extremally small transverse momenta (starting from 30 MeV/c for pions). The comparison of yields of charged particles at high-p_T in $d + Au$ and $Au + Au$ collisions clearly shows that partons created in hard scattering of quarks or gluons interact in the dense matter created in the central $Au + Au$ collisions. Usually at least one of back-to-back emitted partons is stopped and only a jet or a high-p_T particle originating from the second parton is registered.

The analysis [?] of the correlations between a trigger particle with $p_T > 2.5$ GeV/c and other

[a] B.Alver[4], B.B.Back[1], M.D.Baker[2], M.Ballintijn[4], D.S.Barton[2], R.R.Betts[6], A.A.Bickley[7], R.Bindel[7], W.Busza[4], R.Bindel[7], W.Busza[4], A.Carroll[2], Z.Chai[2], V.Chetluru[6], M.P.Decowski[4], E.García[6], T.Gburek[3], N.George[2], K.Gulbrandsen[4], C.Halliwell[6], J.Hamblen[8], I.Harnarine[6], M.Hauer[2], C.Henderson[4], D.J.Hofman[6], R.S.Hollis[6], R.Hołyński[3], B.Holzman[2], A.Iordanova[6], E.Johnson[8], J.L.Kane[4], N.Khan[8], P.Kulinich[4], C.M.Kuo[5], W.Li[4], W.T.Lin[5], C.Loizides[4], S.Manly[8], A.C.Mignerey[7], R.Nouicer[2], A.Olszewski[3], R.Pak[2], A.Olszewski[3], R.Pak[2], C.Reed[4], E.Richardson[7], C.Roland[4], G.Roland[4], J.Sagerer[6], H.Seals[2], I.Sedykh[2], C.E.Smith[6], M.A.Stankiewicz[2], P.Steinberg[2], G.S.F.Stephans[4], A.Sukhanov[2], A.Szostak[2], M.B.Tonjes[7], A.Trzupek[3], C.Vale[4], G.J.van Nieuwenhuizen[4], S.S.Vaurynovich[4], R.Verdier[4], G.I.Veres[4], P.Walters[8], E.Wenger[4], D.Willhelm[7], F.L.H.Wolfs[8], B.Wosiek[3], K.Woźniak[3], S.Wyngaardt[2], B.Wysłouch[4]
[1] Argonne National Laboratory, Argonne, IL 60439-4843, USA
[2] Brookhaven National Laboratory, Upton, NY 11973-5000, USA
[3] Institute of Nuclear Physics PAN, Kraków, Poland
[4] Massachusetts Institute of Technology, Cambridge, MA 02139-4307, USA
[5] National Central University, Chung-Li, Taiwan
[6] University of Illinois at Chicago, Chicago, IL 60607-7059, USA
[7] University of Maryland, College Park, MD 20742, USA
[8] University of Rochester, Rochester, NY 14627, USA

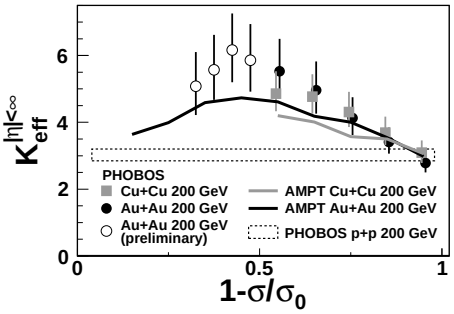

Figure 1: The effective size of the clusters corrected for the acceptance effects, as a function of the fractional cross section, i.e. obtained for similar geometry of $Au + Au$ and $Cu + Cu$ collisions. The cluster parameters obtained for elementary $p+p$ collisions and the results of the same reconstruction procedure performed on the events from AMPT generator are shown for comparison.

charged particles as a function of the difference of pseudorapidity and azimuthal angle, $\Delta\eta$ and $\Delta\phi$, allows to study the interaction of the stopped parton with the medium. In the central $Au + Au$ collisions the yield of particles correlated with the high-p_T trigger particle is larger than in the $p + p$ interactions. In the *near side*, $|\Delta\phi| \approx 0 \pm 1$, a ridge extending up to the end of acceptance range ($-4 < \Delta\eta < 2$) is present. It can be described as an additional yield which adds uniformly in η to the yield observed in $p + p$ interactions. In the *away side*, $\Delta\phi \approx \pi \pm 2$, such additional yield is even larger. Analysis of these yields as a function of centrality shows that they are the largest in central collisions and decrease for peripheral collisions. At $N_{part} \approx 80$ the difference between $Au + Au$ and $p + p$ for the *near side* drops to zero.

The correlations between all charged particles registered in the PHOBOS multiplicity detector were studied in a very wide range, $|\eta| < 3$, for elementary $p+p$ interactions (at 200 GeV and 410 GeV [?]) and nuclei collisions, $Cu + Cu$ and $Au + Au$ at 200 GeV [?,?]. They are represented by a correlation function:

$$R(\Delta\eta, \Delta\phi) = \left\langle (n-1)\left(\frac{\rho_n^{\rm II}(\Delta\eta,\Delta\phi)}{\rho^{\rm mixed}(\Delta\eta,\Delta\phi)} - 1\right)\right\rangle$$

where $\rho(\eta_1, \eta_2, \phi_1, \phi_2)$ is the charged pair density distribution for measured events (in the numerator) or for uncorrelated pairs taken from different events (in the denominator). In the further analysis the function integrated over one of the variables, $R(\Delta\eta)$ or $R(\Delta\phi)$, is used. The first of them has a maximum at $\eta \approx 0$ which is expected for short range correlations. It is thus natural to describe particle production as a two-step process: production of some intermediate objects, clusters, which then decay into finally observed particles [?]. Using the correlation function $R(\Delta\eta)$ it is possible to extract the parameters of the clusters: K_{eff}, the effective cluster size, and δ, width of the two-particle correlation. It is worth to note that even for very large acceptance, six pseudorapidity units, available in PHOBOS, acceptance corrections are large. Already in the elementary interactions[?] the cluster size is large, $K_{eff} \approx 3$. Even larger values, up to $K_{eff} \approx 6$, are found in nuclei collisions [?,?], as shown in Fig.**??**. The width of the clusters (shown later in Fig.**??**) is also large, exceeding that expected for isotropic decay at rest. We observe the same cluster parameters for $Cu + Cu$ and $Au + Au$ collisions with similar geometries even if the number of nucleons participating in the collisions and total multiplicities are much different [?,?].

Also, the correlation function $R(\Delta\phi)$ can be explained by the cluster model. However, a simple assumption that clusters' momenta can be randomly generated from a universal function reproducing only global $dN/d\eta$ and dN/dp_T distributions leads to a shape totally different from that measured experimentally. An agreement can be achieved only after enforcing transverse momentum conservation (by slightly modifying momenta to ensure $\Sigma p_T = 0$) as can be seen in Fig.**??**.

The large acceptance of the PHOBOS detector allows to measure forward-backward correlations at large distances. In this study, an asymmetry variable $C = (N_B - N_F)\sqrt{N_F + N_B}$ is used, where N_B and N_F denote the number of charged particles measured in two pseudorapidity bins, symmetric with respect to $\eta = 0$, at negative and positive η, respectively [?]. This variable is insensitive to the dependence of total multiplicity on centrality of the collision (that is enforcing $\langle N_B \rangle = \langle N_F \rangle$), but the variance σ_C^2 measures the strength of multiplicity fluctuations. For

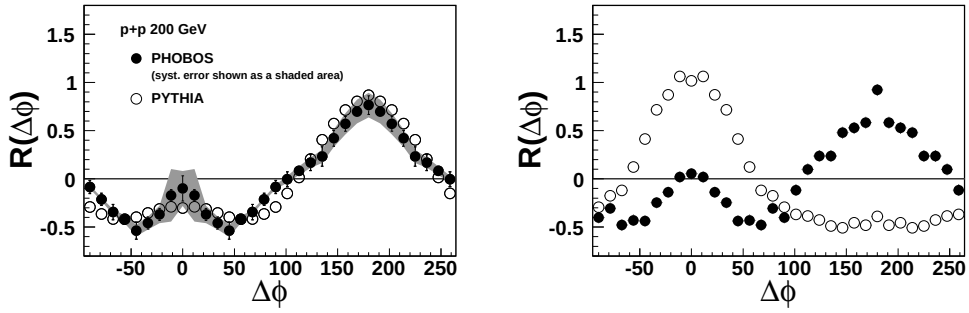

Figure 2: Two-particle correlation functions $R(\Delta\phi)$ obtained for the experimental data (left) and for generated events with identical clusters (decays: $\omega(782) \rightarrow \pi^+\pi^-\pi^0$) (right). In the right plot the correlation for events with randomly generated clusters (open circles) and modified so that sum of all transverse momenta is zero (full circles) are compared.

purely statistical fluctuations we obtain $\sigma_C^2 = 1$. The PHOBOS Collaboration has measured σ_C^2 as a function of the width of pseudorapidity bin, $\Delta\eta$, and the position of bin center, η. σ_C^2 is larger than 1 and increases when η and especially $\Delta\eta$ increase [?]. This agrees qualitatively with the expectation from the cluster model, in which the observed dependencies are explained by acceptance effects. However, in this case it is not possible to extract both parameters of the clusters at the same time, as for large and wide clusters these dependencies may look similar as for small but narrow clusters [?]. Unexpectedly, but consistently with the trends observed for 2-particle correlations, the values of σ_C^2 found for central $Au+Au$ collisions are smaller than for peripheral collisions (see Fig.**??**), indicating different effective cluster sizes (and possibly also δ width).

The centrality dependence of σ_C^2 values, shown in Fig.**??**, is not well reproduced by the models of particle production: UrQMD [?] has wrong centrality dependence, HIJING[?] gives in both cases the same values and AMPT[?] predicts correct trend, but underestimates σ_C^2. The best agreement[?] is observed for the Wounded Nucleon Model[?] which assumes that the nucleons taking part in the collision are the source of the particles which are produced according to a universal fragmentation function, asymmetric in η and about 10 pseudorapidity units wide, extracted from the data on $d+Au$ collisions. The fluctuations observed as large values of σ_C^2 are a sum of these present already in $p+p$ interactions (possibly from production of clusters) and those generated by the fluctuations of the number of wounded nucleons, in forward and backward moving nuclei[?].

The Wounded Nucleon Model may be used to describe not only forward-backward fluctuations, but also 2-particle correlations. In this case, predictions are less precise, as it is more difficult to include short range correlations (from $p+p$). Obviously,2 wounded nucleons should fragment into clusters which then decay into final particles. As an approximation identical clusters with $K_{eff} = 3$ and $\delta = 0.88$, effective parameters found in $p+p$ interactions [?], can be used.

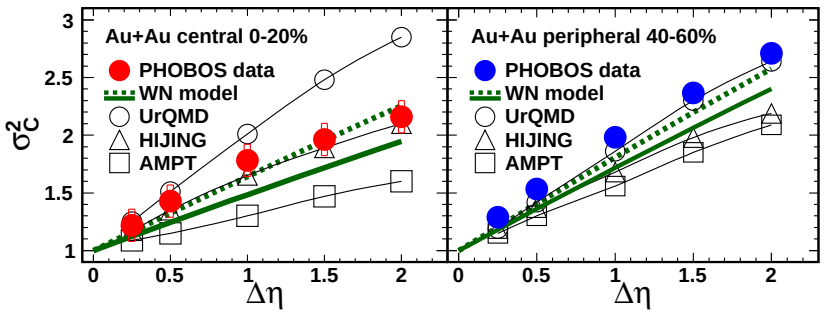

Figure 3: The values of σ_C^2 as a function of pseudorapidity bin width $\Delta\eta$ for central and peripheral $Au+Au$ collisions at $\sqrt{s_{NN}} = 200$ GeV. Experimental results are compared with predictions from several models.

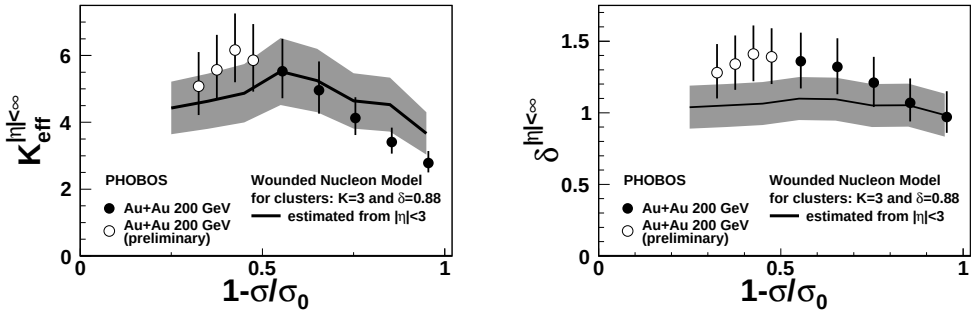

Figure 4: The effective cluster size (left) and the width parameter δ (right) for $Au + Au$ collisions compared with the predictions from the Wounded Nucleon Model in which we assume fragmentation of the wounded nucleons into clusters similar to those observed in $p + p$ interactions.

The fragmentation function into clusters should have similar shape (but K_{eff} times smaller integral) as for fragmentation into particles. These assumptions allow to obtain Wounded Nucleon Model predictions shown in Fig.**??**. Again the main trends are reproduced: the reconstructed cluster size becomes larger for peripheral than for central collisions and the width parameter δ increases. Discrepancies may be due to the fact, that in reality we have a mixture of clusters with various sizes and widths and convolution with wounded nucleons fluctuations gives in this case different reconstruction results than for identical clusters.

In the studies of correlations measured over a wide range of pseudorapidity, strong long-range effects were found. There is a long ridge in the correlation with a high-p_T trigger particle, clusters found in the 2-particle correlations are large and unexpectedly wide. The correlation in the azimuthal angle seems to be determined by the global momentum conservation. Forward-backward and 2-particle correlations can be at least qualitatively described by the Wounded Nucleon Model, in which particles are additionally correlated at large distances because they are emitted according to a fragmentation function, which extends over 10 pseudorapidity units.

Acknowledgments

This work was partially supported by U.S. DOE grants DE-AC02-98CH10886, DE-FG02-93ER40802, DE-FG02-94ER40818, DE-FG02-94ER40865, DE-FG02-99ER41099, and DE-AC02-06CH11357, by U.S. NSF grants 9603486, 0072204, and 0245011, by Polish MNiSW grant N N202 282234 (2008-2010), by NSC of Taiwan Contract NSC 89-2112-M-008-024, and by Hungarian OTKA grant (F 049823).

References

1. B.B. Back *et al.* (PHOBOS Collab.), Nucl. Phys. A757 (2005) 28; I. Arsene *et al.* (BRAHMS Collab.), ib. 1; J. Adams *et al.* (STAR Collab.), ib. 102; K. Adcox *et al.* (PHENIX Collab.), ib. 184.
2. B. Alver *et al.* (PHOBOS Collab.), Phys. Rev. Lett. 104 (2010) 062301.
3. B. Alver *et al.* (PHOBOS Collab.), Phys. Rev. C75 (2007) 054913.
4. B. Alver *et al.* (PHOBOS Collab.), Phys. Rev. C81 (2010) 024904.
5. G.S.F. Stephans *et al.* (PHOBOS Collab.), Nucl. Phys. A 830 (2009) 809c.
6. A. Morel and G. Plaut, Nucl. Phys. B78 (1974) 541.
7. B.B. Back *et al.* (PHOBOS Collab.), Phys. Rev. C74 (2006) 011901.
8. K. Woźniak *et al.* (PHOBOS Collab.), Int. J. Mod. Phys. E 16 (2007) 2187.
9. S. Haussler, M. Abdel-Aziz and M. Bleicher, Nucl. Phys. A785 (2007) 253.
10. X.N. Wang and M. Gyulassy, Phys. Rev. D44 (1991) 3501.
11. Z.W. Lin, C.M. Ko, B.A. Li, B. Zhang and S. Pal, Phys. Rev. C72 (2005) 064901.
12. A.Bzdak and K. Woźniak, Phys. Rev. C81 (2010) 034908.
13. A. Białas, M. Bleszyński and W. Czyż, Nucl. Phys. B111 (1976) 461; A. Białas and W. Czyż, Acta Phys. Polon. B36 (2005) 905.

Measurement of the dielectron continuum in $p+p$ and $\mathrm{Au}+\mathrm{Au}$ collisions at RHIC

T. DAHMS, for the PHENIX Collaboration
CERN,
1211 Geneva 23, Switzerland

PHENIX has measured the e^+e^- pair continuum in $\sqrt{s_{NN}} = 200$ GeV $\mathrm{Au}+\mathrm{Au}$ and $p+p$ collisions over a wide range of mass and transverse momenta. While the $p+p$ data in the mass range below the ϕ meson are well described by known contributions from light meson decays, the $\mathrm{Au}+\mathrm{Au}$ minimum bias inclusive mass spectrum shows an enhancement by a factor of $4.7 \pm 0.4(\mathrm{stat}) \pm 1.5(\mathrm{syst}) \pm 0.9(\mathrm{model})$ in the mass range $0.15 < m_{ee} < 0.75$ GeV/c^2. At low mass ($m_{ee} < 0.3$ GeV/c^2) and high p_T ($1 < p_T < 5$ GeV/c) an enhanced e^+e^- pair yield is observed that is in qualitative agreement with hydrodynamical models of thermal photon emission with initial temperatures ranging from $T_{init} \simeq 300$–600 MeV at times of 0.6–0.15 fm/c after the collision.

1 Introduction

Experimental results from the Relativistic Heavy Ion Collider (RHIC) have established the formation of dense partonic matter in $\mathrm{Au}+\mathrm{Au}$ collisions at $\sqrt{s_{NN}} = 200$ GeV [1]. One of the key questions has been what is the initial temperature of the created matter. Like any medium in thermal equilibrium, the quark-gluon plasma emits black-body radiation characteristic for its temperature in form of real and virtual photons, the latter ones appearing as lepton pairs (e^+e^- or $\mu^+\mu^-$). As photons and lepton pairs do not carry color charge, they do not undergo strong final state interaction while traversing the medium. Thus, they carry all their information from the time they have been created to the detector. But, because they are emitted during all stages of the collision, any measurement will be a time integrated average and the initial temperature can only be derived by comparing to models. One of the main challenges of measuring thermal photons is the huge background due to hadron decay photons. The dominant background contribution due to π^0 decays can be avoided by measuring virtual photons rather than real photons. Any process that creates a real photon can also create a virtual photon which decays into a lepton pair. The invariant mass spectrum of virtual photons created by the quark-gluon Compton scattering ($q+g \rightarrow q+\gamma^*$) is described by the Kroll-Wada equation [2]. For direct virtual photons with $p_T \gg m_{ee}$ this spectrum is proportional to $1/m_{ee}$. Also e^+e^- pairs from π^0 Dalitz decays have the same $1/m_{ee}$ shape at $m_{ee} \ll m_{\pi^0}$, but are suppressed due to the limited phase space when approaching $m_{\pi^0} = 135$ MeV/c^2. Thus, one can measure direct virtual photons above the π^0 mass where the main background source is eliminated.

2 Results

PHENIX has measured e^+e^- pairs from $p+p$ and $\mathrm{Au}+\mathrm{Au}$ collisions at $\sqrt{s_{NN}} = 200$ GeV as a function of mass and p_T. The resulting invariant mass spectra integrated over all p_T are

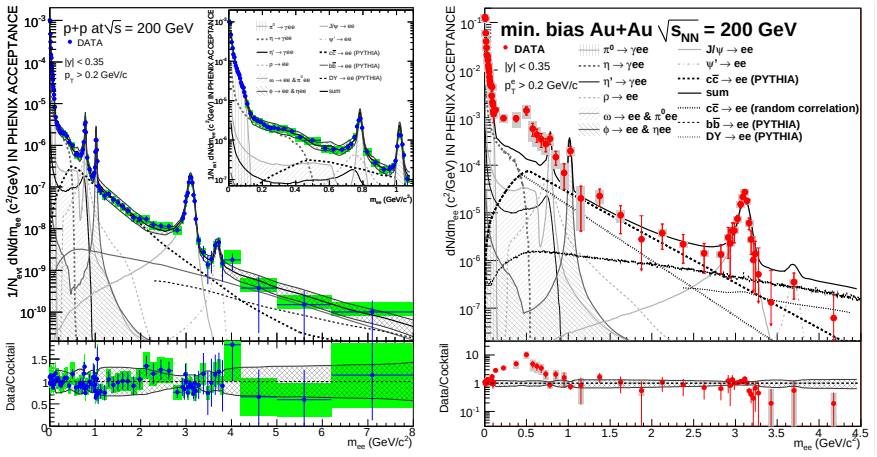

(a) (b)

Figure 1: Invariant mass distribution of e^+e^- pairs in the PHENIX acceptance in $p+p$ (a) and Au + Au (b) collisions. The data are compared to the expectations from the decays of light hadrons and correlated decays of open charm, bottom, and Drell-Yan.

shown in Fig. 1. Contributions from combinatorial and correlated background sources have been subtracted statistically utilizing mixed events and the like-sign pairs. The details of the analysis have been described in Ref.[3,4]. The p+p data are compared to a cocktail of the expected hadronic sources whose cross sections have been measured independently by PHENIX[4]. The contribution from semi-leptonic charm and bottom decays as well as Drell-Yan have been simulated with PYTHIA[5]. The agreement between data and simulation over the full mass range is excellent. By comparing the integrated yield of data and PYTHIA in the intermediate mass region of $1.1 < m_{ee} < 2.5$ GeV/c^2, which is dominated by open charm, a total charm cross section of $\sigma_{c\bar{c}} = 544 \pm 39(\text{stat}) \pm 142(\text{syst}) \pm 200(\text{model})$ μb has been measured in $p+p$ collisions. Alternatively, by fitting the normalization of the simulated shapes to the data, the charm and bottom cross sections of $\sigma_{c\bar{c}} = 518 \pm 47(\text{stat}) \pm 135(\text{syst}) \pm 190(\text{model})$ μb and $\sigma_{b\bar{b}} = 3.9(\text{stat}) \pm 2.4^{+3}_{-2}(\text{syst})$ μb, respectively, have been measured[3]. The charm cross section is in agreement with the result of the non-photon single electron measurement[6]: $\sigma_{c\bar{c}} = 567 \pm 57(\text{stat}) \pm 193(\text{syst})$ μb.

The measurement of e^+e^- pairs in Au + Au collisions is compared to the corresponding cocktail calculation in Fig. 1b. The charm contribution is the same PYTHIA calculation scaled to the number of binary collisions, N_{coll}, times the measured charm cross section of $\sigma_{c\bar{c}} = 567 \pm 57(\text{stat}) \pm 193(\text{syst})$ μb. In contrast to the p+p result, the measured yield of low mass region ($0.15 < m_{ee} < 0.75$ GeV/c^2) in minimum bias Au+Au is enhanced compared to the expectation by a factor $4.7 \pm 0.4(\text{stat}) \pm 1.5(\text{syst}) \pm 0.9(\text{model})$. The intermediate mass region is surprisingly well described by PYTHIA which is shown as dashed line in Fig. 1b. This is interesting to note, as single electron distributions from semi-leptonic charm decays show substantial medium modifications[7]. Thus, it is hard to understand how the dynamical correlation of the $c\bar{c}$ pair at production remains unaffected by the medium. An alternative scenario in which this correlation is washed out by the medium, i. e. the direction of the c and the $\bar{c}$ quark are uncorrelated, is indicated by a dotted line in the same figure. This leads to a much softer spectrum and would leave significant room for other contributions, e. g. thermal radiation emmited by quark-antiquark annihilation processes.

The p_T dependence of the low mass region ($m_{ee} < 1.2$ GeV/c^2) is shown in Fig. 2. The e^+e^- pairs measured in $p+p$ are consistent with the cocktail for the lower p_T bins. At higher p_T however, the data are above the expectation. In Au + Au the enhancement is concentrated at

low p_T but extends to the high p_T region where it is still significantly higher than in $p+p$. The shape of the low mass enhancement in Au + Au differs for $p_T < 1$ GeV/c and $p_T > 1$ GeV/c. At high p_T the excess can be interpreted as due to internal conversions of direct virtual photons which, for $p_T \gg m_{ee}$, has a well defined $1/m_{ee}$ mass dependence [2]. The data have been fit to the cocktail plus a direct photon contribution in the form of $f(m_{ee}) = (1-r)f_c(m_{ee}) + r f_{\rm dir}(m_{ee})$ with the fraction of the direct virtual photon contribution r as the free parameter. From this fraction of the direct virtual photon contribution it is possible to derive the p_T spectrum of direct real photons [8] which is shown for $p+p$ and three Au + Au centrality bins (min. bias, 0–20%, and 20–40%) in Fig. 3a. The data are extended at high p_T with the previous measurements of direct photons in the electromagnetic calorimeter of PHENIX [9,10] which are in good agreement in the overlapping p_T range. The $p+p$ data are are in good agreement with a NLO pQCD calculation of direct photons [11] which is shown for three different theory scales: $\mu = 0.5\,p_T$, p_T, and $2\,p_T$.

In order to compare the $p+p$ data quantitatively with the Au + Au measurement, the $p+p$ direct photon spectrum is fit to a modified power-law function $A_{pp}(1+p_T^2/b)^{-n}$. This fit, scaled by the nuclear overlap function T_{AA} is overlaid with the Au + Au data. For all three centrality bins the data are show a clear enhancement at low p_T. This excess is characterized by fitting the T_{AA} scaled $p+p$ fit plus an exponential $A{\rm e}^{-p_T/T} + T_{AA} \times A_{pp}(1+p_T^2/b)^{-n}$. For the 20% most central collisions, the inverse exponential slope is $T = 221 \pm 19({\rm stat}) \pm 19({\rm syst})$. The result for this centrality bin is compared in Fig. 3b to several hydrodynamical models of thermal photon emission [12,13,14,15,16,17]. The models, which assume the formation of a hot system with initial temperatures ranging from $T_{\rm init} = 300$ MeV at a thermalization time of $\tau_0 = 0.6$ fm/c to $T_{\rm init} = 600$ MeV at $\tau_0 = 0.15$ fm/c, are all in qualitative agreement with the data. Lattice QCD predicts a phase transition from the hadronic phase to the quark-gluon plasma at $T \simeq 170$ MeV.

While for $p_T > 1$ GeV/c the excess yield can be successfully described by internal conversions of direct virtual photons, the excess yield at lower p_T, which is responsible for most of the p_T integrated enhancement, shows a different mass dependence. The transverse mass dependence of the enhancement has been analysed in Ref. [4]. While not shown in this proceedings, it appears that, in addition to the thermal radiation at high m_T, there is a second much softer component at low m_T with an inverse slope of $T \sim 90$ MeV. This low mass, low p_T enhancement is currently not described by any theoretical model calculation.

References

1. K. Adcox *et al.* (PHENIX Collaboration), Nucl. Phys. **A 757**, 184 (2005).
2. N. M. Kroll and W. Wada, Phys. Rev. **98**, 1355 (1955).
3. A. Adare *et al.* (PHENIX Collaboration), Phys. Lett. **B 670**, 313 (2009).
4. A. Adare *et al.* (PHENIX Collaboration), Phys. Rev. C **81**, 034911 (2010).
5. T. Sjöstrand, *et al.*, Comp. Phys. Commun. **135**, 238 (2001).
6. A. Adare *et al.* (PHENIX Collaboration), Phys. Rev. Lett. **97**, 252002 (2006).
7. A. Adare *et al.* (PHENIX Collaboration), Phys. Rev. Lett. **98**, 172301 (2007).
8. A. Adare *et al.* (PHENIX Collaboration), Phys. Rev. Lett. **104**, 132301 (2010).
9. S. S. Adler *et al.* (PHENIX Collaboration), Phys. Rev. Lett. **94**, 232301 (2005).
10. S. S. Adler *et al.* (PHENIX Collaboration), Phys. Rev. Lett. **98**, 012002 (2007).
11. L. E. Gordon and W. Vogelsang, Phys. Rev. D **48**, 3136 (1993)
12. D. d'Enterria and D. Peressounko, Eur. Phys. J. **C 46**, 451 (2006).
13. P. Huovinen, P. V. Ruuskanen, and S. S. Rasanen, Phys. Lett. **B 535**, 109 (2002).
14. D. K. Srivastava and B. Sinha, Phys. Rev. C **64**, 034902 (2001).
15. S. Turbide, R. Rapp, and C. Gale, Phys. Rev. C **69**, 014903 (2004).
16. F. M. Liu *et al.*, Phys. Rev. C **79**, 014905 (2009).
17. Jan-e Alam *et al.*, Phys. Rev. C **63**, 021901(R) (2001).

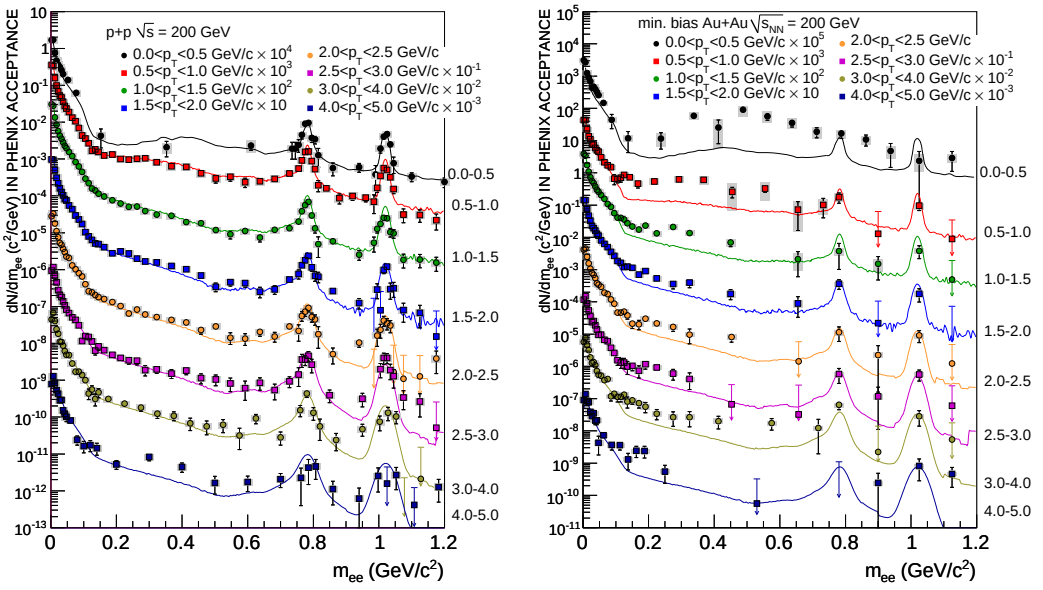

(a) (b)

Figure 2: Invariant mass distribution of e^+e^- pairs in the PHENIX acceptance for different p_T ranges in $p+p$ (a) and Au+Au (b) collisions. The data are compared to the cocktail of hadronic sources which includes the contribution from charm as described in the text.

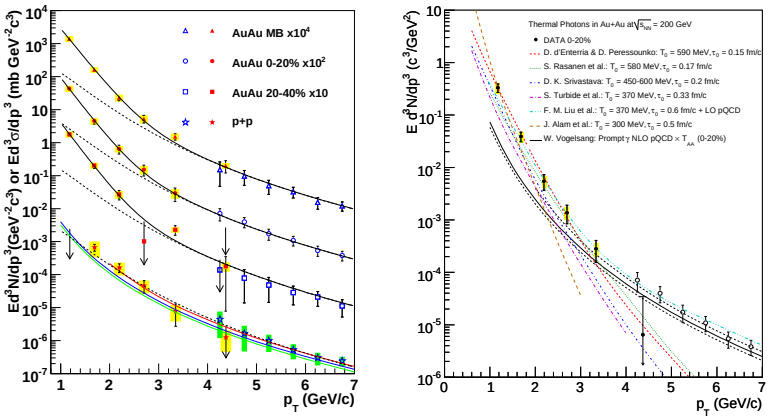

(a) (b)

Figure 3: The invariant cross section ($p+p$) and invariant yield (Au+Au) of direct photons as a function of p_T is shown in (a). Solid points are from the internal conversion analysis, open points from [9,10]. The $p+p$ data are compared to NLO pQCD calculations [11] for three theory scales $\mu = 0.5\,p_T$, p_T, and $2\,p_T$. The $p+p$ data are fit to a modified power-law (dashed curve) which is scaled by T_{AA} and compared to the Au+Au data. The Au+Au data are fitted by the T_{AA} scaled $p+p$ fit plus an exponential (solid lines). In (b) hydrodynamical model calculations of thermal photon emission are compared with the direct photon data in the 20% most central Au + Au collisions. In contrast to the others, the curve of F. M. Liu *et al.* [16] includes contributions from pQCD. The black solid curve show the T_{AA} scaled pQCD calculation [11].

SUPPRESSION OF FORWARD PION CORRELATIONS IN d+Au INTERACTIONS AT STAR

E. BRAIDOT, FOR THE STAR COLLABORATION
Institute for Subatomic Physics, Utrecht University, Princetonplein 5, 3584 CC Utrecht, The Netherlands

During the 2008 run RHIC provided high luminosity in both p+p and d+Au collisions at $\sqrt{s_{NN}} = 200GeV$. Electromagnetic calorimeter acceptance in STAR was enhanced by the new Forward Meson Spectrometer (FMS), and is now almost contiguous from $-1 < \eta < 4$ over the full azimuth. This large acceptance provides sensitivity to the gluon density in the nucleus down to $x \approx 10^{-3}$. Measurements of the azimuthal correlation between a forward π^0 and an associated particle at large rapidity are sensitive to the low-x gluon density. Data exhibit the qualitative features expected from gluon saturation. A comparison to calculations using the Color Glass Condensate (CGC) model is presented.

1 Introduction

Forward acceptance at STAR has been drastically improved in the last few years with the development and commissioning of the Forward Meson Spectrometer (FMS). The FMS is a high granularity electromagnetic calorimeter whose purpose is to measure photons from decays of forward neutral mesons. It extends the fully azimuthal, electromagnetic capability of STAR into the pseudorapidity region $2.5 < \eta < 4.0$, making the overall coverage almost hermetic in the wide $-1.0 < \eta < 4.0$ interval. This allows measurements of correlations of different species of forward- and mid-rapidity particles, over a broad $\Delta\eta \times \Delta\varphi$ range.

One of the main purposes of the FMS [1] is to characterize the p_T dependence of the di-pion azimuthal correlations as a means to search for the onset of saturation effects [2] in the nuclear gluon distribution. It is believed that, as the energy grows, non-linear effects must be included in the nuclear wave-function in order to tame the otherwise divergent rise of the gluon density. At very low values of the longitudinal momentum fraction x of the probed gluon, as accessed in high-energy collisions, the occupation numbers become large, allowing gluon recombination that eventually leads to saturation. Saturation is expected to be revealed at RHIC in d+Au

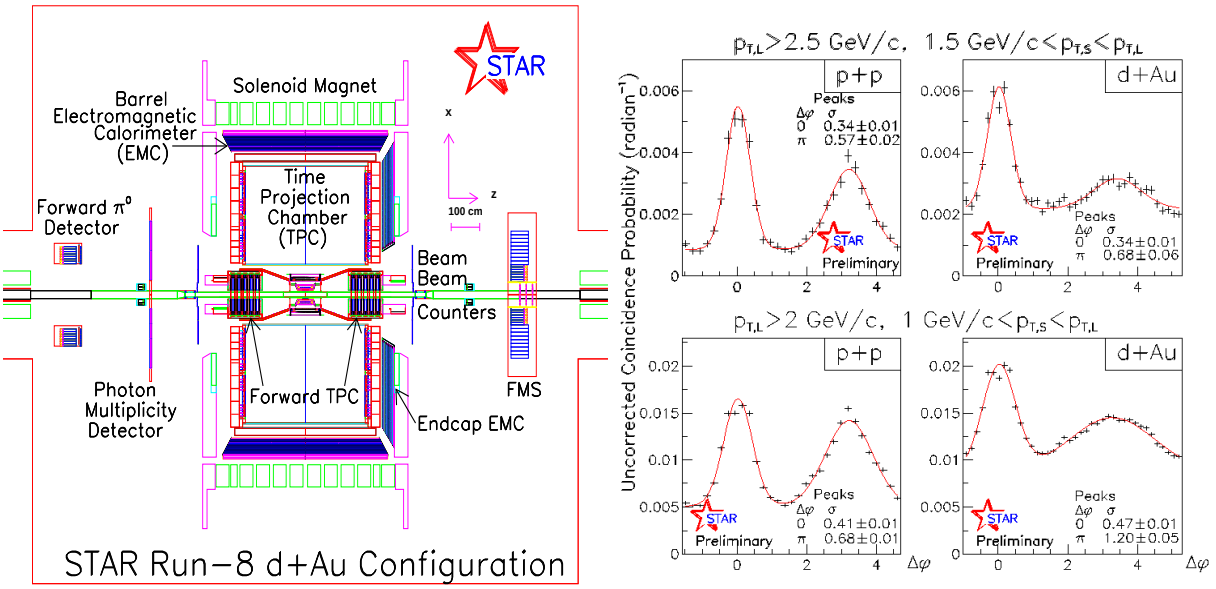

Figure 1: On the left: schematic view of the STAR hall. Gold beam is coming from the West (right in figure) side. On the right: uncorrected coincidence probability versus azimuthal angle difference between two forward neutral pions. Different p_T cuts are indicated inside the figure. The left (right) column shows p+p (d+Au) data with statistical errors. Data are fit with a constant plus two gaussian functions (in red).

collisions, where large densities of nuclear gluons are probed with a much simpler final state than heavy ion collisions. The FMS, facing the deuteron beam direction, provides measurements of forward hadron production in the rapidity region that selects small-x gluons in the nucleus. It probes x down to $x \approx 10^{-3}$ for inclusive particle production at $\langle\eta\rangle \approx 3$ at $\sqrt{s_{NN}} = 200$ GeV [3], well into the range where saturation effects are expected to set in.

2 Azimuthal correlation analysis

Models try to describe forward hadron production from dense nuclear targets by including non-linear effects. One approach [4] extends perturbative QCD factorization by adding contributions of quarks scattering coherently off multiple nucleons, leading to an effective shift in the gluon x. In the Color Glass Condensate (CGC) model [2,5] the low-x gluon density is saturated and non-linearities are treated classically. In both cases the $2 \rightarrow 2$ picture of elastic parton scattering process is replaced by a $2 \rightarrow$ many picture, where the probe scatters coherently off the dense gluon field of the target, which recoils collectively. In the CGC model, the transverse momentum of a jet produced by the large momentum parton (most likely a valence quark) in the deuteron is balanced by many gluons in the nucleus. To quantify this effect, it is instructive to compare the azimuthal angular correlation ($\Delta\varphi$) between the forward π^0 and coincident hadrons. In p+p collisions, one expects to see a peak centered at $\Delta\varphi = \pi$, representing the elastic back-to-back scattering contribution. In forward d+Au collisions, on the other hand, non-linear contributions are expected to cause a loss of correlation between the two particles, leading to a broadening of the back-to-back peak, and eventually to its disappearance (monojet).

A systematic plan of azimuthal correlation measurements has been pursued at STAR using forward prototype calorimeters (Forward Pion Detector, FPD/FPD++) and, more recently, the FMS. The objective has been to probe if the boundaries of the saturation region are accessible at RHIC energies [6] and establish the effect on particle production. Azimuthal correlations between a forward π^0 and a mid-rapidity particle were first measured with the FPD [7] and recently confirmed, and extended, with the FMS [8]. Comparison of $\Delta\varphi$ between p+p and d+Au shows a significant broadening in the back-to-back peak in d+Au. Such effect appears to be stronger as

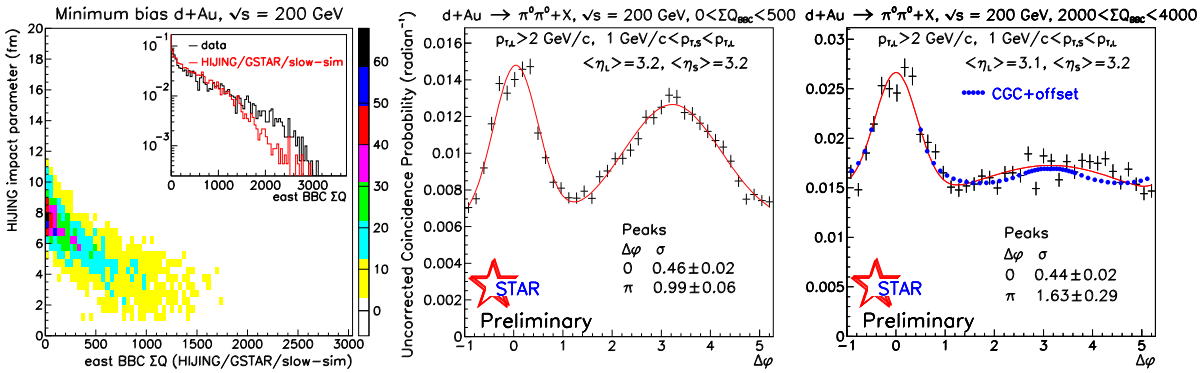

Figure 2: Left: HIJING impact parameter versus charge sum as recorded by the STAR BBC for simulated minimum bias events. Comparison of charge distribution with data is in the inset. Following: uncorrected coincidence probability versus azimuthal angle difference between two forward neutral pions in peripheral (center) and central d+Au collisions (right). Data are shown with statistical errors and fit with a constant plus two gaussian functions (in red). CGC expectations [10] have been superimposed (in blue) to data for central d+Au collisions.

the transverse momentum of the particles decreases, as expected by saturation models. One can approach the saturation region by lowering the x value of the probed gluon by requiring both leading and associated particles to be detected in the forward region, now possible due to the FMS wide acceptance. Results from this analysis, where the lowest x is probed, are shown.

3 Results and Systematics

Centrality averaged azimuthal correlations between two forward π^0 candidates have been measured for different p_T selections. Results are shown on the right-hand side of figure 1. Neutral pions are reconstructed from pairs of photon clusters, found within the FMS fiducial volume ($2.5 < \eta < 4.0$), that present an invariant mass in the interval $0.05 < M_{\gamma\gamma} < 0.25$ GeV/c^2. The pair with the largest p_T is selected as the leading (trigger) π^0 and its azimuthal coordinate is compared inclusively with those of all the other (associated) π^0 candidates. The (efficiency uncorrected) probability to find an associated π^0 per triggered event presents two contributions. The peak centered in $\Delta\varphi = 0$ (near-side peak) represents the contribution from pairs of neutral pions from the same jet. It is not expected to be affected by gluon saturation, hence providing us with a useful tool to check the effective amount of the broadening in the away-side contribution. This second peak, centered at $\Delta\varphi = \pi$, represents the back-to-back contribution to the coincidence probability and it is expected to disappear in going from p+p to d+Au if saturation sets in. Data are fit with a constant plus two gaussians centered at $\Delta\varphi = 0$ and $\Delta\varphi = \pi$ respectively. Figure 1 shows how the width of the near-side peak is not changing from p+p to d+Au, while the away-side peak presents significative broadening, with an effect larger than that found in forward + mid-rapidity particle correlations [8]. The p_T dependence of the broadening effect is studied by applying two different selections to the data. A lower p_T cut for both trigger (2.0 GeV/c$< p_T^{(trg)}$) and associated pions (1.0 GeV/c$< p_T^{(assc)} < p_T^{(trg)}$) shows a stronger broadening of the signal width ($\sigma_{dAu} - \sigma_{pp} = 0.52 \pm 0.05$) than a more restrictive cut (2.5 GeV/c$< p_T^{(trg)}$, 1.5 GeV/c$< p_T^{(assc)} < p_T^{(trg)}$, $\sigma_{dAu} - \sigma_{pp} = 0.11 \pm 0.06$), as expected from saturation models.

Broadening effects are expected to be more significant when the more central part of the nucleus is probed. In order to disentangle peripheral from central collisions, the sum of charges ($\sum Q_{BBC}$) has been recorded using the east side of the STAR Beam-Beam Counter (BBC) that faces the Au beam. This provides a measure of the multiplicity of the event, which is correlated with the impact parameter in the collision, as shown on the left-hand panel of figure 2 for minimum bias events, as simulated by HIJING 1.383 [9]. The multiplicity selections for

peripheral ($0 < \sum Q_{BBC} < 500$) and central d+Au collisions ($2000 < \sum Q_{BBC} < 4000$) result in $\langle b \rangle = 6.8$ fm and $\langle b \rangle = 2.7$ fm respectively. Figure 2 also shows azimuthal correlations for the lower p_T selection, using the charge sum to discriminate between peripheral (central panel) and central (right-hand panel) d+Au collision. Peaks on the near-side appear nearly unchanged from p+p to d+Au, and particularly from peripheral to central d+Au collisions. On the contrary, the away-side peak shows strong differences from peripheral to central d+Au collisions. Peripheral d+Au collisions show back-to-back peak like in p+p, even though it appears to be smaller relative to the near-side peak than in p+p. Central d+Au collisions show instead large broadening of the away-side peak, effectively causing its disappearance.

Theoretical expectations for azimuthal correlations in interactions between a dilute system (deuteron) and a dense target (Gold) have been explored. Inclusive particle production has been calculated within the CGC framework, using a fixed saturation scale Q_S [6], and then used to compute the di-hadron correlations [10]. Calculations consider valence quarks in the deuteron scattering off low-x gluons in the nucleus with impact parameter $b = 0$. A preliminary comparison with data in central d+Au collisions is shown on the right-hand plot of figure 2. Calculations (in blue) have been superimposed to the data after adding a constant offset to emulate the background from underlying event. CGC calculations show qualitative consistency with data in their expectations of a strong suppression of the away-side peak in central d+Au collisions. Comparison between same data and CGC calculations using a different approach can be found in this reference [11].

Further systematic studies are being performed for this analysis. Systematic Pythia investigation found p+p data to be consistent with gluon distribution function that include a rapid rise of the gluon density at low x. Azimuthal correlations were also studied in embedded Pythia+GSTAR events into minimum bias d+Au data in order to rule out the possibility that additional multiplicity in d+Au events compared to p+p could cause loss of correlation.

4 Conclusions

Thanks to a rich d+Au RHIC run in 2008, the Forward Meson Spectrometer is pursuing its primary objective of mapping the boundaries for saturation signatures for back-to-back jet correlations as a function of η and p_T. A new, interesting piece is provided by correlations between two forward neutral pions, which show a strong suppression in the away-side peak in central d+Au collision compared to p+p, qualitatively consistent with CGC expectations.

References

1. L.C. Bland *et al*, *Eur. Phys. J.* C **43**, 427 (2005).
2. L. Gribov, E. Levin, and M. Ryskin, *Phys. Rep.* **100**, 1 (1983); A.H. Mueller and J.Qiu, *Nucl. Phys.* B **268**, 427 (1986); L. McLerran and R. Venugopalan, *Phys. Rev.* D **49**, 3352 (1994).
3. V. Guzey, M. Strickman, and W. Voegelsang, *Phys. Lett.* B **603**, 173 (2004).
4. J. Qiu and I. Vitev, *Phys. Rev. Lett.* **93**, 262301 (2004).
5. A.Dumitru and J. Jalilian-Marian, *Phys. Rev. Lett.* **89**, 022301 (2002); E. Iancu, K. Itakura, and D. N. Triantafyllopoulos, *Nucl. Phys.* A **742**, 182 (2004).
6. J. L. Albacete, C. Marquet, *Phys. Lett.* B **687**, 174 (2010).
7. J. Adams *et al*, *Phys. Rev. Lett.* **97**, 152302 (2006).
8. E. Braidot, *Nucl. Phys.* A **830**, 603 (2009).
9. X. Wang and M. Gyulassy, *Phys. Rev.* D **44**, 3501 (1991).
10. C. Marquet, *Nucl. Phys.* A **796**, 41 (2007).
11. K. Tuchin, arXiv:0912.5479v1, (2009).

NA61/SHINE: HADRON PRODUCTION IN p+p/A AND A+A INTERACTIONS AT THE CERN SPS

ANTONI MARCINEK
FOR THE NA61/SHINE COLLABORATION
Institute of Physics, Jagiellonian University,
Reymonta 4, 30-059 Kraków, Poland

The physics motivations, status and plans of NA61/SHINE experiment are presented. Also the first, preliminary results on π^- production, from the pilot run in 2007, are shown. These data are needed by the T2K experiment for precise neutrino beam simulation. It is explained why the precise hadron production measurements are crucial for various fields of physics. Moreover, it is argued that the 2D scan in system size and collision energy is essential for the study of the onset of deconfinement and search for the critical point of strongly interacting matter.

1 Introduction

The NA61/SHINE (SHINE stands for *SPS Heavy Ion and Neutrino Experiment*) is a successor of the well known NA49 experiment in the field of heavy ion collisions. It is a fixed target experiment on primary (ion) and secondary (hadron and ion) beams from the CERN SPS. The proposal [1] was submitted at the-end of 2006, the pilot run was conducted in October 2007 and the first physics run took place in 2009. The collaboration consists of 131 physicists from 25 institutes from 14 countries.

The physics programme regards three different subjects, the neutrino physics (section 3), cosmic ray physics (section 4) and strongly interacting matter physics (section 5). The first goal are precision measurements of hadron production in p/π+C interactions needed by the T2K (neutrino) and Pierre Auger Observatory and KASCADE (cosmic ray) experiments. The second goal are also precision measurements, to study the properties of the onset of deconfinement in nucleus-nucleus collisions, as well as to measure hadron production at high transverse momenta in p+p and p+Pb collisions as a reference for NA49's Pb+Pb results. Finally there is search for the critical point of strongly interacting matter, which is NA61/SHINE's discovery potential.

2 The NA61/SHINE detector

The main part of NA61/SHINE detector, which is sketched in Fig. 1, was inherited from NA49.[2] This includes four large-volume Time Projection Chambers — VTPC-1 and VTPC-2 inside superconducting dipole magnets for momentum determination, MTPC-L and MTPC-R for energy loss (so-called dE/dx) measurement and two time-of-flight detectors — ToF-L and ToF-R.

However, in order to satisfy the experimental programme, some upgrades [1] were needed. First, a new time-of-flight wall, the so-called Forward-ToF (F-ToF), was added in 2007, which gives *2 times larger* ToF acceptance than NA49 had. Second, new Beam Position Detectors

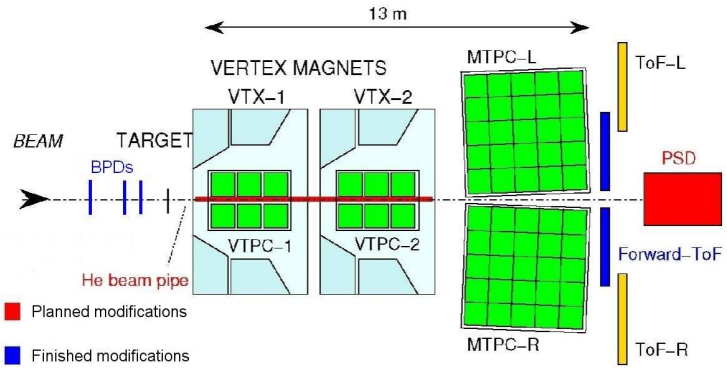

Figure 1: The layout of the NA61/SHINE detector (top-view, not to scale). Blue colour indicates components that were added to original NA49 set-up or upgraded, red indicates elements that will be added.

(BPDs; small Multiwire Proportional Chambers) were built in 2008, which are *2 times bigger* than NA49's. The third finished modification of the original system is a new TPC read-out, commissioned in 2008, which gives *10 times faster* data acquisition than NA49 could have. Moreover two additional upgrades are in progress, the helium filled beam pipe and a new calorimeter, the Projectile Spectator Detector (PSD). The beam pipe will *reduce by a factor of 10* the delta electron background in VTPCs in comparison to NA49. The PSD will in turn have *10 times better* energy resolution than the old NA49's Veto Calorimeter.

Fine performance of the NA61/SHINE detector may be summarized as follows:

- momentum resolution $\sigma(p)/p^2 \approx 10^{-4}\,(\mathrm{GeV/c})^{-1}$,
- time-of-flight resolution $\sigma(tof) \approx 60\,\mathrm{ps}$ for ToF-L and ToF-R and $\sigma(tof) \approx 120\,\mathrm{ps}$ for F-ToF,
- energy loss resolution $\sigma(dE/dx)/ < dE/dx > \approx 4\%$,
- large acceptance $\approx 50\%$ at $p_T \lesssim 2.5\,\mathrm{GeV/c}$.

Thanks to above parameters, depending on momentum, particle identification (PID) might be done with three methods. For very low momenta of particles (below 1 GeV/c) and high momenta (above 6 GeV/c) the dE/dx is used. For low momenta the time-of-flight measurement might be used. Finally, for medium momenta, where dE/dx Bethe-Bloch curves for various particles' species partially overlap as well as the corresponding tof mass-squared spectra, the combined tof and dE/dx method is used.

3 Neutrino physics - first results

The T2K experiment in Japan aims to study neutrino oscillations. [3] The neutrino beam is mainly produced from decays of products (mainly pions and kaons) of the 31 GeV/c proton beam interactions with a carbon target. The proton beam is created in the J-PARC accelerator in Tokai. Neutrinos first pass through the near detector at a distance of 280 m from the target and then through the far detector, Super-Kamiokande, 295 km away. Both detectors are positioned along a line 2.5° off the beam axis.

The study of oscillations is done by the comparison of the energy spectrum of neutrinos of a given flavour (ν_e or ν_μ) measured at the far detector with that extrapolated from measurements at the near detector with and without oscillation hypothesis. Because of the way the neutrinos are produced, the extrapolation is a non-trivial task. It is done using a Monte-Carlo prediction of the neutrino beam. In order to achieve the T2K physics goals, the extrapolation has to be

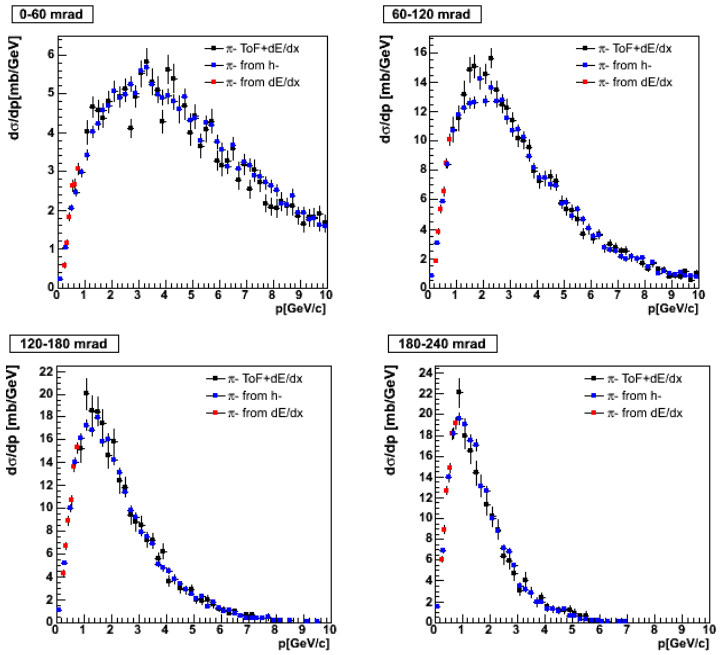

Figure 2: Preliminary cross sections for π^- production in p+C thin target collisions at beam momentum of 31 GeV/c from the pilot run in 2007. Three different methods of analysis (see text) are compared for 4 bins of the production angle. Only statistical errors are plotted.

done with a precision of 2–3%. This implies, that T2K beam MC cannot rely only on hadron production models — it requires *precise knowledge of hadron production* under T2K conditions.[a] This can be provided by the NA61/SHINE measurements.

As there are two strategies to implement the NA61/SHINE data into the T2K beam MC, the measurements are done with two carbon targets — the so-called thin target (4% of nuclear interaction length, λ_I) and the so-called long target (a replica of the T2K target, $1.9\lambda_I$). With the thin target 660k events were taken in 2007 and 6M events in 2009, while with the long target 230k events were registered in 2007 and 4M in 2009.

Preliminary results [4] for p+C thin target collisions at beam momentum of 31 GeV/c from the pilot run in 2007 are shown in the Fig. 2. These are differential cross sections for π^- production, for 4 bins of the production angle (the angle between beam and particle track). In the plot, 3 analysis methods are compared. The first uses combined tof and dE/dx information for momenta above 1 GeV/c, the second assumes that all negatively charged hadrons are π^- and then an MC correction is applied, finally the third one uses solely dE/dx measurement for momenta below 1 GeV/c. Only statistical errors are plotted and systematic ones are less than 20%. Still there is some work in progress to lower them. As one can see, results of these 3 methods are consistent, proving that the detector and analysis is well understood and that NA61/SHINE is ready to analyse a large amount of data collected in 2009.

4 Cosmic rays physics

Modern detectors, like KASCADE and Pierre Auger Observatory, measure composition of cosmic rays, which is of key importance for understanding sources of these particles and exciting structures (*knee, ankle*) in their energy spectrum. The problem is, that the measurement is done indirectly. Really observed are fragments of extensive air showers — cascades of billions of

[a] The same reasoning applies also to prediction of the energy spectrum of neutrinos at the near detector for neutrino cross section measurements.

particles produced in collisions of the primary cosmic ray with a nucleus in the atmosphere and subsequent collisions caused by products of the initial collision. So, a simulation of the shower is needed to say what particle started the shower. This causes a strong model dependence, due mainly to simulation of muon production. This in turn can be related to hadronic interactions at fixed-target energies, where muons are created in decays of products of these interactions. This again means that *a precise knowledge of hadron production* under certain conditions is needed.

For cosmic rays part of the programme, 5M collisions of 158 GeV/c pion beam with a thin carbon target were collected in 2009, along with 6M events with 350 GeV/c pion beam.

5 Physics of strongly interacting matter

Similarly to commonly known substances as water, strongly interacting matter may be found in various phases; there might be phase transitions between them, which may end in critical points. However, the difference is, that the experimental study for the case of strongly interacting matter is indirect. What we actually have access to, are freeze-out points of hadrons created in collisions, in the space of the temperature T and baryochemical potential μ_B. It has been shown, [5] that T and μ_B may be brought into one-to-one correspondence respectively with the system size A and energy E of nuclear collisions.

Lattice QCD calculations predict a first order phase transition between confined and deconfined matter. The idea for the study of the onset of deconfinement is that when the early stage of the collision hits the transition line, one expects to see certain signals in collision energy dependence of hadron production, e.g. the so-called kink, horn and step. These signals were predicted by Gaździcki and Gorenstein [6] and then actually observed by NA49 experiment [7] in central Pb+Pb interactions. Now NA61/SHINE aims to study how these signals develop when the system size is scanned.

There is also a prediction that the mentioned 1^{st} order phase transition ends in a critical point somewhere in the energy range covered by the CERN SPS. The idea for the search for the critical point, given by Stephanov *et al.*[8], is that if freeze-out is close to critical point and system is large enough, when one does a scan in A and E (T and μ_B), then one expects a hill in event-by-event fluctuations of multiplicity and transverse momentum. Important for the search is that one has to take into account fluctuations not related to the critical point. Huge contribution comes from fluctuations in number of participants, so one has to consider only central collisions. This is why *the first 2D (A and E) scan in the history of nucleus-nucleus relativistic collisions* started by NA61/SHINE, [9] is crucial for this search.

For this part of programme, about 19M p+p collisions were registered in 2009 with beam momenta of 20, 31, 40, 80 and 158 GeV/c.

References

1. N. Antoniou *et al.* [NA61 Collaboration], CERN-SPSC-2006-034, SPSC-P-330, (2006). `http://na61.web.cern.ch/`
2. S. Afanasiev *et al.* [NA49 Collaboration], *Nucl. Instrum. Methods* A **430**, 210 (1999).
3. Y. Itow *et al.*, "The JHF-Kamiokande neutrino project", [arXiv:hep-ex/0106019].
4. S. Murphy [NA61 Collaboration], proceedings of the EW session.
5. F. Beccatini, J. Manninen, M. Gaździcki, *Phys. Rev.* C **73**, 044905 (2006).
6. M. Gaździcki, M. Gorenstein, *Acta Phys. Pol.* B **30**, 2705 (1999).
7. C. Alt *et al.* [NA49 Collaboration], *Phys. Rev.* C **77**, 024903 (2008).
8. M. A. Stephanov, K. Rajagopal and E. V. Shuryak, *Phys. Rev.* D **60**, 114028 (1999).
9. N. Abgrall *et al.* [NA61 Collaboration], CERN-SPSC-2009-031, SPSC-P-330-ADD-5, (2009).

ON CONFINEMENT AND CHIRAL SYMMETRY CRITICAL POINTS

P. BICUDO
CFTP, Dep. Física, Instituto Superior Técnico,
Av. Rovisco Pais, 1049-001 Lisboa, Portugal

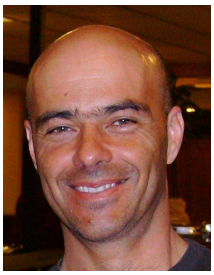

We study the QCD phase diagram, in particular we study the critical points of the two main QCD phase transitions, confinement and chiral symmetry breaking. Confinement drives chiral symmetry breaking, and, due to the finite quark mass, at small density both transitions are a crossover, while they are a first or second order phase transition in large density. We study the QCD phase diagram with a quark potential model including both confinement and chiral symmetry. This formalism, in the Coulomb gauge hamiltonian formalism of QCD, is presently the only one able to microscopically include both a quark-antiquark confining potential and a vacuum condensate of quark-antiquark pairs. This model is able to address all the excited hadrons, and chiral symmetry breaking, at the same token. Our order parameters are the Polyakov loop and the quark mass gap. The confining potential is extracted from the Lattice QCD data of the Bielefeld group. We address how the quark masses affect the critical point location in the phase diagram.

1 Introduction

Our main motivation is to contribute to understand the QCD phase diagram for finite T and μ, to be studied at LHC, RHIC and FAIR [1]. Moreover, our formalism, in the Coulomb gauge hamiltonian formalism of QCD, is presently the only one able to microscopically include both a quark-antiquark confining potential and a vacuum condensate of quark-antiquark pairs. Thus the present work, not only addresses the QCD phase diagram, but it also constitutes the first step to allow us in the future to compute the spectrum of any hadron to finite T .

Here we address the finite temperature string tension, the quark mass gap for a finite current quark mass and temperature, and the deconfinement and chiral restoration crossovers. We conclude on the separation of the critical point for for chiral symmetry restoration from the critical point for deconfinement.

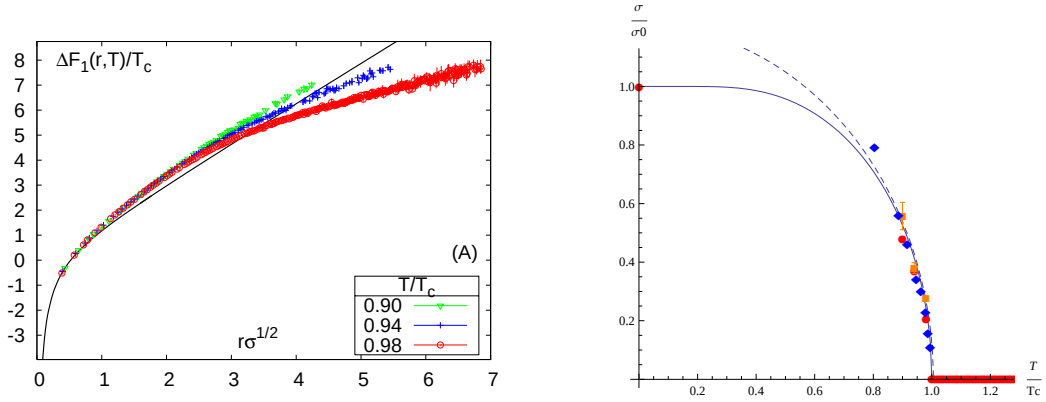

Figure 1: (left) The Bielefeld free F_1 energy at $T < T_c$. (right) Comparing the magnetization critical curve with the string tension σ/σ_0, fitted from the long distance part of F_1, they are quite close.

2 Fits for the finite T string tension from the Lattice QCD energy F_1

At vanishing temperature $T = 0$, the confinement, modelled by a string, is dominant at moderate distances,

$$V(r) \simeq \frac{\pi}{12r} + V_0 + \sigma r \ . \tag{1}$$

At short distances we have the Luscher or Nambu-Gotto Coulomb due to the string vibration + the OGE coulomb, however the Coulomb is not important for chiral symmetry breaking. At finite temperature the string tension $\sigma(T)$ should also dominate chiral symmetry breaking, and thus one of our crucial steps here is the fit of the string tension $\sigma(T)$ from the Lattice QCD data of the Bielefeld Lattice QCD group, [2,3,4,5,6].

The Polyakov loop is a gluonic path, closed in the imaginary time t_4 (proportional to the inverse temperature T^{-1}) direction in QCD discretized in a periodic boundary euclidian Lattice. It measures the free energy F of one or more static quarks,

$$P(0) = Ne^{-F_q/T} \ , \quad P^a(0)\bar{P}^{\bar{a}}(r) = Ne^{-F_{q\bar{q}}(r)/T} \ . \tag{2}$$

If we consider a single solitary quark in the universe, in the confining phase, his string will travel as far as needed to connect the quark to an antiquark, resulting in an infinite energy F. Thus the 1 quark Polyakov loop P is a frequently used order parameter for deconfinement. With the string tension $\sigma(T)$ extracted from the $q\bar{q}$ pair of Polyakov loops we can also estimate the 1 quark Polyakov loop $P(0)$. At finite T, we use as thermodynamic potentials the free energy F_1 and the internal energy U_1, computed in Lattice QCD with the Polyakov loop [2,3,4,5,6]. They are related to the static potential $V(r) = -fdr$ with $F1(r) = -fdr - SdT$ adequate for isothermic transformations. In Fig. 1 we extract the string tensions $\sigma(T)$ from the free energy $F_1(T)$ computed by the Bielefeld group, and we also include string tensions previously computed by the Bielefeld group [7].

We also find an ansatz for the string tension curve, among the order parameter curves of other physical systems related to confinement, i. e. in ferromagnetic materials, in the Ising model, in superconductors either in the BCS model or in the Ginzburg-Landau model, or in string models, to suggest ansatze for the string tension curve. We find that the order parameter curve that best fits our string tension curve is the spontaneous magnetization of a ferromagnet [8], solution of the algebraic equation,

$$\frac{M}{M_{sat}} = \tanh\left(\frac{T_c}{T}\frac{M}{M_{sat}}\right) \ . \tag{3}$$

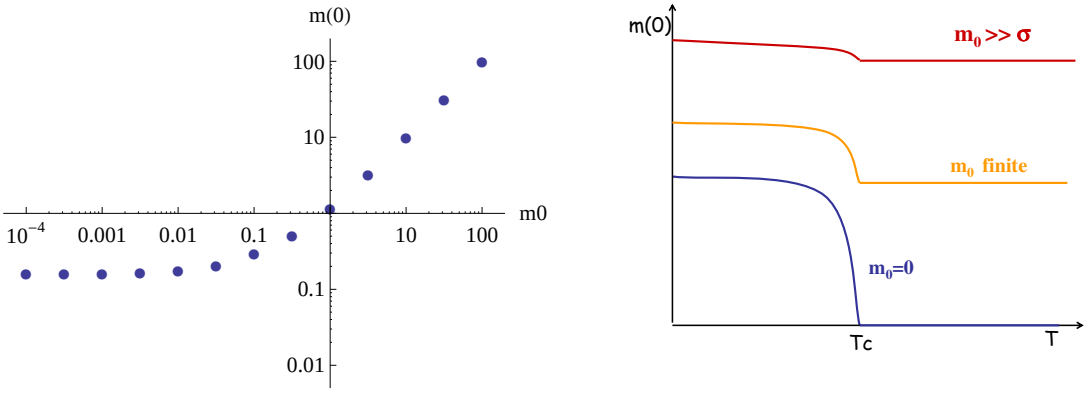

Figure 2: (left) The mass gap $m(0)$ solution of as a function of the quark current mass m_0, in units of $\sigma = 1$. (right) Sketch of the effect of m_0 on the crossover versus phase transition of choral restoration at finite T.

In Fig. 1 we show the solution of Eq. 3 obtained with the fixed point expansion, and compare it with the string tensions computed from lattice QCD data.

3 The mass gap equation with finite T and finite current quark mass m_0.

Now, the critical point occurs when the phase transition changes to a crossover, and the crossover in QCD is produced by the finite current quark mass m0, since it affects the order parameters P or σ, and the mass gap $m(0)$ or the quark condensate $\langle \bar{q}q \rangle$. The mass gap equation at the ladder/rainbow truncation of Coulomb Gauge QCD in equal time reads,

$$m(p) = m_0 + \frac{\sigma}{p^3}\int_0^\infty \frac{dk}{2\pi}\frac{I_A(p,k,\mu)\, m(k) p - I_B(p,k,\mu)\, m(p) k}{\sqrt{k^2 + m(k)^2}} \ , \tag{4}$$

$$I_A(p,k,\mu) = \left[\frac{pk}{(p-k)^2+\mu^2} - \frac{pk}{(p+k)^2+\mu^2}\right] \ ,$$

$$I_B(p,k,\mu) = \left[\frac{pk}{(p-k)^2+\mu^2} + \frac{pk}{(p+k)^2+\mu^2} + \frac{1}{2}\log\frac{(p-k)^2+\mu^2}{(p+k)^2+\mu^2}\right] \ .$$

The mass gap equation (4) for the running mass $m(p)$ is a non-linear integral equation with a nasty cancellation of Infrared divergences[9,10,11]. We devise a new method with a rational ansatz, and with relaxation, to get a maximum precision in the IR where the equation is nearly almost unstable. The solution $m(p)$ is shown in Fig. 2 for a vanishing momentum $p = 0$.

At finite T, one only has to change the string tension to the finite T string tension $\sigma(T)$ [12], and also to replace an integral in ω by a sum in Matsubara Frequencies. Both are equivalent to a reduction in the string tension, $\sigma \to \sigma^*$ and thus all we have to do is to solve the mass gap equation in units of σ^* . The results are depicted in Fig. 2. Thus at vanishing m_0 we have a chiral symmetry phase transition, and at finite m_0 we have a crossover, that gets weaker and weaker when m_0 increases. This is also sketched in Fig. 2.

4 Chiral symmetry and confinement crossovers with a finite current quark mass

In what concerns confinement, the linear confining quark-antiquark potential saturates when the string breaks at the threshold for the creation of a quark-antiquark pair. Thus the free energy $F(0)$ of a single static quark is not infinite, but is the energy of the string saturation, of the order of the mass of a meson i. e. of $2m_0$. For the Polyakov loop we get,

$$P(0) \simeq N e^{-2m_0/T} \ . \tag{5}$$

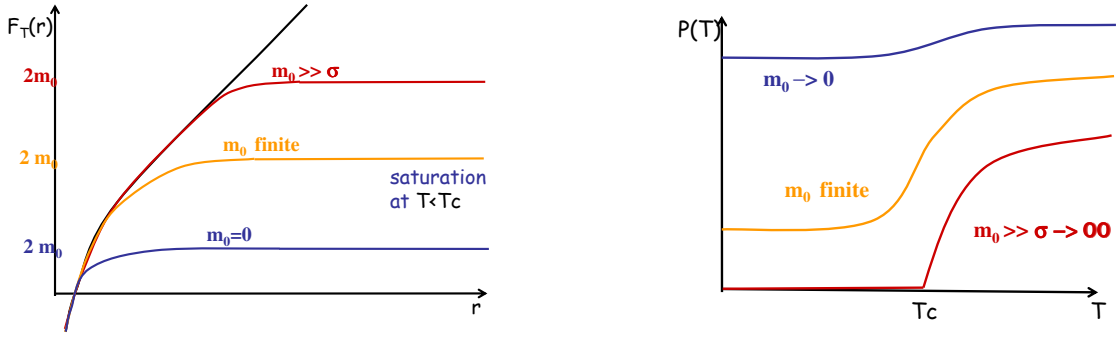

Figure 3: Sketches of the saturation of confinement (left), and of the corresponding crossover in the order parameter P polyakov loop (righ).

Thus at infinite m_0 we have a confining phase transition, while at finite m_0 we have a crossover, that gets weaker and weaker when m_0 decreases. This is sketched in Fig. 3.

Since the finite current quark mass affects in opposite ways the crossover for confinement and the one for chiral symmetry, we conjecture that at finite T and μ there are not only one but two critical points (a point where a crossover separates from a phase transition). Since for the light u and d quarks the current mass m_0 is small, we expect the crossover for chiral symmetry restoration critical to be closer to the $\mu = 0$ vertical axis, and the crossover for deconfinement to go deeper into the finite μ region of the typical critical curve in the QCD phase diagram presently assumed [1].

Acknowledgments

References

1. CBM Progress Report, publicly available at http://www.gsi.de/fair/experiments/CBM, (2009); J. M. Heuser [CBM Collaboration], Nucl. Phys. A **830**, 563C (2009) [arXiv:0907.2136 [nucl-ex]].
2. M. Doring, K. Hubner, O. Kaczmarek and F. Karsch, Phys. Rev. D **75**, 054504 (2007) [arXiv:hep-lat/0702009].
3. K. Hubner, F. Karsch, O. Kaczmarek and O. Vogt, arXiv:0710.5147 [hep-lat].
4. O. Kaczmarek and F. Zantow, Phys. Rev. D **71**, 114510 (2005) [arXiv:hep-lat/0503017].
5. O. Kaczmarek and F. Zantow, arXiv:hep-lat/0506019.
6. O. Kaczmarek and F. Zantow, PoS **LAT2005**, 192 (2006) [arXiv:hep-lat/0510094].
7. O. Kaczmarek, F. Karsch, E. Laermann and M. Lutgemeier, Phys. Rev. D **62**, 034021 (2000) [arXiv:hep-lat/9908010].
8. R. Feynamn, R. Leighton, M. Sands, "The Feynman Lectures on Physics", Vol II, chap. 36 "Ferromagnetism", published by Addison Wesley Publishing Company, Reading, Massachussets, ISBN 0-201-02117-x (1964).
9. S. L. Adler and A. C. Davis, Nucl. Phys. B **244**, 469 (1984).
10. P. J. A. Bicudo and A. V. Nefediev, Phys. Rev. D **68**, 065021 (2003) [arXiv:hep-ph/0307302].
11. F. J. Llanes-Estrada and S. R. Cotanch, Phys. Rev. Lett. **84**, 1102 (2000) [arXiv:hep-ph/9906359].
12. P. Bicudo, arXiv:1003.0936 [hep-lat].

Eccentricity Fluctuations in p-p and Elliptic Flow

Jorge Casalderrey-Solana
Physics Department, Theory Unit, CERN, CH-1211 Genève 23, Switzerland

We discuss under which conditions elliptic flow becomes measurable in high-multiplicity ($dN_{\rm ch}/dy \geq 50$) p-p collisions, which will soon be collected at the LHC. We observe that fluctuations in the p-p interaction region can result in a sizable spacial eccentricity even for the most central p-p collisions. Under relatively mild assumptions on the nature of such fluctuations and on the eccentricity scaling of elliptic flow, we find that the resulting elliptic flow signal in high-multiplicity p-p collisions at the LHC becomes measurable with standard techniques.

1 Introduction

In a high energy nuclear collision at non-zero impact parameter the interaction region is anisotropic in the transverse plane. Collective phenomena, such as final state interactions of the collision products, lead to a transfer of the spacial anisotropy of the collision geometry into a azimuthal momentum anisotropy of the final particles in the collision. This phenomenon is called elliptic flow and it is one of the most important observables in ultrarelativistic heavy ion collisions. The large values of the elliptic flow parameter $v_2 = \langle \cos 2\phi \rangle$ at RHIC signal very strong collective phenomena of the QCD matter created in these collisions.

The large collectivity observed in nucleus-nucleus collisions leads to the question of wether these effects are also present in other hadronic collisions such as in p-p. There is, however a conceptual difference, since the spacial distribution in the nuclear case is due to the distribution of nucleons inside the nuclei, while in the proton there is only one nucleon. However, protons, as nuclei, are extended objects; the spacial distribution of the individual partonic collisions which lead to particle production are the responsible for the spacial anisotropy.

The transverse plane asymmetry in the collision region is not sufficient for elliptic flow, since final state interactions are needed to transfer this anisotropy into momentum distributions. A typical p-p collision produces too few particles for this transfer to occur . However, high energy p-p collisions at the LHC will produce rare very high multiplicity events, in which the final state multiparticle interactions are important and, thus, certain degree of collective behavior for these class of events is expected.

Finally, we would like to remark that even if an azimuthal asymmetry is imprinted into the momentum distribution in p-p, the experimental determination of v_2 is complicated by the finite number of particles involved in these collisions. The main difficulty is to separate true collective effects on the anisotropy to other sources of multiparticle correlations unrelated to flow. One of the most systematic analysis to perform this task is the cumulant analysis, which uses n_p-particle correlations to determine v_2. The effect of non-flow correlations is reduced as the event multiplicity grows; different n_p-correlations lead to a constraint on the minimum value

Table 1: Constraints on the minimum v_2 value so that it is dominated by flow effects as a function of the multiplicity per unit rapidity and for different n_p-cumulants

	$n_p = 2$	$n_p = 4$
v_2 ($n_{\rm mult} = 30$)	> 0.18	> 0.09
v_2 ($n_{\rm mult} = 50$)	> 0.14	> 0.05
v_2 ($n_{\rm mult} = 80$)	> 0.11	> 0.04

of v_2 such that it is dominated by flow. A table summarizing this constraints is shown in Table 1 [1].

2 Eccentricity fluctuations in p-p collisions

Unlike the nucleus-nucleus case, where the matter distribution in the colliding region is determined by the distribution of nucleons involved in the collision, the spacial distribution of matter in a high energy p-p collision is not known. Since flow is sensitive to this distribution, this type of measurements could be potentially used to constraint models of the proton structure at high energy.

The study of flow in heavy ion collisions shows that v_2 is proportional to the (matter density weighted) eccentricity of the colliding region

$$\epsilon = \frac{\langle y^2 \rangle - \langle x^2 \rangle}{\langle y^2 \rangle + \langle x^2 \rangle} \, . \tag{1}$$

where (x, y) are coordinates in the transverse plane with x along the impact parameter. At a fixed impact parameter, different matter distribution for the proton lead to different values of the eccentricity.

Early attempts to asses flow effects in proton-proton considered the proton as a homogenous and smooth distribution of partons [3,4,5]. In these models, the multiplicity distribution is correlated to the centrality of the collision. Thus, sizable eccentricities occur only at finite impact parameter, where the multiplicity of the event is not maximal. This approach leads to small values for $v_2 \leq 0.03$ which are at odds with the constraints in Table 1.

Even if the proton is homogeneous, it is important to take into account the granularity of the matter distribution: even if assuming that all partons are homogeneously distributed within the proton, only a finite number of partonic collisions occur. Thus, on an event-by-event basis, the distribution of these partons changes; as a consequence, even in the most central collisions, where the eccentricity is naively zero, the eccentricity also changes in an event by event basis. Similar fluctuations in the nucleon distribution within the nuclei are important for the correct description of heavy ion v_2 data [7]. In Fig. 1 a the eccentricity distribution for the most central collision for the model of [5] is shown, which, as argued, extends to large eccentricity values.

A different approach is to assume that the scattering centers are not homogeneously distributed within the proton but that they are concentrated in a finite number N_s of "hot spots" with a typical size r_0. As in the previous case, on an event by event basis the hot spots are distributed within the proton and the different configurations lead to different eccentricity values even in the most central collision, which in this case corresponds to those collisions in which all N_s spots interact. The eccentricity distribution for $N_s = 3$ and different values of r_0 is shown in Fig. 1 b [1]. This somewhat extreme model leads to distributions peaked at very large values of the eccentricity. As the number of spots grows, the eccentricity of these central collisions tends to zero as expected.

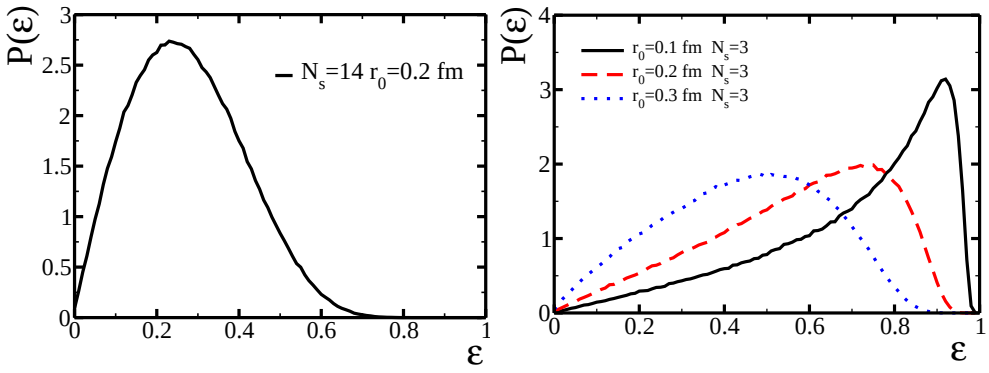

Figure 1: Eccentricity distribution of high multiplicity p-p collisions (central). The left panel shows the distribution for the homogenous model, with $N_s = 14$ scattering. The right panel is for a model in which all the hadronic activity is concentrated in $N_s = 3$ spots of different size r_0.

3 From eccentricity to flow

The eccentricity distributions shown in Fig. 1 are not directly measurable but they are transfered into the momentum distribution via final state interactions. Determining the precise form in which this transfer occurs demands a dynamical calculation along the lines of [4]. However, the flow systematics observed in heavy ion collisions can be used to estimate the final v_2 value. In fact the study of different colliding systems at different energies leads to the conclusion that v_2 is a universal function of the eccentricity of the colliding region and the transverse density of particles[7] . A simple parameterization based on hydrodynamics and which incorporates viscous effects was given in [2]

$$v_2 = \epsilon \left(\frac{v_2}{\epsilon}\right)^{hydro} \frac{1}{1 + \frac{\bar{\lambda}}{K_0}\frac{\langle S\rangle}{\frac{dN}{dy}}}\,, \tag{2}$$

where $< S >$ is the transverse area of the collision, $(v_2/\epsilon)^{hydro}$ is the hydro limit and $\bar{\lambda}/K_0$ is a fitted parameter.

The relation Eq. (2) is valid in an event by event basis. However, the extraction of v_2 demands average over many events, *i. e.*, the distributions in Fig. 1. In particular, the fourth cumulant v_2, $v_2\{4\}$ is proportional to [6]

$$\epsilon\{4\} \equiv \left(2\left\langle\epsilon^2\right\rangle^2 - \left\langle\epsilon^4\right\rangle\right)^{1/4}\,. \tag{3}$$

In Fig. 2 we show the predicted (event averaged) $v_2\{4\}$ for the two different models sketched in the previous section for central (high multiplicity) proton-proton collisions as a function of multiplicity. In both plots, the continuous line is the hydrodynamic limit $\bar{\lambda}/K_0 = 0$, the dashed line correspond to the fitted value $\bar{\lambda}/K_0 = 0.58 fm^{-2}$, and the dotted line is twice this value. On Fig. 2 a we show the results for the homogenous model, with $N_s = 14$ scattering centers: the expected values of v_2 is large and it is comparable to the constraints in Table 1; the value extracted is, in particular, twice as large as the model studies in which the smooth approximation is used. In Fig. 2 b we show the expected v_2 values for the more extreme model in which all the hadronic activity is concentrated in $N_s = 3$ hot spots with radius $r_0 = 0.1$, 0.2, 0.3 fm; in all these cases the values of v_2 are very large and they should be easily distinguishable from non-flow correlations.

In both the cases studied, the density fluctuations in the proton lead to a distinct signal on the azimuthal asymmetry of the produced particles, v_2 which is measurable and distinguishable from non-flow correlations.

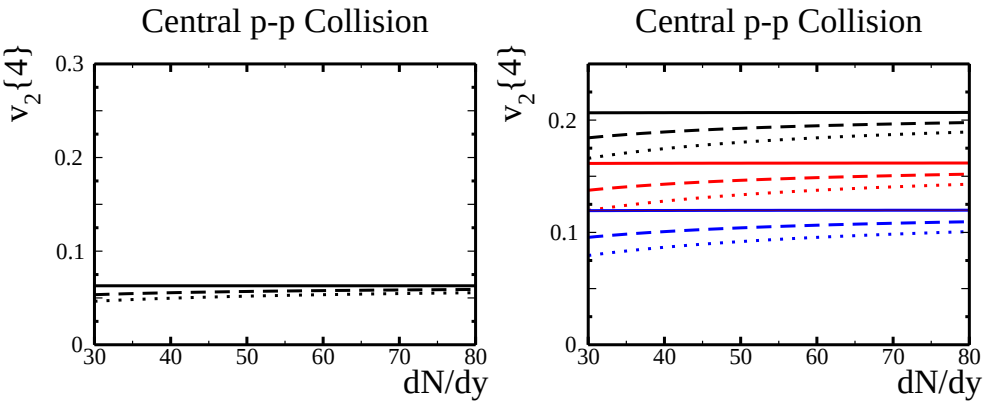

Figure 2: The flow signal $v_2\{4\}$ as a function of multiplicity in most central p-p collisions, for models of $N_s = 14$ (left), $N_s = 3$ (right) interaction regions of radius $r_0 = 0.1$ (top 3 curves), $r_0 = 0.2$ (middle curves), and $r_0 = 0.3$ fm (bottom curves). Signals calculated for $\bar{\lambda}/K_0 = 0$, 5.8 and 11.6 fm^{-2} are displayed by solid, dashed and dotted lines, respectively.

4 Conclusions

In this work we have argued that density fluctuations in the proton wave function play an essential role in determining collective effects in p-p collisions. The effect of these fluctuations is two-fold: on the one hand the eccentricity distribution of the colliding system peaks at sizable values; on the other hand, it allows to have a non vanishing v_2 for those p-p events with highest multiplicity. As shown in Table 1, high multiplicity is an essential requirement for distinguishing flow from non-flow effects on azimuthally asymmetric particle distribution. In both the models studied, the eccentricity fluctuations of the colliding region leads to v_2 values which are measurable for the largest multiplicities achieved in p-p collisions at the LHC.

Determining elliptic flow in p-p is important since it will demonstrate the system independence of the phenomena. Given the small size of the proton, the analysis of collective motion in this smaller system will allow a better constraint of the dissipative and thermalization properties of deconfined QCD matter. Finally, since the elliptic flow signal depends essentially on the density distribution of the proton, this measurement will lead to stringent constraints on models of soft interactions within the proton, as can be concluded from the different values of $v_2\{4\}$ in the models we have analyzed.

Acknowledgments

The work presented in this talk was done in collaboration with U. A. Wiedemann. I have been supported by a Marie Curie Intra-European Fellowship (PIEF-GA-2008-220207).

References

1. J. Casalderrey-Solana and U. A. Wiedemann, Phys. Rev. Lett. **104** (2010) 102301
2. R. S. Bhalerao, J. P. Blaizot, N. Borghini and J. Y. Ollitrault, Phys. Lett. B **627**, 49 (2005).
3. D. d'Enterria, G. K. Eyyubova, V. L. Korotkikh, I. P. Lokhtin, S. V. Petrushanko, L. I. Sarycheva and A. M. Snigirev, arXiv:0910.3029 [hep-ph].
4. M. Luzum and P. Romatschke, arXiv:0901.4588 [nucl-th].
5. L. Cunqueiro, J. Dias de Deus and C. Pajares, arXiv:0806.0523 [hep-ph].
6. M. Miller and R. Snellings, arXiv:nucl-ex/0312008.
7. B. Alver *et al.* [PHOBOS Collaboration], Phys. Rev. Lett. **98**, 242302 (2007).

CGC phenomenology at RHIC and the LHC

J. L. Albacete
Institut de Physique Théorique, CEA/Saclay, 91191 Gif-sur-Yvette cedex, France
URA 2306, unité de recherche associée au CNRS

I present a brief review of the recent phenomenological analyses of RHIC data based on the the Color Glass Condensate and including the use of non-linear evolution equations with running coupling. In particular, I focus in the study of the total multiplicities in Au+Au collisions, and in the single inclusive and double inclusive forward spectra in d+Au collisions. Predictions for the LHC are also discussed

At high energies, QCD scattering enters a novel regime governed by large gluon densities and coherent, non-linear phenomena, including *saturation* of the hadronic wave functions, known as the Color Glass Condensate (CGC) (see e.g., the review [1] and references therein). Nuclear collisions performed at RHIC provide a good opportunity to explore the CGC regime, since the gluon densities in a nucleus are already large even at moderate energies. The recent calculation of running coupling corrections [2,3,4,5] to the BK-JIMWLK evolution equations of the CGC allows for a good quantitative description of several experimental measurements, thus reducing the degree of modelization required in phenomenological studies. Here I present a brief review of the phenomenological analyses of RHIC data based on the use of Balitsky-Kovchegov equation [6,7] including running coupling correction (rcBK) for the description of the small-x degrees of freedom of the wavefunction of the colliding nuclei. We also discuss predictions for the LHC.

The rcBK equation for the small-x evolution of the dipole scattering amplitude reads

$$\frac{\partial \mathcal{N}(x,r)}{\partial \ln(x_0/x)} = \int d^2 r_1 \; K^{\rm run}(r,r_1,r_2)\left[\mathcal{N}(x,r_1)+\mathcal{N}(x,r_2)-\mathcal{N}(x,r)-\mathcal{N}(x,r_1)\,\mathcal{N}(x,r_2)\right] \;, \quad (1)$$

where r_i refers to the dipoles tranverse sizes and x_0 is the starting point for the evolution. The running coupling kernel $K^{\rm run}$ is evaluated according to Balitsly's prescription [2]. In the analyses presented below, the rcBK equation is supplemented with MV initial conditions at the starting evolution point, x_0, $\mathcal{N}_{F(A)}(r,x_0) = 1-\exp\left[-\frac{r^2\,Q_{s0}^2}{4}\,\ln\left(\frac{1}{\Lambda\, r}+e\right)\right]$, with Q_{s0} the initial quark (gluon) saturation scale and $\Lambda = 0.241$ GeV.

1 Multiplicity densities in nucleus-nucleus collisions a RHIC and the LHC.

The total number of particles produced per unit rapidity in RHIC Au+Au collisions turned out to be significantly lower than predicted assuming incoherent superposition of nucleon-nucleon scattering, signaling the importance of coherence effects. Such reduced multiplicities are interpreted in the CGC as a consequence of a reduced flux of scattering centers, i.e. gluons, entering the collision due to saturation effects in the wave function of the colliding nuclei. Thus, the final number of produced particles rises proportional to the number of gluons in the incoming wavefunction, whose growth can be described by the rcBK equation. Even if its applicability to nucleus-nucleus collisions is not completely justified, such idea is realized in the k_T-factorization framework, as proposed in [8], where the multiplicity distributions can be written as :

$$\frac{dN_{ch}}{dy\,d^2b} = C\frac{4\pi N_c}{N_c^2-1}\int \frac{d^2p_t}{p_t^2}\int^{p_t} d^2k_t\,\alpha_s(Q)\,\varphi\left(x_1,\frac{|\underline{k}_t+\underline{p}_t|}{2}\right)\varphi\left(x_2,\frac{|\underline{k}_t-\underline{p}_t|}{2}\right), \quad (2)$$

where p_t and y are the transverse momentum and rapidity of the produced particle, $x_{1,2} = (p_t/\sqrt{s})\,e^{\pm y}$. $\varphi(x,\underline{k}_t) = \int \frac{d^2r}{2\pi\, r^2} e^{i\,k_t\cdot r}\,\mathcal{N}(x,r)$ is the nuclear unintegrated gluon distribution. The

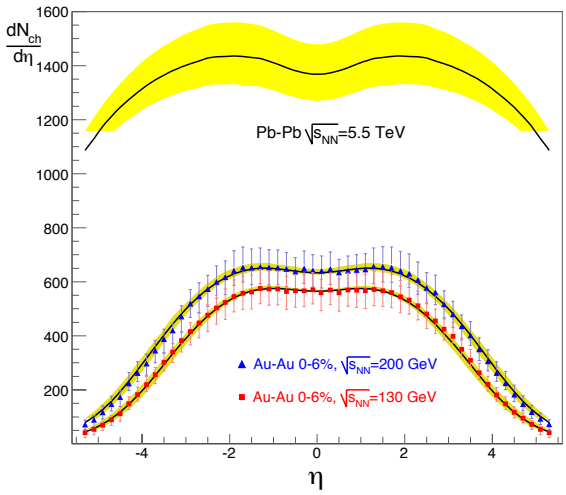

Figure 1: Multiplicity densities as a functiion of pseudorapidity in RHIC Au+Au collisions at $\sqrt{s} = 200$ and 130 GeV (data by the PHOBOS Coll.). Uppermost curves correspond to predictions for Pb+Pb collisions at the LHC ($\sqrt{s} = 5.5$ TeV).

lack of impact parameter integration in this calculation and the gluon to charged hadron ratio are accounted for by the constant C, which sets the normalization. As shown in Fig. 1, the use of Eq. (2) together with rcBK equation for the small-x dynamics of the nuclear ugd provides [9] a good description of the energy and pseudorapidity dependence of data [?] for the multiplicity densities in Au+Au collisions at the highest collision energies at RHIC. With all the parameters in the calculation constrained by RHIC data, the extrapolation to Pb+Pb collisions at the LHC is now completely driven by the small-x dynamics, yielding $\frac{dN_{ch}^{Pb-Pb}}{d\eta}(\sqrt{s}=5.5\,\mathrm{TeV}, \eta = 0) \sim 1290 \div 1480$.

2 Forward single inclusive spectra in p+p, d+Au and p+Pb collisions.

The experimentally observed suppression of forward hadron yields in d+Au collisions compared to those measured in p+p collisions was predicted in CGC base calculations, albeit at a qualitative level[10,11]. Thanks to the new theoretical tools available, now it is also possible to get a good quantitative description of such suppression [12]. At forward rapidities, where the projectile is probed at large-x and the target nucleus at small-x, single inclusive hadron production can be calculated as [13]:

$$\frac{dN_h}{dy_h\, d^2p_t} = \frac{K}{(2\pi)^2} \sum_q \int_{x_F}^1 \frac{dz}{z^2} \left[x_1 f_{q/p}(x_1, p_t^2)\, \tilde{N}_F\left(x_2, \frac{p_t}{z}\right)\, D_{h/q}(z, p_t^2) + x_1 f_{g/p}(x_1, p_t^2)\, \tilde{N}_A\left(x_2, \frac{p_t}{z}\right)\, D_{h/g}(z, p_t^2) \right] , \qquad (3)$$

where p_t and y_h are the transverse momentum and rapidity of the produced hadron, and $f_{i/p}$ and $D_{h/i}$ refer to the parton distribution function of the incoming proton and to the fragmentation function respectively. The gluon distributions representing the target are given by the Fourier transforms of the dipole amplitude: $\tilde{N}_{F(A)}(x,k) = \int d^2\mathbf{r}\, e^{-i\mathbf{k}\cdot\mathbf{r}} \left[1 - \mathcal{N}_{F(A)}(r,x)\right]$, where F(A) stands for fundamental (adjoint) representation.

With $Q_{s0}^2 = 0.4 \div 0.5$ GeV^2 (for quarks) and $0.005 < x_0 < 0.025$, we [12] obtain a very good description of the forward negative charged hadrons at $y = 2.2$ and 3.2 (data by the BRAHMS Collaboration [17]) and neutral pion production at $y = 4$ (data by the STAR collaboration [18]) in minimum bias d+Au collisions, as shown in Fig. 2 (left). An equally good description is

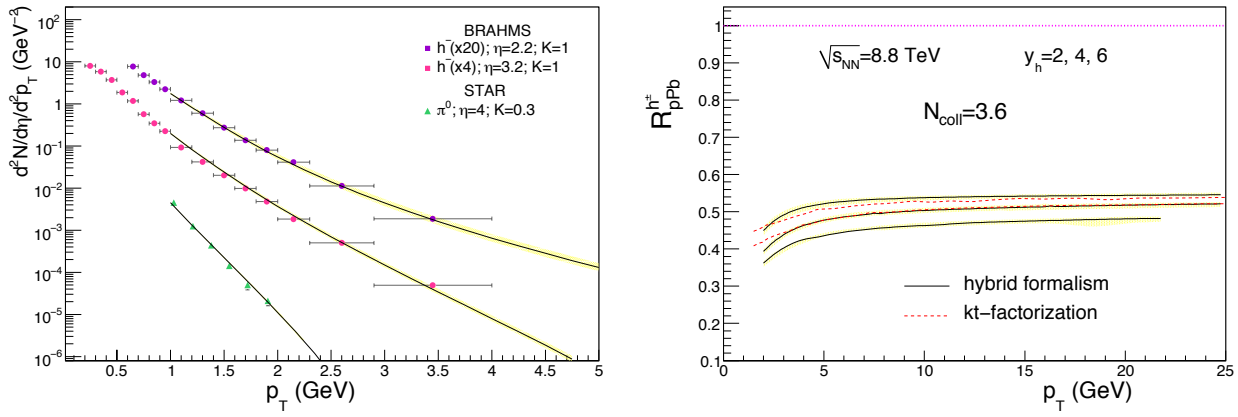

Figure 2: Left: Charged hadron ($y = 2.2$ and 3.2) and neutral pion ($y = 4$) spectra in d+Au collisions. Right: Predicted nuclear modification factor for charged hadron spectra in p+Pb collisions at the LHC.

obtained for proton-proton data at the same collision energy with $Q_{s0}^2 = 0.2$ GeV^2. Remarkably, the description of negative charged hadrons does not require any K-factors, i.e. $K = 1$. However, for neutral pion production we get $K = 0.3\,(0.4)$ in d+Au (p+p) collisions. In agreement with other CGC calculations, we predict a sizable (~ 0.5) suppression for the nuclear modification factor $R_{pPb} = (dN_{h^\pm}^{pPb}/dyd^2p_t)/(dN_{h^\pm}^{pp}/dyd^2p_t)/N_{coll}$ where, following the experimental analyses at RHIC, we have taken $N_{coll} = 3.6$.

3 Di-hadron azimuthal correlations at forward rapidities in d+Au collisions.

Recent measurements of azimuthal forward di-hadron correlations in d+Au collisions by the STAR Collaboration [15] exhibit the feature of *monojet* production, i.e., the suppression of the away-side peak characteristic of approximate back-to-back correlations. Following [16], we calculated the forward double inclusive pion production in d+Au collisions in the CGC framework [14]. More specifically, we are interested in the coincidence probability, which is the experimental measured quantity. It is given by $CP(\Delta\phi) = N_{pair}(\Delta\phi)/N_{trig}$ with

$$N_{pair}(\Delta\phi) = \int\limits_{y_i, |p_{i\perp}|} \frac{dN^{dAu\to h_1h_2X}}{d^3p_1 d^3p_2}\ ,\ N_{trig} = \int\limits_{y,\ p_\perp} \frac{dN^{dAu\to hX}}{d^3p}\ , \tag{4}$$

and it has the meaning of the probability of, given a trigger hadron h_1 in a certain momentum range, produce an associated hadron h_2 in another momentum range and with a difference between the azimuthal angles of the two particles equal to $\Delta\phi$. Following the experimental analysis by the STAR collaboration [15], we set $|p_{1\perp}| > 2$ GeV, 1 GeV $< |p_{2\perp}| < |p_{1\perp}|$ and $2.4 < y_{1,2} < 4$ for the transverse momenta and rapidity of the produced pions. Our results, shifted by an arbitrary offset, are shown in Fig 3, together with the corresponding preliminary data by the STAR collaboration. The disappearance of the away-side peak around $\Delta\phi \sim \pi$ in d+Au collisions exhibited by data is quantitatively well described by our CGC calculation. In our approach, the angular decorrelation is due to the the momentum broadening induced by the propagation of the projectile (or its Fock states) through the nucleus. The momentum

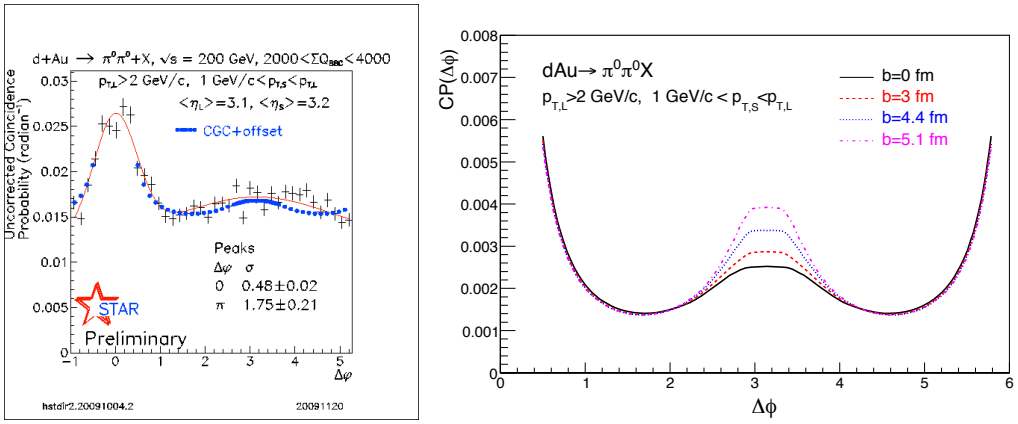

Figure 3: Left: $CP(\Delta\phi)$ for forward pions in d+Au collisions (preliminary data by the STAR Coll.) and CGC theoretical results (blue dots). Right: $CP(\Delta\phi)$ for various collision centralities.

broadening, in turn, is related to the saturation scale of the target nucleus, which is large in the forward region. Fig 3 (right) shows the centrality dependence of our calculation. We predict that the away peak should reappear for more peripheral collisions or, at a fixed rapidity, for larger momenta of the detected particles.

Acknowledgments

This work is supported by a Marie Curie Intra-European Fellowship (FP7- PEOPLE-IEF-2008), contract number 236376.

References

1. F. Gelis, E. Iancu, J. Jalilian-Marian, and R. Venugopalan. arXiv:1002.0333 [hep-ph].
2. I. I. Balitsky. *Phys. Rev. D*, 75:014001, 2007.
3. Y. Kovchegov and H. Weigert. *Nucl. Phys.* **A**, 784:188–226, 2007.
4. E. Gardi, J. Kuokkanen, K. Rummukainen and H. Weigert, Nucl. Phys. A **784** (2007) 282
5. Javier L. Albacete and Yuri V. Kovchegov. *Phys. Rev.*, D75:125021, 2007.
6. I. Balitsky, Nucl. Phys. B **463**, 99 (1996).
7. Y. V. Kovchegov, Phys. Rev. D **60**, 034008 (1999).
8. Dmitri Kharzeev, Eugene Levin, and Marzia Nardi. *Phys. Rev.*, C71:054903, 2005.
9. Javier L. Albacete. *Phys. Rev. Lett.*, 99:262301, 2007.
10. Javier L. Albacete, Nestor Armesto, Alex Kovner, Carlos A. Salgado, and Urs Achim Wiedemann. *Phys. Rev. Lett.*, 92:082001, 2004.
11. Dmitri Kharzeev, Yuri V. Kovchegov, and Kirill Tuchin. *Phys. Rev.*, D68:094013, 2003.
12. Javier L. Albacete and Cyrille Marquet. *Phys. Lett.*, B687:174–179, 2010.
13. Adrian Dumitru, Arata Hayashigaki, and Jamal Jalilian-Marian. *Nucl. Phys.*, A765:464–482, 2006.
14. Javier L. Albacete and Cyrille Marquet. arXiv:1005.4065 [hep-ph].
15. Ermes Braidot for the STAR collaboration. arXiv:1005.2378 [hep-ph]. In these proceedings.
16. Cyrille Marquet. *Nucl. Phys.*, A796:41–60, 2007.
17. I. Arsene *et al.* [BRAHMS Collaboration], Phys. Rev. Lett. **93** (2004) 242303
18. J. Adams *et al.* [STAR Collaboration], Phys. Rev. Lett. **97**, 152302 (2006)

Jet-medium interaction and heavy quark energy loss

LI Shi-Yuan
School of Physics, Shandong University, Jinan, 250100, PR China

In relativistic heavy ion collisions, the interaction between the jet and the quark-gluon medium has an analogy of high energy hadronic scattering. Pionization provides the key for understanding the experimental results of the energy loss of heavy quark, and several other 'puzzles'. The space-time picture of this interaction is discussed. Experimental tests are suggested.

By relativistic heavy ion (A-A) collisions, it is expected to produce de-confined quark-gluon matter (QGM, here refers to any possible state reached after the collision, not necessarily the deconfined or thermalized one), which is a new and special arena for Quantum Chromodynamics (QCD). These matter states present the most dense medium which human being has been able to produce. Investigation on results of their coupling with gravity hence geometry can provide copious information for cosmology study [1].

One of the genius ways to probe these states (e.g., their density) of the medium after the violent A-A collision is 'jet tomography', which relies on the mechanisms of the interactions between the hard parton (with large transverse momentum p_T) created in the initial collisions and the QGM. A lot of phenomena predicted by such an idea have been observed at the relativistic heavy ion collider (RHIC). The list of references on early pioneering works setting up this idea, as well as to-date formulations and experiments can be found in Ref. [2].

Until now, it is adopted that the medium-induced coherent bremsstrahlung from the hard parton is the dominant mechanism of its energy loss, which, physically, is a straightforward extrapolation of the 'parton shower' from vacuum to medium. In consequence, the dead cone e ect for the massive quark (charm or bottom, referred as c or b in the following) case is a typical property [3]. However, experiments [4] on p_T spectra of non-photonic leptons from heavy quark (without distinguishing c or b) decays indicate that the energy loss of the heavy quarks is almost the same as that of the light ones. Recent results of jet in A-A collisions [5] showes that the jet is significantly 'quenched', but contrary to expectations, no apparent modification of the associate fragmentation function (FF) relative to hadron-hadron (h-h) collision is observed.

In this paper we revisit 'pionization' [6,7] common to all high energy hadronic collisions, and apply this property to the 'e ective collision' between the hard jet and QGM. The *stochastic* (rather than collinear) nature of the emission angle of the pionization products is helpful to understand why the dead cone a ects little and why the FF associate with jet in A-A collision is similar as that in h-h collisions. And there are more puzzles can be understood based on this picture (see following). The corresponding process for pionization in the Quantum Electrodynamics (QED) case is (fermion) pair production [6,7]. Electromagnetic energy loss of electron or muon in medium from electron-positron pair production exceeds that from photon bremsstrahlung at enough high energies (see, e.g., [8,9]).

Pionization products correspond to the particles which constitute the 'rapidity plateau' in high energy hadronic scattering [6,7]. They may be important component of the QGM in A-A collision but are irrelevant to the high p_T partons created in the rare hard interactions, which is employed as the hard probe. Here we discuss the pionization in the *e ective high energy jet-QGM scattering*, which mimics the interactions between the hard probe parton and the QGM. The physical picture hence should be first clarified and established now.

With the naïve parton picture, it is easy to find that in any scatterings, if no QGM produced and residual around the overlap region of the two colliding objects, a hard parton created within the space-time scale $1/Q$ in the time of overlap, will never 'meet' anything more than the vacuum in the following time ($t > 1/Q$, if choosing t=0 for the time when the overlap begins). So its following radiation is the hard interaction induced bremsstrahlung. The dominant phase space is collinear and soft, resulting to the 'Sodukov double log' ($LogELogp_T$, with $E \sim p_T \sim Q$)[10]. The most simple example is the $e^+e^- \to q\overline{q}$. Each moves apart back to back, radiations induced by the hard process (say, quark pair hit by the virtual photon or Z^0) develop dominantly soft and collinear. In the Breit frame to observe deeply inelastic scattering, one find the very similar picture. That is, the parton (x is not very large) hit by the virtual photon turns back in the space-time scale $1/Q$, after this interval, the remnant of the hadron (or nuclear) has passed this region (taking into account the Lorentz contraction). So these two issues move apart back to back, contrary to some belief that the hard parton goes through the remnant as passing via 'cold quark gluon matter'. The radiation induced by this hit develops just as the case of e^+e^-. Extra 'initial state radiation' has the similar property. A very simplified example (but containing all the main elements) treated in quantum electrodynamics can be found in Peskin and Schroeder's quantum field theory text book. This analysis can be applied to hadronic interactions. All these suppose that, during the overlap of the two highly Lorentz contracted colliding issues, hard interaction happens, all the other 'underlying reactions' will not change the property of the vacuum, so the hard parton in the following evolution travels in vacuum, leaving apart from all the others from the hadron(s). However, the hard probe issue is just contrary, in which some QGM produced by underlying interactions during the overlap, develops and expands around the overlap region. In this case, the hard parton will collide with gradient(s) of the QGM in subsequential traveling. So, if the behaviour of energy loss in A-A is just the similar as in other processes, e.g., obvious dead cone e ects observed, this could mean no QGM produced. Very the contrary case that dead cone e ects not observed, make it possible to deduce the belief that the vacuum is changed (whether thermalized or not is irrelevant).

Jet is a bundle of collimated, on shell particles, with the invariant mass M of them (as whole) much smaller than the energy/virtuality Q at which the jet (rigorously to say, the hard parton initializing the jet) is created. We use E, p_T to denote its energy and transverse momentum, respectively, with $E \sim p_T \sim Q$ in our discussions. This energetic hard parton evolutes from the space-time scale $\sim 1/p_T$ to $\sim 1/M$ ($M << p_T$) by gluon radiation, and the jet is preliminarily shaped, defined by various infrared safe jet algorithms at partonic level (referred as 'preliminary jet' in the following). Because $1/M << 1fm$, just the asymptotically free region of QCD, any extra interaction or radiation via momentum transfer $\sim> M$ will lead to extra suppression by (small) α_s and (large) denominator of the propagator (all $\sim> M$). So the evolution during $1/p_T$ to $1/M$ (hence the preliminary jet) is hardly di erent whether it is created in h-h, A-A, e^+-e^-, or other collisions. However, the subsequent evolutions to larger space-time scale will recognize the 'environment'. The uniqueness of 'central' A-A collision is the existence of the QGM rather than the vacuum in other more 'simple' scatterings. Because $M << p_T \sim E$, *the jet as a whole can be taken as an energetic composite particle with energy E and mass M hitting and passing through the QGM as target (Such is the jet tomography),* with the space-time picture discussed in last paragraph. Each member (parton) of the jet, as the role of constituent, will interact with the QGM. So *the jet interacting with the QGM is quite in common as the high energy hadronic*

or nuclear scatterings such as a proton or nucleus hitting a target. Based on such a physical picture, without referring to any of the microscopic details of the QGM and the energy and p_T distribution of the preliminary jet, but employing the properties common to any hadronic collisions drawn from experimental facts (e.g., pionization and limiting fragmentation), one can qualitatively explain the above mentioned experimental 'paradoxes' at RHIC[11]. This is desirable since QGM is 'uncharted', while the distribution of the preliminary jet is not well predictable if factorization is broken, at the case that the multiplicity is triggered hence the unitarity of the summation of soft interactions is violated.

Further discussions to be found in [11]. The experimental condition for jet tomography helps to understand why pionization dominant. The hard trigger in A-A only make sure a hard jet produced (hardly soft parton becomes hard by absorbing energy from medium, this even contradicting to the 2nd law of thermodynamics). But the subsequential interactions with the medium are not controllable. So the total inelastic cross section rather than the *rare* hard part of the e ective jet-medium scattering is relevant.

The pionization products are characteristic of the phase space dominated by $k^+ \sim k^-$, i.e., modest rapidity, in center of mass frame. The collinear approximation for the phase space, $k^0 >> k_T$ ($k^+ >> k^-$ or $k^- >> k^+$), only valid for the fragmentation (bremsstrahlung), misses almost all the pionization products. For incorporating pionization, one must take into account the full phase space (all the rapidity region). In which for fixed energy, the angular distribution is random. Systematic calculations and arguments to all orders, with the gluon propagators reggeized, result in the extended eikonal formula (see [6] and refs. therein, which also give brief accounts for the relation with the pomeron), which gives the S-matrix of the scattering process in impact parameter space via the eikonal operator. The extended eikonal formula implies a physical picture of multi-production of high energy scattering. It is a stochastic process in which quanta are created and annihilated in a random way [6]. Though the transverse degrees of freedom distribute according to the specific dynamics and the structure of colliding issues, the longitudinal distribution is just the rapidity plateau, with width proportional to $\ln s$, and s the center of mass energy squared of the scattering. This is the microscopic basis of our extrapolating the property of pionization to the e ective jet-QGM collision and indicates the increase of the relative rate of the pionization energy loss with the jet energy due to the logarithmically increasing rapidity plateau width. The pionization energy loss of the preliminary jet can be estimated to be

$$< \Delta E >= \int_{y_{min}}^{y_{max}} dy d^2k_T \Big(\frac{d\sigma}{dy d^2k_T}\Big) k^0(y, k_T) \Big/ \sigma_{incl} \sim C \int_{y_{min}}^{y_{max}} dy (e^y + e^{-y}). \qquad (1)$$

Here C comes from integration on the transverse distribution, including the information of the concrete dynamics and structure of the QGM, but similar for di erent kinds of energetic quark jets, once the QGM fixed. For the case that pionization is dominant, this calculation can also include the contribution from the limiting fragmentation part, by a slightly modified value of y_{min}, y_{max}, based on the mean value theorem of integration. For central A-A collision in the laboratory frame, neglecting the asymmetry of its thermal movements and assuming the (left-right) symmetry of its longitudinal expansion, in average the QGM can be taken as at rest. So the rapidity y of the created quanta can take values from $y_{min} \sim 0$ to $y_{max} \sim A \ln(E/M)$. Here E, M, are respectively energy and mass of the preliminary jet and $A(> 0)$ is a constant. A can depend on the dynamics, structure and size of the QGM. We then conclude, without concrete values of the constant C and A:

1) $< \Delta E > /E \simeq CE^{A-1}/M^A$. This power behaviour of the dependence on preliminary jet energy relies on the concrete width of the rapidity plateau, and can rise ($A > 1$) or fall ($0 < A < 1$), comparing to the LPM behaviour $\sim 1/E$.

2) The ratio between energy losses of two kinds of jets with same energy E but respective average mass M_1, M_2 is $r_{12}(E) =< \Delta E >_1 / < \Delta E_2 > \simeq (M_2/M_1)^A$. The details of the QGM

(density, temperature, size, etc.) cancels.

3) M_1, M_2 are average masses of the preliminary jets (dressed parton) rather than those of the partons initializing the jets. The initial quark mass can introduce modifications to the average jet mass, but the difference is dramatically reduced by dressing quark mass to be jet mass[a]. This is exactly what RHIC data[4] indicate. Furthermore, the mass of light quark jet can always be an infrared-safe hard scale for perturbative QCD, while the light quark mass can not.

A feasible and decisive test of the above physical picture is to observe the open c, b hadrons (or more practical, non-photonic leptons for the present experimental condition). To measure their nuclear modification factor R_{AA} in the modest rapidity interval (e.g., as for J/Ψ measured by PHENIX, $|y| = 1.2 \sim 2.2$) for central heavy ion collision at RHIC or LHC. Then comparing with the data around $y = 0$. From the above discussion, especially point 1), combining with the bremsstrahlung energy loss, at a linear approximation of the dependence of ΔE on E, we get the similar expression for energy loss as in QED: $\Delta E = \alpha + \beta E$. This means the larger of the jet energy, the more energy lost. So one can predict more suppressed transverse momentum spectrum hence smaller R_{AA} at modest rapidity, because for a definite p_T, one has larger total energy at modest rapidity. This is in fact implied by the J/Ψ spectrum (though now mostly taken as indication of regeneration)[11]. An even clear indication is observed in the central Cu-Cu collision, which also seems a puzzle at first sight. The transverse spectrum of heavy flavour muon at rapidity region $1.4 \sim 1.9$ (PHENIX) is more suppressed than those of the light quark at $y \sim 0$ (STAR)[12]. As is known (and from our physical picture in this paper), the heavy flavour lepton is almost the same suppressed as the light quark but hardly more. So apart from systematics between these two collaborations (and those between electron and muon), and ignoring the rare possibly exceptional strange behaviour that heavy flavour lepton is more suppressed than light hadrons in central Cu-Cu collisions, this implies that even light hadrons may demonstrate such a property. For observing and comparing the open heavy hadrons (or their offspring leptons) in various rapidity region, an even significant signal can be found.

Acknowldgement

This work is partially supported by NSFC with grant Nos. 10775090, 10935012 and Natural Science Foundation of Shandong Province, China (grant no. ZR2009AM001).

1. V.A. De Lorenci, R. Klippert and S.-Y. Li, to be submitted.
2. M. Gyulassy et al., The Proposal for JET Collaboration, http://jet.lbl.gov.
3. Yu. L. Dokshitzer and D. E. Kharzeev, Phys.Lett.B 519:199-206, 2001.
4. See, e.g., S. Mioduszewski, talk on Moriond QCD 2008.
5. S. Salur [STAR Collab.], arXiv:0809.1609 [nucl-ex], and this proceedings; Nathan Grau [PHNIX Collab.], this proceedings; J. Putschke [STAR Collab.], arXiv:0809.1419 [nucl-ex].
6. H. Cheng and T. T. Wu, Expanding protons: Scaterings at high energies , MIT, 1987.
7. H. Cheng and T. T. Wu, Phys. Rev. Lett. 23 (1969) 1311; Phys. Rev. D **3**, (1971) 2195.
8. W. R. Nelson, H. Hirayama and D. W. O. Rogers, SLAC-Report-265.
9. W. Lohmann, R. Kopp and R. Voss, CERN 85-03.
10. V. V. Sudakov, Soviet Physics JETP 3 (1956) 65.
11. S.-Y. Li, arXiv:0804.4776.
12. I. Garishvili [PHENIX Collab.], 0907.5479 [nucl-ex]; B. I. Abelev et al. [STAR Collab.], 0911.3130 [nucl-ex].

[a] By investigating the average jet mass in 2-jet events in e^+-e annihilation for various initial quarks and various center of mass energies, employing Durham algorithm in Pythia/Jetset, we find that the proportion of average masses for light, charm and bottom jets, $M_{jl} : M_{jc} : M_{jb}$, varies from 1 : 1 01 : 1 26 to 1 : 1 01 : 1 08, for jet energies from $6GeV$ to $20GeV$.

10.
Summary

Experimental Summary of Moriond QCD 2010

C. DIACONU
Centre de Physique des Particules de Marseille, 163 Avenue de Luminy, 13288 Marseille France
and
Deustches Elecktronen Synchrotron, Notkestr. 85, 22607, Hamburg, Germany

The experimental contributions to the 45$^{\text{th}}$ Rencontres de Moriond in La Thuile are summarised. Results from the energy frontier, including the first results from LHC, from the precision frontier and from the complexity frontier compose a dynamic picture of the experimental high energy physics. The vast amount of material presented for the first time at this conference displays significant progress in all areas.

1 Introduction

The Standard Model of particle physics is a wonderful dream and a nightmare in the same time. A dream because its predictability is successful over many orders of magnitude in energy and covers an impressive amount of experimental data, most of which exhibit below percent precision. A nightmare because its obvious problems and ad-hoc assumptions happily survived a complex experimental activity, including large installations at the energy, intensity and complexity frontiers. High hopes for further experimental and theoretical paradigms beyond the present *status quo* rely on the LHC, which just started operations. The constant improvements in the understanding of the strong force in soft and hard phenomena is also a huge task and all experimental programs continue to contribute to this effort.

A summary of recent experimental results is presented, grouped into three main experimental frontiers in high energy physics experiments: energy, intensity and complexity. A special place is given to the starting LHC experiments, which sooner or later will cross all of these frontiers.

2 The Dawn of the LHC Era

2.1 Machine operations

The first operation with beams at LHC took place in September 2008, but was unfortunately stopped due to a cooling incident after only a few days. After a successful repair and a (still ongoing) consolidation program, the beams were circulated again in November 2009. With machine safety as the underlying guidance, important milestones were achieved [1]: beam instrumentation checks, first collisions, first energy ramp and finally running with stable beams in collisions. Key ingredients of the machine design were established, such as aperture measurements, multi-bunch beams in collision (up to 16x16) and machine protection checks (injection, beam dump, collimators). The machine operated in luminosity production mode and experiments could take data in true experimental conditions. Collisions took place first at a centre-of-mass energy of 900 GeV

then at 2.36 TeV, thereby establishing a new record. This program, achieved in about three weeks only, open the way to next stage at higher energy and significant luminosity foreseen for 2010 and 2011. Indeed, according to the present plans, LHC will operate in the next two years at a centre-of-mass energy of 3.5 TeV (limited by safety requirements related to the maximal current in inter-magnet connections, for which some instabilities could not be excluded during 2009 shutdown). This energy was first achieved in March 2010. The next challenge is the increase in intensity together with a stability required for luminosity production. The collected data sample should reach 100 pb^{-1} in 2010 and approach 1 fb^{-1} by the end of the 2011 run.

2.2 Data taking and detector performance

All detectors collected data from the delivered collisions, corresponding typically to an integrated luminosity of about 30 $\mu\mathrm{b}^{-1}$ in each experiment. The performance demonstrated using this reduced amount of data is impressive and confirms the careful preparatives based on long cosmic runs during the LHC shutdown.

The detectors were thus able to run with full capabilities during the first collisions at LHC. For instance, the experimental techniques based on the calorimeter timing were used to reject the background from non-colliding bunch interactions [3] and the first physics events were measured and scrutinised with event displays.

The calorimeters show an impressive basic performance, already very close to the design [4,5,6]. In spite of the fact that data was collected relatively recently, refined algorithms are already installed and their performance is very good. The identification of electrons and photons has made the first steps with real data. The first events with jets have been measured and the performance of the hadronic final state reconstruction is now tested with real data. Energy flow algorithms are installed in CMS. The performance of hadronic reconstruction in data is matched by the simulation, thereby preparing on solid ground the future analyses relying on the measurement of missing transverse momentum.

In the tracking area, the same positive tests with real data are observed. The detectors are able to measure charged tracks with the design performance, as demonstrated by the first physics results, briefly described below. The charged tracks are reconstructed in CMS [7,8] using the energy loss measured using an analogue readout by the silicon detector. The material budget in ATLAS was measured with converted photons and agrees within the present statistics with the simulation. The particle identification has been commissioned for the first data sets using the energy loss measurements. The reconstruction of secondary vertices from K^0_s and Λ are instrumental to test the tracking performance and a good agreement with the simulation is observed, demonstrating the good understanding of the resolutions and efficiencies [9,10]. The higher mass baryons decays ($\Xi^- \to \Lambda\pi^-$) and di-photon resonances (π^0, η) provide an additional check of the detector capabilities. After years of tests with cosmic muons, the detectors have been able to measure muons originating from collisions and therefore to test the muon reconstruction with real $p\bar{p}$ data.

Specific sub-detectors have been also used with data and their performance tested with the first data. At LHCb, the RICH detector is able to drastically reduce the combinatorial background, which leads already to a clear peak of $\phi \to K^+K^-$ [11].

An original and inspiring analysis of the beam spot in LHCb provides a method to measure the luminosity [12]. The reconstruction of the effective collisions area is performed by using the excellent precision of the silicon tracker (VELO) of LHCb. Together with intensity information from the machine monitoring, the beam spot measurement allows a luminosity measurement with a precision of 15% and also contributes to the machine tuning during the commissioning.

It is interesting to note that computing also seems to be in good shape, since the data and simulations were processed timely and in line with the rapidly changing experimental conditions.

2.3 First analyses at the LHC

Despite the currently small amount of data LHC, the first physics analyses were presented. The measurement of particle multiplicities was performed by all experiments, with ALICE, ATLAS and CMS obtaining inclusive measurements of charged particles, and with measurements of strange particle production from LHCb. In all cases, even the first data samples are used, the analysis is anything but simple, requiring a very good understanding of the tracking, of the trigger and an overall control of the efficiencies.

The LHCb analysis used a data sample corresponding to an integrated luminosity of 6.8 μb to measure K_s^0 production [13]. Cross sections as a function of K_s^0 transverse momentum were presented in three bins of rapidity. The measurements are in good agreement with Monte Carlo predictions using various options (tunings) of the hadronic final state production.

The charged particle multiplicity was measured by ATLAS [14] using the data collected at $\sqrt{s} = 900$ GeV. The measurement is performed for particles with transverse momenta above 500 MeV in the central rapidity range $|\eta| < 2.5$. The particle multiplicity compares well with various models, but tends to exceed the predictions in the very central region and for transverse momenta around 1 GeV. Similar measurements were previously published by ALICE for $\sqrt{s} =$ 900 GeV, and new measurements at $\sqrt{s} = 2.36$ TeV were presented for the first time [15,16]. The full power of ALICE tracking is employed to remove secondaries and conversions. The particle densities are measured in the central region for various rapidity ranges as a function of the transverse momentum. The results show a reasonable agreement with various predictions based on different tunings and already a very good precision, where it is possible to distinguish between different models in this novel energy range. Similar measurements were performed by CMS [17] in a rapidity range $|\eta| < 2.4$. The measured particle spectra compare very well with ALICE result, when restricted to the same rapidity range ($|\eta| < 0.8$).

These measurements, performed in a record time after the data collection, demonstrate not only that the LHC detectors are already able to execute complex physics analyses, but also that a new energy domain is now reached: the LHC era has truly begun.

The prospects are therefore very encouraging, and the start of the LHC physics will be sound if the projected luminosity or a good fraction of it is indeed collected [2]. The analyses will re-discover the main Standard Model signals (W, top) and will significantly extend the frontiers for new physics searches. The prospects of a few hundreds of $pb^{-}1$ by end 2011 together with an expected increase in energy will enable most of the physics areas. Large data sets to come soon will pose a new challenge to all experiments but the first results show an excellent perspective.

3 The Energy Frontier

3.1 Higgs searches

One of the most hunted particles is the scalar particle (Higgs boson) responsible for the symmetry breaking mechanism within the Standard Model. The best chance is at present at Fermilab, where the scale of the electroweak symmetry breaking is approached in $p\bar{p}$ collisions at a centre-of-mass energy of 1.96 GeV.

Combined Higgs searches at the Tevatron proceed with full speed [18,19,20]. Many channels are combined to add to the sensitivity, including signatures for which the signal over background ratio is as low as 1/100. The first combined paper reports and exclusion domain from 162 to 169 GeV for the Higgs boson mass. The excluded domain is smaller compared to the previous preliminary result from March 2009, although the expected limit has improved significantly, mainly due to the refinements of the analysis. In the high mass domain, the data display a slight excess over the theory, with a limit on the ratio of the observed cross section limit to the Standard Model of 2.7, compared to 1.8 expected at 95% CL. The prospects for Higgs

sensitivity show that a probability better than 30% for a 3σ observation can be reached for all masses below ~ 180 GeV. The improvements in the analysis may in fact exceed the simple luminosity scaling, as has been demonstrated in the past. This *accelerated sensitivity* originates from improvements in the systematics. The large data samples collected in the last 18 months at the Tevatron and the continued large rate of data collection in the next months may lead to significant improvements in analysis techniques and accelerate further the sensitivity pattern. The present situation therefore leaves room for exciting times ahead.

The Higgs mass may also be constrained from the precision measurement [21]. When the direct limits are taken into account, the preference for a low Higgs boson mass persists, as expected. The expected mass range at 2 σ is 114 to 157 GeV. The influence of new physics via loops for precision observables is also studied. The high precision still leaves room for extension of the Standard Model, like for instance the fourth generation leptons and quarks, for which the mass differences allowed regions are determined. Exploring new models within a fit to precision electroweak measurements also provides a useful tool to cross check possible discoveries at LHC and has the potential to include constraints from new physics.

The scalar sector can be further investigated when the hypotheses related to the Standard Model minimal framework are relaxed and theories beyond the Standard Model provide a more complex symmetry breaking mechanism [22,23]. The searches for non-standard Higgs encompasses a large panel of signatures at the Tevatron. For instance, the associated production of a scalar Higgs within a SUSY non-minimal model is investigated. Possible decays to bb or $\tau\tau$ are searched for, using the well established algorithms for b-tagging or τ identification. The CDF and DØ data is combined to exclude Higgs masses up to 200 GeV for $\tan\beta$ below 30 to 50.

The LEP data seem to still have a potential to probe unexplored phase space for Higgs searches: a recent analysis using ALEPH data excludes Higgs masses in the non-MSSM in the region below 107 GeV in decays channels leading to events with four τ leptons and two other leptons or missing energy. This configuration had not been considered in the original searches during LEP experimental lifetime and it is useful to note that large experimental facilities need long term access to their data in order to ensure a coherent coverage of the all possibilities, beyond the current knowledge or fashion.

The meaurement of single top production described below is also used to search for decays to a charged Higgs $t \to H^+ b$ with subsequent decays $H^+ \to W^+ A$ and $A \to \tau^+\tau^-$ (assuming $m_A < 2m_b$), where τ leptons are tagged by isolated charged tracks [24]. The searches exclude charged Higgs boson with masses in the range from 90 to 160 GeV for branching ratios between $10 - 40\%$ for M_A from 9 to 4 GeV.

3.2 The weak bosons

Weak bosons are copiously produced in $p\bar{p}$ collisions at the Tevatron and measurements of the W boson properties (such as mass, width) are a key ingredient in the Standard Model tests. Furthermore, the electroweak sector and the nearby electroweak scale are probed via boson pair-production [25]. This signature reveals rare phenomena with Standard Model cross sections as low as a few pb and constitutes an ideal domain for new physics searches. The multi-boson production may proceed via triple boson couplings and provide thereby a direct probe of the gauge structure of the Standard Model. It is also a necessary analysis to benchmark the experimental capabilities for further searches like Higgs *poursuite*.

The measurement of top pair production at the Tevatron is a sensitive test of the Standard Model [26,27]. The inclusive top pair production cross section has been measured to be 7.70 ± 0.52 pb. The obtained precision of 6.5% challenges the theoretical prediction. Differential measurements have been performed, for instance as a function of the transverse momentum and compared with theoretical predictions at NNLO. The associated production $t\bar{t}$+jets have been

measured for the first time.

Using the selected top candidates in various channels, the top mass is measured most recently to be 173.1 ± 1.3 GeV including new measurements in the lepton-jets and di-lepton channels [28] and combining measurements from CDF and DØ. The mass difference between t and $\bar{t}$ is found to agree with zero, confirming the CPT theorem also for top quarks.

From a top quark discovery place, the Tevatron has become a top quark metrology laboratory. Many properties of the top quark are now measured with a precision approaching 10% opening new opportunities for further developments. The top width is limited to below 7.6 GeV at 95% CL [29]. The t and $\bar{t}$ spin correlations are found in agreement with the prediction and the charge measurements, based on jet charge reconstruction, exclude exotic hypothesis. The analysis of Ws produced in top decays also provides a handle on the properties of the top quark. The W helicity and the search for anomalous couplings in the angular analysis indicate a good agreement with the Standard Model prediction.

The measurement of the single top production offer an unique configuration to test the Standard Model [30,24]. The measurements of the single top cross sections by CDF and DØ were combined to obtain a new measurement: $2.76 + 0.58 - 0.47$ pb. The precision reaches 20% and invites further investigation using this topology. An amazing research program is in place: tests of the s- and t-channels, polarisation analysis of the single top decays, measurements of the top width as well as searches for decays to charged Higgs, as described above.

A clean signal for new physics at the Tevatron is provided by signatures involving several leptons. The inclusive production of two leptons is studied and provides limits on models for new physics with masses approaching 1 TeV [31]. SUSY searches encompass a large number of signature and profit from the large increase in luminosity at the Tevatron [32]. A unique but indirect access to new physics effects is obtained by searching for rare decays. Measurement of rare decays channels $B_{(s)} \to h\mu^+\mu^-$ have been presented and amount to about 10^{-6}. The angular analysis has the potential to detect non-standard contributions. The search for channels strongly suppressed within the Standard Model $B_{d,s} \to \ell^+\ell^-$ now yield a very good sensitivity [33]. Upper limits are obtained at 4.3 10^{-8} for $B_s^0 \to \mu^+\mu^-$ and 7.6 10^{-9} for $B_d^0 \to \mu^+\mu^-$, factors of 10 and 5 respectively above the Standard Model predictions. These measurements have a strong potential to constrain models beyond the Standard Model and are complementary to direct searches and to other similar constraints from b-factories.

The production of single W boson in ep collisions has been measured at HERA [34]. Although the sample is relatively small (only about 100 events are analysed), the W production mechanism in ep collisions is tested for the first time. Furthermore, a previous fluctuation observed by H1 for events with large hadronic transverse momentum is not confirmed in the combined H1 and ZEUS data set. The production of two or three charged leptons in ep collisions at HERA is explained within the Standard Model from photon photon collisions. This *matter-out-of-light* mechanism is investigated for events with large transverse momenta, again using the combined data set of H1 and ZEUS. A good agreement is found in general with the theoretical prediction and the cross section is measured for photon-photon collisions. In the e^+p data set, a small excess of events is found at large transverse momenta $\sum P_T^\ell > 100$GeV by both experiments: 7 events are measured for an Standard Model expectation of 1.9 ± 0.2.

4 The Precision Frontier

4.1 Proton structure and diffraction

The proton structure is an essential ingredient for the physics at LHC but also a fundamental scientific issue. The proton is mainly probed in deep-inelastic scattering at HERA electron- or positron-proton collider and its structure is indirectly investigated using precisely known

processes in hadronic collisions. The huge kinematic coverage at HERA offers a stand-alone picture of the protons, providing the best constrains at low Bjorken x, where the charged partons are predominantly issued from gluon fluctuations. The measurements perfomed by the H1 and ZEUS experiments have been recently combined using a coherent treatment of the systematic errors [35]. The combination yields an improved precision and constrain the parton distribution functions in a region that is crucial for electroweak measurements at LHC. The HERAPDF parameterisation of the structure functions is based only on a coherent data set from HERA and constitutes a useful and necessary exercise, within a clear theoretical framework and taking into account possible parameterisation errors.

The global approach in turn exploits different processes and leads to further constraints, in particular in the separation of quark flavours, also taking on board further tensions between the data sets and unknown theoretical uncertainties from various processes, only available at a fixed order in perturbative QCD calculations.

Measurements of jet production in $p\bar{p}$ collisions at the Tevatron probe the large x region and the precision obtained in recent measurements has the potential to lead to further constraints on PDFs [36].

Further recent developments in the global fits have improved the understanding of the PDFs, in particular in what concerns the uncertainties associated with the proton structure. The NNPDF approach proposes a flexible parameterisation based on neural networks and an estimation of the experimental errors by a Monte Carlo method [37]. This method attempts a realistic estimation of the experimental errors, reducing the influence of the parameterisation choice.

The way forward is two-fold: firstly more precise data will be available, in particular from HERA at high Q^2 and high x, leading to better constraints. Secondly, further improvements in theory (NNLO, low x re-summation, etc.) will necessarily lead to a better theoretical framework. These improvements may lead to further understanding of the mechanisms at work in the proton structure, beyond the otherwise extremely useful determination of PDFs. In longer term, precise measurements of weak bosons production at the LHC can also provide an useful input.

A remarkable role in the understanding of the proton structure is played by diffractive phenomena, in particular the ones involving hard scales, where perturbative QCD may be applicable. Hard diffractive interactions lead to events with activity in the central detector together with intact protons escaping along the beam pipe. At HERA, the diffractive DIS is measured using various techniques, tagging either the rapidity gap associate with the color-less exchange, or measuring the escaping protons in dedicated detectors (roman pots) installed very close to the beam line far from the central detector. The cross sections can be used to extract *diffractive* parton distributions (DPDFs) , assuming that the diffractive colourless exchange factorises from the photon and proton vertices. Recent measurements were presented, using precise data from the HERA II run [38]. Under this hypothesis, the DPDFs can be used to predict diffractive cross sections at the Tevatron or LHC, nevertheless the factorisation hypothesis remains an issue and diffractive phenomena using more exclusive processes (production of jets, vector mesons etc.) provide further information and also open new connections between QCD and low energy phenomenology. A remarkable recent result is the measurement of exclusive di-jet production at the Tevatron [39], which may constitute a testing ground for possible measurement of scalar (Higgs) particle production in diffraction at LHC.

4.2 QCD-related measurements with jets and weak bosons

The strong force manifests itself in a very clear way in particle collisions in the production of hadronic jets from high energy particle collisions. This process incorporate all aspects of the coloured partons interactions, from parton-parton interactions at short distances to long distance effects (hadronisation). The factorisation theorem predicts a decoupling of the partonic

collisions, calculable in the perturbative approximation, from the hadronisation effects. The production of jets is copious in hadronic collisions and is now measured with precision at the Tevatron and HERA, providing stringent tests of QCD.

Measurements of inclusive jet production at the Tevatron allow a test of QCD at very large scales and to constrain the PDFs in a unique region, not accessible at the LHC. In addition, the measurement of events with two or three jets allow to tune the Monte Carlo models in simulation and to scrutinise the highest end of the mass spectra, where signals from new physics may appear [36].

The production of jets is also a tool to access the strong coupling. The measurements at HERA [41] display a very competitive experimental precision of below 1% but are affected by large theoretical uncertainties induced by the limited precision of the cross section calculations, which are only available at NLO. The reduction of these uncertainties will be obtained by further calculations in superior perturbation orders, as well as from further measurements envisaged at HERA using the HERA II data set.

Jet production at the Tevatron is also sensitive to the strong coupling and can be used, in the regions of phase space where the PDFs are well known, to extract the strong coupling at energy scales exceeding 100 GeV, a region never accessed before within the scope of studies of the strong coupling [40]. The measurements are the most precise for hadron-hadron collisions and are in agreement with the DIS results and the world average.

QCD can also be tested in events where a weak boson is measured [42]. The weak boson plays in this case the role of an independent and clean "outgoing" probe, while the bulk of strong-force-related activity recoils against it. The transverse momentum spectra of W bosons is measured with high precision using Tevatron run II data and is compared with theoretical predictions based on perturbative QCD at NLO, MC simulations or leading order multi-leg calculations. The acoplanarity in the events gives access to higher order effects. For instance, the measurement presented by the DØ experiment using a data set with a luminosity of 1 fb^{-1} displays at large acoplanarity a precision that challenges the theoretical calculations and calls for their improvement.

Due to parity violation in weak decays, the production of W bosons in polarised proton-proton collisions at RHIC can offer a handle on the contributions of the quarks spins to the proton. Indeed, the spin asymmetry of the cross sections for W^+ and W^- are sensitive to combinations of spin-dependent parton distributions. The measurements that have only just begun at RHIC with $\sqrt{s} = 500$ GeV, show a good potential to detect W bosons [43] and will be improved by accumulating more statistics. In addition, the run of RHIC at a lower centre-of-mass energy will allow the measurement of W bosons produced from partons in the intermediate range for Bjorken x and lead to unique constraints on the polarised sea quarks.

4.3 Probing strong interactions at low energy

The measurement of the hadronic cross section in $e + e-$ collisions at low energies is a powerful means to test the strong interaction. The measurement of the cross sections for $e^+e^- \to \pi^+\pi^-$ as a function of energy is achieved using the radiative processes, for which a photon, mainly produced by radiation off the incoming leptons is present and measured in the detector. The recent measurements by BaBar [44] present a significant reduction of the statistical errors. A further improvement in precision is obtained by measuring the ratio of hadrons to muons, for which a few significant systematics cancel. The measurement is an essential ingredient for the prediction of the anomalous magnetic moment of the muon $(g-2)_\mu$. The discrepancy between the theoretical prediction and the measurement of the $(g-2)_\mu$ remains at 3 σ level, and associated discussion of this discrepancy remains exciting.

The hadronic cross section is also measured by KLOE experiment [45], collecting data in e^+e^-

collisions at the Φ peak but also at lower energies, down to 1 GeV. The technique of radiative events tag $e^+e^- \to \pi^+\pi^-\gamma$ is also employed. In a new analysis, the photons at large angles are measured, giving access to lower di-pion masses, close to the threshold. The analysed data sample correspond to collision energies below the ϕ peak and is therefore less affected by the less known decays to f_0 resonances. The measurement can be converted into a pion form factor measurement $F_{\pi\pi}$. The result is in agreement with the previous measurements by KLOE and, when translated into the di-pion contribution to the hadronic component of the muon anomalous moment $(g-2)_{had}$, consolidate the above-mentioned discrepancy between measurement and theory for $(g-2)_\mu$.

Strong interactions at low energies are also probed with high precision in photon-photon collisions, obtained at e^+e^- colliders via radiative processes. The tagged or untagged techniques are used the exclusive production of mesons [44,45]. The production of pairs of mesons ($\gamma\gamma \to \pi^0\pi^0, \pi^+\pi^-, \pi^0\eta$) is driven by non-perturbative form factors and can be used to study the di-meson states via a partial-wave analysis. The exclusive production of mesons ($\gamma\gamma \to \pi^0, \eta, \eta_c$) is measured with high precision at b-factories. The measurements compare well with phenomenological models based on parameterisations of the form factors.

4.4 Precision measurements in the heavy quarks sector

Hadrons containing heavy quarks have been long recognised as precious laboratories for the understanding of the strong force. The large scale offered by the heavy quark mass is a level arm for the theoretical calculations, but also provides a valuable experimental handle on detailed measurements of the heavy hadrons production and decays. Massive production of heavy hadrons in charm and beauty factories provide a rich panel of measurements.

The basic properties of the ground states containing heavy quarks are known with high precision. New measurements of the lifetimes have been obtained recently at the Tevatron [46] using a data sample of 4.3 fb^{-1}. The study of heavy hadron decays are informative of their internal dynamics. For instance, the measurement at the Tevatron by CDF of the decay $\Lambda_b^0 \to \Lambda_c^+\pi^-\pi^+\ell^-\nu$ reveals a resonant structure of the final state hadronic structure. This observation is investigated using the decays $\Lambda_b^0 \to \Lambda_c^+\pi^-\pi^+\pi^-$, for which the $\ell\nu$ pair is replaced by a ud pair (a π) and similar features are observed. As another example of the refinement achieved in this area, a measurement of the polarisation structure in non-charm decays $B \to \phi\phi$ has been presented.

The measurements of decay branching fractions of hadrons containing charm quarks are constantly refined [47]. The branching ratios of D^0, D^+ and D_s mesons are measured in the channel with pseudoscalars $D \to PP$ in the Cabibbo-favored, single suppressed and double suppressed configurations. The full data sample of 818 pb^{-1} collected by CLEO-c experiment is used. The measurements are compared with the predictions based on $SU(3)$ symmetry connected with a subset of discrete symmetries. A very good agreement is found, consolidating the basic knowledge of the fundamental role of the symmetries for systems containing a charm quark.

Pure leptonic decays are an unique opportunity to study the built-in mechanism for heavy mesons dynamics, but also to probe the CKM matrix elements. New measurements [48,49] of the decays to tau lepton $D_s^+ \to \tau^+\nu_\tau$ allow the measurement of the decay constant f_{D_s} to a 10% precision, similar to previous measurements of the similar constant f_{D^+} measured in $D_s^+ \to \mu^+\nu_\mu$ decays. The measurements are compared with lattice-based calculations which are now available with similar precision, and allow a test of their basic assumptions.

The large statistics accumulated by Belle and BaBar allow the investigation of new decays channels, and subsequently new domains of the phase space. The measurement of the decay $B_s \to D^{(*)} + D^{(*)-}$ has been reported [50]. The semi-inclusive decays $B \to X_s\eta$, sensitive to hadronic penguins, have been measured by Belle [51] with a significance of around 17 σ for mass

of the strange system X_s exceeding 1 GeV. A contribution at X_s masses above 1 GeV remains so far unexplained.

A crucial measurement in the flavour physics remain refers to the measurement of the CKM matrix elements. The exclusive semi-leptonic decays of B-mesons provide a clean determination of the CKM matrix elements, assuming the non-perturbative form factors can also be determined for zero momentum transfer. Precise BaBar data on $B \to \pi\ell\nu$ and $B \to \rho\ell\nu$ corroborated with a similar measurement at the Tevatron are used in a fit where the shape of the form-factor is also constrained, besides its value at $q = 0$ and V_{ub}. The use of theoretical prejudices for the form factor shape improves the precision on the V_{ub} determination to below 10%, a remarkable result, taking into account the small size of the branching ratios (below 2×10^{-4}) and the difficulty of the kinematic reconstruction.

The spectroscopy of heavy baryons continues to offer a stringent test of QCD. Precise predictions of mass splitting and magnetic moments are obtained using QCD inspired models for systems containing more than one heavy quark. Recent measurements of beauty-strange baryons Ξ_b and Ω_b by the CDF and DØ collaborations were presented. For Ξ_b the experimental results are in agreement with each other and match also the theoretical prediction [52], based on phenomenological approaches, still to be substantiated within QCD. The situation is less clear for Ω_b baryons (ssb) where CDF and DØ obtain significantly different mass measurements, where the CDF result $m_{\Omega_b} = 6054.4 \pm 6.9$ MeV is in agreement with the prediction of 6052.1 ± 5.6 MeV and significantly lower than the DØ measurement.

The excellent start up of the BES III experiment allows new studies of the charmonium states χ_{cJ} and η_c. Such states cannot be produced directly in e^+e^- collisions, but can be studied [53] due to the large statistics sample accumulated at BES III (for instance 110 million $\psi(2s)$ were recorded). The states are produced in the decays $\psi' \to \pi^0 h_c$ followed by $h_c \to \gamma\eta_c$. The mass of the h_c is determined to be in agreement with previous measurements at CLEO and the width has been determined for the first time. Using an inclusive method based on the π^0 recoil mass together with the method using the identification of radiative photon, the branching fractions of the two decays mentioned above are determined for the first time. The radiative decays of charmonium to pairs of π^0s or ηs are an interesting channel for glueball searches. The χ_{cJ} states produced in radiative ψ' decays provide a testing ground to test the color-octet mechanism in P-wave charmonium decays. New measurements improve the precision of the previous measurements by CLEO. The decay channels into ω and ϕ mesons are also studied, as well as the doubly suppressed OZI decays. The decays of the χ_{c1} are observed for the first time in the $\phi\phi$ and $\omega\phi$ modes. The BES III data taking started recently and will certainly provide a rich and interesting physics program in the years to come.

The b-systems produced at factories but also in hadronic decays provide a basis for the study of new states containing $c\bar{c}$ pairs. Indeed, while charmonium excited states have been discovered, several other resonances labelled X, Y, Z discovered in channel with a J/Ψ are assumed to contain also a $c\bar{c}$ pair, but their properties do not fit in the general scheme for charmonium excitations. The experimental data on these charmonium-like states is rich and often corroborated among different experiments, but the phenomenology is nevertheless unclear so far. The measurements using the $\gamma\gamma$ production mechanism provide another handle to pin down the quantum numbers. However, no model is able to describe completely the properties of these states [54].

The phases of the CKM matrix are an ideal place to check for direct signals from the non-standard physics. Of particular importance are the measurement related to the B_s mesons, since some of the associated phases are predicted to be small leading to an unique sensitivity for new physics. The measurements of the $B_s \to J/\psi\ \phi$ decays give access to the phase β_s, predicted to be close to zero within the Standard Model. The recent updates of the measurements by CDF and DØ were combined and a deviation at 2σ level was reported. While this is not yet truly

exciting news, the accuracy of the analysis and the perspectives to include a factor of 4 more data make the subject one of the most interesting to be followed in the end of the data taking at the Tevatron.

5 The Complexity Frontier

The hadronic collisions at high energy, for instance those at the Tevatron, contain besides high energy processes a plethora of associated phenomena related with soft interactions. These phenomena may also be associated with a complexity step beyond the hard scattering ansatz and are an important study case for QCD. In addition, they may become important for the understanding of the final state topologies at LHC. Minimum bias measurements are performed using events selected with uniform acceptance for all possible interactions. Recent measurements include production of Λ, Ω and Σ baryons and reveal the behaviour of particle production in the non-perturbative domain [39]. The underlying event originates from secondary interactions and can be determined by measuring the level of the energy flow between the main jets produced in the hard interactions. Since the theory behind these phenomena is poorly understood, precise measurements are crucial for reliable tuning of the Monte Carlo simulations.

The specific behaviour of the strong force related to the asymptotic freedom and confinement can be studied in collective phenomena, expected to occur in heavy ion collisions. The experimental program developed at the RHIC collider has already produced fundamental results related to a possible phase transition and to its characterisation in various conditions and using different experimental techniques and observables. The ability to run with various nuclei (including protons), the variation of energy and the polarised program (already mentioned in the above) make RHIC a unique facility, in full speed to obtain fundamental results preceding and inspiring the heavy ions program at the LHC.

The hadronic matter at high densities can be probed with pair of leptons [56]. The advantage is the lack of re-interaction of the produced leptons, thereby accessing the original production mechanism. The di-lepton mass spectrum reflects indeed a rich phenomenology. The production of heavy quarks can be identified in the domain of large di-lepton masses. The low mass region is in turn dominated by the production of virtual photons, followed by internal conversions $\gamma^* \rightarrow \ell\ell$. A template fit of the mass spectra allows the measurement of these contributions and the comparison with the theoretical prediction. In particular, the virtual photon production at low masses can be used to study the ratio of direct to inclusive photon production. The ratio measured in *pp* is found to agree with the adjusted "cocktail" of predictions, but exceeds it significantly for *Au-Au* collisions. The di-lepton mass spectra exhibits an excess in the intermediate mass region by around a factor of five, concentrated at low transverse momentum. An enhancement of this type is predicted by some phenomenological models.

The complexity of the final state is also explored by the correlations among the final state particles [57]. The measurement of particle particle correlations allowed to sign the dumping of particles energy in the hot and dense hadronic matter produced in ion-ion collisions. For instance, a large suppression factor (5-10) is observed for the production of π^0's when heavy-ion collisions are compared to *pp* collisions. A different approach is the use of hadronic jets. Indeed, the journey through dense hadronic matter is expected to have a visible impact on the usual hadronisation process of rapid partons, modifying the jet rate and their shape. The measurement of jets in *pp* collisions by STAR experiment show a good agreement with previous measurements, validating the jet technology at RHIC. However, the reliability of jet reconstruction in presence of dense hadronic matter has to be carefully studied before strong conclusions are drawn [58]. Significant progress in experimental studies, including the trigger definition, jet calibrations, final state topologies and so on may lead soon to new measurements using the jet-based techniques.

The collisions of deuterons and heavy ions can be used to study the nuclear structure, since

a "simple" object (the deuteron) could probe the "complex" heavy ion. When the collision probes partons with low momentum fraction x, the main contribution comes from gluons, which is known to increase with decreasing x. This increase, explained by gluon proliferation, is expected to be taken dumped at lower x due to recombinations, leading to what is usually called "saturation". The measurement of particles in the "forward" direction defined by the deuteron beam direction, access the low x domain of the colliding nucleus. The measurement of these particles was enabled recently at the STAR experiment in a new rapidity domain using the Forward Meson Spectrometer. The azimuthal correlations among two π^0's measured with this device show the expected phenomenology of two peaks ('near-side' and 'back-to-back') for *pp* collisions. In *Au-Au* collisions the "near-side" peak is present with comparable size, but the "back-to-back" peak is drastically suppressed. This behaviour is predicted by models of saturations based on Color Glass Condensate, where the perturbative QCD is complemented by coherent scattering of a partons against multiple partons, leading to a suppression of particles above a given threshold in the hemisphere opposite to the leading parton. This suppression is strongest at low transverse momentum, also as expected in the CGC model.

6 Outlook

High energy physics enters every year new domains enlarging the knowledge beyond the energy frontier, the precision frontier and the complexity frontier. From the experimental point of view, a rich panel of installations offer a solid complementarity. A plethora of results allows in many cases combinations, which offer a coherent input for further research areas. This year, the start of the operations at the LHC offers new hope for large excursions into the unknown, with discoveries that may clarify the main issues and weaknesses of the Standard Model, in particular for the long standing issue of the origin of symmetry breaking. The LHC, together with the other experimental programs, at their maturity or in preparation, will make the history of the next decade, and from the top of the La Thuile mountains, this Moriond QCD has been an wonderful opportunity to contemplate the promising landscape of high energy physics into the next decade.

Acknowledgments

I would like to thank our colleagues from Moriond QCD committees for the exquisite scientific program and the professional local organisation. It was a honour for me to have the chance to review such a wealth of new results and I am grateful to all speakers for explaining their cutting-edge research in talks of an excellent quality. I thank David South for the careful reading of the manuscript.

References

1. R. Bailey, these proceedings.
2. I. Vichou, these proceedings.
3. M. Baak, these proceedings.
4. E. Monnier, these proceedings.
5. S. Rappocio, these proceedings.
6. C. Rovelli, these proceedings.
7. D. Giordano, these proceedings.
8. G. Masetti, these proceedings.
9. A. Salzburger, these proceedings.
10. F. Noferini, these proceedings.

11. C. Deplano, these proceedings.
12. V. Balagura, these proceedings.
13. M. Knecht, these proceedings.
14. W.H. Bell, these proceedings.
15. J. Fiete Grosse-Oetringhaust, these proceedings.
16. J. Otwinowski, these proceedings.
17. C. Roland, these proceedings.
18. W.Yao, these proceedings.
19. R. Bernhard, these proceedings.
20. S.Z. Shalhout, these proceedings.
21. J. Haller, these proceedings.
22. S.Greder, these proceedings.
23. S.Beacham, these proceedings.
24. N. Goldschmidt, these proceedings.
25. V. Rusu, these proceedings.
26. M. Begel, these proceedings.
27. S. Parke, these proceedings.
28. H. Lee, these proceedings.
29. V. Sorin, these proceedings.
30. A. Garcia-Bellido , these proceedings.
31. L. Zivković, these proceedings.
32. G. de Lorenzo, these proceedings.
33. G. Simi, these proceedings.
34. S. Levonian, these proceedings.
35. K. Oliver, these proceedings.
36. D. Price, these proceedings.
37. M. Ubiali, these proceedings.
38. V. Sola, these proceedings.
39. M. Rangel, these proceedings.
40. B. Hiroski, these proceedings.
41. G. Grindhammer, these proceedings.
42. S. Grinstein, these proceedings.
43. J. Stevens, these proceedings.
44. F. Anulli, these proceedings.
45. S. Giovanella, these proceedings.
46. M. Dorigo, these proceedings.
47. M. Artuso, these proceedings.
48. S. Stone, these proceedings.
49. J. Dingfelder, these proceedings.
50. T. Aziz, these proceedings.
51. J.M.C. Chang, these proceedings.
52. M. Karliner, these proceedings.
53. Z. Wang, these proceedings.
54. P.N. Pakhlov, these proceedings.
55. L. Oakes, these proceedings.
56. T. Dahms, these proceedings.
57. N. Grau, these proceedings.
58. S. Salur, these proceedings.

Liste of Participants

XLVth Rencontres de Moriond

QCD and High Energy Interactions

List of Participants

Family name	First name	Home institution address	Country	Email address
Abgrall	Nicolas	DPNC	Switzerland	nicolas.abgrall@cern.ch
Abreu	Henso	LAL	France	abreu@lal.in2p3.fr
Antoniadis	Ignatios	CERN	Switzerland	ignatios.antoniadis@cern.ch
Anulli	Fabio	INFN	Italy	fabio.anulli@roma1.infn.it
Arleo	François	LAPTH	France	arleo@cern.ch
Artuso	Marina	Syracuse University	USA	artuso@physics.syr.edu
Autiero	Dario	IPNL	France	autiero@cern.ch
Baak	Max	CERN	Switzerland	mbaak@cern.ch
Bailey	Roger	CERN	Switzerland	roger.bailey@cern.ch
Balagura	Vladislav	CERN	Switzerland	balagura@cern.ch
Beacham	James	New York University	USA	jbb334@nyu.edu
Beelen	Alexandre	IAS	France	alexandre.beelen@ias.u-psud.fr
Bell	William	University of Geneva	Switzerland	W.Bell@cern.ch
Blanchard	Alain	OMP	France	alain.blanchard@ast.obs-mip.fr
Blok	Boris	Technion	Israel	blok@physics.technion.ac.il
Bondar	Alexander	Budker Institute of Nuclear Physics	Russia	bondar@inp.nsk.su
Brau	Benjamin	University of Massachusetts	USA	bbrau@physics.umass.edu
Cabrera Catalan	Maria Eugenia	UAM / CSIC	Spain	maria.cabrera@uam.es
Chardin	Gabriel	CSNSM	France	gabriel.chardin@csnsm.in2p3.fr
Cid Vidal	Xabier	University of Santiago de Compostela	Spain	xabier.cid.vidal@cern.ch
Copeland	Ed	University of Nottingham	UK	ed.copeland@nottingham.ac.uk
Costa	Miguel	Universidade do Porto	Portugal	miguelc@fc.up.pt
Cranmer	Kyle	New York University	USA	cranmer@cern.ch
Dafni	Theopisti	LFNA	Spain	Theopisti.Dafni@cern.ch
Dasgupta	Basudeb	Max Planck Institute	Germany	basu@mppmu.mpg.de
Democles	Jessica	CEA Saclay - SPP	France	jessica.democles@cea.fr
Deplano	Caterina	INFN Cagliari	Italy	caterina.deplano@cern.ch
Diaconu	Cristinel	CPPM	France	diaconu@cppm.in2p3.fr
Dingfelder	Jochen	Physikalisches Institut Freiburg	Germany	jochend@physik.uni-freiburg.de
Dunlop	James	Institute for Astronomy Royal Observatory	UK	jsd@roe.ac.uk
Ehret	Klaus	DESY	Germany	klaus.ehret@desy.de
Finke	Justin	U.S. Naval Research Laboratory	USA	justin.finke@nrl.navy.mil
Fisher	Wade	Michigan State University	USA	wfisher@fnal.gov
Gavela	Belen	UAM	Spain	belen.gavela@uam.es
Giordano	Domenico	CERN	Switzerland	domenico.giordano@cern.ch
Giovannella	Simona	Laboratori Nazionali di Frascati	Italy	simona.giovannella@lnf.infn.it
Grau	Nathan	Columbia University Nevis Laboratories	USA	ncgrau@nevis.columbia.edu
Grindhammer	Guenter	Max Planck Institute	Germany	guenterg@desy.de
Guy	Julien	LPNHE	France	guy@lpnhe.in2p3.fr
Guyonnet	Augustin	LPNHE	France	guyonnet@lpnhe.in2p3.fr
Haller	Johannes	DESY	Germany	haller@mail.desy.de
Hernandez-Monteagudo	Carlos	Max Planck Institute for Astrophysics	Germany	chm@mpa-garching.mpg.de
Hill	Richard	Enrico Fermi Institute	USA	richardhill@uchicago.edu
Hinshaw	Gary	NASA Goddard Space Flight Center	USA	Gary.F.Hinshaw@nasa.gov
Hopchev	Plamen	LAPP	France	hopchev@lapp.in2p3.fr
Hsu	Lauren	Fermilab	USA	llhsu@fnal.gov
Hulsbergen	Wouter	Nikhef	The Netherlands	wouter.hulsbergen@nikhef.nl
Iashvili	Ia	SUNY	USA	iashvili@buffalo.edu
Jones	Christopher	Massachusetts Institute of Technology	USA	c_jones@mit.edu
Jouan	Denis	IPNO	France	jouan@ipno.in2p3.fr
Kinoshita	Kay	University of Cincinnati	USA	kay.kinoshita@uc.edu
Knecht	Mathias	EPFL	Switzerland	mathias.knecht@epfl.ch
Kronborg	Taia	LPNHE	France	taia@lpnhe.in2p3.fr
Kusaka	Akito	University of Chicago	USA	akito@kicp.uchicago.edu

Lafebre	Sven	Pennsylvania State University	USA	s.lafebre@psu.edu
Lavignac	Stéphane	CEA Saclay - IPTh	France	Stephane.Lavignac@cea.fr
Levonian	Sergey	DESY	Germany	levonian@mail.desy.de
Lopez-Cruz	Omar	INAOE	Mexico	omarlx@inaoep.mx
Malaescu	Bogdan	LAL	France	malaescu@lal.in2p3.fr
Marcinek	Antoni	Jagiellonian University	Poland	antoni.marcinek@gmail.com
Marquet	Cyrille	CEA Saclay - IPTh	France	cyrille.marquet@cea.fr
Martini	Luca	INFN	Italy	Luca.Martini@cern.ch
Masetti	Gianni	University of Bologna	Italy	gianni.masetti@bo.infn.it
Matsuoka	Kodai	Kyoto University	Japan	matsuoka@scphys.kyoto-u.ac.jp
Monnier	Emmanuel	CPPM	France	monnier@cppm.in2p3.fr
Mottola	Emil	Los Alamos National Lab	USA	emil@lanl.gov
Murphy	Sébastien	University of Geneva	Switzerland	sebastien.murphy@cern.ch
Novikov	Dmitry	Imperial College	UK	d.novikov@imperial.ac.uk
Nuss	Eric	LPTA	France	eric.nuss@lpta.in2p3.fr
Orloff	Jean	LPC	France	orloff@in2p3.fr
Pain	Reynald	LPNHE	France	rpain@in2p3.fr
Perrozzi	Luca	INFN	Italy	luca.perrozzi@pd.infn.it
Polesello	Giacomo	INFN	Italy	giacomo.polesello@cern.ch
Quiros	Mariano	ICREA	Spain	quiros@ifae.es
Rappoccio	Salvatore	Johns Hopkins University	USA	rappoccio@gmail.com
Raval	Amita	DESY	Germany	amita.raval@cern.ch
Regnault	Nicolas	LPNHE	France	nicolas.regnault@lpnhe.in2p3.fr
Rescigno	Marco	INFN	Italy	marco.rescigno@roma1.infn.it
Rogan	Christopher	California Institute of Technology	USA	crogan@caltech.edu
Roland	Christof	MIT	USA	cer@mit.edu
Rossi	Graziano	KIAS	South Korea	graziano@kias.re.kr
Rovelli	Chiara	University of Rome “La Sapienza”	Italy	chiara.rovelli@roma1.infn.it
Rozanska	Maria	H. Niewodniczanski Inst.of Nuclear Physics	Poland	maria.rozanska@ifj.edu.pl
Rozo	Eduardo	University of Chicago	USA	erozo@kicp.uchicago.edu
Salzburger	Andreas	CERN	Switzerland	Andreas.Salzburger@cern.ch
Schucker	Thomas	CPT	France	thomas.schucker@gmail.com
Serfass	Bruno	University of California	USA	serfass@berkeley.edu
Shanks	Tom	Durham University	UK	tom.shanks@durham.ac.uk
Shushkevich	Stanislav	Max Planck Institute	Germany	shushkev@mppmu.mpg.de
Sola	Valentina	Univ. di Torino - INFN	Italy	vsola@to.infn.it
Stahl	Sascha	Physikalisches Institut	Germany	sstahl@physi.uni-heidelberg.de
Tartari	Andrea	Univ. degli Studi Milano-Bicocca	Italy	andrea.tartari@mib.infn.it
Taylor	Andrew	Institute of Astronomy Royal Observatory	UK	ant@roe.ac.uk
Trocino	Daniele	Univ. degli Studi di Torino	Italy	trocino@to.infn.it
Vainshtein	Arkady	University of Minnesota	USA	vainshte@umn.edu
Varouchas	Dimitris	LBNL	USA	Dimitris.Varouchas@cern.ch
Vichou	Irene	University of Illinois CERN	Switzerland	Irene.Vichou@cern.ch
Vieregg	Abigail	University of California	USA	agoodhue@physics.ucla.edu
Villa	Francesca	LPNHE	France	villa@lpnhe.in2p3.fr
Webber	David	Loomis Laboratory of Physics	USA	dwebber@illinois.edu
Wilkinson	Guy	University of Oxford	UK	guy.wilkinson@cern.ch
Yamada	Satoru	Kamioka Observatory	Japan	yamada@suketto.icrr.u-tokyo.ac.jp